UNIVERSITE PARIS XIII –SORBONNE PARIS NORD

École doctorale Sciences, Technologies, Santé Galilée

Développement d'hydrogel poreux 3D vascularisés à base de polysaccharides pour l'ingénierie tissulaire

Development of vascularized 3D porous polysaccharide-based hydrogel for tissue engineering

THÈSE DE DOCTORAT
présentée par

LE BAO Chau

Laboratory for Vascular Translational Science (LVTS) – INSERM U1148

Hôpital Bichat – Claude Bernard, Paris, France

Pour l'obtention du grade de
DOCTEUR EN SCIENCES DE LA VIE ET DE LA SANTÉ

Soutenue publiquement le 15 décembre 2022 devant le jury d'examen constitué de :

BLANCHEMAIN Nicolas, Université de Lille, Président du jury, Rapporteur
LEROUGE Sophie, École Polytechnique de Montréal, Reportrice
MULLER Laurent, Collège de France, Examinateur
FALENTIN-DAUDRÉ Céline, Université Sorbonne Paris Nord, Examinatrice
CHAUBET Frédéric, Université Sorbonne Paris Nord, Directeur de thèse
SIMON-YARZA Teresa, INSERM U1148, Co-encadrante de thèse

ACKNOWLEDGEMENTS

I am deeply grateful for the people whom have supported me throughout my doctoral thesis. Without you, this would not have been possible.

First, I would like to express my deepest gratitude to both my supervisors Frédéric Chaubet and Teresa Simon-Yarza. Thank you for giving me the opportunity to be a part of your prestigious and amazing team. Thank you for believing in me and for your support throughout these past three years. Thank you for evaluating my manuscript and for providing me with constructive criticism. Most importantly, I thank Teresa for your patience and your consistent source of advice. Your guidance has been extremely invaluable to my professional development and my personal growth. You have provided me the essential tools to begin a new chapter of my life.

I owe my heartfelt gratitude also to Graciela Pavon-Djavid and Cédric Chauvierre for your scientific advices, for your kind assistance during my visa and administrative procedures, and most of all, your genuine interests in me.

I would like to express my gratitude to all the members at the LVTS for their friendship and for all the moments shared at work, in-person and in distance, especially during the confinement periods in 2020 and 2021. Thanks to your constant support and kindness, I have been able to overcome my doubts and gain new perspectives in my professional work and my personal endeavors. Special thanks to Alessandra Dellaquila for all the fruitful discussions, for being a caring colleague and a generous friend. Huge thanks to Paola, Camille, and Rachida for training me and for their advices. I would like to also thank the other PhD students and teammates, Albane, Louise, Chloé, Rodolphe, Fernanda, and Alina for their mutual support and for sharing their experiences with me. I would like to extend my sincere gratitude to all the other members of the LVTS who were somehow involved in this work and the discussion. Without you all, this thesis would not be the same.

I would like to thank my collaborators from Newcastle University, Helen Waller, Daniel Peters, and Jeremy Lakey for your advice and continuing assistance with this work. Many thanks to my collaborators at the LuMIn laboratory (ENS Paris-Saclay), Bruno Le Pioufle, Sakina Bensalem, Alan Raj Jeffrey and Ana Mesic for your advices and expertise.

Many thanks to Samira Benadda at the IMA'CRI photonic imaging platform (CRI 1149) for her training and expertise.

I owe my deepest gratitude to my family, especially my mother, for her unconditional love and support, despite being very far away from me. Your resilience, your patience, your generosity, and your beautiful smile are among many things that have helped me become who I am today. You are my ultimate role model in life.

I am extremely grateful for my friends, my family of choice, for your love and your continuing support. Thank you for all the shared moments as friends and as brothers and sisters. Very special thanks to Raphaël, Lorena, Léo, Lukas, LuLu, Louise, and Antoine for your encouragement and your relentless belief in me. Thank you also for the laughters and for your love beyond limits. You have been my source of inspiration and strength throughout this journey. I am truly and deeply thankful to have you in my life.

Lastly, I owe my gratitude to the doctoral school Institut Galilée and the ANR funding that have financed this PhD work. My horizon has been broadened thanks to this life-changing experience.

RÉSUMÉ

Le réseau vasculaire est essentiel dans plusieurs fonctions biologiques, notamment le maintien de l'homéostasie, l'apport de nutriments, les échanges gazeux et l'élimination des déchets métaboliques [1]. Les limites de diffusion de l'oxygène et des nutriments étant d'environ 200 µm, les cellules situées en périphérie d'un capillaire sont plus susceptibles d'être exposés à un stress hypoxique et d'induire une apoptose [1]. La présence d'un réseau vasculaire fonctionnel est un atout clé dans le développement de modèles physiologiquement pertinents pour l'ingénierie tissulaire et la médecine régénérative. Pour les études *in vitro,* l'utilisation de modèles vascularisés donnerait un aperçu plus réaliste des événements physiopathologiques et de la réponse aux médicaments, contribuant ainsi au développement de modèles plus prédictifs et cliniquement précis [2,3]. L'objectif de ce projet de doctorat est de développer un hydrogel favorisant la formation de vaisseaux pour être utilisé comme modèle *in vitro* pour l'ingénierie tissulaire. Une méthode de fabrication permettant de contrôler la microarchitecture des hydrogels polysaccharides a été mise au point pour former des microcanaux de l'ordre des veinules et des artérioles en utilisant un modèle sacrificiel. Ensuite, une méthode a été développée pour fonctionnaliser les hydrogels à l'aide de protéines recombinantes avec des signaux pro-angiogéniques (YIGSR et VEGF). Différentes combinaisons spatiales de ces séquences bioactives ont permis la modulation de différents comportements des cellules endothéliales. Enfin, les matériaux pro-angiogéniques ont été adaptés pour une plateforme microfluidique afin de permettre le développement d'un organe sur puce imitant le phénomène de lésion hépatique induite par des médicaments.

Mots clés: Hydrogel, modèles *in vitro,* vascularisation, angiogenèse, micromoulage sacrificiel, fonctionnalisation avec contrôle spatial

ABSTRACT

The vasculature is a key element in several biological functions including homeostasis maintenance, nutrients supply, gas exchange, and metabolic waste removal [1]. Since the diffusion limits of oxygen and nutrients has been reported to be around 200 µm, cells located farther from a capillary will most likely undergo hypoxia and apoptosis [1]. Presence of a functional vascular network plays a pivotal role in achieving physiologically relevant bioengineered models for tissue engineering and regenerative medicines. For *in vitro* studies, the use of vascularized models would provide more realistic insights into human pathophysiological events and drug response, thus, contributing to the development of more predictive and clinically accurate *in vitro* models [2,3]. The aim of this doctoral project is to develop a hydrogel favoring vessel formation to be used as an *in vitro* model for tissue engineering applications. Fabrication method to control the microarchitecture of polysaccharide hydrogels were developed and sacrificial templating was employed to form microchannels in the range of venules and arterioles. Next, a spatial control coating method was developed to functionalize the hydrogels using recombinant proteins with pro-angiogenic signals (YIGSR and VEGF). Different spatial combinations of these bioactive sequences modulated different endothelial cell behavior. Finally, the developed pro-angiogenic materials were applied and adapted in a microfluidic platform to support the development of an organ-on-chip device mimicking drugs-induced-liver-injury phenomenon.

Keywords: Hydrogel, *in vitro* models, vascularization, angiogenesis, sacrificial templating, spatial-control coating

GENERAL CONTENTS

LIST OF FIGURES

Figure 4. Microfluidic - based vascularization strategies: soft lithography (top) and 3D patterning (bottom). **(a) Liver sinusoid on-chip fabricated by soft lithography**. LSECs and KCs were seeded on the apical side of a PE membrane while HSCs on its basolateral side and HCs on the PDMS substrate (top). Lateral view of the sinusoidal endothelium (bottom): LSECs (green) and KCs (red) on the top and HSCs (yellow) on the bottom of the membrane. Reproduced with permission.[73] Copyright 2017, The Royal Society of Chemistry. **(b) ECM-based vascularized BBB platform**. (A) HUVECs and fibroblasts were seeded in the vascular channel (VC) and neural cells (astrocytes and neurons) were seeded in the neural channel (NC). The formation of vascular network in the central vascular network channel (VNC) ensured a direct interface between the capillaries and the astrocytes through astrocytic endfeet (B, C- ECs stained in red, astrocytes stained in white). Adapted with permission.[66] Copyright 2017, Springer Nature. **(c) Skin-equivalent platform generated by templating**. (A, B) The culture device was 3D printed and filled with collagen and fibroblasts to form the dermis layer. After removal of the nylon wires, the hollow channel was seeded with HUVECs to form the capillary and keratinocytes were cultured on the top of the dermis and exposed to liquid-air interface for cornification of the epidermal layer. (C) Perfusion of the device via peristaltic pump. Reproduced with permission.[89] Copyright 2017, Elsevier Inc. **(d) Hybrid strategy: 3D printed vascularized proximal tubule model**. (A, B) The colocalized vascular and renal channels are both 3D printed by using a Pluronic F127-based fugitive ink within an ECM solution and different designs can be easily printed. (C, D) The construct is then seeded with epithelial (green) and endothelial (red) cells. Reproduced with permission.[102] Copyright 2019, PNAS. 42

Figure 5. General schematic illustrating strategies used to vascularize spheroids/organoids. **(a) Scaffold-free approach:** Co-culture with ECs/MSCs to form prevascularized network, **(b) Scaffold-based approach:** Co-culture with ECs/MSCs in porous biomaterials. Both (a) and (b) can be followed by spontaneous vascularization via in vivo transplantation in highly vascularized organ such as the brain**. (c) Co-culture of spheroids/organoids inside microfluidic chip to mimic in vivo conditions such as fluid flow.** Created with BioRender.com 49

Figure 6. Vascularization approaches for spheroids and organoids: **(a) Scaffold-free approach to vascularize spheroids**. RNVCMs, HCMECs, hNDFs were co-cultured at optimal cell ratios (70%:15%:15%) and plated into ultralow attachment 96 U-well plates to form cardiac tissue spheroids. Then, the spheroids were collected and plated in low-attachment dishes, allowing them to self-organize into cardiac patch grafts under static conditions. Finally, the cardiac patch grafts were transplanted on the anterior wall of the left ventricle of arhythmic rats to induce spontaneous vascularization. Reproduced with permission.[148] Copyright 2016, Elsevier Inc. **(b) Scaffold-based approach to vascularize spheroids**. PLGA activated by 1-ethyl-3-(3-dimethylaminopropyl) carbodiimide hydrochloride (EDC) and crosslinked with adipic dihydrazide, followed by lyophilization form porous hydrogel. Seeding of ASCs onto

hydrophilic surface induced cell aggregations, which resulted in ASC-spheroids. Then, the spheroids were transplanted in the dorsum of nude mice to induce spontaneous vascularization. Reproduced with permission.[147] Copyright 2017, Elsevier Inc. **(c) Scaffold-free approach to vascularize organoids.** a. Schematic representation of the paper's strategy: hiPSCs, hMSCs, HUVECs co-cultured on Matrigel® to form liver organoids, which were transplanted into mice to induce spontaneous vascularization. b. Observation of cells in co-culture overtime. Organoids formed within 72h. c. Observation of hiPSC-organoids (top panel) and conventional two-dimensional cultures (bottom panel). Scale bar = 1mm. d) Confocal images showing presence of hiPSC-derived hepatic endoderm cells (green) and HUVECs (red) inside liver organoids (left panel) –or- HUVECs (green) and hMSCs (red) inside hiPSC-derived organoids. Scale bar = 100µm. Adapted with permission.[117] Copyright 2013, Springer Nature. **(d) Hybrid strategy**. A. Kidney organoids were cultured in ECM substrate housed inside a perfusable millifluidic chip, subjected to controlled fluidic shear stress. B-E. Confocal 3D observations showing vascular markers in whole-mount organoids, cultured under static U-well, static, low-FSS, and high-FSS conditions. Scale bars = 100 µm. Adapted with permission.[137] Copyright 2019, Springer Nature. 54

Figure 7. Schematic of bioprinting methods. (**a**) Inkjet-based bioprinting involves the formation of droplets of bioink by generating bubbles in the tip of the printer through thermal, piezoelectric or acoustic energy. (**b**) Laser-assisted bioprinting is also based on the generation of droplets of bioink by the incidence of a laser beam on an energy absorbing layer coupled with a donor slide constituted of bioink. The droplets are then recovered on a dedicated platform. (**c**) Extrusion is the most commonly used method; the ink is pressed through the nozzle either with a piston, a screw or using pneumatic pressure. **(d)** Vat photopolymerization requires the presence of a photo-initiator to cure the polymer loaded with cells. Created with Biorender.com 61

Figure 8. Bioprinting – based vascularization strategies: sacrificial casting (top) and coaxial deposition (bottom). **(a) Bioprinting of thick vascularized tissues with sacrificial poloxamer**. (A) Manufacturing process in 4 steps: i) printing of the sacrificial poloxamer-thrombin biomaterial bioink and of cell-laden gelating bioink with endothelial cells; ii) casting of the gelatin/fibrinogen/transglutaminase that interacts with the thrombin diffused from the printed biomaterial causing gelification; iii) removal of the poloxamer by cooling down leading to empty channels; iv) perfusion of the channels with cell media that results in endothelialization of the channels. (B, C, D) Three cell types were incorporated, HUVECs (B), hNDFs (C) and hMSCs (D). (Scale bar: 50 µm.). (E) cell viability and mechanical properties of the construct are affected by gelatin pre-processing temperature. (F, G) hMSCs-laden bioink immediately after printing (F) and after 3 days (G). (H - K) Images of the bioconstruct. (H) Sacrificial bioink colored in red and cell-laden bioink in green. (Scale bar: 2mm). (I) Bright field image from top. (Scale bar: 50 µm.) (J) Construct in a perfusion chamber and (K, L) cross-sections. (Scale bar: 5 mm). Reproduced with permission.[94] Copyright 2016,

LIST OF TABLES

ABBREVIATIONS

ABS: acrylonitrile butadiene styrene

ALI: air-liquid interface

BBB: blood-brain barrier

BMP-2: bone morphogenic protein 2

BVOH: butenediol vinyl alcohol

CM: cardiomyocytes

EC: endothelial cell

ECM: extracellular matrix

ESC: embryonic stem cell

FD: freeze-drying

FGF: fibroblast growth factor

FDM: fuse deposition modeling

Gel: gelatin

GelMA: gelatin methacryloyl

HA: hyaluronic acid

hDMEC: human dermal microvascular endothelial cell

hNDF: human normal dermal fibroblast

hMSC: human mesenchymal stem cell

HUVEC: human umbilical vascular endothelial cell

iPSC: induced pluripotent stem cell

LAB: laser-assisted bioprinting

LbL: layer-by-layer

MOC: multiorgan-on-a-chip

OOaC: Organ-on-a-chip

PAA: polyacrylamide

PEG: polyethylene glycol

PEGDA: polyethylene glycol diacrylate

PDMS: polydimethylsiloxane

PLA: polylactic acid

PVA: polyvinyl alcohol

RT: room temperature

SMC: smooth muscle cell

TE: Tissue engineering

VEGF: vascular endothelial growth factor

1. GENERAL INTRODUCTION

1. GENERAL INTRODUCTION

In physiological environment, tissues and organs are vascularized thanks to an abundant network of blood vessels, known as the vascular network or the vasculature. Presence of a functional vasculature plays a pivotal role in maintaining homeostasis, sufficient nutrients and oxygen supply, and proper gas exchange and waste removal [1]. The role of a healthy and functional vasculature is fundamental on both the macroscale and the microscale, where the diffusion limit of oxygen and nutrients has been reported to be around 200 µm [1]. In bioengineered models, the presence of a functional vascular network would ensure proper nutrients and oxygen supply and prevent cellular death in constructs thicker than 200 µm, better recapitulating the cell microenvironmental cues and the tissue physiology. Indeed, the integration of organ-specific vasculature has been shown to contribute to organ-related pathophysiological events [4].

In tissue engineering, the use of vascularized in vitro models could provide more insights into drug response and pathological conditions [2]. This is particularly of great interest in the pharmaceutical field, where there is a strong demand to speed up the drug development process, lower R&D costs, and overcome the use of inadequate animal models [2,3]. In regenerative medicine, the implantation of pre-vascularized scaffolds would enhance grafting to the host tissue, thus accelerating regeneration. Indeed, the host vasculature needs time to integrate and vascularize the implanted scaffold. The use of avascular implants is generally insufficient to enable perfusion and integration with the host vasculature. While successful implantation of thin constructs like the skin has been reported, it is not the case for thick and metabolically active organs (e.g. liver, heart, kidney). Owing to the diffusion limits of oxygen and nutrients, these organs and their tissues require the presence of a functional vascular network [4]. Therefore, the implantation of pre-vascularized scaffolds represents one of the most relevant strategies for regenerative medicine applications.

Significant efforts have been conducted to build 3D physiologically relevant models that could fully mimic tissue and organ functions. Traditionally, 2D cell culture performed on polystyrene surfaces were the gold standard of *in vitro* models [5]. However, 3D cell culture has been proven to be superior to 2D culture, as it can provide more accurate biological results mimicking cell viability, morphology, differentiation, and proliferation *in vivo* [5]. Consequently, 3D models would give more realistic insights into cellular response to environmental stimuli,

protein synthesis, and drug metabolism [5]. Recognizing these important factors, researchers have shifted from the culture of single cell types on flat and rigid surfaces, to the co-culture cells, first in 2D (e.g. Transwell systems), and later in 3D scaffolds, followed by the emergence of spheroids and organoids [6]. New biomaterials mimicking the cell niche have also emerged in the last decades, with advancements from 2D culture on extracellular matrix mimicking gels (such as Matrigel), to culture on 3D scaffolds with tunable mechanical and physiochemical properties [5,6]. Recently, the incorporation of more complex physiological conditions such as oxygen gradients, fluid flow, mechanical stimuli, or the combinations of these parameters was made possible thanks to the development of microfluidics, which are miniaturized devices containing microchannels with dimensions of tens to hundreds of micrometers [2,7]. In parallel, 3D bioprinting has also been adopted as a promising approach to recreate organ-like microenvironment for 3D cell culture [4]. Nevertheless, the majority of 3D complex models still lack vasculature that could fully recapitulate tissue and organ functions [4,8]. Thus, vascularization remains an unmet need in tissue engineering and regenerative medicines [4].

Within the different classes of biomaterials employed as 3D scaffolds (metals, ceramics, composites, and polymers), polymers represent the highest percentage due to their capability to mimic the extracellular matrix (ECM). In particular, the use of polysaccharides is of great interest thanks to their good biocompatibility and biodegradability, as well as their degradation products, offering great advantages as scaffolds in biomedical engineering. Owing to these unique properties, polysaccharides have been widely investigated for hydrogel synthesis. Thus, hydrogels provide mechanical support and instructive guides to promote cell survival and function. Porous 3D hydrogels are widely employed due to their ability to facilitate nutrient and oxygen diffusion, thus enabling cell migration [9,10]. The addition of channels inside a porous scaffold has been reported to promote cell growth and rapid vascularization, resulting in enhanced tissue formation and function [9,11].

Previously in the team, we have demonstrated the ability to guide endothelial cell (EC) behavior based on the curvature of the microchannel inside porous polysaccharide-based hydrogels [12]. In this doctoral project, improved vessel-like patterning of the hydrogel was explored via two main techniques: 1) sacrificial templates using either polyvinyl alcohol (PVA) or alginate gels; 2) mechanical removal of pharmaceutical-grade polypropylene filaments. To guide endothelial cell

adhesion, proliferation, and migration, a functionalization method which enabled the spatial guidance of pro-angiogenic cues were developed. Finally, as a proof of concept, the polysaccharide hydrogels were applied and adapted to microfluidics for liver tissue engineering. In the context of developing vascularization strategies for 3D models, this doctoral project explored the potential of pullulan-dextran hydrogel as a pro-angiogenic material to create hydrogels that favor vessel formation to be used as an *in vitro* model for tissue engineering applications.

The manuscript is divided into two main parts:

The **bibliographic review (Chapter 2)**, presented in the form of publication, focuses on three main strategies used to vascularize *in vitro* physiologically relevant bioengineered models [4]. These approaches include organ-on-a-chip (OOaC), spheroids and organoids, and 3D bioprinted tissues. Each vascularization strategy was presented separately. To highlight the recent trend towards a combination of these techniques, a fourth section dedicated for hybrid strategies, was also included. Finally, an in-depth discussion on the current technical limitations and evaluations of future perspectives for industrial and clinical applications was presented. This review has been published in Advanced Science (DOI: 10.1002/advs.202100798).

The **experimental work (Chapter 3)** is divided into three chapters. Each chapter is preceded by: 1) an introduction, which briefly situates the developed strategy in the context of the state of the art and the objectives of our project; 2) materials and methods; 3) results and discussions; 4) a conclusion, which summarizes and evaluates the developed technique in the context of the project.

In the first chapter (Chapter 3.1), we present a method to fabricate 3D porous polysaccharide-based hydrogels composed of pharmaceutical-grade pullulan and dextran, with controlled microarchitecture, and channels of various diameters (ranging from 100 to 500 µm) and geometries. The presence of microchannels and interconnecting pores inside the scaffolds serves as a crucial first step in guiding endothelialization. The preformed microchannels were created via sacrificial templates, which were investigated using two separate materials, namely, PVA and alginate hydrogels.

In the second chapter (Chapter 3.2), we present a simple method to functionalize the polysaccharide hydrogels in a spatial-controlled manner. To provide cells with pro-adhesive and pro-angiogenic signals, the hydrogels were coated using a recombinant, engineered bacterial

protein polymer called Caf1. The Caf1 subunits assemble into long, highly stable and flexible polymers, which are bioinert, allowing for insertion of bioactive peptide sequences from the ECM (e.g. YIGSR) as well as growth factors mimicking motifs (e.g. VEGF). Capitalizing on the acidic p.I. of Caf1, hydrogels were functionalized via electrostatic interactions induced by the coating method. The bioactive Caf1 proteins (Caf1-YIGSR and Caf1-VEGF), were spatially coated on the hydrogel through a combination of coating induced by physical absorption and a freeze-drying step. The novel approach described in this chapter demonstrated the ability to guide EC behavior through spatial control of pro-angiogenic cues. This work has been published in International Journal of Molecular Science (DOI: 10.3390/ijms232314604).

In the third chapter (Chapter 3.3), we explore three strategies to develop a hydrogel-based microfluidic platform for tissue engineering applications. The results are preliminary and could serve as a proof of concept to design polysaccharide-based hydrogels that could be incorporated in microfluidic devices, in guiding endothelialization in a more physiological environment. This study demonstrates new potentials of polysaccharides for *in vitro* tissue engineering applications.

A **general discussion** confronts our results to the literature and develops some perspectives regarding the context of the project. Finally, a **general conclusion** and some perspectives closes the presentation of this work.

2. BIBLIOGRAPHY REVIEW

2. BIBLIOGRAPHY REVIEW

Publication in Advanced Science, 2021, DOI: 10.1002/advs.202100798 (the PDF proof is provided in Annex 1):

In vitro strategies to vascularize three-dimensional physiologically relevant models

Dellaquila Alessandra, Chau Le Bao, Didier Letourneur, and Teresa Simon-Yarza*[*]

A. Dellaquila, C. Le Bao, Prof. D. Letourneur, Dr. T. Simon-Yarza
INSERM U1148, Université de Paris, X Bichat Hospital, 75018 Paris, France
E-mail: alessandra.dellaquila@elvesys.com; teresa.simon-yarza@inserm.fr

A. Dellaquila
Elvesys Microfluidics Innovation Center, 75011 Paris, France
Biomolecular Photonics, Department of Physics, University of Bielefeld, 33615 Bielefeld, Germany

C. Le Bao
Université Sorbonne Paris Nord, Galilée Institute, 93430 Villetaneuse, France

Keywords

vascularization, microfluidics, 3D cell culture, bioprinting, tissue engineering

Abstract

Vascularization of three-dimensional (3D) models represents a major challenge of tissue engineering and a key prerequisite for their clinical and industrial application. The use of prevascularized models built from dedicated materials could solve some of the actual limitations, such as suboptimal integration of the bioconstructs within the host tissue, and would provide more *in vivo*-like perfusable tissue and organ-specific platforms. In the last decade, the fabrication of vascularized physiologically relevant 3D constructs has been attempted by numerous tissue engineering strategies, that we classify here in microfluidic technology, 3D co-culture models, namely spheroids and organoids, and biofabrication. In this review, we discuss the recent advancements in prevascularization techniques and the increasing use of natural and synthetic materials to build physiological organ-specific models. Current drawbacks of each technology, future perspectives and translation of vascularized tissue constructs towards clinics, pharmaceutical

field and industry are also presented. By combining complementary strategies, we envision these models to be successfully used for regenerative medicine and drug development in a near future.

List of common abbreviations (alphabetic order)

ALI air-liquid interface**; BBB** blood-brain barrier**; CM** cardiomyocytes; **EC** endothelial cell**; ECM** extracellular matrix; **ESC** embryonic stem cell; **Gel** gelatin**; GelMA** gelatin methacryloyl; **hDMEC** human dermal microvascular endothelial cell; **hNDF** human normal dermal fibroblast; **hMSC** human mesenchymal stem cell; **HUVEC** human umbilical vein endothelial cell; **iPSC** induced pluripotent stem cell; **LAB** laser-assisted bioprinting; **LbL** layer-by-layer; **MOC** multiorgan-on-a-chip; **OOaC** organ-on-a-chip; **PEG** polyethylene glycol; **PDMS** polydimethylsiloxane; **SMC** smooth muscle cell; **VEGF** vascular endothelial growth factor.

1. Introduction

In physiological conditions, the tissues of the human body are vascularized thanks to an abundant network of blood vessels, known as the vascular network. Human vasculature has essential biological functions, such as nutrients and gas exchange, metabolic waste removal and homeostasis maintenance. [1,2] Its role is fundamental at the macro as well as at the microscale, where a diffusion limit of oxygen and nutrients has been reported to be around 200 µm,[3,4] meaning that the cells located farther from a capillary undergo hypoxia and apoptosis. Thus, vascularization plays a pivotal role in achieving physiologically relevant tissue and organ substitutes for tissue engineering and regenerative medicine applications. Despite the unprecedent advancements of tissue engineering in the last decades, the integration of a functional vascular network in tissue constructs still represents a challenge that hampers an efficient and fast scale-up towards the clinical application.

In bioengineered models, the presence of vasculature would ensure the proper exchanges, preventing cellular death in constructs thicker than 200 µm and contribute in mimicking the tissue physiology and cell microenvironmental cues. Overall, a functional capillary network would allow for a long-term maintenance of the construct in terms of viability, morphology and functionality. Furthermore, organ-specific vasculature has shown to strongly affect the behavior of the parenchymal cells and to drive organ-related biological events.[5] Vasculature plays a key role also in many diseases, such as cancer metastasis, atherosclerosis or tumor angiogenesis.[6] For *in vitro* studies, the use of vascularized models could give more realistic insights of human response to drug testing, toxicology assays or in pathological models.[7] Particularly in the pharmaceutical field, the urgent need to speed up the drug development process, lower R&D costs and overcome the use of inadequate animal models strongly relies on the development of more predictive and clinically accurate systems.[8–10] In regenerative medicine, the implantation of prevascularized constructs compared to constructs that spontaneously vascularize *in situ* would enhance the grafting to the host tissue and fasten its regeneration. Moreover, although the successful implantation of thin constructs like skin has been reported, the formation of abundant and functional vascular network is a key prerequisite for the generation of thick and metabolically active organs, such as liver, heart, or kidney.[2] In fact, the host vasculature needs time to integrate and vascularize the implanted tissue and the use of avascular scaffolds could be inefficient due to the impossibility to be instantly

perfused. The implantation of prevascularized scaffolds would thus represent one of the most favorable strategies for regenerative medicine purposes.

Many efforts have been conducted over the past years to build three-dimensional physiologically relevant models that could fully recapitulate the tissues and organs functioning. The traditional two-dimensional cell culture systems on polystyrene surfaces, which have been the gold standard of *in vitro* models for many decades, are unable to mimic the *in vivo* conditions. Tissue engineering has thus developed a plethora of three-dimensional (3D) cell culture models, that have proven to be more physiologically relevant compared to 2D cell culture, providing accurate results in biological studies, such as *in vivo*-like cell viability, morphology, differentiation, and proliferation, as well as cellular response to stimuli, protein synthesis, and drug metabolism (**Figure 1**).[11]

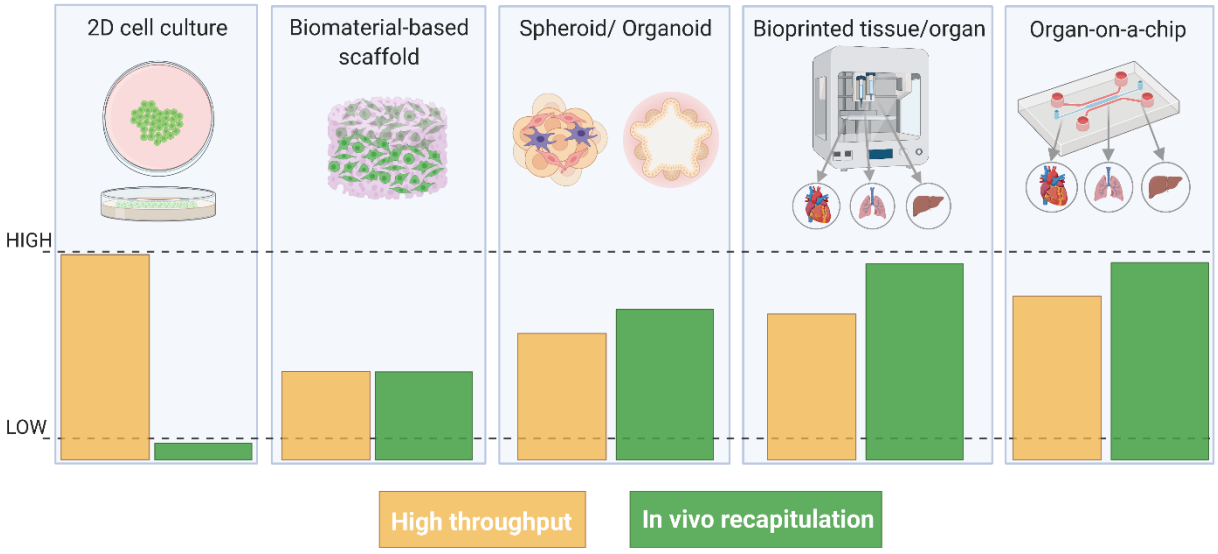

Figure 1. Evolution of tissue engineering platforms from 2D to 3D models. The bottom panel shows the comparison of model throughput versus physiological relevance: the in vivo recapitulation increases when moving from 2D cell cultures to 3D models and the throughput of complex models can be enhanced by means of automated bioprinting processes or parallel microfluidics. Created with BioRender.com

In recent decades, some research lines have thus moved from culturing of single cell types on flat and rigid substrates, to the co-culture of cells, first in 2D (i.e., Transwell® systems) and later in 3D, with the introduction of spheroids and organoids models. Complex physiological conditions,

such as blood flow, oxygen gradients or mechanical stimuli, can be mimicked nowadays by using microfluidic devices, that allow for perfusion of cells by means of microchannels networks. In parallel, new biomaterials have been developed to mimic the cell niche, with advancements from 2D culture on extracellular matrix gels (i.e., Matrigel®) to 3D scaffolds with tunable physical-chemical and mechanical properties.[12–14] These systems have been extensively used as *in vitro* models consisting of multiple cell types and the combination with bioreactors has allowed researchers to provide the cells with physiological-like biochemical and mechanical cues. Recently, these *in vitro* models have often adopted the emerging strategy of 3D bioprinting to engineer more complex systems, eventually replacing the conventional fabrication methods. The synergistic use of these technologies would allow for a precise control of the cell culture conditions and the microenvironment and it would represent a key strategy to engineer biostructures that mirror human tissues and organs while ensuring high throughput, fundamental for the translation of these models towards their application in industrial and clinical settings. Nevertheless, lacking or inefficient perfusion and vascularization remains one of the main limitations of tissue engineered constructs as the need for vascularization exists from the moment the tissue-engineered constructs are assembled *in vitro*, to the moment when they are implanted in a patient.[15]

In this review, we discuss the latest advancements on vascularization strategies in tissue engineering, focusing on different approaches, namely organs-on-a-chip (OOaC), spheroids, organoids and 3D bioprinted tissues. After a brief overview of the physiological properties of the vascular network, we describe the fabrication techniques used to engineer prevascularized 3D physiologically relevant tissue and organ models. Finally, we critically discuss the current technical limitations and evaluate some perspectives for industrial and clinical applications.

2. Physiological properties of the vascular network

The vasculature is a network of blood vessels consisting of the arterial system, the venous system, and the microcirculation (**Figure 2a**). The arterial system, composed of arteries and arterioles, distributes oxygenated blood from the lungs while the venous system, composed of veins and venules, returns low oxygenated blood to the heart. Separating these two systems is the microcirculation, where nutrients and cellular wastes exchange is carried out by the capillaries. The distinct anatomy and size of the blood vessels are dictated by the different physiological functions they play. To withstand high blood pressures and shear stress, the larger vessels, namely arteries

and veins, are composed of three layers. The external layer, called tunica adventitia, is mainly composed of collagen and nerve fibers, with a protective and support function. The middle layer, tunica media, is composed of smooth muscle cells (SMCs) and elastic connective tissue, responsible for vasodilation and vasocontraction. The inner layer, tunica intima, is the lumen wall, lined with endothelial cells (ECs) and surrounded by a thin basement membrane.[16,17] The arteries and veins are large diameter vessels, ranging from 25 mm for the aorta and about 2 mm for the pulmonary veins to hundreds of micrometers for the smallest arteries and veins. While moving down into the vascular tree, the blood pressure decreases and less elasticity is needed: that is why arterioles, with a size of 10-100 μm, are composed of the tunica media and intima only and the capillaries (less than 5 μm) are composed of a single ECs monolayer. It is interesting to notice that with the decrease of the vessels size, the vascular wall also becomes thinner. At the tissue level, the anatomy is extremely complex: in healthy conditions, the capillary density is about 300-400 capillaries/mm^3 in skeletal muscles and above 2000 capillaries/mm^3 in myocardium, brain, liver and kidney.[18] Furthermore, the parenchymal tissues are composed of cells at high concentration, of about 10^5 cells/ mm^3.[19,20] Due to its direct contact with blood, the endothelium participates in numerous physiological functions including selective barrier membrane, thrombosis prevention, blood pressure regulation, and angiogenesis.[21] Although ECs in different regions of the body fulfil similar physiological demands, heterogeneity in their morphology, function, gene expression, and antigen composition has been reported.[22,23] Specifically, the morphology of the endothelium varies to adapt to the specific functions of their underlying tissue (**Figure 2b**). Most of the vessels of the brain, lungs, and skeletal muscles, present a continuous endothelium, where ECs are held together by tight junctions and a continuous basement membrane, allowing mainly for water and ion exchange. For organs that are involved in filtration and secretion (i.e., exocrine and endocrine glands, intestinal villi, kidney glomeruli, choroid in the eyes, and a subpopulation of renal tubules), the endothelium is fenestrated. These fenestrations, or pores, exist along with tight junctions in the endothelial lining, and their permeability can vary depending on the underlying tissue needs. For the vessels in the liver, spleen, and bone marrow, the endothelium is sinusoidal or discontinuous, where the lining has larger fenestration (100-200 μm), extensive intercellular gaps, and an incomplete basement membrane.[21]

For the development of more biomimetic vascularization strategies, we summarize here the main aspects of the two key biological processes through which neovascularization occurs:

vasculogenesis and angiogenesis. Vasculogenesis is the process in which *de novo* blood vessels are generated from endothelial precursors, the angioblasts, in the embryo. Once the primitive vascular network is formed, more blood vessels arise from pre-existing ones and expand through the angiogenesis process. During angiogenesis, ECs are activated through a complex cascade of proangiogenic signals and undergo division, sprouting, branching, and lumen formation to form a network of arteries and veins. Currently, most vascularization approaches intended for clinical applications focus on the latter phenomenon. ECs demonstrate a structural and functional heterogeneity during angiogenesis, when they differentiate into two phenotypes, known as tip cells and stalk cells. Tip cells produce filopodia, which explore and perceive local signals from the environment, while guiding new vessel sprouts and forming connections with neighboring cells to build vessel loops.[24–26] In contrast, stalk cells follow tip cells and proliferate to support sprout elongation and lumen morphogenesis and secrete basement membrane components, which further stabilize newly formed vessels (**Figure 2c**).[27] The phenotypic differentiation of ECs is a transient and reversible process, modulated by complex signaling pathways, as the interplay between the vascular endothelial growth factor (VEGF) and Notch signaling.[28,29] Tip cell migration is regulated by VEGF gradients while the Notch signaling is essential for stalk cell barrier function, polarity, and lumen formation. New vascular network connections are then stabilized through the recruitment of pericytes and vascular smooth muscle cells, followed by the deposition of extracellular matrix (ECM). Once the vessels have been perfused, ECs switch to quiescent state (phalanx phenotype), where they are immobile and non-proliferating and promote vascular stability through increased cell adhesion and reduced response to VEGF signals. Nevertheless, quiescent ECs maintain their plasticity to sense and respond to angiogenic signals.[30] We refer the reader to existing reviews for a detailed overview of the angiogenetic process, see Refs [27,31,32].

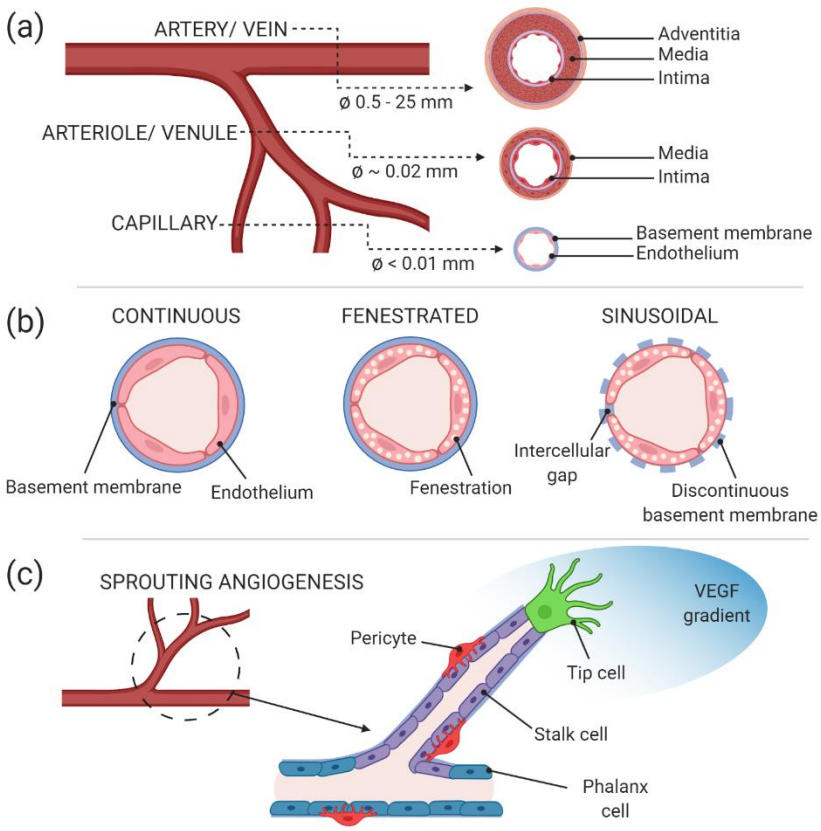

Figure 2. (a) Anatomical properties and dimensions of the human vasculature. (b) Phenotypic heterogeneity of organ-specific endothelium. (c) Differentiated role of endothelial cells during angiogenesis. Created with BioRender.com

3. Requirements for the fabrication of engineered vascularized tissues

Based on the morphological and physiological aspects illustrated so far, the engineering of functional vascularized constructs should fulfill several parameters:

(i) The artificial vessels should have circular cross-section to guarantee optimal cell seeding and physiological-like shear stress, fundamental to maintain healthy endothelial phenotype;[26,33,34]

(ii) The bioengineered vascular network should be branched and multiscale as it is *in vivo*, with larger vessels branching into capillaries to ensure a proper blood flow and gas and nutrients exchange at the microscale. The presence of large vessels (hundreds of µm) is also required when the artificial network needs to be surgically anastomosed to the host vasculature;[3]

(iii) For vessels other than capillaries, a multilayered structure should be recreated *in vitro* and include not only the endothelium composing the tunica intima but also the other cellular

components as the SMCs. Coaxial technology holds great promise for the fabrication of the different vessel layers, as we will illustrate in **Section 4.1.1** and **4.3.2**;

(iv) The tissue construct should take into account the organ-specific morphology of the vascular endothelium (i.e., continuous, fenestrated or sinusoidal ECs), that regulates the barrier properties and the interaction between the parenchymal tissue and the blood.[35] This prerequisite would necessarily require an accurate selection of cell sources, preferring primary cells over cell lines, further complicating the challenge;

(v) The *in vitro* vasculature microenvironment should integrate basement membrane proteins, as laminin and collage type IV, and other ECM components (e.g. fibronectin, glycosaminoglycans),[14,36] that actively influence the endothelial barrier function, differentiation and proliferation during angiogenesis as well as tissue maintenance and remodeling;[37–41]

(vi) The *in vitro* vasculature should be perfused to ensure adequate cell survival and tissue functioning. The perfusion parameters of the vascular network should mirror the hemodynamics and blood flow properties:[42] pulsatile flow should be applied for vessels mimicking the arteries and laminar flow in the microcirculatory system, with shear stresses below 10 dyne/cm^2, values have shown to influence ECs cytoskeleton remodeling and nitric oxide levels.[43] The mechanical properties of the surrounding tissue and ECM components should be designed to match the physiological values;[44–47]

(vii) The prevascularized model should mimic the *in vivo* capillary density and cellular concentration to respect the 200 μm diffusion limit and build functional dense and highly vascularized tissue substitutes or *in vitro* platforms.

4. Vascularization approaches for physiologically relevant 3D models

In this section, the fabrication strategies to prevascularize 3D physiologically relevant tissues are illustrated, classifying the vascularized models in microfluidic-based, 3D cell culture (spheroids and organoids) and 3D bioprinted constructs. The fabrication methods described here,

the features of each 3D approach and their applications are summarized in **Table 1**. It is worth highlighting that some of these approaches are used also as fabrication strategies for other models; in particular, bioprinting is currently used for engineering microfluidic platforms and 3D cell cultures and microfluidic devices have been used for culturing and vascularizing spheroids and organoids. Here, the vascularization strategies of each model are discussed separately while the recent trend towards the combination of these techniques is discussed in **Section 4.4** about hybrid strategies.

Table 1. Fabrication strategies for each vascularized 3D model, comparison of their properties and main applications. SL Soft lithography; T Templating; B Bioprinting; EB Extrusion based; DB Droplet based; LAB Laser assisted; Vat-P Vat photopolymerization. Created with Biorender.com.

3D vascularization strategy	Microfluidics	3D cell culture	Bioprinting
Vessel geometry	• Rectangular cross-section (SL) • Straight circular channels (T) • Branched microvasculature (T, B)	Capillary-like structures *in vitro*	Tubular interconnected channels
Vessel dimensions	Hundreds-tens of μm (> 30 μm)	Hundreds-tens of μm	• Hundreds of μm (EB, DB) • Hundreds-tens of μm (LAB)
Microenvironment	Possibility to integrate ECM proteins and growth factors	• Cell-cell interactions • Possible to integrate ECM proteins and growth factors	Possibility to integrate ECM proteins and growth factors and to print multiple cell types
Advantages	• Physiological shear stress • *In vivo*-like cues (oxygen gradient, mechanical stimuli, …) • Modular and multi-organ platforms • Integration of sensors for monitoring on-chip	• Scalable to various cell culture platforms • Patient specific • Vascular network mimicking *in vivo* complexity and architecture	• Fast method • Multiple cell/materials (EB) • Thick constructs (EB) • Low cost (EB, DB)
Disadvantages	• Use of non-biomimetic polymers (SL) • Expensive equipment for fabrication • Multi-step production • Need for external pumps	• Limited diffusion and nutrient transport as size increases • Difficult to manipulate • Need a large number of cells to generate substantial quantity of tissue	• Low resolution (EB) • Limited cell density • Cell sedimentation during the bioprinting process (EB) • Bioink printability limits mechanical properties (EB) • High cost (LAB)

SL= Soft lithography, T= Templating, B= Bioprinting, EB = Extrusion based, DB = Droplet based, LAB = Laser assisted

4.1. Vascularization techniques for microfluidic-based models

In the last decade, microfluidics has emerged as relevant technology to build 3D *in vitro* microphysiological systems for the study of human pathophysiology and drug development.[48,49] The capability of engineering perfusable channels in microfluidic devices makes this technology particularly interesting to generate vascular networks *in vitro* and important efforts have been

conducted to recreate and integrate microvasculature in organ-on-a-chip (OOaC) models.[50] The recent combination with tissue engineering approaches and biomaterials has accelerated the transition from traditional non-biomimetic materials (glass, silicon and polydimethylsiloxane, PDMS) and 2D cell culture to 3D ECM-like hydrogel-based platforms.[17,51] Microfluidic-based vascular models have been used to study the response of endothelium to a plethora of stimuli under both physiological and pathological conditions,[6,52,53] the interaction between endothelium and parenchyma in organ-specific vascular platforms and to understand key factors in vasculogenesis and angiogenesis processes.[43,54] Microfluidics has been used as well for investigating the interaction between blood cells (platelets, leukocytes, red blood cells) and vasculature and their response to mechanical or biochemical cues, that cannot be studied with static traditional *in vitro* platforms.[55–58]

4.1.1. Strategies to create vasculature on-chip

The vascularization approaches on-chip are commonly classified based on the fabrication method into two main categories, namely prevascularized patterning methods and self-vascularization approaches.[1,59] Prevascularized patterning methods consist of engineering polymeric or biological materials to create a vascular-like network on-chip, which can provide physical support and guidance for cells. To form the vascular component, cells are seeded or patterned and cultured in these pre-formed channels (**Figure 3**). In the self-vascularization approach, ECs are embedded in a matrix and supplied with biological, chemical or mechanical cues to induce spontaneous morphogenesis of the vascular network. Self-vascularized microfluidic platforms are commonly used to study vasculogenesis and angiogenesis processes *in vitro* (see **Section 2**) and they become particularly significant in the context of vasculature-related diseases, such as cancer metastasis or atherosclerosis.[6,48] Comprehensive reviews on the topic are available.[1,17,48,60,61] In this section, we provide an overview of the main prevascularization patterning strategies used for fabricating vascularized microfluidic platforms, focusing on relevant organ-on-a-chip models integrating vasculature and discussing the current bottlenecks of this approach.

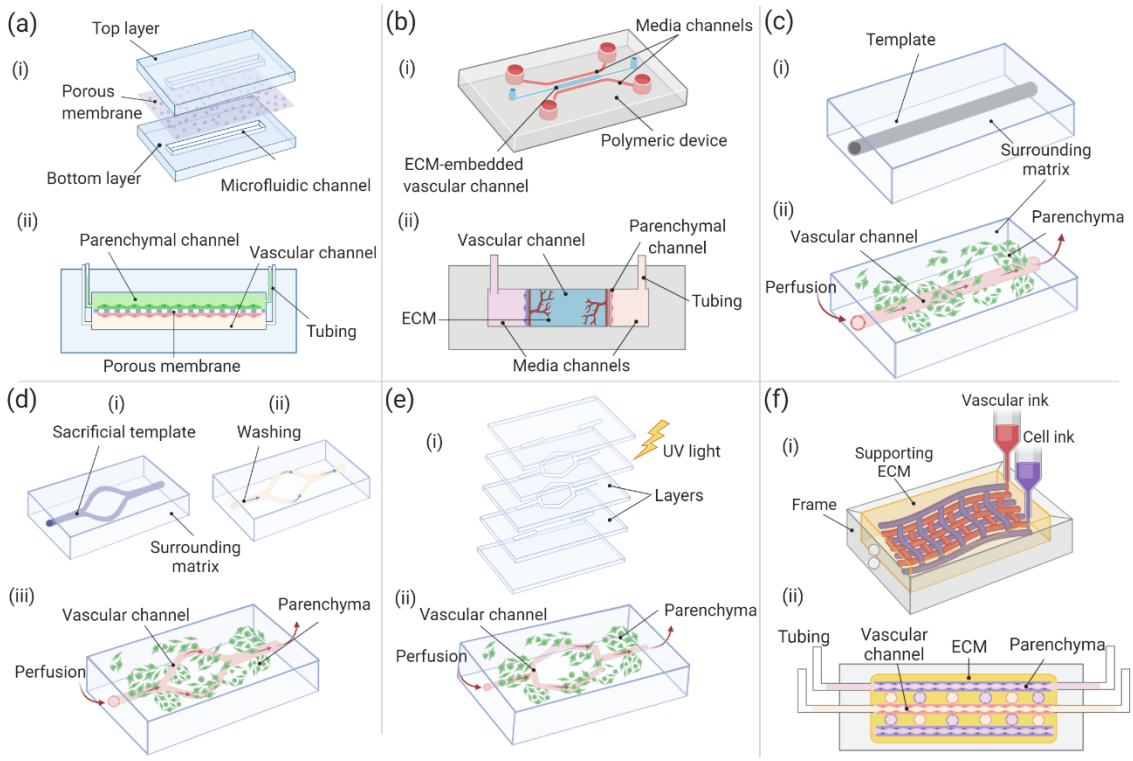

Figure 3. Possible configurations for microfluidics-based vascularization strategies: soft lithography (a, b) and patterning (c, d, e, f). **(a) Membrane-based vascularized device**: the fabrication process consists in assembling the microfluidic layers and a porous membrane (i) and the assembled chip with the typical sandwiched structure. **(b) ECM-based:** the chip usually contains one or more channels filled with ECM proteins (i) that embed the parenchymal and vascular components (ii). **(c) Templating:** (i) a matrix is casted around the template equipment (needle, fiber), that is subsequently removed to form the channel (ii). **(d) Sacrificial molding:** (i) the patterned template is fabricated and encased in the surrounding matrix, (ii) the template is removed and (iii) the device is seeded and perfused. **(e) Layer-by-layer:** the modular layers are assembled, for instance by photo-crosslinking (i) before the device seeding (ii). **(f) Bioprinting for microfluidics:** usually performed on ECM matrix- eventually bioprinted- in which vascular and parenchymal inks can be used to build the tissue (i) before perfusion of the device (ii). Created with BioRender.com

(a) Soft lithography techniques

The mimicry of the vascular interface *in vitro* has been mainly achieved by using microfluidic platforms produced by soft lithography. This approach involves the production of a silicon or glass

mold containing the microchannel features by photolithography and using it as stamp to pattern PDMS devices by replica molding. The device is then sealed by bonding it to a substrate to create perfusable channels (**Figure 3a**).[5] Despite the lack of a proper 3D lumen and geometrical similarity to *in vivo* vasculature, these models have demonstrated to be efficient platforms to build a functional organ-vasculature interface, showing significant advantages compared to static 2D models.

Vascular interface on a membrane

The visionary work of Ingber's group led to the development of the most used organ-on-a-chip model nowadays. They reproduced the Air-Liquid Interface (ALI) of the lung by culturing alveolar epithelial cells and human pulmonary microvascular ECs on two sides of a porous 10 µm thick PDMS membrane in a two-channel PDMS device.[62] Cyclic mechanical strain was applied to mimic physiological breathing by lateral vacuum channels. This simple yet functional platform was used to recreate a long-term model (> 2 weeks) of the ALI, showing *in vivo*-like barrier permeability, enhanced production of surfactants by the epithelium when exposed to air and endothelium alignment under mechanical stretching. Exposure to cytokines and nanoparticles showed the active role of vasculature and mechanical forces under inflammatory conditions, underlying the need to integrate these components to build complex *in vitro* platforms capable of recreating physiological organ functions.[53]

This pioneering platform paved the way for the study of tissue-vasculature interactions in organ-specific models such as kidney, [63,64] brain and blood-brain-barrier (BBB),[65–67] heart, [68,69] gut,[70,71] and liver.[72,73] Recently, a liver sinusoid on chip was built by integrating four primary hepatic cell types from the same murine source.[73] Liver sinusoidal endothelial cells (LSECs) and Kupffer cells (KCs) were cultured on the apical side of a porous polyester membrane to mimic the sinusoidal interface. Hepatic stellate cells (HSCs) were cultured on the basolateral side and hepatocytes (HCs) were seeded on the PDMS bottom channel to recreate the Disse space and the parenchymal tissue respectively (**Figure 4a**). Shear stress was applied in the device and imaging analyses confirmed the formation of a discontinuous endothelium composed of fenestrated LSECs, typical of *in vivo* liver sinusoid.[5] Results showed that the presence of non-parenchymal cells (NPCs) and shear stress enhanced hepatocytes functionality and metabolism compared to HCs static monoculture and neutrophil recruitment resulted to be higher when LSECs were cultured

with the other NPCs under flow. Despite the use of murine cell source and the short-term evaluation, this model reveals the synergistic effect of mechanical cues and paracrine pathways in regulating liver metabolism and its response to inflammatory conditions.

Multiorgan-on-chip: a new promising tool for drug development

The growing need for accurate and reliable *in vitro* models for drug screening and development has led to the design of multiorgan-on-a-chip (MOC) platforms (also known as body-on-a-chip), that allow for the study of PK-PD (pharmacokinetic-pharmacodynamic) pathways of drugs and interactions among organ equivalents.[74] The integration of vasculature is fundamental due to the active role of microvascular circulation in maintaining homeostasis.[48,59] Novak *et al.* have recently engineered a vascularized eight-organ-on-a-chip (BBB, brain, skin, lung, heart, liver, intestine and kidney) coupled with liquid-handling robotics and *in situ* microscopy that enabled automated culture, perfusion and control on chip.[75] Interestingly, the device used a universal blood-like medium for the vascular compartment and a specific medium for each organ. Although the vascular component was part of each organ platform, it was not included in the connections between chips. Schimek *et al.* lined uniformly the connecting tubes of a MOC with primary human dermal microvascular endothelial cells (hDMECs) under pulsatile shear stress and created branching microvessels of 40 μm in diameter by two-photon laser ablation technique.[76] Similarly, PDMS tubes with tunable diameter and thickness that can mimic different blood vessel types have been endothelialized and coupled to MOC platforms and the exposure to drugs showed the formation of a responsive endothelium.[77]

ECM-based microfluidic devices

Standard lithographic processes lead to rectangular or squared cross-sectioned channels, a geometry that has been proven inadequate to build functional microvasculature *in vitro* and to model phenomena such as coagulation.[78,79] Thus, channels with circular cross-sections have been fabricated by different strategies as micromilling of metal molds,[80] flow of nitrogen gas in a PDMS solution,[33] reflow of positive photoresists,[81] or by viscous fingering of ECM substrates, as collagen or Matrigel®.[82,83] Moreover, in standard microfluidic devices, cells are cultured on flat substrates such as polymeric membranes or PDMS sheets. To address these limitations, microfabrication strategies have been adapted to create hydrogel-based microfluidic platform, for instance by molding ECM gels upon PDMS stamps,[84,85] or embedding hydrogels in PDMS

devices (**Figure 3b**).[66,86] In a recent work, Bang *et al.* engineered a BBB device with contact of astrocytes and vascular network through astrocytic endfeet to overcome the lack of direct interface of the two components in common BBB-on-chip platforms, that hampers the achievement of *in vivo*-like barrier permeability values (**Figure 4b**).[66] The PDMS device was composed of two parallel microchannels, representing the vascular and neural compartments respectively, embedded in a fibrin hydrogel and supplied with specific medium through lateral channels. In a first step, a mixture of endothelial cells (HUVECs) and fibroblasts was seeded in the vascular channel and vasculogenesis was induced to create the vascular network. After 3 days, the neural channel was seeded with astrocytes and neurons and the formation of functional BBB was observed within one week. Results confirmed the growth of a functional lumen, the migration of astrocytes to form a direct contact with HUVECs, permeability values comparable to *in vivo* coefficients and formation of synapses.

(b) 3D Patterning methods

The recent adoption of tissue engineering fabrication methods has paved the way for engineering more sophisticated 3D *in vitro* vascular networks on-chip, overcoming the main drawbacks of conventional OOaC platforms, namely the use of non-biomimetic materials and lack of a three-dimensional geometrical complexity.[87] Hydrogel-based devices reproducing the role of ECM *in vivo* offer several advantages such as tunable mechanical properties, biodegradability, control over the cellular microenvironment and a wide choice of materials.[88] We classify below the patterning methods used for microfluidics as templating, layer-by-layer manufacturing and 3D bioprinting.

Templating strategies

Templating, also known as micromolding, is a subtractive technique in which a material with the desired vasculature shape is embedded in a bulk matrix and subsequently removed or dissolved to create a hollow perfusable microvasculature. Microneedles and fibers have been widely used to fabricate simple vascular geometries in gels (**Figure 3c**). Mori *et al.* used needle-based micromolding to create a skin-equivalent model composed of epidermal and dermal layer and perfusable vascular channels.[89] A culture device was 3D printed and nylon wires (500 µm thickness) were used as channel templates. Collagen solution loaded with normal human dermal fibroblasts (hNDFs) was gelled to fabricate the dermal layer and, after removal of the wires, the

vascular channel was formed by seeding HUVECs. The subsequent addition of normal human epidermal keratinocytes (NHEKs) on the top of the dermal layer and exposure to the ALI enabled the formation of the stratum corneum of the epidermis (**Figure 4c**). Water repellency and capacitance tests confirmed the barrier function of the epidermal layer and permeability studies on the vascular channel showed the formation of a selective barrier for the diffusion of nutrients. Percutaneous absorption studies conducted by flowing caffeine and drugs in the vasculature confirmed the adequacy of the model as a platform for vascular absorption studies, fundamental in drug and cosmetics testing.

The needle-based vascularized platforms are mainly limited to straight channel geometries and some manufacturing steps (needle removal, stability of the gel after cross-linking) have to be taken into account during the design process. Sacrificial molding uses templating materials that are dissolved after the hydrogel bulk gelation and represents a versatile technique to create stable and more complex 3D vascular networks.[87] Gelatin,[90] agarose,[91] alginate,[92,93] Pluronic,[94] and PVA[95] have been used as sacrificial materials for creating meshes either by micromolding or 3D printing (**Figure 3d**, **Section 4.3**). Vollert and coworkers fabricated large (15 x 25 x 3 mm^3) perfusable engineered heart tissues for cardiac regeneration by using either straight or branched alginate fibers as lumen template.[92] The tissue was composed of a neonatal rat heart cells mix (cardiomyocytes, ECs, fibroblasts and SMCs), [96] embedded in a fibrin matrix and ECs showed formation of an intima-like layer by spontaneously covering the vessels after alginate dissolution. The engineered tissues showed contractile forces and the continuous perfusion enhanced oxygen concentration, with a significant increase in the cardiomyocytes (CMs) density.

To overcome the use of potential cytotoxic dissolving agents during sacrificial molding, researchers have engineered vascular templates that can be dissolved in cell media, such as Pluronic and 3D-printed self-standing carbohydrate glass lattices and caramel templates, that have been used to create complex hierarchical networks of tubular channels with interconnected lumens and permeable walls.[97,98]

Layer-by-Layer manufacturing

Layer-by-layer (LbL) represents a versatile bottom-up method for manufacturing complex 3D vasculature *in vitro* and consists of assembling 2D pre-patterned gel slabs into multi-layered (modular) 3D devices (**Figure 3e**).[17] Zhang *et al.* fabricated vascularized cardiac and hepatic

constructs by stacking 25 μm thick poly(octamethylene maleate (anhydride) citrate) (POMaC) layers patterned by UV photolithography.[69,99] The presence of microholes and nanopores in the scaffold walls ensured physiological-like mass transport and cell migration and the formation of vessels with a thickness of 2-3 cells. The use of a photo-crosslinkable hydrogel provided for tunable stiffness, thus creating an anisotropic construct that closely mimics the myocardium mechanical properties. The pump-free perfusion *in vitro* was performed by connecting the device to a custom-made bioreactor and the open configuration enabled direct access to the cellular compartments by pipetting. Culturing of the vascular network with HUVECs led to formation of a functional lumen, capable to respond to angiogenic and inflammatory stimuli and compatible with human whole blood flow. By integrating liver or heart parenchymal cells embedded in ECM, functional tissue constructs were built, exhibiting metabolic response to drug administration and contractile behavior, respectively. *In vivo* implantation by anastomosis confirmed the non-thrombogenic properties of the device and successful angiogenesis in a rat model.

3D Bioprinting for microfluidics

Cells and hydrogels can be used as bio-inks for direct fabrication of vascularized organ-on-a-chip platforms by means of 3D bioprinting approaches (**Figure 3f**), that will be mostly discussed in **Section 4.3**. Bioprinting strategies for vasculature and OOaC design have been extensively reviewed elsewhere.[100–105] This approach shows several advantages such as the capability of recreating physiological-like multi-cellular spatial organization within the device and direct manufacturing of 3D perfusable vascular geometries, simplifying the fabrication steps and moving towards more reproducible and automated strategies.[106] Moreover, this technique has shown its potential in vascularizing large tissue constructs and integrating patient-derived cells, representing a valuable tool for personalized medicine.[94,102,107] Coaxial needle technology has been used to fabricate endothelialized perfusable tissues in several studies.[108,109] 3D multi-layer circumferential channels have been recently engineered by using single-step coaxial needle manufacturing to reproduce human tubular tissues as urethra and blood vessels.[110] A gelatin methacryloyl (GelMA) and alginate hydrogel blend combined with eight-arm poly(ethylene glycol) acrylate with tripentaerythritol core (PEGOA) was used as bioink and extruded after cells encapsulation by using up to 3 circumferential needles. Urothelial tissue was created by bioprinting a core layer of human urothelial cells (HUCs) and an external layer of human bladder smooth muscle cells (HBdSMCs)

while vascular tubular tissues were composed of endothelial (HUVECs) and human smooth muscle cells (hSMCs) circumferential layers. Results confirmed long-term viability (2 weeks), proliferation and differentiation and showed the advantages of this method in creating functional tubular constructs for regenerative medicine and modeling.

Although bioprinting techniques are increasingly used for printing perfusable microfluidic networks, the bioprinting step is often limited to the fabrication of polymeric tubular structures, that are successively washed to form hollow channels and seeded with cells.[111] Recent works are focused on the bioprinting of cell laden gels on-chip: this strategy allows a reduction of the fabrication time by eliminating the need for the cell seeding step and it ensures a more precise and homogeneous cellular distribution and alignment, eventually in complex multilayered geometries.[110,112,113]

Recently, 4D bioprinting has emerged as technique for spatiotemporal control of networks self-assembly by using smart materials that respond to external stimuli (e.g. temperature, pH, swelling, etc.). Thus, reversible self-folding tubular constructs can be engineered and their properties controlled over time by tuning the external cues, making this approach particularly interesting for programming the cellular microenvironment and creating functional hybrid hierarchical bioconstructs.[100,114]

Although soft lithography, templating and additive manufacturing are commonly used for fabrication of perfusable vasculature, other methods have been explored. Heintz *et al.* used a laser-based degradation technique to create complex and tortuous 3D microfluidic PEGDA hydrogel networks from a stack image of mouse cerebral cortex vasculature.[115] The high spatial resolution offered by the technique led to microvessels with a diameter of less than 10 μm and a dense network, fundamental for providing the parenchymal tissue with nutrients and oxygen within the diffusion limit.[3]. Interestingly, vascular microfluidic chips have been engineered by reversibly assembling explanted mouse arteries on automated platforms, showing the capability to study intact vessels functionality by performing immunofluorescence studies and quantitative analyses on-chip.[5,116]

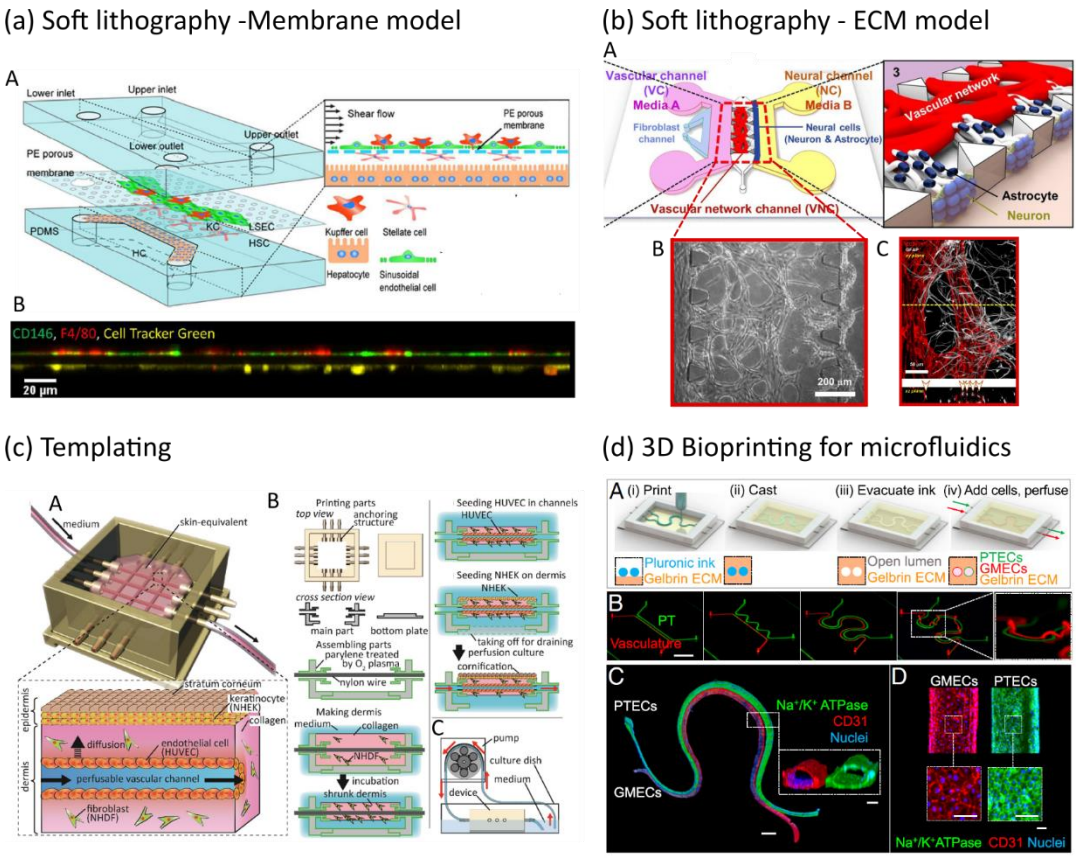

Figure 4. Microfluidic - based vascularization strategies: soft lithography (top) and 3D patterning (bottom). **(a) Liver sinusoid on-chip fabricated by soft lithography**. LSECs and KCs were seeded on the apical side of a PE membrane while HSCs on its basolateral side and HCs on the PDMS substrate (top). Lateral view of the sinusoidal endothelium (bottom): LSECs (green) and KCs (red) on the top and HSCs (yellow) on the bottom of the membrane. Reproduced with permission.[73] Copyright 2017, The Royal Society of Chemistry. **(b) ECM-based vascularized BBB platform**. (A) HUVECs and fibroblasts were seeded in the vascular channel (VC) and neural cells (astrocytes and neurons) were seeded in the neural channel (NC). The formation of vascular network in the central vascular network channel (VNC) ensured a direct interface between the capillaries and the astrocytes through astrocytic endfeet (B, C- ECs stained in red, astrocytes stained in white). Adapted with permission.[66] Copyright 2017, Springer Nature. **(c) Skin-equivalent platform generated by templating**. (A, B) The culture device was 3D printed and filled with collagen and fibroblasts to form the dermis layer. After removal of the nylon wires, the hollow channel was seeded with HUVECs to form the capillary and keratinocytes were cultured on the top of the dermis and exposed to liquid-air interface for cornification of the epidermal layer.

(C) Perfusion of the device via peristaltic pump. Reproduced with permission.[89] Copyright 2017, Elsevier Inc. **(d) Hybrid strategy: 3D printed vascularized proximal tubule model**. (A, B) The colocalized vascular and renal channels are both 3D printed by using a Pluronic F127-based fugitive ink within an ECM solution and different designs can be easily printed. (C, D) The construct is then seeded with epithelial (green) and endothelial (red) cells. Reproduced with permission.[102] Copyright 2019, PNAS.

Table 2 summarizes significant case studies for the microfluidics-based vascularization strategies, cited or discussed in the text. Data such as channel shape, perfusion parameters and duration of *in vitro* studies have been reported to provide the reader with a detailed overview of different specifications and address some drawbacks, that will be discussed in the next paragraph.

Table 2. Summary of case studies for microfluidics-based vascularization strategies. * Bioinks containing cells.

Vascularization method	Organ/ tissue model	Vessel caliber (d)/ Channel size (hxw)	Channel shape	Chip composition	Cellular composition	Perfusion parameters	Duration of *in vitro* study	*In vivo* evaluation/ Drug testing	Refs
Soft lithography	Liver	100 µm x 1 mm	Rectangular, straight	PDMS; PE (polyester) membrane	LSECs, HCs, KCs, HSCs (all primary from mouse)	0.1 or 0.5 dynes/cm^2, syringe pump	1 day	NO/ NO	[73]
	BBB	• Vascular channel: 800 µm, vascular network: < 50 µm • 35-100 µm	Rectangular, straight	• PDMS; fibrin hydrogel • PDMS; fibrin-hyaluronic acid	• HUVECs, lung fibroblasts, rat cortex neural cells • Brain microvascular ECs; HUVECs; pericytes; astrocytes	–	7 days	NO/NO	[66,86]
	Kidney	0.2 x 1 mm (vascular), 1 x 1 mm (urinary)	Rectangular, straight	PDMS (chip, membrane)	Glomerular ECs; hIPS-derived podocytes	0.017 dynes/cm^2 (vascular) 0.0007 dynes/cm^2 (urinary), peristaltic pump	8 days	NO/ YES	[64]
	Intestine	0.15 x 1 mm	Rectangular, straight	PDMS (chip, membrane)	Capillary ECs or lymphatic microvascular ECs, Caco-2 intestinal epithelial cells, immune cells	0.02 dynes/cm2	> 7 days	NO/ YES	[70]
	Multiorgan	(100 x 500 µm) - 40 µm	Rectangular, curved	PDMS	Dermal microvascular ECs	10-40 dynes/cm2, On-chip micropump	Up to 4 weeks	NO/ NO	[76]
Templating	Liver	• 300 µm (main channel) • 100-1000 µm	• Circular, straight • Circular, curved, branched	• Collagen I • GelMA	• HUVECs; hepatocytes (HepG2); MSCs • HUVECs, hepatocytes (HepG2)	• 10^{-1} dynes/cm^2, peristaltic pump • 50 µL/h, syringe pump	• 8 days • 7 days	• NO/ NO • NO/ YES	[19,103]
	Skin	• 520 µm • 100-250 µm	• Circular • Rectangular, curved, branched	• Collagen I • Collagen I	• HUVECs, dermal fibroblasts, epidermal keratinocytes • HUVECs, iPSC-derived ECs, dermal fibroblasts, keratinocytes	• 2-3 mL/h, peristaltic pump • Syringe pump	• 10 days • 21 days for cornification, 2 days at ALI	• NO/ YES • YES/ NO	[89,93]
	Heart	100-500 µm	Circular	Fibrin matrix	Neonatal rat heart cells mix	20 µL/h, syringe pump	21 days	NO/ NO	[92]
3D Bioprinting	Urothelial/ vascular tissue*	~700 µm (inner),~1 mm (outer)	Circular, multilayer, flexible	Bioink: PEGOA + GelMA	Urothelial: Human urothelial cells + human bladder SMCs; vascular: HUVECs + human SMCs	–	14- 21 days	NO/ NO	[104]
	Kidney	200 µm	Circular, colocalized	Gelatin + fibrin ECM; Bioink: Pluronic F127+ PEO	Glomerular microvascular ECs; Proximal tubule epithelial cells	0.3 dynes/cm^2	18 days	NO/ YES	[102]
	Heart	500 µm (200- 900 µm)	Circular, hierarchical, multibranched	Agarose hydrogel, PCL network	Rat cardomiocytes	Syringe pump	5 days	YES/ NO	[98]
	Vasculature*	1.5 x 3 mm	Rectangular, straight	PMMA case, GelMA	Aortic ECs; aortic SMCs; fibroblasts	100 µL/h, peristaltic pump	7 days	NO/ NO	[105]
Alternative strategies	**LbL** Liver/Heart	100 x 50-100 µm	Rectangular, straight	POMaC, Fibrin gel/Matrigel® for parenchyma	Liver: HUVECs + hESCs-derived hepatocytes + hMSCs; Heart: HUVECs + hESC-derived CMs + hMSCs	0.6 dynes/cm^2, bioreactor	7 days	YES/ YES	[69,99]
	Laser-based -	< 10 µm	Tortuous, dense	PEGDA	Mouse brain ECs	10 µL/min	11 days	NO/ NO	[100]
	Explanted vessels Brain	120 µm	Circular, physiological	PDMS	ECs, SMCs	0.5 µL/min, no external pump	–	NO/ YES	[101]

4.1.2. Limitations of microfluidics- based vascularized models

Microfluidic technology has shown great potential for the development of *in vitro* vascularized models for the study of the microenvironment under healthy and pathological conditions and for drugs screening and development. Soft lithography and membrane-based models represent a landmark for recreating the vascular interface and have been used to mimic complex organ-specific pathophysiological mechanisms. However, they fail in recapitulating a 3D microenvironment and the membranes, made usually of artificial polymers, prevent the direct interaction of the vascular and parenchymal components. The use of ECM-based membranes or channels has allowed researchers to move towards more physiologically relevant models,[66,118] but still soft lithography requires expensive equipment and makes the platforms often difficult to be used by a wide end-users range. Templating represents a straightforward method to create hollow channels in a matrix. Although the use of 3D additive manufacturing to print the sacrificial patterns has increased the potential of the technique in fabricating more *in vivo*-like networks,[93] the platforms are usually limited to relatively simple geometries and large vessels of hundreds of micrometers. These methods usually require several fabrication and seeding steps and the template removal step should be designed carefully to avoid device or cellular damage. Layer-by-layer manufacturing, offers the possibility to design more versatile and flexible platforms via a multi-layer assembling process and represents a valuable technique for engineering large scale thick constructs.[108,119] However, the precise alignment of the layers often represents a critical step in the process design. Recently, 3D bioprinting has been widely used for vascularization of biomaterials and fabrication of perfusable vessels due to its scalability, versatility, wide materials selection and precision in engineering complex 3D cell laden constructs,[101,105] and its combined use with microfluidics will be further discussed in **Section 4.3**.

4.2. 3D Cell culture models: spheroids and organoids

Spheroids and organoids are three-dimensional, multi-cellularized structures usually devoid of any exogenous materials. In the last decade, these structures have gained significant popularity in 3D cell culture research due to their ability to mimic the physiological conditions of cells *in vivo*. Although the two terms have been used interchangeably, there are fundamental differences and application varieties between them. Spheroids are established from simple clusters

of cells, ranging from immortalized cell lines, primary cells, or fragments of human tissue.[13,120] Spheroid technology was developed based on the ability of cells to self-organize during embryonic development. This self-assembly process takes place *in vitro* when cells cannot attach to their biomaterial surface, hence aggregate into spherical 3D structures, namely spheroids. Organoids are complex clusters of cells derived from stem cells such as adult stem cells, embryonic stem cells (ESCs), and induced pluripotent stem cells (iPSCs). When given a scaffolding ECM environment (usually collagen or Matrigel® matrix), they self-assemble into microscopic analogs of their parent organs.[121,122] As a result, organoids are widely regarded as miniature versions of organs. Organoids retain the parental organs' genetic features over several passages, which allows for long-term *in vitro* expansion of cells and guaranties long-term viability.

Spheroids have shown potential in mimicking tumor tissues, which could help researchers develop more physiologically relevant cancer models, hence develop better cancer treatments. Vascularized spheroids, which can be achieved via co-culture with ECs, have been employed as a model to study angiogenesis *in vitro* and as a prevascularization approach for tissue engineering applications.[123] However, as spheroids are formed via cell-cell adhesion, they only transiently mimic physiological cell organization.[120] In contrast, organoids formation relies on internal developmental processes, which gives rise to a higher order of self-assembly, hence, the unique ability to recapitulate *in vivo* physiological functions.[121] Since organoids can be derived from patient tissues, they are interesting for disease modeling, development of personalized medicine, as well as drug testing and toxicity studies (see **Section 6**).[124]

4.2.1. Spheroids and organoids generation

Spheroids are formed by culturing cells in hanging drops, round-bottom nonadherent or low adhesive substrates, and in suspension to induce self-aggregation. Alternatively, spinner flask cultures can be employed to induce spontaneous cell aggregation for the fabrication of both spheroids and organoids. In this method, cell suspension is housed inside a spinner flask bioreactor with continuous mixing via a stirring bar, which generates a convectional force that induces cell aggregates formation.

Organoid fabrication methods involve formation of 3D aggregates from stem cells, followed by embedding in a biogel such as Matrigel® and culturing in a specialized mixture of media and factors to obtain specific organoid generation. To date, a wide range of organoid systems including heart, lung, brain, lung, liver, kidney, intestine, retina, etc. have been developed.[125–129]

Table 3 summarizes the different methods for the fabrication of spheroids and organoids, their advantages and challenges. To further explore these topics, we refer the reader to published reviews.[130–133]

Table 3. Overview of spheroid and organoid formation methods.

Method	3D culture system	Description	Advantages	Challenges	Refs
ECM scaffolding	Organoids	Stem cells are placed in Matrigel® (or ECM mix) and maintained in culture	• Replicates microenvironment • Observation of cell adhesion & migration	• Lack of reproducibility using natural ECM • Synthetic ECM requires upregulating reagents	[126,134,135]
Hanging-drop	Spheroids	Cells are suspended in media droplet. Cell aggregation occurs at the air–liquid interface	• Consistent • Does not require ECM • Possible to integrate array production	• Difficulties with media change • Small size • Low throughput	[136,137]
Low-adherent surfaces	Spheroids	Cells are suspended and cultured on a low-adherent plate, or hydrophilic substrates (i.e., hydrogel) to form aggregates	• Does not require ECM • Cost-effective	• Not adaptable to all cell types • Heterogeneous population	[138]
Spinning bioreactor	Spheroids & organoids	Cell suspension is housed inside a spinner flask or a bioreactor with continuous mixing. Cell aggregation is induced by convectional force	• Can generate a wide range of model sizes	• Large & heterogenous structures • Shear forces on cells	[139,140]
Magnetic levitation	Spheroids & organoids	Nanoparticles are ingested by cells, which are then placed in a low-adherent substrate. A magnet lid is used to induce cell aggregation	• Does not require ECM or media	• NPs are expensive and toxic	[141]
Bioprinting	Organoids	Additive manufacture of cytokines, cells, and ECM	• Generates complex & organized structures • Use of multiple cell types	• Bioink selection with desired characteristics	[142–144]
Micropatterning	Spheroids	Microcontact printing & soft-lithography patterning of ECM	• Structure control • Array production	• Expensive equipment • Poor reproducibility • Lack of patterning efficiency	[145]
Microfluidics	Spheroids & organoids	3D structures housed inside microstructures, integrated with microsensors	• Replicates microenvironment • Allows for nutrient delivery • Avoids necrosis • Array production	• Low cell recovery • Post-cell analysis challenges	[146]

4.2.2. Strategies to vascularize spheroids and organoids

Researchers have shown that the incorporation of ECs increases cell viability and functions in multicellular spheroids and enables the formation of rudimentary vascular networks within the spheroid structures.[147–151] The concept of using spheroids containing ECs dated back in 1998 when Korff and Augustin used EC-covered spheroids to analyze angiogenesis *in vitro*: ECs on the spheroids surface exhibited quiescent phenotype, which increased their sensitivity to angiogenic stimulation and differentiation. [151] The incorporation of ECs in the co-culture system mimics the physiological interactions between ECs and other cell types, which consequently preserves cell viability and promotes proliferation and vascularization. Along with ECs, mesenchymal stem cells (MSCs) play a key role in the angiogenic process by facilitating blood vessel stabilization and maturation.[152,153] Specifically, MSCs actively participate in angiogenesis via secretion of proangiogenic factors (i.e., VEGF, MCP-1, IL-6, etc.) and MSC-released paracrine factors are responsible for activation of the ECs angiogenic functions.[152][154] Given their multipotency, MSCs also induce direct differentiation and cell-cell interactions with endothelial lineage, suggesting that MSCs could be used to facilitate vascularization in spheroids and organoids. [153] For example, spheroids fabricated using only MSCs was found to generate vascularized spheroids with improved osteogenic differentiation and bone formation [155]. Similarly, when hMSCs were co-cultured with HUVECs, the resulting spheroids formed capillary-like vessels, hence improved adipogenic differentiation upon transplantation.[156]

In general, the strategies used to vascularize spheroids and organoids are conducted in two steps: first, the spheroids/organoids are formed by co-culturing parenchymal cells with ECs and/or MSCs to induce prevascularization *in vitro*. Then, spontaneous vascularization is induced via *in vivo* transplantation in highly vascularized regions such as skin, liver, heart, lung or brain (**Figure 5**). The co-culture step can be achieved either via i) scaffold-free approach (**Figure 5a**), or ii) scaffold-based approach, with incorporation of a biomaterial as instructive guide (**Figure 5b**), discussed in the next paragraphs. Here, we consider low-adherent substrates, hanging-drop technique (in the case of spheroids) and Matrigel® (in the case of organoids) as scaffold-free since they not require additional procedures, as compared to biomaterial-based scaffolds, which are synthesized in the lab. Alternative options to standard culture techniques is the incorporation of 3D printing, bioprinting, and microfluidic platforms to form vascularized spheroids and organoids (**Figure 5c**).

We refer the integration of several techniques as hybrid strategies for vascularization of *in vitro* models (including 3D cell cultures), which are discussed in **Section 4.4**.

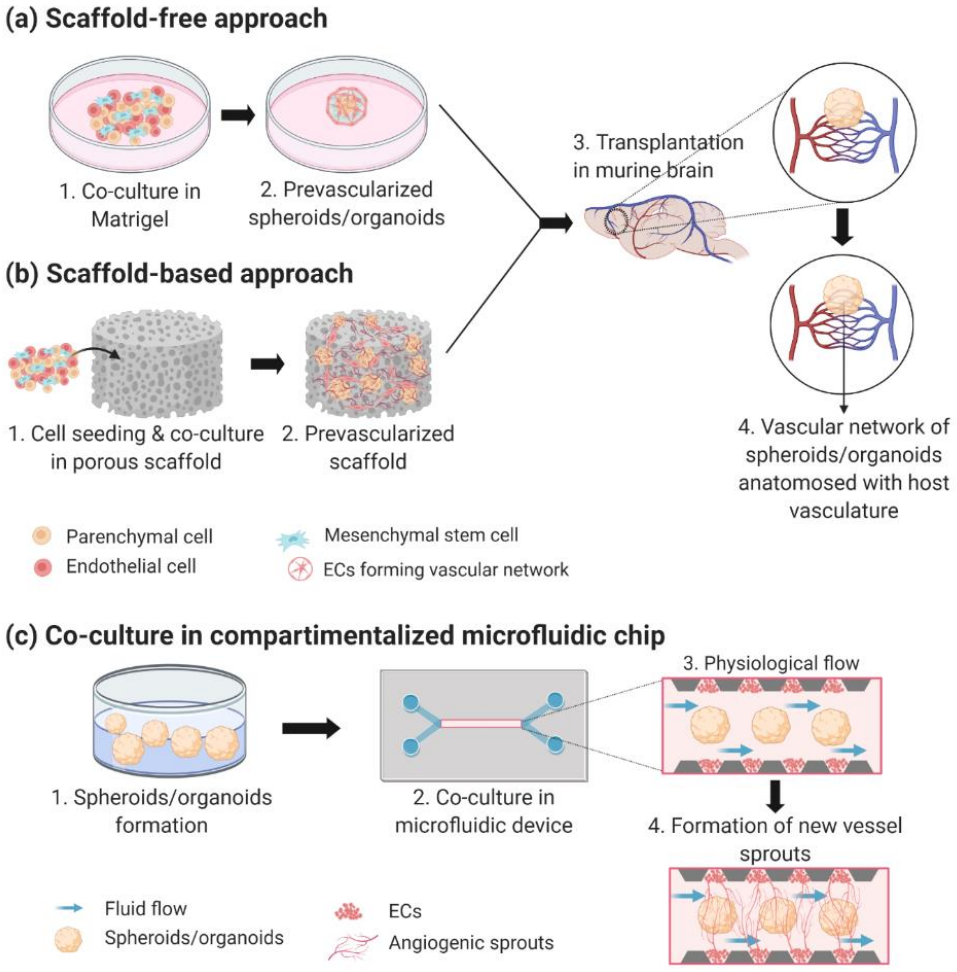

Figure 5. General schematic illustrating strategies used to vascularize spheroids/organoids. **(a) Scaffold-free approach:** Co-culture with ECs/MSCs to form prevascularized network, **(b) Scaffold-based approach:** Co-culture with ECs/MSCs in porous biomaterials. Both (a) and (b) can be followed by spontaneous vascularization via in vivo transplantation in highly vascularized organ such as the brain**. (c) Co-culture of spheroids/organoids inside microfluidic chip to mimic in vivo conditions such as fluid flow.** Created with BioRender.com

Vascularization of spheroids: Scaffold-free approach

Multicellular spheroids consisting of human dermal microvascular endothelial cells (hDMECs), human osteoblasts (HOBs), and normal human dermal fibroblast (hNDFs) were

reported to have promising potential as vascularization units for bone tissue engineering. [148] Spheroids have been generated using the low-adherent surface fabrication method. Co-culture spheroids with round morphology formed after 72 hours, with endothelial cells showing CD31 markers. Additionally, the presence of microvessels formation within the co-culture spheroids suggests prevascularization/ intrinsic vascularization. The prevascularized spheroids were then harvested and transplanted into the dorsal skin of immunodeficient mice for 2 weeks. Intravital analysis of the transplanted spheroids revealed the presence of vessel-like structures: human microvascular networks grew outside of the spheroids border and eventually connected to the host vasculature.

Co-cultures of ECs with other organ-specific cell types such as dental pulp stem cells (DPSCs), rat neonatal cardiomyocytes (RNCMs), rat hepatocytes, and human brain astrocytes and pericytes have also shown vascularization potential. [137,138,149,157] In Dissanayaka's study, DPSCs were co-cultured with HUVECs and results showed microvascular networks forming within the *in vitro* spheroids.[138] Upon *in vivo* transplantation, the lumens of the grafts were lined with ECs and graft vessels and mouse vessels were both present in the implanted site, suggesting integration of prevascularized spheroids into the host vasculature. This study finding highlights the potential of EC-incorporated spheroids as functional vascularized units that can promote successful dental pulp regeneration.

Bhang and colleagues were among the first researchers to demonstrate the feasibility of generating spheroids using only MSCs.[158] Human cord blood MSCs (hCBMSCs)-derived spheroids were grown and transplanted into mouse ischemic tissue. The hCBMSC spheroids were evaluated for apoptotic signaling, angiogenesis-related signal pathways, and blood vessel formation both *in vitro* and *in vivo*. As expected, cell survival was higher in spheroids as compared to cells in monolayer culture. The spheroids improved viability of the transplanted cells and promoted angiogenesis, as evident by an increase in the number of microvessels within the spheroids.[158] Similarly, when β-cell pseudoislets were co-cultured with MSCs, they exhibited insulin-producing phenotype and secreted angiogenic and anti-apoptotic proteins.[150,159] Both reports demonstrated that MSC-incorporated spheroids had enhanced viability, paracrine secretion, and vascularization after transplantation.

Co-culture of EC-incorporated spheroids with fibroblasts can also enhance vascularization. Fibroblasts are essential for production precursors for the ECM and therefore, it contributes to the stabilization of the newly formed vessel-like structure. [160] Noguchi *et al.* developed cardiac tissue spheroids by co-culturing rat neonatal ventricular cardiomyocytes (RNVCMs), human cardiac microvascular endothelial cells (HCMECs), and hNDFs (**Figure 6a**). The spheroids were then fused into a patch-like construct and transplanted into rat hearts. Results showed that microvascular networks formed inside the spheroids, both *in vitro* and *in vivo* experiments.[157]

Vascularization strategies of spheroids: Scaffold-based approach

Biomaterials-based scaffolds have also been adopted for vascularization of spheroids as instructive guides to improve spheroid function and promote angiogenesis. In one study, adipose-derived stem cells (ASCs) spheroids were covered with hyaluronan (HA) gel and chitosan-hyaluronan (CSHA) membrane and seeded onto the wound area on the dorsal skin of Sprague-Dawley male rats. *In vitro* analysis demonstrated that ASC spheroids had higher gene expression of chemokines and cytokines when cultured on HA gel and CSHA membrane, suggesting an improvement in paracrine effects. Following transplantation, spheroids were observed near microvessels in the healing region of the skin. The enhanced paracrine effects upregulate angiogenic factors secretion, thereby stimulating angiogenic and wound healing processes.[161]

In another approach, MSC spheroids were entrapped within RGD-modified alginate hydrogels and transplanted into the dorsum of immunodeficient mice for 8 weeks. *In vitro* analysis demonstrated that these spheroids underwent osteogenic differentiation and exhibited enhanced VEGF secretion and reduced apoptosis. Furthermore, explants of hydrogels containing spheroids demonstrated improved osteogenesis *in vivo*.[155]

Human ASCs were used to generate spheroids, which were then seeded into dried porous poly(lactic-co-glycolic acid) (PLGA) scaffolds. The resulting constructs exhibited improved vascularization and adipogenic differentiation upon transplantation.[156] Similarly, ASC spheroids in porous polyurethane scaffolds demonstrated enhanced angiogenic potential, as evidenced by greater microvessel density.[162] In another study, hMSC/HUVEC spheroids seeded onto poly(propylene fumarate)/fibrin scaffolds showed enhanced vascular network formation.[163]

Vascularization of organoids: Scaffold-free approach

Prevascularized organoids have been transplanted into kidney,[127,128] brain,[125,164,165] and liver.[126] Among the various labs which attempt to form vascularized organoids, the most notable is the work of Takebe's group. They have successfully fabricated complex vascularized organ buds for kidney, heart, lung, brain, intestine, and pancreas using murine PSC-derived progenitors, HUVECs, and MSCs.[135,166]

Watson generated human intestinal organoids using hESCs or hiPSCs and transplanted them in the kidney capsule of immunocompromised mice.[128] The grafted organoids were vascularized by the host vasculature and resembled the native human intestine with crypt-villus architecture and underlying laminated submucosal layers. Cross-section of the transplanted organoids, which showed mucous-filled lumens and sheets of villi with capillary network, further indicated vascularization and good engraftment of organoids into the host kidney. The *in vivo* tissue was more differentiated and matured over time compared to *in vitro* tissue prior to transplantation.[128] Similarly, spontaneous vascularization upon transplantation was also achieved for kidney organoids. Using the ALI method, van den Berg *et al.* generated kidney organoids from podocytes and grafted them into the renal capsule of immunocompromised mice for 28 days. The organoids developed *in vitro* anatomical-like structures resembling a nephron including the glomerulus, the distal and proximal tubes, and the collecting duct. However, the *in vitro* tissue did not form a vascular network, probably due to the limited VEGF production of podocytes and the absence of ECs during *in vitro* development. Upon transplantation to a highly vascularized site, the organoids grew in size, differentiated progressively into mature kidney tissue, and developed their own vascular network that connected to the mouse vasculature, which supplied blood to their core.[127]

Stem cells can be co-differentiated into organ-specific structures and ECs to obtain vascularized organoids and hESCs or hiPSCs have been successfully used to form cerebral organoids and ECs by co-differentiation.[125,165,167] In this case, different protocols and culture conditions have been developed by different research groups and all studies showed organoids which formed tubular structures and perfused vascular networks *in vitro*. In Ham and Pham protocols, hESCs or hiPSCs were induced into neuroectoderms which were then introduced in cerebral organoids media and VEGF-supplemented cerebral organoids media for organoid and

endothelial differentiation, respectively. Alternatively, Cakir *et al.* induced the expression of ETV2, a transcription factor contributing to vessel development, to differentiate hiPSCs into ECs.[125] Moreover, they reported their organoids could promote neuronal maturation and development of vascular networks with BBB characteristics. Thus, the pre-formed functional vessels eventually anastomosed with the host vasculature upon transplantation while the organoids generated without ECs did not survive after 2 weeks of transplantation.[125,167] All results strongly suggest the presence of endothelial cells is highly essential for proper vascularization and engraftment of organoids prior to transplantation.

Along with ECs, mesenchymal stem cells (MSCs) are also included in co-culture experiments for vascularization due to their angiogenesis properties. When liver cells were co-cultured with HUVECs and MSCs to form liver buds, the resulting 3D structures had liver-specific functions, developed vascular networks and integrated with the host transplantation sites (**Figure 6c**).[134,168] Beside the liver, Takebe's group has also successfully developed complex vascularized organ buds for kidney, heart, lung, brain, intestine, and pancreas through self-condensation procedures using murine PSC-derived progenitors, HUVECs, and MSCs following implantation in host mice.[135]

Table 4 summarizes the significant case studies for the 3D cell culture vascularization strategies, cited or discussed in the text.

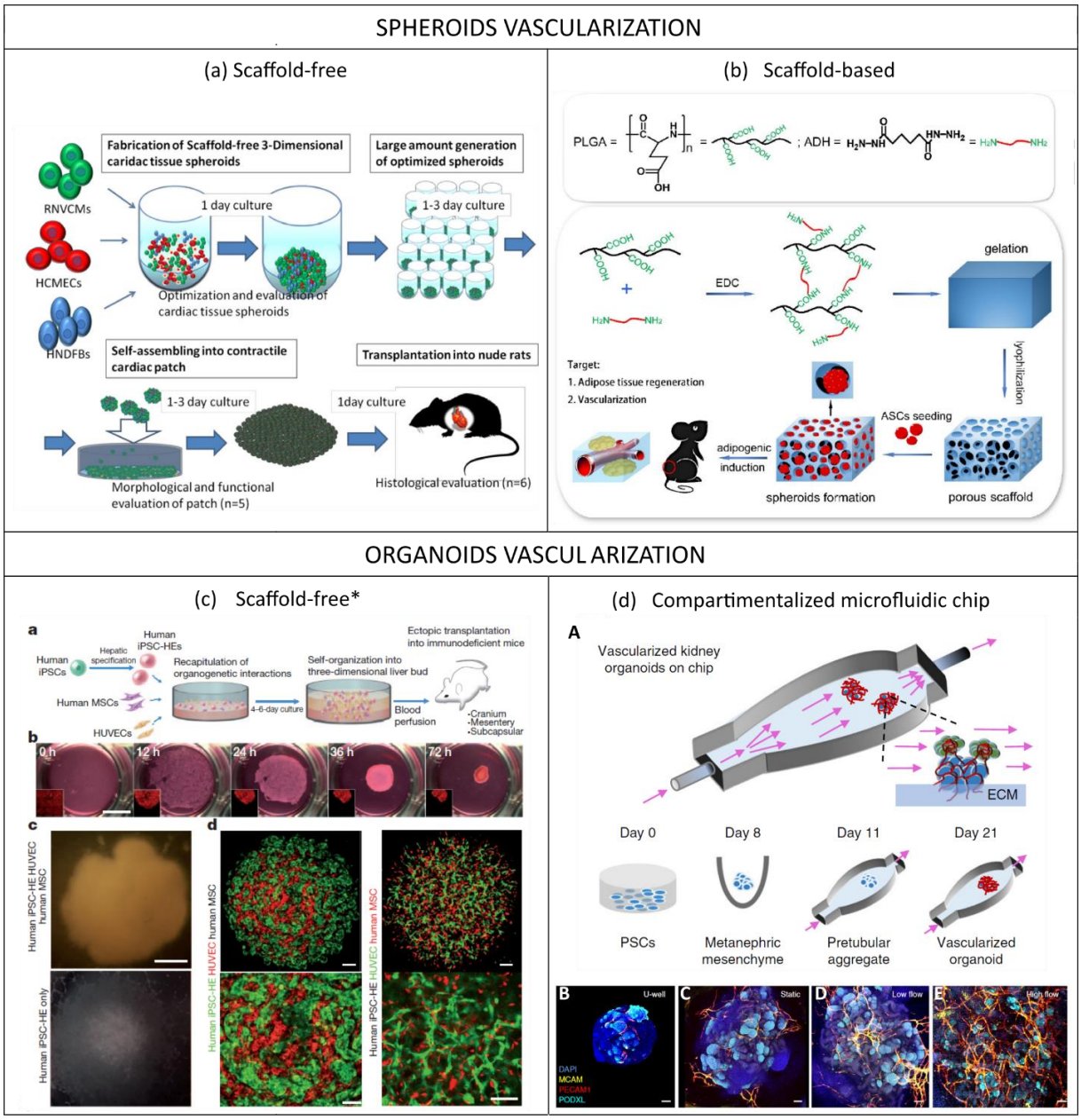

Figure 6. Vascularization approaches for spheroids and organoids: **(a) Scaffold-free approach to vascularize spheroids**. RNVCMs, HCMECs, hNDFs were co-cultured at optimal cell ratios (70%:15%:15%) and plated into ultralow attachment 96 U-well plates to form cardiac tissue spheroids. Then, the spheroids were collected and plated in low-attachment dishes, allowing them to self-organize into cardiac patch grafts under static conditions. Finally, the cardiac patch grafts were transplanted on the anterior wall of the left ventricle of arhythmic rats to induce spontaneous vascularization. Reproduced with permission.[148] Copyright 2016, Elsevier Inc. **(b) Scaffold-based approach to vascularize spheroids**. PLGA activated by 1-ethyl-3-(3-

dimethylaminopropyl) carbodiimide hydrochloride (EDC) and crosslinked with adipic dihydrazide, followed by lyophilization form porous hydrogel. Seeding of ASCs onto hydrophilic surface induced cell aggregations, which resulted in ASC-spheroids. Then, the spheroids were transplanted in the dorsum of nude mice to induce spontaneous vascularization. Reproduced with permission.[147] Copyright 2017, Elsevier Inc. **(c) Scaffold-free approach to vascularize organoids.** a. Schematic representation of the paper's strategy: hiPSCs, hMSCs, HUVECs co-cultured on Matrigel® to form liver organoids, which were transplanted into mice to induce spontaneous vascularization. b. Observation of cells in co-culture overtime. Organoids formed within 72h. c. Observation of hiPSC-organoids (top panel) and conventional two-dimensional cultures (bottom panel). Scale bar = 1mm. d) Confocal images showing presence of hiPSC-derived hepatic endoderm cells (green) and HUVECs (red) inside liver organoids (left panel) –or- HUVECs (green) and hMSCs (red) inside hiPSC-derived organoids. Scale bar = 100µm. Adapted with permission.[117] Copyright 2013, Springer Nature. **(d) Hybrid strategy**. A. Kidney organoids were cultured in ECM substrate housed inside a perfusable millifluidic chip, subjected to controlled fluidic shear stress. B-E. Confocal 3D observations showing vascular markers in whole-mount organoids, cultured under static U-well, static, low-FSS, and high-FSS conditions. Scale bars = 100 µm. Adapted with permission.[137] Copyright 2019, Springer Nature.

Table 4. Summary of case studies for 3D cell culture vascularization strategies

Vascularization method		Tissue/organ model	Biomaterial composition	Cellular composition	Duration of *in vitro* study	*In vivo* evaluation	Refs
Spheroids	Scaffold- free	Bone	-	Osteoblasts, dermal microvascular ECs, normal dermal fibroblasts (all from human)	3 days	2 weeks	[139]
		Dental pulp	-	Dental pulp stem cells, HUVECs	3 days	4 weeks	[129]
		Liver	-	Rat hepatocytes, HUVECs	25 days	NO	[140]
		Heart	-	Rat neonatal ventricular cardiomyocytes, human dermal fibroblasts, human CMECs	7 days	7 days	[148]
		BBB	-	Brain ECs, pericytes, astrocytes (all from primary human source)	3 days	NO	[128]
	Scaffold-based	Skin	Hyaluronan; chitosan	ASCs	3 days	8 days	[152]
		Adipose tissue	PLGA hydrogel	ASCs	2-3 weeks	3 months	[147]
		Bone	• RGD-modified alginate gel • Polyurethane • Poly(propylene fumarate); fibrin	• MSCs • ASCs • hMSCs, HUVECs	• 2-3 days • 3 days • 1-3 weeks	• 2 months • 2 weeks • 9 days	[146,153,154]
Organoids	Scaffold-free	Brain/BBB	-	hiPSCs	Up to 4 months	NO	[156]
		Intestine	-	hESCs/ hiPSCs	35 days	6 weeks	[119]
		Kidney	-	hPSCs	25 days	28 days	[118]
		Brain	• - • -	• hESCs -> ECs & organoids • hiPSCs -> ECs & organoids	• Up to 4 months • 54 days	• 30 days • 7 days	[116,155]
		Liver	-	hiPSC-endoderm cells, hiPSC-ECs, MSCs	3 days	14 days	[125,157]
		Pancreatic islet, brain, heart, lung, intestine, kidney, liver fragments	-	Tissue fragment, HUVECs, hMSCs	1 day	1 month	[126]

4.2.3. Limitations of vascularized 3D cell culture models

Both spheroids and organoids have great potential as vascularized models for disease modelling and drug development purposes. While they bring about promising outlook for the biomedical field, several limitations remain. First of all, both spheroids and organoids generation needs a large number of cells to obtain a substantial quantity of tissue. Secondly, cellular microenvironment is the key factor to achieve viable and functional 3D structures with *in vivo* characteristics, while at the same time promoting angiogenesis.[169] Therefore, ECM or a similar matrix, such as Matrigel®, that is a complex protein mixture from mouse, is commonly used, mainly for organoids. However, due to the heterogeneous composition and immunogenic potential of currently used matrices, an alternative ECM-mimicking source should be considered.[13] Alternatively, biomaterial-based 3D scaffolds have been employed to mimic the components of the ECM while providing structural support and external cues to guide cell-cell and cell-matrix interactions, leading to functional and vascularized spheroids.[156,161–163] While these scaffolds can provide mechanical and biochemical cues for cell growth within the 3D structures, lack of access to adequate supply of oxygen and nutrients to the center of the structure often results to necrotic core and premature growth in the outer layer of organoids, when missing an adequate vascularization of the 3D constructs.[169]

The key requirement for vascularization concerns the surrounding microenvironment, which has to support both angiogenesis and organoid formation.[169] The incorporation of ECs in the cell culture can alleviate this problem by inducing *in vitro* prevascularization, leading to the formation of functional tubular vessels. This increase access to oxygen and nutrients, thanks to functional vessels, promotes cells survival, maturation, and differentiation to specific tissue. HUVEC-covered hepatocyte spheroids had improved cell viability and liver-specific functions such as increased albumin secretion and ammonia removal rates.[149] Cerebral organoids generated from hPSCs formed tubular vessels with pericyte-like cells wrapping around them, while promoting neural differentiation.[165]

As these techniques work with co-cultures, factors such as cell ratios, seeding density, appropriate cell culture medium, co-culture time must be optimized. For example, while it was possible to form spheroids composed of human adipose-derived mesenchymal stromal cells (hASCs) and HUVECs, vascular structures were only observed when 20% ASCs were cultured

with 80% HUVECs in a 1:1 mixture of endothelial and adipogenic medium.[170] Similarly, Noguchi's work showed that contracting vascularized cardiac spheroids were obtained by maintaining the following cell mixture: 70% CMs, 15% ECs, and 15% FBS.[157]

Despite their ability to nourish spheroids/organoids, preformed vessels need to be transplanted in a highly vascularized region to achieve optimal perfusion. The need to experiment on animal models poses a paradox since the one of the main goals of using 3D cell culture models is to reduce animal use in research. Nevertheless, vascularized brain organoids raise ethical concerns and call for consciousness assessment of animal models used in these experiments.[171]

Furthermore, the combination of spheroids/organoids platform with 3D bioprinting and microfluidic technology are necessary to achieve more comprehensive vascularized, physiologically relevant 3D models.[143,146,172] A more in-depth discussion on this topic is presented in **Section 4.4**.

4.3. 3D Bioprinted vascularized models

In the last decades, the word *biofabrication* has been widely used in the scientific community to describe a plethora of processes aimed to manufacture complex products with a biologically-relevant function built from biological building blocks, such as biomaterials, cells or molecules.[173–176] Although biofabrication techniques for tissue engineering and regenerative medicine have been commonly classified into top-down and bottom-up,[177–179] we adopt here the classification proposed by Groll *et al.*[180] Considering the fabrication unit, two approaches can be distinguished, namely bioprinting and bioassembly. While bioprinting uses molecules, that are assembled by means of additive manufacturing techniques based on computer aided design (CAD) models, bioassembly uses pre-fabricated cellular building blocks that can be automatically assembled. Both strategies are followed by a tissue remodeling and maturation phase, which is an integral part of the biofabrication process.[179] Though some bioassembly strategies have achieved successful applications in vascularized tissue models (**BOX 2**), bioprinting represents nowadays the cutting-edge biofabrication technology in the field and will be the main focus of this section.

4.3.1 Current bioprinting technologies

Although the concept of 3D printing encompasses different technologies, as summarized in **Figure 7**, most of them show common advantages for the vascularization of biomaterials: 1) the

possibility to print vessels of different diameters, ranging from microvessels to vessels in the mm range, that can be surgically anastomosed; 2) the use of bioinks, whose composition can improve vascularization; 3) the ability to control the spatial arrangement of cells to promote the formation of vessel networks, eventually with branched, complex geometries.[105] We provide here a general overview of the current 3D bioprinting technologies employed to vascularize tissue constructs. **BOX 1** summarizes the definitions adopted and the critical bioprinting parameters. A more detailed description of the most used commercial bioprinters can be found, for instance, in the work by Ozbolat *et al.*[181]

Inkjet-based

This technology can be applied in a continuous mode or in a drop on demand mode. In the first case the printing ink needs to be electroconductive, which limits its application for biological purposes. Besides, the drop on demand mode is based on the deposition of droplets on the printing surface. To generate and eject the drops, thermal, piezoelectric or acoustic approaches are used (**Figure 7a**). Thermal printing heads heat the bioink locally creating a bubble that pushes the drops through the nozzle. In the case of piezoelectric and acoustic actuators, vibration is at the origin of drop deposition. Compared to other printing techniques, inkjet bioprinting is low-cost and allows for fast printing with high resolution (50 μm). This is a suitable technology for low viscosity bioinks (<10 mPa.s) with a low cell density. Cell viability has been reported in the range of 80-95 % using this method, due to the temperature and the mechanical stress.[182,183]

Laser assisted (LAB)

This technology, also known as laser-induced forward transfer, is a drop on demand method based on the incidence of a pulsed laser beam on top of a donor slide in contact with an energy-absorbing layer. When a bioink is placed next to the energy-absorbing layer, a shockwave appears forming a jet of the bioink that is deposited as a drop on a collector slide (**Figure 7b**). High resolution (5-10 μm) and the possibility to work with a wide range of densities (1-300 mPa.s) and to print the cells on solid or liquid substrates are the main advantages of this strategy. Other benefits are automation, reproducibility and high throughput. Nevertheless, it is a very expensive technology that might cause cell damage. Other drawbacks are cell sedimentation and, when printing 3D constructs, the risk that working wavelengths alter cell organization.

Extrusion based

The most popular 3D bioprinting technologies nowadays are pressure-assisted, that are well adapted for highly viscous and, ideally, structurally stable solutions to avoid loss of shape **(Figure 7c)**. For this purpose, most approaches in the literature combine bioprinting of the ink with *in situ* cross-linking after injection.[105] It is also frequent to work at controlled temperature to assure good viscosity of the bioink and to induce *in situ* gelation. A drawback is that reproducibility depends on numerous parameters, namely needle diameter, air pressure, speed of printing, temperature, humidity. Assuring homogeneity of the bioink during the printing process is particularly relevant in cell-loaded bioinks. Also, excessive pressure can result in cell damage caused by shear stress. Other disadvantages are low speed, low resolution and clogging.

There are several commercially available 3D bioprinters, but the simplicity of the technology leads many research laboratories to manufacture customized printer based on their needs. To print different bioinks without cross-contamination, the use of multiple injectors is often adopted. In the case of vascularized materials, the use of coaxial needles is particularly advantageous to print tubular structures as will be seen in **Section 4.3.2**.

Vat photopolymerization based

The possibility to photocure polymers loaded with biomolecules and/or cells has open new perspectives to create tissue constructs. The process is based on a laser beam that irradiates a resin composed of a solvent, a photo-initiator and a polymer. The photo-initiator reacts to the light source releasing radicals or cations that start the polymerization of the resin. This technology was firstly applied to 3D print low cell compatible resins in the presence of photo-initiators, that were however highly cytotoxic. In the last years, the development of new photo-initiators has expanded the application of this technique to the biomedical field.[175] The high precision and resolution, together with the possibility to incorporate photo-absorbers to prevent photopolymerization in defined regions, makes this technology particularly interesting to engineer vasculature.[176] The extraordinary freedom of design to pattern highly complex hollow vascular-like structures within biomaterials has been recently demonstrated.[177]

Another advantage of vat photopolymerization compared to extrusion is the possibility to use low viscosity resins that improve the resolution compared to high viscosity ones but that can

lead to cell sedimentation. The major drawback of the technology is the cell damage caused by the laser and by oxidative stress due to the activation of the photo-initiators. Laser sources in the UVA-visible spectrum are preferred since they are less toxic than shorter wavelengths in the UVB and UVC regions. In the field of vascularization, the most used photo-initiators are Irgacure 2959 (maximum efficiency wavelength 275 nm) and lithium phenyl-2,4,6-trimethylbenzoylphosphinate (LAP, maximum efficiency wavelength 375 nm), the latter being the less cytotoxic one.[175,178]

Depending on the light source to cure the polymers, vat photopolymerization can be classified in stereolithography (SLA) (polymer cured with a laser), digital light processing (DLP) (polymer cured with a projector), and continuous digital light processing (CDLP)/continuous liquid light processing (CLIP) (polymer cured with oxygen and light emitting diodes).[175,179]

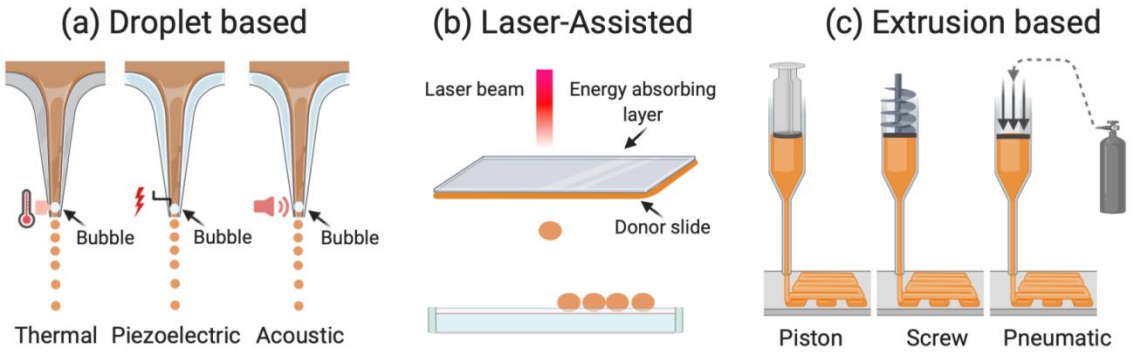

Figure 7. Schematic of bioprinting methods. (**a**) Inkjet-based bioprinting involves the formation of droplets of bioink by generating bubbles in the tip of the printer through thermal, piezoelectric or acoustic energy. (**b**) Laser-assisted bioprinting is also based on the generation of droplets of bioink by the incidence of a laser beam on an energy absorbing layer coupled with a donor slide constituted of bioink. The droplets are then recovered on a dedicated platform. (**c**) Extrusion is the most commonly used method; the ink is pressed through the nozzle either with a piston, a screw or using pneumatic pressure. **(d)** Vat photopolymerization requires the presence of a photo-initiator to cure the polymer loaded with cells. Created with Biorender.com

BOX 1 – DEFINITIONS AND RELEVANT PARAMETERS IN BIOPRINTING

Definitions are given to differentiate between cell-loaded bioinks, hereinafter **"bioinks",** and acellular bioinks that will be named **"biomaterial bioinks",** according to Groll and coll.[272] Most of bioinks are composed of one or several materials, other than cells, being the number of studies using a material-free approach very small, as described in **Section 4.3.2**. Biomaterial bioinks are generally printed to form a scaffold where cells are seeded in a following step, being the risk of heterogenous cell distribution greater, compared to cellular bioinks. In both cases, biomolecules can be incorporated in the ink to exert a biological effect on cells. Other non-biological materials can also be added to affect cell function via mechanical or electrical cues. Materials can also act as mere supports during the printing process, or as sacrificial inks that are removed after the printing process.

Solution viscosity is one of the critical material parameters for inkjet or extrusion bioprinting. The degree of viscosity must permit smooth nozzle extrusion, with homogeneous texture during the whole printing process, and fast solidification after printing.[183] Clogging of the nozzle is frequent due to excessive viscosity or to progressive cell sedimentation. When the solution is not viscous enough, the printed construct risks to collapse or to eventually lose its shape. Viscosity is therefore related to the **printability of the material**, or co-printability of several biomaterials, that must have shear-thinning or thixotropic **rheological behavior** during the printing. To modify the solution viscosity, concentration,[193] or temperature[192] can be tuned. Shao *et al*. used Gel/GelMA solutions cooled at -20 °C for 5 minutes to form a pre-bioink, that was then printed on a platform at 2°C.[192] Additionally, the syringe was turned over every 20 seconds to homogenize cell suspension. A similar approach was followed by Jin *et al*.by using a mixture of gelatin and alginate.[273] For thermal sensitive materials, the printability can be improved by including sacrificial polymers in the bioink solution. Maiullari *et al*. mixed alginate with PEG-fibrinogen, followed by a curing step of the PEG-fibrinogen with UV and the final removal of the alginate with EDTA.[196] Besides printability, viscosity can be also modulated to obtain complex geometries particularly relevant for vascularization. In an elegant work, Lin *et al.* 2019 reported how by increasing the viscosity of a sacrificial bioink made of Pluronic F127, it was possible to avoid viscous fingering at the interface between the printed features and the surrounding material to obtain smooth curved channels.[111] The best way to evaluate viscosity and printability is to perform rheological studies to establish the optimal working ranges of viscosity and storage moduli (for an extensive review about printability and rheological characterization the reader is referred to [274]. Ideal reported values of viscosity are 10 mPa.s for droplet-based bioprinting,[183] with an upper limit of about 100mPa.s,[275] 1-300 mPa.s for LAB and 30-6 x 10^7mPa.s for extrusion.[183] is indicate and has been determined.[275]

The **diameter of the printed element** also affects important physical properties of the final construct, such as porosity, mechanical strength and height of the scaffold.[183] In the case of extrusion, this parameter is closely linked to the needle/ nozzle diameter, the printing pressure and speed, or the flow rate of injection. Low resolution of the extrusion technique remains one of the main limitations to properly vascularize materials by bioprinting and the formation of tubular structures with a diameter similar to small venules, arterioles and capillaries still represents a challenge. Nozzle-free strategies can represent an alternative due to better resolution, compatible with vessels below 100 μm, and less limitation in terms of viscosity and potential cellular toxicity.

Finally, when establishing bioprinting parameters, in addition to the aforementioned, it should not be forgotten that they all affect cell behavior and viability.

4.3.2 Bioprinting strategies for vascularization

Sacrificial bioprinting

Sacrificial bioprinting uses a biomaterial bioink whose sol-gel transition or gelation can be easily controlled. First studies used organic materials soluble in organic solvents,[184,185] and therefore incompatible with the incorporation of cells. Based on previous work where cotton candy was used as sacrificial material to form channels within PDMS, [186] Miller *et al.* reported in 2012 the use of a carbohydrate mixture optimized for bioprinting and subsequent dissolution of interconnected and branched filaments with several diameters.[97] The properties of the printed filaments allowed the formation of microchannels within a wide variety of cell-loaded materials such as agarose, alginate, photopolymerizable polyethylene glycol (PEG), fibrin or Matrigel®. This work inspired numerous studies using the same fugitive ink strategy to mimic the microvascular architecture.[94,111,187–194]

Poloxamers, also known as Pluronic, are poly(ethylene oxide)-poly(propylene oxide)-poly(ethylene oxide)(PEO-PPO-PEO) tri-block polymers with a critical micelle temperature and concentration. This means that at low temperatures they are present in solution, whereas at high temperatures they form micelles and form a gel. In practice, some poloxamers, such as Pluronic-F127, can be bioprinted at temperatures that do not compromise cell viability, and then at 4 °C they become liquid and can be washed, leaving a lumen where endothelial cells can be seeded. This approach has been used by the team of JA Lewis in combination with a fibrin casted gel, in several studies. In 2016, a preliminary study to form a proximal tubule model in a microfluidic chamber was published.[189] Three years later, the same team optimized the composition of the Pluronic-based fugitive ink, and succeeded to print a proximal tubule and a vascular channel that were seeded with epithelial cells and glomerular microvascular endothelial cells respectively, under flow conditions.[111] Also in 2016, they used the same kind of approach to combine HUVECs and hNDFs to form the vasculature, together with osteoinduced hMSC to form a microfluidic platform to create a relevant 3D model of bone (**Figure 8a**).[94] An originality in those works is how the authors made the printed vascular ink interact with the casted cell-loaded hydrogel surrounding it. Briefly, the vascular ink contained thrombin, and the gel that was casted contained fibrinogen and transglutaminase. This way, thrombin diffused from the vascular ink to the surrounding gel causing cross-linking of the material. Using this strategy, the authors were able to form a thick (> 1cm) 3D

chip with endothelialized channels that could be perfused with culture medium to differentiate hMSCs into osteogenic cells.

Gelatin (Gel) is another material that is frequently proposed to form hollow microchannels. Two recent works have used Gel-based fugitive inks to create relevant models of bone. In 2017, Khademhosseini's group reported the use of GelMA with a low degree of substitution to print cylinder rods of around 500 µm within cylinder rods of photocrosslinked gelatin methacryloyl with a high degree of substitution and loaded with hMSC.[190] After removal of the sacrificial ink, HUVECs were seeded in the central channel mimicking the architecture of long bones. Besides, Shao *et al.* have proposed direct co-axial bioprinting to form core-sheath fibers using Gelatin-GelMA, loaded with HUVECs and mouse osteoblast respectively, in a single printing step at 2°C (**Figure 8c**). [191,192] After photocuring GelMA, the temperature is set at 37 °C to liquefy gelatin. The construct is left under static culture conditions for 3 h, to allow HUVECs to adhere, and then dynamic cell culture is done using a shaker. In the same work, authors used this approach to seed HUVECs and human breast cancer cells (MDA-MB-231) to create a cancer model. This biofabrication method presents numerous advantages due to the ability to print complex shapes with controlled heterogenous composition, in a relatively fast way. Nevertheless, further research is needed to confirm the presence of an endothelialized and perfusable lumen.

The use of bioprinting to vascularize hepatic constructs is not yet widespread.[193,195] Recently, a preset extrusion bioprinting technique using alginate as sacrificial ink was employed for liver multiscale tissue engineering.[193] A preset cartridge was prepared with collagen 3 %, loaded with cells, and alginate 3% as fugitive material. The design was established to mimic the hepatic lobule, with EA.hy 926 endothelial cells around the lumen (150-200 µm), in the external surface of the construct and radially interconnecting both surfaces. In the space between ECs, hepatic cells (HepG2/C3A) were printed. Using a preset cartridge allows to control the spatial disposition of the cells with just one printing head. However, compared to other strategies, the dimensions of the printed construct are smaller (4 mm width x 5.2 mm height x 2.5 mm thick). Alginate was also chosen to prepare vascularized cardiac tissue (**Figure 8b**).[194] The aim of this work was to prepare a tissue construct for personalized therapy and drug testing. For this purpose, authors used decellularized omentum (peritoneum) to form a thermoresponsive hydrogel to print

CMs, and sacrificial alginate to bioprint HUVECs. In the cardiovascular field also, the work by Maiullari and coll. describes the use of co-axial bioprinting to prepare a cardiac patch.[196]

Coaxial deposition

Coaxial deposition systems use concentrical nozzles to (i) cross-link the bioink during the extrusion process and (ii) directly print tubular structures that can mimic the multilayered organization of the vasculature. In the mentioned work by Maiullari and coll., a microfluidic printing head was used to perform coaxial microextrusion.[196] The inner needle injected a bioink composed of alginate, PEG-fibrinogen and cells, either HUVECs or iPSC-derived cardiomyocytes, whereas the external needle injected a $CaCl_2$ solution to cross-link the alginate. After bioprinting, UV was applied to cross-link PEG-fibrinogen, and then alginate was removed by ethylenediaminetetraacetic acid (EDTA) washing. Notably, the authors could engineer fibers with the two cell types in a "Janus" conformation that proved to be the most effective to generate vessel-like structures, compared to alternating layers of cells at two different ratios.[196]

Another interesting example of coaxial printing, is the work by the team of A Khademhosseini, that used this technology to print perfusable tubular constructs with needles ranging from 14 G to 30 G leading to internal diameters ranging from about 400 μm to 1 mm (**Figure 8d**).[109] As in previously mentioned works by the same group, GelMA with an adjusted degree of substitution was used together with alginate as sacrificial ink. During the printing process, alginate was ionically cross-linked with Ca^{2+}. Once the GelMA was photo-crosslinked, the construct was washed several times and treated with EDTA to remove all the cationic ions. To obtain a stable tubular construct after removal of the alginate and improve the mechanical properties of the GelMA after cross-linking, different amounts of polyethylene glycol tetra acrylate (PEGTA) were included in the mixture. This study was mainly focus on the biofabrication method to prepare endothelialized constructs, and the cells employed were HUVECs and MSCs. Soon after, they applied the co-axial extrusion technology to prepare an endothelialized myocardium and a heart-on-a-chip.[108,197] In this case, plain microfibers with a diameter of 300 μm were printed leading to homogenous HUVECs distribution. Interestingly, the authors reported a progressive migration of the cells to the surface of the microfibers, as alginate was released. Though cells formed a monolayer similar to an endothelium after 15 days, the final constructs did not present a lumen and were not perfusable.

Pancreatic islets were printed together with endothelial progenitor cells (EPCs) using a coaxial extrusion nozzle for the treatment of type I diabetes.[198] Similar to previous works, a mixture of alginate and GelMA was used for ionic crosslinking and photocrosslinking, respectively, but in this case the endothelial cells were printed around the fiber containing the islets. Unexpectedly, the presence of EPCs did not improve islets function. On the contrary, the authors reported reduced insulin secretion of the islets probably due to reduced diffusion of glucose and hypoxia in the core fibers.

In the work by Leucht *et al.*, authors printed two different compartments with two bioinks to engineer vascularized bone bioconstructs.[199] By mixing Gel, GelMA and acetylated gelatin methacryloyl (AcGelMA), the authors significantly reduced the stiffness of the native G while increasing the swellability. This bioink loaded with human dermal microvascular endothelial cells (hDMECs) was printed in a concentrical compartment next to a second compartment where human adipose derived stem cells (hADSCs) differentiated in osteoblasts were previously bioprinted. The transparent vascularization gels were cured using a LED-UVA lamp (385 nm). The authors demonstrated that softer materials led to better results in terms of number of vascular networks, length and number of nodes. Another way to print different bioinks or biomaterials bioinks, is to use multi-head printers. In the work by Jang *et al.*, 3 different bioinks loaded with human cardiac progenitor (hCPC) cells or hMSC, or a mixture of both were printed to fabricate cell patches for cardiac repair.[200] They used decellularized ECM as biomaterial, with vitamin B_2 and VEGF to improve vascularization, and implanted the construct in a rat model of heart ischemia. Results demonstrated the benefits of a patch with a specific pattern of CPCs and MSCs, that improved cardiac function and reduction of fibrosis, together with an increased neovascularization.

The possibility to print several bioinks in the same construct was exploited to create a gradient of growth factors in a construct for bone vascularization.[190] As described previously in this section,[109] Gel was prepared with two degrees of substitution, low and high. The low GelMA was used as sacrificial biomaterial bioink to form a hollow channel of around 500 µm inside the construct to form a perfusable blood vessel, mimicking the architecture of long bones. Concentric rods with four different formulations were printed to create both vasculogenic and osteogenic niches. By modifying the GelMA composition (low to high), the cells ratio (HUVECs and hMSCs), the silica nanoplatelets and VEGF concentrations, the authors engineered a perfused scaffold with

gradients of biochemical cues to promote both osteogenic differentiation and vascularization. In contrast to the previously mentioned studies,[109,198,201] in this case cross-linking of GelMA occurred in the capillary, before extrusion of the bioink. Another bioactive compound that has been incorporated in a biomaterial bioink for bone tissue engineering is nanohydroxyapatite (nHA).[202] In this work, a mixture of gelatin and nHA was printed using Pluronic as sacrificial support to allow the cross-linker genipin to act during 48 h. Then, Pluronic was removed and HUVECs, hMSCs and/or osteodifferentiated hMSCs were added in a solution made of GelMA-fibrin, that was photocrosslinked.

Stereolithography

The photocuring of polymers to engineer tissue vasculature is still at its early stage. Even if works using this strategy to vascularize tissue relevant constructs are very few, they hold great promise in view of the rapid evolution of the technique. In 2017, Zhu *et al.* used this technique in a pioneer work to bioprint a model of liver including HUVECs, MSCs and HepG2 cells.[200] This construct was subcutaneously implanted in a murine model demonstrating the anastomosis of the implant. Miri and coll., faced one of the main limitations of this technology by building up a microfluidic device to allow stereolithography of a multimaterial construct.[201] This way, they produced a simplified model of breast cancer including HUVECs and MCF7 cancer cells. Another model of breast cancer using SLA was more recently developed by Cui *et al.* to evaluate migration of metastatic cells to bone.[202]

In an elegant work published in 2019 in Science, Grigoryan and coll. proposed the incorporation of food additives as photo-absorbers to form hydrogels with very complex and intricated networks to mimic several tissues, including an alveolar model.[177] They also created a prevascularized construct with a network of HUVECs connected to hepatocyte aggregates, that was subcutaneous implanted. Hepatic cells functionality two weeks after implantation was demonstrated but the benefits of including an endothelial cell network in the production of albumin was not proved, although histological examination evidenced the anastomosis of the implant.

Vat-photopolymerization can be combined with other 3D-printing techniques. This is the case of the recent work by Hann and coll., in which fused deposition modeling (FDM) for sacrificial PVA printing was combined with SLA for GelMA and PEGDA curing to build a channeled construct as model of bone tissue.[203] Compared to the use of photo-absorbers to form hollow

channels, the resolution of FDM was however really low, leading to vessels of several hundreds of microns.

Bioprinting holds great potential in the fabrication of diseased tissues as well, even if studies in this regard are still limited.[192] Besides the case studies already mentioned, Liu *et al.* have recently proposed a model of atopic dermatitis fabricated by hybrid biofabrication combining electrospinning and extrusion bioprinting for the study of this skin disease and drug testing.[203] For a comprehensive review about hybrid biofabrication, we refer the reader to reference [204].

Scaffold-free bioprinting and alternative strategies

A promising bioprinting strategy for vascularization in alternative to scaffold bioprinting is scaffold-free bioprinting, which is based on the capacity of cells to self-assembles after bioprinting and spontaneously form constructs that mimic the native tissue architecture and function. However, this strategy requires a large number of cells as well as a post-printing incubation period that prolongs the process and increases the costs. This explains why the number of studies using this technique to recreate the vasculature is currently limited and mainly focused on the fabrication of larger blood vessels (≥1mm).[205–208]

All the works described in this section so far, deal with extrusion bioprinting. There are however two examples of laser induced forward transfer worth mentioning within the scope of this review. In 2011, Gaebel *et al.* reported the fabrication of a cardiac patch using a polyester urethane urea patch immersed in Matrigel®.[209] Using laser bioprinting, HUVECs and hMSCs were printed on the patch following a defined 2D pattern. This patch was implanted in an infarcted rat model and improvement of some cardiac functions and neovascularization were observed. More recently, intraoperative bioprinting of stem cells from the apical papilla and HUVECs using LAB has been successfully done to treat a mouse calvaria defect.[210] **Table 5** summarizes significant case studies for the bioprinting vascularization strategies, cited or discussed in the text.

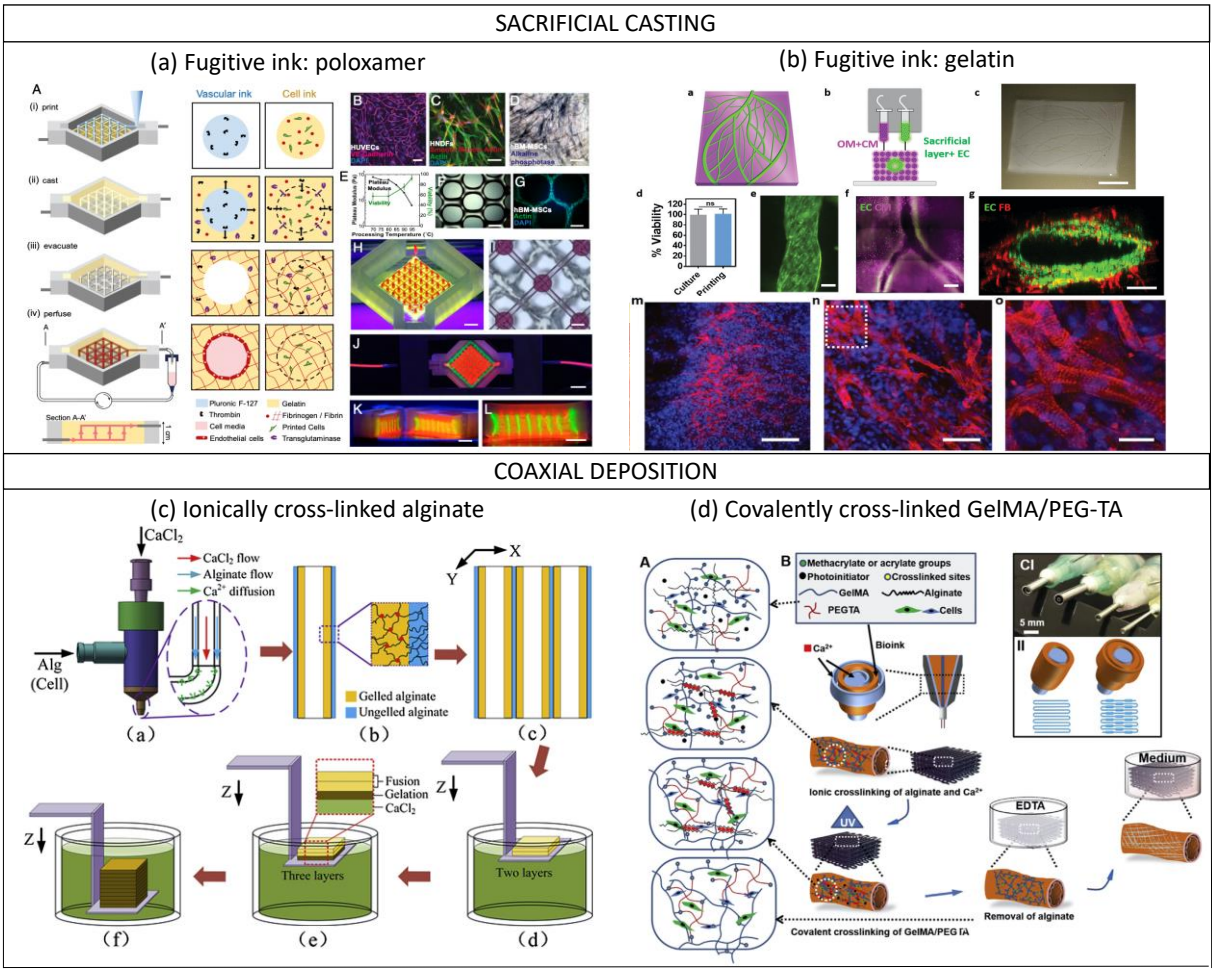

Figure 8. Bioprinting – based vascularization strategies: sacrificial casting (top) and coaxial deposition (bottom). **(a) Bioprinting of thick vascularized tissues with sacrificial poloxamer**. (A) Manufacturing process in 4 steps: i) printing of the sacrificial poloxamer-thrombin biomaterial bioink and of cell-laden gelating bioink with endothelial cells; ii) casting of the gelatin/fibrinogen/transglutaminase that interacts with the thrombin diffused from the printed biomaterial causing gelification; iii) removal of the poloxamer by cooling down leading to empty channels; iv) perfusion of the channels with cell media that results in endothelialization of the channels. (B, C, D) Three cell types were incorporated, HUVECs (B), hNDFs (C) and hMSCs (D). (Scale bar: 50 μm.). (E) cell viability and mechanical properties of the construct are affected by gelatin pre-processing temperature. (F, G) hMSCs-laden bioink immediately after printing (F) and after 3 days (G). (H - K) Images of the bioconstruct. (H) Sacrificial bioink colored in red and cell-laden bioink in green. (Scale bar: 2mm). (I) Bright field image from top. (Scale bar: 50 μm.) (J) Construct in a perfusion chamber and (K, L) cross-sections. (Scale bar: 5 mm). Reproduced with

permission.[94] Copyright 2016, PNAS. **(b) Bioprinting of thick cardiac patches with sacrificial gelatin**. (A) Two bioinks composed of decellularized omentum tissue (OM) + cardiomyocytes differenciated form iPSCs (CM) and sacrificial gelatin + endothelial cells (ECs). (B) 3D-model of the cardiac patch. (C) Printed cardiac patch. (D) Fluorescence images of the printed cardiac patch with the ECs (green), CM (purple), and fibroblasts (red). (Scale bars: 100, 500 and 100 μm, respectively). The cardiac patch was implanted between two layes of the rat omentum and then explanted for analysis. (E) Fluorescence images of the explanted patch showing the sarcomeric actin of the CM in red and nuclei in blue. (Scale bars from left to right: 100, 50, 25 μm). Adapted with permission.[190] Copyright 2019, WILEY-VCH. **(c) Co-axial bioprinting of 3D hydrogels with microchannels using alginate**. (a) Schematics of the co-axial nozzle in which alginate and $CaCl_2$ are co-injected to form (b) channels with an inner layer of ionically cross-linked alginate surrounded by ungelled alginate. (c) Several channels are printed in parallel and then (d) immersed in a bath with $CaCl_2$ to promote € gelation of the non-crosslinked alginate. (e)This step is repeated several times to create a 3D construct. Reproduced with permission.[187] Copyright 2015, Elsevier Inc. **(d) Multi-layer co-axial bioprinting of perfusable 3D constructs with a blend bioink**. (A) The bioink gels through ionical cross-link of alginate with Ca2+ and photo cross-link of GelMA and polyethylene glycol (PEGMA) exposed to UV irradiation. (B) Schematics of the co-axial nozzle in which the blend bioink is injected in between $CaCl_2$ solution to cause immediate alginate gelation. After UV irradiation, the alginate is removed in contact with EDTA and the construct placed in cell culture medium. (C) Multilayered co-axial nozzles (I) and schematics of the channel formation (II). Reproduced with permission.[193] Copyright 2016, Elsevier Inc.

Table 5. Summary of case studies for bioprinting vascularization strategies. Abbreviations not used previously: **Col** collagen; **GMECs** glomerular microvascular endothelial cells; **hiPSC-CM** induced pluripotent stem cells derived cardiomyocytes; **hiPSC-EC** induced pluripotent stem cells derived endothelial cells; **I** inner diameter; **O** outer diameter; **PCL** polycaprolactone; **PTECs** proximal tubule epithelial cells.

Vascularization method	Co-axial	Sacrificial	Organ/tissue model	Needle diameter	Vessel caliber	Biomaterial composition	Cellular composition	Duration of *in vitro* study	*In vivo* evaluation	Refs
Extrusion-based	NO	NO	Bone	0.33 mm (I)	Microvessels	Gel, GelMA, Ac-GelMA	hDMECs, hADSCs, hADSCs differentiated in osteoblasts	14 days	NO	[196]
			Heart	26G	Microvessels	PCL, Heart derived ECM	MSC, CPC	5 days	YES	[197]
			Skin	0.25 mm	Microvessels	PLGA, Fibrin	iPSC-ECs, Perycites, Neonatal fibroblasts, Keratynocytes	7 days	NO	[204]
			Heart	1.6 mm	1 mm	Agarose, Alginate, Platelet rich plasma	HUVECs, H9c2 CM	14 days	NO	[184]
			Liver	0.25 mm	Microvessels	PCL, Col	HUVECs, hLFs, Hepatocytes	14 days	NO	[191]
		YES	Liver	0.5 mm	0.15-0.2 mm	Col 3%, Alginate 3% (sacrificial)	EA.hy 926, HepG2/C3A	10 days	NO	[189]
			Bone	0.7 mm	Microvessels	Gel/nHA, Gel-MA/fibrin	HUVECs, hMSC hMSCs differentiated in osteoblasts	5 weeks	NO	[199]
			Heart	30 G	0.3-0.4 mm	Decellularized omentum, Alginate (sacrificial)	hiPSC-ECs, hiPSC-CMs, HUVECs, Rat CM, fibroblasts	7 days	NO	[190]
			Bone	0.5 mm	0.5 mm	GelMA-high, GelMA-low (sacrificial)	HUVECs, hMSCs	21 days	NO	[186]
			Bone	0.1-0.4 mm	0.4 mm	Gel, Fibrinogen, Thrombin Transglutaminases, Poloxamer (sacrificial)	HUVECs, hNDFs, hMSCs	>6 weeks	NO	[94]
			Kidney	0.41 mm	0.2 mm	Gel, Fibrinogen, Transglutaminase Poloxamer (sacrificial)	GMECs, PTECs	18 days	NO	[102]
	YES	YES	Cancer tissue & Osteogenic tissue	27 G (I), 17G (O)	0.2-1 mm	GelMA, Gel (sacrificial)	HUVECs, MDA-MB-231, MC3T3-E1	20 days	NO	[188]
			Heart	26G (I), 19G (O)	Microvessels	PEG, Fibrinogen, Alginate (sacrificial)	HUVECs, iPSC-CMs	7 days	YES	[192]
			Heart	27G (I), 18G (O)	0.2 mm	GelMA, Alginate (sacrificial)	HUVECs, Neonatal CM	28 days	NO	[194]
			-	27-30G (I), 18-25G (O)	0.3-1.5 mm	GelMA, PEGTA, Alginate (sacrificial)	HUVECs, MSCs	21 days	NO	[193]
			Cardiac	27G (I), 18G (O)	0.3 mm	GelMA, Alginate (sacrificial)	HUVECs, Neonatal CM	33 days	NO	[108]
			Pancreas	0.4 mm	Microvessels	GelMA, Alginate (sacrificial)	hEPCs, Pancreatic islets (organoids)	15 days	YES	[195]
Laser based	-	-	Heart	-	Microvasculature	Polyester urethane urea patch, Matrigel®	HUVECs, hMSC	8 days	YES	[210]
	-	-	Bone	-	Microvasculature	Col	HUVECs, SCAPs	-	YES	[211]

Vat photopolymerization: SLA	-	-	Liver	-	Microvessels	Glycidal methacrylate-HA, GelMA Photo-initiator: LAP	HUVECs, MSCs, HepG2	7 days	YES	[200]
	-	-	Breast cancer	-	Microvessels	GelMA, PEGDA Photo-initiator: LAP	HUVECs, MCF7, C2C12, Fibroblasts, MSCs	7 days	NO	[201]
	-	-	Liver	-	Microvessels	GelMA, PEGDA Photo-initiator: LAP Photo-absorbers: tartrazine, curcumine, anthocyanine	HUVECs, hepatic aggregates (rat primary hepatocytes & NHDFs)	-	YES	[177]
	-	-	Breast cancer	-	500 microns and Microvessels	GelMA, PEGDA Photo-initiator: Irgacure 2959	HUVECs, breast cancer cell lines: MDA-MB-231 and MCF-7, hFob	14 days	NO	[202]
Dual 3D printing (SLA and FDM)	-	-	Bone	-	0.5-1 mm and Microvessels	GelMA, PEGDA, PVA (sacrificial) Photo-initiator: Irgacure 2959	HUVECs, hMSCs	20 days	NO	[203]

4.3.3. Limitations of bioprinted vascularized models

3D bioprinting is an interesting technique for tissue engineering and particularly for vascularization but some current limitations still need to be addressed. As already mentioned, an important drawback concerns the poor resolution that currently makes extrusion printing of objects below 100-200 μm a real challenge. This limitation is even more important when it comes to direct channel printing by co-axial extrusion. That is why obtaining fully prevascularized constructs by bioprinting is not currently possible and the formation of microvasculature requires a post-impression maturation stage that can last several weeks. Other bioprinting techniques, such as LAB, show better resolution, but their use for tissue vascularization is currently limited, mainly due to high cost and limitations to print multiple materials.[211]

The homogeneity of the bioink during the bioprinting process, particularly relevant in the manufacture of larger constructs, represents another drawback. Cells at high concentrations tend to sediment, making the bioink not homogeneous. Moreover, the viscosity of the bioinks fundamental for its printability since it determines the cell density, it affects the mechanical properties of the final construct as well as the cellular viability and behavior (proliferation, differentiation, migration, etc.). Future studies should pay more attention to this aspect and carry out experiments that help to identify the optimal mechanical properties to promote adequate vascularization.[212] In this regard, it is worth mentioning the extrusion bioprinting studies that are already being carried out in space, where microgravity allows the use of less viscous bioinks and the formation of particularly interesting geometries for vascularization, such as voids and tunnels.[213]

Finally, we have seen that a common strategy is the printing of photopolymerizable materials in the presence of a photoinitiator. These materials are often obtained by chemical modification of natural polymers, such as Gel, to incorporate methacrylate groups that polymerize after irradiation at a certain wavelength and in the presence of a photoinitiator. There are many studies focused on the development of cytocompatible photoinitiators, since those currently used are not considered totally harmless to the body and the presence of methacrylate groups can pose a problem for therapeutic use.[214] Furthermore, as already mentioned, the presence of these groups creates materials with mechanical properties that should be further investigated.

Bioprinting is a relatively young technology that has come a long way in the last decade, opening up previously unthinkable possibilities for tissue engineering. Current limitations are

mainly due to the bioprinting method and can be overcome by combining several printing strategies on a single platform.[213] We envision that the advances of this technology over the next few years will contribute considerably to the development of vascularization strategies of physiologically relevant models.

BOX 2 – BIOASSEMBLY STRATEGIES FOR VASCULARIZATION

Micromodule Assembly strategies

Micromodule assembly refers to a category of modular TE strategies in which microscale building blocks are assembled to create larger tissues,[276] with the advantage that the single units provide cells with efficient gas exchange and nutrients supply at the microscale and vascular networks can be easily integrated.[277] The formation of modular vascular tubes is commonly achieved by using micromolds or by creating cell-laden microgels, that are then assembled by photopolymerization,[278], random packing,[279] or direct assembly.[280] Despite the scalability of these technologies, that provide dense cellular population while ensuring perfusion and diffusion and enable to control features at the microscale by tuning the building blocks properties, the lack of some fundamental requirements, as the mechanical stability, hampers their translation towards clinical application and successful engineering of vascularized tissue constructs.[280]

Cell Sheet Engineering

Scaffold-based TE approaches are often limited to low cellular density, lack of a functional vascular network and, consequently, inability to create thick constructs that do not undergo necrosis.[281] Cell sheet engineering has emerged in the 90's as scaffold-free approach for the manufacturing of 3D cellular constructs with native tissue properties,[276] and it has been successfully applied for cornea and trachea reconstruction, production of skin and bladder equivalents and myocardial tissue regeneration.[282,283] The technique consists of growing cells, that spontaneously produce ECM and form sheets, and subsequently assembling of the sheets by stacking or rolling them to obtain 3D or cylindrical tissue engineered blood vessels (TEBVs).[284,285] This technique has been used to engineer artificial vessels composed of up to three cellular layers (adventitia, media and intima) that have been used as artery models and grafted *in vivo* to promote regeneration of the host vasculature.[284,286] Recently, the sheets manipulation has been improved by using temperature-responsive culture substrata as poly(N-isopropylacrylamide) (PIPAAm), that enable sheets release by simply lowering the temperature.[285] Thick cardiac tissues (1 mm), prevascularized *in vitro*, were fabricated by multi-step implantation of stacked sheets into animal models, that showed pulsatile cardiac tubes with beating up to 1 year and formation of microvasculature *in vivo*.[281] Though cell sheet engineering is mainly used in therapeutics and regenerative medicine,[287] the physiological tissue architecture and mechanical properties that can be achieved with this strategy make it interesting for developing highly organized and densely vascularized tissue models.

Nanofabrication

Most of the biofabrication techniques require a maturation phase of the tissue after assembly, usually carried out with bioreactors, that provide the tissue with nutrients, mechanical stimuli and flow under dynamic culturing conditions.[288] To overcome these limitations and provide cells with nanostructured scaffolds, nanotechnology- based strategies have been used to fabricate tissues and vascular-like structures:[174,289] phase separation and self-assembly of peptidic domains of biological polymers, as collagen or elastin, have been used as strategies to engineer nanofibers, nanotubes and nanowires for vascular TE applications.[290,291] However, electrospinning is the main nanofabrication technique for vascularized constructs:[289,292] tubular scaffolds have been electrospun by using rotating mandrels or combination with electrospraying to create highly cellularized constructs,[293] and multilayer core-shell constructs resembling the blood vessels structure have been manufactured by coaxial electrospinning. [294–296] Electrospun scaffolds for vascular TE have been manufactured with a variety of natural and synthetic polymers and their combination in blends leads to devices with physiologically relevant mechanical behavior while promoting cell adhesion and proliferation.[297–300] The fibrous and porous architecture created by electrospinning mimics the *in vivo* ECM nano-environment and the fibers can be easily functionalized or grafted with molecules, peptides, drugs or growth factors to promote cell adhesion, endothelialization and antithrombogenic properties.[301–303] However, few electrospun vascularized organ-specific *in vitro* models have been reported,[304] as most of the works use electrospun membranes or meshes for coculturing of cells with no physiologically relevant 3D vasculature.[305] In fact, although electrospinning has been used for bone, skin, heart, liver, ligament and kidney TE, it finds its main application in tissue repair and regeneration, as wound healing and dressing,[306] osteochondral implants,[307,308] and tissue engineered vascular grafts (TEVGs).[297] Moreover, it shows several limitations as (i) low production rate,[306] (ii) pore size and fibers density that hinders cell infiltration,[302] and (iii) 2D thin shape at the macroscopic scale.[309] Although some drawbacks have been addressed, for instance cell infiltration can be increased by surface treatments or by coupling with other techniques to enhance macro-porosity,[310] and thick scaffolds can be engineered by multilayered electrospinning,[311] bioprinting remains nowadays the most used and versatile technique for the biofabrication 3D vascularized tissue models.

4.4. Hybrid strategies

In the last years, the need to engineer sophisticated biomimetic *in vitro* models has led researchers to combine different vascularization techniques discussed so far in the same manufacturing process, making classification in distinct classes often reductive. The rise of hybrid strategies for vascularization has the advantage that the unique features and strengths of different fabrication strategies for vascularization of physiologically relevant 3D models can be recapitulated on a single platform and we report here some significant examples of this approach (**Figure 9**).[216,217]

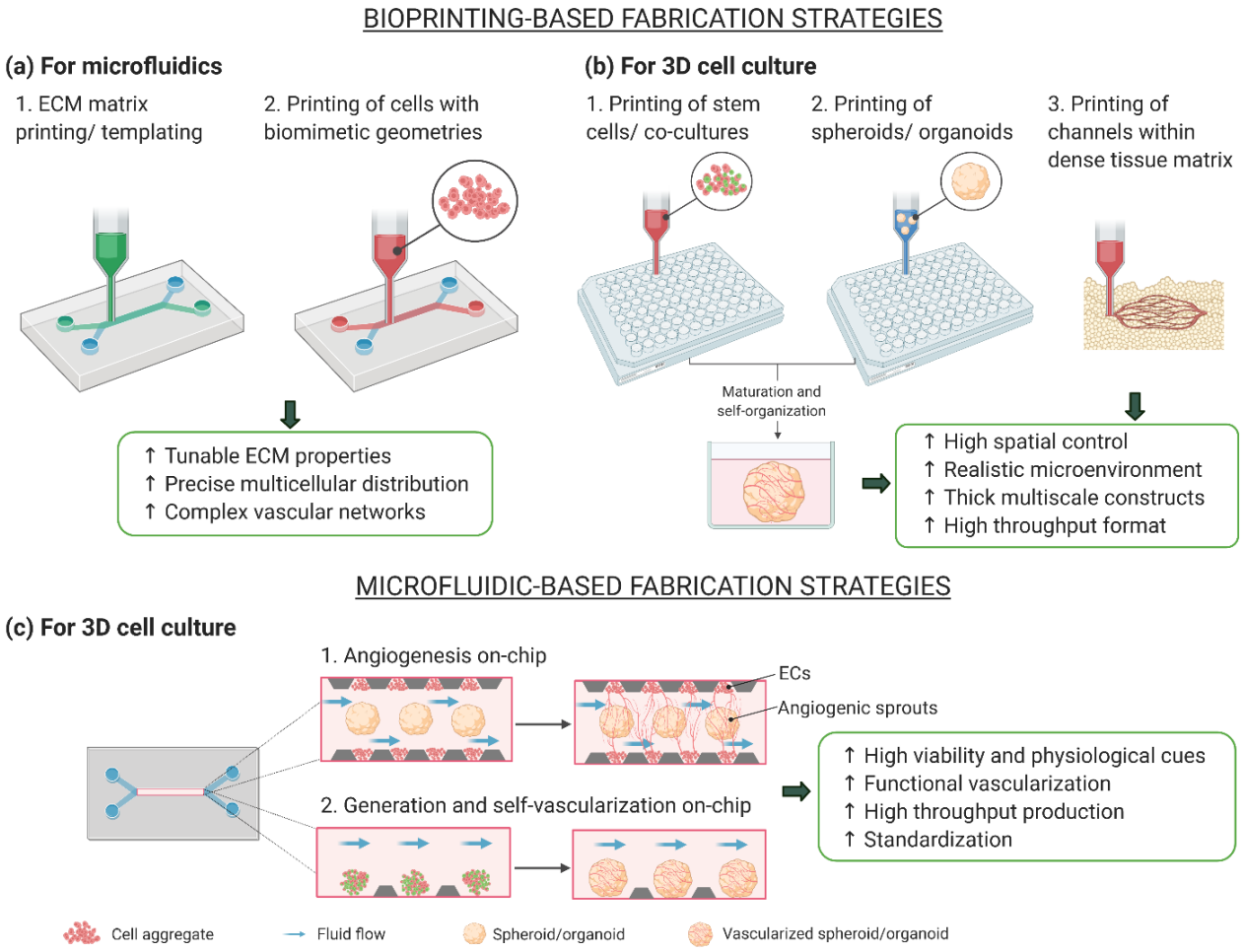

Figure 9. Hybrid strategies for vascularization. The hybrid approaches are divided into (a) bioprinting-based and (b) microfluidic-based. The main advantages of the application of these fabrication strategies for each model are shown in the green panels. Created with BioRender.com

4.4.1. Bioprinting-based hybrid fabrication strategies

Many studies have focused on the use of 3D bioprinting strategies, discussed in detail in **Section 4.3**, for the fabrication of vascularized organ-on-a-chip platforms (**Figure 3f**). This approach shows several advantages such as the capability of recreating physiological-like multi-cellular spatial organization within the device and direct manufacturing of 3D perfusable vascular geometries, reducing the fabrication steps and moving towards more reproducible and automated strategies.[218] Moreover, this technique has shown its potential in vascularizing large tissue constructs and integrating patient-derived cells, representing a valuable tool for personalized medicine.[94,219,220] Bioprinting can be used either to (i) print hydrogels as template for channels fabrication on-chip or to (ii) directly print vascular networks on-chip from cell-laden boinks (**Figure 9a**). These models, often embedded in an ECM matrix, are commonly perfused by integration within microfluidic bioreactors, produced by soft-lithography or 3D printing technologies.[19,221–223]

In a recent work, a perfusable liver model was fabricated with GelMA hydrogel loaded with hepatocytes by using agarose as fiber template.[103] The cell-laden matrix was casted in a PMMA mold and the agarose was bioprinted in the shape of a channel by microextrusion. After UV photocrosslinking of GelMA, the agarose fiber was removed to form the hollow channel and the device was embedded in a PDMS-PMMA bioreactor for perfusion. A functional lumen was obtained by subsequent seeding of HUVECs in the empty channel and the platform was used for drug toxicity assays. Lin *et al.* used extrusion-based sacrificial bioprinting to engineer 3D vascularized proximal tubule models for the study of kidney reabsorption phenomena.[102] They used Pluronic F127 and high-molecular-weight poly(ethyleneoxide) (PEO) as fugitive ink to print colocalized convoluted proximal tubule and vascular channel embedded in an ECM matrix of gelatin and fibrin (**Figure 4d,** see **Section 4.3.2**).[185] A silicon gasket holding the structures allowed for perfusion of the tubule after dissolution of the fugitive ink at 4°C. Proximal tubule epithelial cells and glomerular microvascular endothelial cells were seeded to form a functional epithelium and endothelium respectively. Studies of albumin and inulin uptake confirmed selective reabsorption mechanism from the tubule to the vascular network and glucose reabsorption 5- to 10-fold higher compared to Transwell®-based models. The reabsorption functions of the tubule and the role of the endothelium were investigated as well after administration of glucose transport inhibiting drug and simulation of hyperglycemia conditions.

Although bioprinting techniques are increasingly used for printing perfusable microfluidic networks, the bioprinting step is often limited to the fabrication of polymeric tubular structures, that are successively washed to form hollow channels and seeded with cells, as described above.[102] Recent works are focused on the bioprinting of cell laden gels on-chip: this strategy allows a reduction of the fabrication time by eliminating the need for the cell seeding step and it ensures a more precise and homogeneous cellular distribution and alignment, eventually in complex multilayered geometries.[104,105,224] In this context, coaxial needle technology has been used in several studies to directly fabricate endothelialized perfusable tissues.[108,193] 3D multi-layer circumferential channels have been recently engineered by using single-step coaxial needle manufacturing to reproduce human tubular tissues as urethra and blood vessels.[104] A GelMA and alginate hydrogel blend combined with eight-arm poly(ethylene glycol) acrylate with tripentaerythritol core (PEGOA) was used as bioink and extruded after cells encapsulation by using up to 3 circumferential needles. Urothelial tissue was created by bioprinting a core layer of human urothelial cells (HUCs) and an external layer of human bladder smooth muscle cells (HBdSMCs) while vascular tubular tissues were composed of HUVECs and hSMCs circumferential layers. Results confirmed long-term viability (2 weeks), proliferation and differentiation and showed the advantages of this method in creating functional tubular constructs for regenerative medicine and modeling (**Table 2**).

Recently, 4D bioprinting has emerged as technique for spatiotemporal control of networks self-assembly by using smart materials that respond to external stimuli (temperature, pH, swelling, …). Thus, reversible self-folding tubular constructs can be engineered and their properties controlled over time by tuning the external cues, making this approach particularly interesting for programming the cellular microenvironment and creating functional hybrid hierarchical bioconstructs.[225,226] Bioprinting strategies for vasculature and OOaC design have been extensively reviewed elsewhere.[109,110,220,226–228]

3D bioprinting has been also used for fabrication of 3D cell cultures so as to overcome some of the current drawbacks, as spheroids/organoids variability and low throughput,[160,229] and spheroids/organoids models bioprinted on multi-well plates have been successfully developed for high throughput screening of compounds. Different bioprinting techniques have been adopted for either (i) printing of PSCs-only bioinks, subsequently self-organized in 3D aggregates, or (ii)

spheroid/organoid-laden hydrogels (**Figure 9b**).[230–233] Using a commercial 3D bioprinter, Higgins et al. generated large numbers of homogeneous functional kidney organoids in an automated fashion. Organoids were bioprinted from hPCSs bioink into 96-well plates and results showed formation of glomerular, epithelial and endothelial components and the capability to respond to drug-induced toxicity. The bioprinter enabled the production of more than 600 organoids per hour while the manual generation was estimated to be about 30 organoids in the same timeframe.[230] Vascularized adipose microtissues were created starting from a coculture of adipose-derived stem cells and HUVECs spheroids. [134] The spheroids were successfully used as bioprinting blocks encapsulated in a GelMA hydrogel mixed with a lithium-based photoinitiator. The spheroid-laden bioink was printed into a multi-layer structure and the GelMA matrix was cross-linked through UVA irradiation. Results confirmed adipogenic differentiation, formation of vasculature and spheroids growth up to 14 days of culture. Vascularization of iPSC-derived organ building blocks has been achieved via sacrificial writing into functional tissue (SWIFT) by the group of J Lewis.[234] A matrix of collagen I and Matrigel® was used as scaffold to tightly pack thousands of organoids that led to a highly dense tissue matrix after centrifugation. SWIFT was used for 3D printing of gelatin as sacrificial material within the matrix. After gelatin removal, the system could be perfused and functional lumens were formed by flow of HUVECs. This technique was used to generate perfusable cerebral organoids and cardiac spheroids and results confirmed the formation of functional tissue constructs with high cell density and *in vivo*-like microarchitecture. Recently, complex tissues with relevant micro and macro-scale organization have been fabricated by bioprinting organoids building blocks within support hydrogels.[233] The findings suggest the feasibility of engineering organoid-based tissues at the centimeter scale, providing innovative functional constructs for regenerative medicine and drug research.

Bioprinted structures have also been used as delivery vehicles for organoids. Soltanian and coll. 3D printed PLA tissue trapper containing collagen I and Matrigel® for the transplantation of pancreatic organoids from human embryonic stem cells into the abdominal cavity of immunodeficient mice, observing anastomosis with the host vasculature and enhanced production of insulin thanks to the proper cell-cell and cell-matrix interactions.[135]

4.4.2. Microfluidic-based hybrid fabrication strategies

The use of microfluidics for the production and culture of organoids, also defined as organoid-on-a-chip technology, is showing great potential in overcoming some of the main limitations of static 3D culture systems, as inefficient nutrients exchange, lack of standardization and low throughput.[124,216,235] Over the past years, microfluidic strategies have been used for generation of spheroids and organoids,[236] in situ analysis and monitoring of organoids behavior,[194] and to build automated platforms for drug screening and personalized medicine.[237,238]

In the context of organoids vascularization, the two main microfluidic-based approaches are (i) direct generation on-chip of the vascularized spheroid/organoid and (ii) embedding of the spheroid/organoid and subsequent vascularization on-chip (**Figure 9c**).[137,239–241] By using the first strategy, Jin and coll. created vascularized liver organoids on-chip. The liver organoids were composed of induced hepatic cells cocultured with HUVECs and they were embedded in a 3D decellularized liver ECM, used as scaffold. The system was integrated in a pump-free microfluidic device under continuous flow. The encapsulation of hepatic and endothelial cells under flow led to the formation of functional liver organoids with enhanced metabolism compared to static conditions and increased intercellular interaction and reduced apoptosis due to the presence of HUVECs. The system was used for drug testing on a microfluidic array for high-throughput and the integration of intestinal organoids enabled the simulation of multiorgan response to the screened drugs.[239]

Recently, Isshiki and coll. vascularized brain organoids on a compartmentalized microfluidic device.[241] Brain organoids were generated from hiPSCs, followed by co-culturing with HUVECs within the microfluidic chip. The microfluidic platform had five parallel channels: one for organoid-HUVEC co-culture, which was sandwiched between two sets of microchannels where HUVECs and hLFs were suspended in cell culture media to form vasculature. Results showed that on-chip vasculature promoted differentiation and brain organogenesis with specific *in vivo* features as compared to conventional mono-culture. Homan and coworkers developed kidney organoids in perfused 3D millifluidic device (**Figure 6d**).[137] Once harvested, organoids were introduced into the device, connected with external tubing where media was perfused through the chip via a closed loop circuit. The results showed that organoids grown under controlled high

fluidic shear stress had enhanced glomerular vascularization and increase in adult gene expression as compared to organoids grown in static conditions, with development stages comparable to *in vivo*. Meanwhile, when organoids were grown in a prevascularized gel composed of HUVECs and hNDFs under static conditions, they were found to inhibit nephrogenesis, as compared to mono-culture organoids grown under controlled flow. These findings suggest a preference for fluid flow during early stages development of kidney. The study could not prove that microvasculature formed in the kidney organoids were perfusable. Nevertheless, the feasibility to induce flow-enhanced on-chip organogenesis opens new strategies to form physiologically relevant *in vitro* models with functional vasculature. For a comprehensive review about vascularization strategies of organoids on-chip, we refer the reader to reference [242].

By using bioprinting-based and microfluidic-based fabrication methods, researchers have already successfully proved the capability to engineer complex models, as 3D printed perfusable tissue equivalents and vascularized physiologically relevant models on-chip.[243–246] The combined use of these strategies has shown the possibility to create more reproducible and standardized constructs, laying the groundwork for the development of high throughput technologies.

5. Unmet needs of current vascularized 3D models

Despite the enormous progresses of the recent years, the biological complexity of vascularized 3D tissue models poses a challenge for the development of sophisticated platforms. Consequently, several limitations of the current constructs remain (**BOX 3**). Nowadays, the biological environment is recreated by 3D matrices, integration of multi-cellular cultures that assemble in tissue relevant structures and by providing physiologically relevant stimuli. However, cell lines are still widely used in research and ECs from umbilical vein (HUVECs) remain the top choice for endothelium modeling due to easy handling, reliability in long-term culture and affordable costs. Even though this common feature can be convenient when comparing results from different studies, it limits the establishment of organ-specific models, hampering the study of tissue-specific mechanisms at the vascular interface. Therefore, tissue specific human-derived primary endothelial cells represent a more valid source and have been used to engineer patient-specific platforms. However, access to human tissue and isolation protocols are often difficult and laborious operations.[228] For this reason, many studies are still based on animal cell sources, which once again impede data and system scalability towards “human-sized” models. Stem cell biology

might be an alternative to address the current limitations and develop platforms for personalized medicine. Hence, vascular models using endothelial cells derived from multipotent or pluripotent stem cell sources have been already successfully engineered.[229,230] These cells present also the advantage of being suitable for further clinical development, such as in the case of bioprinted tissue constructs.

Another current limitation is the establishment of long-term models. As presented in **Table 2, 4** and **5**, most of the vascularized models are used as *in vitro* platforms for short-term studies (about 2 weeks) and this hampers the assessment of vascularized tissue constructs in several ways, basing on their main application. Specifically, in the case of bioprinted devices, the long-term evaluation of their stability is fundamental for their *in vivo* application while, for 3D cell culture and microfluidics, the establishment of long-term models would ensure more accurate pathology-related and drug testing studies.[231–233]

The 3D geometrical complexity and the dimensions of the microcirculatory system can be more easily replicated with self-vascularization strategies compared to prevascularization techniques due to the spontaneous assembly of ECs, with sprouts diameters often below 30 μm.[234,235] However, this technique is not reproducible and it takes a longer time for the vasculature to be functional and perfusable. Current bioprinting strategies have shown the capability to 3D print complex vascular geometries,[99,189] as well as dense tissue constructs,[236] that could not be achieved otherwise. However, vessels size is still restricted by the resolution limit of many fabrication techniques and relatively few works have obtained capillary-like diameters, mainly by laser-based strategies, which have proved effective to create multi-scale vascular networks with capillaries of less than 10 μm.[109,115]

As discussed in **Section 4.1.**, the incorporation of biochemical and mechanical stimuli have been successfully achieved with microfluidics-based strategies,[19,109] yet engineering models that fully recapitulate the physiological cues of the microenvironment is still a challenge. In this context, 3D cell culture models such as spheroids and organoids present a solution to achieve both geometrical complexity and recapitulate the *in vivo* microenvironment thanks to their unique feature to self-organize. The generation of these *in vivo* like constructs manifests from cell culture systems, which make it possible to amend this technology to various cell culture platforms, enabling high-throughput screening and batch production, hence, highly translational to the

industry. In terms of vascularization, spheroids/organoids present a different set of challenges. As discussed in **Section 4.2**, vascularized spheroids/organoids can achieve capillary-like structures both *in vitro* and *in vivo* via co-culture with ECs and transplantation in animal models. Therefore, all the technical and ethical issues associated with using ECs (cell source, availability, etc.) and animal models encompass the challenges of using vascularized spheroids/organoids for research, clinical, and industrial purposes.

The incorporation of the lymphatic system must also be considered to create more comprehensive microcirculatory models.[237,238] This network plays a fundamental role in tissue fluid homeostasis, immune cells trafficking, and actively participates in cardiovascular pathophysiology, cancer metastases and several diseases progression.[239–241]

Automation represents another key requirement in the development of reliable and high throughput platforms and, although sophisticated devices for automated manipulation, testing and analysis on-chip have been recently developed,[75,116] most of the works do not consider this feature. In parallel, the further integration of sensors for *in situ* monitoring of construct performances would speed up the automation, scalability and readouts of these models, while boosting their value in both academic and industrial setups.[201,242–244]

BOX 3 – UNMET NEEDS OF PREVASCULARIZED MODELS: KEY POINTS

- Extensive use of cell lines
- Short-term evaluation *in vitro*
- Difficult to replicate the capillaries size
- Limited examples of dense microvasculature
- Limited examples of thick vascularized tissues
- Need to integrate biochemical/ mechanical cues
- Need for automation and *in situ* monitoring

6. Industrial and clinical translation of current vascularized 3D models

Scaling up

The development of scalable vascularized models should take into account the following requirements: a reproducible, time, and cost-effective fabrication process to obtain robust, high throughput, automated, physiologically relevant and user-friendly constructs or platforms. [245] As

aforementioned, technologies such as additive manufacturing hold potential for producing sophisticated constructs by means of reliable and rapid fabrication processes, that can be scaled-up to mass production. However, it is important to keep in mind the need to create models that can be operated in a simple and proper way by a wide range of end-users.

The scalability of microfluidics-based technology is still limited by use of external bulky perfusion systems. To cope with this challenge, the multi-well format, that consists of many 3D microfluidic devices on a single plate, has been proposed successfully and produced in both academic and industrial settings.[5,246] This technology enables researchers to work with high throughput devices while ensuring compact designs and user-friendly formats, conventionally used in biology and pharmaceutical fields. The multiwell format-based and pumpless Organoplate® platforms produced by the Dutch biotech company MIMETAS have been largely used for creating vascularized OOaC models and study angiogenesis without the need for external perfusion, paving the way for a tangible industrial translation of OOaC technology.[234,247]

Organoids are considered a powerful model for drug testing and development as well as for personalized medicine. The establishment of organoids biobanks from either healthy or diseased tissues has boosted the scale-up of this technology,[267,268] and protocols for large-scale production of organoids in compliance with Good Manufacturing Practices (GMP) requirements have been recently published.[269,270] As discussed in **Section 4.4**, the use of microfluidic and bioprinting fabrication strategies could accelerate the scalability of 3D cell cultures by providing automated high throughput platforms and standardized production.[230] The translation of the technology from basic research to industry and clinic poses however several challenges and questions from both the ethical and the logistic points of view. Aspects as informed consent of the donors, commercial ownership and public versus private biobanks still need to be defined in a clear regulatory framework to enable the scale up of organoids models.[113,271]

As for bioprinting technology, difficulties in scaling up functional tissues with adequate size to achieve vascularization limits its use for tissue repair. More importantly, questions regarding the mechanical strength and stability of bioengineered tissues, as well as their integration, innervation, immunogenicity and maintenance of long-term functionality after implantation, must also be considered.[181,211] For example, pilot studies to determine the vascularization degree of skin substitutes after *in vivo* implantation could contribute to the development of tissue constructs with

relevant sizes to be used in the clinic but more preclinical studies are required to address such concerns.[248]

It is worth noting however that one of the major challenges for the scale up of constructs for regenerative medicine still remains the large-scale expansion of human cells. Since billions of functional cells per patient are required for implantation,[273] researchers have worked in the past years on the scalability of culture systems in line with current GMP. In this perspective, large-scale expansion methods have moved from 2D culture systems, in which cells are expanded by multiplying the number of culture dishes, to bioreactor systems, with the advantage of introducing dynamic culturing conditions, monitoring and controlling of the culture environment, less user-dependent variability and higher cost and time efficiency. With the variety of bioreactors and culture methods established nowadays,[274] protocols for scalable GMP production of PSCs, hiPSCs- derived cells and multipotent SCs, especially MSCs, fundamental during the angiogenesis process, have been successfully developed,[275–277] although some critical aspects are still debated. For instance, media formulation still represents one of the bottlenecks and an homogenization is required, notably to prevent any unwanted differentiation during the expansion process and to cope with the high costs of the components.[278] Furthermore, for the compliance with GMP standards, many other parameters, as donors selection, facilities control, storage and distribution of the final products need to be standardized.[279] The establishment of reliable and automated mass cellular production protocols is thus an essential precondition for the industrial and clinical scale up of tissue engineered constructs.

Drug development

Drug development is a long and expensive multi-step process that involves basic research and drug discovery, pre-clinical and clinical trials and, after the approval, post-market monitoring. The estimated cost for the development of one new drug is of 2.5 billion dollars, of which 60 % in clinical trials, and the process takes about 12 years, with less than 10% of the drug candidates succeeding in human clinical trial phases.[10,280,281] Although the inadequacy of animals in modeling human response and related ethical issues, mammalian models are still necessary for drugs testing in preclinical phase.[8–10]

In this context, OOaC technology has been extensively investigated as tool to speed up drug research by better mimicking *in vivo* behavior and combining interactions between different

tissues. Similar to spheroids/organoids, OOaC technology can lower the R&D costs and overcome the use of animal models by means of more predictive and representative preclinical systems.[282–285] Particularly, OOaC models can be used in preclinical trials for the study of pharmacokinetics-pharmacodynamics (PK-PD) mechanisms and to test drugs already on the market for safety monitoring. The use of multiorgan-on-chip platforms with integrated vasculature results of particular interest for studying absorption, distribution, metabolism, excretion (ADME) pathways of new drug candidates.[280,286] With the European Union's full ban on testing cosmetic ingredients or products on animals in 2013, OOaC technology has emerged as well as alternative *in vitro* model for toxicology studies and safety assessment in cosmetics field.[89,287] All over the world, public and private institutions have funded OOaC-related programs to promote and accelerate the translation of the technology from fundamental research to the industry, leading to the establishment of many OOaC start-ups.[281,288,289] Leading pharmaceutical and cosmetic companies are actively collaborating with some of the major start-ups and academic centers to integrate OOaC platforms in drug testing and safety assessment in an industrial context. OOaC models have already shown higher complexity and better predictability compared to other *in vitro* systems. Thus, further development of these platforms to address the unmet needs could have a tremendous impact on the current drug development process.

In oncology drug research, where only ≤5% of new anticancer drug candidates is approved, tumor organoids and spheroids present a promising strategy to improve drug approval rates and serve as potential preclinical drug screening platforms.[290][291] For instance, colon cancer organoids were used to screen 83 drugs currently used in clinics or in clinical trials for cancer treatments. The findings demonstrated that colon cancer organoids were suitable for high throughput screening of drug candidates and could better mimic tumor microenvironment such as oxygen and nutrient gradients compared to existing models.[290,292] Tumor organoids have also been used successfully as preclinical models for pharmacodynamic profiling of human tumors.[293] Companies like Fluofarma and InSphero offer fast-growing 3D tumor spheroids, which can be adapted for high throughput single-cell analysis, functional assays, drug testing, preclinical and clinical models. Besides oncology, spheroids and organoids are also widely employed to speed up drug testing and to overcome difficulties associated with predictions of outcomes in other pathologies.[115,291,294] InSphero develops models for diabetes and liver diseases such as non-alcoholic fatty liver disease (NAFLD) and non-alcoholic steatohepatitis (NASH) and organoids generated from *ex vivo* biopsy

samples have been used to model genetic diseases such as cystic fibrosis (CF) for the development of precision therapies.[295]

The pharmaceutical industry has adopted as well bioprinted models, also due to a recent increase of the number of bioprinters on the market.[172] Since 2014, liver tissue models bioprinted by Organovo are used in the pharma industry to screen liver toxicity of drugs.[133] Other companies, such as Aspect Biosystems, have more recently established joint programs with pharmaceutical companies for the screening of immuno-therapeutics to treat cancer using 3D printed models,[296] as well as with multinational research organizations to develop vascularized human liver lobules by means of their microfluidic 3D bioprinting technology.[297]

Towards clinical application of vascularized models

Although recent attempts to use microfluidics and 3D cell culture constructs for tissue repair and regenerative medicine have been made,[93,298–301] their application remains mainly focused on drug research and development of personalized treatments, as discussed above.[99,282,292] Particularly, patient-derived organoids hold great potential for transplant application since they would solve the major issues of using allogenic materials, with related immune response, and of shortage of donors.[300] However, even if preclinical animal studies have shown the possible application of organoids for cell or organ transplantation, the use of models integrating vasculature remains limited.[302–304] In the clinical context, bioprinting-based vascularization strategies represent currently the most advanced technology. Intraoperative bioprinting, i.e., the direct printing of tissue on the patient in the operating theater, holds great promise together with several challenges and pre-clinical studies, mainly in mice, have already been successfully performed.[305] Kérourédan *et al.* printed by LAB stem cells from apical papilla mixed with HUVEC, during surgical procedure for the treatment of murine bone calvary defect.[211] The main advantage of LAB is the lack of contact between the printer and the patient tissue, when compared to extrusion methods. Nevertheless, to translate this technology to an operating room, 3D bioprinters still need to be adapted: miniaturization of the system, low printing speed, that might prolong the surgery, and the need to precisely control the light source represent important challenges.[305] Besides, to assure proper vascularization of the printed tissue, 3D bioprinters should ideally print macrovessels in tandem with microvessels to enable the anastomosis with the patient circulation while ensuring instant blood supply to the construct.

Since the aim of this technology is to adapt to each patient and be performed on-site, aspects such as standardization, customization, quality control, GMP, etc. should be defined for its application in human clinical trials. In fact, regulatory aspects for use on patients need to be defined urgently since tissues obtained by bioprinting are not yet subject to dedicated regulatory standards.[306,307] The elements involved in the manufacture of these tissues are i) the material, ii) the cells, iii) the software, iv) the bioprinter. In some cases, a maturation stage is also added. Some of these elements are considered medical products (cells) and others medical devices (software), thus they would be under different regulations. The origin of the material (animal, synthetic, recombinant proteins etc.) and cells (autologous / heterologous, embryonic etc.), or the type of maturation (using growth factors, bioreactors etc.) also determines the rules to follow in the different countries.[308] It is therefore necessary to establish a clear framework to determine the classification of the tissues obtained by bioprinting and to define the regulatory requirements. For more information on this topic, the reader is referred to the book chapter of Li., published in 2018.[306]

The use of vascularized 3D models with physiological relevance can bridge the gap between *in vitro* research, drug development and clinical trials. Here, we have discussed how 3D cell culture models and microfluidic platforms are promising tools to improve the robustness and reliability of preclinical research data, minimize the need for animal testing and develop more efficient drug screening platforms and personalized therapies. Although their potential for transplantation and regenerative medicine has been proven, the use of complete models including vasculature is still in its infancy. On the hand, 3D bioprinting has been more widely investigated as technology for organs repair and regeneration but ethical and regulatory aspects still need to be addressed carefully to enable its safe and rapid translation.

7. Conclusion

The recent achievements of research in developing 3D physiological *in vitro* models hold promise to revolutionize the conventional regenerative medicine approaches by creating new tools for basic research, personalized medicine, drug development and clinical application. The use of complex models integrating vasculature is a key requirement for their successful translation. Current efforts are closer than ever to engineer complex, dense and thick vascularized organ-specific models and the continuous improvements of tissue engineering have already shown great

potential in fabricating three-dimensional physiological relevant constructs for clinical and industrial settings. Nevertheless, certain drawbacks, regarding the technical challenges, the scale-up and the regulatory framework still need to be addressed. On a scientific level, the combination of different and complementary tissue engineering strategies would allow researchers to overcome some of the current fabrication limits, as we have illustrated here. At the same time, the close cooperation and open dialogue of researchers, clinicians and industry would contribute in speeding up the translational process in the near future.

Conflict of Interest

The authors declare no conflict of interest.

Acknowledgements

This work has been supported by Inserm, Université Sorbonne Paris Nord, and Université de Paris. A.D. acknowledges funding from the European Union's Horizon 2020 research and innovation programme under the Marie Skłodowska-Curie grant agreement No. 766181. C.L.B. acknowledges funding from the "Recherche Hospitalo-universitaire" Innovations for Liver Tissue Engineering (RHU iLite), grant number ANR-16-RHUS-0005.

References

[1] C. Hu, Y. Chen, M. J. A. Tan, K. Ren, H. Wu, *Analyst* **2019**, *144*, 4461.

[2] K. Haase, R. D. Kamm, *Regen. Med.* **2017**, *12*, 285.

[3] J. Rouwkema, A. Khademhosseini, *Trends Biotechnol.* **2016**, *34*, 733.

[4] H. Jian, M. Wang, S. Wang, A. Wang, S. Bai, *Bio-Design Manuf.* **2018**, *1*, 45.

[5] D. S. Y. Lin, F. Guo, B. Zhang, *Nanotechnology* **2019**, *30*, 024002.

[6] S. Kim, W. Kim, S. Lim, J. S. Jeon, *Bioengineering* **2017**, *4*, DOI 10.3390/bioengineering4010008.

[7] A. D. Bannerman, R. X. Ze Lu, A. Korolj, L. H. Kim, M. Radisic, *Curr. Opin. Biomed. Eng.* **2018**, *6*, 8.

[8] I. A. Freires, J. de C. O. Sardi, R. D. de Castro, P. L. Rosalen, *Pharm. Res.* **2017**, *34*, 681.

[9] K. Ronaldson-Bouchard, G. Vunjak-Novakovic, *Cell Stem Cell* **2018**, *22*, 310.

[10] J. M. Wilkinson, in *Organ-on-a-Chip Eng. Microenviron. Saf. Effic. Test.*, (Eds: J. Hoeng, D. Bovard, M. C. Peitsch), Elsevier **2020**, Ch. 1.

[11] D. Antoni, H. Burckel, E. Josset, G. Noel, *Int. J. Mol. Sci.* **2015**, *16*, 5517.

[12] J. Grenier, H. Duval, F. Barou, P. Lv, B. David, D. Letourneur, *Acta Biomater.* **2019**, *94*, 195.

[13] M.-N. Labour, C. Le Guilcher, R. Aid-Launais, N. El Samad, S. Lanouar, T. Simon-Yarza, D. Letourneur, *Int. J. Mol. Sci.* **2020**, *21*, 3644.

[14] S. Jalili-Firoozinezhad, M. Filippi, F. Mohabatpour, D. Letourneur, A. Scherberich, *Mater. Today* **2020**, *40*, 193.

[15] F. A. Auger, L. Gibot, D. Lacroix, *Annu. Rev. Biomed. Eng.* **2013**, *15*, 177.

[16] W. D. Tucker, Y. Arora, K. Mahajan, *Anatomy, Blood Vessels*, StatPearls Publishing, Treasure Island, FL **2018**.

[17] A. Hasan, A. Paul, N. E. Vrana, X. Zhao, A. Memic, Y. S. Hwang, M. R. Dokmeci, A. Khademhosseini, *Biomaterials* **2014**, *35*, 7308.

[18] E. Witzleb, in *Hum. Physiol.*, (Eds: R. F. Schmidt, G. Thews), Springer, Berlin, Germany **1989**, Ch. 20.

[19] N. Mori, Y. Akagi, Y. Imai, Y. Takayama, Y. S. Kida, *Sci. Rep.* **2020**, *10*, 5646.

[20] E. Bianconi, A. Piovesan, F. Facchin, A. Beraudi, R. Casadei, F. Frabetti, L. Vitale, M. C. Pelleri, S. Tassani, F. Piva, S. Perez-Amodio, P. Strippoli, S. Canaider, *Ann. Hum. Biol.* **2013**, *40*, 463.

[21] J. G. Betts, K. A. Young, J. A. Wise, E. Johnson, B. Poe, D. H. Kruse, O. Korol, J. E. Johnson, M. Womble, P. DeSaix, in *Anatomy and Physiology*, OpenStax, Houston, Texas 2013, Ch. 20.

[22] W. C. Aird, *Circ. Res.* **2007**, *100*, 158.

[23] M. E. Gerritsen, *Biochem. Pharmacol.* **1997**, *36*, 2701-2711.

[24] H. Gerhardt, M. Golding, M. Fruttiger, C. Ruhrberg, A. Lundkvist, A. Abramsson, M. Jeltsch, C. Mitchell, K. Alitalo, D. Shima, C. Betsholtz, *J. Cell Biol.* **2003**, *161*, 1163.

[25] H. M. Eilken, R. H. Adams, *Curr. Opin. Cell Biol.* **2010**, *22*, 617.

[26] T. Simon-Yarza, M. N. Labour, R. Aid, D. Letourneur, *Mater. Sci. Eng. C* **2021**, *118*, 111369.

[27] L. K. Phng, H. Gerhardt, *Dev. Cell* **2009**, *16*, 196.

[28] R. Benedito, S. F. Rocha, M. Woeste, M. Zamykal, F. Radtke, O. Casanovas, A. Duarte, B. Pytowski, R. H. Adams, *Nature* **2012**, *484*, 110.

[29] T. Simón-Yarza, F. R. Formiga, E. Tamayo, B. Pelacho, F. Prosper, M. J. Blanco-Prieto, *Theranostics* **2012**, *2*, 541.

[30] W. Risau, *Nature* **1997**, *386*, 671.

[31] M. Shibuya, *Genes and Cancer* **2011**, *2*, 1097.

[32] D. R. Senger, G. E. Davis, *Cold Spring Harb. Perspect. Biol.* **2011**, *3*, 1.

[33] L. K. Fiddes, N. Raz, S. Srigunapalan, E. Tumarkan, C. A. Simmons, A. R. Wheeler, E. Kumacheva, *Biomaterials* **2010**, *31*, 3459.

[34] J. He, R. Chen, Y. Lu, L. Zhan, Y. Liu, D. Li, Z. Jin, *Mater. Sci. Eng. C* **2016**, *59*, 53.

[35] K. K. Sørensen, P. McCourt, T. Berg, C. Crossley, D. Le Couteur, K. Wake, B. Smedsrød, *Am. J. Physiol. Integr. Comp. Physiol.* **2012**, *303*, R1217.

[36] G. R. Martin, R. Timpl, *Annu. Rev. Cell Biol.* **1987**, *3*, 57.

[37] T. Tilling, D. Korte, D. Hoheisel, H. J. Galla, *J. Neurochem.* **1998**, *71*, 1151.

[38] Y. Kubota, H. K. Kleinman, G. R. Martin, T. J. Lawley, *J. Cell Biol.* **1988**, *107*, 1589.

[39] D. M. Form, B. M. Pratt, J. A. Madri, *Lab. Investig.* **1986**, *55*, 521.

[40] J. S. Lowe, P. G. Anderson, in *Stevens Lowes Hum. Histol.*, Elsevier, **2015**, pp. 55–70.

[41] J. H. Miner, N. M. Nguyen, in *Encycl. Respir. Med. Four-Volume Set*, Elsevier, **2006**, pp. 157–162.

[42] T. W. Secomb, *Compr. Physiol.* **2016**, *6*, 975.

[43] S. Kim, H. Lee, M. Chung, N. L. Jeon, *Lab Chip* **2013**, *13*, 1489.

[44] C. F. Guimarães, L. Gasperini, A. P. Marques, R. L. Reis, *Nat. Rev. Mater.* **2020**, *5*, 351.

[45] R. Pimentel C., S. K. Ko, C. Caviglia, A. Wolff, J. Emnéus, S. S. Keller, M. Dufva, *Acta Biomater.* **2018**, *65*, 174.

[46] M. Chaouat, C. Le Visage, W. E. Baille, B. Escoubet, F. Chaubet, M. A. Mateescu, D. Letourneur, *Adv. Funct. Mater.* **2008**, *18*, 2855.

[47] M. Atlan, T. Simon-Yarza, J. M. Ino, V. Hunsinger, L. Corté, P. Ou, R. Aid-Launais, M. Chaouat, D. Letourneur, *Sci. Rep.* **2018**, *8*, 7417.

[48] S. Lee, J. Ko, D. Park, S. R. Lee, M. Chung, Y. Lee, N. L. Jeon, *Lab Chip* **2018**, *18*, 2686.

[49] Q. Smith, S. Gerecht, *Curr. Opin. Chem. Eng.* **2014**, *3*, 42.

[50] J. Tien, *Curr. Opin. Chem. Eng.* **2014**, *3*, 36.

[51] R. Ning, Q. Zhuang, J.-M. Lin, in *Cell Analysis on Microfluidics. Integrated Analytical Systems*, (Eds: J. M. Lin), Springer, Singapore 2018, pp. 181–224.

[52] I. K. Zervantonakis, S. K. Hughes-Alford, J. L. Charest, J. S. Condeelis, F. B. Gertler, R. D. Kamm, *Proc. Natl. Acad. Sci. U. S. A.* **2012**, *109*, 13515.

[53] A. Dellaquila, E. K. Thomée, A. H. McMillan, S. C. Lesher-Pérez, in *Organ-on-a-Chip Eng. Microenviron. Saf. Effic. Test.*, (Eds. J. Hoeng, D. Bovard, M. C. Peitsch), Elsevier **2020**, Ch. 4.

[54] R. Sudo, S. Chung, I. K. Zervantonakis, V. Vickerman, Y. Toshimitsu, L. G. Griffith, R. D. Kamm, *FASEB J.*

2009, *23*, 2155.

[55] B. Sebastian, P. S. Dittrich, *Annu. Rev. Fluid Mech.* **2018**, *50*, 483.

[56] B. Prabhakarpandian, M. C. Shen, K. Pant, M. F. Kiani, *Microvasc. Res.* **2011**, *82*, 210.

[57] D. R. Myers, Y. Sakurai, R. Tran, B. Ahn, E. T. Hardy, R. Mannino, A. Kita, M. Tsai, W. A. Lam, *J. Vis. Exp.* **2012**, e3958.

[58] R. G. Mannino, D. R. Myers, B. Ahn, Y. Wang, Margo Rollins, H. Gole, A. S. Lin, R. E. Guldberg, D. P. Giddens, L. H. Timmins, W. A. Lam, *Sci. Rep.* **2015**, *5*, 1.

[59] S. H. Lee, J. H. Sung, *Adv. Healthc. Mater.* **2018**, *7*, 1700419.

[60] E. W. K. Young, *J. Lab. Autom.* **2013**, *18*, 427.

[61] A. M. A. O. Pollet, J. M. J. den Toonder, *Bioengineering* **2020**, *7*, 17.

[62] D. Huh, B. D. Matthews, A. Mammoto, M. Montoya-Zavala, H. Yuan Hsin, D. E. Ingber, *Science* **2010**, *328*, 1662.

[63] L. Wang, T. Tao, W. Su, H. Yu, Y. Yu, J. Qin, *Lab Chip* **2017**, *17*, 1749.

[64] S. Musah, A. Mammoto, T. C. Ferrante, S. S. F. Jeanty, M. Hirano-Kobayashi, T. Mammoto, K. Roberts, S. Chung, R. Novak, M. Ingram, T. Fatanat-Didar, S. Koshy, J. C. Weaver, G. M. Church, D. E. Ingber, *Nat. Biomed. Eng.* **2017**, *1*, 0069.

[65] J. A. Brown, V. Pensabene, D. A. Markov, V. Allwardt, M. Diana Neely, M. Shi, C. M. Britt, O. S. Hoilett, Q. Yang, B. M. Brewer, P. C. Samson, L. J. McCawley, J. M. May, D. J. Webb, D. Li, A. B. Bowman, R. S. Reiserer, J. P. Wikswo, *Biomicrofluidics* **2015**, *9*, 054124.

[66] S. Bang, S. R. Lee, J. Ko, K. Son, D. Tahk, J. Ahn, C. Im, N. L. Jeon, *Sci. Rep.* **2017**, *7*, 1.

[67] S. W. L. Lee, M. Campisi, T. Osaki, L. Possenti, C. Mattu, G. Adriani, R. D. Kamm, V. Chiono, *Adv. Healthc. Mater.* **2020**, *9*, 1901486.

[68] M. B. Chen, S. Srigunapalan, A. R. Wheeler, C. A. Simmons, *Lab Chip* **2013**, *13*, 2591.

[69] B. Zhang, B. Fook, L. Lai, R. Xie, L. Davenport Huyer, M. Montgomery, M. Radisic, *Nat Protoc* **2018,** 13, 1793–1813.

[70] H. J. Kim, H. Li, J. J. Collins, D. E. Ingber, *Proc. Natl. Acad. Sci. U. S. A.* **2016**, *113*, E7.

[71] A. Bein, W. Shin, S. Jalili-Firoozinezhad, M. H. Park, A. Sontheimer-Phelps, A. Tovaglieri, A. Chalkiadaki, H. J. Kim, D. E. Ingber, *CMGH* **2018**, *5*, 659.

[72] Y. B. A. Kang, T. R. Sodunke, J. Lamontagne, J. Cirillo, C. Rajiv, M. J. Bouchard, M. Noh, *Biotechnol. Bioeng.* **2015**, *112*, 2571.

[73] Y. Du, N. Li, H. Yang, C. Luo, Y. Gong, C. Tong, Y. Gao, S. Lü, M. Long, *Lab Chip* **2017**, *17*, 782.

[74] S. Jalili-Firoozinezhad, C. C. Miranda, J. M. S. Cabral, *Trends Biotechnol.* **2021**, DOI 10.1016/j.tibtech.2021.01.004.

[75] R. Novak, M. Ingram, S. Marquez, D. Das, A. Delahanty, A. Herland, B. M. Maoz, S. S. F. Jeanty, M. R. Somayaji, M. Burt, E. Calamari, A. Chalkiadaki, A. Cho, Y. Choe, D. B. Chou, M. Cronce, S. Dauth, T. Divic, J. Fernandez-Alcon, T. Ferrante, J. Ferrier, E. A. FitzGerald, R. Fleming, S. Jalili-Firoozinezhad, T. Grevesse, J. A. Goss, T. Hamkins-Indik, O. Henry, C. Hinojosa, T. Huffstater, K.-J. Jang, V. Kujala, L. Leng, R. Mannix, Y. Milton, J. Nawroth, B. A. Nestor, C. F. Ng, B. O'Connor, T.-E. Park, H. Sanchez, J. Sliz, A. Sontheimer-Phelps, B. Swenor, G. Thompson, G. J. Touloumes, Z. Tranchemontagne, N. Wen, M. Yadid, A. Bahinski, G. A. Hamilton, D. Levner, O. Levy, A. Przekwas, R. Prantil-Baun, K. K. Parker, D. E. Ingber, *Nat. Biomed. Eng.* **2020**, *4*, 407.

[76] K. Schimek, M. Busek, S. Brincker, B. Groth, S. Hoffmann, R. Lauster, G. Lindner, A. Lorenz, U. Menzel, F. Sonntag, H. Walles, U. Marx, R. Horland, *Lab Chip* **2013**, *13*, 3588.

[77] W. Zhang, Y. S. Zhang, S. M. Bakht, J. Aleman, S. R. Shin, K. Yue, M. Sica, J. Ribas, M. Duchamp, J. Ju, R. B. Sadeghian, D. Kim, M. R. Dokmeci, A. Atala, A. Khademhosseini, *Lab Chip* **2016**, *16*, 1579.

[78] J. T. Borenstein, M. M. Tupper, P. J. MacK, E. J. Weinberg, A. S. Khalil, J. Hsiao, G. García-Cardeña, *Biomed. Microdevices* **2010**, *12*, 71.

[79] M. B. Esch, D. J. Post, M. L. Shuler, T. Stokol, *Tissue Eng. Part A* **2011**, *17*, 2965.

[80] M. E. Wilson, N. Kota, Y. Kim, Y. Wang, D. B. Stolz, P. R. Leduc, O. B. Ozdoganlar, *Lab Chip* **2011**, *11*, 1550.

[81] J. S. Choi, Y. Piao, T. S. Seo, *Bioprocess Biosyst. Eng.* **2013**, *36*, 1871.

[82] L. L. Bischel, E. W. K. Young, B. R. Mader, D. J. Beebe, *Biomaterials* **2013**, *34*, 1471.

[83] A. Herland, A. D. Van Der Meer, E. A. FitzGerald, T. E. Park, J. J. F. Sleeboom, D. E. Ingber, *PLoS One* **2016**, *11*, e0150360.

[84] Y. Zheng, J. Chen, M. Craven, N. W. Choi, S. Totorica, A. Diaz-Santana, P. Kermani, B. Hempstead, C. Fischbach-Teschl, J. A. López, A. D. Stroock, *Proc. Natl. Acad. Sci. U. S. A.* **2012**, *109*, 9342.

[85] G. Ligresti, R. J. Nagao, J. Xue, Y. J. Choi, J. Xu, S. Ren, T. Aburatani, S. K. Anderson, J. W. MacDonald, T. K. Bammler, S. M. Schwartz, K. A. Muczynski, J. S. Duffield, J. Himmelfarb, Y. Zheng, *J. Am. Soc. Nephrol.* **2016**, *27*, 2370.

[86] S. Lee, M. Chung, S. R. Lee, N. L. Jeon, *Biotechnol. Bioeng.* **2020**, *117*, 748.

[87] R. Xie, W. Zheng, L. Guan, Y. Ai, Q. Liang, *Small* **2019**, *1902838*, 1.

[88] J. Liu, H. Zheng, P. Poh, H.-G. Machens, A. Schilling, *Int. J. Mol. Sci.* **2015**, *16*, 15997.

[89] N. Mori, Y. Morimoto, S. Takeuchi, *Biomaterials* **2017**, *116*, 48.

[90] A. P. Golden, J. Tien, *Lab Chip* **2007**, *7*, 720.

[91] L. E. Bertassoni, M. Cecconi, V. Manoharan, M. Nikkhah, J. Hjortnaes, A. L. Cristino, G. Barabaschi, D. Demarchi, M. R. Dokmeci, Y. Yang, A. Khademhosseini, *Lab Chip* **2014**, *14*, 2202.

[92] I. Vollert, M. Seiffert, J. Bachmair, M. Sander, A. Eder, L. Conradi, A. Vogelsang, T. Schulze, J. Uebeler, W. Holnthoner, H. Redl, H. Reichenspurner, A. Hansen, T. Eschenhagen, *Tissue Eng. - Part A* **2014**, *20*, 854.

[93] H. E. Abaci, Z. Guo, A. Coffman, B. Gillette, W. H. Lee, S. K. Sia, A. M. Christiano, *Adv. Healthc. Mater.* **2016**, *5*, 1800.

[94] D. B. Kolesky, K. A. Homan, M. A. Skylar-Scott, J. A. Lewis, *Proc. Natl. Acad. Sci. U. S. A.* **2016**, *113*, 3179.

[95] W. H. Goh, M. Hashimoto, *Macromol. Mater. Eng.* **2018**, *303*, 1700484.

[96] A. Hansen, A. Eder, M. Bönstrup, M. Flato, M. Mewe, S. Schaaf, B. Aksehirlioglu, A. Schwörer, J. Uebeler, T. Eschenhagen, *Circ. Res.* **2010**, *107*, 35.

[97] J. S. Miller, K. R. Stevens, M. T. Yang, B. M. Baker, D. H. T. Nguyen, D. M. Cohen, E. Toro, A. A. Chen, P. A. Galie, X. Yu, R. Chaturvedi, S. N. Bhatia, C. S. Chen, *Nat. Mater.* **2012**, *11*, 768.

[98] D. Lei, Y. Yang, Z. Liu, B. Yang, W. Gong, S. Chen, S. Wang, L. Sun, B. Song, H. Xuan, X. Mo, B. Sun, S. Li, Q. Yang, S. Huang, S. Chen, Y. Ma, W. Liu, C. He, B. Zhu, E. M. Jeffries, F. L. Qing, X. Ye, Q. Zhao, Z. You, *Mater. Horizons* **2019**, *6*, 1197.

[99] B. Zhang, M. Montgomery, M. D. Chamberlain, S. Ogawa, A. Korolj, A. Pahnke, L. A. Wells, S. Masse, J. Kim, L. Reis, A. Momen, S. S. Nunes, A. R. Wheeler, K. Nanthakumar, G. Keller, M. V. Sefton, M. Radisic, *Nat. Mater.* **2016**, *15*, 669.

[100] K. A. Heintz, M. E. Bregenzer, J. L. Mantle, K. H. Lee, J. L. West, J. H. Slater, *Adv. Healthc. Mater.* **2016**, *5*, 2153.

[101] S. Yasotharan, S. Pinto, J. G. Sled, S. S. Bolz, A. Günther, *Lab Chip* **2015**, *15*, 2660.

[102] N. Y. C. Lin, K. A. Homan, S. S. Robinson, D. B. Kolesky, N. Duarte, A. Moisan, J. A. Lewis, H. John, A. Paulson, *Proc. Natl. Acad. Sci. U. S. A.* **2019**, *116*, 5399.

[103] S. Massa, M. A. Sakr, J. Seo, P. Bandaru, A. Arneri, S. Bersini, E. Zare-Eelanjegh, E. Jalilian, B. H. Cha, S. Antona, A. Enrico, Y. Gao, S. Hassan, J. P. Acevedo, M. R. Dokmeci, Y. S. Zhang, A. Khademhosseini, S. R. Shin, *Biomicrofluidics* **2017**, *11*, 044109.

[104] Q. Pi, S. Maharjan, X. Yan, X. Liu, B. Singh, A. M. van Genderen, F. Robledo-Padilla, R. Parra-Saldivar, N. Hu, W. Jia, C. Xu, J. Kang, S. Hassan, H. Cheng, X. Hou, A. Khademhosseini, Y. S. Zhang, *Adv. Mater.* **2018**, *30*, 1706913.

[105] M. Abudupataer, N. Chen, S. Yan, F. Alam, Y. Shi, L. Wang, H. Lai, J. Li, K. Zhu, C. Wang, *Biomed. Microdevices* **2020**, *22*, 1.

[106] M. Humayun, C. W. Chow, E. W. K. Young, *Lab Chip* **2018**, *18*, 1298.

[107] J. Cui, H. Wang, Z. Zheng, Q. Shi, T. Sun, Q. Huang, T. Fukuda, *Biofabrication* **2019**, *11*, 015016.

[108] Y. S. Zhang, A. Arneri, S. Bersini, S. R. Shin, K. Zhu, Z. Goli-Malekabadi, J. Aleman, C. Colosi, F. Busignani, V. Dell'Erba, C. Bishop, T. Shupe, D. Demarchi, M. Moretti, M. Rasponi, M. R. Dokmeci, A. Atala, A. Khademhosseini, *Biomaterials* **2016**, *110*, 45.

[109] D. Richards, J. Jia, M. Yost, R. Markwald, Y. Mei, *Ann. Biomed. Eng.* **2017**, *45*, 132.

[110] A. K. Miri, E. Mostafavi, D. Khorsandi, S. K. Hu, M. Malpica, A. Khademhosseini, *Biofabrication* **2019**, *11*, 042002.

[111] Y. Fang, R. M. Eglen, *SLAS Discov.* **2017**, *22*, 456.

[112] M. A. Lancaster, J. A. Knoblich, *Nat. Protoc.* **2014**, *9*, 2329.

[113] F. Schutgens, H. Clevers, *Annu. Rev. Pathol. Mech. Dis.* **2020**, *15*, 211.

[114] M. W. Laschke, M. D. Menger, *Trends Biotechnol.* **2017**, *35*, 133.

[115] T. Takahashi, *Annu. Rev. Pharmacol. Toxicol.* **2019**, *59*, 447.

[116] B. Cakir, Y. Xiang, Y. Tanaka, M. H. Kural, M. Parent, Y. Kang, K. Chapeton, B. Patterson, Y. Yuan, C. He, M. S. B. Raredon, J. Dengelegi, K. Kim, P. Sun, M. Zhong, S. Lee, P. Patra, F. Hyder, L. E. Niklason, S. Lee, Y. Yoon, I. Park, **2019**, *16*, 1169.

[117] T. Takebe, K. Sekine, M. Enomura, H. Koike, M. Kimura, T. Ogaeri, R. R. Zhang, Y. Ueno, Y. W. Zheng, N. Koike, S. Aoyama, Y. Adachi, H. Taniguchi, *Nature* **2013**, *499*, 481.

[118] C. W. van den Berg, L. Ritsma, M. C. Avramut, L. E. Wiersma, B. M. van den Berg, D. G. Leuning, E. Lievers, M. Koning, J. M. Vanslambrouck, A. J. Koster, S. E. Howden, M. Takasato, M. H. Little, T. J. Rabelink, *Stem Cell Reports* **2018**, *10*, 751.

[119] C. L. Watson, M. M. Mahe, J. Múnera, J. C. Howell, N. Sundaram, H. M. Poling, J. I. Schweitzer, J. E. Vallance, C. N. Mayhew, Y. Sun, G. Grabowski, S. R. Finkbeiner, J. R. Spence, N. F. Shroyer, J. M. Wells, M. A. Helmrath, *Nat. Med.* **2014**, *20*, 1310.

[120] R. Vassena, C. Eguizabal, B. Heindryckx, K. Sermon, C. Simon, A. M. M. van Pelt, A. Veiga, F. Zambelli, *Hum Reprod* **2015**, *30*, 2014.

[121] E. Fennema, N. Rivron, J. Rouwkema, C. van Blitterswijk, J. De Boer, *Trends Biotechnol.* **2013**, *31*, 108.

[122] C. Shao, J. Chi, H. Zhang, Q. Fan, Y. Zhao, F. Ye, *Adv. Mater. Technol.* **2020**, *5*, 1.

[123] A. Ashok, D. Choudhury, Y. Fang, W. Hunziker, *Biotechnol. Adv.* **2020**, *39*, 107460.

[124] V. Velasco, S. A. Shariati, R. Esfandyarpour, *Microsystems Nanoeng.* **2020**, *6*, 76.

[125] T. Takebe, K. Sekine, M. Kimura, E. Yoshizawa, S. Ayano, M. Koido, S. Funayama, N. Nakanishi, T. Hisai,

T. Kobayashi, T. Kasai, R. Kitada, A. Mori, H. Ayabe, Y. Ejiri, N. Amimoto, Y. Yamazaki, S. Ogawa, M. Ishikawa, Y. Kiyota, Y. Sato, K. Nozawa, S. Okamoto, Y. Ueno, H. Taniguchi, *Cell Rep.* **2017**, *21*, 2661.

[126] Y. Takahashi, K. Sekine, T. Kin, T. Takebe, H. Taniguchi, *Cell Rep.* **2018**, *23*, 1620.

[127] C. Shao, Y. Liu, J. Chi, Z. Chen, J. Wang, Y. Zhao, *Langmuir* **2019**, *35*, 3832.

[128] E. Urich, C. Patsch, S. Aigner, M. Graf, R. Iacone, P. O. Freskgård, *Sci. Rep.* **2013**, *3*, 1500.

[129] W. L. Dissanayaka, L. Zhu, K. M. Hargreaves, L. Jin, C. Zhang, *J. Dent. Res.* **2014**, *93*, 1296.

[130] R. A. Vertrees, M. McCarthy, T. Solley, V. L. Popov, J. Roaten, M. Pauley, X. Wen, T. J. Goodwin, *Cancer Biol. Ther.* **2009**, *8*, 356.

[131] A. Przepiorski, V. Sander, T. Tran, J. A. Hollywood, B. Sorrenson, J. H. Shih, E. J. Wolvetang, A. P. McMahon, T. M. Holm, A. J. Davidson, *Stem Cell Reports* **2018**, *11*, 470.

[132] C. Adine, K. K. Ng, S. Rungarunlert, G. R. Souza, J. N. Ferreira, *Biomaterials* **2018**, *180*, 52.

[133] I. T. Ozbolat, W. Peng, V. Ozbolat, *Drug Discov. Today* **2016**, *21*, 1257.

[134] L. Benmeridja, L. De Moor, E. De Maere, F. Vanlauwe, M. Ryx, L. Tytgat, C. Vercruysse, P. Dubruel, S. Van Vlierberghe, P. Blondeel, H. Declercq, *J. Tissue Eng. Regen. Med.* **2020**, *14*, 840.

[135] A. Soltanian, S. Mardpour, Z. Ghezelayagh, H. Baharvand, **2019**, 9564.

[136] J. Fukuda, K. Nakazawa, *Biomicrofluidics* **2011**, *5*, 1.

[137] K. A. Homan, N. Gupta, K. T. Kroll, D. B. Kolesky, M. Skylar-Scott, T. Miyoshi, D. Mau, M. T. Valerius, T. Ferrante, J. V. Bonventre, J. A. Lewis, R. Morizane, *Nat. Methods* **2019**, *16*, 255.

[138] K. Kusamori, M. Nishikawa, N. Mizuno, T. Nishikawa, A. Masuzawa, Y. Tanaka, Y. Mizukami, K. Shimizu, S. Konishi, Y. Takahashi, Y. Takakura, *Pharm. Res.* **2016**, *33*, 247.

[139] R. Walser, W. Metzger, A. Görg, T. Pohlemann, M. D. Menger, M. W. Laschke, **2013**, *26*, 222.

[140] T. Okudaira, N. Amimoto, H. Mizumoto, T. Kajiwara, *J. Biosci. Bioeng.* **2016**, *122*, 213.

[141] C. Wittig, M. W. Laschke, C. Scheuer, M. D. Menger, **2013**, *8*, e69975.

[142] L. A. Kunz-Schughart, J. A. Schroeder, M. Wondrak, F. Van Rey, K. Lehle, F. Hofstaedter, D. N. Wheatley, M. W. Laschke, M. D. Menger, T. Korff, H. G. Augustin, *J. Cell Biol.* **1998**, *290*, 782.

[143] J. Rezaie, M. Heidarzadeh, M. Hassanpour, H. Amini, E. Shokrollahi, M. Ahmadi, R. Rahbarghazi, in *Updat. Mesenchymal Induc. Pluripotent Stem Cells*, (Eds: K. A. Al-Anazi), IntechOpen **2020**, Ch. 6.

[144] H. Tao, Z. Han, Z. C. Han, Z. Li, *Stem Cells Int.* **2016**, *2016*, 1314709.

[145] L. Bussche, G. R. Van de Walle, *Stem Cells Transl Med* **2015**, *3*, 1514.

[146] S. Ho, K. Murphy, B. Binder, C. Vissers, J. K. Leach, *Stem Cells Transl. Med.* **2016**, 1.

[147] K. Zhang, L. Song, J. Wang, S. Yan, G. Li, L. Cui, J. Yin, *Acta Biomater.* **2017**, *51*, 246.

[148] R. Noguchi, K. Nakayama, M. Itoh, K. Kamohara, K. Furukawa, J. I. Oyama, K. Node, S. Morita, *J. Hear. Lung Transplant.* **2016**, *35*, 137.

[149] S. H. Bhang, S. Lee, J. Y. Shin, T. J. Lee, B. S. Kim, *Tissue Eng. - Part A* **2012**, *18*, 2138.

[150] J.-Y. Shin, J.-H. Jeong, J. Han, S. H. Bhang, G.-J. Jeong, M. R. Haque, T. A. Al-Hilal, M. Noh, Y. Byun, B.-S. Kim, *Tissue Eng. Part A* **2015**, *21*, 1024.

[151] L. A. Kunz-Schughart, J. A. Schroeder, M. Wondrak, F. Van Rey, K. Lehle, F. Hofstaedter, D. N. Wheatley, *Am. J. Physiol. - Cell Physiol.* **2006**, *290*, 1385.

[152] S. Hsu, P. Hsieh, *Wound Repair Reneg* **2015**, *23*, 57.

[153] M. W. Laschke, T. E. Schank, C. Scheuer, S. Kleer, S. Schuler, W. Metzger, D. Eglin, *Acta Biomater.* **2013**, *9*, 6876.

[154] R. Mishra, B. M. Roux, M. Posukonis, E. Bodamer, E. M. Brey, J. P. Fisher, D. Dean, *Biomaterials* **2016**, *77*, 255.

[155] M. T. Pham, K. M. Pollock, M. D. Rose, W. A. Cary, H. R. Stewart, P. Zhou, J. A. Nolta, B. Waldau, *Neuroreport* **2018**, *29*, 588.

[156] O. Ham, Y. B. Jin, J. Kim, M. O. Lee, *Biochem. Biophys. Res. Commun.* **2020**, *521*, 84.

[157] T. Takebe, R. R. Zhang, H. Koike, M. Kimura, E. Yoshizawa, M. Enomura, N. Koike, K. Sekine, H. Taniguchi, *Nat. Protoc.* **2014**, *9*, 396.

[158] M. T. Pham, K. M. Pollock, M. D. Rose, W. A. Cary, H. R. Stewart, P. Zhou, J. A. Nolta, B. Waldau, **2019**, *29*, 588.

[159] T. Takebe, N. Koike, K. Sekine, R. Fujiwara, T. Amiya, Y. W. Zheng, H. Taniguchi, *Organogenesis* **2014**, *10*, 260.

[160] S. Grebenyuk, A. Ranga, *Front. Bioeng. Biotechnol.* **2019**, *7*, 1.

[161] F. Verseijden, S. J. Posthumus-van Sluijs, E. Farrell, J. W. Van Neck, S. E. R. Hovius, S. O. P. Hofer, G. J. V. M. Van Osch, *Cell Transplant.* **2010**, *19*, 1007.

[162] A. Lavazza, M. Massimini, *J. Med. Ethics* **2018**, *44*, 606.

[163] A. Soltanian, Z. Ghezelayagh, Z. Mazidi, M. Halvaei, S. Mardpour, M. K. Ashtiani, E. Hajizadeh-Saffar, Y. Tahamtani, H. Baharvand, *J. Cell. Physiol.* **2019**, *234*, 9564.

[164] R. D. Pedde, B. Mirani, A. Navaei, T. Styan, S. Wong, M. Mehrali, A. Thakur, N. K. Mohtaram, A. Bayati, A. Dolatshahi-Pirouz, M. Nikkhah, S. M. Willerth, M. Akbari, *Adv. Mater.* **2017**, *29*, 1606061.

[165] V. Mironov, T. Trusk, V. Kasyanov, S. Little, R. Swaja, R. Markwald, *Biofabrication* **2009**, *1*, 022001.

[166] Y. Liu, E. Kim, R. Ghodssi, G.W. Rubloff, J. N. Culver, W. E. Bentley, G. F. Payne, *Biofabrication* **2010**, *2*, 2.

[167] L. Moroni, J. A. Burdick, C. Highley, S. J. Lee, Y. Morimoto, S. Takeuchi, J. J. Yoo, *Nat. Rev. Mater.* **2018**, *3*, 21.

[168] J. G. Nemeno-Guanzon, S. Lee, J. R. Berg, Y. H. Jo, J. E. Yeo, B. M. Nam, Y.-G. Koh, J. I. Lee, *J. Biomed. Biotechnol.* **2012**, *2012*, 956345.

[169] P. Bajaj, R. M. Schweller, A. Khademhosseini, J. L. West, R. Bashir, *Annu. Rev. Biomed. Eng.* **2014**, *16*, 247.

[170] T. Woodfield, K. Lim, P. Morouço, R. Levato, J. Malda, F. Melchels, *Compr. Biomater. II* **2017**, *5*, 236.

[171] J. Groll, T. Boland, T. Blunk, J. A. Burdick, D.-W. Cho, P. D. Dalton, B. Derby, G. Forgacs, Q. Li, V. A. Mironov, *Biofabrication* **2016**, *8*, 13001.

[172] I. T. Ozbolat, K. K. Moncal, H. Gudapati, *Addit. Manuf.* **2017**, *13*, 179.

[173] S. Derakhshanfar, R. Mbeleck, K. Xu, X. Zhang, W. Zhong, M. Xing, *Bioact. Mater.* **2018**, *3*, 144.

[174] I. Matai, G. Kaur, A. Seyedsalehi, A. McClinton, C. T. Laurencin, *Biomaterials* **2020**, *226*, 119536.

[175] W. L. Ng, J. M. Lee, M. Zhou, Y. W. Chen, K. X. A. Lee, W. Y. Yeong, Y. F. Shen, *Biofabrication* **2020**, *12*, 022001.

[176] N. A. Chartrain, C. B. Williams, A. R. Whittington, *Acta Biomater.* **2018**, *74*, 90.

[177] B. Grigoryan, S. J. Paulsen, D. C. Corbett, D. W. Sazer, C. L. Fortin, A. J. Zaita, P. T. Greenfield, N. J. Calafat, J. P. Gounley, A. H. Ta, F. Johansson, A. Randles, J. E. Rosenkrantz, J. D. Louis-Rosenberg, P. A. Galie, K. R. Stevens, J. S. Miller, *Science* **2019**, *364*, 458.

[178] H. Xu, J. Casillas, S. Krishnamoorthy, C. Xu, *Biomed. Mater.* **2020**, *15*, 055021.

[179] M. Pagac, J. Hajnys, Q.-P. Ma, L. Jancar, J. Jansa, P. Stefek, J. Mesicek, *Polymers* **2021**, *13*, 598.

[180] D. Therriault, S. R. White, J. A. Lewis, *Nat. Mater.* **2003**, *2*, 265.

[181] W. Wu, C. J. Hansen, A. M. Aragón, P. H. Geubelle, S. R. White, J. A. Lewis, *Soft Matter* **2010**, *6*, 739.

[182] L. M. Bellan, S. P. Singh, P. W. Henderson, T. J. Porri, H. G. Craighead, J. A. Spector, *Soft Matter* **2009**, *5*, 1354.

[183] R. Sooppan, S. J. Paulsen, J. Han, A. H. Ta, P. Dinh, A. C. Gaffey, C. Venkataraman, A. Trubelja, G. Hung, J. S. Miller, P. Atluri, *Tissue Eng. - Part C Methods* **2016**, *22*, 1.

[184] Q. Zou, B. E. Grottkau, Z. He, L. Shu, L. Yang, M. Ma, C. Ye, *Mater. Sci. Eng. C* **2020**, *108*, 110205.

[185] K. A. Homan, D. B. Kolesky, M. A. Skylar-Scott, J. Herrmann, H. Obuobi, A. Moisan, J. A. Lewis, *Sci. Rep.* **2016**, *6*, 1.

[186] B. Byambaa, N. Annabi, K. Yue, G. Trujillo-de Santiago, M. M. Alvarez, W. Jia, M. Kazemzadeh-Narbat, S.

R. Shin, A. Tamayol, A. Khademhosseini, *Adv. Healthc. Mater.* **2017**, *6*, 1.

[187] Q. Gao, Y. He, J. zhong Fu, A. Liu, L. Ma, *Biomaterials* **2015**, *61*, 203.

[188] L. Shao, Q. Gao, C. Xie, J. Fu, M. Xiang, Y. He, *Biofabrication* **2020**, *12*, 035014.

[189] D. Kang, G. Hong, S. An, I. Jang, W. S. Yun, J. H. Shim, S. Jin, *Small* **2020**, *1905505*, 1.

[190] N. Noor, A. Shapira, R. Edri, I. Gal, L. Wertheim, T. Dvir, *Adv. Sci.* **2019**, *6*, 1900344.

[191] J. W. Lee, Y. J. Choi, W. J. Yong, F. Pati, J. H. Shim, K. S. Kang, I. H. Kang, J. Park, D. W. Cho, *Biofabrication* **2016**, *8*, 015007.

[192] F. Maiullari, M. Costantini, M. Milan, V. Pace, M. Chirivì, S. Maiullari, A. Rainer, D. Baci, H. E. S. Marei, D. Seliktar, C. Gargioli, C. Bearzi, R. Rizzi, *Sci. Rep.* **2018**, *8*, 1.

[193] W. Jia, P. S. Gungor-Ozkerim, Y. S. Zhang, K. Yue, K. Zhu, W. Liu, Q. Pi, B. Byambaa, M. R. Dokmeci, S. R. Shin, A. Khademhosseini, *Biomaterials* **2016**, *106*, 58.

[194] Y. S. Zhang, J. Aleman, S. R. Shin, T. Kilic, D. Kim, S. A. M. Shaegh, S. Massa, R. Riahi, S. Chae, N. Hu, H. Avci, W. Zhang, A. Silvestri, A. S. Nezhad, A. Manbohi, F. De Ferrari, A. Polini, G. Calzone, N. Shaikh, P. Alerasool, E. Budina, J. Kang, N. Bhise, J. Ribas, A. Pourmand, A. Skardal, T. Shupe, C. E. Bishop, M. R. Dokmeci, A. Atala, A. Khademhosseini, *Proc. Natl. Acad. Sci. U. S. A.* **2017**, *114*, E2293.

[195] X. Liu, S. S. D. Carter, M. J. Renes, J. Kim, D. M. Rojas-Canales, D. Penko, C. Angus, S. Beirne, C. J. Drogemuller, Z. Yue, P. T. Coates, G. G. Wallace, *Adv. Healthc. Mater.* **2019**, *8*, 1.

[196] A. Leucht, A. C. Volz, J. Rogal, K. Borchers, P. J. Kluger, *Sci. Rep.* **2020**, *10*, 1.

[197] J. Jang, H. J. Park, S. W. Kim, H. Kim, J. Y. Park, S. J. Na, H. J. Kim, M. N. Park, S. H. Choi, S. H. Park, S. W. Kim, S. M. Kwon, P. J. Kim, D. W. Cho, *Biomaterials* **2017**, *112*, 264.

[198] Y. S. Zhang, Q. Pi, A. M. van Genderen, *J. Vis. Exp.* **2017**, *2017*, 1.

[199] I. Chiesa, C. De Maria, A. Lapomarda, G. M. Fortunato, F. Montemurro, R. Di Gesù, R. S. Tuan, G. Vozzi, R. Gottardi, *Biofabrication* **2020**, *12*, 025013.

[200] W. Zhu, X. Qu, J. Zhu, X. Ma, S. Patel, J. Liu, P. Wang, C. S. E. Lai, M. Gou, Y. Xu, K. Zhang, S. Chen, *Biomaterials* **2017**, *124*, 106.

[201] A. K. Miri, D. Nieto, L. Iglesias, H. Goodarzi Hosseinabadi, S. Maharjan, G. U. Ruiz-Esparza, P. Khoshakhlagh, A. Manbachi, M. R. Dokmeci, S. Chen, S. R. Shin, Y. S. Zhang, A. Khademhosseini, *Adv. Mater.* **2018**, *30*, 1800242.

[202] H. Cui, T. Esworthy, X. Zhou, S. Y. Hann, R. I. Glazer, R. Li, L. G. Zhang, *Adv. Healthc. Mater.* **2020**, *9*, 1900924.

[203] S. Y. Hann, H. Cui, T. Esworthy, X. Zhou, S. jun Lee, M. W. Plesniak, L. G. Zhang, *Acta Biomater.* **2021**, *123*, 263.

[204] X. Liu, S. Michael, K. Bharti, M. Ferrer, M. J. Sont, *Biofabrication* **2020**, *12*, 035002.

[205] P. D. Dalton, T. B. F. Woodfield, V. Mironov, J. Groll, *Adv. Sci.* **2020**, *7*, 1902953.

[206] Y. Tan, D. J. Richards, T. C. Trusk, R. P. Visconti, M. J. Yost, M. S. Kindy, C. J. Drake, W. S. Argraves, R. R. Markwald, Y. Mei, *Biofabrication* **2014**, *6*, 024111.

[207] C. Kucukgul, S. B. Ozler, I. Inci, E. Karakas, S. Irmak, D. Gozuacik, A. Taralp, B. Koc, *Biotechnol. Bioeng.* **2015**, *112*, 811.

[208] M. Itoh, K. Nakayama, R. Noguchi, K. Kamohara, K. Furukawa, K. Uchihashi, S. Toda, J. I. Oyama, K. Node, S. Morita, *PLoS One* **2015**, *10*, e0136681.

[209] C. Norotte, F. S. Marga, L. E. Niklason, G. Forgacs, *Biomaterials* **2009**, *30*, 5910.

[210] R. Gaebel, N. Ma, J. Liu, J. Guan, L. Koch, C. Klopsch, M. Gruene, A. Toelk, W. Wang, P. Mark, F. Wang, B. Chichkov, W. Li, G. Steinhoff, *Biomaterials* **2011**, *32*, 9218.

[211] O. Kérourédan, D. Hakobyan, M. Rémy, S. Ziane, N. Dusserre, J.-C. Fricain, S. Delmond, N. B. Thébaud, R. Devillard, *Biofabrication* **2019**, *11*, 045002.

[212] P. Datta, B. Ayan, I. T. Ozbolat, *Acta Biomater.* **2017**, *51*, 1.

[213] L. Lucas, A. Aravind, P. Emma, M. Christophe, C. Edwin-Joffrey, *Bioprinting* **2021**, *21*, e00119.

[214] W. Sun, B. Starly, A. C. Daly, J. A. Burdick, J. Groll, G. Skeldon, W. Shu, Y. Sakai, M. Shinohara, M. Nishikawa, J. Jang, D.-W. Cho, M. Nie, S. Takeuchi, S. Ostrovidov, A. Khademhosseini, R. D. Kamm, V. Mironov, L. Moroni, I. T. Ozbolat, *Biofabrication* **2020**, *12*, 22002.

[215] A. Bagheri, J. Jin, *ACS Appl. Polym. Mater.* **2019**, *1*, 593.

[216] F. Yu, W. Hunziker, D. Choudhury, *Micromachines* **2019**, *10*, 165.

[217] F. Yu, D. Choudhury, *Drug Discov. Today* **2019**, *24*, 1248.

[218] S. Knowlton, B. Yenilmez, S. Tasoglu, *Trends Biotechnol.* **2016**, *34*, 685.

[219] D. D. Monie, S. K. Bhatia, in *Bioprinting Regen. Med.*, Eds: K. Turksen, Springer International Publishing, Switzerland **2015**, pp. 123–137.

[220] K. Fetah, P. Tebon, M. J. Goudie, J. Eichenbaum, L. Ren, N. Barros, R. Nasiri, S. Ahadian, N. Ashammakhi, M. R. Dokmeci, A. Khademhosseini, *Prog. Biomed. Eng.* **2019**, *1*, 012001.

[221] V. K. Lee, D. Y. Kim, H. Ngo, Y. Lee, L. Seo, S. S. Yoo, P. A. Vincent, G. Dai, *Biomaterials* **2014**, *35*, 8092.

[222] Y. S. Zhang, J. Aleman, A. Arneri, S. Bersini, S. R. Shin, M. R. Dokmeci, A. Khademhosseini, S. Arabia, *Biomaterials* **2016**, *110*, 45.

[223] J. Y. Park, H. Ryu, B. Lee, D. H. Ha, M. Ahn, S. Kim, J. Y. Kim, N. L. Jeon, D. W. Cho, *Biofabrication* **2019**, *11*, 015002.

[224] A. Dobos, F. Gantner, M. Markovic, J. Van Hoorick, L. Tytgat, S. Van Vlierberghe, A. Ovsianikov, *Biofabrication* **2021**, *13*, 015016.

[225] G. Gao, X. Cui, *Biotechnol. Lett.* **2016**, *38*, 203.

[226] A. K. Miri, A. Khalilpour, B. Cecen, S. Maharjan, S. Ryon, S., A. Khademhosseini, *Biomaterials* **2019**, *198*, 08006.

[227] P. Sasmal, P. Datta, Y. Wu, I. T. Ozbolat, *Microphysiological Syst.* **2018**, *1*, 1.

[228] I. S. Kinstlinger, J. S. Miller, *Lab Chip* **2016**, *16*, 2025.

[229] W. Peng, P. Datta, Y. Wu, M. Dey, B. Ayan, A. Dababneh, I. T. Ozbolat, in *Adv. Exp. Med. Biol.*, Vol. 1107, Springer, New York 2018, pp. 53–71.

[230] J. W. Higgins, A. Chambon, K. Bishard, A. Hartung, D. Arndt, J. Brugnano, P. X. Er, K. T. Lawlor, J. M. Vanslambrouck, S. Wilson, A. N. Combes, S. E. Howden, K. S. Tan, S. V. Kumar, L. J. Hale, B. Shepherd, S. Pentoney, S. C. Presnell, A. E. Chen, M. H. Little, *bioRxiv* **2018**, 505396.

[231] A. Kjar, B. McFarland, K. Mecham, N. Harward, Y. Huang, *Bioact. Mater.* **2021**, *6*, 460.

[232] E. Maloney, C. Clark, H. Sivakumar, K. Yoo, J. Aleman, S. A. P. Rajan, S. Forsythe, A. Mazzocchi, A. W. Laxton, S. B. Tatter, R. E. Strowd, K. I. Votanopoulos, A. Skardal, *Micromachines* **2020**, *11*, 208.

[233] J. A. Brassard, M. Nikolaev, T. Hübscher, M. Hofer, M. P. Lutolf, *Nat. Mater.* **2020**, *20*, 22.

[234] M. A. Skylar-Scott, S. G. M. Uzel, L. L. Nam, J. H. Ahrens, R. L. Truby, S. Damaraju, J. A. Lewis, *Sci. Adv.* **2019**, *5*, eaaw2459.

[235] T. Takebe, B. Zhang, M. Radisic, *Cell Stem Cell* **2017**, *21*, 297.

[236] R. Vadivelu, H. Kamble, M. Shiddiky, N.-T. Nguyen, *Micromachines* **2017**, *8*, 94.

[237] A. Skardal, T. Shupe, A. Atala, *Drug Discov. Today* **2016**, *21*, 1399.

[238] B. Schuster, M. Junkin, S. S. Kashaf, I. Romero-Calvo, K. Kirby, J. Matthews, C. R. Weber, A. Rzhetsky, K. P. White, S. Tay, *Nat. Commun.* **2020**, *11*, 1.

[239] Y. Jin, J. Kim, J. S. Lee, S. Min, S. Kim, D. Ahn, Y. Kim, S. Cho, **2018**, *1801954*, 1.

[240] Y. Nashimoto, T. Hayashi, I. Kunita, A. Nakamasu, Y. S. Torisawa, M. Nakayama, H. Takigawa-Imamura, H. Kotera, K. Nishiyama, T. Miura, R. Yokokawa, *Integr. Biol.* **2017**, *9*, 506.

[241] Y. Isshiki, T. Kaneko, A. Tamada, K. Muguruma, R. Yokokawa, *Proc. IEEE Int. Conf. Micro Electro Mech. Syst.* **2020**, 1024.

[242] S. Zhang, Z. Wan, R. D. Kamm, *Lab Chip* **2021**, *21*, 473.

[243] T. Grix, A. Ruppelt, A. Thomas, A.-K. Amler, B. Noichl, R. Lauster, L. Kloke, *Genes* **2018**, *9*, 176.

[244] H. Zhao, Y. Chen, L. Shao, M. Xie, J. Nie, J. Qiu, P. Zhao, H. Ramezani, J. Fu, H. Ouyang, Y. He, *Small* **2018**,

14, 1802630.

[245] L. Serex, K. Sharma, V. Rizov, A. Bertsch, J. D. McKinney, P. Renaud, *Biofabrication* **2021**, *13*, 025006

[246] N. S. Bhise, V. Manoharan, S. Massa, A. Tamayol, M. Ghaderi, M. Miscuglio, Q. Lang, Y. S. Zhang, S. R. Shin, G. Calzone, N. Annabi, T. D. Shupe, C. E. Bishop, A. Atala, M. R. Dokmeci, A. Khademhosseini, *Biofabrication* **2016**, *8*, 014101.

[247] A. Wnorowski, H. Yang, J. C. Wu, *Adv. Drug Deliv. Rev.* **2019**, *140*, 3.

[248] A. Cochrane, H. J. Albers, R. Passier, C. L. Mummery, A. van den Berg, V. V. Orlova, A. D. van der Meer, *Adv. Drug Deliv. Rev.* **2019**, *140*, 68.

[249] A. Geraili, P. Jafari, M. S. Hassani, B. H. Araghi, M. H. Mohammadi, A. M. Ghafari, S. H. Tamrin, H. P. Modarres, A. R. Kolahchi, S. Ahadian, A. Sanati-Nezhad, *Adv. Healthc. Mater.* **2018**, *7*, 1700426.

[250] J. Drost, H. Clevers, *Nat. Rev. Cancer* **2018**, *18*, 407.

[251] L. Prodanov, R. Jindal, S. S. Bale, M. Hegde, W. J. Mccarty, I. Golberg, A. Bhushan, M. L. Yarmush, O. B. Usta, *Biotechnol. Bioeng.* **2016**, *113*, 241.

[252] L. A. van Grunsven, *Adv. Drug Deliv. Rev.* **2017**, *121*, 133.

[253] V. van Duinen, D. Zhu, C. Ramakers, A. J. van Zonneveld, P. Vulto, T. Hankemeier, *Angiogenesis* **2019**, *22*, 157.

[254] W. Y. Wang, D. Lin, E. H. Jarman, W. J. Polacheck, B. M. Baker, *Lab Chip* **2020**, *20*, 1153.

[255] R. Pimentel C., S. K. Ko, C. Caviglia, A. Wolff, J. Emnéus, S. S. Keller, M. Dufva, *Acta Biomater.* **2018**, *65*, 174.

[256] K. H. K. Wong, J. G. Truslow, A. H. Khankhel, K. L. S. Chan, J. Tien, *J. Biomed. Mater. Res. Part A* **2013**, *101A*, 2181.

[257] M. Sato, N. Sasaki, M. Ato, S. Hirakawa, K. Sato, K. Sato, PloS ONE **2015**, *10*, e0137301.

[258] I. Choi, S. Lee, Y. K. Hong, *Cold Spring Harb. Perspect. Med.* **2012**, *2*, a006445.

[259] A. Aspelund, M. R. Robciuc, S. Karaman, T. Makinen, K. Alitalo, *Circ. Res.* **2016**, *118*, 515.

[260] T. P. Padera, E. F. J. Meijer, L. L. Munn, *Annu. Rev. Biomed. Eng.* **2016**, *18*, 125.

[261] J. P. Wikswo, F. E. Block, D. E. Cliffel, C. R. Goodwin, C. C. Marasco, D. A. Markov, D. L. McLean, J. A. McLean, J. R. McKenzie, R. S. Reiserer, P. C. Samson, D. K. Schaffer, K. T. Seale, S. D. Sherrod, *IEEE Trans. Biomed. Eng.* **2013**, *60*, 682.

[262] J. F. Wong, M. D. Mohan, E. W. K. Young, C. A. Simmons, *Biosens. Bioelectron.* **2020**, *147*, 111757.

[263] S. Jalili-Firoozinezhad, F. S. Gazzaniga, E. L. Calamari, D. M. Camacho, C. W. Fadel, A. Bein, B. Swenor, B. Nestor, M. J. Cronce, A. Tovaglieri, O. Levy, K. E. Gregory, D. T. Breault, J. M. S. Cabral, D. L. Kasper,

R. Novak, D. E. Ingber, *Nat. Biomed. Eng.* **2019**, *3*, 520.

[264] P. N. Joshi, in *Lab-on-a-Chip Fabr. Appl.*, (Eds: M. Stoytcheva, R. Zlatev), IntechOpen, **2016**, Ch. 5.

[265] X. Wang, D. T. T. Phan, A. Sobrino, S. C. George, C. C. W. Hughes, A. P. Lee, *Lab Chip* **2016**, *16*, 282.

[266] A. Petrosyan, P. Cravedi, V. Villani, A. Angeletti, J. Manrique, A. Renieri, R. E. De Filippo, L. Perin, S. Da Sacco, *Nat. Commun.* **2019**, *10*, 1.

[267] V. Sander, A. Przepiorski, A. E. Crunk, N. A. Hukriede, T. M. Holm, A. J. Davidson, *STAR Protoc.* **2020**, *1*, 100150.

[268] F. Jacob, R. D. Salinas, D. Y. Zhang, P. T. T. Nguyen, J. G. Schnoll, S. Z. H. Wong, R. Thokala, S. Sheikh, D. Saxena, S. Prokop, D. ao Liu, X. Qian, D. Petrov, T. Lucas, H. I. Chen, J. F. Dorsey, K. M. Christian, Z. A. Binder, M. Nasrallah, S. Brem, D. M. O'Rourke, G. li Ming, H. Song, *Cell* **2020**, *180*, 188.

[269] M. Dossena, R. Piras, A. Cherubini, M. Barilani, E. Dugnani, F. Salanitro, T. Moreth, F. Pampaloni, L. Piemonti, L. Lazzari, *Stem Cell Res. Ther.* **2020**, *11*, 94.

[270] J. Vives, L. Batlle-Morera, *Stem Cell Res. Ther.* **2020**, *11*, 1.

[271] S. N. Boers, J. J. Delden, H. Clevers, A. L. Bredenoord, *EMBO Rep.* **2016**, *17*, 938.

[272] Y. Huyan, Q. Lian, T. Zhao, D. Li, J. He, *Int. J. Bioprinting* **2020**, *6*, 53.

[273] C. Kropp, D. Massai, R. Zweigerdt, *Process Biochem.* **2017**, *59*, 244.

[274] A. J. Want, A. W. Nienow, C. J. Hewitt, K. Coopman, *Regen. Med.* **2012**, *7*, 71.

[275] C. Kropp, H. Kempf, C. Halloin, D. Robles-Diaz, A. Franke, T. Scheper, K. Kinast, T. Knorpp, T. O. Joos, A. Haverich, U. Martin, R. Zweigerdt, R. Olmer, *Stem Cells Transl. Med.* **2016**, *5*, 1289.

[276] V. Bunpetch, H. Wu, S. Zhang, H. Ouyang, *Stem Cells Dev.* **2017**, *26*, 1662.

[277] V. C. Chen, S. M. Couture, J. Ye, Z. Lin, G. Hua, H. I. P. Huang, J. Wu, D. Hsu, M. K. Carpenter, L. A. Couture, *Stem Cell Res.* **2012**, *8*, 388.

[278] C. García-Fernández, A. López-Fernández, S. Borrós, M. Lecina, J. Vives, *Biochem. Eng. J.* **2020**, *159*, 107601.

[279] J. P. K. Armstrong, T. J. Keane, A. C. Roques, P. S. Patrick, C. M. Mooney, W. L. Kuan, V. Pisupati, R. O. C. Oreffo, D. J. Stuckey, F. M. Watt, S. J. Forbes, R. A. Barker, M. M. Stevens, *Sci. Transl. Med.* **2020**, *12*, eaaz2253.

[280] Y. A. Jodat, M. G. Kang, K. Kiaee, G. J. Kim, A. F. H. Martinez, A. Rosenkranz, H. Bae, S. R. Shin, *Curr. Pharm. Des.* **2019**, *24*, 5471.

[281] B. Zhang, M. Radisic, *Lab Chip* **2017**, *17*, 2395.

[282] R. Mittal, F. W. Woo, C. S. Castro, M. A. Cohen, J. Karanxha, J. Mittal, T. Chhibber, V. M. Jhaveri, *J. Cell.*

Physiol. **2019**, *234*, 8352.

[283] N. Franzen, W. H. van Harten, V. P. Retèl, P. Loskill, J. van den Eijnden-van Raaij, M. IJzerman, *Drug Discov. Today* **2019**, *24*, 1720.

[284] C. C. Miranda, J. M. S. Cabral, in *Precis. Med. Investig. Pract. Provid.*, Elsevier **2020**, Ch. 45.

[285] T. Simon-Yarza, A. Mielcarek, P. Couvreur, C. Serre, *Adv. Mater.* **2018**, *30*, 1707365.

[286] Y. Zhao, R. K. Kankala, S. Bin Wang, A. Z. Chen, *Molecules* **2019**, *24*, 675.

[287] A. Almeida, B. Sarmento, F. Rodrigues, *Int. J. Pharm.* **2017**, *519*, 178.

[288] M. Mastrangeli, S. Millet, the O. partners, J. van den E. Raaij, *Preprints* **2019**, 2019030031.

[289] H. Kimura, Y. Sakai, T. Fujii, *Drug Metab. Pharmacokinet.* **2018**, *33*, 43.

[290] M. Zanoni, S. Pignatta, C. Arienti, M. Bonafè, A. Tesei, *Expert Opin. Drug Discov.* **2019**, *14*, 289.

[291] M. Zanoni, M. Cortesi, A. Zamagni, C. Arienti, S. Pignatta, A. Tesei, *J. Hematol. Oncol.* **2020**, *13*, 1.

[292] S. Bartfeld, H. Clevers, *J. Mol. Med.* **2017**, *95*, 729.

[293] V. Vaira, G. Fedele, S. Pyne, E. Fasoli, G. Zadra, D. Bailey, E. Snyder, A. Faversani, G. Coggi, R. Flavin, S. Bosari, M. Loda, *Proc. Natl. Acad. Sci. U. S. A.* **2010**, *107*, 8352.

[294] Z. Gilazieva, A. Ponomarev, C. Rutland, A. Rizvanov, V. Solovyeva, *Cancers (Basel).* **2020**, *12*, 1.

[295] J. F. Dekkers, G. Berkers, E. Kruisselbrink, A. Vonk, H. R. De Jonge, H. M. Janssens, I. Bronsveld, E. A. Van De Graaf, E. E. S. Nieuwenhuis, R. H. J. Houwen, F. P. Vleggaar, J. C. Escher, Y. B. De Rijke, C. J. Majoor, H. G. M. Heijerman, K. M. De Winter-De Groot, H. Clevers, C. K. Van Der Ent, J. M. Beekman, *Sci. Transl. Med.* **2016**, *8*, 344ra84.

[296] Aspects Biosystems, "Aspect Byosystems partners with Merck, GSK and McGill", **2019**.

[297] Aspects Biosystems, "Aspects Biosystems annouces liver tissue collaboration with JSR", **2018**.

[298] T. Nakamura, T. Sato, *CMGH* **2018**, *5*, 51.

[299] G. Rossi, A. Manfrin, M. P. Lutolf, *Nat. Rev. Genet.* **2018**, *19*, 671-687.

[300] C. Corrò, L. Novellasdemunt, V. S. W. Li, *Am. J. Physiol. - Cell Physiol.* **2020**, *319*, C151.

[301] N. Ashammakhi, E. Elkhammas, A. Hasan, *J. Biomed. Mater. Res. Part B Appl. Biomater.* **2019**, *107*, 2006.

[302] J. Yu, *Int. J. Stem Cells* **2020**, DOI 10.15283/ijsc20143.

[303] M. Li, J. C. Izpisua Belmonte, *N. Engl. J. Med.* **2019**, *380*, 569.

[304] G. Kaushik, M. P. Ponnusamy, S. K. Batra, *Stem Cells* **2018**, *36*, 1329.

[305] Y. Wu, D. J. Ravnic, I. T. Ozbolat, *Trends Biotechnol.* **2020**, *38*, 594.

[306] P. Li, in *3D Bioprinting Reconstr. Surg. Tech. Appl.* (Eds.: D.J. Thomas, Z.M. Jessop, I.S. Whitaker), Woodhead Publishing, **2018**, Ch. 11.

[307] F. Gilbert, C. D. O'Connell, T. Mladenovska, S. Dodds, *Sci. Eng. Ethics* **2018**, *24*, 73.

[308] P. Aprile, D. Letourneur, T. Simon-Yarza, *Adv. Healthc. Mater.* **2020**, *9*, 2000707.

[309] J. Groll, J. A. Burdick, D. W. Cho, B. Derby, M. Gelinsky, S. C. Heilshorn, T. Jüngst, J. Malda, V. A. Mironov, K. Nakayama, A. Ovsianikov, W. Sun, S. Takeuchi, J. J. Yoo, T. B. F. Woodfield, *Biofabrication* **2019**, *11*, 013001.

[310] Y. P. Jin, C. Shi, Y. Y. Wu, J. L. Sun, J. P. Gao, Y. Yang, *Chin. Med. J. (Engl).* **2020**, *133*, 424.

[311] A. Schwab, R. Levato, M. D'Este, S. Piluso, D. Eglin, J. Malda, *Chem. Rev.* **2020**, *120*, 11028.

[312] P. Datta, B. Ayan, I. T. Ozbolat, *Acta Biomater.* **2017**, *51*, 1.

[313] J. W. Nichol, A. Khademhosseini, *Soft Matter* **2009**, *5*, 1312.

[314] Y. Du, M. Ghodousi, H. Qi, N. Haas, W. Xiao, A. Khademhosseini, *Biotechnol. Bioeng.* **2011**, *108*, 1693.

[315] R. Gauvin, A. Khademhosseini, *ACS Nano* **2011**, *5*, 4258.

[316] A. P. McGuigan, M. V. Sefton, *Proc. Natl. Acad. Sci. U. S. A.* **2006**, *103*, 11461.

[317] M. D. Sarker, S. Naghieh, N. K. Sharma, X. Chen, *J. Pharm. Anal.* **2018**, *8*, 277.

[318] T. Shimizu, H. Sekine, Y. Isoi, M. Yamato, A. Kikuchi, T. Okano, *Tissue Eng.* **2006**, *12*, 499.

[319] J. Yang, M. Yamato, T. Shimizu, H. Sekine, K. Ohashi, M. Kanzaki, T. Ohki, K. Nishida, T. Okano, *Biomaterials* **2007**, *28*, 5033.

[320] M. Y. Tondreau, F. A. Auger, in *Proc. of WC8*, ALTEX Proceedings, Montreal, Canada, **2011.**

[321] N. L'Heureux, N. Dusserre, G. Konig, B. Victor, P. Keire, T. N. Wight, N. A. F. Chronos, A. E. Kyles, C. R. Gregory, G. Hoyt, R. C. Robbins, T. N. McAllister, *Nat. Med.* **2006**, *12*, 361.

[322] S. Masuda, T. Shimizu, *Adv. Drug Deliv. Rev.* **2016**, *96*, 103.

[323] N. L'heureux, S. Pâquet, R. Labbé, L. Germain, F. A. Auger, *FASEB J.* **1998**, *12*, 47.

[324] K. Kim, R. Utoh, K. Ohashi, T. Kikuchi, T. Okano, *J. Tissue Eng. Regen. Med.* **2017**, *11*, 2071.

[325] L. Moroni, J. A. Burdick, C. Highley, S. J. Lee, Y. Morimoto, S. Takeuchi, J. J. Yoo, *Nat. Rev. Mater.* **2018**, *3*, 21.

[326] L. A. Smith, P. X. Ma, *Colloids Surfaces B Biointerfaces* **2004**, *39*, 125.

[327] V. Mironov, V. Kasyanov, Z. S. Xiao, C. Eisenberg, L. Eisenberg, S. Gonda, T. Trusk, R. R. Markwald, G. D. Prestwich, *Biomaterials* **2005**, *26*, 7628.

[328] A. E. Reimer, K. M. Feher, D. Hernandez, K. Slowinska, *J. Mater. Chem.* **2012**, *22*, 7701.

[329] A. Hasan, A. Memic, N. Annabi, M. Hossain, A. Paul, M. R. Dokmeci, F. Dehghani, A. Khademhosseini, *Acta Biomater.* **2014**, *10*, 11.

[330] J. J. Stankus, L. Soletti, K. Fujimoto, Y. Hong, D. A. Vorp, W. R. Wagner, *Biomaterials* **2007**, *28*, 2738.

[331] L. Ye, J. Cao, L. Chen, X. Geng, A.-Y. Zhang, L.-R. Guo, Y.-Q. Gu, Z.-G. Feng, *J. Biomed. Mater. Res. Part A* **2015**, *103*, 3863.

[332] N. Duan, X. Geng, L. Ye, A. Zhang, Z. Feng, L. Guo, Y. Gu, *Biomed. Mater.* **2016**, *11*, 035007.

[333] P. Coimbra, P. Santos, P. Alves, S. P. Miguel, M. P. Carvalho, K. D. de Sá, I. J. Correia, P. Ferreira, *Colloids Surfaces B Biointerfaces* **2017**, *159*, 7.

[334] S. A. Sell, M. J. McClure, K. Garg, P. S. Wolfe, G. L. Bowlin, *Adv. Drug Deliv. Rev.* **2009**, *61*, 1007.

[335] H. Liu, X. Li, G. Zhou, H. Fan, Y. Fan, *Biomaterials* **2011**, *32*, 3784.

[336] J. Han, P. Lazarovici, C. Pomerantz, X. Chen, Y. Wei, P. I. Lelkes, *Biomacromolecules* **2011**, *12*, 399.

[337] W. Fu, Z. Liu, B. Feng, R. Hu, X. He, H. Wang, M. Yin, H. Huang, H. Zhang, W. Wang, *Int. J. Nanomedicine* **2014**, *9*, 2335.

[338] E. Ercolani, C. Del Gaudio, A. Bianco, *J. Tissue Eng. Regen. Med.* **2015**, *9*, 861.

[339] N. Goonoo, *Biomed. Phys. Eng. Express* **2018**, *4*, 32001.

[340] T. Simón-Yarza, A. Rossi, K.-H. Heffels, F. Prósper, J. Groll, M. J. Blanco-Prieto, *Tissue Eng. Part A* **2015**, *21*, 1654.

[341] S. Salerno, F. Tasselli, E. Drioli, L. De Bartolo, *Membranes (Basel).* **2020**, *10*, 112.

[342] T. P. Burton, A. Callanan, *Tissue Eng. Regen. Med.* **2018**, *15*, 301.

[343] M. Liu, X. P. Duan, Y. M. Li, D. P. Yang, Y. Z. Long, *Mater. Sci. Eng. C* **2017**, *76*, 1413.

[344] A. De Mori, M. P. Fernández, G. Blunn, G. Tozzi, M. Roldo, *Polymers (Basel).* **2018**, *10*, 285.

[345] T. Wu, M. Ding, C. Shi, Y. Qiao, P. Wang, R. Qiao, X. Wang, J. Zhong, *Chinese Chem. Lett.* **2020**, *31*, 617.

[346] A. Martins, J. V. Araújo, R. L. Reis, N. M. Neves, *Nanomedicine* **2007**, *2*, 929.

[347] V. S. Joshi, N. Y. Lei, C. M. Walthers, B. Wu, J. C. Y. Dunn, *J. Surg. Res.* **2013**, *183*, 18.

[348] S. B. Orr, A. Chainani, K. J. Hippensteel, A. Kishan, C. Gilchrist, N. W. Garrigues, D. S. Ruch, F. Guilak, D. Little, *Acta Biomater.* **2015**, *24*, 117.

3. EXPERIMENTAL WORK (PART 1)

3. EXPERIMENTAL WORK (PART 1)

3.1. DEVELOPMENT OF 3D POROUS POLYSACCHARIDE-BASED HYDROGELS WITH PREFORMED MICROCHANNELS OF VARYING DIAMETERS AND GEOMETRIES

1. Introduction

The development of hydrogel-based biomaterials that can promote vascularization presents a great challenge in tissue engineering. 3D hydrogels which can mimic soft tissue mechanical properties are promising candidates as scaffolds for tissue regeneration. For vascularization strategies, porous hydrogels are often employed due to their ability to facilitate nutrient and oxygen diffusion and enable cell migration [1]. However, interconnected pores alone are not sufficient to promote anastomoses with host vasculature upon transplantation. Numerous studies have shown that the addition of channels inside a porous scaffold can facilitate cell growth and rapid vascularization, resulting in enhanced tissue formation [2].

Over the past decades, researchers have utilized biofabrication methods coupled with sacrificial printing to produce scaffolds with preformed vascular network, as described in depth in Chapter 2. Both 3D printing of hydrogel and sacrificial materials enable precise spatial control over the final scaffold geometry and the geometry of the sacrificial template with channel structures. Briefly, the sacrificial templates are first printed, then encased inside a hydrogel-based scaffolds (referred to as the encapsulating hydrogel), and finally dissolved to produce a hydrogel construct with preformed vascular networks [3]. However, this strategy still presents several limitations. The first disadvantage concerns the use of bioink, which is associated with the low mechanical properties of natural hydrogels, leading to channel collapse during direct printing. The most common choice for encapsulating hydrogel is GelMA (gelatin methacryloyl) [3]. GelMA offers high levels of tunability: mechanical properties can be adjusted based on polymer concentration, type of photoinitiator, photocrosslinking time, and UV (ultraviolet) dose during photoinitiation. It must be noted that the use of GelMA for 3D bioprinting requires sufficient solution viscosity. Low-viscosity of GelMA solution tends to result in cell deposition during DLP (digital light processing)

printing [4]. While increasing GelMA concentration to more than 15% (w/v) could improve rheological properties for printing, it could impair cell viability due to high density of the encapsulated hydrogel network [5]. Thickening agent such as alginate could be added to GelMA solution to overcome the solution viscosity, but at the cost of cell growth [6].

Other commonly used sacrificial materials include carbohydrate glass, gelatin, agarose, Pluronic F127 [3]. Gelatin and Pluronic F127 have weak mechanical properties, which often leads to collapse of sacrificial templates. Meanwhile, gelatin has a fast and uncontrolled dissolving rate, causing the sacrificial template to dissolve before fully encapsulated by the main hydrogel [7,8]. Recently, researchers have used polyvinyl alcohol (PVA) as sacrificial material to print simple to complex vessel geometries and generate preformed microchannel inside hydrogel-based scaffolds. Pan and colleagues employed GelMA hydrogel to encase 3D-printed PVA templates. They replaced bioprinting with simple additive manufacturing such as fuse deposition modeling (FDM) to print PVA models with tubular structures, then casted GelMA solution over the PVA templates and the GelMA was photocrosslinked with a photoinitiator, lithium phenyl-2,4,6-trimethylbenzoylphosphinate (LAP). Their work demonstrated the ability to produce hydrogel scaffolds with different channel patterns and diameters, and the channels were perfusable in stained PBS solution [9]. Zou et al. 3D printed PVA template, then bioprinted a hydrogel composite made of sodium alginate, agarose solution, and platelet-rich plasma (PRP) mixed with human umbilical vein endothelial cells (HUVECs). The PVA templates were dissolved in cell media, resulting in a large-scale construct with microchannel networks, high cell survival rate, and positive collagen content after 14 days in culture [10].

Both of these studies still present limitations. In the study of Zou and colleagues, the exposure of PVA templates along with $CaCl_2$ and agarose introduced complex interactions between the sacrificial component and the encasing hydrogel mesh. While agarose facilitated rapid solidification of alginate hydrogel, it reduced the dissolution rate of PVA in water. Similarly, the release of calcium ions, which crosslinked with sodium alginate, prevented PVA from dissolving further. Thus, the incorporation of cells within the hydrogel composite bioink increased the complexity of interactions between the PVA template, the encasing scaffold, and the cellular components. More importantly, the microchannels in both studies remained in the hundreds of micron level (400 to 1000 μm), far from the target diameters of capillaries, arterioles and venules

in the organism [9,10]. Finally, the scaffolds lacked pores, which is also essential to facilitate rapid cell growth and vascularization [2].

Therefore, in the context of developing hydrogel scaffolds using sacrificial templates for microchannel construction, two main factors must be taken into account: First, the encapsulating hydrogel must have adequate mechanical strength to ensure scaffold stability and channel rigidity after hydrogel crosslinking. Second, the sacrificial material must facilitate easy incorporation within the encapsulating hydrogel and have the right dissolution rate, to promote good channel formation, and maintain structural integrity after encapsulation.

The first part of the PhD project attempts to solve the aforementioned technical challenges. Here, the encapsulating hydrogel is chemically crosslinked, which avoids all issues associated with photopolymerization on cell viability due to cytotoxicity caused by the photoinitiators and by the oxygen radicals formed during the photocrosslinking process. These chemical hydrogels are made of pharmaceutical-grade pullulan and dextran (referred to as PUDNA), with defined porosity, controlled swelling, and adequate mechanical properties. The hydrogel crosslinking was previously described in various publications and the crosslinking method has been patented (**Figure 10**) [11–14]. The hydrogel synthesis protocol was then adapted to include the incorporation of sacrificial templates, which gave rise to preformed microchannel inside the hydrogel. These vessel-like tubular structures were created via additive manufacturing. The initial sacrificial material employed in this study was commercial water-soluble PVA (**Figure 11a**). By using FDM 3D printing method, we were able to create sacrificial templates exhibiting simple tubular structure with channel diameters ranging from 400 µm to 500 µm. After optimization work, alginate hydrogel was employed as sacrificial material to generate complex geometries mimicking arterioles and capillaries (100 - 200 µm) (**Figure 11b**). Additionally, the technical challenges of FDM 3D printing in regards to fabricating sacrificial templates for tissue engineering applications will also be reported and discussed.

2. Materials and Methods

2.1. Materials and equipment

Pullulan (Mw 200 kDa) and dextran (Mw 500 kDa) were obtained from Hayashibara Inc., Okayama, Japan and Pharmacosmos, respectively. FITC-dextran (dextran labeled with fluorescein

isocyanate, TdB consultancy®) was used to label the hydrogels. All other chemicals were obtained from Sigma-Aldrich®. The 3D printer (Ultimaker S3) and polymer filaments (polyvinyl alcohol, PVA, and polylactic acid, PLA) were purchased from Ultimaker.

2.2. Hydrogel synthesis without microchannel

Five different formulations were prepared with the same concentration of polysaccharides and varying concentrations of crosslinker, sodium trimetaphosphate (STMP). Hydrogels were prepared using a patented method developed previously by our team [11–14]. Briefly, pullulan and dextran (75:25 w/w) and NaCl (0.35g/mL) were dissolved in miliQ water. STMP solution was then added under alkaline conditions obtained by the addition of NaOH 10M solution into the polysaccharide mixture. Five STMP solutions with varying concentrations (1% (w/v), 2% (w/v), 3% (w/v), 4% (w/v), and 5% (w/v)) were used to obtain five hydrogel formulations, namely: PUDNA-S1, PUDNA-S2, PUDNA-S3, PUDNA-S4, and PUDNA-S5 respectively. Additionally, 1% FITC-dextran was also added to the hydrogel precursor solution as a fluorescent tracer. The hydrogel was molded by pouring the crosslinked solution onto a silicon spacer (1 mm in thickness) sandwiched between two rectangular glass slides (**Figure 10**). This hydrogel slab was then immediately incubated for 20 minutes at 50 ºC. Afterwards, hydrogels were cut into disc shapes using a biopsy cutter (Harris Uni-Core, Sigma Aldrich) of 5.0 mm in diameter. The scaffolds were then washed extensively in phosphate buffer saline (PBS) 10X to remove unreacted NaOH and neutralize the pH. Next, the gels were rinsed again in miliQ water until the ionic force of the rinsing solution was below 20 µS/cm (Conductivity Meter Thermo Orion model 145). Then, the hydrogels were rinsed in NaCl (0.025% w/v) solution until the ionic force reached around 540 µS/cm.

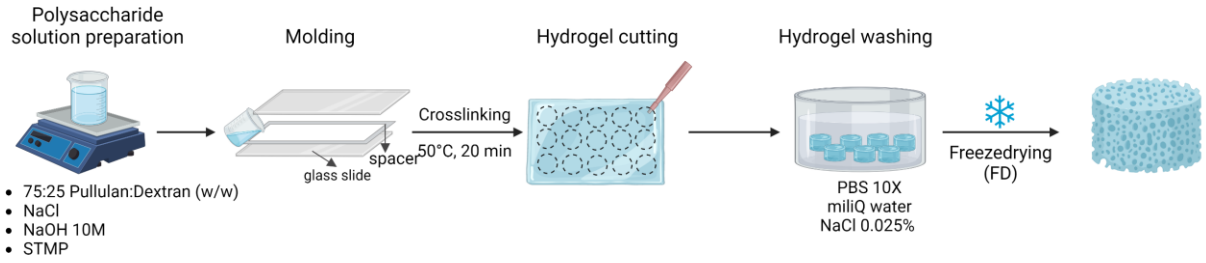

Figure 10. Hydrogel synthesis protocol (without microchannel). Created with Biorender.com.

2.3. Pore formation via freeze drying process

Hydrogels swollen in NaCl (0.025% w/v) were drained to remove excess solvent, then put in Petri dishes (VWR, 391-0875) and placed on freeze-dryer trays (MUT 004, Cryotec®). The freeze-drying protocol consists of three stages: freezing under atmospheric pressure from 15 ºC to -20 ºC at a constant rate of -0.1 ºC/min, followed by a phase at constant temperature of -20 ºC for 90 minutes. Primary drying was performed at low pressure (0.010 mbar) and -5 ºC for 8 hours. Secondary drying was run at 30 ºC for 1 hour [14].

2.4. Design and 3D printing of sacrificial templates

Sacrificial templates made of soluble PVA and molds made of PLA were designed and converted into Standard Triangle Language (STL) files using Fusion 360 Autodesk software. All STL files were then processed by Cura software (Ultimaker) to generate G-code instructions for the 3D printer. Then, PVA templates or PLA molds were printed using the Ultimaker S3 and the adapted print cores (AA print core for PLA filament and BB print core for PVA filament). Different designs were developed to generate microvessel-like structures with diameters ranging from 100 to 500 µm (**Figure 11**). Printing parameters such as print speed (mm/s) and extruded layer height (mm) were optimized for each 3D printed design in order to produce smooth prints with no deformation inside the microchannel.

2.5. Hydrogel synthesis with microchannel via sacrificial templates

PVA templates

PVA filament and the 3D printer UltimakerS3 were purchased from Ultimaker. A set up consisting of two glass slides and the PVA template between them was used to prepare the patterned hydrogels (**Figure 11a.ii**). Hydrogel was prepared as described in section 2.2. After the crosslinking step at 50 ºC, the hydrogels were washed and freeze-dried for pore formation (**Section 2.3**). PVA structures were dissolved during the washing step with miliQ water.

Alginate hydrogel templates

In order to determine the optimal crosslinking condition for alginate hydrogel, a series of alginic acid sodium solutions (Alg) and $CaCl_2$ solutions at different concentrations were prepared: 5%, 10%, 20%, 30% (w/v) in miliQ water. After mixing alginic acid sodium in miliQ water at both

room temperature (RT) and at 30 ºC, only 5% and 10% (w/v) were fully dissolved. However, Alg 10% (w/v) solution was more viscous than Alg 5% (w/v). Similarly, two $CaCl_2$ solutions 5% and 20% (w/v) were prepared and were used to crosslink Alg 5% and 10% (w/v) solutions. Crosslinked alginate hydrogel was casted into a mold with a simple tubular structure and was observed for hydrogel retraction to determine optimal crosslinking parameters.

Once the optimal crosslinking parameters of alginate hydrogel were determined, hydrogel templates were prepared as follows. First, PLA molds with bifurcating networks (**Figure 11b.i**) were printed using as print settings a print speed of 70 mm/s, a layer height of 0.2 mm, and a wall thickness of 0.8 mm. Next, alginic acid sodium salt 10 % (w/v) and calcium chloride 5 % (w/v) solutions were prepared in miliQ water. The alginate solution was casted onto the PLA template by spreading the solution with a spatula. Immediately afterwards, the PLA-containing alginate template was immersed into calcium chloride solution to crosslink the alginate gel. The crosslinked alginate gel (sacrificial component) was placed between two silicon spacers (0.5 mm in thickness, to control the final gel thickness) and two glass-slides during the synthesis of the hydrogel. The alginate sacrificial template was dissolved by submerging hydrogels in ethylene diamine tetraacetic acid (EDTA 0.1 M) overnight, following the hydrogel washing step.

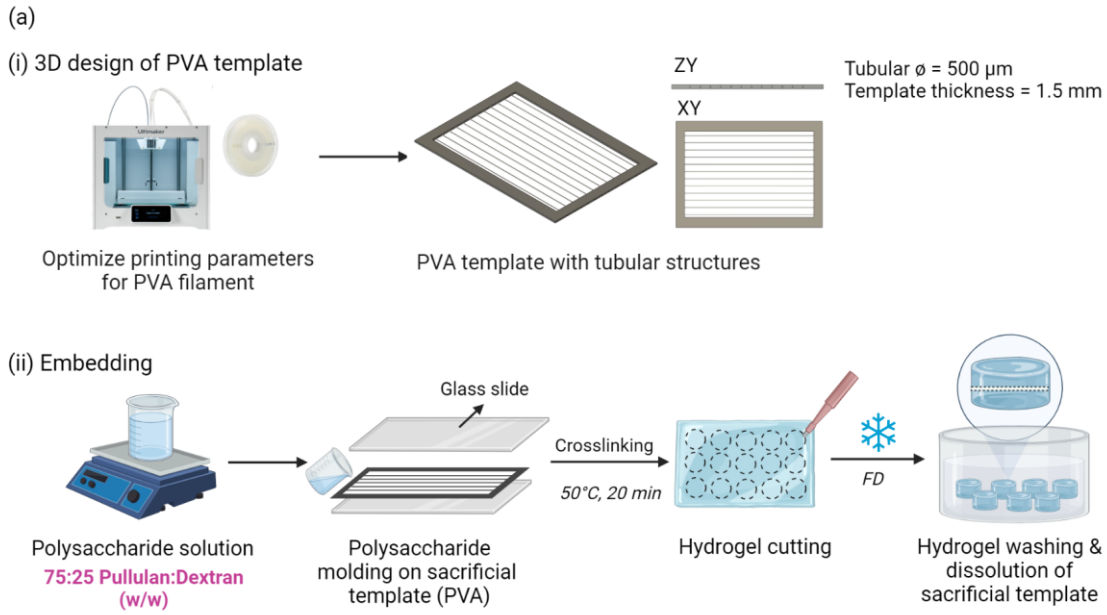

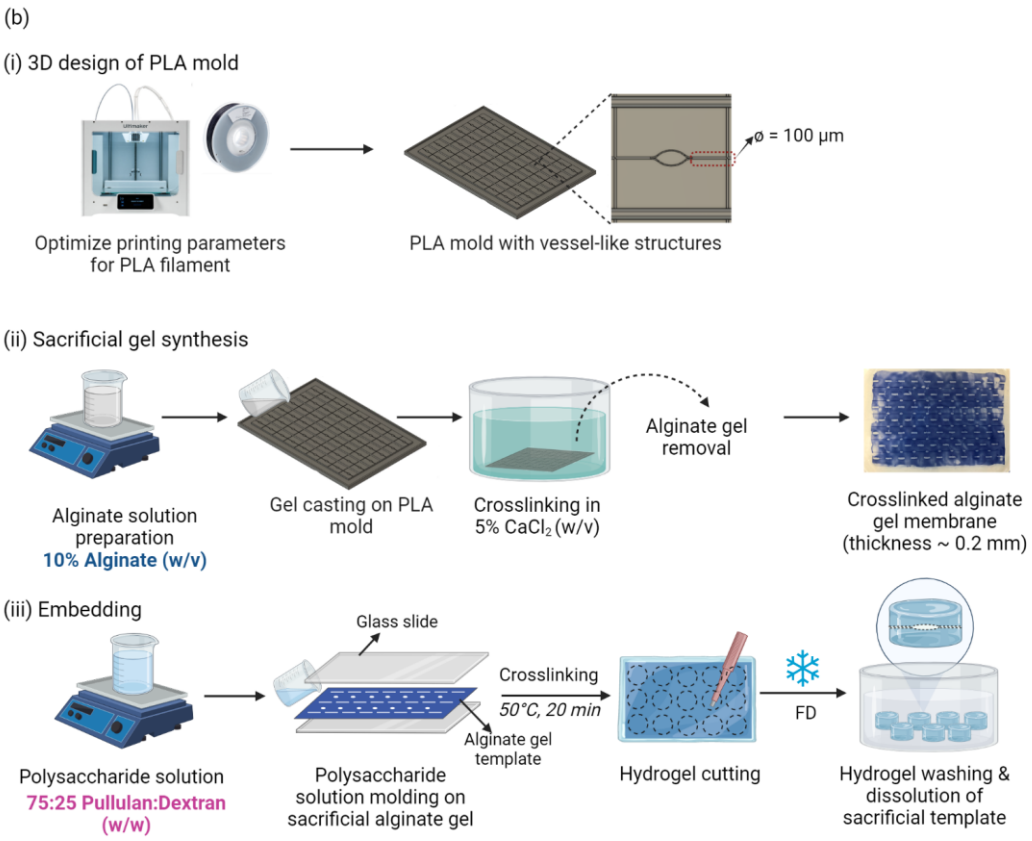

Figure 11. (a) Fabrication protocol using PVA sacrificial templates for simple geometric channels of 400 – 500 µm; (b) Fabrication protocol using alginate hydrogel sacrificial templates for complex geometric channels of 100 – 300 µm in diameter. Created with Biorender.com.

2.6. Scanning electron microscopy (SEM)

The topography of freeze-dried polysaccharide-based hydrogels was observed at the Jacques Monod Institute (Paris, France) using a scanning electron microscope (JEOL JSM-IT100), software InTouch Scope v.1.060) under low vacuum conditions.

2.7. Porosity measurements

Porosity of hydrogels was determined based on published protocol which calculates the water amount absorbed in the hydrogel before and after manual squeezing tests [15]. Experiments were performed by soaking samples (n = 3) in phosphate buffered saline (PBS) in a 12-well cell culture plate (Corning®) for 2 hours under mechanical shaking at RT. Samples were then weighted after removing the excess of liquid by placing them on the plastic lid. This was considered weight of swollen gel ($M_{swollen}$, mg). Follow this step, samples were weighed again after squeezing out

remaining liquid using tissue paper and gentle pressing using a spatula. This was considered the "squeezed" weight ($M_{squeezed}$, mg). The porosity calculated by this method corresponds to the large pores that entrap water molecules free or weakly bound to the polysaccharide matrix that are release by gentle mechanical compression. The pores volume percentage was calculated using the following equation (**Eq. 1**):

$$Volume\ of\ macropores\ (\%) = \frac{(M_{swollen} - M_{squeezed})}{M_{swollen}} \times 100 \qquad \textbf{(Eq. 1)}$$

2.8. Swelling measurements

Scaffolds were weighted before (M_{dry}) and after ($M_{swollen}$) rehydration in PBS for 2 days, 3 days, and 7 days. Swelling ratios at different time points were determined using the following equation (**Eq. 2**):

$$\text{Swelling ratio} = \frac{(M_{swollen} - M_{dry})}{M_{dry}} \qquad \textbf{(Eq. 2)}$$

2.9. Confocal microscopy

Confocal microscopy of hydrated samples was conducted using a confocal microscope from Leica (Leica SP8). Images were acquired using LSA-X (Leica App Suite X) software and image analysis was performed with ImageJ/Fiji software.

3. Results

3.1. Hydrogel preparation and characterization (without microchannel)

The formation of a microscale tubular structure within a small circular shape hydrogel requires consideration of the hydrogel's swelling behavior since it will have a direct impact on the final diameter of the channel. Therefore, prior to developing different sacrificial templates for microchannel formation, the hydrogel formulation needed to be optimized. The standard protocol for preparing these porous hydrogels is described in Section 2.2 and 2.3 and illustrated in **Figure 10**.

In order to determine the optimal crosslinker concentration required to yield hydrogels with controlled swelling, we prepared five different hydrogel formulations: PUDNA-S1, PUDNA-S2, PUDNA-S3, PUDNA-S4 and PUDNA-S5. The STMP solution was used according to the synthesis

protocol. After freeze-drying, the samples were used for further characterization and analysis. To study the influence of the STMP feeding ratio, hydrogel's porosity (%) and swelling ratio were evaluated. Porosity measurements were conducted in PBS and determined based on **Eq. 1**. The porosity globally decreased with increasing STMP concentration (**Figure 12**).

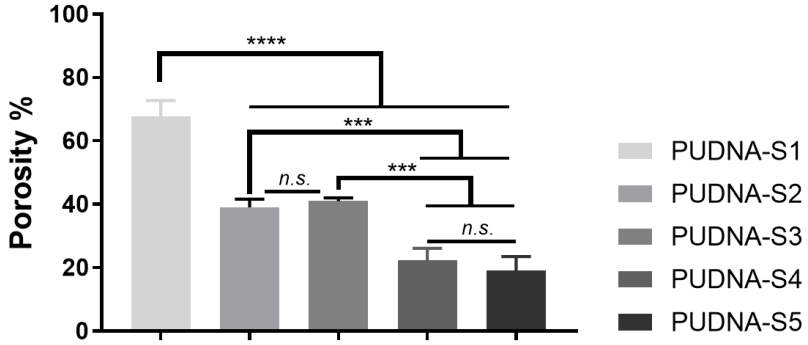

Figure 12. Porosity values of PUDNA hydrogels (n = 3). Ordinary one-way ANOVA analysis (with multiple comparisons) was performed. * $p < 0.05$, ** $p < 0.01$, *** $p < 0.001$, **** $p < 0.0001$.

Swelling measurements were conducted in PBS. Measurements were taken at several intervals and recorded over 7 days. Overall, the increase in the amount of STMP introduced into the hydrogel formulation led to a decrease in swelling of hydrogels (**Figure 13**). The water content of each hydrogel condition followed the trend observed in swelling ratio (**Figure 14**), where water absorption capacity decreased with an increase in crosslinker concentration. After 7 days of rehydration in PBS, only PUDNA-S1 samples continued to swell and absorb water.

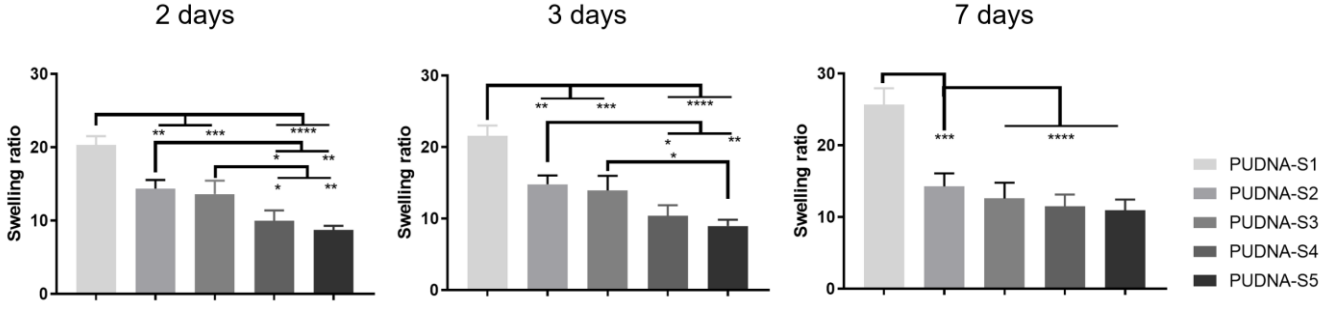

Figure 13. Swelling ratio of PUDNA hydrogels (n = 3) on day 2, day 3, and day 7. Ordinary one-way ANOVA analysis (with multiple comparisons) and post test for linear trend were performed. * $p < 0.05$, ** $p < 0.01$, *** $p < 0.001$, **** $p < 0.0001$.

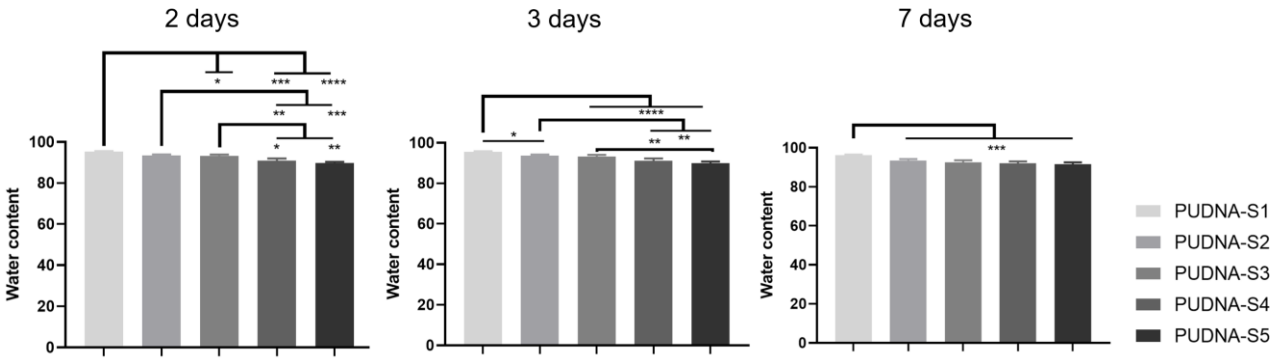

Figure 14. Water content of PUDNA hydrogels (n = 3) on day 2, day 3, and day 7, respectively. Ordinary one-way ANOVA analysis (with multiple comparisons) and post test for linear trend were performed. * $p < 0.05$, ** $p < 0.01$, *** $p < 0.001$, **** $p < 0.0001$.

The solubility of each STMP solution concentration was also monitored. After 30 minutes of mixing at RT, images of all STMP solutions were taken for visual observation. As shown in **Figure 15**, at 4% and 5%, STMP did not dissolve completely, resulting in cloudy solutions.

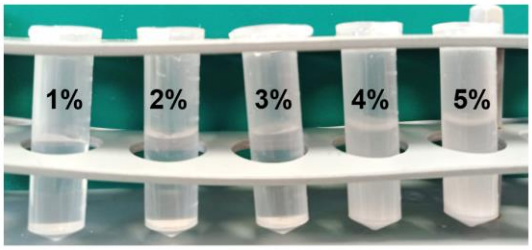

Figure 15. Photos of the five STMP solutions after 1h of dissolution.

Furthermore, during manipulation, it was observed that the lower crosslinked samples (PUDNA-S1 and PUDNA-S2) in the swollen state were prone to breakage. It has been reported in the team that the increase in STMP feeding concentration resulted in an increase in storage modulus (G') of the polysaccharide gels. Therefore, at low STMP amount, the hydrogels were softer and broke easily. Thus, the high swelling ratio would not allow us to have control over the final diameter of the preformed microchannel in the next part of the study. AS for PUDNA-S4 and PUDNA-S5, the immiscibility of STMP would lead to heterogeneously crosslinking with the polysaccharides, hence, resulting in heterogeneity in pore formation in each batch of production, as well as heterogeneity among different samples of the same condition.

Taking together these results, we determined that that PUDNA-S3 was the optimal formulation with adequately desirable porosity (30 - 40 %) and controlled swelling after 3-7 days of rehydration. Therefore, from this point on, PUDNA-S3 was chosen as the formulation to carry on the next part of this work: fabrication of hydrogels with preformed microchannels. From now on, the hydrogels are simply referred to as PUDNA.

3.2. Sacrificial templating: PVA as sacrificial templates

3D printing of PVA mold with tubular structures

First, rectangular templates made of PVA were designed and printed. These templates had a thickness of 1.0 mm. Inside the "frame" part of the template, several parallel tubular structures of 500 µm in diameter were printed (**Figure 16**). The "frame" component was created in order to control the thickness of the encapsulating hydrogel, while the tubular structures were included to form microchannel inside the hydrogel (**Figure 16**). As a control, the first model was printed using default settings from Cura (**Table 6**): profile of 0.2 mm, print speed of 70.0 mm/s, layer height of 0.2 mm, and wall thickness of 0.8 mm. Overall, the printed template showed smooth surface; the channel structure was relatively smooth and remained intact. The diameter of the tubular component was 500 ± 20 µm.

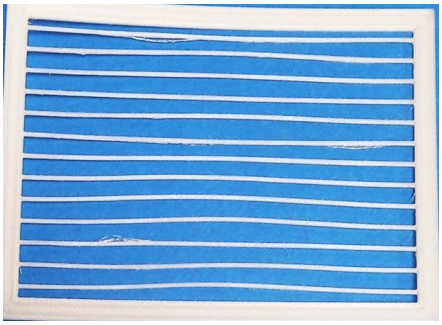

Figure 16. PVA template comprised of a rectangular frame and parallel tubular structures (ø = 500 µm).

Table 6. Printing parameters used for molds with tubular structures (vary in diameter)

Tubular diameter (µm)	Print speed (mm/s)	Layer height (mm)	Wall thickness (mm)
500	70.0	0.2	0.8
450	35.0	0.2	0.8

450	70.0	0.3	0.8
450	70.0	0.2	0.8
450	70.0	0.1	0.8
400	70.0	0.3	0.8
400	70.0	0.2	0.8
400	70.0	0.1	0.8
350	70.0	0.3	0.8
350	70.0	0.2	0.8
350	70.0	0.2	0.8

Next, print speed and layer height were varied to evaluate their effect on the quality of the final print, with a focus on the tubular structures of the printed template. When print speed was reduced, the channel structure was serrated: for each channel, 3 to 4 strands of melted polymer were bound in the extremities and remained loose in the middle section. Reducing the print speed allowed more time for the extruded polymer to cool down in the middle region, hence, leading to non-intact channel formation (**Figure 17**). Taking this observation into account, we kept the print speed at 70.0 mm/s as a constant value. For the following templates with channel diameters ranging from 350 to 450 µm, layer height was varied: 0.1, 0.2, and 0.3 mm. Reducing the layer height led to more serrated, un-fused filaments, while increasing layer height lowered the number of un-fused filaments. Nonetheless, the increase in layer height did not solve this issue. Only templates having channel diameter between 350 and 400 µm could be printed and the resulting templates had tubular structure smaller than the designed value. When attempting to print a template with channel diameter of 300 µm, we only obtained the frame component (**Figure 18**).

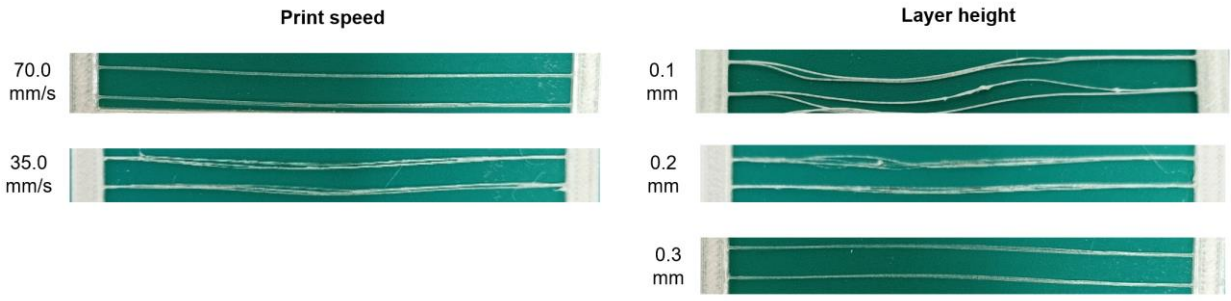

Figure 17. Resulting PVA templates with tubular diameter of 400 µm

Figure 18. PVA template of which the design has tubular structure of 300 µm in diameter

Regarding printing PVA templates, the optimal printing parameters were determined: print speed of 70.0 mm/s, layer height of 0.2 mm, and wall thickness of 0.8 mm. Now that the optimal print settings were determined, we attempted to print single tubular structure at smaller diameters: 300, 250, 200, 150, 100, 50 µm. The parameters used to print these structures were: print speed of 70 mm/s, layer height of 0.2 mm, and a wall thickness of 0.8 mm (**Table 7**).

Table 7. Printing parameters used for single microchannel (small diameter)

Tubular diameter (µm)	**Print speed (mm/s)**	**Layer height (mm)**	**Wall thickness (mm)**
300	70.0	0.2	0.8
250	70.0	0.2	0.8
200	70.0	0.2	0.8
150	70.0	0.2	0.8
100	70.0	0.2	0.8
50	70.0	0.2	0.8

All structures with diameters between 100 and 300 µm were printed successfully without any deformation and had smooth surfaces. The structure of 50 µm in diameter could not be printed as the Cura software could not recognize the print (discussed in **Appendix 1**). Unfortunately, in terms of handleability, these printed singular tubes were not optimal as they can be easily damaged or deformed during removal from the print platform. Therefore, these tubular structures were not utilized to produce scaffolds with preformed channels. They remained a proof of concept for this work. In order to precisely control the final thickness of the hydrogel, only the frame-like PVA templates were used for the embedding step (**Figure 11a**).

To prepare hydrogels with microchannel, the main hydrogel (PUDNA) solution was prepared according to the synthesis protocol (Section 2.2). **Figure 19** presents hydrogels that were created using PVA templates with tubular structures of 500 µm in diameter. Observation with the naked eye showed hydrogel with pores and the preformed microchannel (when hold at a certain angle) **(Figure 19a**). SEM images further confirm the initial observations. On the surface of the hydrogel, we could see both macropores (> 100 µm) and micropores (< 100 µm) (**Figure 19b**), according to standard nomenclature [16]. Presence of the preformed microchannel was also visible on the side (**Figure 19c**) and in the cross-sections of the samples (**Figure 19d**). The microchannel demonstrated a circle-like cross-section and an overall cylindrical profile. The channel surface was relatively smooth. Interconnected pores and macropores and micropores inside the channel structure were also observed. After crosslinking and washing, the channel formed in the hydrogel had an average diameter between 800 and 850 µm, which was 1.6 to 1.7 times greater than the diameter of PVA tubular structures (500 µm).

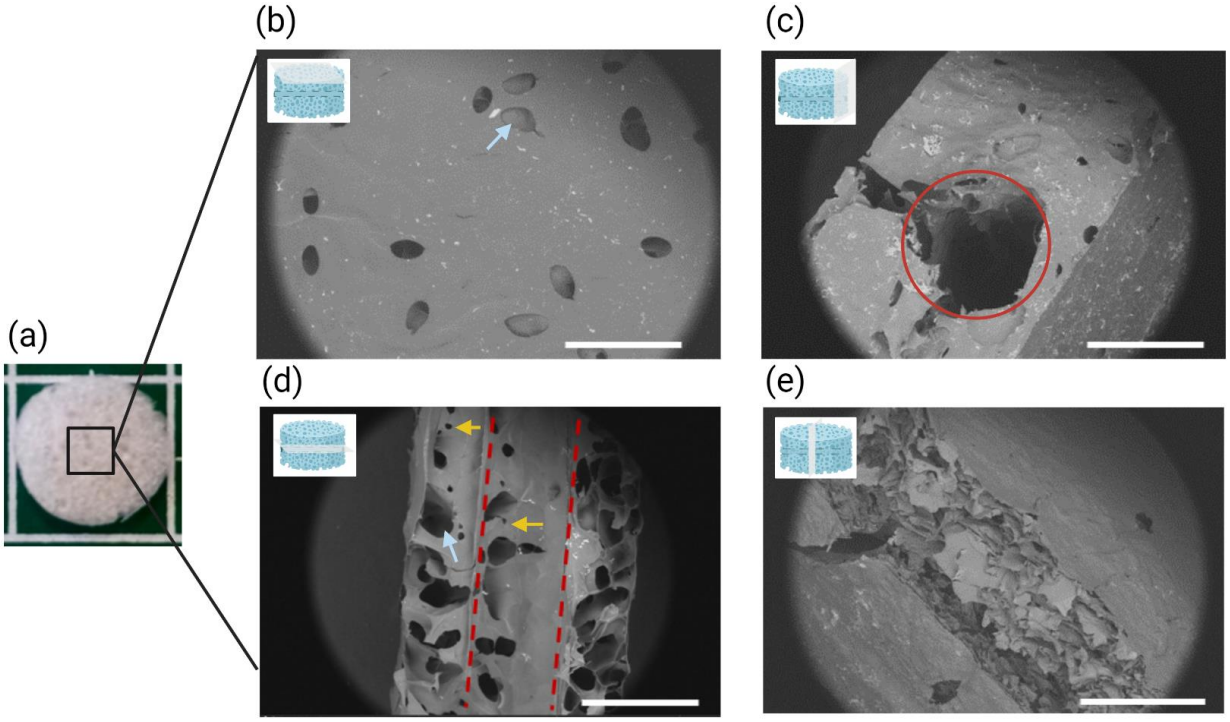

Figure 19. a) Freeze-dried hydrogel with microchannel using template of 500 µm; SEM images of hydrogel showing: b) top surface; c) side with the presence of a microchannel, as indicated by a red dash circle; d) the microchannel located in the middle of the hydrogel. Red dash lines separate

the limit between the surface of the microchannel and the hydrogel; e) the cross-section of the hydrogel. Scale bar = 1.0 mm. Yellow arrows = macropores. Blue arrows = micropores.

3.3. Sacrificial templating: alginate hydrogel as sacrificial component

3D printing of PLA mold with vessel-like structures

In order to overcome the printing limits associated with water soluble PVA filaments, we changed the strategy to 3D print molds with PLA with a vessel-like pattern to mold the sacrificial templates made of alginate. Overall, the microchannels inside the PLA mold had smooth surfaces to ensure formation of uniform sacrificial tubular structures in the next part of this work.

Alginate hydrogel as sacrificial templates

The first step was to define the optimal alginic acid and $CaCl_2$ concentration to obtain stable gels. Observations after crosslinking showed that: increase in alginic acid sodium concentration led to less retraction, while increase in $CaCl_2$ led to more retracted structure. Although retraction might allow the formation of smaller, thinner structures, it might cause the final template to be more fragile. To avoid retraction of alginate hydrogel, alginic acid sodium 10% (w/v) and $CaCl_2$ 5% (w/v) were chosen for the casting step (**Figure 11b.ii**). The resulting alginate template showed good fidelity of microchannel (**Figure 20**).

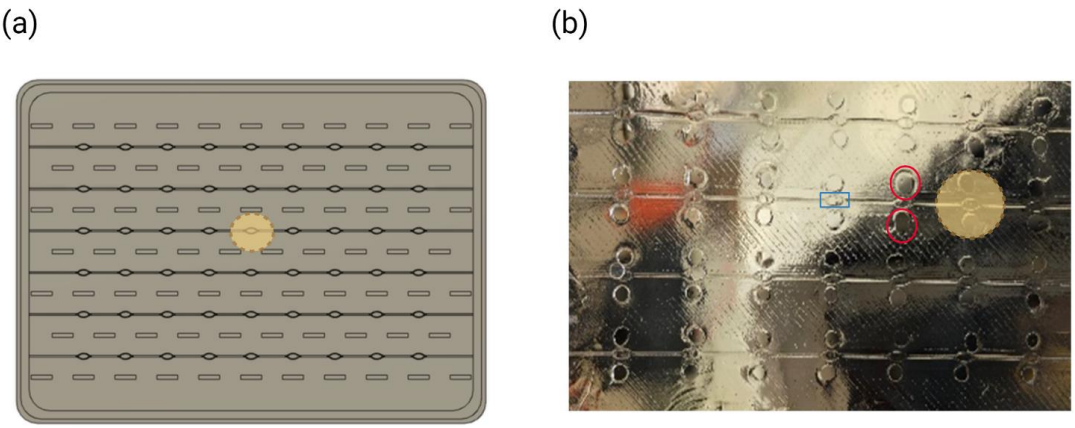

Figure 20. a) 3D design of master mold. Yellow circle indicates the region where the encased hydrogel will be cut to capture only the vessel loop structure; b) Alginate hydrogel forming after casting on the 3D-printed master mold. Red circles indicate cut-out regions above and below the

vessel loop structure to enable PUDNA hydrogel fusion between the top and bottom layer. Blue rectangles highlight the vessel loop regions. The microchannel formed was 100 µm in diameter.

As a proof of concept, we printed another mold, which has a multi-scale bifurcating structure with vessel diameters from 1.0 mm to 0.1 mm (**Figure S2**). Using the same casting method, we were able to achieve a hydrogel membrane/template that was sturdy enough for manipulation and could be transferred to another surface for visualization (**Figure 21**). The alginate membrane was also easily dissolved in EDTA 0.1 M at RT overnight. This large scale alginate template with bifurcating structures of varying diameters could be integrated in larger scaffolds for study of endothelial cell behavior inside a vessel with changing size.

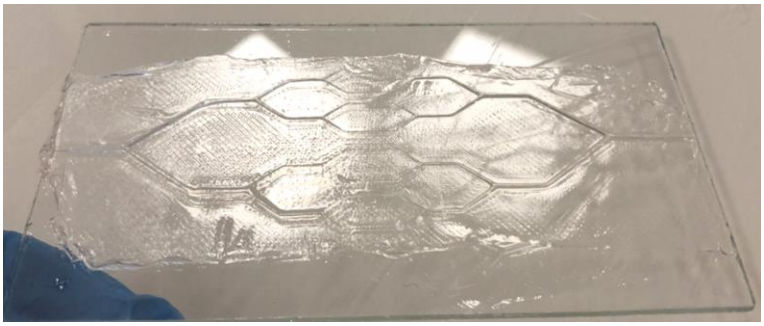

Figure 21. Crosslinked alginate hydrogel template (large scale) retrieved on a glass panel

To prepare small circular hydrogels with vessel-loop microchannel, the main hydrogel (PUDNA) solution was prepared according to the synthesis protocol (**Section 2.2**), followed by an embedding step (**Figure 11b.iii**). The alginate sacrificial template was dissolved during the hydrogel washing step. PUDNA hydrogels before and after dissolution of sacrificial template were observed (**Figure 22**). Due to the transparency of these samples, it was difficult to see the vessel loop structures using bright-field microscopy. When holding these hydrogels under the light, we could see the vessel structures, which remained the same before and after freeze-drying as well as after rehydration of freeze-dried samples.

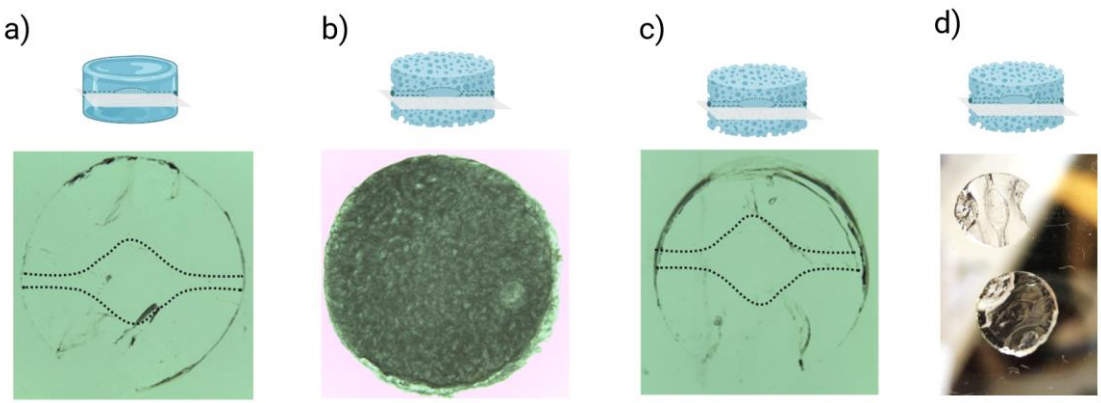

Figure 22. Viewing of samples under a bright-field microscope: a) After washing step and alginate hydrogel template dissolution. The sample was cut in half to facilitate viewing of the microchannel structure; b) Freeze-dried hydrogel; c) Freeze-dried hydrogel after 24h rehydration in PBS 1X. Black dash lines outline the shape of the vessel loop geometries. d) Observation of rehydrated sample (cut in half) viewed by the naked eye.

To confirm the formation of the vessel loop structure within the hydrogels, a confocal light scanning microscopy (CLSM) was employed. Tile scan capture of the whole channel structure (**Figure 23**) presented infidel pattern transfer. The left side and right side of channel were not on the same plane. The inlet and outlet regions of the vessel loop appeared irregular. A Z-stack was also performed to capture the channel full thickness. However, the resulting image did not provide a better observation of the channel formation inside the hydrogel (image not shown).

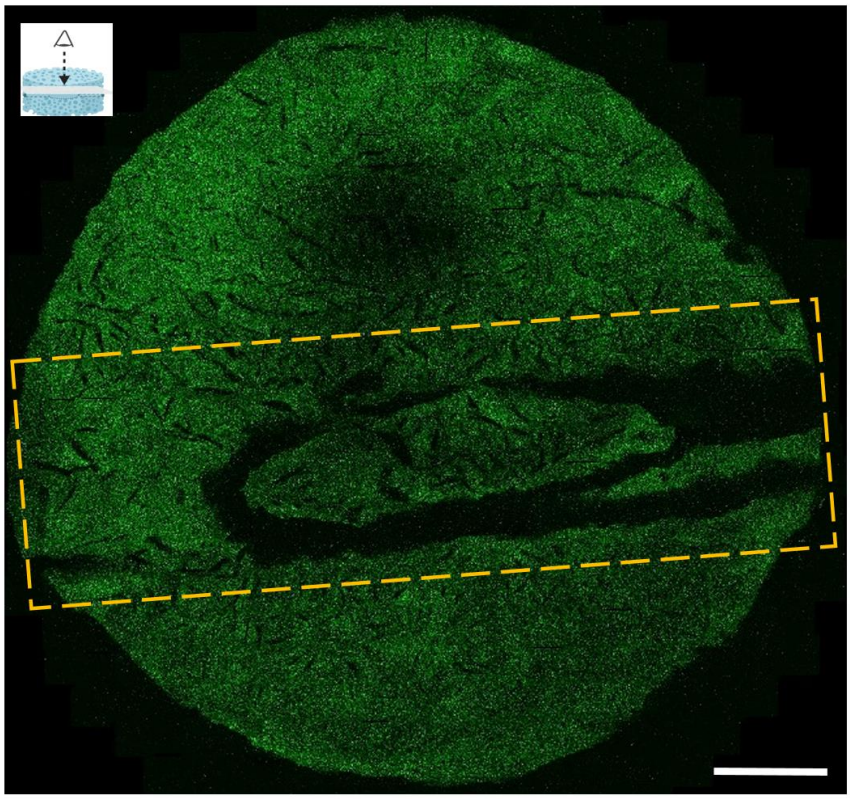

Figure 23. FITC-Dex containing hydrogels with vessel loop structure observed using CLSM. Scale bar = 1.0 mm. Yellow dash rectangle indicates the vessel loop region on hydrogel.

4. Discussion

4. Hydrogel characterization

Crosslinker feeding ratio in hydrogels is known to impact the swelling and stiffness of a hydrogel [17]. Indeed, maximum swelling ability was observed in less crosslinked hydrogels (PUDNA-S1), while lower swelling ability was seen in hydrogels with higher crosslinker density (PUDNA-S5) (**Figure 13**). This can be explained by an increase in crosslinker density, consequence of a greater quantity of STMP introduced during the synthesis, resulting in more crosslinked polymer chains that limit expansion of the macromolecular structure. As a result, less swelling and lower water absorption was observed when STMP was increased in the synthesis of the hydrogel. Besides, a decrease in porosity was observed in more crosslinked hydrogels (PUDNA-S3, PUDNA-S4 and PUDNA-S5) due to a decrease in the hydrogel mesh size, hence, reducing the size of interconnecting pores within the polymer network. Although the mesh sizes of

the developed hydrogels were not determined in this work, the decrease in swelling ratio and porosity with increasing crosslinker density is in accordance with previous work from the team. Under 100% dextran or 100% pullulan assumptions, the computed mesh sizes from the end-to-end distance of the chains were determined to be around 25 and 40 nm and were reported to decrease with increasing STMP feeding ratio [18,19]. It was also reported that the computed mesh size was higher in the swollen state than in the relaxed state and decreased with increasing STMP feeding ratio. Together, these results further support the change in porosity as an effect of crosslinker density. Thus, we have demonstrated the ability to tune hydrogel swelling and porosity by the amount of STMP introduced in the polymer solution. Regarding the stiffness of the different formulation, quantitative data could not be conducted due to inaccessibility to the testing instrument. However, during manipulation, the lower crosslinked samples (PUDNA-S2 and PUDNA-S1) in the swollen state were prone to breakage. These observations could be related to the hydrogel stiffness, which decreased linearly with decreasing STMP amount (from 14 kPa to 3 kPa), as previously reported in the team [18,19].

4.1. Advantages and disadvantages of PVA sacrificial templates

PVA is a synthetic polymer that is obtained by partial or complete hydrolysis of acetate group from polyvinyl acetate [20]. Water-soluble PVA enables printing complex geometries that require support for large overhang, deep internal cavities, and intricate structures, without the risk of breaking the 3D-printed model. These structures can be generated through dual extrusion mode on the FDM printer [20]. Once the print is finished, the entire model can be placed in water to dissolve the sacrificial PVA structures.

In this work, we used PVA as the main printing material in order to develop sacrificial templates for the formation of microchannels, which were embedded within the PUDNA hydrogels. These channel-like structures were created with the aim to mimic micron-scale vessels. As sacrificial material, PVA offers several advantages. First, the printed PVA template did not dissolve during our hydrogel synthesis protocol but dissolved during the hydrogel washing step. The channel structure formed by PVA tubular template was observed as soon as the encapsulating hydrogel was crosslinked. This tubular structure remained intact during the hydrogel washing step and PVA dissolution step. Moreover, PVA templates when stored properly (e.g. absence of humidity) could be preserved for a long period of time (at least 30 days), offering easy usability.

Nevertheless, in practice, working with PVA filaments entailed several challenges. Even when stored properly, PVA was highly susceptible to moisture, especially during the warm months. The PVA filaments were stored in the PolyBox™ (Ultimaker) with silica gel desiccant sachets to control and absorb moisture from the air. The PolyBox™ purchased from Ultimaker played a role maintaining the humidity in the box to be below 15%. In the cold months, the box humidity reached to 20% within a month, although it was still possible to print with PVA at this moisture level, it was not recommended. In the warm months, humidity could reach to 20% after 2 weeks. Changing of the silica gel desiccant sachets frequently was necessary to ensure proper storage of the PVA filament. Another issue was filament smoothness. Marks or scratches on the filament resulting from handling, installing of the filament, or moving of the printer, could easily induced filament breakage during polymer extrusion, leading to clogging of the print core. The process of troubleshooting and fixing all technical issues related to the 3D printer and the PVA filament (e.g. nozzle clog due to scratched filament or filament reaching moisture above 20%), significantly reduced production time.

To obtain a precise hollow, smooth tubular structure at the microscale, optimal printing parameters were defined: printing temperature 225ºC (adapted for PVA filament), printing speed of 70.0 mm/s, profile of 0.2 mm, and layer height of 0.8 mm. The aforementioned printing settings are considered as user deterministic parameters. The nozzle diameter, a non-user deterministic parameter, is associated with the print core type adapted for PVA printing filament. Non-user deterministic features along with the use of appropriate print core type contributed to all technical challenges of working with PVA as sacrificial templates. An in-depth discussion is presented in **Appendix 1**.

4.2. Advantages and disadvantages of using alginate hydrogel as sacrificial templates

Alginate hydrogel offers a simple mean to fabricate sacrificial templates with different geometries and varying diameter. A precursor polymer solution of 10 % (w/v) was easily casted on the 3D printed mold and through rapid immersion in $CaCl_2$ 5% (w/v) solution, alginate hydrogel was crosslinked. The resulting hydrogel template resulted in good structure fidelity and enabled the formation of microchannels inside the PUDNA encapsulating hydrogel. Although this material enabled creation of vessel-like structures with more complex geometries as compared to PVA, it presented other challenges. The casting method could only allow generation of very thin template

and did not enable accurate control over the thickness of the whole template. Additionally, the stiffness of alginate hydrogel template was much lower than PVA template adding difficulty to the manipulation and to the incorporation during the synthesis of the PUDNA hydrogel. As a result, the formation of microchannel inside PUDNA hydrogel was not even in the XY-plane (**Figure 21**). While the channel shape heterogeneity resembles native vessels, it poses challenges regarding the 3D imaging of 3D scaffolds, which is essential for characterization and validation of tissue-engineered biomaterials. As shown in **Figure 21**, the tile scan of the hydrogel with vessel-loop structure was only captured in a single XY-plane. Image acquisition of the entire bioengineered vasculature (in XYZ) could take up to several hours, depending on the structure's thickness, size, and its location within the hydrogel scaffold. An alternative to confocal laser scanning microscopy is light sheet imaging technique. However, access to this equipment was not available for us during this stage of the project.

5. Conclusions

In this work, the influence of crosslinking on hydrogel swelling behavior and porosity was evaluated. By changing the amount of STMP introduced in the polymer solution, we could tune swelling ratio and porosity % of the hydrogel. Both swelling ratio and porosity decreased with increasing feeding ratio of STMP. Specifically, PUDNA-S3 was the optimal formulation that allowed us to obtain scaffolds with controlled swelling, that could be optimal to use for microchannels formation inside the hydrogels. PUDNA-S3 hydrogels were also more mechanically stable and did not break easily during manipulation. Using this optimized formulation, we demonstrated the ability to form microchannels using two different materials as sacrificial templates (PVA and alginate hydrogels). Each material had its own advantages and disadvantages from the synthesis step (of the template), to manipulation, integration into the hydrogel scaffold (encasing), and impact on the overall manufacturing protocol. The use of 3D-printed templates made of PVA allowed us to easily print sacrificial templates with fast production time and high throughput. PVA templates had controlled dissolution, smooth channel surface, as well as channel structure with high robustness and high fidelity (in the case of "frame" template with tubular structures of 400 to 500 µm). Although we could print single PVA tubes with diameter as small as 100 µm, these structures were prone to damage upon removal from the printer platform. The limitation in producing channels smaller than 400 µm was associated with the fabrication using

FDM technique and the nature of PVA, rendering this approach non-user-friendly. However, the 3D printed templates were easily integrated into the hydrogels. To overcome issues related to working with PVA, alginate gel template was created as an alternative. Alginate gel was crosslinked using a simple crosslinking method and crosslinked gel was easily dissolved in EDTA 0.1M. The resulting membrane could be easily scaled up or scaled down depending on the final use and had channels of diameters ranging from 100 µm to 1.0 mm (Figure 11 and 12). On a smaller scale, we were able to produce a sacrificial template with multiple vessel loop structures of 100 µm (Figure 11). Although it was relatively easy to encase alginate templates inside PUDNA hydrogel, the hydrogel manufacturing step had to be adapted: holes above and below each channel structure had to be cut to ensure fusion of the PUDNA gel in the Z-axis (Figure 11b), thus, creating an additional step in the manufacturing process. The production time of hydrogels with microchannels using alginate templates was much longer than the approach using PVA templates. Thus, the final scaffold (with alginate templates) did not have uniform microchannel (uneven on the XY plane), possible due to the thin nature of the alginate membrane, of which thickness could not be precisely controlled. We consider that this strategy holds promise for microvasculature patterning within hydrogels but further optimization is still needed.

To advance with the objectives of the PhD project, in the following studies for hydrogel functionalization (**Chapter 3.2**), our team's published protocol was chosen to prepare samples with preformed microchannels [2]. This method was referred to as mechanical removal of filament. Briefly, the channel formation was guided by placement of suture filaments placed between two spacers and two glass slides. This method allowed us to produce hydrogels with straight microchannels of 100 ± 20 µm and cylindrical profile (tubular structure). Although it was not possible to form complex bifurcated structures mimicking the vascular tree, it allowed us to avoid all technical challenges associated with PVA and alginate manipulation and long production time. Compared to sacrificial templating, the filament removal strategy had shorter production time as well as easy and fast scale-up process. The protocol of this strategy will be described in detail in **Chapter 3.2**.

6. Appendix

Appendix 1. Challenges of FDM-based 3D printing and using PVA as sacrificial templates

In this section, the challenges of FDM 3D printing as well as the associated issues of using PVA in regard to producing sacrificial tubular structures of diameters < 400 μm are discussed. The limitations of working with PVA include two main factors: 1) choosing the right print core and 2) choosing the right printing parameters.

Choosing the right print core

Depending on the printing materials, two main types of print cores (AA and BB) are used in FDM, with AA print core intended for build materials and BB print core intended for support materials. The most commonly employed build materials in additive manufacturing are PLA, ABS (acrylonitrile butadiene styrene), and nylon [21]. On the other hand, BB print cores are exclusively used for water-soluble materials such as PVA and BVOH (butenediol vinyl alcohol) [21]. The main difference between AA and BB print cores relies on the nozzle's internal structure, which affects the quality of extruded polymer filament (**Figure S1**) [22]. The AA print core shape is designed to allow extruded material to 'pool up', which reduces material oozing. This is why PVA cannot be used with AA print core as when PVA is pooled up this causes clogging of the AA nozzle. Consequently, BB nozzle has a straighter design to prevent 'pooling' of extruded polymer (**Table S1** and **Figure S1**) [22].

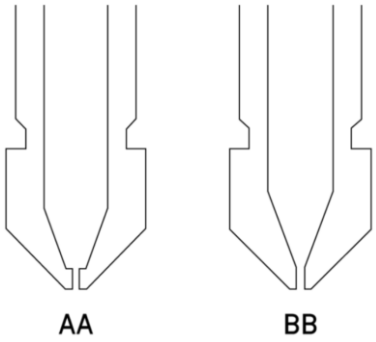

Figure S8. Different internal structures of AA and BB print cores

Table S3. Print core types and printing materials used in FDM

Print core type	Print material	Polymers
AA	Build	PLA, ABS, Nylon
BB	Support	PVA, BVOH

Printing parameters: layer height and nozzle diameter

FDM printing is based on the extrusion of melted polymer, which is related to the layer height and nozzle diameter. These two properties are crucial to the dimensions of the extruded material. Layer height is a user-determined print setting that can be controlled using the 3D printer slicer software (e.g. Cura). On the other hand, nozzle diameter is a fixed value and a feature of the nozzle, which is associated with the print core type. Nozzle diameter determines the layer height's minimum and maximum values [23].

Layer height affects the Z-axis, whereas nozzle diameter affects the X-axis and Y-axis. In general, a lower layer height results in better Z-axis resolution, while a smaller nozzle results in better X-Y resolution. These two parameters can be adjusted independently, depending on the type of extrude material and intended application of the final 3D model.

In practice, with any given print core and nozzle combination, the layer height can be set to be about 75% of the nozzle diameter or less. This means that, with a 0.4 mm, a layer height of up to 0.3 mm can be used [23,24]. This only works if the resulting value is not lower than the smaller possible increment of the stepper motor controlling Z-axis movement, which is usually around 0.04 mm.

Using a BB print core with a nozzle diameter of 0.4 mm, we could theoretically print a tubular structure by using a minimum layer height of 0.1 mm (**Table S2**). However, when applied this minimum layer height setting, we could not print any smooth tubular structure smaller than 400 µm (**Figure 18**). Thus, the layer-by-layer nature of FDM method led to less fused channels in the case of PVA frame-like templates (**Figure 17**). Regarding single tubular structures of diameters ranging from 100 to 300 µm, the wall thickness did not significantly affect the final print quality, yet it remains the limiting factor to print smaller channels (< 100 µm). Thus, removal of these thin single cylindrical structures from the print platform risks deforming their shape, and further

preventing their use as sacrificial templates. The ideal FDM printed parts for sacrificial template should allow facile manipulation. Finally, to print finer and smaller tubular structures made of PVA, ideally, we would need to use a BB print core with a 0.25 nozzle diameter. However, this option is not currently available in the market.

Table S4. Guidelines to select the right layer height matching a nozzle diameter

Nozzle diameter (mm)	Print core type available	Min. layer height (mm)	Max. layer height (mm)	Standard layer height (mm)
0.25	AA only	0.06	0.2	0.13
0.4	AA and BB	0.1	0.32	0.2
0.6	AA and BB	0.15	0.48	0.3
0.8	AA and BB	0.2	0.64	0.4

Appendix 2. Proof of concept: Use of alginate hydrogel as sacrificial template to build bifurcating vessel structure

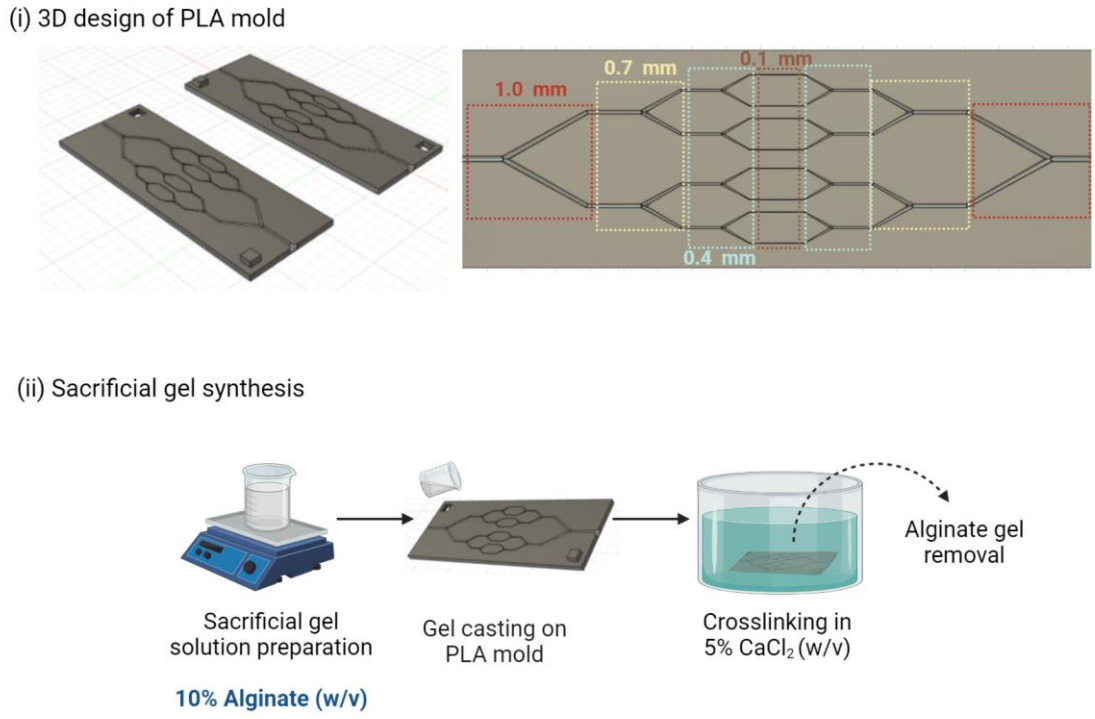

Figure S9. (**i**) 3D design of the PLA mold with multi-scale bifurcating tubular network. Each highlighted region represents the channel diameter with matching values indicated above the dash

rectangle; (**ii**) Protocol to prepare alginate hydrogel template with multi-scale bifurcating tubular network. Figure created with Biorender.com.

References

[1] Y. Kang, J. Chang, Channels in a porous scaffold: A new player for vascularization, Regen. Med. 13 (2018) 705–715. https://doi.org/10.2217/rme-2018-0022.

[2] T. Simon-Yarza, M.N. Labour, R. Aid, D. Letourneur, Channeled polysaccharide-based hydrogel reveals influence of curvature to guide endothelial cell arrangement in vessel-like structures, Mater. Sci. Eng. C. 118 (2021) 111369. https://doi.org/10.1016/j.msec.2020.111369.

[3] A. Dellaquila, C. Le Bao, D. Letourneur, T. Simon-Yarza, In Vitro Strategies to Vascularize 3D Physiologically Relevant Models, Adv. Sci. 8 (2021). https://doi.org/10.1002/advs.202100798.

[4] W. Ye, H. Li, K. Yu, C. Xie, P. Wang, Y. Zheng, P. Zhang, J. Xiu, Y. Yang, F. Zhang, Y. He, Q. Gao, 3D printing of gelatin methacrylate-based nerve guidance conduits with multiple channels, Mater. Des. 192 (2020) 108757. https://doi.org/10.1016/j.matdes.2020.108757.

[5] M. Zhou, B.H. Lee, Y.J. Tan, L.P. Tan, Microbial transglutaminase induced controlled crosslinking of gelatin methacryloyl to tailor rheological properties for 3D printing, Biofabrication. 11 (2019). https://doi.org/10.1088/1758-5090/ab063f.

[6] D. Chimene, R. Kaunas, A.K. Gaharwar, Hydrogel Bioink Reinforcement for Additive Manufacturing: A Focused Review of Emerging Strategies, Adv. Mater. 32 (2020) 1–22. https://doi.org/10.1002/adma.201902026.

[7] S. Calixto, N. Ganzherli, S. Gulyaev, S. Figueroa-Gerstenmaier, Gelatin as a photosensitive material, Molecules. 23 (2018) 1–22. https://doi.org/10.3390/molecules23082064.

[8] S. Mohanty, L.B. Larsen, J. Trifol, P. Szabo, H.V.R. Burri, C. Canali, M. Dufva, J. Emnéus, A. Wolff, Fabrication of scalable and structured tissue engineering scaffolds using water dissolvable sacrificial 3D printed moulds, Mater. Sci. Eng. C. 55 (2015) 569–578. https://doi.org/10.1016/j.msec.2015.06.002.

[9] B. Pan, L. Shao, J. Jiang, S. Zou, H. Kong, R. Hou, Y. Yao, J. Du, Y. Jin, 3D printing sacrificial templates for manufacturing hydrogel constructs with channel networks, Mater. Des. 222 (2022) 111012. https://doi.org/10.1016/j.matdes.2022.111012.

[10] Q. Zou, B.E. Grottkau, Z. He, L. Shu, L. Yang, M. Ma, C. Ye, Biofabrication of valentine-shaped heart with a composite hydrogel and sacrificial material, Mater. Sci. Eng. C. 108 (2020) 110205. https://doi.org/10.1016/j.msec.2019.110205.

[11] A. Autissier, C. Le Visage, C. Pouzet, F. Chaubet, D. Letourneur, Fabrication of porous polysaccharide-based scaffolds using a combined freeze-drying/cross-linking process, Acta Biomater. 6 (2010) 3640–3648. https://doi.org/10.1016/j.actbio.2010.03.004.

[12] S. Lanouar, R. Aid-Launais, A. Oliveira, L. Bidault, B. Closs, M.N. Labour, D. Letourneur, Effect of cross-linking on the physicochemical and in vitro properties of pullulan/dextran microbeads, J. Mater. Sci. Mater. Med. 29 (2018). https://doi.org/10.1007/s10856-018-6085-x.

[13] M.-N. Labour, C. Le Guilcher, R. Aid-Launais, N. El Samad, S. Lanouar, T. Simon-Yarza, D. Letourneur, Development of 3D Hepatic Constructs Within Polysaccharide-Based Scaffolds with Tunable Properties, Int. J. Mol. Sci. Artic. (n.d.). https://doi.org/10.3390/ijms21103644.

[14] J. Grenier, H. Duval, F. Barou, P. Lv, B. David, D. Letourneur, Acta Biomaterialia Mechanisms of pore formation in hydrogel scaffolds textured by freeze-drying, Acta Biomater. 94 (2019) 195–203. https://doi.org/10.1016/j.actbio.2019.05.070.

[15] E. Campodoni, M. Montanari, S.M. Dozio, E.B. Heggset, S. Panseri, M. Montesi, A. Tampieri, K. Syverud, M. Sandri, Blending Gelatin and Cellulose Nanofibrils : Biocomposites with Tunable Degradability and Mechanical Behavior, (n.d.).

[16] ASTM International, Polymeric Scaffolds for use in tissue-engineered medical products, (2019). https://doi.org/10.1520/F2450-18.

[17] A. Abed, N. Assoul, M. Ba, S.M. Derkaoui, P. Portes, L. Louedec, P. Flaud, I. Bataille, D. Letourneur, A. Meddahi-Pellé, Influence of polysaccharide composition on the biocompatibility of pullulan/dextran-based hydrogels, J. Biomed. Mater. Res. - Part A. 96 A (2011) 535–542. https://doi.org/10.1002/jbm.a.33007.

[18] Jerôme Grenier, Hydrogel poreux pour la reconstruction osseuse : élaboration, caractérisation et mise en œuvre dans un bioréacteur à perfusion, Université Paris-Saclay, 2019. https://tel.archives-ouvertes.fr/tel-02638200.

[19] S. Lanouar, Conception and validation of new tridimensional porous matrices for cutaneous wound healing and regeneration, Université Sorbonne Paris Nord, 2020. https://www.theses.fr/2020PA131016.

[20] C. Wei, N.G. Solanki, J.M. Vasoya, A. V. Shah, A.T.M. Serajuddin, Development of 3D Printed Tablets by Fused Deposition Modeling Using Polyvinyl Alcohol as Polymeric Matrix for Rapid Drug Release, J. Pharm. Sci. 109 (2020) 1558–1572. https://doi.org/10.1016/j.xphs.2020.01.015.

[21] P. Siemiński, Introduction to fused deposition modeling, Addit. Manuf. (2021) 217–275. https://doi.org/10.1016/B978-0-12-818411-0.00008-2.

[22] Ultimaker, Difference between AA 0.4 and BB 0.4 nozzle - Ultimaker 3D printers - Ultimaker Community of 3D Printing Experts, (n.d.). https://community.ultimaker.com/topic/21217-difference-between-aa-04-and-bb-04-nozzle/ (accessed October 27, 2022).

[23] D. Fischer, C. Eßbach, R. Schönherr, D. Dietrich, D. Nickel, Improving inner structure and properties of additive manufactured amorphous plastic parts: The effects of extrusion nozzle diameter and layer height, Addit. Manuf. 51 (2022). https://doi.org/10.1016/j.addma.2022.102596.

[24] Shop3DUniverse, Which Ultimaker Print Cores Should I Use?, (n.d.). https://support.shop3duniverse.com/portal/en/kb/articles/which-ultimaker-print-cores-should-i-use.

3. EXPERIMENTAL WORK (PART 2)

3. EXPERIMENTAL WORK (PART 2)

3.2. HYDROGEL FUNCTIONALIZATION VIA SPATIAL-CONTROL COATING

Publication in International Journal of Molecular Science, 2022, DOI: 10.3390/ijms232314604

(the PDF proof is provided in Annex 2):

Spatial-controlled coating of pro-angiogenic proteins on 3D porous hydrogels guides endothelial cell behavior

Chau Le Bao[1*], Helen Waller[2], Alessandra Dellaquila[1], Daniel Peters[2], Jeremy Lakey[2], Frédéric Chaubet[1], and Teresa Simon-Yarza[1*]

[1] Laboratory for Vascular Translational Science (LVTS) INSERM U1148, Université Paris Cité, Université Sorbonne Paris Nord, CEDEX 18, 75877 Paris, France; dellaquila.alessandra@gmail.com (A.D.); fchaubet@gmail.com (F.C.)

[2] Newcastle University Biosciences Institute, Newcastle upon Tyne NE1 7RU, UK; helen.waller@newcastle.ac.uk (H.W.); daniel.peters@newcastle.ac.uk (D.P.); jeremy.lakey@newcastle.ac.uk (J.L.)

* Correspondence: chau.le-bao@inserm.fr (C.L.B.); teresa.simon-yarza@inserm.fr (T.S.-Y.)

Abstract: In tissue engineering, the composition and the structural arrangement of molecular components within the extracellular matrix (ECM) determine the physical and biochemical features of a scaffold, which consequently modulate cell behavior and function. The microenvironment of the ECM plays a fundamental role in regulating angiogenesis. Numerous strategies in tissue engineering have attempted to control the spatial cues mimicking in vivo angiogenesis by using simplified systems. The aim of this study was to develop 3D porous crosslinked hydrogels with different spatial presentation of pro-angiogenic molecules to guide endothelial cell (EC) behavior. Hydrogels with pores and preformed microchannels were made with pharmaceutical-grade pullulan and dextran and functionalized with novel pro-angiogenic protein polymers (Caf1-YIGSR and Caf1-VEGF). Hydrogel functionalization was achieved by electrostatic interactions via

incorporation of diethylaminoethyl (DEAE)-dextran. Spatial-controlled coating of hydrogels was realized through a combination of freeze-drying and physical absorption with Caf1 molecules. Cells in functionalized scaffolds survived, adhered, and proliferated over seven days. When incorporated alone, Caf1-YIGSR mainly induced cell adhesion and proliferation, whereas Caf1-VEGF promoted cell migration and sprouting. Most importantly, directed cell migration required the presence of both proteins in the microchannel and in the pores, highlighting the need for an adhesive substrate provided by Caf1-YIGSR for Caf1-VEGF to be effective. This study demonstrates the ability to guide EC behavior through spatial control of pro-angiogenic cues for the study of pro-angiogenic signals in 3D and to develop pro-angiogenic implantable materials.

Keywords: hydrogels; electrostatic interactions; spatial-controlled coating; angiogenesis; tissue engineering

1. Introduction

Tissue engineering has offered the tantalizing possibility to regenerate tissues and organs, allowing the treatment of a multitude of conditions and pathologies. Despite numerous significant progresses with in vitro and small animal studies, clinical applications have been scarce [1]. Even the most advanced solutions delivered to physicians lack sufficient vascularization within the tissue engineered constructs [2]. This is because the diffusion of oxygen and nutrient supply present major limits on the size and complexity of bioengineered scaffolds. For this reason, vascularization of biomaterials remains the highlighted focus in tissue engineering and regenerative medicines. In this context, one main current challenge in tissue engineering is the development of biomaterials that can promote angiogenesis, ultimately integrating with the host vasculature to form anastomosis.

Angiogenesis, the formation of new blood vessels from existing ones, is a complex process. During angiogenesis, quiescent endothelial cells (ECs) from pre-existing vessels are activated by the increase in concentration of pro-angiogenic factors induced by inflammation or by hypoxia [3]. Activated ECs proliferate and differentiate into tip cells, which results in the elongation of new blood vessels in the direction of the pro-angiogenic stimulus. This sprouting process is modulated by the migration of ECs led by tip cells, characterized by lamellipodia and filopodia in their cytoskeleton, followed by stalk cells, which are found between quiescent cells and the tip cells. Stalk cells continue to proliferate and constitute the new endothelium, while ensuring a continuum

with the original vessel through regulated proliferation [4,5]. Once the capillary is formed, ECs secrete attractant molecules to recruit perivascular cells, which migrate along the newly formed vessels and provide stability, support cell differentiation, and regulate vessel permeability [6].

Angiogenesis is partially modulated by the ECM, which provides essential structural support and biochemical cues for cell morphogenesis and physiological functions [7]. Numerous strategies employing hydrogels with functionalized pro-angiogenic molecules have been proposed to promote vessel formation. Most of these approaches are based on the delivery of growth factors (GFs), such as vascular endothelial growth factor (VEGF), to facilitate vascularization in vivo [8]. Recently, pre-vascularization of biomaterials has been proposed as an approach to promote in vitro vessel formation prior to implantation. The idea is to stimulate in vitro vessel formation within 3D biomaterials which present pre-formed channels. Different techniques to develop hydrogels with pre-formed channels have been investigated. These include the use of syringes or glass micropipettes [9], or sacrificial templates [10–13]. To promote cell adhesion, ECM proteins (e.g., collagen, fibrin, or fibronectin) and cell adhesive molecules (e.g., RGD, YIGSR sequences) are often incorporated into the hydrogel composition [8,14,15]. Besides interaction with the ECM, angiogenesis also depends on spatial presentation of pro-angiogenic cues that direct vessel sprouting and maturation [3]. Over the past decades, various approaches have attempted to fabricate hydrogels with spatial guidance either through direct patterning of vascular cells, or through spatial distribution of pro-angiogenic molecules (e.g., VEGF, FGF, angiopoietin, YIGSR) [16–20]. The use of ECM molecules presents promising outcomes for in vitro and in vivo vascularization. Nevertheless, clinical translation still remains a hurdle due to high cost and immunogenic potential of animal-origin ECM molecules.

Several important factors must be taken into account when designing hydrogels that favor endothelialization for tissue engineering and regenerative medicines: (1) presence of interconnected pores favoring cell–cell interactions and migration; (2) presence of a hollow channel having a wide range of diameters to mimic native vessels; (3) ability to promote EC arrangement leading to the formation of microvessel-like networks; (4) biocompatible composition (pharmaceutical-grade materials); (5) integration of basement membrane proteins (BM), such as laminin and collagen type IV, and other ECM proteins to induce endothelial proliferation and differentiation during angiogenesis; (6) easy fabrication protocol; and (7) cost efficient.

For vascularization purposes, porous 3D hydrogels are widely employed due to their ability to facilitate nutrient and oxygen diffusion, thus enabling cell migration [21,22]. Additionally, the presence of channels within porous scaffolds has been reported to promote cell growth and rapid vascularization [23,24]. The channels in 3D hydrogels play a key role in guiding EC arrangement and should also be utilized to induce angiogenic behavior in ECs.

Polysaccharides are widely employed as tissue engineered biomaterials due to their physicochemical properties that can mimic the ECM [25]. In this context, we utilized 3D porous hydrogels, composed of pullulan and dextran. Notably, our team has demonstrated in several studies the versatility of pullulan- and dextran-based hydrogels, where the scaffold geometry, mechanical properties, porosity, and swelling behavior of these hydrogels could be controlled [25–28]. The hydrogel crosslinking method was previously described in numerous publications and has been patented [29,30]. Thus, these hydrogels have been investigated in various in vitro and in vivo studies [29,31,32]. Most recently, we have demonstrated the ability to guide EC arrangement based on channel curvature on the 3D polysaccharide hydrogels [28].

In the context of promoting in vitro vessel formation, this study aimed to develop 3D porous hydrogels with different spatial presentation of pro-angiogenic signals to guide ECs towards angiogenic behavior. The challenge of this work was to functionalize the chemically crosslinked hydrogels to promote EC adhesion and to direct sprouting through spatial guidance using pro-angiogenic cues. Here, we present a simple method to produce biomimetic 3D porous hydrogels, made from pharmaceutical-grade pullulan and dextran, with preformed microchannels (**Figure 24**). To provide cells with pro-adhesive and pro-angiogenic signals, the hydrogels were functionalized using a recombinant, engineered bacterial protein polymer called Caf1. Caf1 subunits assemble into long, highly stable and flexible polymers, which are bioinert, allowing bioactive peptide motifs from the ECM and growth factors to be inserted and hence provide exquisite control over the biological signals supplied to the cells [33–35]. In this work, we demonstrate an innovative strategy to functionalize chemical hydrogels in a spatial-controlled manner. Capitalizing on the acidic pI of Caf1, we could functionalize hydrogels simply via electrostatic interactions induced by the coating method (**Figure 24b**). Then, spatial cues of the pro-angiogenic motifs were modulated through a combination of hydrogel coating and a freeze-drying process (**Figure 24c**).

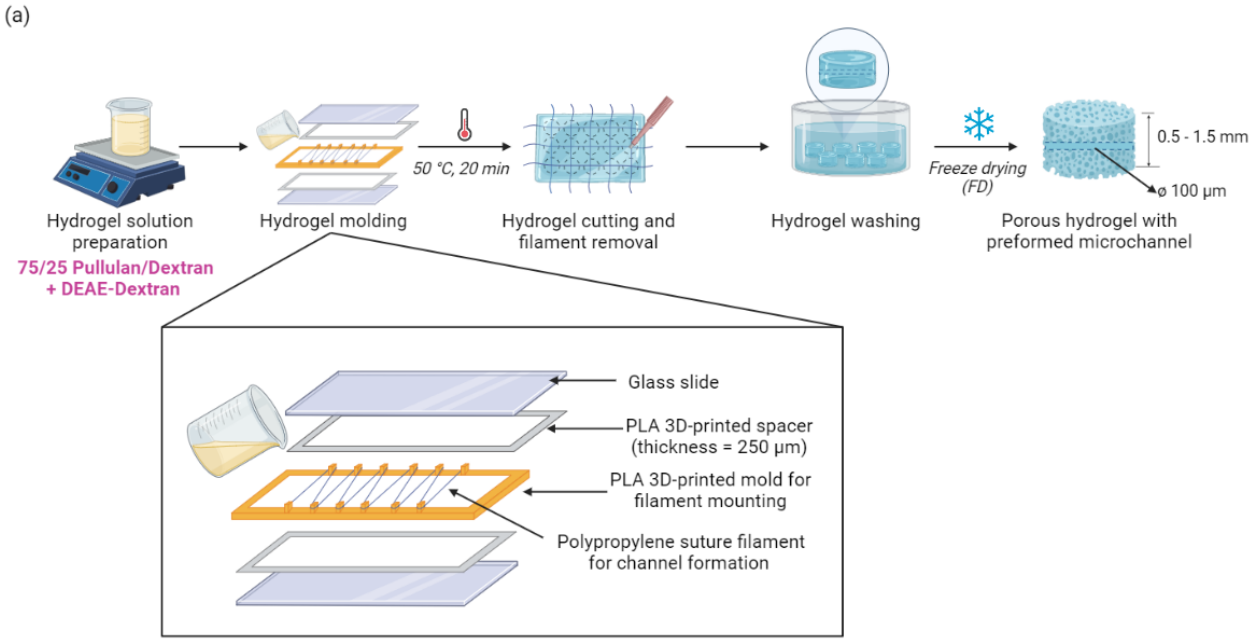
(a)
Hydrogel solution preparation
75/25 Pullulan/Dextran + DEAE-Dextran
Hydrogel molding
50 °C, 20 min
Hydrogel cutting and filament removal
Hydrogel washing
Freeze drying (FD)
0.5 - 1.5 mm
ø 100 µm
Porous hydrogel with preformed microchannel
Glass slide
PLA 3D-printed spacer (thickness = 250 µm)
PLA 3D-printed mold for filament mounting
Polypropylene suture filament for channel formation

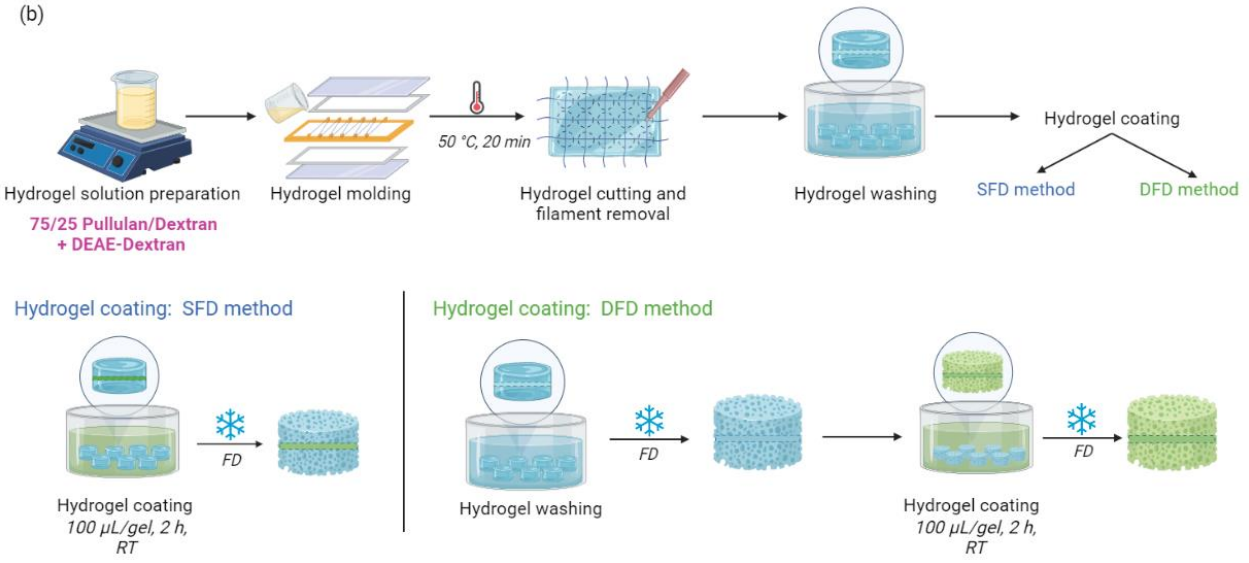
(b)
Hydrogel solution preparation
75/25 Pullulan/Dextran + DEAE-Dextran
Hydrogel molding
50 °C, 20 min
Hydrogel cutting and filament removal
Hydrogel washing
Hydrogel coating
SFD method
DFD method
Hydrogel coating: SFD method
FD
Hydrogel coating 100 µL/gel, 2 h, RT
Hydrogel coating: DFD method
Hydrogel washing
FD
FD
Hydrogel coating 100 µL/gel, 2 h, RT

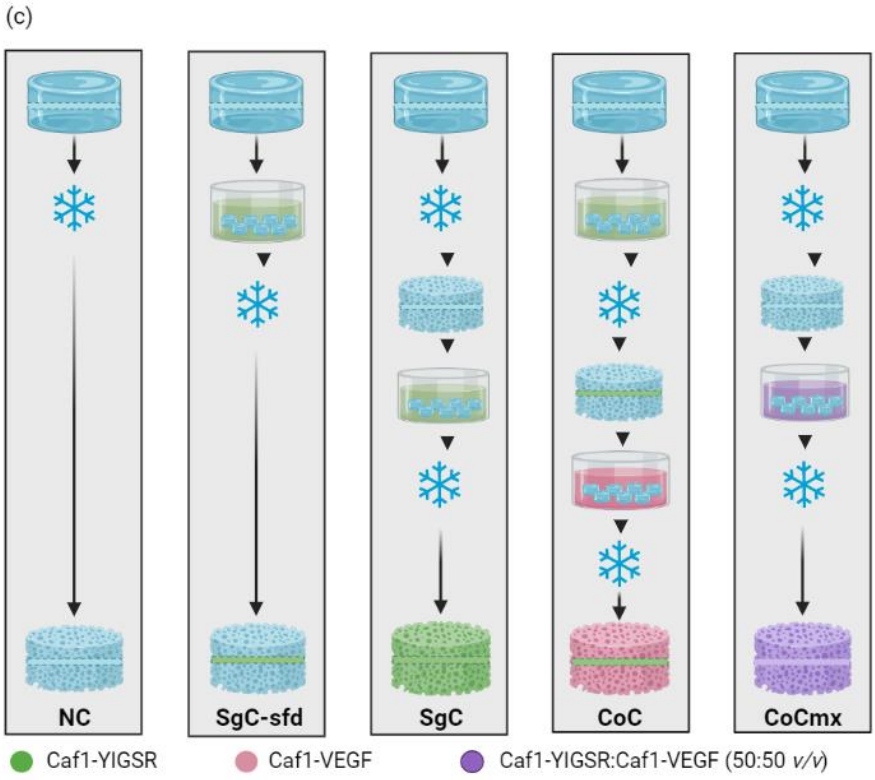

Figure 24. (**a**) Fabrication protocol of 3D porous hydrogels without coating; (**b**) Fabrication protocol of 3D porous hydrogels with coating (SFD: single freeze-drying; DFD: double freeze-drying); (**c**) Schematic plan of spatially controlled coating methods. NC: non-coated; SgC-sfd: single-coated-single-freeze-drying; SgC: single-coated; CoC: Co-coated; CoCmix: co-coated-co-mixed.

The developed scaffolds were evaluated based on: (1) porosity; (2) presence of the hollow channels formed within the 3D scaffolds; (3) ability to promote EC cell adhesion as well as migration; (4) ability to induce pro-angiogenic behavior of ECs. Furthermore, our approach offers a facile protocol for both scaffold fabrication and functionalization. The use of Caf1 overcomes the high cost and immunogenic potential of traditional ECM molecules. The functionalized scaffolds exhibited good EC adhesion and proliferation. Scaffolds with different spatial distribution of pro-angiogenic moieties induced different EC behaviors. Based on the results obtained from this study, we report the first work, to our knowledge, in using animal-free ECM-like molecules to control the spatial cues of hydrogel-based scaffolds, which modulates EC behavior and guides them towards angiogenic sprouting.

2. Results

2.1. Hydrogel preparation and characterization

Hydrogels molded using spacers and cut into discs had an average thickness of 550 ± 20 µm after freeze-drying. Surface pores were clearly visible with the naked eye (**Figure 25a**). Scanning electron microscopy (SEM) observations confirmed the porous structure, revealing the macro- and micro-architecture of the hydrogels (**Figure 25b**). Larger pores (>50 µm) were present on the surface, while interconnected smaller pores (<50 µm) were seen in the cross-section of these hydrogels. Additionally, the presence of a hollow channel in the middle of the hydrogel was observed along with pores inside the channel structure (**Figure 25b**, bottom left).

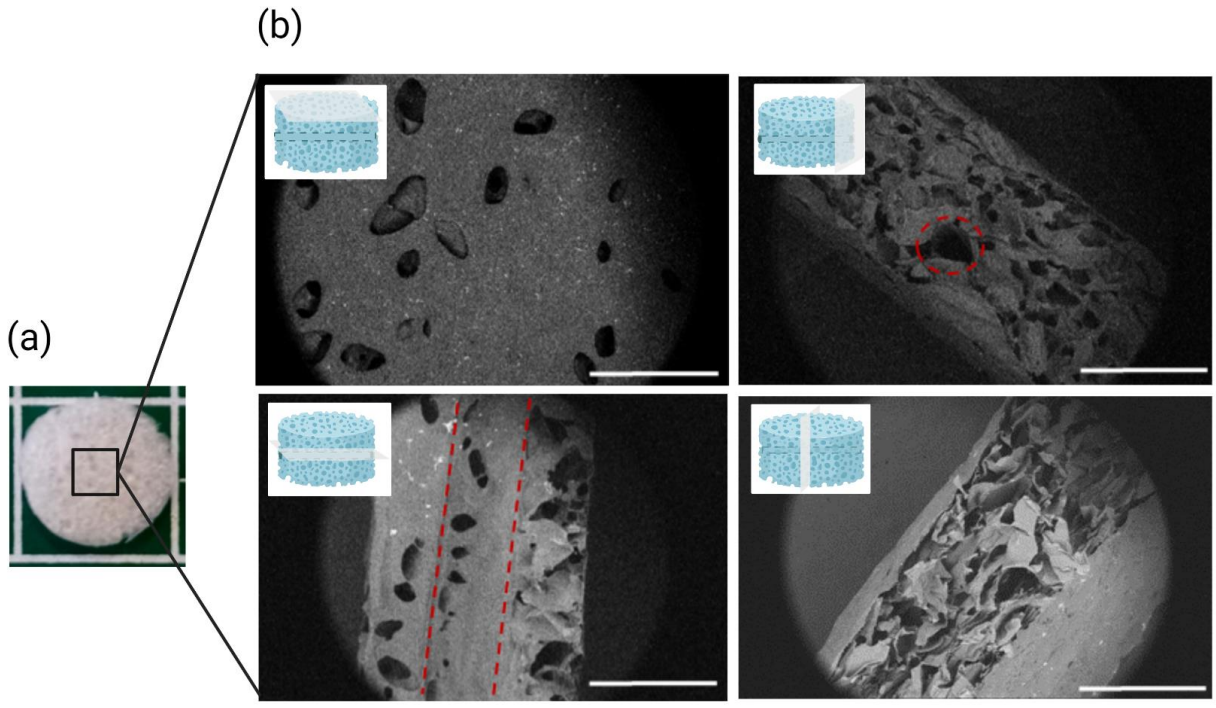

Figure 25. (**a**) Image of the hydrogel showing pores visible to the naked eyes. Scale bar = 5 mm; (**b**) SEM images of the surface, the edges and the cross-section of the hydrogel with a preformed channel. Red dash circle shows the circular cross-section of the microchannel (ø ~ 100 µm), observed on the side of the hydrogel. Red dashed lines represent the limit between the hollow channel and the hydrogel surface. Scale bar = 1 mm.

The cationization by DEAE–Dex (DD) on pullulan–dextran-based hydrogels, previously described by our team [25–28] (referred to as PUDNA), was proven by an increase in the zeta

potential of the hydrogel (from −22.3 mV to +8.28 mV) when replacing dextran with DD. Based on these results, a series of experiments were carried out to determine the optimal concentration of DD needed to facilitate electrostatic interactions between the cationized hydrogel and the negatively charged Caf1 protein polymer. Hydrogel solutions with various DD concentrations were prepared (25%, 50%, 75%, and 100% DD:Dex *w*/*w*) and hydrogels were formulated following the protocol described, as shown in Figure 1. These hydrogels were referred to as D0 for non-cationized samples, and D25, D50, D75, D100 for cationized samples with varying DD concentrations aforementioned. Upon rehydration of the hydrogels for further characterization, it was observed that the opacity increased with the increase in DD concentration added to the hydrogel (**Figure 26a**). Between D25 and D50, the samples were already quite opaque but the structures next to the surfaces were still visible under the microscope (**Figure 26b**). However, above D25, the gels were too opaque to allow observation, using confocal laser scanning microscopy (CLSM) or biphoton microscopy, of the microchannel which was embedded in the middle of the hydrogel (z-axis). Therefore, another opacity-coating efficiency test was conducted at the lower range of DD concentration: 5%, 10%, 15%, and 20% (DD:Dex *w*/*w*) (**Figure 26**). Here, all the hydrogels and their channel structures were visible via the confocal microscope (**Figure 26c**). Thus, all four conditions (D5, D10, D15, D20) were used for further hydrogel characterization as well as for in vitro studies with ECs.

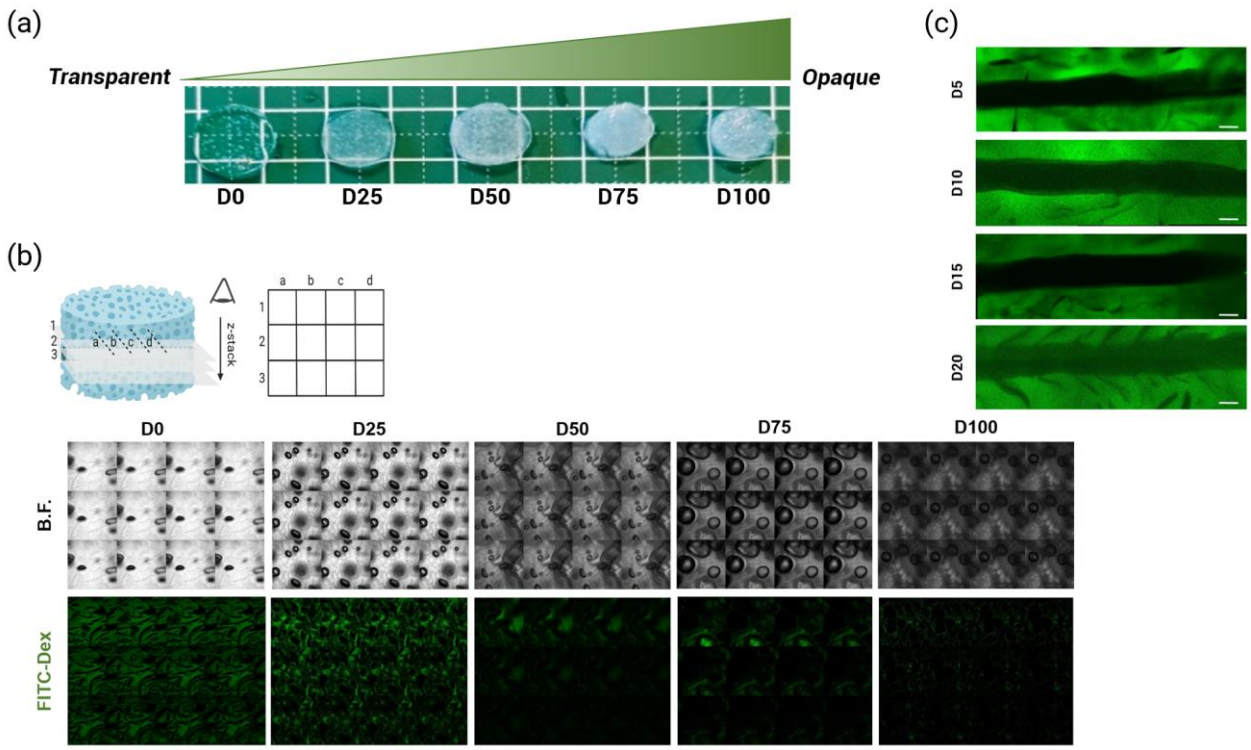

Figure 26. (**a**) Hydrogel opacity increased with an increase in DD concentration; (**b**) Hydrogel opacity as observed using CLSM: under bright-field and fluorescence (FITC). Z-stack images of hydrogels without DD (D0) and with DD 25–100% (DD:Dex *w*/*w*) were compiled as collages to demonstrate the increase in sample opacity with an increase in sample depth. (**c**) Z-projection (average intensity) of FITC-Dex hydrogels observed using CLSM.

Porosity measurements of non-cationized (PUDNA) and cationized hydrogels containing DEAE-dextran (PUDNA-D5, PUDNA-D10, PUDNA-D15, and PUDNA-D20) showed porosity values of 25–28 % (**Table 8**). Swelling ratios for all conditions were around 12, meaning that water content after swelling was around 93 % (*w*/*w*) (**Table 8**). It should be noted that we did not find statistical differences between the different formulations.

Table 8. Effect of polysaccharide formulation on hydrogel properties: porosity %, swelling ratio, and water content. Results are expressed as mean values ± SD.

Scaffold Name	Porosity %	Swelling Ratio	Water Content (%)
PUDNA	26.1 ± 3.7	13.6 ± 1.8	93.1 ± 0.8
PUDNA-D5	28.0 ± 2.0	14.2 ± 3.7	94.2 ± 0.7
PUDNA-D10	25.0 ± 2.2	10.8 ±1.4	91.5 ± 0.6
PUDNA-D15	25.6 ± 4.3	12.2 ± 2.3	91.9 ± 1.3
PUDNA-D20	25.5 ± 3.1	13.2 ± 2.2	92.8 ± 0.7

The degree of crosslinking by sodium trimetaphosphate (STMP) within the hydrogels was evaluated by quantifying the amount of phosphorus present after matrix degradation with HNO_3, an indicator of phosphate bridges between chains of pullulan–dextran. The phosphorus content in all hydrogel conditions ranged from 113 to 143 μmol per gram of hydrogel. These results suggest that the incorporation of DEAE–dextran did not affect the crosslinking degree of the polysaccharide-based hydrogels.

2.2. In vitro endothelial cell studies

To ensure cell adhesion on the materials, Caf1-YIGSR (a Caf1 polymer containing a pro-adhesive peptide sequence from laminin) was used to functionalize the hydrogels via electrostatic interactions. First, hydrogels were cationized by incorporating DD at various concentrations (5–20% DD:Dex *w*/*w*). Then, the cationized scaffolds were coated with the solution of Caf1-YIGSR (1 mg/mL, p.I. = 4.6) [13], at pH 7.0, room temperature (RT) via the vacuum-induced syringe method (**Figure S3**). This technique ensured that only the channel was coated. Subsequently, after the syringe coating step, the scaffolds were submerged in the same Caf1-YIGSR solution for 2 h, RT and immediately rinsed with PBS before the freeze-drying step (**Figure 24b**, SFD method). The scaffolds were exposed to UV light for at least 1 h before cell seeding experiments.

2.2.1. Selection of cationized hydrogel for optimal coating efficiency

To establish the optimal concentration of DD required to functionalize the scaffolds via electrostatic interactions, samples with increasing DD concentration (5–20% DD:Dex *w*/*w*) were coated, then loaded with HUVECs at a seeding density of $5.0*10^6$ cells/mL. Coating efficiency was determined based on cell adhesion and cell morphology. After 7 days in culture, cellularized scaffolds were fixed and stained with DAPI and phalloidin TRITC. Coated, cationized scaffolds with 5–20% DD:Dex (*w*/*w*) were referred to as PUDNA-D5C, PUDNA-D10C, PUDNA-D15C, and PUDNA-D20C, respectively.

HUVECs seeded on PUDNA-D5C formed large aggregates inside the coated channel section (**Figure 27a**). On PUDNA-D10C, a few polarized cells could be detected, where they exhibited filopodia and connections to neighboring cells (**Figure 27a**). On PUDNA-D15C scaffolds, the number of cells that adhered inside the channel appeared to increase slightly. The cell clusters seemed to reduce, while more polarized cells appeared inside the channel. Finally, on PUDNA-D20C scaffolds, cell morphology and behavior significantly improved. The entire channel edge was lined with elongated cells. These cells formed connections with their neighboring cells, showing filopodia structure and stress fibers, and less cell aggregates were detected. Regarding the porous regions outside the channel structure, numerous cell clusters were observed in the pores neighboring the channel (y-axis) as well as in the macropores outside the channel (z-axis) (**Figure 27b**).

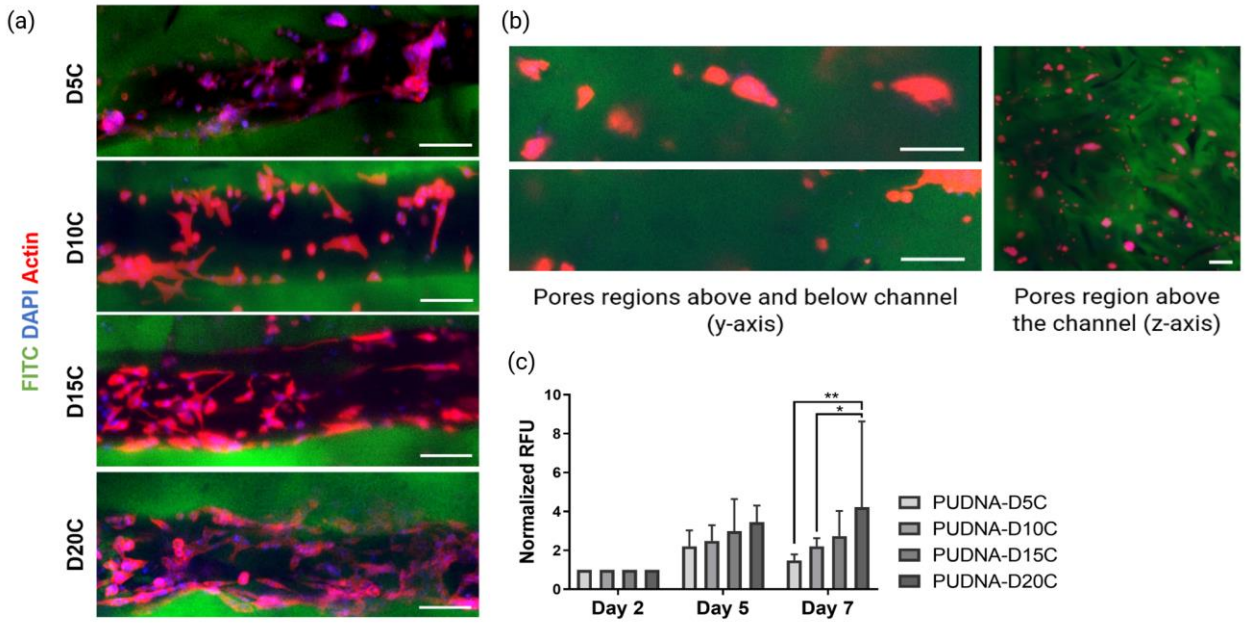

Figure 27. Cell analysis of seeded HUVECs on coated, cationized hydrogels with increasing DD concentrations: (**a**) Images represent Z-Projection, average intensity, showing cell morphology at day 7 via CLSM. Scale bar = 100 µm; (**b**) Representative image (Z-Projection) of cells in the pore region outside the channel on coated scaffold. Scale bar = 100 µm; (**c**) Cell metabolic activity determined by resazurin assay on days 2, 5, and 7. All resofurin fluorescence unit (RFU) values of each condition were normalized to their own RFU value on day 2. Statistical analysis was performed using a two-way ANOVA with multiple comparisons. * $p < 0.05$, ** $p < 0.01$.

Cell metabolic activity on all coated, cationized scaffolds was also investigated (**Figure 27c**). Overtime, there was an increase in cell metabolic activity for all coating conditions. On day 7, metabolic activity reached its peak for all conditions, with PUDNA-D20C showing the highest value and statistically greater than the metabolic activity on PUDNA-D5C and PUDNA-D10C. Although the cell metabolic activity on PUDNA-D15C vs. PUDNA-D20C did not differ, the morphological organization of HUVECs on PUDNA-D20C appeared more superior to those on PUDNA-D15C. From here on, PUDNA-D20C which showed optimal coating efficiency, was chosen as the standard cationized hydrogel for future functionalization experiments.

2.2.2. Spatial-controlled coating: Caf1-YIGSR facilitated cell adhesion in both SFD and DFD coating methods

We hypothesized that the coating of hydrogels could be modulated by integrating the coating step (via vacuum-induced syringe method) before and after the freeze-drying (FD) step (**Figure 24**). To confirm this hypothesis, cationized hydrogels (PUDNA-D20) were functionalized twice: the first coating was performed before FD, then the second coating was performed after FD. Samples which were coated once, were only freeze-dried once, in which only the channel was coated. These samples were named SFD and were used as controls. On the other hand, samples that were coated twice, hence freeze-dried twice, were named DFD, in which both the channel and the pores were coated.

The coated hydrogels were seeded with HUVECs at 5.0×10^6 cells/mL and cultured for 9 days. Then, cellularized scaffolds were analyzed for cell adhesion, cell morphology, and cell metabolic activity. Similar to the SFD scaffolds, cells on the DFD scaffolds adhered in a monolayer along the channel lining and more cell spreading (elongation) was detected after 7 days in culture. Additionally, more polarized cells were observed inside the channel (**Figure 28a**, bottom). When looking at the pores near the channel edges, migrating cells were observed: the cell filopodia reached towards the pores outside the channel and formed connections with neighboring cells residing in the pores (external of channel) (Figure 5a, bottom). Cell clusters were also detected: inside the channel, the clusters were comprised of both polarized and round cells; outside the channel, the clusters were composed of mostly round cells. On day 9 (results not shown), the cell's presence began to block visibility under the CLSM, making it inconclusive for further analysis.

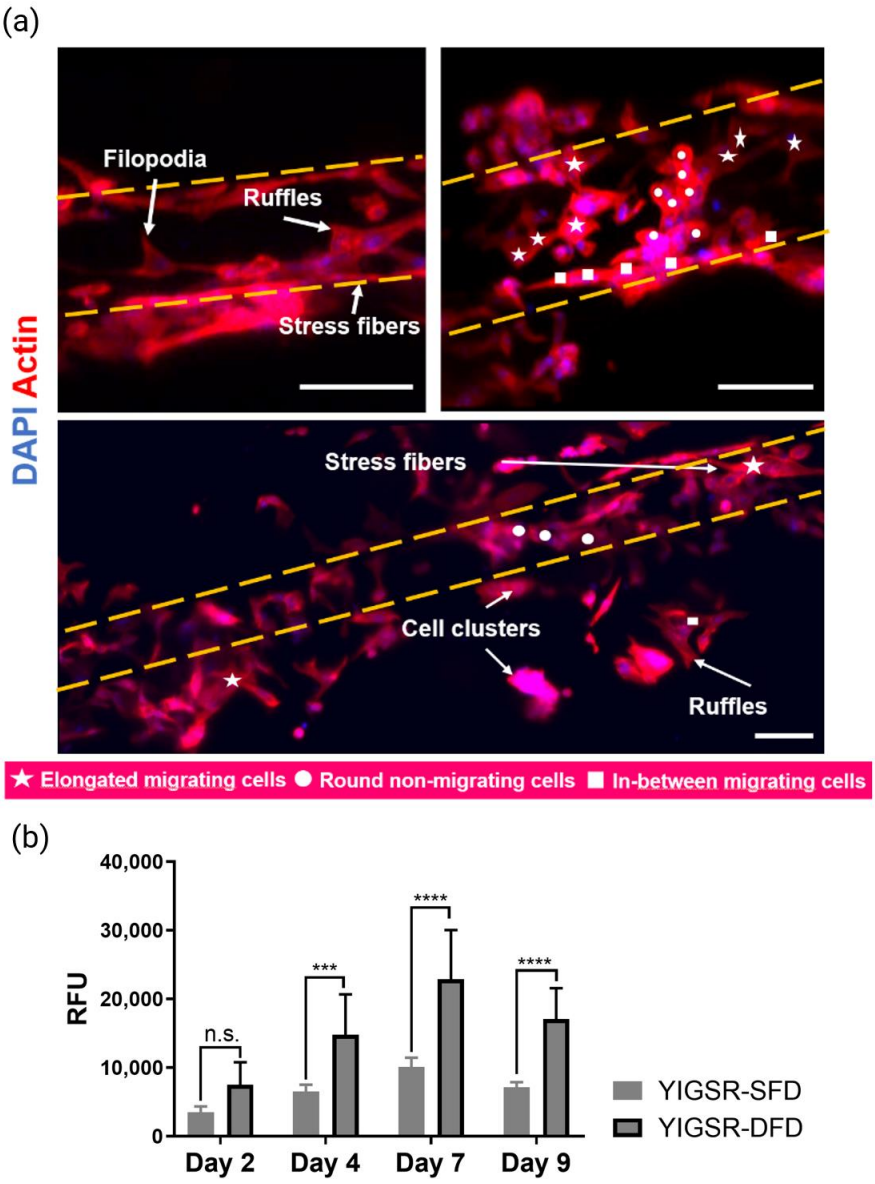

Figure 28. Cell analysis of seeded HUVECs on PUDNA-D20C scaffolds (SgC-SFD, top; SgC-DFD, bottom). (**a**) Images represent Z-Projection (average intensity) showing cell morphology at day 7 via CLSM. Scale bar = 100 µm; (**b**) Cell metabolic activity determined by resazurin assay on days 2, 5, 7, and 9. Statistical analysis was performed using a two-way ANOVA. *** $p < 0.001$, **** $p < 0.0001$.

Cell metabolic activity from resazurin assay (**Figure 28b**) was analyzed to support the cell adhesion and cell morphology observations. For both SFD and DFD scaffolds (YIGSR-SFD and

YIGSR-DFD), there was an increase of metabolic activity from day 2 to day 7. After 7 days, the metabolic activity dropped. Compared to SFD, cells on DFD scaffolds had a significantly higher metabolic activity, with a peak on day 7.

2.2.3. Spatial-controlled coating (DFD Method): Caf1-YIGSR and Caf1-VEGF influenced cell behavior differently

Two different recombinant Caf1 proteins containing peptide sequences from laminin (YIGSR) and VEGF, were tested on DFD hydrogels. Those coated with Caf1-YIGSR and with Caf1-VEGF, were named YIGSR-DFD and VEGF-DFD, respectively. Regarding the cell morphology, cells seeded on hydrogels coated with YIGSR exhibited different shape than those seeded on VEGF-coated hydrogels (**Figure 29a**). On VEGF-DFD samples, very few cells adhered inside the channel and the channel edge. Those that remained adhered inside the channel started to polarize. In contrast, on YIGSR-DFD samples, a greater number of cells adhered inside the channel and lined the channel edge while fewer cells showed signs of migration or polarization.

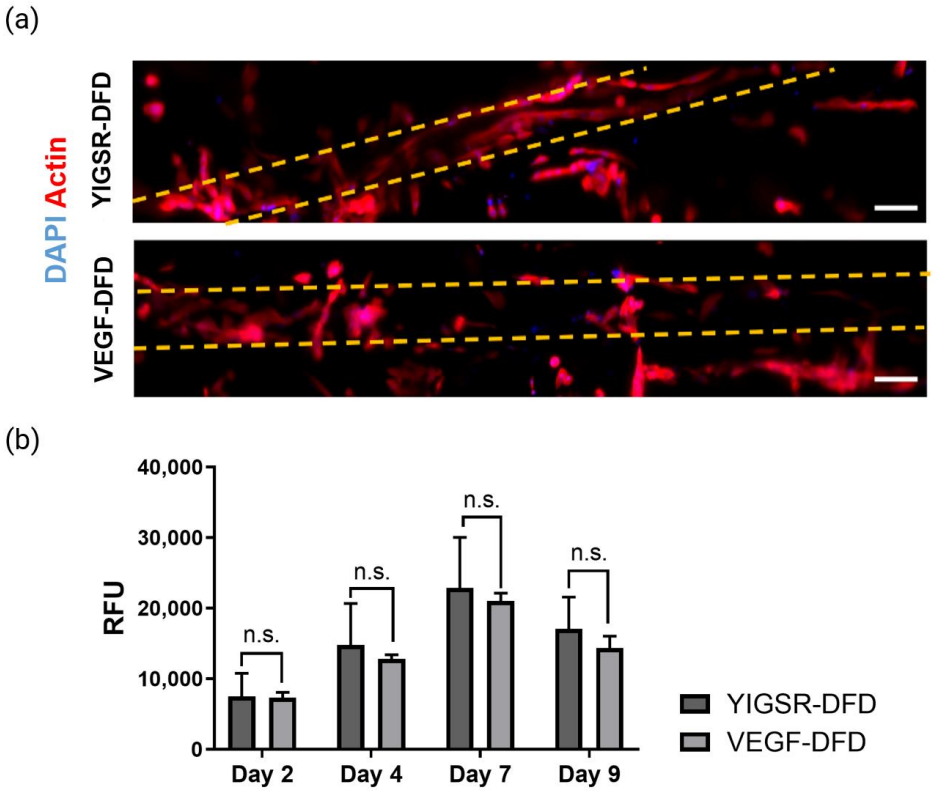

Figure 29. Cell analysis of seeded HUVECs on scaffolds functionalized with Caf1-YIGSR and Caf1-VEGF via the DFD method. (**a**) Tile-scan images represent Z-Projections (average intensity) showing cell morphology inside the scaffold channel (full length) at day 7 via CLSM. Scale bar = 100 µm. Yellow dashed lines represent the limit of the microchannel; (**b**) Cell metabolic activity of seeded HUVECs determined by resazurin assay on days 2, 4, 7, and 9. Statistical analysis was performed using a two-way ANOVA.

Overtime, cell metabolic activity followed the previously observed trend, with the highest cellular activity observed on day 7 and a slight decrease on day 9. The differences in cellular activity of seeded HUVECs on YIGSR-DFD and VEGF-DFD were insignificant (**Figure 29b**), but the variations of cell morphology seen on the differently coated scaffolds were more obvious (**Figure 29a**). These results confirmed that Caf1-YIGSR had a stronger cell-adhesive effect than Caf1-VEGF.

2.2.4. Spatial-Controlled Coating (SgC, CoC, CoCmx): Caf1-YIGSR and Caf1-VEGF spatial distribution on scaffolds can provoke different angiogenic behaviors

Using the optimal coating protocol (DFD = double freeze-drying, coating of both channel and pores), the next step was to determine whether (i) the presence of different protein types (Caf1-YIGSR and Caf1-VEGF) and (ii) their spatial presentation on the scaffolds (pores and/or microchannel) could influence cell behavior. To answer this question, several coatings were performed as described in Figure 1c. DFD scaffolds with only one type of coating (Caf1-YIGSR) were named SgC. Scaffolds with two types of coating (Caf1-YIGSR and Caf1-VEGF) were named CoC and CoCmx. In CoC, Caf1-YIGSR were coated only in the channel and Caf1-VEGF were coated in the pores. In CoCmx, both Caf1 sequences were mixed at a 50:50 ratio (*v*/*v*) so that the pores and the channel were simultaneously coated at the same time with both Caf1-YIGSR and Caf1-VEGF (**Figure 27**). The non-coated, cationized hydrogels (D20C) were used as control and were named NC.

As expected, the NC scaffolds did not support cell adhesion or proliferation overtime (**Figure 30**). On the NC scaffolds, only cell aggregates were observed inside the channel and cell metabolic activity was lower compared to those on the coated scaffolds. Initial examination of cell morphology on all the coated scaffolds (SgC, CoC, CoCmx) showed interesting outcomes. Both SgC and CoCmx resulted in elongated cells lining the channel edges, a high density of polarized

cells inside the channel, large number of cells forming connections with neighboring cells. While both CoC and CoCmx scaffolds encouraged adhered cells to migrate outwards of the channel, SgC scaffolds only contained adhered cells within the channel (**Figure 30a**). Further observations on CoCmx scaffolds demonstrated that the co-presence of Caf1-YIGSR and Caf1-VEGF also had an effect on ECs outside the channel (**Figure 31**). Here, the cells in the pores did not form aggregates but rather exhibited an elongated morphology, conforming their shape to the curvature of the pores (**Figure 31a**, right panel and **Figure 31b**).

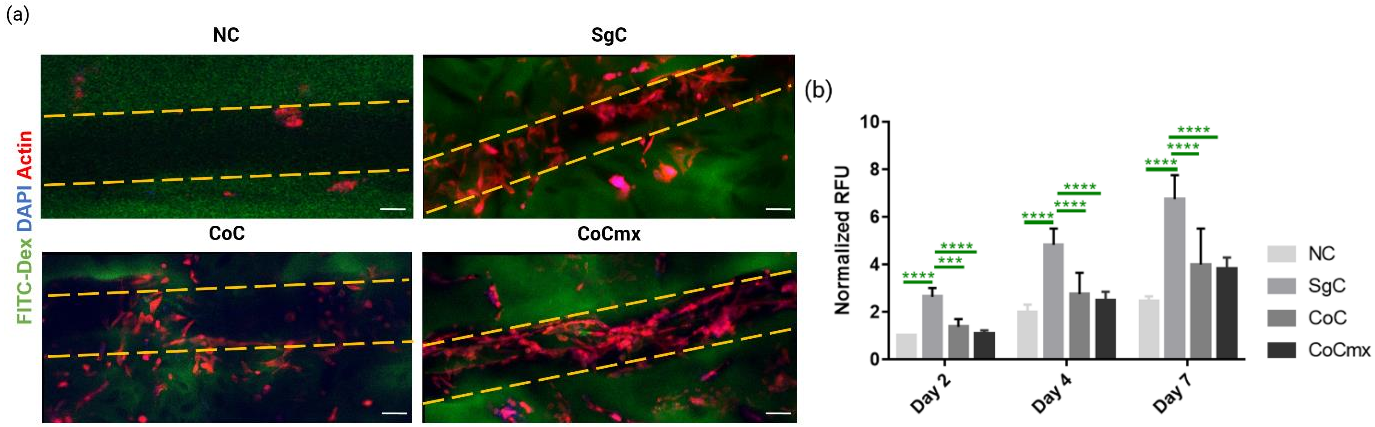

Figure 30. Cell analysis of seeded HUVECs on non-functionalized (NC) and functionalized scaffolds with a different spatial distribution of Caf1-YIGSR and Caf1-VEGF (SgC, CoC, and CoCmx) via the DFD method. (**a**) Images represent Z-Projection (average intensity) showing cell morphology at day 7 via CLSM. Scale bar = 100 µm. Yellow dashed lines represent the limit of the microchannel; (**b**) Cell metabolic activity (resazurin-based assay) at days 2, 4, and 7. Statistical analysis using two-way ANOVA of all hydrogels compared to SgC. Statistical analysis was performed using a two-way ANOVA. *** $p < 0.001$, **** $p < 0.0001$.

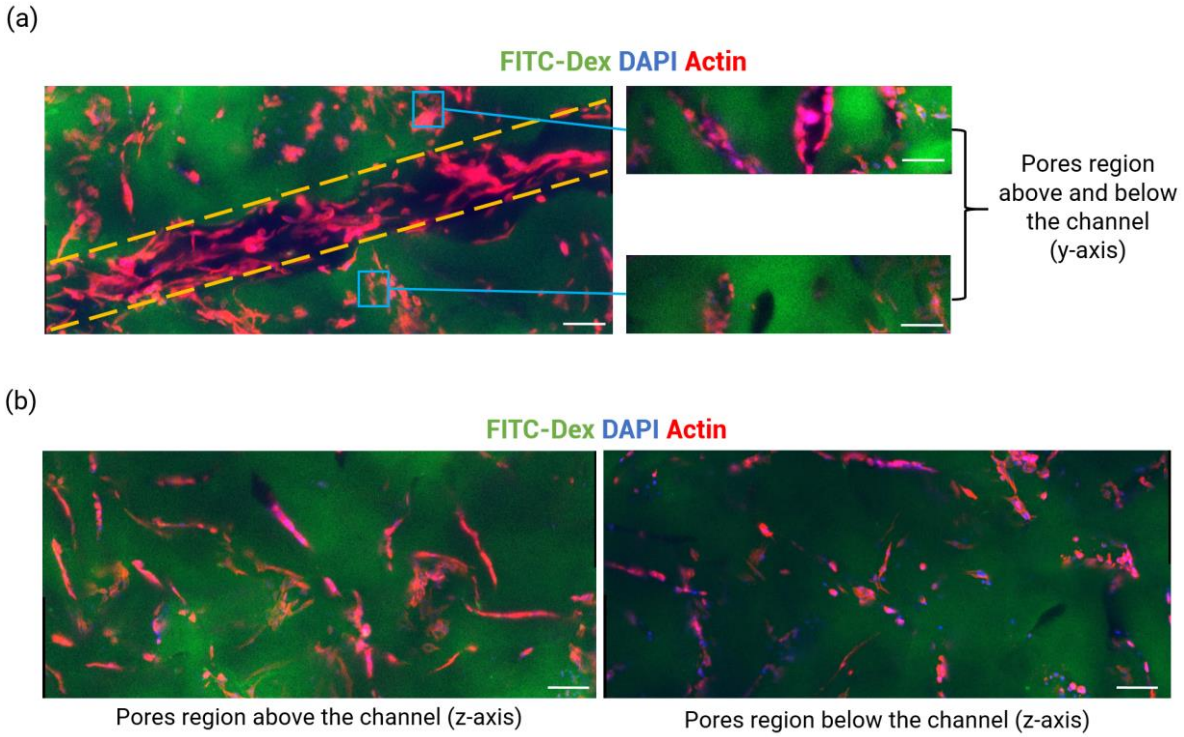

Figure 31. Cell analysis of seeded HUVECs on CoCmx scaffolds. (**a**) Images represent Z-Projection (average intensity) inside the scaffold's channel. Scale bar = 100 µm. Yellow dashed lines represent the limit of the microchannel; (**b**) Images represent Z-Projection (average intensity) of the same scaffold, in the porous regions outside the channel (z-axis). Scale bar = 100 µm.

Overall cell metabolic activity showed the expected trend with the highest activity observed on day 7 for all scaffold conditions. NC scaffolds resulted in the lowest cell metabolic activity, which is representative of the cell morphology outcome. As for coated scaffolds, the cell metabolic activity on SgC samples was significantly greater compared to those on the CoC and CoCmx scaffolds (**Figure 30b**).

2.2.5. Protein bulk concentration

Previously, we observed that the cell metabolic activity of HUVECs seeded on all functionalized hydrogels was statistically higher than on non-functionalized ones. Moreover, cell morphology drastically improved when seeded on spatially controlled coated DFD gels (SgC, CoC, CoCmx) (**Figure 30a**). Therefore, we hypothesized that the enhancement in cell behaviors was contributed by an increase in protein concentration on the functionalized scaffolds.

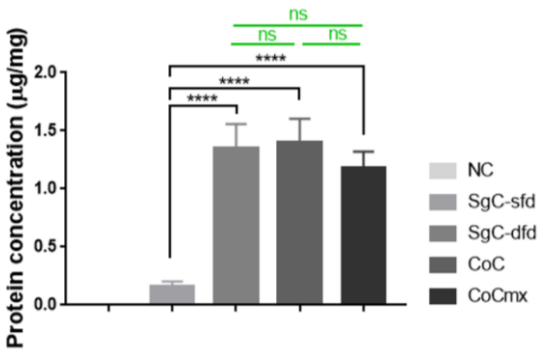

Figure 32. Protein concentration of cationized hydrogels (20% DEAE–Dextran) with spatial-control coating. Statistical analysis was performed using a one-way ANOVA. **** $p < 0.0001$.

Among the SgC scaffolds where only one type of protein (Caf1-YIGSR) was employed and the coating was performed either once (SFD, channel coated only) or twice (DFD, channel and pores coated), the DFD scaffolds had a significantly greater protein concentration (µg per mg hydrogel). Similarly, when comparing all the DFD samples to the SgC-SFD samples, CoC and CoCmx showed a higher protein concentration **(Figure 32**). These values were expected since the DFD scaffolds were coated twice, hence the amount of proteins grafted onto the hydrogels would be greater on these scaffolds.

3. Discussion

Porous hydrogels made of pullulan and dextran were synthesized by chemical crosslinking with sodium trimetaphosphate (STMP), as previously described [29]. First, the hydroxyl groups in the polysaccharides were activated at basic pH using NaOH, resulting in the opening of cyclic STMP and crosslinking between the polysaccharides, leading to hydrogel formation [36]. Previous studies have demonstrated the potential of these biocompatible hydrogels as scaffolds for 3D cell culture, tissue engineering, and cell therapy applications [25,27,37,38]. However, due to the high water content (~93%) and the chemical structures of pullulan and dextran, endothelial cells do not adhere spontaneously to these hydrogels [28,38], as shown **in Figure 30a** (NC sample). The neutral polysaccharides were cationized by incorporating diethylaminoethyl dextran (DEAE–Dex) to facilitate electrostatic interactions with the negatively-charged ECM-like molecules (Caf1-YIGSR and Caf1-VEGF). The shape and diameter of the channel remained 100 ± 20 µm before and after swelling. These observations are in correspondence with the swelling behavior observed

in all formulations. Here, we demonstrated the ability to form straight microchannels with circular cross-section and controlled diameter.

Cell analysis of HUVECs seeded on functionalized scaffolds with various coating methods (SFD vs. DFD) and spatial distribution of the two Caf1 motifs (YIGSR and VEGF) confirmed that the Caf1 solution (p.I. = 4.6; 1 mg/mL; ζ = −23.6 mV) was adequate to facilitate electrostatic interactions with cationized hydrogels (PUDNA-D20; ζ = +29.5 mV). Through the addition of microchannels within the polysaccharide scaffolds and sufficient surface functionalization via electrostatic interactions, ECs were able to adhere, leading to good cell proliferation and cell spreading within the microchannel. In this work, spatial control of the ECM-mimicking moieties was shown to induce different EC behaviors that could be interesting for vascularization applications. An in-depth discussion on this part is presented in **Sections 3.2–3.4**.

3.1. The impact of DEAE–Dex concentration on hydrogel opacity and functionalization

As seen in **Figure 26**, an increase in the concentration of DEAE–Dex added to the polysaccharide solution contributed an increase in hydrogel opacity, which limited sample visibility under the microscope. Even with a multiphoton microscope or a high-resolution confocal laser scanning microscope and sufficient image treatment and analysis, it was very difficult to locate the microchannel embedded in the middle of the sample depth. Consequently, these observations suggest that a balance between hydrogel transparency and the cationic polymer concentration need to be considered to ensure sample visibility for microscopy analysis, which is essential to monitor cell behavior in the scaffolds. Moreover, this balance must also allow sufficient interactions between the charged materials in order to facilitate cell adhesion on the functionalized scaffolds.

After a series of optimization work, by synthesizing cationized hydrogels with varying DEAE–Dex concentrations (5–100% DD:Dex *w*/*w*), we were able to determine the best cationic parameters to yield optimal hydrogel opacity and favorable EC behavior outcomes. At 20% (DD:Dex *w*/*w*), the scaffold surface and microchannel were still visible under the CLSM (**Figure 26a**). More importantly, ECs were also observable after 7 days in culture (**Figure 27a**). On day 7, PUDNA-D20C scaffolds facilitated better EC adhesion, where more elongated cells were present inside the channel (**Figure 27a**) and cell metabolic activity was statistically higher than the metabolic activity on the rest of the other conditions (**Figure 27c**). These results strongly suggest

that PUDNA-D20C was the optimal hydrogel condition for most favorable EC adhesion and morphology.

3.2. Caf1-YIGSR induced cell adhesion on SFD hydrogels and enhanced cell proliferation on DFD hydrogels

Cell morphology and behavior on SFD scaffolds using Caf1-YIGSR (**Figure 28a**) confirmed that the YIGSR sequence could be used as a cell-adhesive coating material.

Recent works on functionalized biomaterials have demonstrated the ability to modulate cell behavior by varying the concentration of cell-adhesive ligands in the scaffolds, with an increase in ligand concentration leading to an improvement in cell adhesion, spreading, and proliferation [39]. The results obtained from this study are in accordance with these findings. When both the channel and pores were coated (DFD coating method: YIGSR-DFD), the amount of Caf1 protein detected on the SgC-DFD scaffolds was higher than that on the SgC-SFD scaffolds, suggesting an increase in bulk ligand concentration (**Figure 32**). As a result, cell morphology on the DFD scaffolds greatly improved (**Figure 28a**) and greater cell metabolic activity was observed after 7 days in culture (**Figure 28b**). The decrease in cell metabolic activity on day 9 could be due to high cell confluency. This is supported by the fact that no signs of cell death were observed after 9 days. In conclusion, the increase in spatial distribution of the YIGSR sequence, contributed to an increase in ligand bulk concentration on the scaffold, leading to an enhancement of EC morphology and behavior.

3.3. Caf1-VEGF induced cell migration and angiogenic sprouting depending on its spatial presentation on porous hydrogels

When Caf1-VEGF was used alone as the coating material in the DFD method, few cells adhered inside the channel and did not completely line the channel edge. Adhered cells showed polarization characteristics and sprouting-like behaviors. It is well known that VEGF is a pro-migratory factor that induces filopodia elongation in ECs during angiogenesis [5]. This explains why ECs in VEGF-DFD scaffolds showed filopodia structure resembling migration behaviors (**Figure 28a**). Additionally, cells on the top side of the channel protruded and connected to cells on the bottom side (**Figure 29a**). Due to lack of cell-adhesive moieties (i.e., Caf1-YIGSR), not enough cells adhered inside the channel, resulting in lower cell proliferation, as demonstrated by

the lower cell metabolic activity (**Figure 29b**). This drop in metabolic activity could also be linked to cell confluency on day 9.

Taking these results into consideration, CoC scaffolds were prepared, where two different Caf1 proteins were presented on the hydrogels in different spatial distribution. First, the channel was coated with Caf1-YIGSR, then the pore-filled region was coated with Caf1-VEGF (**Figure 24c**). On co-coating scaffolds, the cell morphology and behaviors significantly altered. Adhered cells inside the channel started to migrate outwards to the pore-filled region. Some cells even exhibited filopodia structure. These results strongly suggest that different spatial presentations of Caf1-VEGF on porous hydrogels drive distinct cell behaviors.

During the last decades, cell–ECM interaction research has shown that when cell-adhesive molecules were spatially presented to the cells in different manners, they induced different patterns of cellular behavior [40,41]. In the case of CoC hydrogels, cell adhesion was achieved thanks to the contribution of the Caf1-YIGSR coating in the channel during the first coating step (**Figure 27**). The presence of Caf1-YIGSR facilitated proper cell adhesion, where cells could form a strong anchor to the substrate at focal complexes [4]. The presence of Caf1-VEGF promoted protrusion formation of ECs and transformed protrusion into forward movement. This explains the observation of filopodia structure, stress fibers, and polarization of HUVECs seeded on the CoC hydrogels (**Figure 30a**). The adhered cells sensed migratory signals from the VEGF sequence, which stimulated cell migration processes. In other words, our results suggest that the presence of Caf1-VEGF moieties in the pores created cell directionality, leading to cells moving from the channel outwards to the porous region (exterior of the channel).

3.4. Synergistic effects of Caf1-YIGSR and Caf1-VEGF on EC morphologies and behavior

Taken the outcomes discovered from CoC hydrogels, a question regarding Caf1-YIGSR and Caf1-VEGF spatial distribution on hydrogel was considered. What will be the effect of these two Caf1 proteins on cell morphology and cell behavior, if they were both presented on the hydrogel in similar spatial organization? This question led to the creation of CoCmx hydrogels, where Caf1-YIGSR and Caf1-VEGF solutions were mixed in equal parts (50:50 *v*/*v*) and used to coat the scaffolds via the DFD method. Here, both the channel and the pores were functionalized with Caf1-YIGSR and Caf1-VEGF at the same time. Initial inspection of cell morphology on CoCmx scaffolds showed good cell adhesion (where cells fully lined the channel) and elongated

filopodia (which indicated cell sprouting and migration) (**Figure 30a**, top panel). Moreover, migrating cells connected with non-migrating cells both inside the channel and outside the channel (**Figure 30a**, bottom panel). These observations suggested the synergistic effect of Caf1-YIGSR and Caf1-VEGF. Both VEGF and YIGSR are known to play a role in angiogenesis, with YIGSR contributing to cell adhesion, cell–cell interactions, and tubule formation, while VEGF stimulates cell migration [4,42,43]. The presence of both Caf1-YIGSR and Caf1-VEGF inside the channel induced a stabilizing adhesive effect on ECs. These ECs then migrated towards the VEGF stimulus that was also available in the pores of the scaffolds. Consequently, the dual presence of YIGSR and VEGF sequences, both exhibiting angiogenic effects, promoted greater EC proliferation. These ECs possibly produced their own ECM, which further stabilized the vessel-like network and induced EC differentiation towards angiogenic phenotypes. This explains why elongated migrating cells were observed in both the channel section and the porous regions outside the channel only on CoCmx scaffolds (**Figure 31**).

In other words, the dual presence of Caf1-YIGSR and Caf1-VEGF functionalized on our 3D porous hydrogels created a synergistic effect on seeded HUVECs. Previously, a Caf1 mosaic co-polymer containing two pro-osteogenic motifs was seen to promote the early stages of bone formation in primary human mesenchymal stromal cells in a 2D system [35]. The synergistic effect described here further demonstrates the benefits of the Caf1 system, where bioactive peptides can be easily introduced and placed in close proximity in a single material, allowing these synergistic effects to take place. Thus, these effects mimicked the in vitro angiogenesis, where ECs adhered and became activated, then proliferated and differentiated into tip cells, resulting in elongation in the direction of the VEGF stimulus.

3.5. Comparison of the developed method with current vascularization strategies

Over the past decades, numerous attempts have been made to develop vascularized constructs using three main strategies: microfluidic-based approaches, 3D bioprinting, and organoids/spheroids-based techniques. The readers are invited to read more on this topic in the published review [2].

The use of ECM-based membranes integrated in microfluidic platforms has allowed researchers to develop more physiologically relevant models thanks to the ability to perfuse the

systems. However, most models require soft lithography for materials fabrication, which is expensive and is difficult to be used by a wide end-user's range.

The use of 3D additive manufacturing, such as fuse deposition modeling (FDM), facilitates printing of sacrificial components that better mimic in vivo vasculature. However, these techniques often require several manufacturing steps and still present major issue in terms of resolution. Most vessel geometries remain relatively simple and the vessel diameters are in the range of hundreds of microns. Channels obtained using co-axial bioprinting or with sacrificial bioinks remain in the same range. More recently, the use of laser-assisted bioprinting (LAB) offers high resolution (5–10 μm) of printed channels, automation, reproducibility, and high throughput. Similarly, the use of Vat photopolymerization-based bioprinting opens new possibility to create complex vascular patterns with high precision and high resolution. However, these approaches are still far from translation due to the high cost of equipment, and the need to work with photosensitive materials and photoinitiators further limit their application for therapy.

Spheroids and organoids are another alternative approach to promote the vascularization of hydrogel constructs. They offer the ability to recapitulate the microenvironment, thus present great potential as vascularized models. However, to reach a substantial quantity of tissue, a large number of cells are needed. The use of ECM proteins with heterogeneous composition and high immunogenic potential (e.g., collagen and Matrigel), further prevents translation of these models in the industry and clinical settings.

In this work, we employed a simple method to form microchannels at the microcapillaries range (≥100 μm). Although the filament templating/removal technique is limiting in terms of producing complex designs, it enables high reproducibility and facile fabrication. Our system, porous hydrogels with channels, functionalized in a spatial-controlled manner, present several advantages compared to other aforementioned vascularization strategies.

Compared to other hydrogel-based vascularization strategies, our polysaccharide-based hydrogels support long-term cell culture of up to 9 days, as demonstrated in this study, and could be kept up to 14 days in other studies without being degraded [27]. With a small amount of protein (~0.25–1.8 μg/mg hydrogel), we were able to induce initial cell adhesion, followed by cell proliferation and migration on functionalized scaffolds. Thus, the spatial cues (e.g., YIGSR and VEGF) further direct cell migration mimicking the first step of sprouting angiogenesis. Even

though the electrostatic bonds are weaker than covalent bonds, our functionalization method was stable enough to enable observation of grafted Caf1 on the hydrogels (as shown in **Figure S5**). Moreover, the concomitant presence of channels and pores offers the possibility to promote vascularization of tissue constructs, while enabling co-culture with other cell types for the development of different bioengineered models. Caf1 molecules are manufactured in vitro using bacterial expression systems in high quantities and with a lower cost [33]. Thus, the animal-free origin of Caf1 would reduce immunogenic potential, making them ideal materials for implantable constructs. Our coating method based on ionic interactions is performed in a one-step process and uses green chemistry. In this study we focused on YIGSR and VEGF, but in the future, it will be possible to use the same strategy to incorporate other Caf1 peptides to confer new properties to the material. Finally, from an industrial point of view, our fabrication technique and the choice of materials are highly beneficial: The production method is simple and can be easily scaled-up and the freeze-dried hydrogels allow for long-term storage, all contributing to low-cost production and maintenance.

4. Materials and Methods

4.1. Materials

Pullulan (Mw 200 kDa) and dextran (Mw 500 kDa) were obtained from Hayashibara Inc. (Okayama, Japan) and Pharmacosmos (Holbaeck, Denmark), respectively. FITC-dextran (dextran labeled with fluorescein isocyanate, TdB consultancy®) was used to label the hydrogels. All other chemicals were obtained from Sigma-Aldrich® (Saint-Quentin-Fallavier, France). Caf1-YIGSR and Caf1-VEGF as freeze-dried powder were provided to us by Newcastle University (Newcastle, UK).

4.2. Hydrogel synthesis: 3D porous polysaccharide-based hydrogel with microchannel

Briefly, a solution of pullulan and dextran (75:25 *w*/*w*) and NaCl was prepared in ultrapure water. This solution is referred to as PUDNA. Then, NaOH 10M was added to the PUDNA solution to activate the hydroxyl groups before reacting with the crosslinker STMP (sodium trimetaphosphate) (3% *w*/*v*) at room temperature under magnetic stirring. The crosslinked solution was poured in between two glass slides, separated by polypropylene suture filaments ø 70 µm (6.0, Ethicon®) (Raritan, NJ, USA) and two spacers of 250 µm thickness, before crosslinking in an oven

at 50 °C for 20 min. This incubation step was carried out to facilitate the crosslinking reaction and to form microchannels within the hydrogel. Afterwards, the hydrogels were cut into discs of 5 mm in diameter using a biopsy disc-cutter from Harris Uni-Score (Sigma-Aldrich®) (**Figure 24a**).

Hydrogels were neutralized in PBS 10X and washed in distilled water until equilibrium (*ca.* 15 µS/cm). The conductivity was measured with an Orion 145 A+ conductivity meter purchased from Thermo Fisher Scientific (Asnières-sur-Seine, France). A second wash was performed in NaCl 0.025% (Sigma-Aldrich®) until equilibrium (*ca.* 500 µS/cm). Finally, the hydrogels were freeze-dried to promote pore formation.

The freeze-drying protocol consisted of three stages: freezing under atmospheric pressure from 15 °C to −20 °C at a constant rate of −0.1 °C/min, followed by a phase at constant temperature of −20 °C for 90 min. Primary drying was performed at low pressure (0.001 mbar) and −5 °C for 8 h and secondary drying at 30 °C for 1 h [26].

4.3. Hydrogel Characterization

4.3.1. SEM

The topography of freeze-dried hydrogels was observed using the JEOL JSM-IT100 system (software InTouch Scope v.1.060) under low-vacuum conditions. The SEM system was located at the Institute Jacques Monod (Paris, France).

4.3.2. Porosity

The porosity of hydrogels was determined based on a published protocol which calculates the water amount absorbed in the hydrogel before and after manual squeezing tests [44]. Experiments were performed by soaking 5 samples in PBS 1X in a 24-well cell culture plate (Corning®) (Corning, NY, USA) for 2 h under mechanical shaking. Samples were then weighed after removing the excess liquid by placing them on the plastic lid. This was considered the weight of the swollen gel (Mswollen, mg). Following this step, samples were weighed again after squeezing out the remaining liquid using tissue paper and gentle pressing using a spatula. This was considered the “squeezed” weight (Msqueezed, mg). The porosity calculated by this method corresponds to the large pores that entrap water molecules free or weakly bound to the polysaccharide matrix that are release by gentle mechanical compression. The pore volume

percentage was calculated using Equation (1). At least three scaffolds were analyzed per condition. Results were expressed as mean values ± SD.

$$\text{Volume of macropores (\%)} = \frac{(M_{swollen} - M_{squeezed})}{M_{swollen}} \times 100 \qquad (1)$$

4.3.3. Swelling Ratio

Scaffolds were weighed before (Mdry) and after (Mswollen) rehydration in PBS 1X for 48 h. The swelling ratio was determined using Equation (2). At least three scaffolds were analyzed per condition. Results were expressed as mean values ± SD.

$$\text{Swelling ratio} = \frac{(M_{swollen} - M_{dry})}{M_{dry}} \qquad (2)$$

4.3.4. Water content (WC)

The water content was calculated by using the sample weight after 48 h post-rehydration (Mswollen) and the sample weights before rehydration (Mdry). The water content was calculated using Equation (3). At least three scaffolds were analyzed per condition. Results were expressed as mean values ± SD.

$$WC = \frac{(M_{swollen} - M_{dry})}{M_{swollen}} * 100 \qquad (3)$$

4.4. Hydrogel functionalization via electrostatic interactions

4.4.1. Caf1 solution preparation

To assure cell adhesion onto the polysaccharide-based hydrogels, recombinant, engineered Caf1 proteins displaying pro-adhesive and pro-angiogenic peptide motifs were used to functionalize the hydrogels. Briefly, the sequence encoding the peptide was inserted into the *caf1* gene, present on a standard expression plasmid, and the protein was expressed and purified from an *E. coli* culture using tangential flow filtration and size exclusion chromatography [33,35].

The Caf1 proteins with cell-adhesive motifs are called Caf1-YIGSR and Caf1-VEGF. Solutions of 1.0 mg/mL (ζ = −23.6 mV for Caf1-YIGSR and ζ = −21.7 mV for Caf1-VEGF) were prepared by diluting the freeze-dried powder in miliQ water at room temperature and stored at −20

°C. These solutions were then thawed on the day of hydrogel coating and allowed to cool to room temperature, before being used.

4.4.2. Cationization of polysaccharide hydrogel

Briefly, a predetermined amount of diethylaminoethyl (DEAE)–dextran (Mw 500 kDa) from Pharmacosmos (Holbaeck, Denmark) was added into the standard hydrogel solution to obtain a solution at various concentrations: 5–20% (DD:Dex *w*/*w*; ζ = +29.5 mV) and mixed well at room temperature (RT) until fully dissolved. The hydrogel precursor solution was degassed overnight at RT and used for hydrogel synthesis the next day.

4.4.3. Spatial-controlled hydrogel coating

To facilitate electrostatic interactions, positive charges were added to the hydrogel network (by incorporation of DEAE–Dextran) to react with the negatively charged protein solution (pI = 4.46). Once the hydrogels were synthesized and rinsed thoroughly (**Section 4.1**), they were immediately coated via the syringe vacuum-induced method (**Figure S3**) (100 µL/ gel) and incubated for 2 h at RT. This coating step was performed either only before, or both before and after the freeze-drying step to coat the gel channel only (SFD coating method) or both the channel and pores (DFD coating method) (**Figure 24**).

4.5. Cell culture and cell seeding

Human umbilical vein endothelial cells (HUVECs) (ATCC-CRL-1730) purchased from ATCC® (Manassas, VA, USA) were maintained and subcultured in T75 surface-treated flasks (Corning®) in complete endothelial growth medium (EGM-2) (Lonza) following the manufacturer's recommendations. To prevent bacterial contamination, 1% antibiotic-antimyotic (AA 100X) (Gibco™) purchased from Thermo Fisher Scientific, was also added to the complete growth medium. Cells splitting was performed according to manufacturer and kept in an incubator prior to use (37 °C, 5% CO_2).

Prior to cell seeding, hydrogels were sterilized under UV light for at least 1 h. Cells were first detached with 1 mL of Trypsin solution (1X, Gibco) at 37 °C for 5 min. Trypsin was inactivated by performing cell dispersion in EGM-2, followed by centrifugation and cell counting. Cell dilution in cell culture medium was conducted to reach the desired concentration. Cell loading

was performed via the syringe vacuum-induced method to ensure cell seeding only inside the preformed microchannel. Briefly, hydrogels and cell suspension were introduced in a 10 mL syringe barrel. A 3-way stopcock was used to close the system and the plunger was pulled to make cell suspension circulate inside the channels. Then, cell-loaded hydrogels were placed in a 24 well-plate (Corning®), complete cell medium was added, and the plates were placed in an incubator.

The optimal seeding density was determined to be 5.0×10^6 cells/mL. Culture medium (EGM-2) was refreshed every 2–3 days. To facilitate cell lining of the channels, the hydrogels were turned 180° twice following the protocol described in **Figure S4**.

4.6. Cell metabolic activity

Cell metabolic activity was determined using the In Vitro Toxicology Assay Kit (Resazurin-based, TOX8-1KT, Sigma-Aldrich, France). Briefly, cells were cultured as previously described (**Section 4.5**). On day 2, 4, 7, and 10, cell medium was removed and 0.5 mL of fresh culture medium containing 10% resazurin solution was added. After 3 h of incubation (37 °C, 5% CO_2), 100 µL (in triplicates per sample) of the supernatant was transferred to a 96-well plate. Fluorescence was measured using an Infinite M200 Pro microplate reader (TECAN®) at 560Ex/590Em. All samples were analyzed in triplicate, in three different experiments. Results were expressed as mean values ± SD.

4.7. Cell staining for confocal microscopy

Cellularized hydrogels were fixed with paraformaldehyde 4% (Sigma-Aldrich®) in PBS for 1 h at 4 °C. After rinsing with PBS, membranes were permeabilized with Triton X-100 (Sigma-Aldrich®) 0.1% in PBS for 1 h at RT. Actin filaments were labeled by incubation with TRITC-conjugated phalloidin (Sigma-Aldrich®) (1/200, 1 h incubation time at RT) and nuclei were stained with DAPI (1/2000). Samples with FITC (λ_{ex} 488 nm) and cellularized samples stained with phalloidin actin marker (λ_{ex} 561 nm) and DAPI nuclear marker (λ_{ex} 405 nm) were observed using a Leica SP8 confocal microscope. Images were acquired using the LSA-X software (LAS X Core 3.7.6) and image analysis was performed with ImageJ/Fiji software (Window, version 153, Java8).

4.8. Immunofluoresence staining of the Caf1 protein polymers

In order to confirm the presence of Caf1 protein polymer functionalized on the hydrogel channel (SFD coating method), we conjugated Caf1 with fluorescent markers. Briefly, the primary antibody YPF19 (Yersinia pestis F1 antigen antibody, mouse monoclonal, GTX28275) from GeneTex (Irvine, CA, USA) was prepared in PBS (1/200) to conjugate the Caf1 presented on hydrogels. The functionalized, freeze-dried hydrogels were incubated overnight at 4 °C. After thorough washing in PBS, the samples were incubated with a secondary antibody (Alexa Fluo 647, goat anti-mouse, 1/1000) for 45 min at 37 °C. Finally, the samples were washed in PBS several times for at least 30 min. Then, the samples were observed using CLSM.

5. Conclusions

In this study, 3D porous polysaccharide-based hydrogels made of pullulan and dextran that do not promote cell adhesion, were functionalized with animal-free ECM-like molecules via electrostatic interactions promoted by the incorporation of cationized dextran (DEAE–dextran). Although the cationization resulted in slightly opaque samples, we were still able to visualize cell morphology and evaluate in vitro cellular behaviors using 3D microscopy. Our work has demonstrated that electrostatic bonding between the charged hydrogels and Caf1 molecules was stable enough to induce adequate cell adhesion and proliferation. The spatial cues on these scaffolds were controlled through a combination of hydrogel coating and a freeze-drying step. On one hand, ECs adhered and showed sprouting according to how they exposed the cell-adhesive Caf1-YIGSR. On the other hand, the VEGF-like molecule (Caf1-VEGF) functioned as a migratory factor in the presence of the adhesive moiety (Caf1-YIGSR). When ECs were exposed to both Caf1-YIGSR and Caf1-VEGF, they exhibited angiogenic behavior. These results strongly suggest that our functionalized polysaccharide-based hydrogels can provoke different EC behaviors thanks to spatially controlled presentation of these ECM-like, animal-free, pro-angiogenic molecules. Moreover, we also demonstrated that scaffold functionalization via electrostatic interactions was sufficient to promote cell adhesion and cell proliferation for a week, which allowed ECs to further differentiate into their angiogenic phenotypes when exposed properly to the different Caf1 moieties.

The novel approach described here represents an advance in the study of the effect different peptide sequences of the ECM have on ECs behavior. This work represents a proof of concept and opens the door to future studies to determine the effect of other spatial combinations using different Caf1 motifs in different cell types. The pro-angiogenic materials prepared here could be implanted in vivo for regenerative medicine applications. Furthermore, previously in the team, we have demonstrated the formation of soft tissue constructs (e.g., liver spheroids) using the non-functionalized polysaccharide hydrogels [27,45] (Le Guilcher et al. 2022 under revision). These 3D hepatic constructs showed long-term liver functions, including biliary functions, holding promise to be used as 3D models of the liver for theragnostic purposes. The developed polysaccharide hydrogels could be further optimized and integrated with the aforementioned hepatic constructs to build better organ-specific in vitro models. In the near future, we hope to contribute to the translation of vascularized constructs towards clinical applications and drug development.

Author Contributions: "Conceptualization, C.L.B and T.S-Y..; methodology, C.L.B., A.D., F.C, and T.S.-Y.; validation, T.S.-Y, F.C., H.W., D.P., and J.L.; formal analysis, C.L.B.; investigation, C.L.B.; resources, H.W., D.P., and J.L.; data curation, C.L.B.; writing—original draft preparation, C.L.B.; writing—review and editing, C.L.B. T.S.-Y., J.L. and D.P.; visualization, C.L.B.; supervision,T.S.-Y. and F.C.; project administration, T.S.-Y. and F.C.; funding acquisition, T.S.-Y. All authors have read and agreed to the published version of the manuscript."

Funding: This research was funded by "Recherche Hospitalo-universitaire" Innovations for Liver Tissue Engineering (RHU iLite, grant number ANR-16-RHUS-0005), DILI-on-chip (grant number ANR-21-CE19-0025), EXCALYBUR (grant number ANR-20-CE18-0001), and Université Paris Cité (IDEX UP AAP EMERGENCE SIMON).

Acknowledgments: This work was supported by INSERM, Université Paris Cité, and Université Sorbonne Paris Nord. The authors would like to thank Helen Waller, Daniel Peters, and Jeremy Lakey from Newcastle University for their scientific expertise and for providing us with the recombinant peptides used in this study. The authors also greatly acknowledge Samira Benadda of the CRI U1149 Imaging Facility. Figures and illustrations were created with BioRender.

Conflicts of Interest: The co-authors declare conflict of interest. Jeremy Lakey and Daniel Peters are directors at MarraBio Limited, an active company incorporated on 10 August 2022 with the

registered office located in Newcastle upon Tyne, Northumberland. The funders had no role in the design of the study; in the collection, analyses, or interpretation of data; in the writing of the manuscript; or in the decision to publish the results.

6. Supplementary Materials

6.1. Hydrogel coating via syringe vacuum-induced method

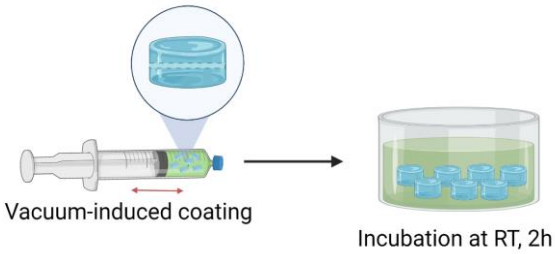

Figure S10. Scheme of syringe coating method which allows to selectively coat only the channel within the hydrogels before pore formation.

6.2. Protocol for cell seeding of microchannel within hydrogels

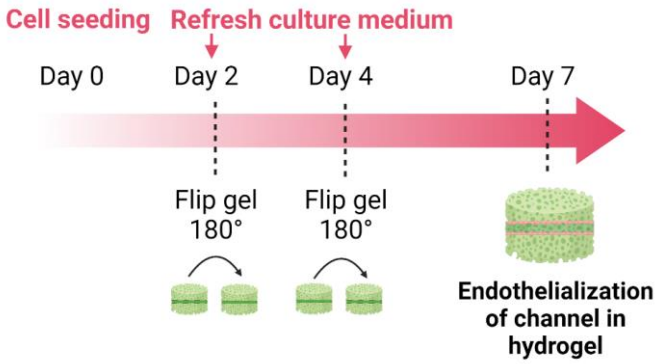

Figure S11. Cell culture protocol of 5 mm-long hydrogel channels. At day 0, endothelial cells ($5.0*10^3$ cells/µL) were seeded in the channels. Complete endothelial cell culture medium was changed 3 times at day 2, 4 and 6. Hydrogels were turned 180° at day 2 and 4.

6.3. Bulk mechanical properties

Bulk storage and loss moduli of scaffolds were measured by using the Elastosens™ Bio (Rheolution, Inc., Montreal, QC, Canada). Samples of dimension 22 mm in diameter and 2 mm in

height were prepared to fit inside the Elastosens™ Bio sample holder. Samples were tested in triplicates and results were expressed as mean values ± SD.

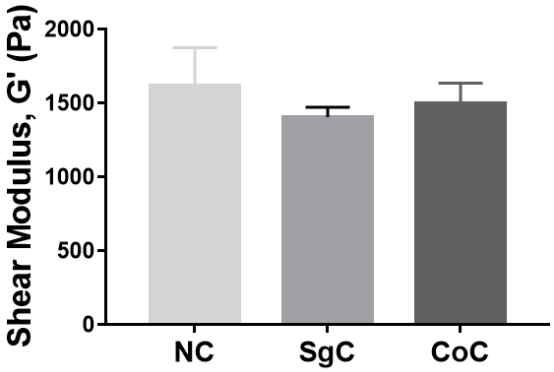

Figure S12. Shear storage modulus of non-coated hydrogels (NC) and coated hydrogels with different spatial controlled coating (SgC and CoC).

6.4. Nanoindentation mapping

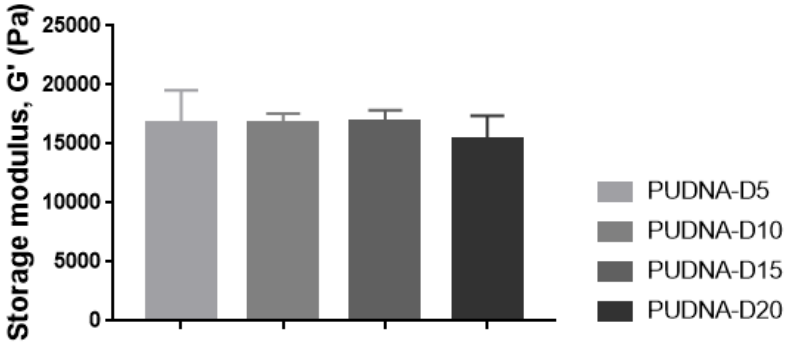

Figure S13. Young's modulus of hydrogels using nanoindentation mapping.

6.5. Immunofluorescence staining of the Caf1 protein polymers

In order to confirm the presence of Caf1 protein polymer functionalized on the hydrogel channel (SFD coating method), we conjugated Caf1 with fluorescent markers. Here, we could observe the markers of Caf1 in the channel of the hydrogel (**Figure S7**). The ablity to observe Caf1 presence on the hydrogel after 2 days of conjugation and rinsage in PBS indicates electrostatic stability. Since the criticial time for cells to adhere and to remodel the ECM remains within the first 24 hours after cell seeding, we did not pursue further observation of the functionalized molecules. Plus, this would require multiple colors in the immunofluorescence protocol, which will further complicate microscopy observation given the sample thickness, opacity, and presence of cells.

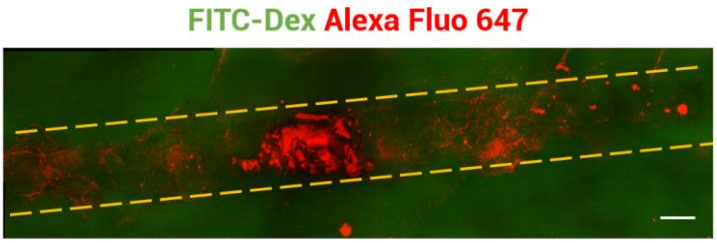

Figure S14. Presence of Caf1-YIGSR on SFD coated hydrogel without cells. Scale bar = 100 µm.

References

1. Williams, D.F. Challenges with the Development of Biomaterials for Sustainable Tissue Engineering. *Front. Bioeng. Biotechnol.* **2019**, *7*, 1–10. https://doi.org/10.3389/fbioe.2019.00127.

2. Dellaquila, A.; Le Bao, C.; Letourneur, D.; Simon-Yarza, T. In Vitro Strategies to Vascularize 3D Physiologically Relevant Models. *Adv. Sci.* **2021**, *8*, 2100798. https://doi.org/10.1002/advs.202100798.

3. Mastrullo, V.; Cathery, W.; Velliou, E.; Madeddu, P.; Campagnolo, P. Angiogenesis in Tissue Engineering: As Nature Intended? *Front. Bioeng. Biotechnol.* **2020**, *8*, 1–13. https://doi.org/10.3389/fbioe.2020.00188.

4. Gerhardt, H.; Golding, M.; Fruttiger, M.; Ruhrberg, C.; Lundkvist, A.; Abramsson, A.; Jeltsch, M.; Mitchell, C.; Alitalo, K.; Shima, D.; et al. VEGF guides angiogenic sprouting utilizing endothelial tip cell filopodia. *J. Cell Biol.* **2003**, *161*, 1163–1177. https://doi.org/10.1083/jcb.200302047.

5. Michaelis, U.R. Mechanisms of endothelial cell migration. *Cell. Mol. Life Sci.* **2014**, *71*, 4131–4148. https://doi.org/10.1007/s00018-014-1678-0.

6. Cathery, W.; Faulkner, A.; Maselli, D.; Madeddu, P. Concise Review: The Regenerative Journey of Pericytes Toward Clinical Translation. *Stem Cells* **2018**, *36*, 1295–1310. https://doi.org/10.1002/stem.2846.

7. Yue, Biology of the Extracellular Matrix: An Overview Beatri. *J. Glaucoma* **2014**, *23*, 1–7. https://doi.org/10.1097/IJG.0000000000000108.Biology.

8. Yin, N.; Han, Y.; Xu, H.; Gao, Y.; Yi, T.; Yao, J.; Dong, L.; Cheng, D.; Chen, Z. VEGF-conjugated alginate hydrogel prompt angiogenesis and improve pancreatic islet engraftment and function in type 1 diabetes. *Mater. Sci. Eng. C* **2016**, *59*, 958–964. https://doi.org/10.1016/j.msec.2015.11.009.

9. Linville, R.M.; Boland, N.F.; Covarrubias, G.; Price, G.M.; Tien, J. Physical and Chemical Signals That Promote Vascularization of Capillary-Scale Channels. *Cell Mol. Bioeng.* **2016**, *9*, 73–84. https://doi.org/10.1007/s12195-016-0429-8.

10. Tseng, T.C.; Hsieh, F.Y.; Theato, P.; Wei, Y.; Hsu, S.H. Glucose-sensitive self-healing hydrogel as sacrificial materials to fabricate vascularized constructs. *Biomaterials* **2017**, *133*, 20–28. https://doi.org/10.1016/j.biomaterials.2017.04.008.

11. Pan, B.; Shao, L.; Jiang, J.; Zou, S.; Kong, H.; Hou, R.; Yao, Y.; Du, J.; Jin, Y. 3D printing sacrificial templates for manufacturing hydrogel constructs with channel networks. *Mater. Des.* **2022**, *222*, 111012. https://doi.org/10.1016/j.matdes.2022.111012.

12. Mohanty, S.; Larsen, L.B.; Trifol, J.; Szabo, P.; Burri, H.V.R.; Canali, C.; Dufva, M.; Emnéus, J.; Wolff, A. Fabrication of scalable and structured tissue engineering scaffolds using water dissolvable sacrificial 3D printed moulds. *Mater. Sci. Eng. C* **2015**, *55*, 569–578. https://doi.org/10.1016/j.msec.2015.06.002.

13. Pimentel, C.R.; Ko, S.K.; Caviglia, C.; Wolff, A.; Emnéus, J.; Keller, S.S.; Dufva, M. Three-dimensional fabrication of thick and densely populated soft constructs with complex and actively perfused channel network. *Acta Biomater.* **2018**, *65*, 174–184. https://doi.org/10.1016/j.actbio.2017.10.047.

14. Rocha, L.A.; Sousa, R.A.; Learmonth, D.A.; Salgado, A.J. The role of biomaterials as angiogenic modulators of spinal cord injury: Mimetics of the spinal cord, cell and angiogenic factor delivery agents. *Front. Pharmacol.* **2018**, *9*, 1–7. https://doi.org/10.3389/fphar.2018.00164.

15. Belair, D.G.; Miller, M.J.; Wang, S.; Darjatmoko, S.R.; Binder, B.Y.; Sheibani, N.; Murphy, W.L. Differential regulation of angiogenesis using degradable VEGF binding microspheres. *Biomaterials* **2016**, *93*, 27–37. https://doi.org/10.1016/j.biomaterials.2016.03.021.

16. Chiu, L.L.Y.; Radisic, M. Scaffolds with covalently immobilized VEGF and Angiopoietin-1 for vascularization of engineered tissues. *Biomaterials* **2010**, *31*, 226–241. https://doi.org/10.1016/j.biomaterials.2009.09.039.

17. Kuttappan, S.; Mathew, D.; Jo, J.; Tanaka, R.; Menon, D.; Ishimoto, T.; Nakano, T.; Nair, S.V.; Nair, M.B.; Tabata, Y. Dual release of growth factor from nanocomposite fibrous scaffold promotes vascularisation and bone regeneration in rat critical sized calvarial defect. *Acta Biomater.* **2018**, *78*, 36–47. https://doi.org/10.1016/j.actbio.2018.07.050.

18. Fittkau, M.H.; Zilla, P.; Bezuidenhout, D.; Lutolf, M.P.; Human, P.; Hubbell, J.A.; Davies, N. The selective modulation of endothelial cell mobility on RGD peptide containing surfaces by YIGSR peptides. *Biomaterials* **2005**, *26*, 167–174. https://doi.org/10.1016/j.biomaterials.2004.02.012.

19. Alsop, A.T.; Pence, J.C.; Weisgerber, D.W.; Harley, B.A.C.; Bailey, R.C. Photopatterning of vascular endothelial growth factor within collagen-glycosaminoglycan scaffolds can induce a spatially confined response in human umbilical vein endothelial cells. *Acta Biomater.* **2014**, *10*, 4715–4722. https://doi.org/10.1016/j.actbio.2014.07.002.

20. Rich, M.H.; Lee, M.K.; Baek, K.; Jeong, J.H.; Kim, D.H.; Millet, L.J.; Bashir, R.; Kong, H. Material-mediated proangiogenic factor release pattern modulates quality of regenerated blood vessels. *J. Control. Release* **2014**, *196*, 363–369. https://doi.org/10.1016/j.jconrel.2014.10.020.

21. Chiu, Y.C.; Cheng, M.H.; Engel, H.; Kao, S.W.; Larson, J.C.; Gupta, S.; Brey, E.M. The role of pore size on vascularization and tissue remodeling in PEG hydrogels. *Biomaterials* **2011**, *32*, 6045–6051. https://doi.org/10.1016/j.biomaterials.2011.04.066.

22. Wang, Y.; Kankala, R.K.; Ou, C.; Chen, A.; Yang, Z. Advances in hydrogel-based vascularized tissues for tissue repair and drug screening. *Bioact. Mater.* **2022**, *9*, 198–220. https://doi.org/10.1016/j.bioactmat.2021.07.005.

23. Kang, Y.; Chang, J. Channels in a porous scaffold : A new player for vascularization. *Regen. Med.* **2018**, *13*, 705–715.

24. Wang, X.; Nie, Z.; Chang, J.; Lu, M.L.; Kang, Y. Multiple channels with interconnected pores in a bioceramic scaffold promote bone tissue formation. *Sci. Rep.* **2021**, *11*, 20447. https://doi.org/10.1038/s41598-021-00024-z.

25. Lanouar, S.; Aid-Launais, R.; Oliveira, A.; Bidault, L.; Closs, B.; Labour, M.N.; Letourneur, D. Effect of cross-linking on the physicochemical and in vitro properties of pullulan/dextran microbeads. *J. Mater. Sci. Mater. Med.* **2018**, *29*, 1–9. https://doi.org/10.1007/s10856-018-6085-x.

26. Grenier, J.; Duval, H.; Barou, F.; Lv, P.; David, B.; Letourneur, D. Acta Biomaterialia Mechanisms of pore formation in hydrogel scaffolds textured by freeze-drying. *Acta Biomater.* **2019**, *94*, 195–203. https://doi.org/10.1016/j.actbio.2019.05.070.

27. Labour, M.N.; Le Guilcher, C.; Aid-Launais, R.; Samad, N.E.; Lanouar, S.; Simon-Yarza, T.; Letourneur, D. Development of 3D hepatic constructs within polysaccharide-based scaffolds with tunable properties. *Int. J. Mol. Sci.* **2020**, *21*, 3644. https://doi.org/10.3390/ijms21103644.

28. Simon-Yarza, T.; Labour, M.N.; Aid, R.; Letourneur, D. Channeled polysaccharide-based hydrogel reveals influence of curvature to guide endothelial cell arrangement in vessel-like structures. *Mater. Sci. Eng. C* **2021**, *118*, 111369. https://doi.org/10.1016/j.msec.2020.111369.

29. Autissier, A.; Le Visage, C.; Pouzet, C.; Chaubet, F.; Letourneur, D. Fabrication of porous polysaccharide-based scaffolds using a combined freeze-drying/cross-linking process. *Acta Biomater.* **2010**, *6*, 3640–3648. https://doi.org/10.1016/j.actbio.2010.03.004.

30. Le Visage, C.; Letourneur, D.; Chaubet, F.; Autissier, A. Method for Preparing Porous Scaffold for Tissue Engineering. U.S. Patent, US9028857B2, 12 May, 2015.

31. Autissier, A.; Letourneur, D.; Le Visage, C. Pullulan-based hydrogel for smooth muscle cell culture. *J. Biomed. Mater. Res. Part A* **2007**, *82*, 336–342. https://doi.org/10.1002/jbm.a.30998.

32. Lanouar, S. *Conception and Validation of New Tridimensional Porous Matrices for Cutaneous Wound Healing and Regeneration*; Université Sorbonne Paris Nord, Paris, France, 2020.

33. Roque, A.I.; Soliakov, A.; Birch, M.A.; Philips, S.R.; Shah, D.S.H.; Lakey, J.H. Reversible non-stick behaviour of a bacterial protein polymer provides a tuneable molecular mimic for cell and tissue engineering. *Adv. Mater.* **2014**, *26*, 2704–2709. https://doi.org/10.1002/adma.201304645.

34. Dura, G.; Crespo-Cuadrado, M.; Waller, H.; Peters, D.T.; Ferreira, A.M.; Lakey, J.H.; Fulton, D.A. Hydrogels of engineered bacterial fimbriae can finely tune 2D human cell culture. *Biomater. Sci.* **2021**, *9*, 2542–2552. https://doi.org/10.1039/d0bm01966f.

35. Peters, D.T.; Waller, H.; Birch, M.A.; Lakey, J.H. Engineered mosaic protein polymers; A simple route to multifunctional biomaterials. *J. Biol. Eng.* **2019**, *13*, 1–14. https://doi.org/10.1186/s13036-019-0183-2.

36. Lack, S.; Dulong, V.; Picton, L.; Cerf, D.L.; Condamine, E. High-resolution nuclear magnetic resonance spectroscopy studies of polysaccharides crosslinked by sodium trimetaphosphate: A proposal for the reaction mechanism. *Carbohydr. Res.* **2007**, *342*, 943–953. https://doi.org/10.1016/j.carres.2007.01.011.

37. Pietrzyk-Nivau, A.; Poirault-Chassac, S.; Gandrille, S.; Derkaoui, S.M.; Kauskot, A.; Letourneur, D.; Le Visage, C.; Baruch, D.; Eaves, C.J. Three-dimensional environment sustains hematopoietic stem cell differentiation into platelet-producing megakaryocytes. *PLoS ONE* **2015**, *10*, 1–19. https://doi.org/10.1371/journal.pone.0136652.

38. Purnama, A.; Aid-Launais, R.; Haddad, O.; Maire, M.; Mantovani, D.; Letourneur, D.; Hlawaty, H.; Le Visage, C. Fucoidan in a 3D scaffold interacts with vascular endothelial growth factor and promotes neovascularization in mice. *Drug Deliv. Transl. Res.* **2015**, *5*, 187–197. https://doi.org/10.1007/s13346-013-0177-4.

39. Jeon, O.; Alsberg, E. Photofunctionalization of alginate hydrogels to promote adhesion and proliferation of human mesenchymal stem cells. *Tissue Eng. Part A* **2013**, *19*, 1424–1432. https://doi.org/10.1089/ten.tea.2012.0581.

40. Akhmanova, M.; Osidak, E.; Domogatsky, S.; Rodin, S.; Domogatskaya, A. Physical, Spatial, and Molecular Aspects of Extracellular Matrix of in Vivo Niches and Artificial Scaffolds Relevant to Stem Cells Research. *Stem Cells Int.* **2015**, *2015*, 167025. https://doi.org/10.1155/2015/167025.

41. González-pérez, F.; Alonso, M.; Torre, I.G.D.; Santos, M.; Rodríguez-cabello, J.C. Laminin-Derived Peptide Sequences within Elastin-Like Recombinamer Scaffolds Provide Spatiotemporally Synchronized Guidance of Angiogenesis and Neurogenesis. *Adv. Healthc. Mater.* **2022**, *11*, 2201646. https://doi.org/10.1002/adhm.202201646.

42. Ali, S.; Saik, J.E.; Gould, D.J.; Dickinson, M.E.; West, J.L. Immobilization of Cell-Adhesive Laminin Peptides in Degradable PEGDA Hydrogels Influences Endothelial Cell Tubulogenesis. *Biores. Open Access* **2013**, *2*, 241–249. https://doi.org/10.1089/biores.2013.0021.

43. Grant, D.S.; Tashiro, K.I.; Segui-Real, B.; Yamada, Y.; Martin, G.R.; Kleinman, H.K. Two different laminin domains mediate the differentiation of human endothelial cells into capillary-like structures in vitro. *Cell* **1989**, *58*, 933–943. https://doi.org/10.1016/0092-8674(89)90945-8.

44. Campodoni, E.; Montanari, M.; Dozio, S.M.; Heggset, E.B.; Panseri, S.; Montesi, M.; Tampieri, A.; Syverud, K.; Sandri, M. Blending Gelatin and Cellulose Nanofibrils : Biocomposites with Tunable Degradability and Mechanical Behavior. *Nanomaterials* **2020**, *10*, 1219.

45. Le Guilcher, C.; Franck, G.; Dellaquila, A.; Labour, M.-N.; Aid, R.; Tordjmann, T.; Letourneur, D.; Simon-Yarza, T. Engineered Human Liver Based on Pullulan-Dextran Hydrogel Promotes Mice Survival after Liver Failure. 2022.

3. EXPERIMENTAL WORK (PART 3)

3. EXPERIMENTAL WORK (PART 3)

3.3. DEVELOPMENT OF A POLYSACCHARIDE-BASED HYDROGEL FOR MICROFLUIDIC APPLICATIONS

1. Introduction

Microfluidics is a newly emerged field which has evolved from the convergence of principles and technologies from pre-existing domains such as physics, biology, chemistry, fluid dynamics, microelectronics, and materials science [1,2]. Microfluidic chips are mainly miniaturized chips containing microchannels with dimensions of tens to hundreds of micrometers, connected in a specific design to achieve a set of defined functions [1,3]. These microscale devices are practical to conduct chemical and/or biological operations such as reactions, separations, or the detection of various compounds [4]. The interdisciplinary aspect of microfluidics makes it a useful platform to build physiologically relevant, 3D in vitro models for disease modeling, drug discovery and development, and personalized medicine strategies [5]. For biomedical applications, working with microfluidic devices presents several advantages including small sample and reagent volume requirements, potential for efficient mass transport to functionalized surfaces, ease of automation, low-cost, and disposability [1]. This is why microfluidic chips are often referred to as lab-on-a-chip, or organ-on-a-chip. Lab-on-chip devices enable integration of one or several functions that would normally require an entire laboratory. These includes microfluidic-based sensors and microreactors utilized as novel methods for nanoparticles synthesis [6,7]. Organ-on-chip devices are microphysiological systems that aim to recapitulate the organ-specific microenvironment of the organ of interest [5].

Generally, microfluidic systems consist of: microfluidic chip, reservoirs, flow controllers, and tubing. Microfluidic experiments are performed on the chip. Reservoirs are generally small laboratory tubes containing reagents and buffers for the experiment. Flow controllers, often pressure-based, allow the injection of fluid from the reservoirs to the microfluidic chip. Tubing connects all the other components together. A microscope is often included to performed live-analysis of microfluidic experiments (e.g. flow experiment, cell culture) Additionally, accessories (e.g. valves, pumps, flow sensors) are also used. Automation of the system is enabled by the use of a software and a computer [1].

Despite their promise as lab-on-chip devices, in reality, working with microfluidic systems is more like 'lab-around-a-chip' due to several operational challenges. To build a complete and functional microfluidic platform, it often requires: 1) expensive tool for fabrication; 2) multistep production; 3) complex peripheral equipment (i.e. flow controller, external pumps); 4) use of non-biomimetic polymers [1,5,8]. Together, these operational challenges further limit the potential of microfluidic devices in point-of-care settings [8].

When working with microfluidics, we are working in a microscale environment, where physical properties such as fluid mechanics are much more amplified. In particular, small dimensions and volumes used in microfluidics lead to specific phenomena of fluid mechanics. For example, laminar flow and hydrodynamic resistance are two dominating fluid mechanics principles should be considered while performing microfluidic experiments [9]. In addition, the wettability and contact angles of an aqueous solution on the chip's surface, capillary pressure, flow rate in a microchannel are also fundamental concepts and parameters that underpin microfluidic operations [10]. Therefore, the material used to fabricate the microfluidic chip will influence microfluidic properties as well as microfluidic applications [3].

A large range production methods and materials exist for microfluidic fabrication. Microfabrication techniques such as photolithography, thermomolding, casting, 3D printing, photopolymerization, and photolithography are often employed to produce microfluidic devices [1]. Each fabrication material corresponds with specific physical properties and microfabrication strategies [3]. In addition, the chip design must also be adapted to the desired material properties (e.g. biocompatibility, rigidity, sterile environment, optical transparency, surface treatment, fast prototyping) and the type of use (e.g. research vs. commercial applications) [9]. Other important properties that must be carefully evaluated when selecting a material are: ease of fabrication, durability, chemical compatibility with reagents, biocompatibility, transparency for microscopy observation, and surface functionalization capability [2].

One fundamental element of microfluidic applications is to select the optimal material for device fabrication. A plethora of materials attempts to match these properties could be used to manufacture microfluidic devices. Typically, these include glass, silicon, metals, polymers, and

ceramics. Depending on their destination use, each material has its own advantages and disadvantages [2,3,11].

Glass is chemically inert, electrically insulating, thermally stable, biocompatible, and is easy to perform surface modification [11,12]. These properties make glass suitable as microreactors to perform chemical reactions that often require extreme conditions (e.g. high temperatures, high pressures, and aggressive solvents) [11]. Thanks to its high resolution at the microscale, glass makes superior microcapillary reactors for synthesis of emulsions and polymeric nanoparticles [13]. Glass offers excellent optical transparency for microscopy observation for evaluations of diffusion and flow experiments, and evaluations of cell morphology and behavior during cell culture. Additionally, glass rigidity renders it facile to integrate with valves and pumps made of other materials (e.g. silicon, polymer). The most common glass compositions include soda-lime glass, borosilicate glass, and fused quartz [11]. Nonetheless, manufacturing of glass-based microfluidic devices can be quite expensive, time consuming, and requires preparation in cleanrooms [11].

In contrast to the high-cost manufacturing of glass, metals are cheap and easily accessible. Metals can withstand high heat load, high pressure, and toxic chemicals (except for strong acids). Its robustness allows easy cleaning protocol. The most commonly used metals for microfluidic fabrication includes aluminum, copper, and iron [14]. However, they are often used as alloys with other metals to fine-tune their chemical resistances [14]. Metal-based microfluidic devices are utilized for nanomaterial synthesis [13].

Ceramics have good resistance to corrosive chemicals and excellent thermal stability. However, their high brittleness, high porosity, and limited in dimensional stability make ceramics a less ideal substrate to integrate into a complete microfluidic platform [11,13].

Silicons are known for its readily availability, chemical compatibility, thermostability, ease of fabrication, design flexibility, semiconducting properties, and possibility of surface modifications. These properties make silicons a dominant choice for microfluidic fabrication [11]. However, there are several drawbacks with most silicons for microfluidic fabrication. Due to its opacity, they are often incompatible for optical detection. Many of them are fragile, due to their high modulus, making it difficult to integrate external pumps and valves [11]. However, one of the most representative materials of polymers for microfluidic manufacturing belongs to the family of

silicons: polydimethylsiloxane (PDMS). As an elastomer, PDMS offers excellent microchip fabrication properties: easy to mold, good for prototyping, and low cost [11]. Other advantages of PDMS include optical transparency, low auto-fluorescence, hydrophobicity, high elasticity, gas permeability, and biocompatibility [2,3,11]. Owing to these properties, PDMS-based microfluidics are highly valuable for biomedical research, including long-term cell culture experiments, cell screening, and biochemical assays [3]. The porosity of PDMS renders it an adsorptive substrate, through which many molecules can diffuse. These properties make PDMS incompatible with organic solvents (e.g. hexane, toluene, and chloroform) as their molecules can be adsorbed into the channel walls, thus, swell the platform [2,3,11]. Another issue that could arise is water evaporation through the channel walls, which changes the solution concentration [3]. For biomimetic use, such as in organ-on-chip devices, an important drawback of PDMS derives from its very high ridigity that poses a problem to create physiologically relevant and organ-specific models, specifically in the case of soft tissues and organs. The average stiffness of PDMS ranges from 100 kPa to 3MPa depending on the composition [15], whereas the average stiffness of soft organs such as the liver ranges between 2 and 6 KPa [16]. To overcome these problems, other polymeric materials have been investigated as an alternative material for microfluidic fabrication.

Hydrogels represents a class of materials that offers promising potential in tissue engineering applications such as 3D cell culture, cell encapsulation, drug delivery, biosensors, and actuators [3]. As already mentioned in previous chapters, they are known for their biocompatibility, low cytotoxicity, tunable biodegradability and porosity. Their 3D aqueous nature enables mimicking the natural mechanical and structural cues of the ECM, which are important criteria to guide proper cell adhesion, proliferation, and differentiation. Hydrogels facilitate diffusion of small molecules and particles. These properties render hydrogels an excellent alternative to PDMS substrate. The ability to fine tune stiffness and degradability makes hydrogels good candidate materials in building some compartments of the microfluidic chips. As promising as this may sound, the challenges to entirely replace PDMS using hydrogels for microfluidic fabrication remain numerous. Compared to PDMS, hydrogels have much lower viscoelastic moduli, which presents several operational challenges (e.g. maintain the device integrity, integrate with peripheral components like flow controllers, connecting of tubing), limiting their use in the long term [3].

Over the past decades, microfluidic-based vascular models have been developed by incorporating endothelial cells and parenchymal cells in organ-specific vascular platforms [5]. In the context of creating a more physiological relevant hydrogel that can replace PDMS in microfluidic chips, several attempts have been investigated. In general, the PDMS substrate is partially or entirely replaced with a hydrogel having stiffness closer to the native ECM. These strategies aim to promote better cell adhesion, proliferation, and differentiation inside the microfluidic chip. There are two main methods: 1) coating the microchannel of the PDMS chip with hydrogels; 2) incorporating hydrogels as an additional compartment inside the chip. In general, the gel can be natural or synthetic functionalized with ECM proteins (e.g. fibrin, gelatin, and collagen) and endothelial cells are either seeded after gel loading or suspended into the hydrogel prior to seeding [17–19]. In the method reported by Chen et al. HUVECs and fibroblasts were suspended in fibrin gels and injected into parallel microchannels of a standard PDMS chip [18]. After gel polymerization, cell culture media filled the microchannel and the perfusion was carried out to promote lumen formation. Upon 5 days in culture, self-organized microvascular networks and lumen formation were observed [18]. More recently, a synthetic hydrogel with fine-tuned adhesiveness and degradability was developed and incorporated as a cell-supportive compartment next to a parent channel seeded with HUVECs and a neighboring channel filled with growth factors that simulate angiogenic sprouting [17]. The channel seeded with endothelial cells was simply coated with gelatin and the PDMS chip was unmodified.

Previously, in our team, we have demonstrated the ability to form soft tissue constructs, in particular liver tissue, using polysaccharide hydrogels composed of pharmaceutical-grade pullulan and dextran [20,21] (Le Guilcher et al. 2022, under revision). These 3D hepatic constructs showed long-term liver functions, including biliary functions, holding promise to be used as 3D models of the liver for theranostic purposes. An important improvement for liver-on-chip development would be the incorporation of the vascular compartment. In this thesis, we have proved the potential of using pullulan-dextran hydrogels as pro-angiogenic substrates that could guide endothelial sprouting and migration (**Chapter 3.2**). As a stretch goal, the work in this chapter aimed to develop a hydrogel-based substrate to be integrated into a microfluidic chip as a vascularization strategy for liver-on-chip.

In this chapter, the development of a polysaccharide hydrogel integrated in microfluidic platforms for angiogenesis promotion is summarized. Three main strategies with preliminary results are presented: 1) Development of an injectable hydrogel as cell culture matrix for microfluidic devices (**Figure 33**); 2) Development of a polysaccharide hydrogel as microfluidic device (**Figure 34**); 3) Development of a photocrosslinked hydrogel as microfluidic device (**Figure 35**).

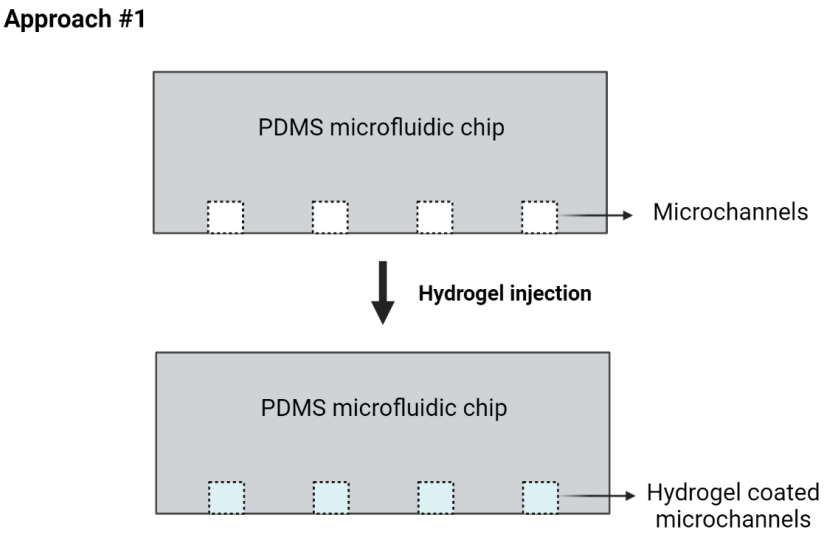

Figure 33. Scheme of approach #1: Development of an injectable hydrogel as cell culture matrix for microfluidic devices. Created with Biorender.com

Approach #2

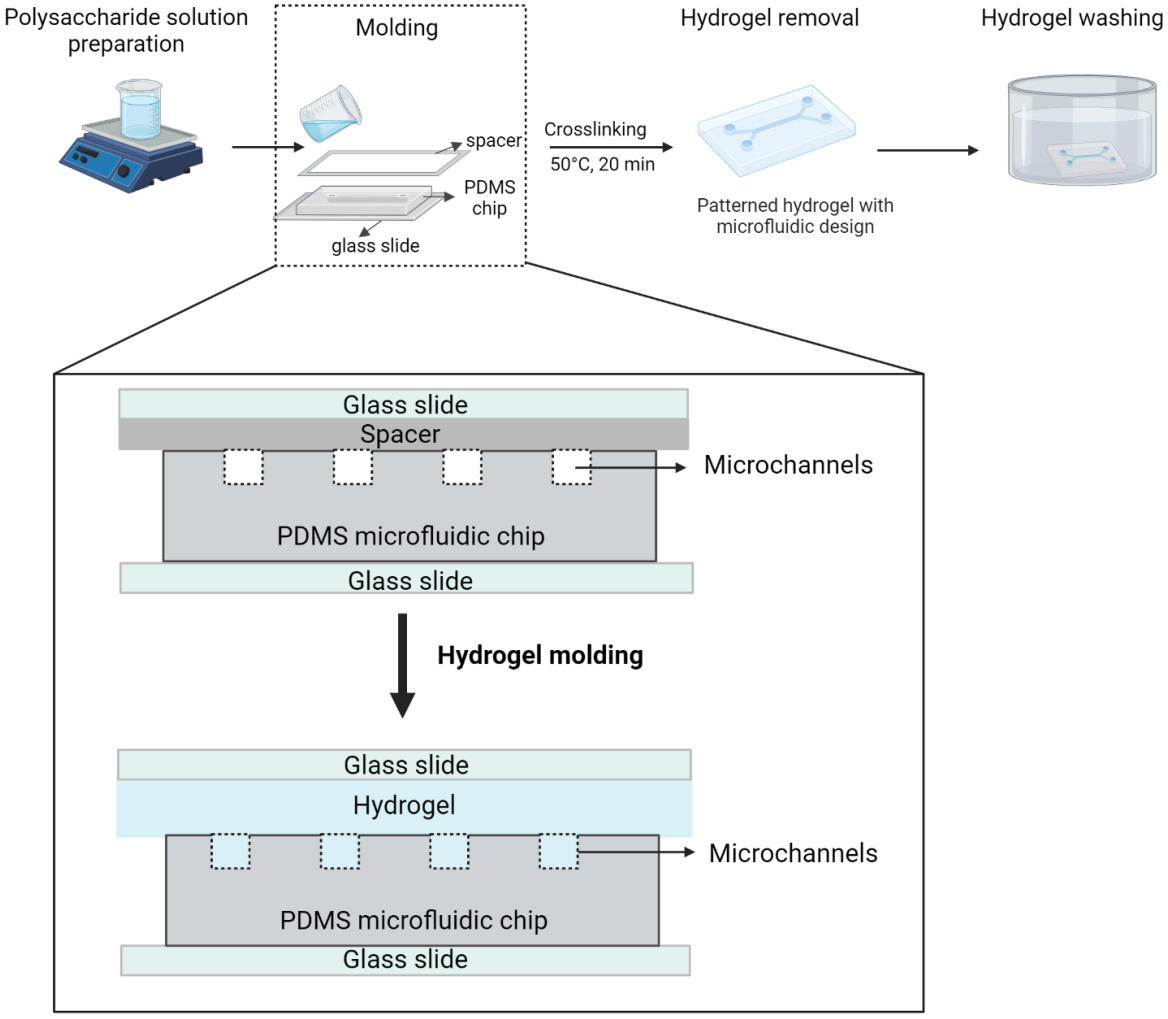

Figure 34. Scheme of approach #2: Development of a polysaccharide hydrogel as microfluidic device. Created with Biorender.com

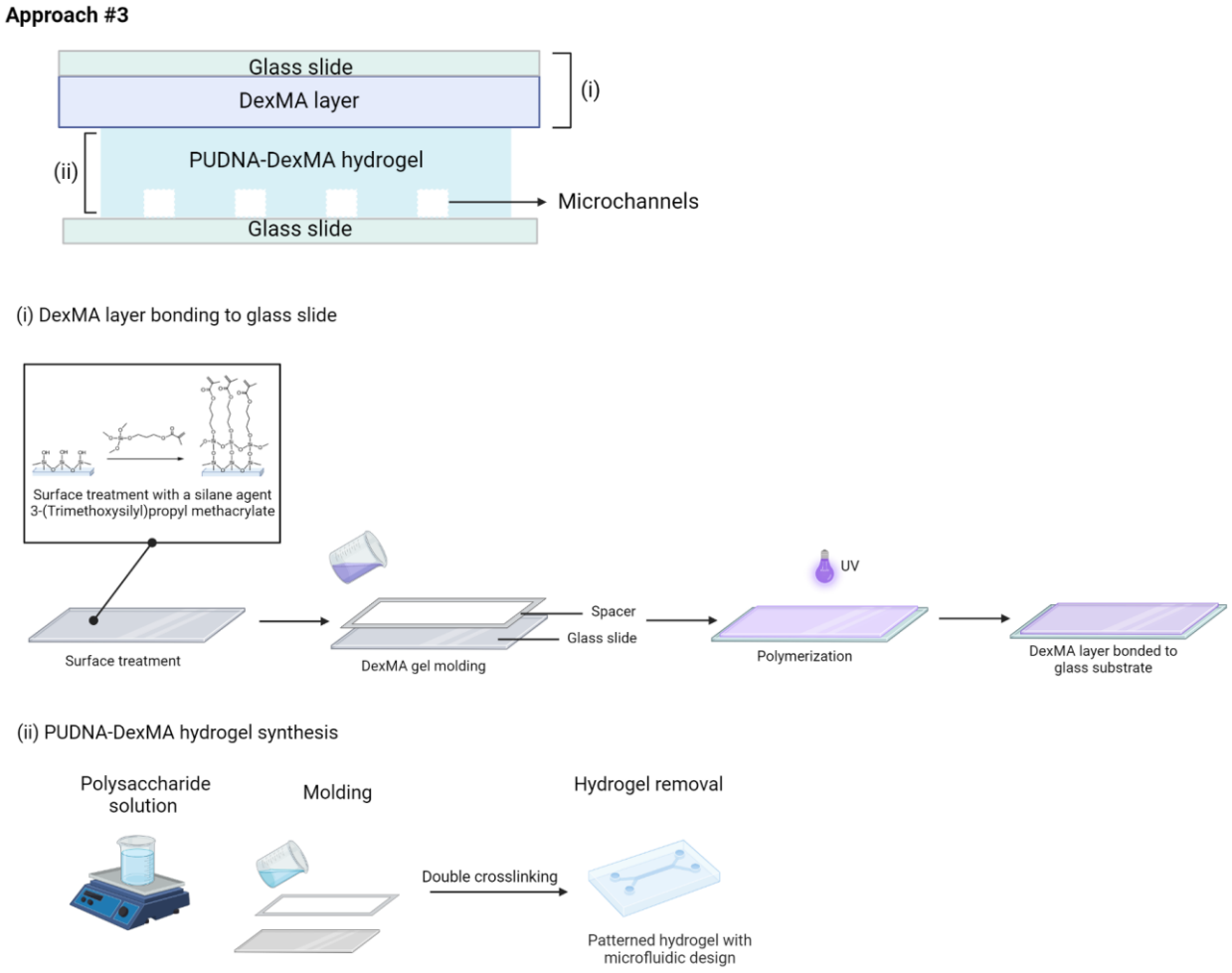

Figure 35. Scheme of approach #3: Development of a photocrosslinked hydrogel as microfluidic device. Figure created with Biorender.com.

2. Materials and Methods

2.1. Materials and equipment

Pullulan (Mw 200 kDa) was purchased from Hayashibara Inc, Okayama, Japan. Dextran70 and dextran of various molecular weights (Mw 70 kDa and Mw 500 kDa) were obtained from Pharmacosmos (Holbaek, Denmark). FITC-dextran (dextran labeled with fluorescein isocyanate) from TdB consultancy® was used to label the hydrogels. Dextran-methacrylate (Mw 35-50 kDa, DS: 45-65%), and Irgacure 2959 were purchased from Advanced Biomatrix (U.S.A). All other chemicals were obtained from Sigma-Adrich®. Polydimethylsiloxane (PDMS) microfluidic chips were fabricated and provided by our collaborator from the LUMIN laboratory (Laboratoire Lumière, Matière et Interfaces) at École National Supérieure Paris-Saclay (France).

2.2. Pressure-based flow control for hydrogel loading

Flow-controlled loading was performed by using a pressure-based microfluidic flow controller (microfluidic flow control system, MFCS™) (Fluigent, France). Polypropylene tubes and appropriate fittings were used to deliver the hydrogel solution. A 2-ml Eppendorf vial was used as reservoir for the gel solution. The pressure-based flow was controlled by Fluigent software. Air pressure of 3 mbar to 80 mbar was utilized to induce flow of hydrogel solution into the tubing and to deliver hydrogel solution into the microchannel of the PDMS chip.

Four different polysaccharide solution compositions with different swelling behavior were investigated: PUD, PUDNA, PUD70, and PUD70. Solutions without NaCl were PUD and PUD70 (for dextran 70 kDa). Solutions with NaCl were PUDNA and PUD70NA. Briefly, pullulan and dextran (75:25 w/w) and NaCl (0.35g/mL) were dissolved in miliQ water and placed in an ice bath. Then STMP 3% (w/v) solution was then added under alkaline condition obtained by the addition of NaOH 10M solution into the polysaccharide mixture. The crosslinking reaction was carried out at cold temperature in order to slow down the crosslinking of the polymer chain, which would allow enough time for the hydrogel solution to be delivered into the targeted microfluidic channel. As soon as STMP was added, the hydrogel solution was transferred to a reservoir (2-mL Eppendorf vial). Finally, loading of the hydrogel was carried out by varying the pressure from the flow controller. Live analysis of solution flow into the microfluidic chip was observed via an inverted microscope (Nikon® Eclipse Ti2). Image acquisition was conducted by Image Software NIS-Elements (Nikon®).

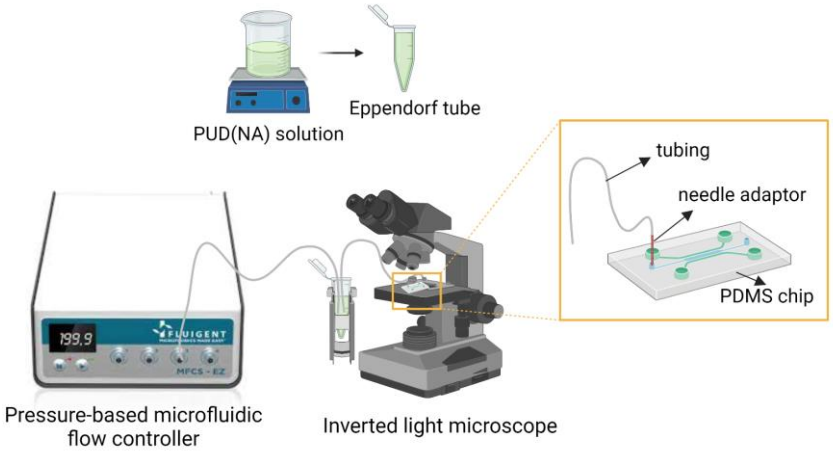

Figure 36. Scheme of hydrogel loading via a microfluidic flow control system. Figure created with Biorender.com

2.3. Real-time crosslinking kinetics study of PUD/PUDNA hydrogels

Hydrogel crosslinking kinetics was evaluated using a contact-free viscoelasticity measurement device (ElastoSens™ Bio, Rheolution). During gel formation, the evolution of the shear elastic modulus (G') of hydrogels was measured with the ElastoSens™ Bio. Briefly, the PUD or PUDNA solution was prepared and crosslinked as described (**Section 2.2**). Once STMP was added to the PUD/PUDNA solution, the hydrogel was transferred immediately into a sample holder of the ElastoSens™ Bio. All measurements were conducted over time at 37 ºC. Crosslinking time of each sample was determined based on the time the shear modulus reached a plateau (**Figure 37**).

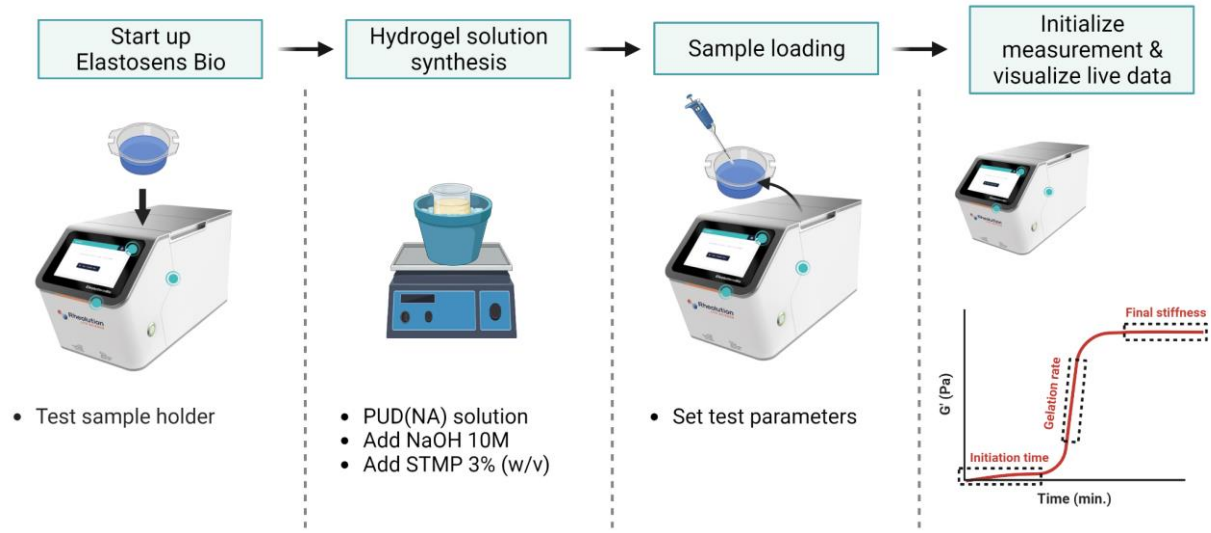

Figure 37. Protocol for real-time crosslinking analysis with ElastoSens™ Bio. Figure created with Biorender.com.

2.4. Direct molding to create PUDNA hydrogels with microfluidic patterns

PDMS microfluidic chip with hepatic lobule design (**Figure 38**) was used as a template for hydrogel molding. The PUDNA solution was prepared follows: aqueous solution of pullulan:dextran 75:25 (w/w), 0.3 g/mL) containing NaCl (0.35 g/mL), reacted with sodium trimetaphosphate (STMP) (0.3 g/mL) under alkaline conditions (after addition of NaOH 10M). The molding setup was prepared as followed: PDMS microfluidic chip was placed on top of a glass slide. Then a silicon spacer of 1.0 mm thickness (with dimensions matching that of the glass slide)

was placed on the PDMS chip to control the thickness of the hydrogel. Once the crosslinker STMP solution was added, the hydrogel solution was rapidly casted (**Figure 34**) and placed in the oven at 50 ºC for 20 minutes. The patterned hydrogel was then washed thoroughly with PBS 10X, PBS 1X, and NaCl 0.025% (w/v). Peeling of the patterned hydrogel was done during the first bath in PBS 10X.

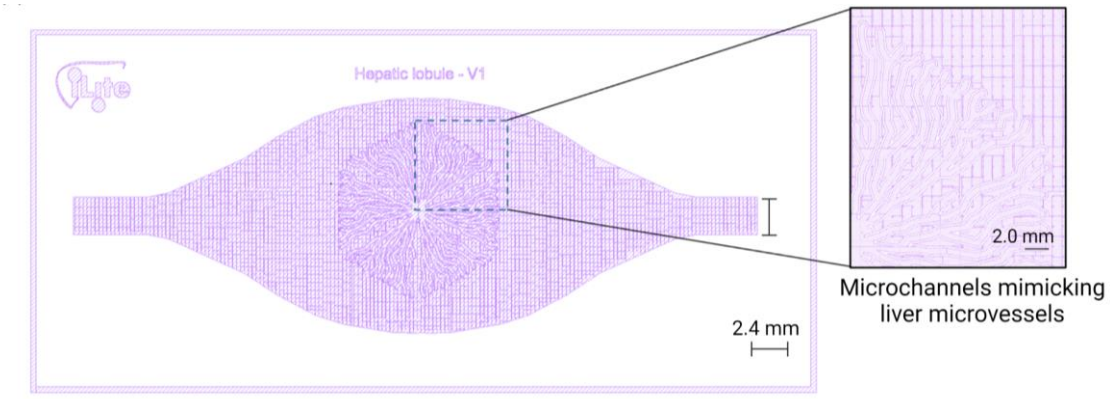

Figure 38. 3D design of the microfluidic pattern used for approach #2

2.5. Fluid flow experiment (gravity-driven perfusion)

The patterned hydrogel was turned over so that the patterned side was in contact with the glass slide. Then a small volume of commercial cyanoacrylate was placed on the four corners of the hydrogel-based microfluidic chip to facilitate adhesion of the chip onto the glass substrate. A biopsy puncher was used to cut two holes of 3.0 mm in diameter on the extremities of the channel structure on the hydrogel. A small volume of diluted organic dye was added to the cutout regions. A microfluidic adaptor was fitted to one of the cut-out regions (**Figure 39**). The adaptor acted as a reservoir to hold liquid and organic food dye was added to fill the reservoir half-way. This promotes a liquid-liquid interaction, instead of a solid-liquid interaction (hydrogel substrate and organic dye, respectively). Liquid flow was evaluated based on how far the fluid travels inside the microchannel design of the patterned hydrogel.

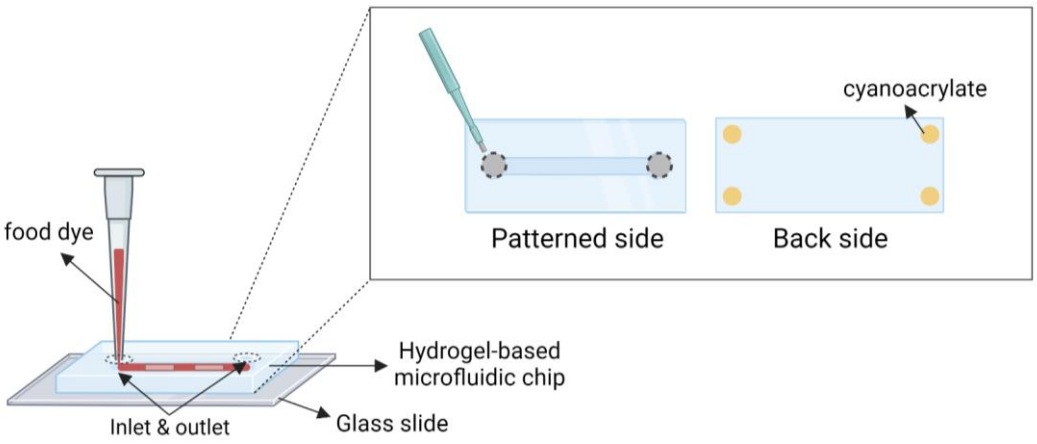

Figure 39. Scheme of fluid flow experiment. Gray circles: cut-out regions at the inlet and outlet of the microfluidic chip. Figure created with Biorender.com.

2.6. 3D printing and designs of encasing system

The holder was designed and converted into STL files using Fusion 360 Autodesk software. All STL files were then processed by Cura software (Ultimaker) to generate G-code instructions for the 3D printer (Ultimaker S3). Sample holder was printed using polylactic acid (PLA) filament. The setup for the encasing system is presented in **Figure 40**.

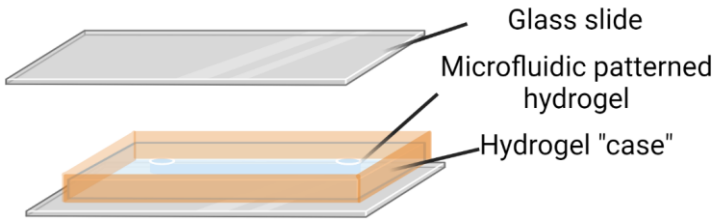

Figure 40. Scheme of hydrogel encasing system. Figure created with Biorender.com.

2.7. Real-time crosslinking kinetics study of DexMA-Dex hydrogels

A real-time crosslinking analysis was performed to understand DexMA crosslinking behavior in the presence of a non-photocrosslinkable polysaccharide. Aqueous solutions of DexMA-Dex at various ratios were prepared: 100:0, 80:20, 50:50, and 20:80 (w/w). Photoinitiator Irgacure 2959 (0.01% v/v) was added immediately before the kinetic test was launched. UV light source (365 nm) from the ElastoSens™ Bio was employed to carry out photocrosslinking.

2.8. Real-time crosslinking kinetics study of DexMA-PUDNA hydrogels

To determine if DexMA could crosslink with the PUD(NA) hydrogel network, and whether interpenetrating networks (IPNs) could be formed, kinetic tests were performed. Solutions of different PUD(NA):DexMA weight ratios were prepared: 100:0, 90:10, and 80:20 (w/w). We also investigated the order of crosslinking: chemical crosslinking – photocrosslinking and vice versa. To do this, the addition order of crosslinker (STMP) and photoinitiator (Irgacure 2959) were evaluated (**Table 9**). The purpose was to understand how the addition of Irgacure 2959 could affect gelation of chemical hydrogel (PUDNA) and how NaOH and STMP could affect the irradiation of photopolymerized hydrogel (DexMA).

Table 9. Experimental protocol to evaluate crosslinking order

	Chem - UV	**UV – Chem**
Synthesis protocol	1. Add NaOH and STMP to the PUDNA-DexMA solution. Magnetic stirring at RT, 5 min. 2. Place hydrogel inside the sample holder. 3. Launch kinetic test 4. Once sequence 2 finishes, pause kinetic test 5. Open the sample chamber, add Irgacure 2959 on top of the sample 6. Close the chamber and resume the test to launch sequence 3	1. Add Irgacure 2959 to the PUDNA-DexMA solution. Magnetic stirring at RT, 5 min. 2. Place hydrogel inside the sample holder. 3. Launch kinetic test 4. Once sequence 2 finishes, pause kinetic test 5. Open the sample chamber, add Irgacure 2959 on top of the sample 6. Close the chamber and resume the test to launch sequence 3
Test parameters	• Sequence 1: 50ºC, 20 min, UV light off • Sequence 2: 20ºC, 5 min, UV light off • Sequence 3: 20ºC, 20 min, UV light on • UV light source: 365 nm • UV light intensity: 50% (eq. of 14.4 mW/cm^2)	• Sequence 1: 20ºC, 20 min, UV light on Sequence 2: 20ºC, 5 min, UV light off • Sequence 3: 50ºC, 20 min, UV light off • UV light source: 365 nm • UV light intensity: 50% (eq. of 14.4 mW/cm2)

3. Results

3.1. Approach #1: Development of an injectable polysaccharide hydrogel as cell culture matrix

To study the injectability of PUDNA hydrogel, two loading methods were tested. When the hydrogel solution was injected using a syringe, the solution flowed into all channels of the microfluidic chip due to non-preferential flow (**Figure 41**). Therefore, a pressure-based flow controller was employed (**Figure 36**). Four different hydrogel formulations were investigated: PUD, PUD70, PUDNA and PUD70NA. D70 represents dextran (Mw 70 kDa) and NA refers to solutions with NaCl. Upon crosslinking reaction with STMP, the hydrogel solution was transferred to a reservoir, which was connected to tubes for pressure-controlled flow experiments.

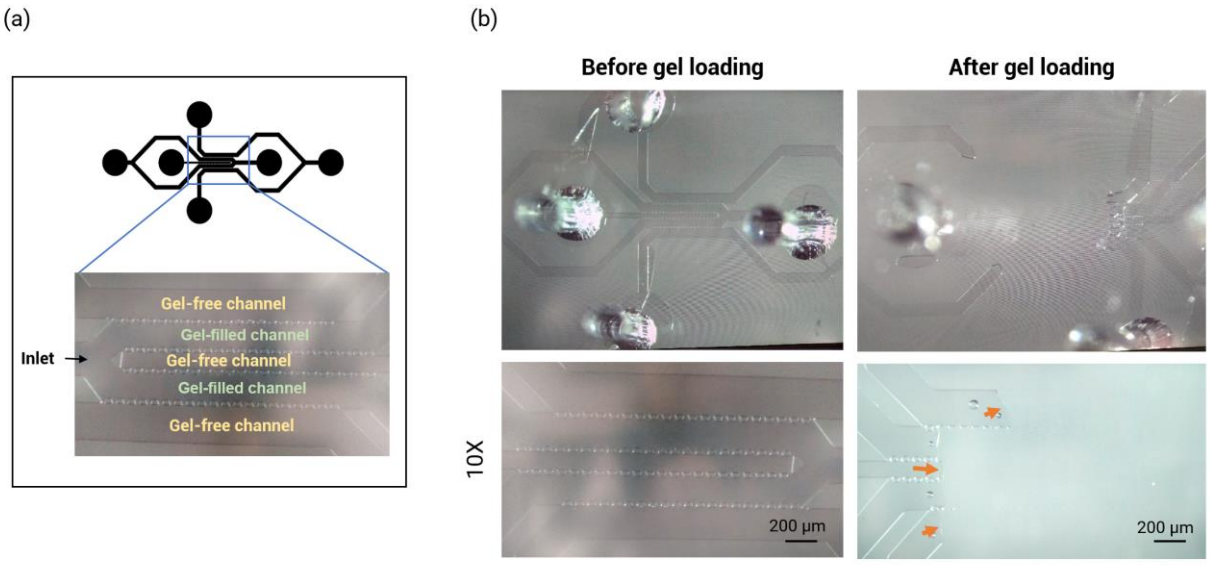

Figure 41. (**a**) Scheme shows the targeted channels to be loaded with hydrogel; (**b**) Observation of PDMS microfluidic chip before and after hydrogel loading via syringe injection. Orange arrows indicate hydrogel leaked in unwanted regions.

Real-time analysis of hydrogel injection/loading inside the PDMS microfluidic chip was observed. For both PUD and PUDNA, the hydrogel solutions were rather viscous and presented shear thinning behavior. Therefore, an initial pressure of 100 mbar was needed to force the hydrogel solution from the Eppendorf reservoir into the connected tube. Then, as soon as flow was observed through the needle adaptor and into the inlet of the PDMS chip, pressure was lowered to 5 mbar to

ensure a slow and controlled flow inside the microchannel. After 20 minutes, flow was observed through the target channels. However, after initial flow within the target channel, the hydrogel leaked out and all channels appeared filled with it. This event was observed in both PUD and PUDNA formulations (**Figure 42**). For PUD70 and PUD70NA, a pressure of 100 mbar was also used in the beginning to force the hydrogel solution from the Eppendorf reservoir into the connected tube. Then as soon as flow was observed through the needle adaptor and into the inlet of the PDMS chip, pressure was lowered to 5 mbar to ensure a slow and controlled flow inside the target channel. When the hydrogel solution approached the pillars of the microchannel, flow became slower. An increase in pressure was necessary to push the viscous hydrogel solution through these pillars. Pressures of 8 mbar and 25 mbar were used for PUD70 and PUD70NA solution, respectively. It was noted that the PUD70NA solution was more viscous than PUD70 solution, which corresponds to the need for an increase in pressure of the flow controller. A steady flow was achieved for both hydrogel formulations and the solutions remained well-contained inside the targeted channel (**Figure 42**). However, when the gel-loaded chip was immersed in PBS solution for the washing step, hydrogel swelling was observed (**Figure 42b**).

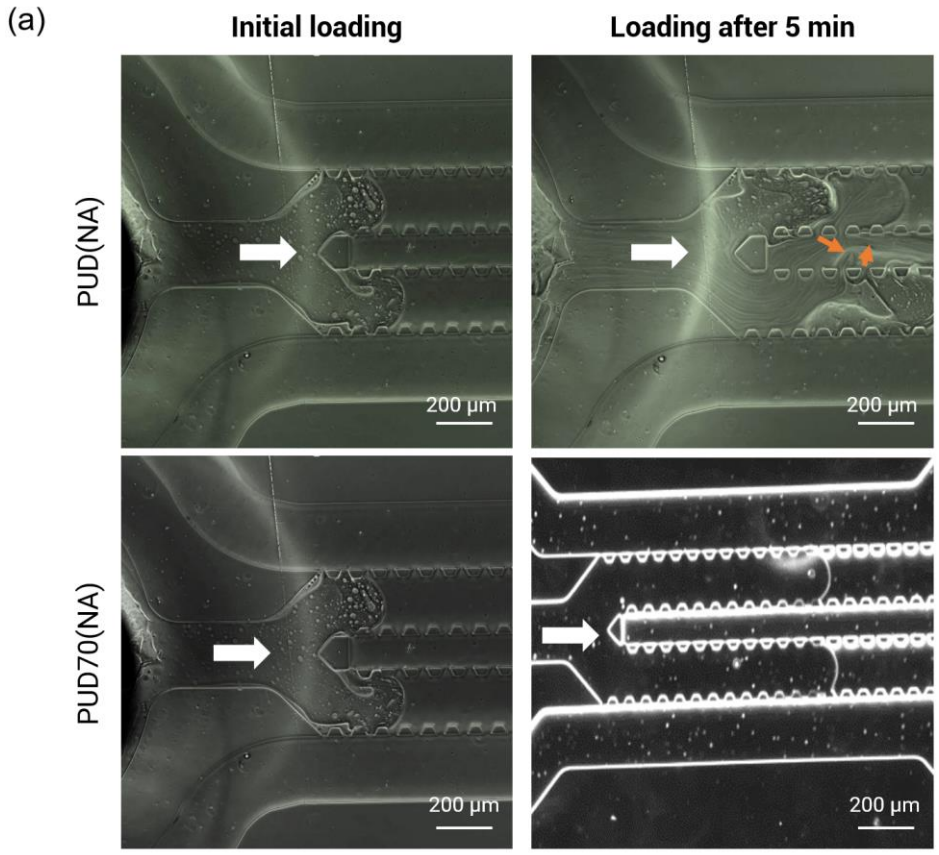

(b)

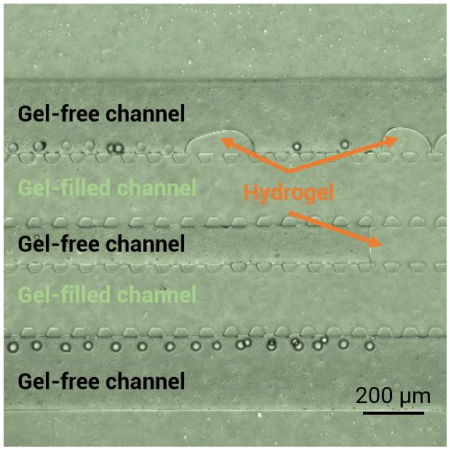

Figure 42. (**a**) Live-analysis of hydrogel injection into microfluidic chip. Zoom: 10X. White arrows indicate flow direction. Orange arrows represent leaked hydrogel in unwanted channel; (**b**) microscopy observation (10X) of injected PUD70 and PUD70NA hydrogel after washing step.

To further understand the behavior of hydrogels during loading, we performed hydrogel crosslinking kinetic experiments on the four hydrogel formulations. **Figure 43** presents the evolution of storage modulus of four hydrogels overtime. The presence of salt (NaCl) in both PUDNA and PUD70NA solutions lead to an increase in gelation rate, with steeper slope and shorter initiation time. Lower MW dextran resulted in a shorter initiation time. Longer crosslinking time was observed in the formulation with salt and lower MW dextran (PUD70NA) as compared to the one without salt (PUD70).

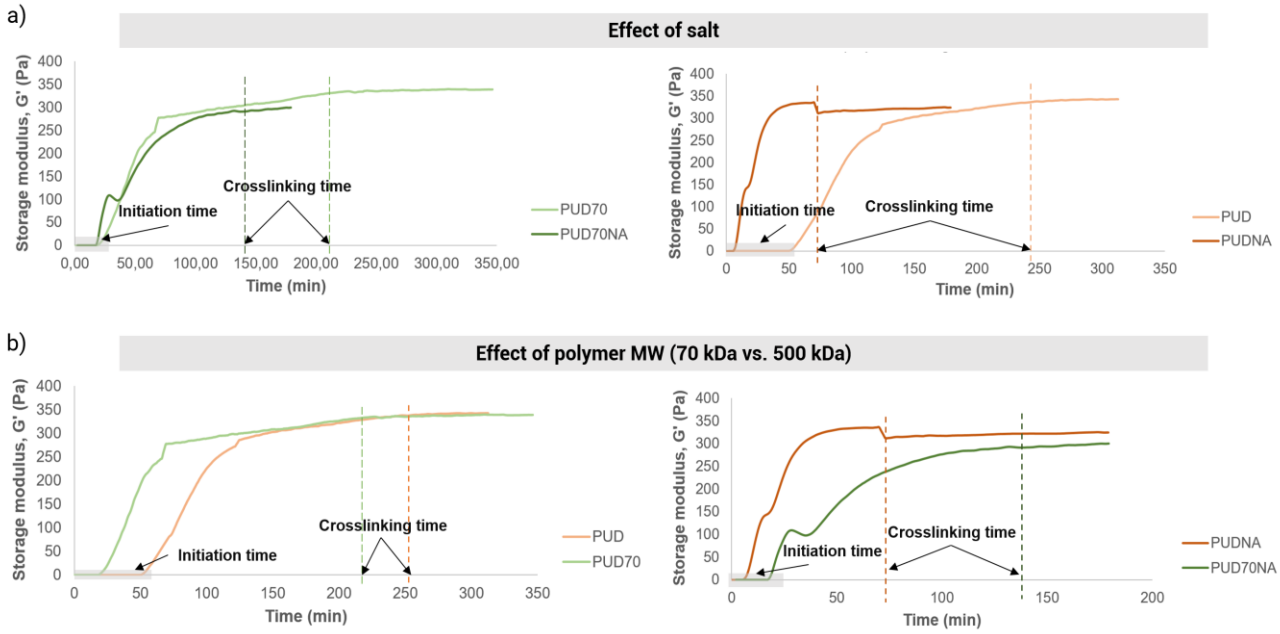

Figure 43. Real-time crosslinking analysis of PUDNA, PUD, PUD70NA, and PUD70 hydrogels to evaluate: (**a**) effect of salt on crosslinking kinetics and (**b**) effect of lower MW dextran on hydrogel crosslinking kinetics.

3.2. Approach #2. Polysaccharide-based hydrogel as microfluidic chip via direct molding

First, we tested the feasibility of replicating microfluidic patterns on PUDNA hydrogel. The hydrogel molding was conducted described in **Section 2.4**. Confocal scanning light microscopy was performed to observe the microfluidic patterns imprinted in the PUDNA hydrogel. Here, we could see that the microfluidic patterns were well preserved within the hydrogel (**Figure 44a**). There was a high-fidelity transfer of the patterned liver microvasculature network from the PDMS master mold onto the PUDNA hydrogel. Since fluid flow and perfusion are essential features of a functional microfluidic device, we next tested gravity driven perfusion on the patterned hydrogel using the protocol described in **Section 2.5**. Initial observation after fluid injection demonstrated that the liquid dye flowed through the inlet and outlet of the chip pattern. However, the dye did not pass through the microchannels resembling the liver microvasculature (ø = 150 - 200 µm). After 1h, the liquid dye still remained in the surrounding of the microchannel and did not pass through them (**Figure 44b**).

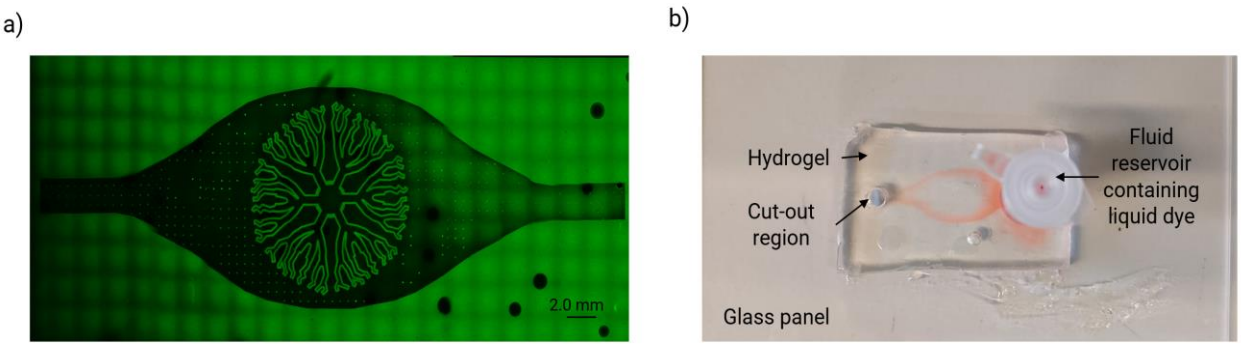

Figure 44. (**a**) FITC-dextran labelled microfluidic patterned PUDNA hydrogel; (**b**) Observation of fluid flow in patterned PUDNA hydrogel.

3.3. Encasing system to hold hydrogel-based microfluidic chip

To better accommodate the fluid flow experiment setup, a hydrogel case was proposed. The role of this case is to contain and support the soft hydrogel chip, which may enable fitting with rigid tubing. The case was designed and 3D printed using PLA (**Figure 45**). Holder #1 was used to encase the microfluidic hydrogel, while holder #2 was created to allow easy removal of hydrogel from holder #1. With this system, we could prevent sample damage during standard microfluidic setup (e.g. connecting to tubing). As demonstrated, it was possible to place the soft hydrogel with microfluidic patterns inside the 3D-printed case. In addition, it was relatively easy to remove the hydrogel from the case.

However, with this system, the microfluidic patterned side was only put in contact with the glass slide and not adhered to it. As a result, there was no complete seal of the system, which is required for microfluidic cell culture experiments. The use of cyanoacrylate was a temporary solution to perform fluid flow experiments, but cyanoacrylate is not a sustainable strategy as there are risks of cyanoacrylate dispersion leading to possible cytotoxicity during cell culture experiments. Thus, an alternative to the use of cyanoacrylate glue was explored in approach #3.

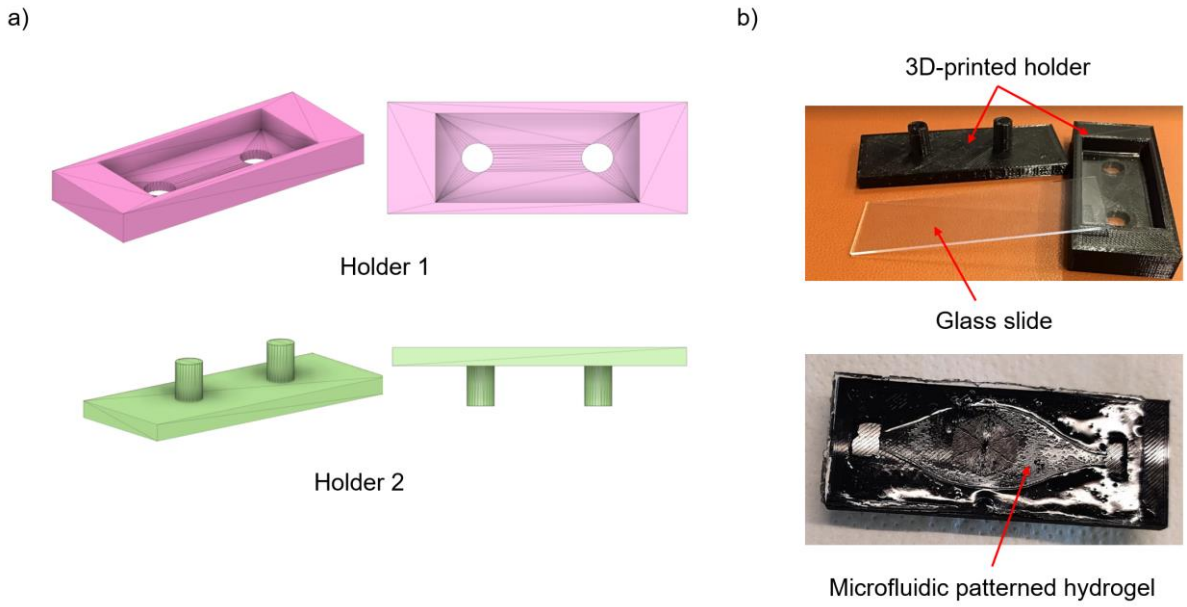

Figure 45. (**a**) 3D design of hydrogel holder as viewed with Autodesk Fusion 360; (**b**) 3D printed PLA holder with the encased hydrogel.

3.4. Approach #3. Development of a photocrosslinked hydrogel as microfluidic device

To avoid issues associated with our chemically cross-linked hydrogel (e.g. high swelling, crosslinking under alkaline condition), we explored the possibility of using a photocrosslinked hydrogel. This method was selected with the aim to incorporate an IPN hydrogel in the microfluidic device and to control hydrogel swelling. Indeed, according to previous studies, the swelling degree of DexMA (dextran methacrylate) hydrogels can be controlled by the degree of methacrylate ion substitution. It was reported that the higher degree of substitution led a decrease in hydrogel swelling [17]. Moreover, we also employed DexMA a co-polymer for PUD or PUDNA to develop an IPN hydrogel.

Hydrogel precursor solution was transferred into the ElastoSens™ Bio holder and kinetic test was launched. Once the shear storage modulus of the hydrogel reached a plateau, crosslinking reaction was considered completed. Photocrosslinked DexMA-Dex (100:0) hydrogel was opaque, which is an undesirable characteristic for our final application. Indeed, lower amounts of DexMA concentration decreased hydrogel opacity (**Figure 46a**). The concentration of DexMA also had an effect on hydrogel shear modulus. Lower DexMA amount led to lower shear modulus (**Figure 46a**). For 100:0 DexMA:Dex hydrogel, the final stiffness reached was around 350 Pa, whereas for

50:50 and 20:80 DexMA-Dex samples, the modulus decreased to 200 Pa and 77 Pa, respectively. Interestingly, pure DexMA hydrogel exhibited longer initiation time compared to the other hydrogels with lower DexMA concentrations. The 80:20, 50:50, and 20:80 followed a trend: lower amount of DexMA resulted in longer initiation time and thus, slower crosslinking time.

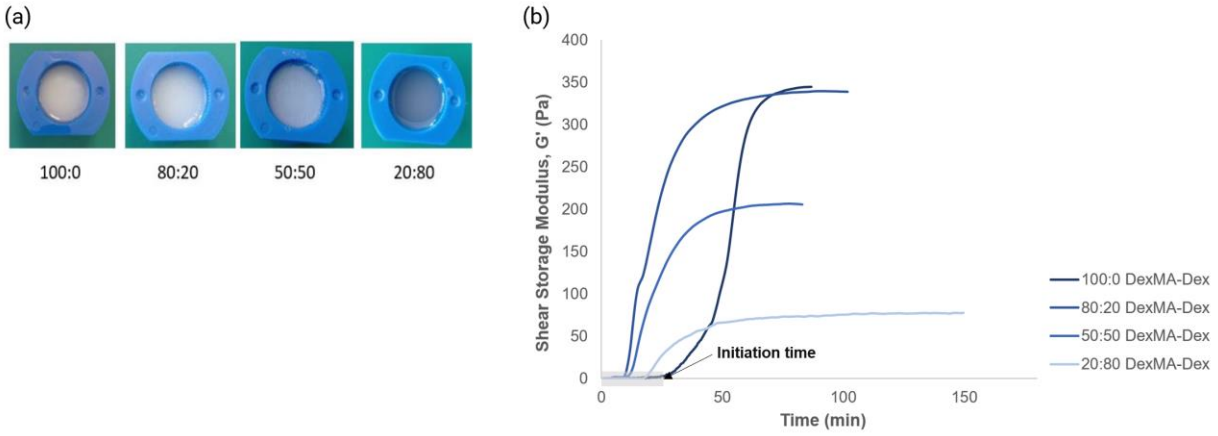

Figure 46. (**a**) Photocrosslinked DexMA-Dex hydrogels at various DexMA-Dex weight ratios; (**b**) Shear storage modulus (G') evolution of photocrosslinked hydrogels overtime.

3.5. Crosslinking kinetics of PUDNA-DexMA hydrogel

Figure 47 summarizes the crosslinking kinetics observed on hydrogels that were crosslinked by two different orders, as previously described in **Section 2.7**, **Table 9**. All Chem-UV hydrogels crosslinked to a further extent than UV-Chem hydrogels. Incomplete crosslinking was demonstrated by presence of liquid remaining in UV-Chem hydrogels after 1h of monitoring. Both PUDNA-DexMA formulations that underwent UV-Chem approach did not crosslink completely, despite exposure under UV light. Increase in DexMA concentration resulted in a decreased in hydrogel's stiffness. PUDNA-DexMA 100:0 had a final G' of 315 Pa, while PUDNA-DexMA 90:10 had G' of 310 Pa. PUDNA-DexMA 90:10 samples were opaque, as expected, due to the presence of DexMA.

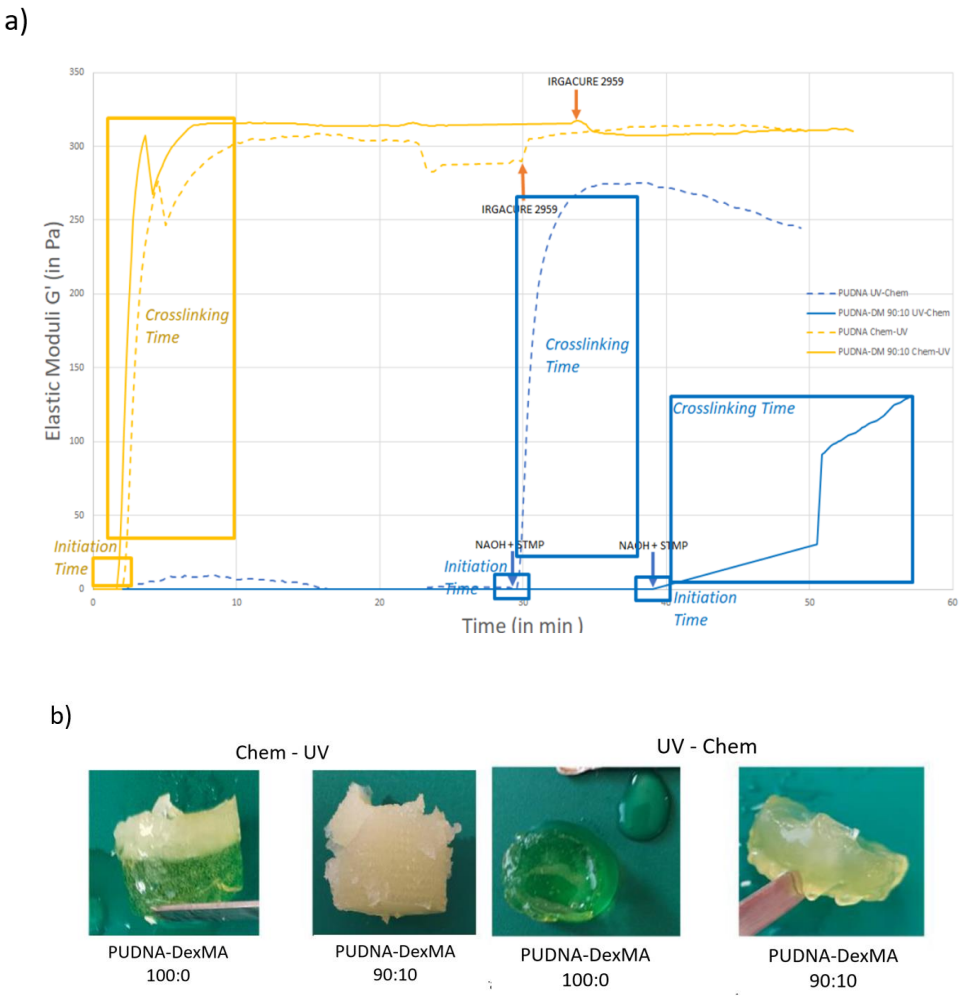

Figure 47. (**a**) The evolution of the shear storage modulus, G' (kPa) as a function of time of different PUDNA-DexMA hydrogel formulations, crosslinked with STMP (0.1% *v/v*) and Irgacure 2959 (0.01% *v/v*); (**b**) Photos of crosslinked hydrogels after kinetic measurements.

3.6. Crosslinking kinetics of PUD-DexMA hydrogel

Figure 48 summarizes the crosslinking kinetics observed on hydrogels, here without salt, that were crosslinked by two different orders, as previously described in Section 2.8, Table 1. All PUD-DexMA hydrogels that underwent Chem-UV approach reached final stiffness plateau after 20 minutes, corresponding to the crosslinking duration set for chemical crosslinking part. Interestingly, when these hydrogels were subjected to the UV-Chem approach, the shear storage modulus had a high starting point (around 200-250 kPa) and drastically dropped to 100-150 kPa

when NaOH and STMP were added to launch the chemical crosslinking sequence. Photos of UV-Chem hydrogels demonstrated incomplete crosslinking.

a)

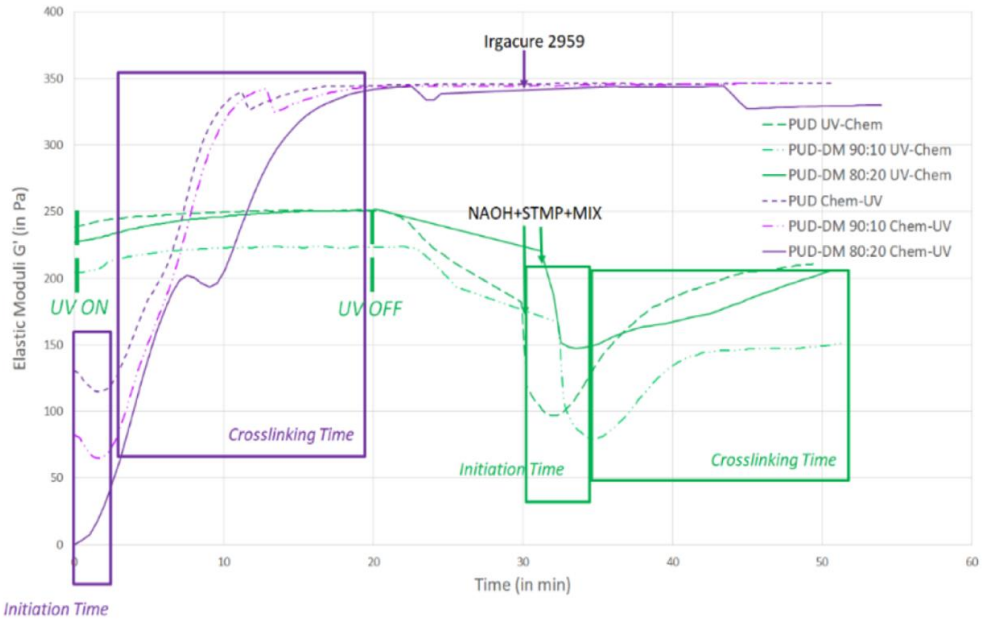

b)

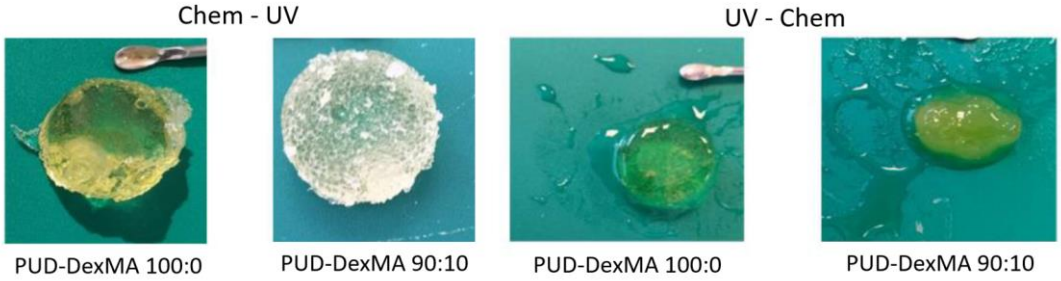

Figure 48. (**a**) The evolution of the shear storage modulus, G' (kPa) as a function of time of different PUD-DexMA hydrogel formulations, crosslinked with STMP (0.1% v/v) and Irgacure 2959 (0.01% v/v); (**b**) Photos of crosslinked hydrogels after kinetic measurements.

4. Discussions

4.1. Approach #1. Development of an injectable polysaccharide hydrogel as cell culture matrix

By conducting simple injection experiments and crosslinking kinetic studies, we have demonstrated the role of salt (NaCl) in PUDNA final properties. When salt was introduced in the hydrogel precursor solution, it reduced initiation time, hence, accelerated crosslinking time (**Figure 43**). For our application, this feature is not ideal, as the polymer solution required some time to travel from the reservoir into the microfluidic chip. Plus, the presence of salt also increased the polymer solution viscosity, making it more difficult to control flow in a spatial-controlled manner. In contrast, when salt was removed from the polymer precursor solution, initiation time took longer and crosslinking time was doubled (**Figure 43**). The molecular weight of dextran also affected crosslinking kinetics and solution viscosity. In the absence of salt, the use of low MW dextran (PUD70) resulted in shorter crosslinking time. Thus, the precursor solution was easily injected inside the microchannel of the PDMS microfluidic chip. In the presence of salt and low MW dextran (PUD70NA), it was also possible to inject the hydrogel solution in a spatial-controlled manner. These observations suggest that at lower MW dextran, the effect of salt of hydrogel solution was less significant as compared to solutions with higher MW dextran (**Figure 43**). Upon loading and after hydrogel washing step, swelling was observed (**Figure 42b**). Previously, in **Chapter 3.1**, we demonstrated the effect of crosslinker density in hydrogel swelling, where higher crosslinked hydrogels showed less swelling. Therefore, in the case of PUD70 injectable hydrogel, we could reduce swelling by increasing the amount of STMP introduced in the polymer precursor solution.

4.2. Approach #2. Polysaccharide hydrogel as microfluidic chip

We have demonstrated the feasibility to fabricate hydrogels with microfluidic patterns through direct molding. By simply using the PDMS microfluidic chip as a master mold, we could easily transfer all microfluidic patterns onto our soft polysaccharide hydrogel (**Figure 44a**).

However, since PUDNA hydrogel is much softer than PDMS, it poses several technical challenges for end-user applications. The first issue is fluid flow. As shown in **Figure 44b**, fluid flow through the hydrogel-based microfluidic chip was only possible through the inlet and outlet (diameter = 2400 µm). This flow was contributed by simple fluid diffusion from the inlet to the outlet. No flow was observed through the microvasculature branches of diameter 150 – 200 µm. This could be due to lack of differential in pressure. Another technical issue arised throughout this experiment was the glass-to-hydrogel adhesion. In conventional microfluidic systems, PDMS is permanently bonded to the glass substrate by plasma treatment. In our case, the hydrogel-based microfluidic chip was merely glued to the glass panel by using cyanoacrylate. Overtime, this could leak into the hydrogel and all the media used in subsequent cell culture experiments. Therefore, hydrogel-glass bonding posed as a technical problem. For this reason, glass methacrylation was proposed to addressed this issue (Approach #3).

4.3. Approach #3. Development of a photocrosslinked hydrogel glue layer to bond hydrogel-based microfluidic device with glass substrate

The purpose of methacrylation of glass surfaces is to covalently bind methacrylate functional groups to the glass substrate. This enables the glass surface to participate in the photocrosslinking reaction, hence, covalently bond methacrylate-containing hydrogel for cell culture experiments. Dextran methacrylate (DexMA) was chosen to perform preliminary experiments due to its similar chemical nature with dextran. The following approach was proposed to fabricate an adaptor layer made of dextran methacrylate (DexMA). On one side, the adaptor DexMA hydrogel will then be bonded to the glass panel via a silane agent, 3-(trimethoxysilyl)propyl methacrylate (TMSPMA) (**Figure 35**). This silane agent has a moderate hydrophobicity and is suitable for copolymerization with acrylate, methacrylate and styrene type of monomers [22]. On the other side, the DexMA layer will be bonded to the polysaccharide hydrogel via *in situ* crosslinking (**Figure 35**).

As observed in **Figure 46a**, photocrosslinked DexMA hydrogel (DexMA-Dex 100:0) was opaque. Real-time analysis of crosslinking analysis allowed us to determine the crosslinking parameters for DexMA gel glue layer. However, as the gel was opaque, the use of DexMA as a glue layer was re-considered. An alternative solution would be to incorporate DexMA hydrogel only in the regions that do not overlap with the microchannel, yet still provide enough surface to adhere with the glass panel (as proposed in Approach 3, Figure 3, step i). Other polymers that could

be covalently crosslinked with the silanes on treated glass surfaces include PEGMA (poly(ethylene glycol) methacrylate) [23], PEGDA (poly(ethylene glycol) diacrylate) [24], poly(GMA-co-EGDMA) (poly(glycidyl methacrylate-co-ethylene glycol dimethacrylate) [25]. To avoid the use of synthetic polymers, alternatives combining pullulan, dextran, and dextran-MA, to prepare a hydrogel 100 % polysaccharidic were evaluated.

In the presence of salt, the introduction of DexMA in the hydrogel formulation, when followed the Chem-UV sequence, increased the hydrogel stiffness (G' > 300 Pa), as compared to pure PUDNA (G' < 300 Pa) (**Figure 47**). In the reverse sequence, UV-Chem, the storage modulus was only detected after NaOH and STMP were introduced in the hydrogel precursor solution. This could mean a few things: First, the feed ratio of DexMA was too low to photocrosslink along with PUDNA. During photopolymerization, free radical product from the dissociation of Irgacure is released [26]. These free radicals could react with NaCl (presence in PUDNA), forming crystals and preventing polymer precursors to crosslink. The hydrogel opacity of PUDNA-DexMA 90:10 in Chem-UV approach was contributed by the salt crystals and to the presence of DexMA (as previously demonstrated). Similar analogy could also be done for STMP and Irgacure 2959. When NaCl is removed from the polymer precursor solution (PUD-DexMA 90:10), under Chem-UV sequence, the final sample was less opaque (**Figure 48**). Future characterizations including nuclear magnetic resonance spectroscopy (NMR) and Fourier-transformed inferred spectroscopy (FTIR) will be conducted to evaluate the crosslinking degree and crosslinking mechanisms between PUDNA and DexMA networks.

In regards to hydrogel stiffness, the incorporation of DexMA in PUDNA solution was not a viable solution. Even at higher values of storage modulus, the value we could obtain remain below 400 Pa, whereas the targeted G' to mimic the stiffness of native liver is 2-6.5 kPa [16]. Although we could expect to obtain stiffer hydrogels by increasing the feed ratio of DexMA, the final hydrogel would be too opaque for our final application.

5. Conclusions

In this chapter, three main strategies to develop a polysaccharide hydrogel to be integrated in microfluidic chips for angiogenesis promotion was presented. In the first approach, we developed an injectable polysaccharide hydrogel for loading inside targeted channels of PDMS

microfluidic chips. The polysaccharide solution viscosity was shown to be affected by the presence of salt and the MW weight of the polysaccharide (dextran). Successful loading was achieved using PUD and PUD70 solutions, where the crosslinked hydrogel remained in the targeted channel and did not leak into un-target channels (**Figure 42a**). Upon hydrogel washing, swelling was observed. To control swelling, we could increase the concentration of STMP introduced in the polysaccharide solutions (PUD and PUD70). Future work of this approach includes evaluation of solution viscosity and shear thinning properties by rheological measurements as well as crosslinking kinetics of solutions with increased STMP concentrations. Quantitative analysis of fluid properties such as flow resistance will also be determined.

In the second approach, we attempted to entirely replace PDMS substrate with polysaccharide to produce a hydrogel-based microfluidic chip (**Figure 34**). Through direct molding, we could easily transfer the microfluidic patterns on the polysaccharide hydrogel. Fluid flow only took place via diffusion from the inlet/outlet of the microfluidic, but not through the microchannels (diameter around 150 μm). Fitting of microfluidic tubing was another issue that prevented further fluid flow experiments to be performed. Several optimizations such as selection of softer tubing materials, case design, hydrogel-glass bonding experiments, and microfluidic chip design could be performed in the future.

In the third approach, we explored the potential of using photocrosslinked polymer (DexMA) and IPN hydrogel composed of 100% polysaccharide (PUDNA-DexMA) to incorporate in microfluidic chips. The aim of this strategy is to replace the use of cyanoacrylate for hydrogel-glass bonding. Although we determined the crosslinking parameters for the DexMA gel layer, the hydrogel's opacity presented an undesirable characteristic, especially for optical detection. Thus, the crosslinking of PUDNA and DexMA and PUD and DexMA hydrogels were incomplete and the final stiffness were too low for our final applications (400 Pa as compared to targeted G' of 2-6 kPa). Therefore, we propose another solution: Using approach #2 as discussed, but instead of crosslinking the hydrogel for 20 minutes, we could remove it from the oven after 15 minutes. Then a small volume of DexMA solution would be poured over the PUDNA hydrogel to form a thin DexMA layer and a UV source will be applied to crosslink the DexMA hydrogel, before putting back the whole system in the oven, to finish the crosslinking of PUDNA hydrogel.

References

[1] G.M. Whitesides, The origins and the future of microfluidics, Nat. 2006 4427101. 442 (2006) 368–373. https://doi.org/10.1038/nature05058.

[2] A.G. Niculescu, C. Chircov, A.C. Bîrcă, A.M. Grumezescu, Fabrication and applications of microfluidic devices: A review, Int. J. Mol. Sci. 22 (2021) 1–26. https://doi.org/10.3390/ijms22042011.

[3] K. Ren, J. Zhou, H. Wu, Materials for microfluidic chip fabrication, Acc. Chem. Res. 46 (2013) 2396–2406. https://doi.org/10.1021/ar300314s.

[4] S.I. Hamdallah, R. Zoqlam, P. Erfle, M. Blyth, A.M. Alkilany, A. Dietzel, S. Qi, Microfluidics for pharmaceutical nanoparticle fabrication: The truth and the myth, Int. J. Pharm. 584 (2020) 119408. https://doi.org/10.1016/J.IJPHARM.2020.119408.

[5] A. Dellaquila, C. Le Bao, D. Letourneur, T. Simon-Yarza, In Vitro Strategies to Vascularize 3D Physiologically Relevant Models, Adv. Sci. 8 (2021). https://doi.org/10.1002/advs.202100798.

[6] N. Wongkaew, M. Simsek, C. Griesche, A.J. Baeumner, Functional Nanomaterials and Nanostructures Enhancing Electrochemical Biosensors and Lab-on-a-Chip Performances: Recent Progress, Applications, and Future Perspective, Chem. Rev. 119 (2019) 120–194. https://doi.org/10.1021/acs.chemrev.8b00172.

[7] P. Sengupta, K. Khanra, A.R. Chowdhury, P. Datta, Lab-on-a-chip sensing devices for biomedical applications, Elsevier Ltd, 2019. https://doi.org/10.1016/B978-0-08-102420-1.00004-2.

[8] J. Weigle, Bernhard; Domingo, Gonzalo; LaBarre, Paul; Gerlach, Towards non- and minimally instrumented, microfluidics-based diagnostic devices, 8 (2008) 1–30. https://doi.org/10.1039/b811314a.Towards.

[9] A. Anbari, H.T. Chien, S.S. Datta, W. Deng, D.A. Weitz, J. Fan, Microfluidic Model Porous Media: Fabrication and Applications, Small. 14 (2018). https://doi.org/10.1002/smll.201703575.

[10] A. Olanrewaju, M. Beaugrand, M. Yafia, D. Juncker, Capillary microfluidics in microchannels: From microfluidic networks to capillaric circuits, Lab Chip. 18 (2018) 2323–2347. https://doi.org/10.1039/c8lc00458g.

[11] J.B. Nielsen, R.L. Hanson, H.M. Almughamsi, C. Pang, T.R. Fish, A.T. Woolley, Microfluidics: innovations in materials and their fabrication and functionalization, Anal. Chem. 92 (2020) 150–168. https://doi.org/10.1021/acs.analchem.9b04986.

[12] A. Shakeri, N.A. Jarad, A. Leung, L. Soleymani, T.F. Didar, Biofunctionalization of Glass- and Paper-Based Microfluidic Devices: A Review, Adv. Mater. Interfaces. 6 (2019) 1–16. https://doi.org/10.1002/admi.201900940.

[13] V.S. Cabeza, High and Efficient Production of Nanomaterials by Microfluidic Reactor Approaches, Adv. Microfluid. - New Appl. Biol. Energy, Mater. Sci. (2016). https://doi.org/10.5772/64347.

[14] M. James, R.A. Revia, Z. Stephen, M. Zhang, Microfluidic synthesis of iron oxide nanoparticles, Nanomaterials. 10 (2020) 1–19. https://doi.org/10.3390/nano10112113.

[15] F. Akther, P. Little, Z. Li, N.-T. Nguyen, H.T. Ta, Hydrogels as artificial matrices for cell seeding in microfluidic devices, (2020). https://doi.org/10.1039/d0ra08566a.

[16] C.F. Guimarães, L. Gasperini, A.P. Marques, R.L. Reis, The stiffness of living tissues and its implications for tissue engineering, Nat. Rev. Mater. 5 (2020) 351–370. https://doi.org/10.1038/s41578-019-0169-1.

[17] J. Liu, H. Long, D. Zeuschner, A.F.B. Räder, W.J. Polacheck, H. Kessler, L. Sorokin, B. Trappmann, Synthetic extracellular matrices with tailored adhesiveness and degradability support lumen formation during angiogenic sprouting, Nat. Commun. 12 (2021). https://doi.org/10.1038/s41467-021-23644-5.

[18] M.B. Chen, J.A. Whisler, J. Fröse, C. Yu, Y. Shin, R.D. Kamm, On-chip human microvasculature assay for visualization and quantification of tumor cell extravasation dynamics, Nat. Protoc. 12 (2017) 865–880. https://doi.org/10.1038/nprot.2017.018.

[19] D. Sharma, W. Jia, F. Long, S. Pati, Q. Chen, Y. Qyang, B. Lee, C.K. Choi, F. Zhao, Polydopamine and collagen coated micro-grated polydimethylsiloxane for human mesenchymal stem cell culture, Bioact. Mater. 4 (2019) 142–150. https://doi.org/10.1016/j.bioactmat.2019.02.002.

[20] M.N. Labour, C. Le Guilcher, R. Aid-Launais, N. El Samad, S. Lanouar, T. Simon-Yarza, D. Letourneur, Development of 3D hepatic constructs within polysaccharide-based scaffolds with tunable properties, Int. J. Mol. Sci. 21 (2020) 1–20. https://doi.org/10.3390/ijms21103644.

[21] T. Le Guilcher, Camille; Franck, Grégory; Dellaquila, Alessandra; Labour, Marie-Noelle; Aid, Rachida; Tordjmann, Thierry; Letourneur, Didier; Simon-Yarza, Engineered human liver based on pullulan-dextran hydrogel promotes mice survival after liver failure, (2022).

[22] E. Korzhikova-Vlakh, M. Antipchik, T. Tennikova, Macroporous polymer monoliths in thin layer format, Polymers (Basel). 13 (2021). https://doi.org/10.3390/polym13071059.

[23] H. Yuk, T. Zhang, S. Lin, G.A. Parada, X. Zhao, Tough bonding of hydrogels to diverse non-porous surfaces, Nat. Mater. 15 (2016) 190–196. https://doi.org/10.1038/nmat4463.Tough.

[24] Y. Zhu, D. Sazer, J.S. Miller, A. Warmflash, Rapid fabrication of hydrogel micropatterns by projection stereolithography for studying self-organized developmental patterning, PLoS One. 16 (2021) 1–13. https://doi.org/10.1371/journal.pone.0245634.

[25] I. Urbanova, F. Svec, Monolithic polymer layer with gradient of hydrophobicity for separation of peptides using two-dimensional thin layer chromatography and MALDI-TOF-MS detection, J. Sep. Sci. 34 (2011) 2345–2351. https://doi.org/10.1002/jssc.201100202.

[26] S.J.P. Marlton, B.I. McKinnon, N.S. Hill, M.L. Coote, A.J. Trevitt, Electrostatically Tuning the Photodissociation of the Irgacure 2959 Photoinitiator in the Gas Phase by Cation Binding, J. Am. Chem. Soc. 143 (2021) 2331–2339. https://doi.org/10.1021/jacs.0c11978.

4. GENERAL DISCUSSION

4. General Discussion

In the context of developing prevascularized hydrogels for *in vitro* models, this work aimed to create hydrogels with: i) tubular structures mimicking some aspects of the native vasculature, such as circular cross-section and vessel-like branched and multiscale geometries, ii) integrated basement membrane such as laminin and other ECM components that promote proper cell adhesion, proliferation, and differentiation during angiogenesis, tissue maintenance, and remodeling. The first part of the PhD work managed to meet the first goal where biocompatible 3D porous hydrogels with microchannels of varying diameters and geometries were generated. Then in the second part, the second goal was achieved: the hydrogels were functionalized to integrate a laminin-mimic peptide (Caf1-YIGSR) and a VEGF-mimic molecule (Caf1-VEGF) into the hydrogel-based scaffolds, resulting in enhanced endothelial cell adhesion, proliferation, and signs of endothelial cell migration and sprouting. Lastly, the final experimental work presented and extended the possibility to finely tune our hydrogels and to develop a more physio-mechanically relevant substrate for cell culture in microfluidic systems. Overall, the developed hydrogels exhibited some fundamental requirements for angiogenesis, which contribute to a class of biomaterials that can promote angiogenesis for *in vitro* tissue engineering applications.

Hydrogel-based scaffolds composed of crosslinked polymers are preferred over reconstituted ECM of collagen, fibrin, or basement membrane. This is due to the ability to independently control the physical and chemical properties of hydrogels (such as matrix elasticity, porosity, ligand density, etc.). The main challenge in developing tissue engineered hydrogels is to mimic the native ECM microenvironment and ensure proper cellular interactions with the engineered ECM. For this reason, natural polymers such as collagen, hyaluronic acid, alginate, pullulan, dextran are the preferred choice due to their biomimetic potential. Based on this, in this thesis project, I chose to work with polysaccharide hydrogels composed of pullulan and dextran.

In the first experimental section (**Chapter 3.1**), a fabrication method to control the microarchitecture of polysaccharide hydrogels were developed and sacrificial templating was employed to form microchannels in the range of microvessels (ø = 500 – 100 µm). The resulting vessel-mimic constructs had circular cross-section (**Figure 19**), which shall ensure optimal cell colonization. Indeed, in the second experimental section (**Chapter 3.2**), we showed that when the hydrogel was coated with the laminin-mimic protein (Caf1-YIGSR), optimal cell colonization was

achieved. In particular, when HUVECs were seeded on the functionalized hydrogels, at optimal cell seeding density, adhesion and proliferation were observed after 7 days in static culture. Thus, the cells exhibited healthy phenotype (**Figure 28**). However, this study still presents some shortcomings. Firstly, the system lacked flow and perfusion, which are fundamental to ensure adequate cell survival and tissue functioning [1]. For the moment, cellularized scaffolds were only maintained in static conditions. On-going strategies are being explored to integrate flow into our hydrogel scaffolds. For example, using fuse deposition modeling (FDM), we could design and print a platform that holds the hydrogels in place, while connecting them to a flow system. Once a flow system would be well adapted to our 3D soft hydrogels, we could then optimize perfusion parameters to mimic the hemodynamics and blood flow properties. It has been reported that pulsatile flow with shear stresses below 10 dyne/cm^2 can influence ECs cytoskeleton remodeling and nitric oxide levels [2], thus further contributing to promote sprouting angiogenesis.

Regarding the microchannel dimensions, we managed to form tubular structures as small as 100 µm using both PVA and alginate templates. On such a small scale, and given the manufacturing technique developed, the integration of these tubular networks pose several operational challenges (e.g. complex integration protocol of hydrogel and sacrificial components, handleability of alginate sacrificial templates, etc.) As discussed previously in the bibliography review, current approaches in vascularization of 3D cell culture models merely produced constructs of 500 microns to a few millimeters [1,3,4]. In particular, of the approaches using sacrificial materials for channels patterning within hydrogel scaffolds, the smallest diameter reported was 200 µm [5]. Scaffolds with large channels (ø = 1 mm) were perfused via an external custom-made perfusion system [3,4], while those of smaller diameters (ø ~ 250 µm) were perfused upon transplantation in an animal model [6]. In most cases, natural hydrogels (e.g. fibrin, gelatin, and collagen) were employed [4–7]. Some studies demonstrated the manufacturing of thick constructs with interconnected hollow channels, but the channel dimensions remain relatively large (ø = 1 mm to 500). In the first chapter, we also discussed the technical challenges in working with PVA as sacrificial templates, which further highlights the current challenge in microfabrication, specifically in realizing microvasculature constructs for patterning in hydrogels.

In the second experimental chapter (**Chapter 3.2**), the polysaccharide hydrogels, with straight tubular structures of ø 100 µm, were functionalized to promote cell adhesion. Since the

hydrogels were crosslinked under alkaline condition (pH – 14), direct incorporation of cell-adhesive biomolecules was unsuitable. Therefore, electrostatic interactions were chosen as the functionalization method. After synthesis of cationized hydrogels via the incorporation of the cationic polymer (DEAE-Dextran), the hydrogels were exposed to the bioactive solutions (pI – 4.6). We demonstrated that by increasing the bulk concentration of the functionalized Caf1-YIGSR (DFD coating method), better cell morphology was also observed, where cells showed polarization and filopodia structures, and increased cell proliferation was achieved after 7 days in culture. Additionally, we demonstrated the ability to modulate endothelial cell behavior through combinations of pro-angiogenic signals in a specific spatial organization.

For the past decades, various attempts have been made to fabricate hydrogels with spatial-guided distribution of bioactive molecules. Current techniques are classified into two main strategies: i) direct patterning of cells through bioprinting or ii) organizing the spatial distribution of pro-angiogenic biomolecules. Bioprinting of synthetic hydrogels and natural hydrogels has been explored for both techniques. Thus, a plethora of proteins and peptides (e.g. RGD, YIGSR, RoY) and GFs (e.g. FGF, VEGF) have been incorporated either alone or in combination. Specifically, VEGF is the most commonly used GF for patterning of hydrogels. Using photolithography, VEGF was printed onto a collagen-glycosaminoglycan scaffolds in a spatially defined configuration and was reported to promote formation of immature vascular networks [8]. Similarly, hydrogels have been designed to incorporate VEGF with pre-defined patterning of VEGF. When VEGF was patterned in parallel channels, they promoted formation of aligned vasculature within PEGDA hydrogels [9]. These results further implicate the importance of precise spatial control in promoting vessels formation. In addition to the use of spatially-defined deposition of GF, researchers have also investigated combinations of different GFs to better replicate the different stages of angiogenesis. For example, improved angiogenesis and maturation of vessels have been reported both with VEGF and Angiopoietin [10] as well as with a combination of VEGF, FGF (fibroblast growth factor), and BMP2 (Bone morphogenetic *protein* 2) [11]. Presence of YIGSR peptides on RGD functionalized PEG (polyethylene glycol) hydrogels were reported to induced cell migration, as compared to scaffolds only functionalized with RGD alone [12].

Besides GFs, peptides have also been employed to functionalize scaffolds to facilitate vessel formation. When functionalized onto chitosan hydrogels, RoY, a 12 amino acid synthetic

peptide, resulted in increased tube formation *in vivo*, as compared to non-functionalized scaffolds [13]. Similarly, incorporation of peptide motifs KLT (which mimics VEGF and binds to VEGF receptors) and PRG (repetitive RGD sequence) into self-assembling peptide scaffolds resulted in an increase in cell viability, cell adhesion, and cell proliferation [14]. Compared to GFs, peptides are more stable than GFs and allow incorporation of angiogenic domains through covalent binding to the scaffolds [15].

From the on-going discussion, it is strongly implicated that simple incorporation of bioactive molecules and GFs and the patterning of vascular cells serve as a good starting point to control the initial organization of vascular networks. This gives a good control over the initial stage of vessel formation and remodeling, where ECs will remodel these networks during *in vitro* and after implantation of the engineered constructs. However, when there are no additional cues left to guide this remodeling process, random organization of the vascular network could occur. Therefore, one or more methods to control vascular remodeling and maturation must be included to ensure good vascular organization as well as functionality in the long term [16].

Indeed, with regards to our approach, we controlled the spatial distribution of pro-angiogenic cues which resulted in control over ECs organization as well as their different phenotypes inside the porous channeled hydrogels. Our simplified system has not yet fully recapitulated the complexity of *in vivo* angiogenesis. However, the developed approach demonstrated the ability to control initial stage of angiogenesis and the potential to influence initial organization of the vascular networks.

In the third experimental chapter, we explored the different ways to incorporate polysaccharide hydrogels in microfluidic devices. Our work presents a proof of concept to synthesize pullulan, dextran, and DexMA hydrogels as alternative solutions to PDMS for microfluidic fabrication. The integration of microfluidics and 3D hydrogels are of great interest to take a step forward in conducting *in vitro* experiments with more physiologically relevant parameters. The work presented in this manuscript attempts to increase the complexity and functionality of microfluidic devices.

To increase microfluidic device functionality, researchers have incorporated numerous materials in the fabrication process. The use of hydrogels enables integration of semi-permeable barriers, smart valves, and sensors [17–19]. Hydrogels composed of polyethylene glycol diacrylate

(PEGDA), 2-(dimethylamino)ethyl methacrylate, and 2-hydroxyethyl methacrylate were entrapped with enzyme dots to carry out multi-enzymatic reactions in microfluidic devices [18]. For cell culture experiments, hydrogels have been often integrated either as a coating matrix or a specific compartment dedicated for cell culture [20]. The main role of hydrogels in microfluidic 3D cell culture is to mimic the native tissues-specific microenvironment and provide specific cell attachment cues to promote cell proliferation, differentiation, and migration. Natural hydrogels, synthetic hydrogels, and combinations of both have been investigated. Commonly used natural hydrogels include collagen type I, gelatin, alginate, chitosan, agarose, and hyaluronic acid (HA) [20]. Synthetic hydrogels employed in microfluidic systems include PEG and PAA [20]. For vascular models and microvascular-on-chip platforms, natural hydrogels and combination of different natural polymers have been the preferred choice. Agarose hydrogels have been employed to build perfusable microfluidic networks [21]. Similarly, agarose/gelatin composites were used to fabricate a microvasculature-on-a-chip platform, with stiffness mimicking the native blood-vessel intima, basement membrane functionality, and perfusable networks [22]. HA and collagen hydrogels incorporated in microfluidic chips were reported to improve EC adhesion, migration, and proliferation: a chemical gradient was modeled in a PDMS microfluidic channel by simulating VEGF distribution during cellular interactions. HUVECs were seeded in two separate channels and collagen type I was coated in parallel channels with VEGF gradients. The study reported sprouting angiogenesis from endothelial monolayer (HUVECs) into the collagen-coated regions [23]. In light of guiding ECs towards sprouting angiogenesis, our work presented in **Chapter 3.2** demonstrated the potential of polysaccharide hydrogels and Caf1-YIGSR/VEGF in achieving specific EC angiogenic behavior. Therefore, we strongly believe that the developed hydrogels could eventually be integrated into microfluidic devices to develop *in vitro* vascular models for tissue engineering and regenerative medicines.

5. GENERAL CONCLUSION

5. General Conclusion

Vascularization plays an essential role in physiological conditions at both the macroscale and the microscale. Considerable efforts in the biomedical field have demonstrated the feasibility to engineer complex, dense, and thick vascularized organ-specific models. Nevertheless, the integration of a functional vascular network in bioconstructs remains a major challenge in tissue engineering and regenerative medicines. The development of *in vitro* vascularized models with physiologically relevant outcomes is an essential starting point towards successful research to clinical translation.

This doctoral project aimed to develop a novel polysaccharide-based hydrogel that promote vessel formation as a potential *in vitro* model for tissue engineering applications.

In the first part, polysaccharide hydrogels with controlled microarchitecture and channel geometries were developed. The formation of microchannels mimicking the capillaries and arterioles size and geometries were demonstrated by using sacrificial templating. Further development of the material will serve to create complex microscale vessel-like structures with enhanced structural integrity inside hydrogel. In addition, we hope to improve the manufacturing protocol for better scalability and reproducibility. Overall, the strategies presented in this work provide a proof of concept and hold promise for microvasculature patterning within hydrogels.

In the second part, the developed hydrogels were further optimized to promote angiogenic behavior of endothelial cells. The hydrogels are biocompatible, non-cytotoxic, and can be functionalized with pro-angiogenic molecules synthesized from a non-animal source, rendering them non-immunogenic. Our spatial-controlled coating technique mimics endothelial guidance in sprouting angiogenesis. Overall, this work offers an alternative class of pro-angiogenic materials and a simple functionalization method that could serve as spatial guidance for cell behavior.

In the third part, the polysaccharide hydrogels, namely, pullulan, dextran, and dextran methacrylate were investigated and adapted to a microfluidic platform. This work presents a proof of concept to synthesize hydrogels, as alternative solutions to PDMS for microfluidic fabrication. Future work regarding formulation optimization, materials characterization, microfluidic characterization and integration will be conducted after this doctoral project.

In closing, we hope to contribute to the development of novel polysaccharide-based hydrogels as pro-angiogenic materials. The developed protocols are safe and simple to conduct. Freeze-dried scaffolds allow long-term storage and good handleability. The use of polysaccharides and bioactive molecules from a non-animal source offer potential for clinical translation in various biomedical applications.

6. GENERAL REFERENCES

6. References *(for General Introduction and General Discussion sections)*

[1] J. Rouwkema, B.F.J.M. Koopman, C.A.V. Blitterswijk, W.J.A. Dhert, J. Malda, Supply of nutrients to cells in engineered tissues, Biotechnol. Genet. Eng. Rev. 26 (2009) 163–178. https://doi.org/10.5661/bger-26-163.

[2] K. Ronaldson-Bouchard, G. Vunjak-Novakovic, Organs-on-a-Chip: A Fast Track for Engineered Human Tissues in Drug Development, Cell Stem Cell. 22 (2018) 310–324. https://doi.org/10.1016/j.stem.2018.02.011.

[3] P.H. King, Organ-on-a-Chip Engineered Microenvironments for Safety and Efficacy Testing, IEEE Pulse. 11 (2020) 49–50. https://doi.org/10.1109/mpuls.2020.3008454.

[4] A. Dellaquila, C. Le Bao, D. Letourneur, T. Simon-Yarza, In Vitro Strategies to Vascularize 3D Physiologically Relevant Models, Adv. Sci. 8 (2021). https://doi.org/10.1002/advs.202100798.

[5] D. Anton, H. Burckel, E. Josset, G. Noel, Three-dimensional cell culture: A breakthrough in vivo, Int. J. Mol. Sci. 16 (2015) 5517–5527. https://doi.org/10.3390/ijms16035517.

[6] S. Alhaque, M. Themis, H. Rashidi, Three-dimensional cell culture: From evolution to revolution, Philos. Trans. R. Soc. B Biol. Sci. 373 (2018). https://doi.org/10.1098/rstb.2017.0216.

[7] K. Ren, J. Zhou, H. Wu, Materials for microfluidic chip fabrication, Acc. Chem. Res. 46 (2013) 2396–2406. https://doi.org/10.1021/ar300314s.

[8] V. Mastrullo, W. Cathery, E. Velliou, P. Madeddu, P. Campagnolo, Angiogenesis in Tissue Engineering: As Nature Intended?, Front. Bioeng. Biotechnol. 8 (2020) 1–13. https://doi.org/10.3389/fbioe.2020.00188.

[9] Y. Kang, J. Chang, Channels in a porous scaffold: A new player for vascularization, Regen. Med. 13 (2018) 705–715. https://doi.org/10.2217/rme-2018-0022.

[10] J. Grenier, H. Duval, F. Barou, P. Lv, B. David, D. Letourneur, Acta Biomaterialia Mechanisms of pore formation in hydrogel scaffolds textured by freeze-drying, Acta Biomater. 94 (2019) 195–203. https://doi.org/10.1016/j.actbio.2019.05.070.

[11] X. Wang, Z. Nie, J. Chang, M.L. Lu, Y. Kang, Multiple channels with interconnected pores in a bioceramic scaffold promote bone tissue formation, Sci. Rep. 11 (2021) 1–15. https://doi.org/10.1038/s41598-021-00024-z.

[12] T. Simon-Yarza, M.N. Labour, R. Aid, D. Letourneur, Channeled polysaccharide-based hydrogel reveals influence of curvature to guide endothelial cell arrangement in vessel-like structures, Mater. Sci. Eng. C. 118 (2021) 111369. https://doi.org/10.1016/j.msec.2020.111369.

[13] W. Ye, H. Li, K. Yu, C. Xie, P. Wang, Y. Zheng, P. Zhang, J. Xiu, Y. Yang, F. Zhang, Y. He, Q. Gao, 3D printing of gelatin methacrylate-based nerve guidance conduits with multiple channels, Mater. Des. 192 (2020) 108757. https://doi.org/10.1016/j.matdes.2020.108757.

[14] M. Zhou, B.H. Lee, Y.J. Tan, L.P. Tan, Microbial transglutaminase induced controlled crosslinking of gelatin methacryloyl to tailor rheological properties for 3D printing, Biofabrication. 11 (2019). https://doi.org/10.1088/1758-5090/ab063f.

[15] D. Chimene, R. Kaunas, A.K. Gaharwar, Hydrogel Bioink Reinforcement for Additive Manufacturing: A Focused Review of Emerging Strategies, Adv. Mater. 32 (2020) 1–22. https://doi.org/10.1002/adma.201902026.

[16] S. Calixto, N. Ganzherli, S. Gulyaev, S. Figueroa-Gerstenmaier, Gelatin as a photosensitive material, Molecules. 23 (2018) 1–22. https://doi.org/10.3390/molecules23082064.

[17] S. Mohanty, L.B. Larsen, J. Trifol, P. Szabo, H.V.R. Burri, C. Canali, M. Dufva, J. Emnéus, A. Wolff, Fabrication of scalable and structured tissue engineering scaffolds using water dissolvable sacrificial 3D printed moulds, Mater. Sci. Eng. C. 55 (2015) 569–578. https://doi.org/10.1016/j.msec.2015.06.002.

[18] B. Pan, L. Shao, J. Jiang, S. Zou, H. Kong, R. Hou, Y. Yao, J. Du, Y. Jin, 3D printing sacrificial templates for manufacturing hydrogel constructs with channel networks, Mater. Des. 222 (2022) 111012. https://doi.org/10.1016/j.matdes.2022.111012.

[19] Q. Zou, B.E. Grottkau, Z. He, L. Shu, L. Yang, M. Ma, C. Ye, Biofabrication of valentine-shaped heart with a composite hydrogel and sacrificial material, Mater. Sci. Eng. C. 108 (2020) 110205. https://doi.org/10.1016/j.msec.2019.110205.

[20] A. Autissier, C. Le Visage, C. Pouzet, F. Chaubet, D. Letourneur, Fabrication of porous polysaccharide-based scaffolds using a combined freeze-drying/cross-linking process, Acta Biomater. 6 (2010) 3640–3648. https://doi.org/10.1016/j.actbio.2010.03.004.

[21] S. Lanouar, R. Aid-Launais, A. Oliveira, L. Bidault, B. Closs, M.N. Labour, D. Letourneur, Effect of cross-linking on the physicochemical and in vitro properties of pullulan/dextran microbeads, J. Mater. Sci. Mater. Med. 29 (2018). https://doi.org/10.1007/s10856-018-6085-x.

[22] M.-N. Labour, C. Le Guilcher, R. Aid-Launais, N. El Samad, S. Lanouar, T. Simon-Yarza, D. Letourneur, Development of 3D Hepatic Constructs Within Polysaccharide-Based Scaffolds with Tunable Properties, Int. J. Mol. Sci. Artic. (n.d.). https://doi.org/10.3390/ijms21103644.

[23] E. Campodoni, M. Montanari, S.M. Dozio, E.B. Heggset, S. Panseri, M. Montesi, A. Tampieri, K. Syverud, M. Sandri, Blending Gelatin and Cellulose Nanofibrils : Biocomposites with Tunable Degradability and Mechanical Behavior, (n.d.).

[24] ASTM International, Polymeric Scaffolds for use in tissue-engineered medical products, (2019). https://doi.org/10.1520/F2450-18.

[25] A. Abed, N. Assoul, M. Ba, S.M. Derkaoui, P. Portes, L. Louedec, P. Flaud, I. Bataille, D. Letourneur, A. Meddahi-Pellé, Influence of polysaccharide composition on the biocompatibility of pullulan/dextran-based hydrogels, J. Biomed. Mater. Res. - Part A. 96 A (2011) 535–542. https://doi.org/10.1002/jbm.a.33007.

[26] Jerôme Grenier, Hydrogel poreux pour la reconstruction osseuse : élaboration, caractérisation et mise en œuvre dans un bioréacteur à perfusion, Université Paris-Saclay, 2019. https://tel.archives-ouvertes.fr/tel-02638200.

[27] S. Lanouar, Conception and validation of new tridimensional porous matrices for cutaneous wound healing and regeneration, Université Sorbonne Paris Nord, 2020. https://www.theses.fr/2020PA131016.

[28] C. Wei, N.G. Solanki, J.M. Vasoya, A. V. Shah, A.T.M. Serajuddin, Development of 3D Printed Tablets by Fused Deposition Modeling Using Polyvinyl Alcohol as Polymeric Matrix for Rapid Drug Release, J. Pharm. Sci. 109 (2020) 1558–1572. https://doi.org/10.1016/j.xphs.2020.01.015.

[29] P. Siemiński, Introduction to fused deposition modeling, Addit. Manuf. (2021) 217–275. https://doi.org/10.1016/B978-0-12-818411-0.00008-2.

[30] Ultimaker, Difference between AA 0.4 and BB 0.4 nozzle - Ultimaker 3D printers - Ultimaker Community of 3D Printing Experts, (n.d.). https://community.ultimaker.com/topic/21217-difference-between-aa-04-and-bb-04-nozzle/ (accessed October 27, 2022).

[31] D. Fischer, C. Eßbach, R. Schönherr, D. Dietrich, D. Nickel, Improving inner structure and properties of additive manufactured amorphous plastic parts: The effects of extrusion nozzle diameter and layer height, Addit. Manuf. 51 (2022). https://doi.org/10.1016/j.addma.2022.102596.

[32] Shop3DUniverse, Which Ultimaker Print Cores Should I Use?, (n.d.). https://support.shop3duniverse.com/portal/en/kb/articles/which-ultimaker-print-cores-should-i-use (accessed October 27, 2022).

[33] G.M. Whitesides, The origins and the future of microfluidics, Nat. 2006 4427101. 442 (2006) 368–373. https://doi.org/10.1038/nature05058.

[34] A.G. Niculescu, C. Chircov, A.C. Bîrcă, A.M. Grumezescu, Fabrication and applications of microfluidic devices: A review, Int. J. Mol. Sci. 22 (2021) 1–26. https://doi.org/10.3390/ijms22042011.

[35] S.I. Hamdallah, R. Zoqlam, P. Erfle, M. Blyth, A.M. Alkilany, A. Dietzel, S. Qi, Microfluidics for pharmaceutical nanoparticle fabrication: The truth and the myth, Int. J. Pharm. 584 (2020) 119408. https://doi.org/10.1016/J.IJPHARM.2020.119408.

[36] N. Wongkaew, M. Simsek, C. Griesche, A.J. Baeumner, Functional Nanomaterials and Nanostructures Enhancing Electrochemical Biosensors and Lab-on-a-Chip Performances: Recent Progress, Applications, and Future Perspective, Chem. Rev. 119 (2019) 120–194. https://doi.org/10.1021/acs.chemrev.8b00172.

[37] P. Sengupta, K. Khanra, A.R. Chowdhury, P. Datta, Lab-on-a-chip sensing devices for biomedical applications, Elsevier Ltd, 2019. https://doi.org/10.1016/B978-0-08-102420-1.00004-2.

[38] J. Weigle, Bernhard; Domingo, Gonzalo; LaBarre, Paul; Gerlach, Towards non- and minimally instrumented, microfluidics-based diagnostic devices, 8 (2008) 1–30. https://doi.org/10.1039/b811314a.Towards.

[39] A. Anbari, H.T. Chien, S.S. Datta, W. Deng, D.A. Weitz, J. Fan, Microfluidic Model Porous Media: Fabrication and Applications, Small. 14 (2018). https://doi.org/10.1002/smll.201703575.

[40] A. Olanrewaju, M. Beaugrand, M. Yafia, D. Juncker, Capillary microfluidics in microchannels: From microfluidic networks to capillaric circuits, Lab Chip. 18 (2018) 2323–2347. https://doi.org/10.1039/c8lc00458g.

[41] J.B. Nielsen, R.L. Hanson, H.M. Almughamsi, C. Pang, T.R. Fish, A.T. Woolley, Microfluidics: innovations in materials and their fabrication and functionalization, Anal. Chem. 92 (2020) 150–168. https://doi.org/10.1021/acs.analchem.9b04986.

[42] A. Shakeri, N.A. Jarad, A. Leung, L. Soleymani, T.F. Didar, Biofunctionalization of Glass- and Paper-Based Microfluidic Devices: A Review, Adv. Mater. Interfaces. 6 (2019) 1–16. https://doi.org/10.1002/admi.201900940.

[43] V.S. Cabeza, High and Efficient Production of Nanomaterials by Microfluidic Reactor Approaches, Adv. Microfluid. - New Appl. Biol. Energy, Mater. Sci. (2016). https://doi.org/10.5772/64347.

[44] M. James, R.A. Revia, Z. Stephen, M. Zhang, Microfluidic synthesis of iron oxide nanoparticles, Nanomaterials. 10 (2020) 1–19. https://doi.org/10.3390/nano10112113.

[45] F. Akther, P. Little, Z. Li, N.-T. Nguyen, H.T. Ta, Hydrogels as artificial matrices for cell seeding in microfluidic devices, (2020). https://doi.org/10.1039/d0ra08566a.

[46] C.F. Guimarães, L. Gasperini, A.P. Marques, R.L. Reis, The stiffness of living tissues and its implications for tissue engineering, Nat. Rev. Mater. 5 (2020) 351–370. https://doi.org/10.1038/s41578-019-0169-1.

[47] J. Liu, H. Long, D. Zeuschner, A.F.B. Räder, W.J. Polacheck, H. Kessler, L. Sorokin, B. Trappmann, Synthetic extracellular matrices with tailored adhesiveness and degradability support lumen formation during angiogenic sprouting, Nat. Commun. 12 (2021). https://doi.org/10.1038/s41467-021-23644-5.

[48] M.B. Chen, J.A. Whisler, J. Fröse, C. Yu, Y. Shin, R.D. Kamm, On-chip human microvasculature assay for visualization and quantification of tumor cell extravasation dynamics, Nat. Protoc. 12 (2017) 865–880. https://doi.org/10.1038/nprot.2017.018.

[49] D. Sharma, W. Jia, F. Long, S. Pati, Q. Chen, Y. Qyang, B. Lee, C.K. Choi, F. Zhao, Polydopamine and collagen coated micro-grated polydimethylsiloxane for human mesenchymal stem cell culture, Bioact. Mater. 4 (2019) 142–150. https://doi.org/10.1016/j.bioactmat.2019.02.002.

[50] M.N. Labour, C. Le Guilcher, R. Aid-Launais, N. El Samad, S. Lanouar, T. Simon-Yarza, D. Letourneur, Development of 3D hepatic constructs within polysaccharide-based scaffolds with tunable properties, Int. J. Mol. Sci. 21 (2020) 1–20. https://doi.org/10.3390/ijms21103644.

[51] T. Le Guilcher, Camille; Franck, Grégory; Dellaquila, Alessandra; Labour, Marie-Noelle; Aid, Rachida; Tordjmann, Thierry; Letourneur, Didier; Simon-Yarza, Engineered human liver based on pullulan-dextran hydrogel promotes mice survival after liver failure, (2022).

[52] E. Korzhikova-Vlakh, M. Antipchik, T. Tennikova, Macroporous polymer monoliths in thin layer format, Polymers (Basel). 13 (2021). https://doi.org/10.3390/polym13071059.

[53] H. Yuk, T. Zhang, S. Lin, G.A. Parada, X. Zhao, Tough bonding of hydrogels to diverse non-porous surfaces, Nat. Mater. 15 (2016) 190–196. https://doi.org/10.1038/nmat4463.Tough.

[54] Y. Zhu, D. Sazer, J.S. Miller, A. Warmflash, Rapid fabrication of hydrogel micropatterns by projection stereolithography for studying self-organized developmental patterning, PLoS One. 16 (2021) 1–13. https://doi.org/10.1371/journal.pone.0245634.

[55] I. Urbanova, F. Svec, Monolithic polymer layer with gradient of hydrophobicity for separation of peptides using two-dimensional thin layer chromatography and MALDI-TOF-MS detection, J. Sep. Sci. 34 (2011) 2345–2351. https://doi.org/10.1002/jssc.201100202.

[56] S.J.P. Marlton, B.I. McKinnon, N.S. Hill, M.L. Coote, A.J. Trevitt, Electrostatically Tuning the Photodissociation of the Irgacure 2959 Photoinitiator in the Gas Phase by Cation Binding, J. Am. Chem. Soc. 143 (2021) 2331–2339. https://doi.org/10.1021/jacs.0c11978.

7. ANNEXES

7. ANNEXES

7.1. Annex 1. Bibliography review (PDF proof)

REVIEW

ADVANCED SCIENCE Open Access

www.advancedscience.com

In Vitro Strategies to Vascularize 3D Physiologically Relevant Models

Alessandra Dellaquila, Chau Le Bao, Didier Letourneur, and Teresa Simon-Yarza**

Vascularization of 3D models represents a major challenge of tissue engineering and a key prerequisite for their clinical and industrial application. The use of prevascularized models built from dedicated materials could solve some of the actual limitations, such as suboptimal integration of the bioconstructs within the host tissue, and would provide more in vivo-like perfusable tissue and organ-specific platforms. In the last decade, the fabrication of vascularized physiologically relevant 3D constructs has been attempted by numerous tissue engineering strategies, which are classified here in microfluidic technology, 3D coculture models, namely, spheroids and organoids, and biofabrication. In this review, the recent advancements in prevascularization techniques and the increasing use of natural and synthetic materials to build physiological organ-specific models are discussed. Current drawbacks of each technology, future perspectives, and translation of vascularized tissue constructs toward clinics, pharmaceutical field, and industry are also presented. By combining complementary strategies, these models are envisioned to be successfully used for regenerative medicine and drug development in a near future.

1. Introduction

In physiological conditions, the tissues of the human body are vascularized thanks to an abundant network of blood vessels, known as the vascular network. Human vasculature has essential biological functions, such as nutrients and gas exchange, metabolic waste removal, and homeostasis maintenance.[1,2] Its role is fundamental at the macro as well as at the microscale, where a diffusion limit of oxygen and nutrients has been reported to be around 200 µm,[3,4] meaning that the cells located farther from a capillary undergo hypoxia and apoptosis. Thus, vascularization plays a pivotal role in achieving physiologically relevant tissue and organ substitutes for tissue engineering (TE) and regenerative medicine applications. Despite the unprecedent advancements of tissue engineering in the last decades, the integration of a functional vascular network in tissue constructs still represents a challenge that hampers an efficient and fast scale-up toward the clinical application.

In bioengineered models, the presence of vasculature would ensure the proper exchanges, preventing cellular death in constructs thicker than 200 µm and contribute in mimicking the tissue physiology and cell microenvironmental cues. Overall, a functional capillary network would allow for a long-term maintenance of the construct in terms of viability, morphology, and functionality. Furthermore, organ-specific vasculature has shown to strongly affect the behavior of the parenchymal cells and to drive organ-related biological events.[5] Vasculature plays a key role also in many diseases, such as cancer metastasis, atherosclerosis, or tumor angiogenesis.[6] For in vitro studies, the use of vascularized models could give more realistic insights of human response to drug testing, toxicology assays, or in pathological models.[7] Particularly in the pharmaceutical field, the urgent need to speed up the drug development process, lower R&D costs, and overcome the use of inadequate animal models strongly relies on the development of more predictive and clinically accurate systems.[8–10] In regenerative medicine, the implantation of prevascularized constructs compared to constructs that spontaneously vascularize in situ would enhance the grafting to the host tissue and fasten its regeneration. Moreover, although the successful implantation of thin constructs like skin has been reported, the formation of abundant and functional vascular network is a key prerequisite for the generation of thick and metabolically active organs, such as liver, heart, or kidney.[2] In fact, the

A. Dellaquila, C. Le Bao, Prof. D. Letourneur, Dr. T. Simon-Yarza
Université de Paris
INSERM U1148
X Bichat Hospital
Paris F-75018, France
E-mail: alessandra.dellaquila@inserm.fr; teresa.simon-yarza@inserm.fr
A. Dellaquila
Elvesys Microfluidics Innovation Center
Paris 75011, France
A. Dellaquila
Biomolecular Photonics
Department of Physics
University of Bielefeld
Bielefeld 33615, Germany
C. Le Bao
Université Sorbonne Paris Nord
Galilée Institute
Villetaneuse F-93430, France

The ORCID identification number(s) for the author(s) of this article can be found under https://doi.org/10.1002/advs.202100798

DOI: 10.1002/advs.202100798

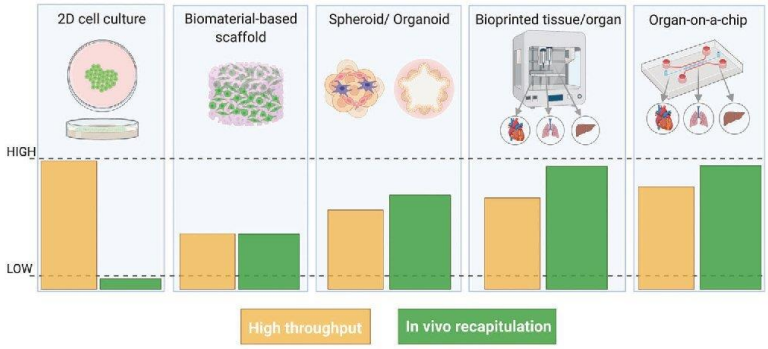

Figure 1. Evolution of tissue engineering platforms from 2D to 3D models. The bottom panel shows the comparison of model throughput versus physiological relevance: the in vivo recapitulation increases when moving from 2D cell cultures to 3D models and the throughput of complex models can be enhanced by means of automated bioprinting processes or parallel microfluidics. Created with BioRender.com.

host vasculature needs time to integrate and vascularize the implanted tissue and the use of avascular scaffolds could be inefficient due to the impossibility to be instantly perfused. The implantation of prevascularized scaffolds would thus represent one of the most favorable strategies for regenerative medicine purposes.

Many efforts have been conducted over the past years to build 3D physiologically relevant models that could fully recapitulate the tissues and organs functioning. The traditional 2D cell culture systems on polystyrene surfaces, which have been the gold standard of in vitro models for many decades, are unable to mimic the in vivo conditions. Tissue engineering has thus developed a plethora of 3D cell culture models, which have proven to be more physiologically relevant compared to 2D cell culture, providing accurate results in biological studies, such as in vivo-like cell viability, morphology, differentiation, and proliferation, as well as cellular response to stimuli, protein synthesis, and drug metabolism (**Figure 1**).[11]

In recent decades, some research lines have thus moved from culturing of single cell types on flat and rigid substrates, to the coculture of cells, first in 2D (i.e., Transwell systems) and later in 3D, with the introduction of spheroids and organoids models. Complex physiological conditions, such as blood flow, oxygen gradients, or mechanical stimuli, can be mimicked nowadays by using microfluidic devices, that allow for perfusion of cells by means of microchannels networks. In parallel, new biomaterials have been developed to mimic the cell niche, with advancements from 2D culture on extracellular matrix (ECM) gels (i.e., Matrigel) to 3D scaffolds with tunable physical–chemical and mechanical properties.[12–14] These systems have been extensively used as in vitro models consisting of multiple cell types and the combination with bioreactors has allowed researchers to provide the cells with physiological-like biochemical and mechanical cues. Recently, these in vitro models have often adopted the emerging strategy of 3D bioprinting to engineer more complex systems, eventually replacing the conventional fabrication methods. The synergistic use of these technologies would allow for a precise control of the cell culture conditions and the microenvironment and it would represent a key strategy to engineer biostructures that mirror human tissues and organs while ensuring high throughput, fundamental for the translation of these models toward their application in industrial and clinical settings. Nevertheless, lacking or inefficient perfusion and vascularization remains one of the main limitations of tissue engineered constructs as the need for vascularization exists from the moment the tissue-engineered constructs are assembled in vitro, to the moment when they are implanted in a patient.[15]

In this review, we discuss the latest advancements on vascularization strategies in tissue engineering, focusing on different approaches, namely, organs-on-a-chip (OOaC), spheroids, organoids, and 3D bioprinted tissues. After a brief overview of the physiological properties of the vascular network, we describe the fabrication techniques used to engineer prevascularized 3D physiologically relevant tissue and organ models. Finally, we critically discuss the current technical limitations and evaluate some perspectives for industrial and clinical applications.

2. Physiological Properties of the Vascular Network

The vasculature is a network of blood vessels consisting of the arterial system, the venous system, and the microcirculation (**Figure 2a**). The arterial system, composed of arteries and arterioles, distributes oxygenated blood from the lungs while the venous system, composed of veins and venules, returns low oxygenated blood to the heart. Separating these two systems is the microcirculation, where nutrients and cellular wastes exchange is carried out by the capillaries. The distinct anatomy and size of the blood vessels are dictated by the different physiological functions they play. To withstand high blood pressures and shear stress, the larger vessels, namely, arteries and veins, are composed of three layers. The external layer, called tunica adventitia, is mainly composed of collagen and nerve fibers, with a protective and support function. The middle layer, tunica media, is composed of smooth muscle cells (SMCs) and elastic connective tissue, responsible for vasodilation and vasocontraction. The inner layer, tunica intima, is the lumen wall, lined with endothelial cells (ECs) and surrounded by a thin basement membrane.[16,17] The arteries and veins are large diameter vessels, ranging from 25 mm

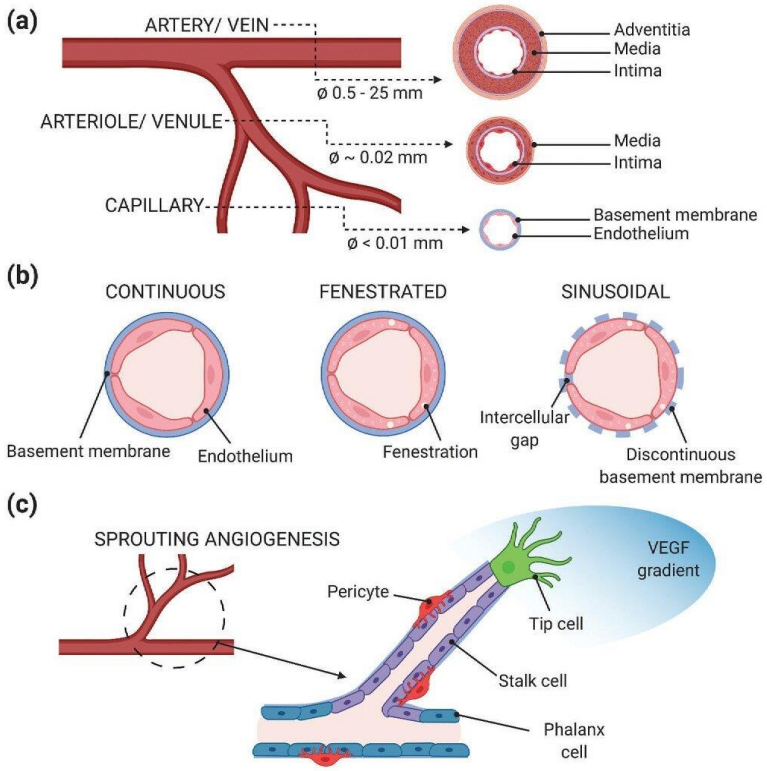

Figure 2. Physiological properties of the vascular network. a) Anatomical properties and dimensions of the human vasculature. b) Phenotypic heterogeneity of organ-specific endothelium. c) Differentiated role of endothelial cells during angiogenesis. Created with BioRender.com.

for the aorta and about 2 mm for the pulmonary veins to hundreds of micrometers for the smallest arteries and veins. While moving down into the vascular tree, the blood pressure decreases and less elasticity is needed: that is why arterioles, with a size of 10–100 µm, are composed of the tunica media and intima only and the capillaries (less than 5 µm) are composed of a single ECs monolayer. It is interesting to notice that with the decrease of the vessels size, the vascular wall also becomes thinner. At the tissue level, the anatomy is extremely complex: in healthy conditions, the capillary density is about 300–400 capillaries mm^{-3} in skeletal muscles and above 2000 capillaries mm^{-3} in myocardium, brain, liver, and kidney.[18] Furthermore, the parenchymal tissues are composed of cells at high concentration, of about 10^5 cells mm^{-3}.[19,20] Due to its direct contact with blood, the endothelium participates in numerous physiological functions including selective barrier membrane, thrombosis prevention, blood pressure regulation, and angiogenesis.[21] Although ECs in different regions of the body fulfil similar physiological demands, heterogeneity in their morphology, function, gene expression, and antigen composition has been reported.[22,23] Specifically, the morphology of the endothelium varies to adapt to the specific functions of their underlying tissue (Figure 2b). Most of the vessels of the brain, lungs, and skeletal muscles, present a continuous endothelium, where ECs are held together by tight junctions and a continuous basement membrane, allowing mainly for water and ion exchange. For organs that are involved in filtration and secretion (i.e., exocrine and endocrine glands, intestinal villi, kidney glomeruli, choroid in the eyes, and a subpopulation of renal tubules), the endothelium is fenestrated. These fenestrations, or pores, exist along with tight junctions in the endothelial lining, and their permeability can vary depending on the underlying tissue needs. For the vessels in the liver, spleen, and bone marrow, the endothelium is sinusoidal or discontinuous, where the lining has larger fenestration (100–200 µm), extensive intercellular gaps, and an incomplete basement membrane.[21]

For the development of more biomimetic vascularization strategies, we summarize here the main aspects of the two key biological processes through which neovascularization occurs: vasculogenesis and angiogenesis. Vasculogenesis is the process in which de novo blood vessels are generated from endothelial precursors, the angioblasts, in the embryo. Once the primitive vascular network is formed, more blood vessels arise from preexisting ones and expand through the angiogenesis process. During angiogenesis, ECs are activated through a complex cascade of

proangiogenic signals and undergo division, sprouting, branching, and lumen formation to form a network of arteries and veins. Currently, most vascularization approaches intended for clinical applications focus on the latter phenomenon. ECs demonstrate a structural and functional heterogeneity during angiogenesis, when they differentiate into two phenotypes, known as tip cells and stalk cells. Tip cells produce filopodia, which explore and perceive local signals from the environment, while guiding new vessel sprouts and forming connections with neighboring cells to build vessel loops.[24–26] In contrast, stalk cells follow tip cells and proliferate to support sprout elongation and lumen morphogenesis and secrete basement membrane components, which further stabilize newly formed vessels (Figure 2c).[27] The phenotypic differentiation of ECs is a transient and reversible process, modulated by complex signaling pathways, as the interplay between the vascular endothelial growth factor (VEGF) and Notch signaling.[28,29] Tip cell migration is regulated by VEGF gradients while the Notch signaling is essential for stalk cell barrier function, polarity, and lumen formation. New vascular network connections are then stabilized through the recruitment of pericytes and vascular smooth muscle cells, followed by the deposition of ECM. Once the vessels have been perfused, ECs switch to quiescent state (phalanx phenotype), where they are immobile and nonproliferating and promote vascular stability through increased cell adhesion and reduced response to VEGF signals. Nevertheless, quiescent ECs maintain their plasticity to sense and respond to angiogenic signals.[30] We refer the reader to existing reviews for a detailed overview of the angiogenetic process.[27,31,32]

3. Requirements for the Fabrication of Engineered Vascularized Tissues

Based on the morphological and physiological aspects illustrated so far, the engineering of functional vascularized constructs should fulfill several parameters:

i) The artificial vessels should have circular cross-section to guarantee optimal cell seeding and physiological-like shear stress, fundamental to maintain healthy endothelial phenotype.[26,33,34]
ii) The bioengineered vascular network should be branched and multiscale as it is in vivo, with larger vessels branching into capillaries to ensure a proper blood flow and gas and nutrients exchange at the microscale. The presence of large vessels (hundreds of micrometers) is also required when the artificial network needs to be surgically anastomosed to the host vasculature.[3]
iii) For vessels other than capillaries, a multilayered structure should be recreated in vitro and include not only the endothelium composing the tunica intima but also the other cellular components as the SMCs. Coaxial technology holds great promise for the fabrication of the different vessel layers, as we will illustrate in Sections 4.1.1 and 4.3.2.
iv) The tissue construct should take into account the organ-specific morphology of the vascular endothelium (i.e., continuous, fenestrated or sinusoidal ECs), which regulates the barrier properties and the interaction between the parenchymal tissue and the blood.[35] This prerequisite would necessarily require an accurate selection of cell sources, preferring primary cells over cell lines, further complicating the challenge.
iv) The in vitro vasculature microenvironment should integrate basement membrane proteins, as laminin and collage type IV, and other ECM components (fibronectin, glycosaminoglycans, ...),[14,36] which actively influence the endothelial barrier function, differentiation, and proliferation during angiogenesis as well as tissue maintenance and remodeling.[37–41]
v) The in vitro vasculature should be perfused to ensure adequate cell survival and tissue functioning. The perfusion parameters of the vascular network should mirror the hemodynamics and blood flow properties:[42] pulsatile flow should be applied for vessels mimicking the arteries and laminar flow in the microcirculatory system, with shear stresses below 10 dyne cm^{-2}, values have shown to influence ECs cytoskeleton remodeling and nitric oxide levels.[43] The mechanical properties of the surrounding tissue and ECM components should be designed to match the physiological values.[44–47]
vi) The prevascularized model should mimic the in vivo capillary density and cellular concentration to respect the 200 µm diffusion limit and build functional dense and highly vascularized tissue substitutes or in vitro platforms.

4. Vascularization Approaches for Physiologically Relevant 3D Models

In this section, the fabrication strategies to prevascularize 3D physiologically relevant tissues are illustrated, classifying the vascularized models in microfluidic-based, 3D cell culture (spheroids and organoids), and 3D bioprinted constructs. The fabrication methods described here, the features of each 3D approach, and their applications are summarized in **Table 1**. It is worth highlighting that some of these approaches are used also as fabrication strategies for other models; in particular, bioprinting is currently used for engineering microfluidic platforms and 3D cell cultures and microfluidic devices have been used for culturing and vascularizing spheroids and organoids. Here, the vascularization strategies of each model are discussed separately while the recent trend toward the combination of these techniques is discussed in Section 4.4 about hybrid strategies.

4.1. Vascularization Techniques for Microfluidic-Based Models

In the last decade, microfluidics has emerged as relevant technology to build 3D in vitro microphysiological systems for the study of human pathophysiology and drug development.[48,49] The capability of engineering perfusable channels in microfluidic devices makes this technology particularly interesting to generate vascular networks in vitro and important efforts have been conducted to recreate and integrate microvasculature in OOaC models.[50] The recent combination with tissue engineering approaches and biomaterials has accelerated the transition from traditional nonbiomimetic materials (glass, silicon, and polydimethylsiloxane (PDMS)) and 2D cell culture to 3D ECM-like hydrogel-based platforms.[17,51] Microfluidic-based vascular models have been used to study the response of endothelium to a plethora of stimuli under both physiological and

Table 1. Fabrication strategies for each vascularized 3D model, comparison of their properties, and main applications. SL: soft lithography; T: templating; B: bioprinting; EB: extrusion-based; DB: droplet-based; LAB: laser-assisted; Vat-P: vat photopolymerization. Created with Biorender.com.

	Vascularized 3D model		
	Microfluidic-based	3D cell culture	Bioprinted
Fabrication strategy	• Soft lithography • Templating • Bioprinting	• ECM scaffolding • Hanging drop • Low adherent plate • Bioreactor-based • Magnetic levitation • Micropatterning • Microfluidics • Bioprinting	• Extrusion-based • Laser-based • Inkjet-based • Vat photopolymerization
Vessel geometry	• Rectangular cross-section (SL) • Straight circular channels (T) • Branched microvasculature (T, B)	Capillary-like structures in vitro	Tubular interconnected channels
Vessel dimensions	Hundreds to tens of micrometers (>30 µm)	Hundreds to tens of micrometers	• Tens of micrometers (Vat-P) • Hundreds of micrometers (EB, DB) • Hundreds to tens of micrometers (LAB)
Microenvironment	Possibility to integrate ECM proteins and growth factors	• Cell–cell interactions • Possible to integrate ECM proteins and growth factors	Possibility to integrate ECM proteins and growth factors and to print multiple cell types
Advantages	• Physiological shear stress • In vivo-like cues (oxygen gradient, mechanical stimuli, ...) • Modular and multiorgan platforms • Integration of sensors for monitoring on-chip	• Scalable to various cell culture platforms • Patient specific • Vascular network mimicking in vivo complexity and architecture	• Fast method • Multiple cell/materials (EB) • Thick constructs (EB) • Low cost (E, DB, Vat-P)
Disadvantages	• Use of nonbiomimetic polymers (SL) • Expensive equipment for fabrication • Multistep production • Need for external pumps	• Limited diffusion and nutrient transport as size increases • Difficult to manipulate • Need for a large number of cells to generate substantial quantity of tissue	• Low resolution (EB) • Limited cell density • Cell sedimentation during the bioprinting process (EB) • Bioink printability limits mechanical properties (EB) • High cost (LAB)
Application	• Disease modeling • Drug discovery and development • Personalized medicine	• Disease modeling • Drug discovery and development • Personalized medicine	• Clinical application • Disease modeling • Drug discovery and development • Personalized medicine

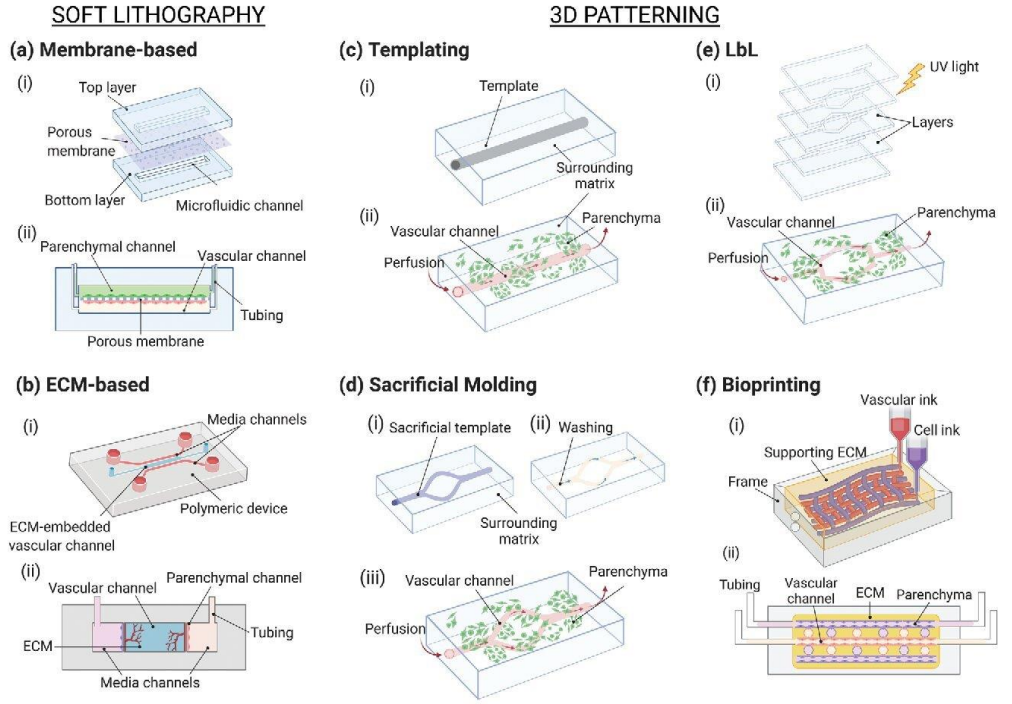

Figure 3. Schematic of the strategies used to vascularize microfluidic-based models. a,b) Soft lithography and c–f) patterning. a) Membrane-based vascularized device: i) the fabrication process consists of assembling the microfluidic layers and a porous membrane and the assembled chip with the typical sandwiched structure. b) ECM-based microfluidic platform: i) the chip usually contains one or more channels filled with ECM proteins that ii) embed the parenchymal and vascular components. c) Templating: i) a matrix is casted around the template equipment (needle, fiber), which is ii) subsequently removed to form the channel. d) Sacrificial molding: i) the patterned template is fabricated and encased in the surrounding matrix, ii) the template is removed, and iii) the device is seeded and perfused. e) Layer-by-layer: the modular layers are assembled, for instance, i) by photocrosslinking before ii) the device seeding. f) Bioprinting for microfluidics: usually performed on ECM matrix—eventually bioprinted—in which vascular and parenchymal inks can be used to i) build the tissue before ii) perfusion of the device. Created with BioRender.com.

pathological conditions,[6,52,53] the interaction between endothelium and parenchyma in organ-specific vascular platforms and to understand key factors in vasculogenesis and angiogenesis processes.[43,54] Microfluidics has been used as well for investigating the interaction between blood cells (platelets, leukocytes, and red blood cells) and vasculature and their response to mechanical or biochemical cues, which cannot be studied with static traditional in vitro platforms.[55–58]

4.1.1. Strategies to Create Vasculature On-Chip

The vascularization approaches on-chip are commonly classified based on the fabrication method into two main categories, namely, prevascularized patterning methods and self-vascularization approaches.[1,59] Prevascularized patterning methods consist of engineering polymeric or biological materials to create a vascular-like network on-chip, which can provide physical support and guidance for cells. To form the vascular component, cells are seeded or patterned and cultured in these preformed channels (**Figure 3**). In the self-vascularization approach, ECs are embedded in a matrix and supplied with biological, chemical or mechanical cues to induce spontaneous morphogenesis of the vascular network. Self-vascularized microfluidic platforms are commonly used to study vasculogenesis and angiogenesis processes in vitro (see Section 2) and they become particularly significant in the context of vasculature-related diseases, such as cancer metastasis or atherosclerosis.[6,48] Comprehensive reviews on the topic are available.[1,17,48,60,61] In this section, we provide an overview of the main prevascularization patterning strategies used for fabricating vascularized microfluidic platforms, focusing on relevant organ-on-a-chip models integrating vasculature and discussing the current bottlenecks of this approach.

Soft Lithography Techniques: The mimicry of the vascular interface in vitro has been mainly achieved by using microfluidic platforms produced by soft lithography. This approach involves the production of a silicon or glass mold containing the

microchannel features by photolithography and using it as stamp to pattern PDMS devices by replica molding. The device is then sealed by bonding it to a substrate to create perfusable channels (Figure 3a).[5] Despite the lack of a proper 3D lumen and geometrical similarity to in vivo vasculature, these models have demonstrated to be efficient platforms to build a functional organ-vasculature interface, showing significant advantages compared to static 2D models.

Vascular Interface on a Membrane: The visionary work of Ingber's group led to the development of the most used organ-on-a-chip model nowadays. They reproduced the air–liquid interface (ALI) of the lung by culturing alveolar epithelial cells and human pulmonary microvascular ECs on two sides of a porous 10 µm thick PDMS membrane in a two-channel PDMS device.[62] Cyclic mechanical strain was applied to mimic physiological breathing by lateral vacuum channels. This simple yet functional platform was used to recreate a long-term model (>2 weeks) of the ALI, showing in vivo-like barrier permeability, enhanced production of surfactants by the epithelium when exposed to air and endothelium alignment under mechanical stretching. Exposure to cytokines and nanoparticles showed the active role of vasculature and mechanical forces under inflammatory conditions, underlying the need to integrate these components to build complex in vitro platforms capable of recreating physiological organ functions.[53]

This pioneering platform paved the way for the study of tissue-vasculature interactions in organ-specific models such as kidney,[63,64] brain and blood–brain barrier (BBB),[65–67] heart,[68,69] gut,[70,71] and liver.[72,73] Recently, a liver sinusoid on-chip was built by integrating four primary hepatic cell types from the same murine source.[73] Liver sinusoidal endothelial cells (LSECs) and Kupffer cells (KCs) were cultured on the apical side of a porous polyester membrane to mimic the sinusoidal interface. Hepatic stellate cells (HSCs) were cultured on the basolateral side and hepatocytes (HCs) were seeded on the PDMS bottom channel to recreate the Disse space and the parenchymal tissue respectively (**Figure 4**a). Shear stress was applied in the device and imaging analyses confirmed the formation of a discontinuous endothelium composed of fenestrated LSECs, typical of in vivo liver sinusoid.[5] Results showed that the presence of nonparenchymal cells (NPCs) and shear stress enhanced hepatocytes functionality and metabolism compared to HCs static monoculture and neutrophil recruitment resulted to be higher when LSECs were cultured with the other NPCs under flow. Despite the use of murine cell source and the short-term evaluation, this model reveals the synergistic effect of mechanical cues and paracrine pathways in regulating liver metabolism and its response to inflammatory conditions.

Multiorgan-on-a-Chip (MOC): A New Promising Tool for Drug Development: The growing need for accurate and reliable in vitro models for drug screening and development has led to the design of MOC platforms (also known as body-on-a-chip), that allow for the study of pharmacokinetic–pharmacodynamic (PK–PD) pathways of drugs and interactions among organ equivalents.[76] The integration of vasculature is fundamental due to the active role of microvascular circulation in maintaining homeostasis.[48,59] Novak et al. have recently engineered a vascularized eight-organ-on-a-chip (BBB, brain, skin, lung, heart, liver, intestine, and kidney) coupled with liquid-handling robotics and in situ microscopy that enabled automated culture, perfusion and control on-chip.[77] Interestingly, the device used a universal blood-like medium for the vascular compartment and a specific medium for each organ. Although the vascular component was part of each organ platform, it was not included in the connections between chips. Schimek et al. lined uniformly the connecting tubes of a MOC with primary human dermal microvascular endothelial cells (hDMECs) under pulsatile shear stress and created branching microvessels of 40 µm in diameter by two-photon laser ablation technique.[78] Similarly, PDMS tubes with tunable diameter and thickness that can mimic different blood vessel types have been endothelialized and coupled to MOC platforms and the exposure to drugs showed the formation of a responsive endothelium.[79]

ECM-Based Microfluidic Devices: Standard lithographic processes lead to rectangular or squared cross-sectioned channels, a geometry that has been proven inadequate to build functional microvasculature in vitro and to model phenomena such as coagulation.[80,81] Thus, channels with circular cross-sections have been fabricated by different strategies as micromilling of metal molds,[82] flow of nitrogen gas in a PDMS solution,[33] reflow of positive photoresists,[83] or by viscous fingering of ECM substrates, as collagen or Matrigel.[84,85] Moreover, in standard microfluidic devices, cells are cultured on flat substrates such as polymeric membranes or PDMS sheets. To address these limitations, microfabrication strategies have been adapted to create hydrogel-based microfluidic platform, for instance, by molding ECM gels upon PDMS stamps,[86,87] or embedding hydrogels in PDMS devices (Figure 3b).[66,88] In a recent work, Bang et al. engineered a BBB device with contact of astrocytes and vascular network through astrocytic endfeet to overcome the lack of direct interface of the two components in common BBB-on-chip platforms, that hampers the achievement of in vivo-like barrier permeability values (Figure 4b).[66] The PDMS device was composed of two parallel microchannels, representing the vascular and neural compartments respectively, embedded in a fibrin hydrogel and supplied with specific medium through lateral channels. In a first step, a mixture of endothelial cells (human umbilical vein endothelial cells, HUVECs) and fibroblasts was seeded in the vascular channel and vasculogenesis was induced to create the vascular network. After 3 days, the neural channel was seeded with astrocytes and neurons and the formation of functional BBB was observed within one week. Results confirmed the growth of a functional lumen, the migration of astrocytes to form a direct contact with HUVECs, permeability values comparable to in vivo coefficients and formation of synapses.

3D Patterning Methods: The recent adoption of tissue engineering fabrication methods has paved the way for engineering more sophisticated 3D in vitro vascular networks on-chip, overcoming the main drawbacks of conventional OOaC platforms, namely, the use of nonbiomimetic materials and lack of a 3D geometrical complexity.[89] Hydrogel-based devices reproducing the role of ECM in vivo offer several advantages such as tunable mechanical properties, biodegradability, control over the cellular microenvironment, and a wide choice of materials.[90] We classify

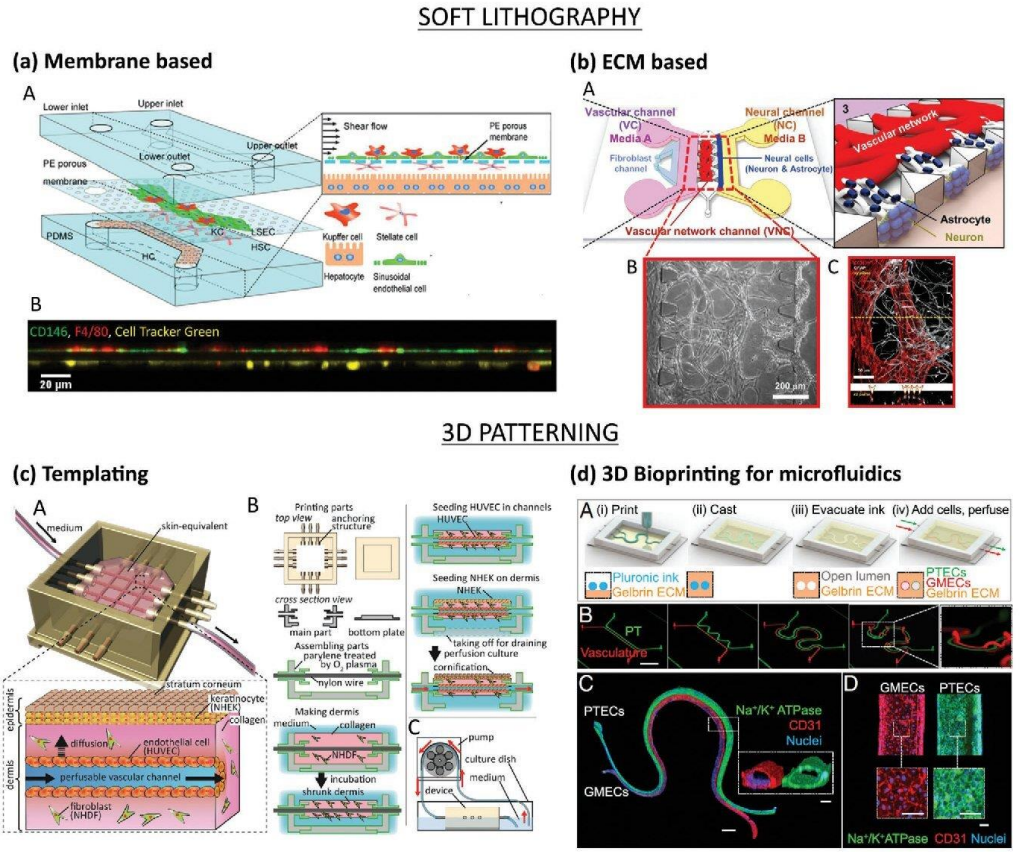

Figure 4. Microfluidic-based vascularization strategies: soft lithography (top) and 3D patterning (bottom). a) Liver sinusoid on-chip fabricated by soft lithography. LSECs and KCs were seeded on the apical side of a PE membrane while HSCs on its basolateral side and HCs on the PDMS substrate (top). Lateral view of the sinusoidal endothelium (bottom): LSECs (green) and KCs (red) on the top and HSCs (yellow) on the bottom of the membrane. Reproduced with permission.[73] Copyright 2017, The Royal Society of Chemistry. b) ECM-based vascularized BBB platform: A) HUVECs and fibroblasts were seeded in the vascular channel (VC), and neural cells (astrocytes and neurons) were seeded in the neural channel (NC). The formation of vascular network in the central vascular network channel (VNC) ensured a direct interface between the capillaries and the astrocytes through astrocytic endfeet (B,C: ECs stained in red, astrocytes stained in white). Adapted with permission.[66] Copyright 2017, Springer Nature. c) Skin-equivalent platform generated by templating: A,B) The culture device was 3D printed and filled with collagen and fibroblasts to form the dermis layer. After removal of the nylon wires, the hollow channel was seeded with HUVECs to form the capillary, and keratinocytes were cultured on the top of the dermis and exposed to liquid–air interface for cornification of the epidermal layer. C) Perfusion of the device via peristaltic pump. Reproduced with permission.[74] Copyright 2017, Elsevier Inc. d) Hybrid strategy: 3D printed vascularized proximal tubule model. A,B) The colocalized vascular and renal channels are both 3D printed by using a Pluronic F127-based fugitive ink within an ECM solution and different designs can be easily printed. C,D) The construct is then seeded with epithelial (green) and endothelial (red) cells. Reproduced with permission.[75] Copyright 2019, PNAS.

below the patterning methods used for microfluidics as templating, layer-by-layer (LbL) manufacturing and 3D bioprinting.

Templating Strategies: Templating, also known as micromolding, is a subtractive technique in which a material with the desired vasculature shape is embedded in a bulk matrix and subsequently removed or dissolved to create a hollow perfusable microvasculature. Microneedles and fibers have been widely used to fabricate simple vascular geometries in gels (Figure 3c). Mori et al. used needle-based micromolding to create a skin-equivalent model composed of epidermal and dermal layer and perfusable vascular channels.[74] A culture device was 3D printed and nylon wires (500 µm thickness) were used as channel templates. Collagen solution loaded with normal human dermal fibroblasts (hNDFs) was gelled to fabricate the dermal layer and, after removal of the wires, the vascular channel was formed by seeding HUVECs. The subsequent addition of normal human epidermal keratinocytes (NHEKs) on the top of the dermal layer and

exposure to the ALI enabled the formation of the stratum corneum of the epidermis (Figure 4c). Water repellency and capacitance tests confirmed the barrier function of the epidermal layer and permeability studies on the vascular channel showed the formation of a selective barrier for the diffusion of nutrients. Percutaneous absorption studies conducted by flowing caffeine and drugs in the vasculature confirmed the adequacy of the model as a platform for vascular absorption studies, fundamental in drug and cosmetics testing.

The needle-based vascularized platforms are mainly limited to straight channel geometries and some manufacturing steps (needle removal, stability of the gel after crosslinking) have to be taken into account during the design process. Sacrificial molding uses templating materials that are dissolved after the hydrogel bulk gelation and represents a versatile technique to create stable and more complex 3D vascular networks.[89] Gelatin (Gel),[91] agarose,[92] alginate,[93,94] Pluronic,[95] and poly(vinyl alcohol) (PVA)[96] have been used as sacrificial materials for creating meshes either by micromolding or 3D printing (Figure 3d and Section 4.3). Vollert et al. fabricated large ($15 \times 25 \times 3$ mm^3) perfusable engineered heart tissues for cardiac regeneration by using either straight or branched alginate fibers as lumen template.[93] The tissue was composed of a neonatal rat heart cells mix (cardiomyocytes (CMs), ECs, fibroblasts, and SMCs),[97] embedded in a fibrin matrix and ECs showed formation of an intima-like layer by spontaneously covering the vessels after alginate dissolution. The engineered tissues showed contractile forces and the continuous perfusion enhanced oxygen concentration, with a significant increase in the CMs density.

To overcome the use of potential cytotoxic dissolving agents during sacrificial molding, researchers have engineered vascular templates that can be dissolved in cell media, such as Pluronic and 3D-printed self-standing carbohydrate glass lattices and caramel templates, which have been used to create complex hierarchical networks of tubular channels with interconnected lumens and permeable walls.[98,99]

Layer-by-Layer Manufacturing: LbL represents a versatile bottom-up method for manufacturing complex 3D vasculature in vitro and consists of assembling 2D prepatterned gel slabs into multilayered (modular) 3D devices (Figure 3e).[17] Zhang et al. fabricated vascularized cardiac and hepatic constructs by stacking 25 µm thick poly(octamethylene maleate (anhydride) citrate) (POMaC) layers patterned by UV photolithography.[69,100] The presence of microholes and nanopores in the scaffold walls ensured physiological-like mass transport and cell migration and the formation of vessels with a thickness of 2–3 cells. The use of a photocrosslinkable hydrogel provided for tunable stiffness, thus creating an anisotropic construct that closely mimics the myocardium mechanical properties. The pump-free perfusion in vitro was performed by connecting the device to a custom-made bioreactor and the open configuration enabled direct access to the cellular compartments by pipetting. Culturing of the vascular network with HUVECs led to formation of a functional lumen, capable to respond to angiogenic and inflammatory stimuli and compatible with human whole blood flow. By integrating liver or heart parenchymal cells embedded in ECM, functional tissue constructs were built, exhibiting metabolic response to drug administration and contractile behavior, respectively. In vivo implantation by anastomosis confirmed the nonthrombogenic properties of the device and successful angiogenesis in a rat model.

3D Bioprinting for Microfluidics: Cells and hydrogels can be used as bioinks for direct fabrication on-chip of perfusable or vascularized models with complex geometries by means of 3D bioprinting approaches (Figure 3f). Here, we consider 3D bioprinting for fabrication of microfluidic devices as hybrid strategy, discussed in Section 4.4.

Although soft lithography, templating and additive manufacturing are commonly used for fabrication of perfusable vasculature, other methods have been explored. Heintz et al. used a laser-based degradation technique to create complex and tortuous 3D microfluidic poly(ethylene glycol diacrylate) (PEGDA) hydrogel networks from a stack image of mouse cerebral cortex vasculature.[101] The high spatial resolution offered by the technique led to microvessels with a diameter of less than 10 µm and a dense network, fundamental for providing the parenchymal tissue with nutrients and oxygen within the diffusion limit.[3] Interestingly, vascular microfluidic chips have been engineered by reversibly assembling explanted mouse arteries on automated platforms, showing the capability to study intact vessels functionality by performing immunofluorescence studies and quantitative analyses on-chip.[5,102]

Table 2 summarizes significant case studies for the microfluidic-based vascularization strategies, cited or discussed in the text. Data such as channel shape, perfusion parameters and duration of in vitro studies have been reported to provide the reader with a detailed overview of different specifications and address some drawbacks, which will be discussed in the next paragraph.

4.1.2. Limitations of Microfluidic-Based Vascularized Models

Microfluidic technology has shown great potential for the development of in vitro vascularized models for the study of the microenvironment under healthy and pathological conditions and for drugs screening and development. Soft lithography and membrane-based models represent a landmark for recreating the vascular interface and have been used to mimic complex organ-specific pathophysiological mechanisms. However, they fail in recapitulating a 3D microenvironment and the membranes, made usually of artificial polymers, prevent the direct interaction of the vascular and parenchymal components. The use of ECM-based membranes or channels has allowed researchers to move toward more physiologically relevant models,[66,106] but still soft lithography requires expensive equipment and makes the platforms often difficult to be used by a wide end-users range. Templating represents a straightforward method to create hollow channels in a matrix. Although the use of 3D additive manufacturing to print the sacrificial patterns has increased the potential of the technique in fabricating more in vivo-like networks,[94] the platforms are usually limited to relatively simple geometries and large vessels of hundreds of micrometers. These methods usually require several fabrication and seeding steps and the template removal step should be designed carefully to avoid device or cellular damage. Layer-by-layer manufacturing, offers the possibility

Table 2. Summary of case studies for microfluidic-based vascularization strategies.

Vascularization method	Organ/tissue model	Vessel caliber (d)/channel size ($h \times w$)	Channel shape	Chip composition	Cellular composition	Perfusion parameters	Duration of in vitro study	In vivo evaluation/drug testing	Refs.
Soft lithography	Liver	100 µm × 1 mm	Rectangular, straight	PDMS; PE (polyester) membrane	LSECs, HCs, KCs, HSCs (all primary from mouse)	0.1 or 0.5 dynes cm^{-2}, syringe pump	1 day	No/No	[73]
	BBB	• Vascular channel: 800 µm, vascular network: <50 µm • 35–100 µm	Rectangular, straight	• PDMS; fibrin hydrogel • PDMS; fibrin-hyaluronic acid	• HUVECs, lung fibroblasts, rat cortex neural cells • Brain microvascular ECs; HUVECs; pericytes; astrocytes	–	7 days	No/No	[66,88]
	Kidney	0.2 × 1 mm (vascular), 1 × 1 mm (urinary)	Rectangular, straight	PDMS (chip, membrane)	Glomerular ECs; hiPS-derived podocytes	0.017 dynes cm^{-2} (vascular), 0.0007 dynes cm^{-2} (urinary), peristaltic pump	8 days	No/Yes	[64]
	Intestine	0.15 × 1 mm	Rectangular, straight	PDMS (chip, membrane)	Capillary ECs or lymphatic microvascular ECs, Caco-2 intestinal epithelial cells, immune cells	0.02 dynes cm^{-2}	>7 days	No/Yes	[70]
	Multiorgan	(100 × 500 µm) to 40 µm	Rectangular, curved	PDMS	Dermal microvascular ECs	10–40 dynes cm^{-2}, on-chip micropump	Up to 4 weeks	No/No	[78]
Templating	Liver	• 300 µm (main channel) • 100–1000 µm	• Circular, straight • Circular, curved, branched	• Collagen I • GelMA	• HUVECs; hepatocytes (HepG2); MSCs • HUVECs, hepatocytes (HepG2)	• 10^{-1} dynes cm^{-2}, peristaltic pump • 50 µL h^{-1}, syringe pump	• 8 days • 7 days	• No/No • No/Yes	[19,103]

(*Continued*)

Table 2. (Continued).

Vascularization method	Organ/tissue model	Vessel caliber (d)/channel size ($h \times w$)	Channel shape	Chip composition	Cellular composition	Perfusion parameters	Duration of in vitro study	In vivo evaluation/drug testing	Refs.
	Skin	• 520 µm • 100–250 µm	• Circular • Rectangular, curved, branched	• Collagen I • Collagen I	• HUVECs, dermal fibroblasts, epidermal keratinocytes • HUVECs, iPSC-derived ECs, dermal fibroblasts, keratinocytes	• 2–3 mL h^{-1}, peristaltic pump • Syringe pump	• 10 days • 21 days for cornification, 2 days at ALI	• No/Yes • Yes/No	[74,94]
	Heart	100–500 µm	Circular	Fibrin matrix	Neonatal rat heart cells mix	20 µL h^{-1}, syringe pump	21 days	No/No	[93]
3D bioprinting	Urothelial/vascular tissue[a]	≈700 µm (inner), ≈1 mm (outer)	Circular, multilayer, flexible	Bioink: PEGOA + GelMA	Urothelial: human urothelial cells + human bladder SMCs; vascular: HUVECs + human SMCs	–	14–21 days	No/No	[104]
	Kidney	200 µm	Circular, colocalized	Gelatin + fibrin ECM; bioink: pluronic F127 + PEO	Glomerular microvascular ECs; proximal tubule epithelial cells	0.3 dynes cm^{-2}	18 days	No/Yes	[75]
	Heart	500 µm (200–900 µm)	Circular, hierarchical, multibranched	Agarose hydrogel, PCL network	Rat cardiomiocytes	Syringe pump	5 days	Yes/No	[99]
	Vasculature[a]	1.5 × 3 mm	Rectangular, straight	PMMA case, GelMA	Aortic ECs; aortic SMCs; fibroblasts	100 µL h^{-1}, peristaltic pump	7 days	No/No	[105]
Alternative strategies	LbL Liver/heart	100 × 50 to 100 µm	Rectangular, straight	POMaC, fibrin gel/Matrigel for parenchyma	Liver: HUVECs + hESC-derived hepatocytes + hMSCs; heart: HUVECs + hESC-derived CMs + hMSCs	0.6 dynes cm^{-2}, bioreactor	7 days	Yes/Yes	[69,100]
	Laser-based –	<10 µm	Tortuous, dense	PEGDA	Mouse brain ECs	10 µL min^{-1}	11 days	No/No	[101]
	Explanted vessels Brain	120 µm	Circular, physiological	PDMS	ECs, SMCs	0.5 µL min^{-1}, no external pump	–	No/Yes	[102]

[a] Bioinks containing cells.

to design more versatile and flexible platforms via a multilayer assembling process and represents a valuable technique for engineering large-scale thick constructs.[107,108] However, the precise alignment of the layers often represents a critical step in the process design. Recently, 3D bioprinting has been widely used for vascularization of biomaterials and fabrication of perfusable vessels due to its scalability, versatility, wide materials selection, and precision in engineering complex 3D cell laden constructs,[109,110] and its combined use with microfluidics will be further discussed in Section 4.4.

4.2. 3D Cell Culture Models: Spheroids and Organoids

Spheroids and organoids are 3D, multicellularized structures usually devoid of any exogenous materials. In the last decade, these structures have gained significant popularity in 3D cell culture research due to their ability to mimic the physiological conditions of cells in vivo. Although the two terms have been used interchangeably, there are fundamental differences and application varieties between them. Spheroids are established from simple clusters of cells, ranging from immortalized cell lines, primary cells, or fragments of human tissue.[13,111] Spheroid technology was developed based on the ability of cells to self-organize during embryonic development. This self-assembly process takes place in vitro when cells cannot attach to their biomaterial surface, hence aggregate into spherical 3D structures, namely, spheroids. Organoids are complex clusters of cells derived from stem cells such as adult stem cells, embryonic stem cells (ESCs), and induced pluripotent stem cells (iPSCs). When given a scaffolding ECM environment (usually collagen or Matrigel matrix), they self-assemble into microscopic analogs of their parent organs.[112,113] As a result, organoids are widely regarded as miniature versions of organs. Organoids retain the parental organs' genetic features over several passages, which allows for long-term in vitro expansion of cells and guaranties long-term viability.

Spheroids have shown potential in mimicking tumor tissues, which could help researchers develop more physiologically relevant cancer models, hence develop better cancer treatments. Vascularized spheroids, which can be achieved via coculture with ECs, have been employed as a model to study angiogenesis in vitro and as a prevascularization approach for tissue engineering applications.[114] However, as spheroids are formed via cell–cell adhesion, they only transiently mimic physiological cell organization.[111] In contrast, organoids formation relies on internal developmental processes, which gives rise to a higher order of self-assembly, hence, the unique ability to recapitulate in vivo physiological functions.[112] Since organoids can be derived from patient tissues, they are interesting for disease modeling, development of personalized medicine, as well as drug testing and toxicity studies (see Section 6).[115]

4.2.1. Spheroids and Organoids Generation

Spheroids are formed by culturing cells in hanging drops, round-bottom nonadherent or low adhesive substrates, and in suspension to induce self-aggregation. Alternatively, spinner flask cultures can be employed to induce spontaneous cell aggregation for the fabrication of both spheroids and organoids. In this method, cell suspension is housed inside a spinner flask bioreactor with continuous mixing via a stirring bar, which generates a convectional force that induces cell aggregates formation.

Organoid fabrication methods involve formation of 3D aggregates from stem cells, followed by embedding in a biogel such as Matrigel and culturing in a specialized mixture of media and factors to obtain specific organoid generation. To date, a wide range of organoid systems including heart, lung, brain, lung, liver, kidney, intestine, retina, etc., have been developed.[116–120]

Table 3 summarizes the different methods for the fabrication of spheroids and organoids, their advantages, and challenges. To further explore these topics, we refer the reader to published reviews.[121–124]

4.2.2. Strategies to Vascularize Spheroids and Organoids

Researchers have shown that the incorporation of ECs increases cell viability and functions in multicellular spheroids and enables the formation of rudimentary vascular networks within the spheroid structures.[138–142] The concept of using spheroids containing ECs dated back in 1998 when Korff and co-workers used EC-covered spheroids to analyze angiogenesis in vitro: ECs on the spheroids surface exhibited quiescent phenotype, which increased their sensitivity to angiogenic stimulation and differentiation.[142] The incorporation of ECs in the coculture system mimics the physiological interactions between ECs and other cell types, which consequently preserves cell viability and promotes proliferation and vascularization. Along with ECs, mesenchymal stem cells (MSCs) play a key role in the angiogenic process by facilitating blood vessel stabilization and maturation.[143,144] Specifically, MSCs actively participate in angiogenesis via secretion of proangiogenic factors (i.e., VEGF, MCP-1, IL-6, etc.) and MSC-released paracrine factors are responsible for activation of the ECs angiogenic functions.[143,145] Given their multipotency, MSCs also induce direct differentiation and cell–cell interactions with endothelial lineage, suggesting that MSCs could be used to facilitate vascularization in spheroids and organoids.[144] For example, spheroids fabricated using only MSCs was found to generate vascularized spheroids with improved osteogenic differentiation and bone formation.[146] Similarly, when human mesenchymal stem cells (hMSCs) were cocultured with HUVECs, the resulting spheroids formed capillary-like vessels, hence improved adipogenic differentiation upon transplantation.[147]

In general, the strategies used to vascularize spheroids and organoids are conducted in two steps: first, the spheroids/organoids are formed by coculturing parenchymal cells with ECs and/or MSCs to induce prevascularization in vitro. Then, spontaneous vascularization is induced via in vivo transplantation in highly vascularized regions such as skin, liver, heart, lung, or brain (**Figure 5**). The coculture step can be achieved either via i) scaffold-free approach (Figure 5a), or ii) scaffold-based approach, with incorporation of a biomaterial as instructive guide (Figure 5b), discussed in the next paragraphs. Here, we consider low-adherent substrates, hanging-drop technique (in the case of spheroids) and Matrigel (in the case of organoids) as scaffold-free since they do not require additional

Table 3. Overview of spheroid and organoid formation methods.

Method	3D culture system	Description	Advantages	Challenges	Refs.
ECM scaffolding	Organoids	Stem cells are placed in Matrigel (or ECM mix) and maintained in culture	• Replicates microenvironment • Observation of cell adhesion and migration	• Lack of reproducibility using natural ECM • Synthetic ECM requires upregulating reagents	[117,125,126]
Hanging drop	Spheroids	Cells are suspended in media droplet. Cell aggregation occurs at the air–liquid interface	• Consistent • Does not require ECM • Possible to integrate array production	• Difficulties with media change • Small size • Low throughput	[127,128]
Low-adherent surfaces	Spheroids	Cells are suspended and cultured on a low-adherent plate, or hydrophilic substrates (i.e., hydrogel) to form aggregates	• Does not require ECM • Cost-effective	• Not adaptable to all cell types • Heterogeneous population	[129]
Spinning bioreactor	Spheroids and organoids	Cell suspension is housed inside a spinner flask or a bioreactor with continuous mixing. Cell aggregation is induced by convectional force	• Can generate a wide range of model sizes	• Large and heterogenous structures • Shear forces on cells	[130,131]
Magnetic levitation	Spheroids and organoids	Nanoparticles are ingested by cells, which are then placed in a low-adherent substrate. A magnet lid is used to induce cell aggregation	• Does not require ECM or media	• NPs are expensive and toxic	[132]
Bioprinting	Organoids	Additive manufacture of cytokines, cells, and ECM	• Generates complex and organized structures • Use of multiple cell types	• Bioink selection with desired characteristics	[133–135]
Micropatterning	Spheroids	Microcontact printing and soft-lithography patterning of ECM	• Structure control • Array production	• Expensive equipment • Poor reproducibility • Lack of patterning efficiency	[136]
Microfluidics	Spheroids and organoids	3D structures housed inside microstructures, integrated with microsensors	• Replicates microenvironment • Allows for nutrient delivery • Avoids necrosis • Array production	• Low cell recovery • Postcell analysis challenges	[137]

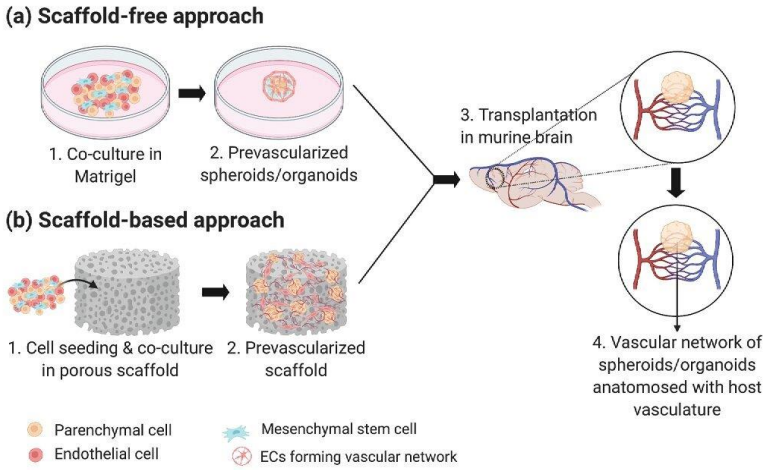

Figure 5. Schematic of the strategies used to vascularize 3D cell culture models. a) Scaffold-free approach: Coculture with ECs/MSCs to form prevascularized network. b) Scaffold-based approach: Coculture with ECs/MSCs in porous biomaterials. Both (a) and (b) can be followed by spontaneous vascularization via in vivo transplantation in highly vascularized organ such as the brain. Created with BioRender.com.

procedures, as compared to biomaterial-based scaffolds, which are synthesized in the lab. Alternative options to standard culture techniques are the incorporation of 3D printing, bioprinting, and microfluidic platforms to form vascularized spheroids and organoids. We refer the integration of several techniques as hybrid strategies for vascularization of in vitro models, including 3D cell cultures, which are discussed in Section 4.4.

Vascularization of Spheroids: Scaffold-Free Approach: Multicellular spheroids consisting of hDMECs, human osteoblasts (HOBs), and normal hNDFs were reported to have promising potential as vascularization units for bone tissue engineering.[139] Spheroids have been generated using the low-adherent surface fabrication method. Coculture spheroids with round morphology formed after 72 h, with endothelial cells showing CD31 markers. Additionally, the presence of microvessels formation within the coculture spheroids suggests prevascularization/intrinsic vascularization. The prevascularized spheroids were then harvested and transplanted into the dorsal skin of immunodeficient mice for 2 weeks. Intravital analysis of the transplanted spheroids revealed the presence of vessel-like structures: human microvascular networks grew outside of the spheroids border and eventually connected to the host vasculature.

Cocultures of ECs with other organ-specific cell types such as dental pulp stem cells (DPSCs), rat neonatal cardiomyocytes (RNCMs), rat hepatocytes, and human brain astrocytes and pericytes have also shown vascularization potential.[128,129,140,148] In Dissanayaka's study, DPSCs were cocultured with HUVECs and results showed microvascular networks forming within the in vitro spheroids.[129] Upon in vivo transplantation, the lumens of the grafts were lined with ECs and graft vessels and mouse vessels were both present in the implanted site, suggesting integration of prevascularized spheroids into the host vasculature. This study finding highlights the potential of EC-incorporated spheroids as functional vascularized units that can promote successful dental pulp regeneration.

Bhang and colleagues were among the first researchers to demonstrate the feasibility of generating spheroids using only MSCs.[149] Human cord blood MSC (hCBMSC)-derived spheroids were grown and transplanted into mouse ischemic tissue. The hCBMSC spheroids were evaluated for apoptotic signaling, angiogenesis-related signal pathways, and blood vessel formation both in vitro and in vivo. As expected, cell survival was higher in spheroids as compared to cells in monolayer culture. The spheroids improved viability of the transplanted cells and promoted angiogenesis, as evident by an increase in the number of microvessels within the spheroids.[149] Similarly, when β-cell pseudoislets were cocultured with MSCs, they exhibited insulin-producing phenotype and secreted angiogenic and anti-apoptotic proteins.[141,150] Both reports demonstrated that MSC-incorporated spheroids had enhanced viability, paracrine secretion, and vascularization after transplantation.

Coculture of EC-incorporated spheroids with fibroblasts can also enhance vascularization. Fibroblasts are essential for production precursors for the ECM and therefore, it contributes to the stabilization of the newly formed vessel-like structure.[151] Noguchi et al. developed cardiac tissue spheroids by coculturing rat neonatal ventricular cardiomyocytes (RNVCMs), human cardiac microvascular endothelial cells (HCMECs), and hNDFs (**Figure 6a**). The spheroids were then fused into a patch-like construct and transplanted into rat hearts. Results showed that microvascular networks formed inside the spheroids, both in vitro and in vivo experiments.[148]

Vascularization Strategies of Spheroids: Scaffold-Based Approach: Biomaterial-based scaffolds have also been adopted for vascularization of spheroids as instructive guides to improve spheroid function and promote angiogenesis. In one study, adipose-derived stem cells (ASCs) spheroids were covered with

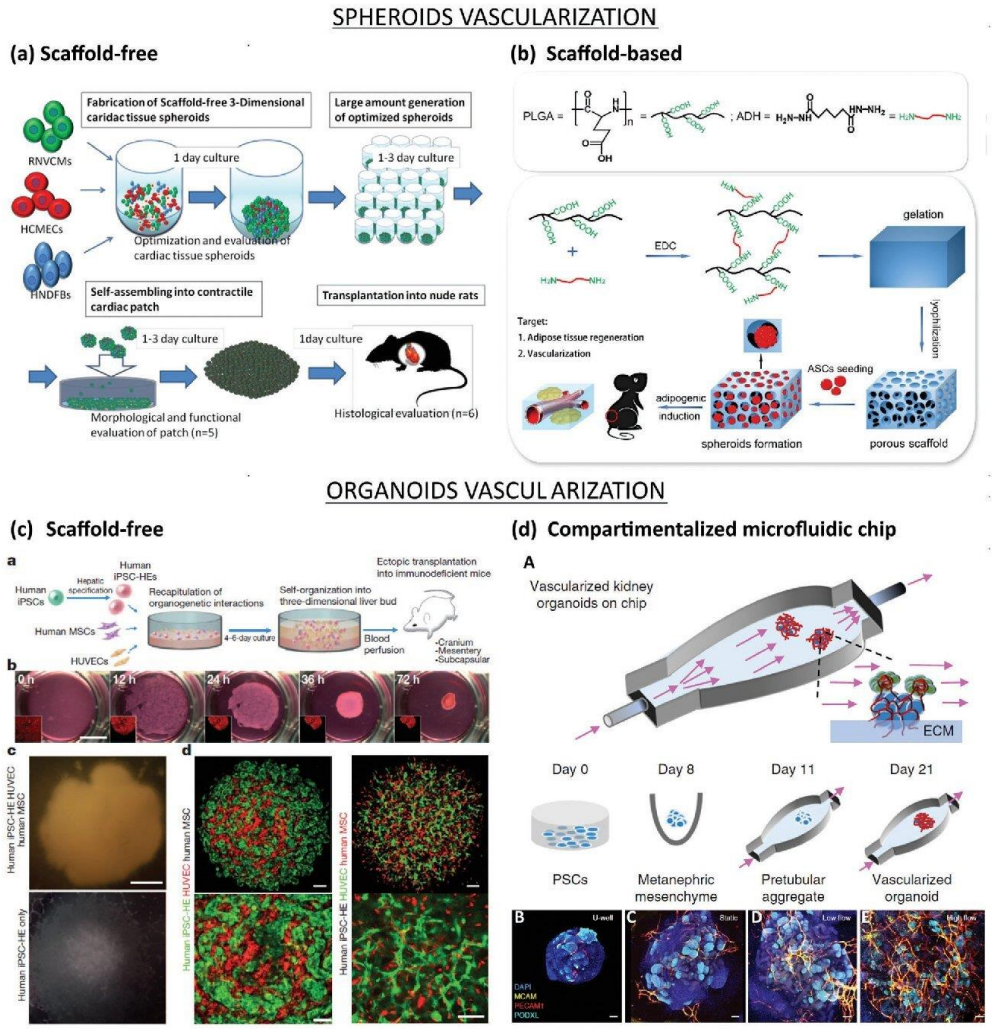

Figure 6. Vascularization approaches for spheroids (top) and organoids (bottom). a) Scaffold-free approach to vascularize spheroids. RNVCMs, HCMECs, and hNDFs were cocultured at optimal cell ratios (70%:15%:15%) and plated into ultralow attachment 96 U-well plates to form cardiac tissue spheroids. Then, the spheroids were collected and plated in low-attachment dishes, allowing them to self-organize into cardiac patch grafts under static conditions. Finally, the cardiac patch grafts were transplanted on the anterior wall of the left ventricle of arhythmic rats to induce spontaneous vascularization. Reproduced with permission.[148] Copyright 2016, Elsevier Inc. b) Scaffold-based approach to vascularize spheroids. PLGA activated by 1-ethyl-3-(3-dimethylaminopropyl) carbodiimide hydrochloride (EDC) and crosslinked with adipic dihydrazide, followed by lyophilization forms porous hydrogel. Seeding of ASCs onto hydrophilic surface induced cell aggregations, which resulted in ASC-spheroids. Then, the spheroids were transplanted in the dorsum of nude mice to induce spontaneous vascularization. Reproduced with permission.[147] Copyright 2017, Elsevier Inc. c) Scaffold-free approach to vascularize organoids: a) Schematic representation of the paper's strategy: hiPSCs, hMSCs, and HUVECs cocultured on Matrigel to form liver organoids, which were transplanted into mice to induce spontaneous vascularization. b) Observation of cells in coculture overtime. Organoids formed within 72 h. c) Observation of hiPSC-organoids (top panel) and conventional 2D cultures (bottom panel). Scale bar = 1 mm. d) Confocal images showing the presence of hiPSC-derived hepatic endoderm cells (green) and HUVECs (red) inside liver organoids (left panel), or HUVECs (green) and hMSCs (red) inside hiPSC-derived organoids. Scale bar = 100 µm. Adapted with permission.[117] Copyright 2013, Springer Nature. d) Compartmentalized microfluidic-based hybrid strategy: A) Kidney organoids were cultured in ECM substrate housed inside a perfusable millifluidic chip, subjected to controlled fluidic shear stress. B–E) Confocal 3D observations showing vascular markers in whole-mount organoids, cultured under static U-well, static, low-FSS, and high-FSS conditions. Scale bars = 100 µm. Adapted with permission.[137] Copyright 2019, Springer Nature.

hyaluronan (HA) gel and chitosan–hyaluronan (CSHA) membrane and seeded onto the wound area on the dorsal skin of Sprague-Dawley male rats. In vitro analysis demonstrated that ASC spheroids had higher gene expression of chemokines and cytokines when cultured on HA gel and CSHA membrane, suggesting an improvement in paracrine effects. Following transplantation, spheroids were observed near microvessels in the healing region of the skin. The enhanced paracrine effects upregulate angiogenic factors secretion, thereby stimulating angiogenic and wound healing processes.[152]

In another approach, MSC spheroids were entrapped within Arginine-Glycine-Aspartate (RGD)-modified alginate hydrogels and transplanted into the dorsum of immunodeficient mice for 8 weeks. In vitro analysis demonstrated that these spheroids underwent osteogenic differentiation and exhibited enhanced VEGF secretion and reduced apoptosis. Furthermore, explants of hydrogels containing spheroids demonstrated improved osteogenesis in vivo.[146]

Human ASCs were used to generate spheroids, which were then seeded into dried porous poly(lactic-*co*-glycolic acid) (PLGA) scaffolds. The resulting constructs exhibited improved vascularization and adipogenic differentiation upon transplantation.[147] Similarly, ASC spheroids in porous polyurethane scaffolds demonstrated enhanced angiogenic potential, as evidenced by greater microvessel density.[153] In another study, hMSC/HUVEC spheroids seeded onto poly(propylene fumarate)/fibrin scaffolds showed enhanced vascular network formation.[154]

Vascularization of Organoids: Scaffold-Free Approach: Prevascularized organoids have been transplanted into kidney,[118,119] brain,[116,155,156] and liver.[117] Among the various labs which attempt to form vascularized organoids, the most notable is the work of Takebe's group. They have successfully fabricated complex vascularized organ buds for kidney, heart, lung, brain, intestine, and pancreas using murine PSC-derived progenitors, HUVECs, and MSCs.[126,157]

Watson generated human intestinal organoids using hESCs or hiPSCs and transplanted them in the kidney capsule of immunocompromised mice.[119] The grafted organoids were vascularized by the host vasculature and resembled the native human intestine with crypt-villus architecture and underlying laminated submucosal layers. Cross-section of the transplanted organoids, which showed mucous-filled lumens and sheets of villi with capillary network, further indicated vascularization and good engraftment of organoids into the host kidney. The in vivo tissue was more differentiated and matured over time compared to in vitro tissue prior to transplantation.[119] Similarly, spontaneous vascularization upon transplantation was also achieved for kidney organoids. Using the ALI method, van den Berg et al. generated kidney organoids from podocytes and grafted them into the renal capsule of immunocompromised mice for 28 days. The organoids developed in vitro anatomical-like structures resembling a nephron including the glomerulus, the distal and proximal tubes, and the collecting duct. However, the in vitro tissue did not form a vascular network, probably due to the limited VEGF production of podocytes and the absence of ECs during in vitro development. Upon transplantation to a highly vascularized site, the organoids grew in size, differentiated progressively into mature kidney tissue, and developed their own vascular network that connected to the mouse vasculature, which supplied blood to their core.[118]

Stem cells can be codifferentiated into organ-specific structures and ECs to obtain vascularized organoids and hESCs or hiPSCs have been successfully used to form cerebral organoids and ECs by codifferentiation.[116,156,155] In this case, different protocols and culture conditions have been developed by different research groups and all studies showed organoids which formed tubular structures and perfused vascular networks in vitro. In Ham and Pham protocols, hESCs or hiPSCs were induced into neuroectoderms which were then introduced in cerebral organoids media and VEGF-supplemented cerebral organoids media for organoid and endothelial differentiation, respectively. Alternatively, Cakir et al. induced the expression of ETV2, a transcription factor contributing to vessel development, to differentiate hiPSCs into ECs.[116] Moreover, they reported their organoids could promote neuronal maturation and development of vascular networks with BBB characteristics. Thus, the preformed functional vessels eventually anastomosed with the host vasculature upon transplantation while the organoids generated without ECs did not survive after 2 weeks of transplantation.[116,155] All results strongly suggest the presence of endothelial cells is highly essential for proper vascularization and engraftment of organoids prior to transplantation.

Along with ECs, MSCs are also included in coculture experiments for vascularization due to their angiogenesis properties. When liver cells were cocultured with HUVECs and MSCs to form liver buds, the resulting 3D structures had liver-specific functions, developed vascular networks and integrated with the host transplantation sites (Figure 6c).[125,158] Beside the liver, Takebe's group has also successfully developed complex vascularized organ buds for kidney, heart, lung, brain, intestine, and pancreas through self-condensation procedures using murine PSC-derived progenitors, HUVECs, and MSCs following implantation in host mice.[126]

Table 4 summarizes the significant case studies for the 3D cell culture vascularization strategies, cited or discussed in the text.

4.2.3. Limitations of Vascularized 3D Cell Culture Models

Both spheroids and organoids have great potential as vascularized models for disease modelling and drug development purposes. While they bring about promising outlook for the biomedical field, several limitations remain. First of all, both spheroids and organoids generation need a large number of cells to obtain a substantial quantity of tissue. Second, cellular microenvironment is the key factor to achieve viable and functional 3D structures with in vivo characteristics, while at the same time promoting angiogenesis.[159] Therefore, ECM or a similar matrix, such as Matrigel, which is a complex protein mixture from mouse, is commonly used, mainly for organoids. However, due to the heterogeneous composition and immunogenic potential of currently used matrices, an alternative ECM-mimicking source should be considered.[13] Alternatively, biomaterial-based 3D scaffolds have been employed to mimic the components of the ECM while providing structural support and external cues to guide cell–cell and cell–matrix interactions, leading to functional and vascularized spheroids.[147,152–154] While these scaffolds can

Table 4. Summary of case studies for 3D cell culture vascularization strategies.

Vascularization method		Tissue/organ model	Biomaterial composition	Cellular composition	Duration of in vitro study	In vivo evaluation	Refs.
Spheroids	Scaffold-free	Bone	–	Osteoblasts, dermal microvascular ECs, normal dermal fibroblasts (all from human)	3 days	2 weeks	[139]
		Dental pulp	–	Dental pulp stem cells, HUVECs	3 days	4 weeks	[129]
		Liver	–	Rat hepatocytes, HUVECs	25 days	No	[140]
		Heart	–	Rat neonatal ventricular cardiomyocytes, human dermal fibroblasts, human CMECs	7 days	7 days	[148]
		BBB	–	Brain ECs, pericytes, astrocytes (all from primary human source)	3 days	No	[128]
	Scaffold-based	Skin	Hyaluronan; chitosan	ASCs	3 days	8 days	[152]
		Adipose tissue	PLGA hydrogel	ASCs	2–3 weeks	3 months	[147]
		Bone	• RGD-modified alginate gel • Polyurethane • Poly(propylene fumarate); fibrin	• MSCs • ASCs • hMSCs, HUVECs	• 2–3 days • 3 days • 1–3 weeks	• 2 months • 2 weeks • 9 days	[146,153,154]
Organoids	Scaffold-free	Brain/BBB	–	hiPSCs	Up to 4 months	No	[156]
		Intestine	–	hESCs/hiPSCs	35 days	6 weeks	[119]
		Kidney	–	hPSCs	25 days	28 days	[118]
		Brain	• – • –	• hESCs → ECs and organoids • hiPSCs → ECs and organoids	• Up to 4 months • 54 days	• 30 days • 7 days	[116,155]
		Liver	–	hiPSC-endoderm cells, hiPSC-ECs, MSCs	3 days	14 days	[125,157]
		Pancreatic islet, brain, heart, lung, intestine, kidney, liver fragments	–	Tissue fragment, HUVECs, hMSCs	1 day	1 month	[126]

provide mechanical and biochemical cues for cell growth within the 3D structures, lack of access to adequate supply of oxygen and nutrients to the center of the structure often results to necrotic core and premature growth in the outer layer of organoids, when missing an adequate vascularization of the 3D constructs.[159]

The key requirement for vascularization concerns the surrounding microenvironment, which has to support both angiogenesis and organoid formation.[159] The incorporation of ECs in the cell culture can alleviate this problem by inducing in vitro prevascularization, leading to the formation of functional tubular vessels. This increase access to oxygen and nutrients, thanks to functional vessels, promotes cells survival, maturation, and differentiation to specific tissue. HUVEC-covered hepatocyte spheroids had improved cell viability and liver-specific functions such as increased albumin secretion and ammonia removal rates.[140] Cerebral organoids generated from hPSCs formed tubular vessels with pericyte-like cells wrapping around them, while promoting neural differentiation.[156]

As these techniques work with cocultures, factors such as cell ratios, seeding density, appropriate cell culture medium, and coculture time must be optimized. For example, while it was possible to form spheroids composed of human adipose-derived mesenchymal stromal cells (hASCs) and HUVECs, vascular structures were only observed when 20% ASCs were cultured with 80% HUVECs in a 1:1 mixture of endothelial and adipogenic medium.[160] Similarly, Noguchi's work showed that contracting vascularized cardiac spheroids were obtained by maintaining the following cell mixture: 70% CMs, 15% ECs, and 15% FBS.[148]

Despite their ability to nourish spheroids/organoids, preformed vessels need to be transplanted in a highly vascularized region to achieve optimal perfusion. The need to experiment on animal models poses a paradox since the one of the main goals of using 3D cell culture models is to reduce animal use in research. Nevertheless, vascularized brain organoids raise ethical concerns and call for consciousness assessment of animal models used in these experiments.[161]

Furthermore, the combination of spheroids/organoids platform with 3D bioprinting and microfluidic technology are necessary to achieve more comprehensive vascularized, physiologically relevant 3D models.[134,137,162] A more in-depth discussion on this topic is presented in Section 4.4.

4.3. 3D Bioprinted Vascularized Models

In the last decades, the word biofabrication has been widely used in the scientific community to describe a plethora of processes aimed to manufacture complex products with a biologically relevant function built from biological building blocks, such as biomaterials, cells, or molecules.[163–166] Although biofabrication techniques for tissue engineering and regenerative medicine have been commonly classified into top-down and bottom-up,[167–169] we adopt here the classification proposed by Groll et al.[170] Considering the fabrication unit, two approaches can be distinguished, namely, bioprinting and bioassembly. While bioprinting uses molecules, that are assembled by means of additive manufacturing techniques based on computer-aided design (CAD) models, bioassembly uses prefabricated cellular building blocks that can be automatically assembled. Both strategies are followed by a tissue remodeling and maturation phase, which is an integral part of the biofabrication process.[169] Though some bioassembly strategies have achieved successful applications in vascularized tissue models (Section 4.3.4), bioprinting represents nowadays the cutting-edge biofabrication technology in the field and will be the main focus of this section.

4.3.1. Current Bioprinting Technologies

Although the concept of 3D printing encompasses different technologies, as summarized in **Figure 7**, most of them show common advantages for the vascularization of biomaterials: 1) the possibility to print vessels of different diameters, ranging from microvessels to vessels in the mm range, that can be surgically anastomosed; 2) the use of bioinks, whose composition can improve vascularization; 3) the ability to control the spatial arrangement of cells to promote the formation of vessel networks, eventually with branched, complex geometries.[109] We provide here a general overview of the current 3D bioprinting technologies employed to vascularize tissue constructs. Later in this section, we summarize the definitions adopted and the critical bioprinting parameters. A more detailed description of the most used commercial bioprinters can be found, for instance, in the work by Ozbolat et al.[171]

Inkjet-Based: This technology can be applied in a continuous mode or in a drop on demand mode. In the first case the printing ink needs to be electroconductive, which limits its application for biological purposes. Besides, the drop on demand mode is based on the deposition of droplets on the printing surface. To generate and eject the drops, thermal, piezoelectric, or acoustic approaches are used (Figure 7a). Thermal printing heads heat the bioink locally creating a bubble that pushes the drops through the nozzle. In the case of piezoelectric and acoustic actuators, vibration is at the origin of drop deposition. Compared to other printing techniques, inkjet bioprinting is low-cost and allows for fast printing with high resolution (50 μm). This is a suitable technology for low viscosity bioinks (<10 mPa s) with a low cell density. Cell viability has been reported in the range of 80–95% using this method, due to the temperature and the mechanical stress.[172,173]

Laser-Assisted Bioprinting (LAB): This technology, also known as laser-induced forward transfer, is a drop on demand method based on the incidence of a pulsed laser beam on top of a donor slide in contact with an energy-absorbing layer. When a bioink is placed next to the energy-absorbing layer, a shockwave appears forming a jet of the bioink that is deposited as a drop on a collector slide (Figure 7b). High resolution (5–10 μm) and the possibility to work with a wide range of densities (1–300 mPa s) and to print the cells on solid or liquid substrates are the main advantages of this strategy. Other benefits are automation, reproducibility, and high throughput. Nevertheless, it is a very expensive technology that might cause cell damage. Other drawbacks are cell sedimentation and, when printing 3D constructs, the risk that working wavelengths alter cell organization.

Extrusion-Based: The most popular 3D bioprinting technologies nowadays are pressure-assisted, which are well adapted for highly viscous and, ideally, structurally stable solutions to avoid loss of shape (Figure 7c). For this purpose, most approaches in the literature combine bioprinting of the ink with in situ

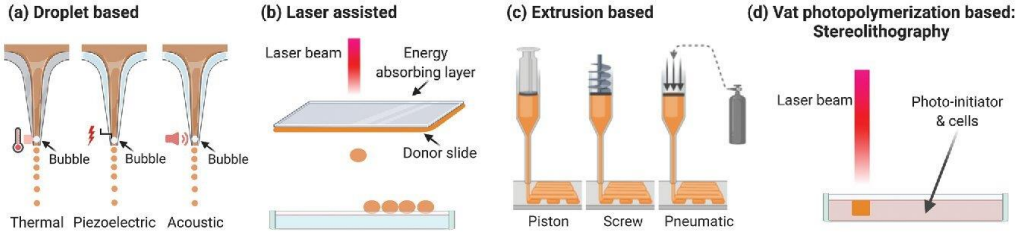

Figure 7. Schematic of bioprinting methods. a) Inkjet-based bioprinting involves the formation of droplets of bioink by generating bubbles in the tip of the printer through thermal, piezoelectric, or acoustic energy. b) Laser-assisted bioprinting is also based on the generation of droplets of bioink by the incidence of a laser beam on an energy absorbing layer coupled with a donor slide constituted of bioink. The droplets are then recovered on a dedicated platform. c) Extrusion is the most commonly used method; the ink is pressed through the nozzle either with a piston, a screw, or using pneumatic pressure. d) Vat photopolymerization requires the presence of a photoinitiator to cure the polymer loaded with cells. Created with Biorender.com.

crosslinking after injection.[109] It is also frequent to work at controlled temperature to assure good viscosity of the bioink and to induce in situ gelation. A drawback is that reproducibility depends on numerous parameters, namely, needle diameter, air pressure, speed of printing, temperature, and humidity. Assuring homogeneity of the bioink during the printing process is particularly relevant in cell-loaded bioinks. Also, excessive pressure can result in cell damage caused by shear stress. Other disadvantages are low speed, low resolution, and clogging.

There are several commercially available 3D bioprinters, but the simplicity of the technology leads many research laboratories to manufacture customized printer based on their needs. To print different bioinks without crosscontamination, the use of multiple injectors is often adopted. In the case of vascularized materials, the use of coaxial needles is particularly advantageous to print tubular structures as will be seen in Section 4.3.2.

Vat Photopolymerization-Based: The possibility to photocure polymers loaded with biomolecules and/or cells has open new perspectives to create tissue constructs. The process is based on a laser beam that irradiates a resin composed of a solvent, a photoinitiator and a polymer. The photoinitiator reacts to the light source releasing radicals or cations that start the polymerization of the resin. This technology was first applied to 3D print low cell compatible resins in the presence of photoinitiators, which were however highly cytotoxic. In the last years, the development of new photoinitiators has expanded the application of this technique to the biomedical field.[174] The high precision and resolution, together with the possibility to incorporate photoabsorbers to prevent photopolymerization in defined regions, makes this technology particularly interesting to engineer vasculature.[175] The extraordinary freedom of design to pattern highly complex hollow vascular-like structures within biomaterials has been recently demonstrated.[176]

Another advantage of vat photopolymerization compared to extrusion is the possibility to use low viscosity resins that improve the resolution compared to high viscosity ones but that can lead to cell sedimentation. The major drawback of the technology is the cell damage caused by the laser and by oxidative stress due to the activation of the photoinitiators. Laser sources in the UVA–visible spectrum are preferred since they are less toxic than shorter wavelengths in the UVB and UVC regions. In the field of vascularization, the most used photoinitiators are Irgacure 2959 (maximum efficiency wavelength 275 nm) and lithium phenyl-2,4,6-trimethylbenzoylphosphinate (LAP, maximum efficiency wavelength 375 nm), the latter being the less cytotoxic one.[174,177]

Depending on the light source to cure the polymers, vat photopolymerization can be classified in stereolithography (SLA) (polymer cured with a laser), digital light processing (DLP) (polymer cured with a projector), and continuous digital light processing (CDLP)/continuous liquid light processing (CLIP) (polymer cured with oxygen and light emitting diodes (LEDs)).[174,178]

Definitions and Relevant Parameters in Bioprinting: Definitions are given to differentiate between cell-loaded bioinks, hereinafter "bioinks," and acellular bioinks that will be named "biomaterial bioinks," according to Groll et al.[179] Most of bioinks are composed of one or several materials, other than cells, being the number of studies using a material-free approach very small, as described in Section 4.3.2. Biomaterial bioinks are generally printed to form a scaffold where cells are seeded in a following step, being the risk of heterogenous cell distribution greater, compared to cellular bioinks. In both cases, biomolecules can be incorporated in the ink to exert a biological effect on cells. Other nonbiological materials can also be added to affect cell function via mechanical or electrical cues. Materials can also act as mere supports during the printing process, or as sacrificial inks that are removed after the printing process.

Solution viscosity is one of the critical material parameters for inkjet or extrusion bioprinting. The degree of viscosity must permit smooth nozzle extrusion, with homogeneous texture during the whole printing process, and fast solidification after printing.[173] Clogging of the nozzle is frequent due to excessive viscosity or to progressive cell sedimentation. When the solution is not viscous enough, the printed construct risks to collapse or to eventually lose its shape. Viscosity is therefore related to the printability of the material, or coprintability of several biomaterials, which must have shear-thinning or thixotropic rheological behavior during the printing. To modify the solution, viscosity, concentration,[180] or temperature[181] can be tuned. Shao et al. used Gel/gelatin methacryloyl (GelMA) solutions cooled at −20 °C for 5 min to form a prebioink, which was then printed on a platform at 2 °C.[181] Additionally, the syringe was turned over every 20 s to homogenize cell suspension. A similar approach was followed by Jin et al. by using a mixture of gelatin and alginate.[182] For thermal sensitive materials, the printability

can be improved by including sacrificial polymers in the bioink solution. Maiullari et al. mixed alginate with polyethylene glycol (PEG)–fibrinogen, followed by a curing step of the PEG–fibrinogen with UV and the final removal of the alginate with ethylenediaminetetraacetic acid (EDTA).[183] Besides printability, viscosity can be also modulated to obtain complex geometries particularly relevant for vascularization. In an elegant work, Lin et al. 2019 reported how by increasing the viscosity of a sacrificial bioink made of Pluronic F127, it was possible to avoid viscous fingering at the interface between the printed features and the surrounding material to obtain smooth curved channels.[75] The best way to evaluate viscosity and printability is to perform rheological studies to establish the optimal working ranges of viscosity and storage moduli (for an extensive review about printability and rheological characterization, the reader is referred to ref. [184]). Ideal reported values of viscosity are 10 mPa s for droplet-based bioprinting,[173] with an upper limit of about 100 mPa s,[185] 1–300 mPa s for LAB, and 30 to 6×10^7 mPa s for extrusion.[173]

The diameter of the printed element also affects important physical properties of the final construct, such as porosity, mechanical strength, and height of the scaffold.[173] In the case of extrusion, this parameter is closely linked to the needle/nozzle diameter, the printing pressure and speed, or the flow rate of injection. Low resolution of the extrusion technique remains one of the main limitations to properly vascularize materials by bioprinting and the formation of tubular structures with a diameter similar to small venules, arterioles, and capillaries still represents a challenge. Nozzle-free strategies can represent an alternative due to better resolution, compatible with vessels below 100 µm, and less limitation in terms of viscosity and potential cellular toxicity.

Finally, when establishing bioprinting parameters, in addition to the aforementioned, it should not be forgotten that they all affect cell behavior and viability.

4.3.2. Bioprinting Strategies for Vascularization

Sacrificial Bioprinting: Sacrificial bioprinting uses a biomaterial bioink whose sol–gel transition or gelation can be easily controlled. First studies used organic materials soluble in organic solvents,[186,187] and therefore incompatible with the incorporation of cells. Based on previous work where cotton candy was used as sacrificial material to form channels within PDMS,[188] Miller et al. reported in 2012 the use of a carbohydrate mixture optimized for bioprinting and subsequent dissolution of interconnected and branched filaments with several diameters.[98] The properties of the printed filaments allowed the formation of microchannels within a wide variety of cell-loaded materials such as agarose, alginate, photopolymerizable PEG, fibrin, or Matrigel. This work inspired numerous studies using the same fugitive ink strategy to mimic the microvascular architecture.[95,75,189–193,181,180,194]

Poloxamers, also known as Pluronic, are poly(ethylene oxide)–poly(propylene oxide)–poly(ethylene oxide) (PEO–PPO–PEO) triblock polymers with a critical micelle temperature and concentration. This means that at low temperatures they are present in solution, whereas at high temperatures they form micelles and form a gel. In practice, some poloxamers, such as Pluronic-F127, can be bioprinted at temperatures that do not compromise cell viability, and then at 4 °C they become liquid and can be washed, leaving a lumen where endothelial cells can be seeded. This approach has been used by the team of JA Lewis in combination with a fibrin casted gel, in several studies. In 2016, a preliminary study to form a proximal tubule model in a microfluidic chamber was published.[191] Three years later, the same team optimized the composition of the Pluronic-based fugitive ink, and succeeded to print a proximal tubule and a vascular channel that were seeded with epithelial cells and glomerular microvascular endothelial cells, respectively, under flow conditions.[75] Also in 2016, they used the same kind of approach to combine HUVECs and hNDFs to form the vasculature, together with osteoinduced hMSC to form a microfluidic platform to create a relevant 3D model of bone (**Figure 8**a).[95] An originality in those works is how the authors made the printed vascular ink interact with the casted cell-loaded hydrogel surrounding it. Briefly, the vascular ink contained thrombin, and the gel that was casted contained fibrinogen and transglutaminase. This way, thrombin diffused from the vascular ink to the surrounding gel causing crosslinking of the material. Using this strategy, the authors were able to form a thick (>1 cm) 3D chip with endothelialized channels that could be perfused with culture medium to differentiate hMSCs into osteogenic cells.

Gel is another material that is frequently proposed to form hollow microchannels. Two recent works have used Gel-based fugitive inks to create relevant models of bone. In 2017, Khademhosseini's group reported the use of GelMA with a low degree of substitution to print cylinder rods of around 500 μm within cylinder rods of photocrosslinked gelatin methacryloyl with a high degree of substitution and loaded with hMSC.[192] After removal of the sacrificial ink, HUVECs were seeded in the central channel mimicking the architecture of long bones. Besides, Shao et al. have proposed direct coaxial bioprinting to form core–sheath fibers using Gelatin–GelMA, loaded with HUVECs and mouse osteoblast, respectively, in a single printing step at 2 °C (Figure 8c).[193,181] After photocuring GelMA, the temperature is set at 37 °C to liquefy gelatin. The construct is left under static culture conditions for 3 h, to allow HUVECs to adhere, and then dynamic cell culture is done using a shaker. In the same work, authors used this approach to seed HUVECs and human breast cancer cells (MDA-MB-231) to create a cancer model. This biofabrication method presents numerous advantages due to the ability to print complex shapes with controlled heterogenous composition, in a relatively fast way. Nevertheless, further research is needed to confirm the presence of an endothelialized and perfusable lumen.

The use of bioprinting to vascularize hepatic constructs is not yet widespread.[180,196] Recently, a preset extrusion bioprinting technique using alginate as sacrificial ink was employed for liver multiscale tissue engineering.[180] A preset cartridge was prepared with collagen 3%, loaded with cells, and alginate 3% as fugitive material. The design was established to mimic the hepatic lobule, with EA.hy 926 endothelial cells around the lumen (150–200 µm), in the external surface of the construct and radially interconnecting both surfaces. In the space between ECs, hepatic cells (HepG2/C3A) were printed. Using a preset cartridge allows to control the spatial disposition of the cells with just one printing head. However, compared to other strategies, the dimensions of the printed construct are smaller (4 mm width

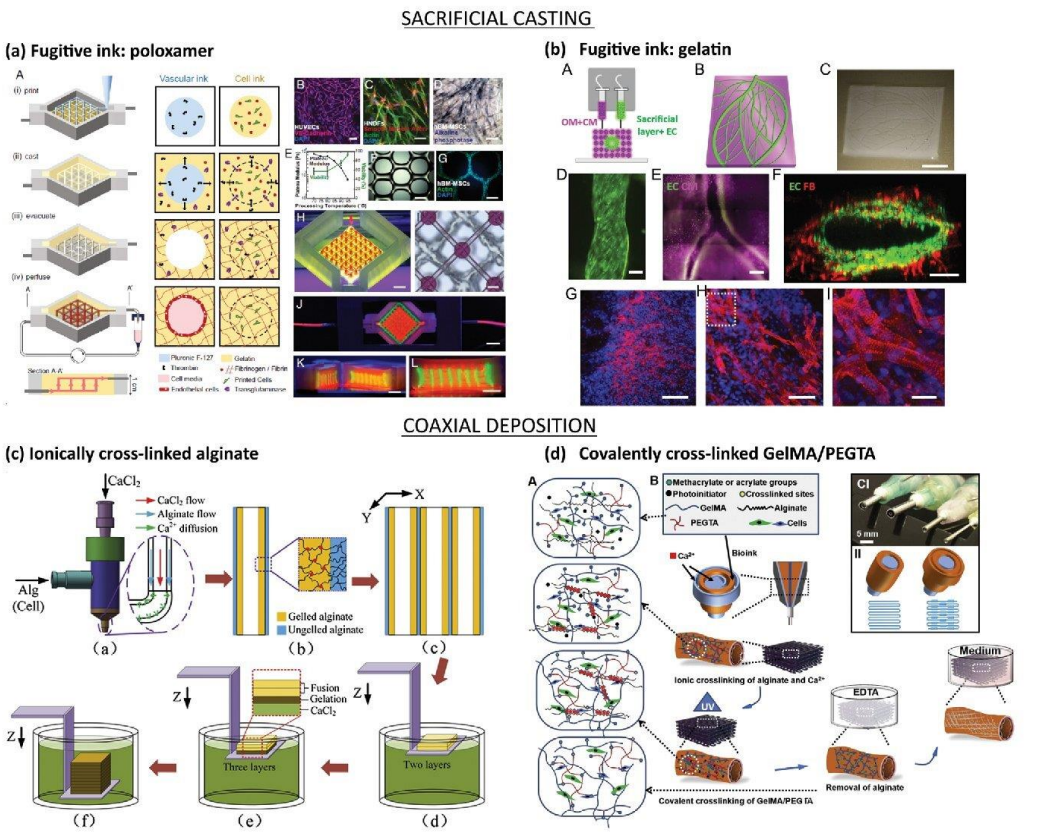

Figure 8. Bioprinting-based vascularization strategies: sacrificial casting (top) and coaxial deposition (bottom). a) Bioprinting of thick vascularized tissues with sacrificial poloxamer: A) Manufacturing process in four steps: i) printing of the sacrificial poloxamer-thrombin biomaterial bioink and of cell-laden gelating bioink with endothelial cells; ii) casting of the gelatin/fibrinogen/transglutaminase that interacts with the thrombin diffused from the printed biomaterial causing gelification; iii) removal of the poloxamer by cooling down leading to empty channels; iv) perfusion of the channels with cell media that results in endothelialization of the channels. Three cell types were incorporated: B) HUVECs, C) hNDFs, and D) hMSCs. (Scale bar: 50 µm.) E) Cell viability and mechanical properties of the construct are affected by gelatin preprocessing temperature. hMSC-laden bioink F) immediately after printing and G) after 3 days. H–K) Images of the bioconstruct. H) Sacrificial bioink colored in red and cell-laden bioink in green. (Scale bar: 2 mm.) I) Bright-field image from top. (Scale bar: 50 µm.) J) Construct in a perfusion chamber and K,L) cross-sections. (Scale bar: 5 mm.) Reproduced with permission.[95] Copyright 2016, PNAS. b) Bioprinting of thick cardiac patches with sacrificial gelatin. A) Two bioinks composed of decellularized omentum tissue (OM) + cardiomyocytes differentiated form iPSCs (CM) and sacrificial gelatin + endothelial cells (ECs). B) 3D- model of the cardiac patch. C) Printed cardiac patch. D–F) Fluorescence images of the printed cardiac patch with the ECs (green), CM (purple), and fibroblasts (red). (Scale bars: 100, 500 and 100 µm, respectively). The cardiac patch was implanted between two layes of the rat omentum and then explanted for analysis. G-I) Fluorescence images of the explanted patch showing the sarcomeric actin of the CM in red and nuclei in blue. (Scale bars from left to right: 100, 50, 25 µm). Adapted with permission.[190] Copyright 2019, WILEY-VCH. Copyright 2019, The Authors. Published by Wiley-VCH. c) Coaxial bioprinting of 3D hydrogels with microchannels using alginate: a) Schematics of the coaxial nozzle in which alginate and $CaCl_2$ are co-injected to form b) channels with an inner layer of ionically crosslinked alginate surrounded by ungelled alginate. c) Several channels are printed in parallel and then d) immersed in a bath with $CaCl_2$ to promote e) gelation of the noncrosslinked alginate. f) This step is repeated several times to create a 3D construct. Reproduced with permission.[193] Copyright 2015, Elsevier Inc. d) Multilayer coaxial bioprinting of perfusable 3D constructs with a blend bioink: A) The bioink gels through ionical crosslink of alginate with Ca^{2+} and photocrosslink of GelMA and polyethylene glycol (PEGMA) exposed to UV irradiation. B) Schematics of the coaxial nozzle in which the blend bioink is injected in between $CaCl_2$ solution to cause immediate alginate gelation. After UV irradiation, the alginate is removed in contact with EDTA and the construct placed in cell culture medium. C-I) Multilayered coaxial nozzles and II) schematics of the channel formation. Reproduced with permission.[195] Copyright 2016, Elsevier Inc.

× 5.2 mm height × 2.5 mm thick). Alginate was also chosen to prepare vascularized cardiac tissue (Figure 8b).[194] The aim of this work was to prepare a tissue construct for personalized therapy and drug testing. For this purpose, authors used decellularized omentum (peritoneum) to form a thermoresponsive hydrogel to print CMs, and sacrificial alginate to bioprint HUVECs. In the cardiovascular field also, the work by Maiullari et al. describes the use of coaxial bioprinting to prepare a cardiac patch.[183]

Coaxial Deposition: Coaxial deposition systems use concentrical nozzles to i) crosslink the bioink during the extrusion process and ii) directly print tubular structures that can mimic the multilayered organization of the vasculature. In the mentioned work by Maiullari et al., a microfluidic printing head was used to perform coaxial microextrusion.[183] The inner needle injected a bioink composed of alginate, PEG–fibrinogen and cells, either HUVECs or iPSC-derived cardiomyocytes, whereas the external needle injected a $CaCl_2$ solution to crosslink the alginate. After bioprinting, UV was applied to crosslink PEG–fibrinogen, and then alginate was removed by EDTA washing. Notably, the authors could engineer fibers with the two cell types in a "Janus" conformation that proved to be the most effective to generate vessel-like structures, compared to alternating layers of cells at two different ratios.[183]

Another interesting example of coaxial printing is the work by the team of Khademhosseini, which used this technology to print perfusable tubular constructs with needles ranging from 14G to 30G leading to internal diameters ranging from about 400 µm to 1 mm (Figure 8d).[195] As in previously mentioned works by the same group, GelMA with an adjusted degree of substitution was used together with alginate as sacrificial ink. During the printing process, alginate was ionically crosslinked with Ca^{2+}. Once the GelMA was photocrosslinked, the construct was washed several times and treated with EDTA to remove all the cationic ions. To obtain a stable tubular construct after removal of the alginate and improve the mechanical properties of the GelMA after crosslinking, different amounts of polyethylene glycol tetra acrylate (PEGTA) were included in the mixture. This study was mainly focus on the biofabrication method to prepare endothelialized constructs, and the cells employed were HUVECs and MSCs. Soon after, they applied the coaxial extrusion technology to prepare an endothelialized myocardium and a heart-on-a-chip.[108,197] In this case, plain microfibers with a diameter of 300 µm were printed leading to homogenous HUVECs distribution. Interestingly, the authors reported a progressive migration of the cells to the surface of the microfibers, as alginate was released. Though cells formed a monolayer similar to an endothelium after 15 days, the final constructs did not present a lumen and were not perfusable.

Pancreatic islets were printed together with endothelial progenitor cells (EPCs) using a coaxial extrusion nozzle for the treatment of type I diabetes.[198] Similar to previous works, a mixture of alginate and GelMA was used for ionic crosslinking and photocrosslinking, respectively, but in this case the endothelial cells were printed around the fiber containing the islets. Unexpectedly, the presence of EPCs did not improve islets function. On the contrary, the authors reported reduced insulin secretion of the islets probably due to reduced diffusion of glucose and hypoxia in the core fibers.

In the work by Leucht et al., the authors printed two different compartments with two bioinks to engineer vascularized bone bioconstructs.[199] By mixing Gel, GelMA, and acetylated gelatin methacryloyl (AcGelMA), the authors significantly reduced the stiffness of the native G while increasing the swellability. This bioink loaded with hDMECs was printed in a concentrical compartment next to a second compartment where human adipose-derived stem cells (hADSCs) differentiated in osteoblasts were previously bioprinted. The transparent vascularization gels were cured using a LED-UVA lamp (385 nm). The authors demonstrated that softer materials led to better results in terms of number of vascular networks, length and number of nodes. Another way to print different bioinks or biomaterials bioinks, is to use multihead printers. In the work by Jang et al., three different bioinks loaded with human cardiac progenitor cells (hCPC) or hMSC, or a mixture of both were printed to fabricate cell patches for cardiac repair.[200] They used decellularized ECM as biomaterial, with vitamin B_2 and VEGF to improve vascularization, and implanted the construct in a rat model of heart ischemia. Results demonstrated the benefits of a patch with a specific pattern of CPCs and MSCs, which improved cardiac function and reduction of fibrosis, together with an increased neovascularization.

The possibility to print several bioinks in the same construct was exploited to create a gradient of growth factors in a construct for bone vascularization.[192] As described previously in this section,[195] Gel was prepared with two degrees of substitution, low and high. The low GelMA was used as sacrificial biomaterial bioink to form a hollow channel of around 500 µm inside the construct to form a perfusable blood vessel, mimicking the architecture of long bones. Concentric rods with four different formulations were printed to create both vasculogenic and osteogenic niches. By modifying the GelMA composition (low to high), the cells ratio (HUVECs and hMSCs), the silica nanoplatelets, and VEGF concentrations, the authors engineered a perfused scaffold with gradients of biochemical cues to promote both osteogenic differentiation and vascularization. In contrast to the previously mentioned studies,[195,198,201] in this case, crosslinking of GelMA occurred in the capillary, before extrusion of the bioink. Another bioactive compound that has been incorporated in a biomaterial bioink for bone tissue engineering is nanohydroxyapatite (nHA).[202] In this work, a mixture of gelatin and nHA was printed using Pluronic as sacrificial support to allow the crosslinker genipin to act during 48 h. Then, Pluronic was removed and HUVECs, hMSCs, and/or osteodifferentiated hMSCs were added in a solution made of GelMA–fibrin, which was photocrosslinked.

Stereolithography: The photocuring of polymers to engineer tissue vasculature is still at its early stage. Even if works using this strategy to vascularize tissue relevant constructs are very few, they hold great promise in view of the rapid evolution of the technique. In 2017, Zhu et al. used this technique in a pioneer work to bioprint a model of liver including HUVECs, MSCs, and HepG2 cells.[203] This construct was subcutaneously implanted in a murine model demonstrating the anastomosis of the implant. Miri et al., faced one of the main limitations of this technology by building up a microfluidic device to allow stereolithography of a multimaterial construct.[204] This way, they produced a simplified model of breast cancer including HUVECs and MCF7 cancer cells. Another model of breast cancer using SLA was

more recently developed by Cui et al. to evaluate migration of metastatic cells to bone.[205]

In an elegant work published in 2019 in Science, Grigoryan et al. proposed the incorporation of food additives as photoabsorbers to form hydrogels with very complex and intricated networks to mimic several tissues, including an alveolar model.[176] They also created a prevascularized construct with a network of HUVECs connected to hepatocyte aggregates, which was subcutaneous implanted. Hepatic cells functionality two weeks after implantation was demonstrated but the benefits of including an endothelial cell network in the production of albumin was not proved, although histological examination evidenced the anastomosis of the implant.

Vat-photopolymerization can be combined with other 3D-printing techniques. This is the case of the recent work by Hann et al., in which fused deposition modeling (FDM) for sacrificial PVA printing was combined with SLA for GelMA and PEGDA curing to build a channeled construct as model of bone tissue.[206] Compared to the use of photoabsorbers to form hollow channels, the resolution of FDM was however really low, leading to vessels of several hundreds of micrometers.

Bioprinting holds great potential in the fabrication of diseased tissues as well, even if studies in this regard are still limited.[181] Besides the case studies already mentioned, Liu et al. have recently proposed a model of atopic dermatitis fabricated by hybrid biofabrication combining electrospinning and extrusion bioprinting for the study of this skin disease and drug testing.[207] For a comprehensive review about hybrid biofabrication, we refer the reader to ref. [208].

Scaffold-Free Bioprinting and Alternative Strategies: A promising bioprinting strategy for vascularization in alternative to scaffold bioprinting is scaffold-free bioprinting, which is based on the capacity of cells to self-assembles after bioprinting and spontaneously form constructs that mimic the native tissue architecture and function. However, this strategy requires a large number of cells as well as a postprinting incubation period that prolongs the process and increases the costs. This explains why the number of studies using this technique to recreate the vasculature is currently limited and mainly focused on the fabrication of larger blood vessels (≥1 mm).[209–212]

All the works described in this section so far deal with extrusion bioprinting. There are however two examples of laser induced forward transfer worth mentioning within the scope of this review. In 2011, Gaebel et al. reported the fabrication of a cardiac patch using a polyester urethane urea patch immersed in Matrigel.[213] Using laser bioprinting, HUVECs and hMSCs were printed on the patch following a defined 2D pattern. This patch was implanted in an infarcted rat model and improvement of some cardiac functions and neovascularization were observed. More recently, intraoperative bioprinting of stem cells from the apical papilla and HUVECs using LAB has been successfully done to treat a mouse calvaria defect.[214] **Table 5** summarizes significant case studies for the bioprinting vascularization strategies, cited or discussed in the text.

4.3.3. Limitations of Bioprinted Vascularized Models

3D bioprinting is an interesting technique for tissue engineering and particularly for vascularization but some current limitations still need to be addressed. As already mentioned, an important drawback concerns the poor resolution that currently makes extrusion printing of objects below 100–200 µm a real challenge. This limitation is even more important when it comes to direct channel printing by coaxial extrusion. That is why obtaining fully prevascularized constructs by bioprinting is not currently possible and the formation of microvasculature requires a postimpression maturation stage that can last several weeks. Other bioprinting techniques, such as LAB, show better resolution, but their use for tissue vascularization is currently limited, mainly due to high cost and limitations to print multiple materials.[185]

The homogeneity of the bioink during the bioprinting process, particularly relevant in the manufacture of larger constructs, represents another drawback. Cells at high concentrations tend to sediment, making the bioink not homogeneous. Moreover, the viscosity of the bioinks fundamental for its printability since it determines the cell density, it affects the mechanical properties of the final construct as well as the cellular viability and behavior (proliferation, differentiation, migration, etc.). Future studies should pay more attention to this aspect and carry out experiments that help to identify the optimal mechanical properties to promote adequate vascularization.[215] In this regard, it is worth mentioning the extrusion bioprinting studies that are already being carried out in space, where microgravity allows the use of less viscous bioinks and the formation of particularly interesting geometries for vascularization, such as voids and tunnels.[216]

Finally, we have seen that a common strategy is the printing of photopolymerizable materials in the presence of a photoinitiator. These materials are often obtained by chemical modification of natural polymers, such as Gel, to incorporate methacrylate groups that polymerize after irradiation at a certain wavelength and in the presence of a photoinitiator. There are many studies focused on the development of cytocompatible photoinitiators, since those currently used are not considered totally harmless to the body and the presence of methacrylate groups can pose a problem for therapeutic use.[217] Furthermore, as already mentioned, the presence of these groups creates materials with mechanical properties that should be further investigated.

Bioprinting is a relatively young technology that has come a long way in the last decade, opening up previously unthinkable possibilities for tissue engineering. Current limitations are mainly due to the bioprinting method and can be overcome by combining several printing strategies on a single platform.[216] We envision that the advances of this technology over the next few years will contribute considerably to the development of vascularization strategies of physiologically relevant models.

4.3.4. Bioassembly Strategies for Vascularization

Micromodule Assembly Strategies: Micromodule assembly refers to a category of modular TE strategies in which microscale building blocks are assembled to create larger tissues,[218] with the advantage that the single units provide cells with efficient gas exchange and nutrients supply at the microscale and vascular networks can be easily integrated.[219] The formation of modular vascular tubes is commonly achieved by using micromolds or by creating cell-laden microgels, which are then assembled by photopolymerization,[220] random packing,[221] or direct assembly.[222] Despite the scalability of these technologies, which

Table 5. Summary of case studies for bioprinting vascularization strategies. Abbreviations not used previously: Col: collagen; GMECs: glomerular microvascular endothelial cells; hFob: human fetal osteoblasts; hiPSC-CM: induced pluripotent stem cell-derived cardiomyocytes; hiPSC-EC: induced pluripotent stem cell-derived endothelial cells; I: inner diameter; LAP: lithium phenyl-2,4,6-trimethyl-benzoyl-phosphinate; O: outer diameter; PCL: polycaprolactone; PTECs: proximal tubule epithelial cells; SCAPs: stem cells from the apical papilla.

Vascularization method	Coaxial	Sacrificial	Organ/tissue model	Needle diameter	Vessel caliber	Biomaterial composition	Cellular composition	Duration of in vitro study	In vivo evaluation	Refs.
Extrusion-based	No	No	Bone	0.33 mm (I)	Microvessels	Gel, GelMA, Ac-GelMA	hDMECs, hADSCs, hADSCs differentiated in osteoblasts	14 days	No	[199]
			Heart	26G	Microvessels	PCL, heart-derived ECM	MSC, CPC	5 days	Yes	[200]
			Skin	0.25 mm	Microvessels	PLGA, fibrin	iPSC-ECs, perycites, neonatal fibroblasts, keratynocytes	7 days	No	[207]
			Heart	1.6 mm	1 mm	Agarose, alginate, platelet rich plasma	HUVECs, H9c2 CM	14 days	No	[190]
			Liver	0.25 mm	Microvessels	PCL, Col	HUVECs, hLFs, hepatocytes	14 days	No	[196]
		Yes	Liver	0.5 mm	0.15–0.2 mm	Col 3%, alginate 3% (sacrificial)	EA.hy 926, HepG2/C3A	10 days	No	[180]
			Bone	0.7 mm	Microvessels	Gel/nHA, Gel-MA/fibrin	HUVECs, hMSC hMSCs differentiated in osteoblasts	5 weeks	No	[202]
			Heart	30G	0.3–0.4 mm	Decellularized momentum, alginate (sacrificial)	hiPSC-ECs, hiPSC-CMs, HUVECs, rat CM, fibroblasts	7 days	No	[194]
			Bone	0.5 mm	0.5 mm	GelMA-high, GelMA-low (sacrificial)	HUVECs, hMSCs	21 days	No	[192]
			Bone	0.1–0.4 mm	0.4 mm	Gel, fibrinogen, thrombin transglutaminases, poloxamer (sacrificial)	HUVECs, hNDFs, hMSCs	>6 weeks	No	[95]
			Kidney	0.41 mm	0.2 mm	Gel, fibrinogen, transglutaminase, poloxamer (sacrificial)	GMECs, PTECs	18 days	No	[75]
	Yes	Yes	Cancer tissue and osteogenic tissue	27G (I), 17G (O)	0.2–1 mm	GelMA, Gel (sacrificial)	HUVECs, MDA-MB-231, MC3T3-E1	20 days	No	[181]
			Heart	26G (I), 19G (O)	Microvessels	PEG, fibrinogen, alginate (sacrificial)	HUVECs, iPSC-CMs	7 days	Yes	[183]
			Heart	27G (I), 18G (O)	0.2 mm	GelMA, Alginate (sacrificial)	HUVECs, neonatal CM	28 days	No	[197]
			–	27–30G (I), 18–25G (O)	0.3–1.5 mm	GelMA, PEGTA, alginate (sacrificial)	HUVECs, MSCs	21 days	No	[195]
			Cardiac	27G (I), 18G (O)	0.3 mm	GelMA, alginate (sacrificial)	HUVECs, neonatal CM	33 days	No	[108]
			Pancreas	0.4 mm	Microvessels	GelMA, alginate (sacrificial)	hEPCs, pancreatic islets (organoids)	15 days	Yes	[198]
Laser-based	–	–	Heart	–	Microvasculature	Polyester urethane urea patch, Matrigel	HUVECs, hMSC	8 days	Yes	[213]
	–	–	Bone	–	Microvasculature	Col	HUVECs, SCAPs	–	Yes	[214]

(*Continued*)

Table 5. (Continued).

Vascularization method	Coaxial	Sacrificial	Organ/tissue model	Needle diameter	Vessel caliber	Biomaterial composition	Cellular composition	Duration of in vitro study	In vivo evaluation	Refs.
Vat photopolymerization: SLA	–	–	Liver	–	Microvessels	Glycidal methacrylate-HA, GelMA Photoinitiator: LAP	HUVECs, MSCs, HepG2	7 days	Yes	[203]
	–	–	Breast cancer	–	Microvessels	GelMA, PEGDA Photoinitiator: LAP	HUVECs, MCF7, C2C12, fibroblasts, MSCs	7 days	No	[204]
	–	–	Liver	–	Microvessels	GelMA, PEGDA Photoinitiator: LAP Photoabsorbers: tartrazine, curcumine, anthocyanine	HUVECs, hepatic aggregates (rat primary hepatocytes and NHDFs)	–	Yes	[176]
	–	–	Breast cancer	–	500 μm and microvessels	GelMA, PEGDA Photoinitiator: Irgacure 2959	HUVECs, breast cancer cell lines: MDA-MB-231 and MCF-7, hFob	14 days	No	[205]
Dual 3D printing (SLA and FDM)	–	–	Bone	–	0.5–1 mm and microvessels	GelMA, PEGDA, PVA (sacrificial) Photoinitiator: Irgacure 2959	HUVECs, hMSCs	20 days	No	[206]

provide dense cellular population while ensuring perfusion and diffusion and enable to control features at the microscale by tuning the building blocks properties, the lack of some fundamental requirements, as the mechanical stability, hampers their translation toward clinical application and successful engineering of vascularized tissue constructs.[222]

Cell Sheet Engineering: Scaffold-based TE approaches are often limited to low cellular density, lack of a functional vascular network and, consequently, inability to create thick constructs that do not undergo necrosis.[223] Cell sheet engineering has emerged in the 90's as scaffold-free approach for the manufacturing of 3D cellular constructs with native tissue properties,[218] and it has been successfully applied for cornea and trachea reconstruction, production of skin and bladder equivalents and myocardial tissue regeneration.[224,225] The technique consists of growing cells, that spontaneously produce ECM and form sheets, and subsequently assembling of the sheets by stacking or rolling them to obtain 3D or cylindrical tissue engineered blood vessels (TEBVs).[226,227] This technique has been used to engineer artificial vessels composed of up to three cellular layers (adventitia, media, and intima) that have been used as artery models and grafted in vivo to promote regeneration of the host vasculature.[226,228] Recently, the sheets manipulation has been improved by using temperature-responsive culture substrata as poly(*N*-isopropylacrylamide) (PIPAAm), that enable sheets release by simply lowering the temperature.[227] Thick cardiac tissues (1 mm), prevascularized in vitro, were fabricated by multistep implantation of stacked sheets into animal models, that showed pulsatile cardiac tubes with beating up to 1 year and formation of microvasculature in vivo.[223] Though cell sheet engineering is mainly used in therapeutics and regenerative medicine,[229] the physiological tissue architecture and mechanical properties that can be achieved with this strategy make it interesting for developing highly organized and densely vascularized tissue models.

Nanofabrication: Most of the biofabrication techniques require a maturation phase of the tissue after assembly, usually carried out with bioreactors, which provide the tissue with nutrients, mechanical stimuli, and flow under dynamic culturing conditions.[166] To overcome these limitations and provide cells with nanostructured scaffolds, nanotechnology-based strategies have been used to fabricate tissues and vascular-like structures:[164,230] phase separation and self-assembly of peptidic domains of biological polymers, as collagen or elastin, have been used as strategies to engineer nanofibers, nanotubes and nanowires for vascular TE applications.[231,232] However, electrospinning is the main nanofabrication technique for vascularized constructs:[230,233] tubular scaffolds have been electrospun by using rotating mandrels or combination with electrospraying to create highly cellularized constructs,[234] and multilayer core–shell constructs resembling the blood vessels structure have been manufactured by coaxial electrospinning.[235–237] Electrospun scaffolds for vascular TE have been manufactured with a variety of natural and synthetic polymers and their combination in blends leads to devices with physiologically relevant mechanical behavior while promoting cell adhesion and proliferation.[238–241] The fibrous and porous architecture created by electrospinning mimics the in vivo ECM nanoenvironment and the fibers can be easily functionalized or grafted with molecules, peptides, drugs, or growth factors to promote cell adhesion, endothelialization, and antithrombogenic properties.[242–244] However, few electrospun vascularized organ-specific in vitro models have been reported,[245] as most of the works use electrospun membranes or meshes for coculturing of cells with no physiologically

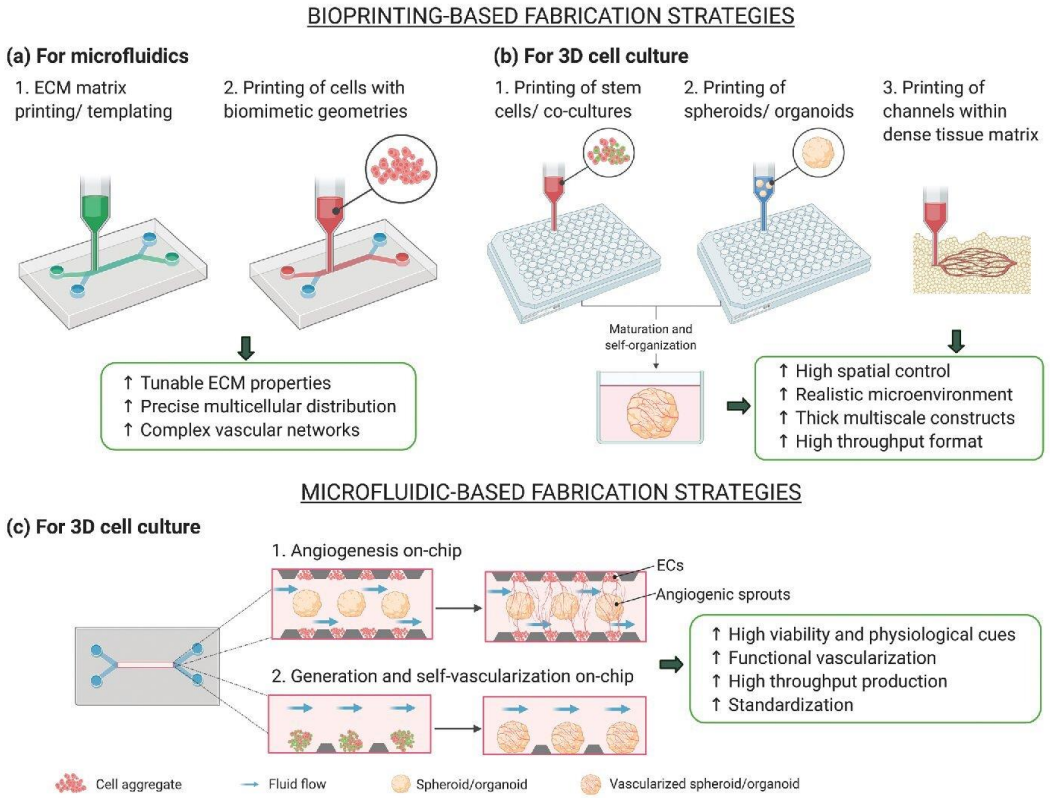

Figure 9. Hybrid strategies for vascularization. The hybrid approaches are divided into a,b) bioprinting-based and c) microfluidic-based. The main advantages of the application of these fabrication strategies for each model are shown in the green panels. Created with BioRender.com.

relevant 3D vasculature.[246] In fact, although electrospinning has been used for bone, skin, heart, liver, ligament, and kidney TE, it finds its main application in tissue repair and regeneration, as wound healing and dressing,[247] osteochondral implants,[248,249] and tissue engineered vascular grafts (TEVGs).[238] Moreover, it shows several limitations as i) low production rate,[250] ii) pore size and fibers density that hinders cell infiltration,[243] and iii) 2D thin shape at the macroscopic scale.[250] Although some drawbacks have been addressed, for instance, cell infiltration can be increased by surface treatments or by coupling with other techniques to enhance macroporosity,[251] and thick scaffolds can be engineered by multilayered electrospinning,[252] bioprinting remains nowadays the most used and versatile technique for the biofabrication 3D vascularized tissue models.

4.4. Hybrid Strategies

In the last years, the need to engineer sophisticated biomimetic in vitro models has led researchers to combine different vascularization techniques discussed so far in the same manufacturing process, making classification in distinct classes often reductive. The rise of hybrid strategies for vascularization has the advantage that the unique features and strengths of different fabrication strategies for vascularization of physiologically relevant 3D models can be recapitulated on a single platform and we report here some significant examples of this approach (**Figure 9**).[251,252]

4.4.1. Bioprinting-Based Hybrid Fabrication Strategies

Many studies have focused on the use of 3D bioprinting strategies, discussed in detail in Section 4.3, for the fabrication of vascularized organ-on-a-chip platforms (Figure 3f). This approach shows several advantages such as the capability of recreating physiological-like multicellular spatial organization within the device and direct manufacturing of 3D perfusable vascular geometries, reducing the fabrication steps and moving toward more reproducible and automated strategies.[253] Moreover, this technique has shown its potential in vascularizing large tissue constructs and integrating patient-derived cells, representing a valuable tool for personalized medicine.[95,254,255] Bioprinting can be

used either to i) print hydrogels as template for channels fabrication on-chip or to ii) directly print vascular networks on-chip from cell-laden boinks (Figure 9a). These models, often embedded in an ECM matrix, are commonly perfused by integration within microfluidic bioreactors, produced by soft lithography or 3D printing technologies.[19,256–258]

In a recent work, a perfusable liver model was fabricated with GelMA hydrogel loaded with hepatocytes by using agarose as fiber template.[103] The cell-laden matrix was casted in a poly(methyl methacrylate) (PMMA) mold and the agarose was bioprinted in the shape of a channel by microextrusion. After UV photocrosslinking of GelMA, the agarose fiber was removed to form the hollow channel and the device was embedded in a PDMS–PMMA bioreactor for perfusion. A functional lumen was obtained by subsequent seeding of HUVECs in the empty channel and the platform was used for drug toxicity assays. Lin et al. used extrusion-based sacrificial bioprinting to engineer 3D vascularized proximal tubule models for the study of kidney reabsorption phenomena.[75] They used Pluronic F127 and high-molecular-weight poly(ethyleneoxide) (PEO) as fugitive ink to print colocalized convoluted proximal tubule and vascular channel embedded in an ECM matrix of gelatin and fibrin (Figure 4d; see Section 4.3.2).[191] A silicon gasket holding the structures allowed for perfusion of the tubule after dissolution of the fugitive ink at 4 °C. Proximal tubule epithelial cells and glomerular microvascular endothelial cells were seeded to form a functional epithelium and endothelium, respectively. Studies of albumin and inulin uptake confirmed selective reabsorption mechanism from the tubule to the vascular network and glucose reabsorption five- to tenfold higher compared to Transwell-based models. The reabsorption functions of the tubule and the role of the endothelium were investigated as well after administration of glucose transport inhibiting drug and simulation of hyperglycemia conditions.

Although bioprinting techniques are increasingly used for printing perfusable microfluidic networks, the bioprinting step is often limited to the fabrication of polymeric tubular structures, which are successively washed to form hollow channels and seeded with cells, as described above.[75] Recent works are focused on the bioprinting of cell laden gels on-chip: this strategy allows a reduction of the fabrication time by eliminating the need for the cell seeding step and it ensures a more precise and homogeneous cellular distribution and alignment, eventually in complex multilayered geometries.[104,105,259] In this context, coaxial needle technology has been used in several studies to directly fabricate endothelialized perfusable tissues.[108,195] 3D multilayer circumferential channels have been recently engineered by using single-step coaxial needle manufacturing to reproduce human tubular tissues as urethra and blood vessels.[104] A GelMA and alginate hydrogel blend combined with eight-arm poly(ethylene glycol) acrylate with tripentaerythritol core (PEGOA) was used as bioink and extruded after cells encapsulation by using up to 3 circumferential needles. Urothelial tissue was created by bioprinting a core layer of human urothelial cells (HUCs) and an external layer of human bladder smooth muscle cells (HBdSMCs) while vascular tubular tissues were composed of HUVECs and hSMCs circumferential layers. Results confirmed long-term viability (2 weeks), proliferation, and differentiation and showed the advantages of this method in creating functional tubular constructs for regenerative medicine and modeling (Table 2).

Recently, 4D bioprinting has emerged as technique for spatiotemporal control of networks self-assembly by using smart materials that respond to external stimuli (temperature, pH, swelling, ...). Thus, reversible self-folding tubular constructs can be engineered and their properties controlled over time by tuning the external cues, making this approach particularly interesting for programming the cellular microenvironment and creating functional hybrid hierarchical bioconstructs.[260,261] Bioprinting strategies for vasculature and OOaC design have been extensively reviewed elsewhere.[109,110,255,261–263]

3D bioprinting has been also used for fabrication of 3D cell cultures so as to overcome some of the current drawbacks, as spheroids/organoids variability and low throughput,[159,264] and spheroids/organoids models bioprinted on multiwell plates have been successfully developed for high throughput screening of compounds. Different bioprinting techniques have been adopted for either i) printing of PSC-only bioinks, subsequently self-organized in 3D aggregates, or ii) spheroid/organoid-laden hydrogels (Figure 9b).[265–268] Using a commercial 3D bioprinter, Higgins et al. generated large numbers of homogeneous functional kidney organoids in an automated fashion. Organoids were bioprinted from hPCSs bioink into 96-well plates and results showed formation of glomerular, epithelial and endothelial components and the capability to respond to drug-induced toxicity. The bioprinter enabled the production of more than 600 organoids per hour while the manual generation was estimated to be about 30 organoids in the same timeframe.[265] Vascularized adipose microtissues were created starting from a coculture of adipose-derived stem cells and HUVECs spheroids.[134] The spheroids were successfully used as bioprinting blocks encapsulated in a GelMA hydrogel mixed with a lithium-based photoinitiator. The spheroid-laden bioink was printed into a multilayer structure and the GelMA matrix was crosslinked through UVA irradiation. Results confirmed adipogenic differentiation, formation of vasculature and spheroids growth up to 14 days of culture. Vascularization of iPSC-derived organ building blocks has been achieved via sacrificial writing into functional tissue (SWIFT) by the group of J Lewis.[269] A matrix of collagen I and Matrigel was used as scaffold to tightly pack thousands of organoids that led to a highly dense tissue matrix after centrifugation. SWIFT was used for 3D printing of gelatin as sacrificial material within the matrix. After gelatin removal, the system could be perfused and functional lumens were formed by flow of HUVECs. This technique was used to generate perfusable cerebral organoids and cardiac spheroids and results confirmed the formation of functional tissue constructs with high cell density and in vivo-like microarchitecture. Recently, complex tissues with relevant micro- and macroscale organization have been fabricated by bioprinting organoids building blocks within support hydrogels.[268] The findings suggest the feasibility of engineering organoid-based tissues at the centimeter scale, providing innovative functional constructs for regenerative medicine and drug research.

Bioprinted structures have also been used as delivery vehicles for organoids. Soltanian et al. 3D printed PLA tissue trapper containing collagen I and Matrigel for the transplantation of pancreatic organoids from human embryonic stem cells into the abdominal cavity of immunodeficient mice, observing anastomosis with the host vasculature and enhanced production of insulin thanks to the proper cell–cell and cell–matrix interactions.[135]

4.4.2. Microfluidic-Based Hybrid Fabrication Strategies

The use of microfluidics for the production and culture of organoids, also defined as organoid-on-a-chip technology, is showing great potential in overcoming some of the main limitations of static 3D culture systems, as inefficient nutrients exchange, lack of standardization, and low throughput.[124,251,270] Over the past years, microfluidic strategies have been used for generation of spheroids and organoids,[271] in situ analysis and monitoring of organoids behavior,[197] and to build automated platforms for drug screening and personalized medicine.[272,273]

In the context of organoids vascularization, the two main microfluidic-based approaches are i) direct generation on-chip of the vascularized spheroid/organoid and ii) embedding of the spheroid/organoid and subsequent vascularization on-chip (Figure 9c).[137,274–276] By using the first strategy, Jin et al. created vascularized liver organoids on-chip. The liver organoids were composed of induced hepatic cells cocultured with HUVECs and they were embedded in a 3D decellularized liver ECM, used as scaffold. The system was integrated in a pump-free microfluidic device under continuous flow. The encapsulation of hepatic and endothelial cells under flow led to the formation of functional liver organoids with enhanced metabolism compared to static conditions and increased intercellular interaction and reduced apoptosis due to the presence of HUVECs. The system was used for drug testing on a microfluidic array for high-throughput and the integration of intestinal organoids enabled the simulation of multiorgan response to the screened drugs.[274]

Recently, Isshiki et al. vascularized brain organoids on a compartmentalized microfluidic device.[276] Brain organoids were generated from hiPSCs, followed by coculturing with HUVECs within the microfluidic chip. The microfluidic platform had five parallel channels: one for organoid-HUVEC coculture, which was sandwiched between two sets of microchannels where HUVECs and hLFs were suspended in cell culture media to form vasculature. Results showed that on-chip vasculature promoted differentiation and brain organogenesis with specific in vivo features as compared to conventional monoculture. Homan et al. developed kidney organoids in perfused 3D millifluidic device (Figure 6d).[137] Once harvested, organoids were introduced into the device, connected with external tubing where media was perfused through the chip via a closed loop circuit. The results showed that organoids grown under controlled high fluidic shear stress had enhanced glomerular vascularization and increase in adult gene expression as compared to organoids grown in static conditions, with development stages comparable to in vivo. Meanwhile, when organoids were grown in a prevascularized gel composed of HUVECs and hNDFs under static conditions, they were found to inhibit nephrogenesis, as compared to monoculture organoids grown under controlled flow. These findings suggest a preference for fluid flow during early stages development of kidney. The study could not prove that microvasculature formed in the kidney organoids were perfusable. Nevertheless, the feasibility to induce flow-enhanced on-chip organogenesis opens new strategies to form physiologically relevant in vitro models with functional vasculature. For a comprehensive review about vascularization strategies of organoids on-chip, we refer the reader to ref. [277].

By using bioprinting-based and microfluidic-based fabrication methods, researchers have already successfully proved the capability to engineer complex models, as 3D printed perfusable tissue equivalents and vascularized physiologically relevant models on-chip.[278–281] The combined use of these strategies has shown the possibility to create more reproducible and standardized constructs, laying the groundwork for the development of high throughput technologies.

5. Unmet Needs of Current Vascularized 3D Models

Despite the enormous progresses of the recent years, the biological complexity of vascularized 3D tissue models poses a challenge for the development of sophisticated platforms. Consequently, several limitations of the current constructs remain (**Table 6**). Nowadays, the biological environment is recreated by 3D matrices, integration of multicellular cultures that assemble in tissue relevant structures and by providing physiologically relevant stimuli. However, cell lines are still widely used in research and ECs from umbilical vein (HUVECs) remain the top choice for endothelium modeling due to easy handling, reliability in long-term culture, and affordable costs. Even though this common feature can be convenient when comparing results from different studies, it limits the establishment of organ-specific models, hampering the study of tissue-specific mechanisms at the vascular interface. Therefore, tissue specific human-derived primary endothelial cells represent a more valid source and have been used to engineer patient-specific platforms. However, access to human tissue and isolation protocols are often difficult and laborious operations.[282] For this reason, many studies are still based on animal cell sources, which once again impede data and system scalability toward "human-sized" models. Stem cell biology might be an alternative to address the current limitations and develop platforms for personalized medicine. Hence, vascular models using endothelial cells derived from multipotent or pluripotent stem cell sources have been already successfully engineered.[283,284] These cells present also the advantage of being suitable for further clinical development, such as in the case of bioprinted tissue constructs.

Another current limitation is the establishment of long-term models. As presented in Table 2, 4, and 5, most of the vascularized models are used as in vitro platforms for short-term studies (about 2 weeks) and this hampers the assessment

Table 6. Unmet needs of prevascularized models.

Model feature	Unmet need
Model design	• Difficult to replicate the capillaries size • Limited examples of dense microvasculature • Limited examples of thick vascularized tissues
In vitro cell culture	• Extensive use of cell lines • Short-term evaluation in vitro
Environmental control	• Need to integrate biochemical/ mechanical cues • Need for automation • Need for in situ monitoring via sensors integration

of vascularized tissue constructs in several ways, basing on their main application. Specifically, in the case of bioprinted devices, the long-term evaluation of their stability is fundamental for their in vivo application while, for 3D cell culture and microfluidics, the establishment of long-term models would ensure more accurate pathology-related and drug testing studies.[285–287]

The 3D geometrical complexity and the dimensions of the microcirculatory system can be more easily replicated with self-vascularization strategies compared to prevascularization techniques due to the spontaneous assembly of ECs, with sprouts diameters often below 30 µm.[288,289] However, this technique is not reproducible and it takes a longer time for the vasculature to be functional and perfusable. Current bioprinting strategies have shown the capability to 3D print complex vascular geometries,[100,191] as well as dense tissue constructs,[45] which could not be achieved otherwise. However, vessels size is still restricted by the resolution limit of many fabrication techniques and relatively few works have obtained capillary-like diameters, mainly by laser-based strategies, which have proved effective to create multiscale vascular networks with capillaries of less than 10 µm.[101,195]

As discussed in Section 4.1, the incorporation of biochemical and mechanical stimuli have been successfully achieved with microfluidic-based strategies,[19,195] yet engineering models that fully recapitulate the physiological cues of the microenvironment is still a challenge. In this context, 3D cell culture models such as spheroids and organoids present a solution to achieve both geometrical complexity and recapitulate the in vivo microenvironment thanks to their unique feature to self-organize. The generation of these in vivo like constructs manifests from cell culture systems, which make it possible to amend this technology to various cell culture platforms, enabling high-throughput screening and batch production, hence, highly translational to the industry. In terms of vascularization, spheroids/organoids present a different set of challenges. As discussed in Section 4.2, vascularized spheroids/organoids can achieve capillary-like structures both in vitro and in vivo via coculture with ECs and transplantation in animal models. Therefore, all the technical and ethical issues associated with using ECs (cell source, availability, etc.) and animal models encompass the challenges of using vascularized spheroids/organoids for research, clinical, and industrial purposes.

The incorporation of the lymphatic system must also be considered to create more comprehensive microcirculatory models.[290,291] This network plays a fundamental role in tissue fluid homeostasis, immune cells trafficking, and actively participates in cardiovascular pathophysiology, cancer metastases and several diseases progression.[292–294]

Automation represents another key requirement in the development of reliable and high throughput platforms and, although sophisticated devices for automated manipulation, testing, and analysis on-chip have been recently developed,[77,102] most of the works do not consider this feature. In parallel, the further integration of sensors for in situ monitoring of construct performances would speed up the automation, scalability, and readouts of these models, while boosting their value in both academic and industrial setups.[201,295–297]

6. Industrial and Clinical Translation of Current Vascularized 3D Models

6.1. Scaling Up

The development of scalable vascularized models should take into account the following requirements: a reproducible, time, and cost-effective fabrication process to obtain robust, high throughput, automated, physiologically relevant, and user-friendly constructs or platforms.[298] As aforementioned, technologies such as additive manufacturing hold potential for producing sophisticated constructs by means of reliable and rapid fabrication processes, that can be scaled-up to mass production. However, it is important to keep in mind the need to create models that can be operated in a simple and proper way by a wide range of end-users.

The scalability of microfluidic-based technology is still limited by use of external bulky perfusion systems. To cope with this challenge, the multiwell format, which consists of many 3D microfluidic devices on a single plate, has been proposed successfully and produced in both academic and industrial settings.[5,299] This technology enables researchers to work with high throughput devices while ensuring compact designs and user-friendly formats, conventionally used in biology and pharmaceutical fields. The multiwell format-based and pumpless Organoplate platforms produced by the Dutch biotech company MIMETAS have been largely used for creating vascularized OOaC models and study angiogenesis without the need for external perfusion, paving the way for a tangible industrial translation of OOaC technology.[288,300]

Organoids are considered a powerful model for drug testing and development as well as for personalized medicine. The establishment of organoids biobanks from either healthy or diseased tissues has boosted the scale-up of this technology,[301,302] and protocols for large-scale production of organoids in compliance with Good Manufacturing Practices (GMP) requirements have been recently published.[303,304] As discussed in Section 4.4, the use of microfluidic and bioprinting fabrication strategies could accelerate the scalability of 3D cell cultures by providing automated high throughput platforms and standardized production.[265] The translation of the technology from basic research to industry and clinic poses however several challenges and questions from both the ethical and the logistic points of view. Aspects as informed consent of the donors, commercial ownership, and public versus private biobanks still need to be defined in a clear regulatory framework to enable the scale up of organoids models.[113,305]

As for bioprinting technology, difficulties in scaling up functional tissues with adequate size to achieve vascularization limits its use for tissue repair. More importantly, questions regarding the mechanical strength and stability of bioengineered tissues, as well as their integration, innervation, immunogenicity, and maintenance of long-term functionality after implantation, must also be considered.[171,185] For example, pilot studies to determine the vascularization degree of skin substitutes after in vivo implantation could contribute to the development of tissue constructs with relevant sizes to be used in the clinic but more preclinical studies are required to address such concerns.[306]

It is worth noting however that one of the major challenges for the scale-up of constructs for regenerative medicine still remains the large-scale expansion of human cells. Since billions of functional cells per patient are required for implantation,[307] researchers have worked in the past years on the scalability of culture systems in line with current GMP. In this perspective, large-scale expansion methods have moved from 2D culture systems, in which cells are expanded by multiplying the number of culture dishes, to bioreactor systems, with the advantage of introducing dynamic culturing conditions, monitoring and controlling of the culture environment, less user-dependent variability, and higher cost and time efficiency. With the variety of bioreactors and culture methods established nowadays,[308] protocols for scalable GMP production of PSCs, hiPSC-derived cells and multipotent SCs, especially MSCs, fundamental during the angiogenesis process, have been successfully developed,[309–311] although some critical aspects are still debated. For instance, media formulation still represents one of the bottlenecks and an homogenization is required, notably to prevent any unwanted differentiation during the expansion process and to cope with the high costs of the components.[312] Furthermore, for the compliance with GMP standards, many other parameters, as donors selection, facilities control, storage, and distribution of the final products need to be standardized.[313] The establishment of reliable and automated mass cellular production protocols is thus an essential precondition for the industrial and clinical scale-up of tissue engineered constructs.

6.2. Drug Development

Drug development is a long and expensive multistep process that involves basic research and drug discovery, preclinical and clinical trials and, after the approval, postmarket monitoring. The estimated cost for the development of one new drug is of 2.5 billion dollars, of which 60% in clinical trials, and the process takes about 12 years, with less than 10% of the drug candidates succeeding in human clinical trial phases.[10,314,315] Although the inadequacy of animals in modeling human response and related ethical issues, mammalian models are still necessary for drugs testing in preclinical phase.[8–10]

In this context, OOaC technology has been extensively investigated as tool to speed up drug research by better mimicking in vivo behavior and combining interactions between different tissues. Similar to spheroids/organoids, OOaC technology can lower the R&D costs and overcome the use of animal models by means of more predictive and representative preclinical systems.[316–319] Particularly, OOaC models can be used in preclinical trials for the study of PK–PD mechanisms and to test drugs already on the market for safety monitoring. The use of multiorgan-on-chip platforms with integrated vasculature results of particular interest for studying absorption, distribution, metabolism, excretion (ADME) pathways of new drug candidates.[314,320] With the European Union's full ban on testing cosmetic ingredients or products on animals in 2013, OOaC technology has emerged as well as alternative in vitro model for toxicology studies and safety assessment in cosmetics field.[74,321] All over the world, public and private institutions have funded OOaC-related programs to promote and accelerate the translation of the technology from fundamental research to the industry, leading to the establishment of many OOaC start-ups.[315,322,323] Leading pharmaceutical and cosmetic companies are actively collaborating with some of the major start-ups and academic centers to integrate OOaC platforms in drug testing and safety assessment in an industrial context. OOaC models have already shown higher complexity and better predictability compared to other in vitro systems. Thus, further development of these platforms to address the unmet needs could have a tremendous impact on the current drug development process.

In oncology drug research, where only ≤5% of new anticancer drug candidates is approved, tumor organoids and spheroids present a promising strategy to improve drug approval rates and serve as potential preclinical drug screening platforms.[324,325] For instance, colon cancer organoids were used to screen 83 drugs currently used in clinics or in clinical trials for cancer treatments. The findings demonstrated that colon cancer organoids were suitable for high throughput screening of drug candidates and could better mimic tumor microenvironment such as oxygen and nutrient gradients compared to existing models.[324,326] Tumor organoids have also been used successfully as preclinical models for pharmacodynamic profiling of human tumors.[327] Companies like Fluofarma and InSphero offer fast-growing 3D tumor spheroids, which can be adapted for high throughput single-cell analysis, functional assays, drug testing, and preclinical and clinical models. Besides oncology, spheroids and organoids are also widely employed to speed up drug testing and to overcome difficulties associated with predictions of outcomes in other pathologies.[115,325,328] InSphero develops models for diabetes and liver diseases such as nonalcoholic fatty liver disease (NAFLD) and nonalcoholic steatohepatitis (NASH) and organoids generated from ex vivo biopsy samples have been used to model genetic diseases such as cystic fibrosis (CF) for the development of precision therapies.[329]

The pharmaceutical industry has adopted as well bioprinted models, also due to a recent increase of the number of bioprinters on the market.[171] Since 2014, liver tissue models bioprinted by Organovo are used in the pharma industry to screen liver toxicity of drugs.[133] Other companies, such as Aspect Biosystems, have more recently established joint programs with pharmaceutical companies for the screening of immuno-therapeutics to treat cancer using 3D printed models,[330] as well as with multinational research organizations to develop vascularized human liver lobules by means of their microfluidic 3D bioprinting technology.[331]

6.3. Toward Clinical Application of Vascularized Models

Although recent attempts to use microfluidics and 3D cell culture constructs for tissue repair and regenerative medicine have been made,[94,332–335] their application remains mainly focused on drug research and development of personalized treatments, as discussed above.[100,316,326] Particularly, patient-derived organoids hold great potential for transplant application since they would solve the major issues of using allogenic materials, with related immune response, and of shortage of donors.[334] However, even if preclinical animal studies have shown the possible application of organoids for cell or organ transplantation, the use of

models integrating vasculature remains limited.[336–338] In the clinical context, bioprinting-based vascularization strategies represent currently the most advanced technology. Intraoperative bioprinting, i.e., the direct printing of tissue on the patient in the operating theater, holds great promise together with several challenges and preclinical studies, mainly in mice, have already been successfully performed.[339] Kérourédan et al. printed by LAB stem cells from apical papilla mixed with HUVEC, during surgical procedure for the treatment of murine bone calvary defect.[214] The main advantage of LAB is the lack of contact between the printer and the patient tissue, when compared to extrusion methods. Nevertheless, to translate this technology to an operating room, 3D bioprinters still need to be adapted: miniaturization of the system, low printing speed, which might prolong the surgery, and the need to precisely control the light source represent important challenges.[339] Besides, to assure proper vascularization of the printed tissue, 3D bioprinters should ideally print macrovessels in tandem with microvessels to enable the anastomosis with the patient circulation while ensuring instant blood supply to the construct.

Since the aim of this technology is to adapt to each patient and be performed on-site, aspects such as standardization, customization, quality control, GMP, etc., should be defined for its application in human clinical trials. In fact, regulatory aspects for use on patients need to be defined urgently since tissues obtained by bioprinting are not yet subject to dedicated regulatory standards.[340,341] The elements involved in the manufacture of these tissues are i) the material, ii) the cells, iii) the software, and iv) the bioprinter. In some cases, a maturation stage is also added. Some of these elements are considered medical products (cells) and others medical devices (software), thus they would be under different regulations. The origin of the material (animal, synthetic, recombinant proteins, etc.) and cells (autologous/heterologous, embryonic, etc.), or the type of maturation (using growth factors, bioreactors, etc.) also determines the rules to follow in the different countries.[342] It is therefore necessary to establish a clear framework to determine the classification of the tissues obtained by bioprinting and to define the regulatory requirements. For more information on this topic, the reader is referred to the book chapter of Li., published in 2018.[340]

The use of vascularized 3D models with physiological relevance can bridge the gap between in vitro research, drug development and clinical trials. Here, we have discussed how 3D cell culture models and microfluidic platforms are promising tools to improve the robustness and reliability of preclinical research data, minimize the need for animal testing and develop more efficient drug screening platforms and personalized therapies. Although their potential for transplantation and regenerative medicine has been proven, the use of complete models including vasculature is still in its infancy. On the hand, 3D bioprinting has been more widely investigated as technology for organs repair and regeneration but ethical and regulatory aspects still need to be addressed carefully to enable its safe and rapid translation.

7. Conclusion

The recent achievements of research in developing 3D physiological in vitro models hold promise to revolutionize the conventional regenerative medicine approaches by creating new tools for basic research, personalized medicine, drug development, and clinical application. The use of complex models integrating vasculature is a key requirement for their successful translation. Current efforts are closer than ever to engineer complex, dense and thick vascularized organ-specific models and the continuous improvements of tissue engineering have already shown great potential in fabricating 3D physiological relevant constructs for clinical and industrial settings. Nevertheless, certain drawbacks, regarding the technical challenges, the scale-up, and the regulatory framework still need to be addressed. On a scientific level, the combination of different and complementary tissue engineering strategies would allow researchers to overcome some of the current fabrication limits, as we have illustrated here. At the same time, the close cooperation and open dialogue of researchers, clinicians, and industry would contribute in speeding up the translational process in the near future.

Acknowledgements

This work was supported by Inserm, Université Sorbonne Paris Nord, and Université de Paris. A.D. acknowledges funding from the European Union's Horizon 2020 research and innovation programme under the Marie Skłodowska-Curie Action - Innovative Training Network (MSCA-ITN) DeLIVER, grant agreement no. 766181. C.L.B. acknowledges funding from the "Recherche Hospitalo-universitaire" Innovations for Liver Tissue Engineering (RHU iLite), grant no. ANR-16-RHUS-0005.

Conflict of Interest

The authors declare no conflict of interest.

Keywords

3D cell culture, bioprinting, microfluidics, tissue engineering, vascularization

Received: February 26, 2021
Revised: April 23, 2021
Published online:

[1] C. Hu, Y. Chen, M. J. A. Tan, K. Ren, H. Wu, *Analyst* **2019**, *144*, 4461.
[2] K. Haase, R. D. Kamm, *Regener. Med.* **2017**, *12*, 285.
[3] J. Rouwkema, A. Khademhosseini, *Trends Biotechnol.* **2016**, *34*, 733.
[4] H. Jian, M. Wang, S. Wang, A. Wang, S. Bai, *Bio-Des. Manuf.* **2018**, *1*, 45.
[5] D. S. Y. Lin, F. Guo, B. Zhang, *Nanotechnology* **2019**, *30*, 024002.
[6] S. Kim, W. Kim, S. Lim, J. S. Jeon, *Bioengineering* **2017**, *4*, 8.
[7] A. D. Bannerman, R. X. Ze Lu, A. Korolj, L. H. Kim, M. Radisic, *Curr. Opin. Biomed. Eng.* **2018**, *6*, 8.
[8] I. A. Freires, J. d. C. O. Sardi, R. D. de Castro, P. L. Rosalen, *Pharm. Res.* **2017**, *34*, 681.
[9] K. Ronaldson-Bouchard, G. Vunjak-Novakovic, *Cell Stem Cell* **2018**, *22*, 310.
[10] J. M. Wilkinson, in *Organ-on-a-Chip: Engineered Microenvironments for Safety and Efficacy Testing* (Eds: J. Hoeng, D. Bovard, M. C. Peitsch), Elsevier, Amsterdam **2020**, Ch. 1.
[11] D. Antoni, H. Burckel, E. Josset, G. Noel, *Int. J. Mol. Sci.* **2015**, *16*, 5517.

[12] J. Grenier, H. Duval, F. Barou, P. Lv, B. David, D. Letourneur, *Acta Biomater.* **2019**, *94*, 195.
[13] M.-N. Labour, C. Le Guilcher, R. Aid-Launais, N. El Samad, S. Lanouar, T. Simon-Yarza, D. Letourneur, *Int. J. Mol. Sci.* **2020**, *21*, 3644.
[14] S. Jalili-Firoozinezhad, M. Filippi, F. Mohabatpour, D. Letourneur, A. Scherberich, *Mater. Today* **2020**, *40*, 193.
[15] F. A. Auger, L. Gibot, D. Lacroix, *Annu. Rev. Biomed. Eng.* **2013**, *15*, 177.
[16] W. D. Tucker, Y. Arora, K. Mahajan, *Anatomy, Blood Vessels*, StatPearls Publishing, Treasure Island, FL **2018**.
[17] A. Hasan, A. Paul, N. E. Vrana, X. Zhao, A. Memic, Y. S. Hwang, M. R. Dokmeci, A. Khademhosseini, *Biomaterials* **2014**, *35*, 7308.
[18] E. Witzleb, in *Human Physiology* (Eds: R. F. Schmidt, G. Thews), Springer, Berlin **1989**, Ch. 20.
[19] N. Mori, Y. Akagi, Y. Imai, Y. Takayama, Y. S. Kida, *Sci. Rep.* **2020**, *10*, 5646.
[20] E. Bianconi, A. Piovesan, F. Facchin, A. Beraudi, R. Casadei, F. Frabetti, L. Vitale, M. C. Pelleri, S. Tassani, F. Piva, S. Perez-Amodio, P. Strippoli, S. Canaider, *Ann. Hum. Biol.* **2013**, *40*, 463.
[21] J. G. Betts, K. A. Young, J. A. Wise, E. Johnson, B. Poe, D. H. Kruse, O. Korol, J. E. Johnson, M. Womble, P. DeSaix, *Anatomy and Physiology*, OpenStax, Houston, TX **2013**, Ch. 20.
[22] W. C. Aird, *Circ. Res.* **2007**, *100*, 158.
[23] M. E. Gerritsen, *Biochem. Pharmacol.* **1997**, *36*, 2701.
[24] H. Gerhardt, M. Golding, M. Fruttiger, C. Ruhrberg, A. Lundkvist, A. Abramsson, M. Jeltsch, C. Mitchell, K. Alitalo, D. Shima, C. Betsholtz, *J. Cell Biol.* **2003**, *161*, 1163.
[25] H. M. Eilken, R. H. Adams, *Curr. Opin. Cell Biol.* **2010**, *22*, 617.
[26] T. Simon-Yarza, M. N. Labour, R. Aid, D. Letourneur, *Mater. Sci. Eng., C* **2021**, *118*, 111369.
[27] L. K. Phng, H. Gerhardt, *Dev. Cell* **2009**, *16*, 196.
[28] R. Benedito, S. F. Rocha, M. Woeste, M. Zamykal, F. Radtke, O. Casanovas, A. Duarte, B. Pytowski, R. H. Adams, *Nature* **2012**, *484*, 110.
[29] T. Simón-Yarza, F. R. Formiga, E. Tamayo, B. Pelacho, F. Prosper, M. J. Blanco-Prieto, *Theranostics* **2012**, *2*, 541.
[30] W. Risau, *Nature* **1997**, *386*, 671.
[31] M. Shibuya, *Genes Cancer* **2011**, *2*, 1097.
[32] D. R. Senger, G. E. Davis, *Cold Spring Harbor Perspect. Biol.* **2011**, *3*, a005090.
[33] L. K. Fiddes, N. Raz, S. Srigunapalan, E. Tumarkan, C. A. Simmons, A. R. Wheeler, E. Kumacheva, *Biomaterials* **2010**, *31*, 3459.
[34] J. He, R. Chen, Y. Lu, L. Zhan, Y. Liu, D. Li, Z. Jin, *Mater. Sci. Eng., C* **2016**, *59*, 53.
[35] K. K. Sørensen, P. McCourt, T. Berg, C. Crossley, D. Le Couteur, K. Wake, B. Smedsrød, *Am. J. Physiol.: Regul., Integr. Comp. Physiol.* **2012**, *303*, R1217.
[36] G. R. Martin, R. Timpl, *Annu. Rev. Cell Biol.* **1987**, *3*, 57.
[37] T. Tilling, D. Korte, D. Hoheisel, H. J. Galla, *J. Neurochem.* **1998**, *71*, 1151.
[38] Y. Kubota, H. K. Kleinman, G. R. Martin, T. J. Lawley, *J. Cell Biol.* **1988**, *107*, 1589.
[39] D. M. Form, B. M. Pratt, J. A. Madri, *Lab. Invest.* **1986**, *55*, 521.
[40] J. S. Lowe, P. G. Anderson, *Stevens & Lowe's Human Histology*, Elsevier, Amsterdam **2015**, pp. 55–70.
[41] J. H. Miner, N. M. Nguyen, *Encyclopedia of Respiratory Medicine, Four-Volume Set*, Elsevier, Amsterdam **2006**, pp. 157–162.
[42] T. W. Secomb, *Compr. Physiol.* **2016**, *6*, 975.
[43] S. Kim, H. Lee, M. Chung, N. L. Jeon, *Lab Chip* **2013**, *13*, 1489.
[44] C. F. Guimarães, L. Gasperini, A. P. Marques, R. L. Reis, *Nat. Rev. Mater.* **2020**, *5*, 351.
[45] R. Pimentel C, S. K. Ko, C. Caviglia, A. Wolff, J. Emnéus, S. S. Keller, M. Dufva, *Acta Biomater.* **2018**, *65*, 174..
[46] M. Chaouat, C. Le Visage, W. E. Baille, B. Escoubet, F. Chaubet, M. A. Mateescu, D. Letourneur, *Adv. Funct. Mater.* **2008**, *18*, 2855.
[47] M. Atlan, T. Simon-Yarza, J. M. Ino, V. Hunsinger, L. Corté, P. Ou, R. Aid-Launais, M. Chaouat, D. Letourneur, *Sci. Rep.* **2018**, *8*, 7417.
[48] S. Lee, J. Ko, D. Park, S. R. Lee, M. Chung, Y. Lee, N. L. Jeon, *Lab Chip* **2018**, *18*, 2686.
[49] Q. Smith, S. Gerecht, *Curr. Opin. Chem. Eng.* **2014**, *3*, 42.
[50] J. Tien, *Curr. Opin. Chem. Eng.* **2014**, *3*, 36.
[51] R. Ning, Q. Zhuang, J.-M. Lin, in *Cell Analysis on Microfluidics* (Eds: J. M. Lin), Integrated Analytical Systems, Springer, Singapore **2018**, pp. 181–224.
[52] I. K. Zervantonakis, S. K. Hughes-Alford, J. L. Charest, J. S. Condeelis, F. B. Gertler, R. D. Kamm, *Proc. Natl. Acad. Sci. USA* **2012**, *109*, 13515.
[53] A. Dellaquila, E. K. Thomée, A. H. McMillan, S. C. Lesher-Pérez, in *Organ-on-a-Chip: Engineered Microenvironments for Safety and Efficacy Testing* (Eds: J. Hoeng, D. Bovard, M. C. Peitsch), Elsevier, Amsterdam **2020**, Ch. 4.
[54] R. Sudo, S. Chung, I. K. Zervantonakis, V. Vickerman, Y. Toshimitsu, L. G. Griffith, R. D. Kamm, *FASEB J.* **2009**, *23*, 2155.
[55] B. Sebastian, P. S. Dittrich, *Annu. Rev. Fluid Mech.* **2018**, *50*, 483.
[56] B. Prabhakarpandian, M. C. Shen, K. Pant, M. F. Kiani, *Microvasc. Res.* **2011**, *82*, 210.
[57] D. R. Myers, Y. Sakurai, R. Tran, B. Ahn, E. T. Hardy, R. Mannino, A. Kita, M. Tsai, W. A. Lam, *J. Visualized Exp.* **2012**, e3958.
[58] R. G. Mannino, D. R. Myers, B. Ahn, Y. Wang, M. Rollins, H. Gole, A. S. Lin, R. E. Guldberg, D. P. Giddens, L. H. Timmins, W. A. Lam, *Sci. Rep.* **2015**, *5*, 12401.
[59] S. H. Lee, J. H. Sung, *Adv. Healthcare Mater.* **2018**, *7*, 1700419.
[60] E. W. K. Young, *J. Lab. Autom.* **2013**, *18*, 427.
[61] A. M. A. O. Pollet, J. M. J. den Toonder, *Bioengineering* **2020**, *7*, 17.
[62] D. Huh, B. D. Matthews, A. Mammoto, M. Montoya-Zavala, H. Yuan Hsin, D. E. Ingber, *Science* **2010**, *328*, 1662.
[63] L. Wang, T. Tao, W. Su, H. Yu, Y. Yu, J. Qin, *Lab Chip* **2017**, *17*, 1749.
[64] S. Musah, A. Mammoto, T. C. Ferrante, S. S. F. Jeanty, M. Hirano-Kobayashi, T. Mammoto, K. Roberts, S. Chung, R. Novak, M. Ingram, T. Fatanat-Didar, S. Koshy, J. C. Weaver, G. M. Church, D. E. Ingber, *Nat. Biomed. Eng.* **2017**, *1*, 0069.
[65] J. A. Brown, V. Pensabene, D. A. Markov, V. Allwardt, M. Diana Neely, M. Shi, C. M. Britt, O. S. Hoilett, Q. Yang, B. M. Brewer, P. C. Samson, L. J. McCawley, J. M. May, D. J. Webb, D. Li, A. B. Bowman, R. S. Reiserer, J. P. Wikswo, *Biomicrofluidics* **2015**, *9*, 054124.
[66] S. Bang, S. R. Lee, J. Ko, K. Son, D. Tahk, J. Ahn, C. Im, N. L. Jeon, *Sci. Rep.* **2017**, *7*, 8083.
[67] S. W. L. Lee, M. Campisi, T. Osaki, L. Possenti, C. Mattu, G. Adriani, R. D. Kamm, V. Chiono, *Adv. Healthcare Mater.* **2020**, *9*, 1901486.
[68] M. B. Chen, S. Srigunapalan, A. R. Wheeler, C. A. Simmons, *Lab Chip* **2013**, *13*, 2591.
[69] B. Zhang, B. Fook, L. Lai, R. Xie, L. Davenport Huyer, M. Montgomery, M. Radisic, *Nat. Protoc.* **2018**, *13*, 1793.
[70] H. J. Kim, H. Li, J. J. Collins, D. E. Ingber, *Proc. Natl. Acad. Sci. USA* **2016**, *113*, E7.
[71] A. Bein, W. Shin, S. Jalili-Firoozinezhad, M. H. Park, A. Sontheimer-Phelps, A. Tovaglieri, A. Chalkiadaki, H. J. Kim, D. E. Ingber, *Cell. Mol. Gastroenterol. Hepatol.* **2018**, *5*, 659.
[72] Y. B. A. Kang, T. R. Sodunke, J. Lamontagne, J. Cirillo, C. Rajiv, M. J. Bouchard, M. Noh, *Biotechnol. Bioeng.* **2015**, *112*, 2571.
[73] Y. Du, N. Li, H. Yang, C. Luo, Y. Gong, C. Tong, Y. Gao, S. Lü, M. Long, *Lab Chip* **2017**, *17*, 782.
[74] N. Mori, Y. Morimoto, S. Takeuchi, *Biomaterials* **2017**, *116*, 48.
[75] N. Y. C. Lin, K. A. Homan, S. S. Robinson, D. B. Kolesky, N. Duarte, A. Moisan, J. A. Lewis, H. John, A. Paulson, *Proc. Natl. Acad. Sci. USA* **2019**, *116*, 5399.

[76] S. Jalili-Firoozinezhad, C. C. Miranda, J. M. S. Cabral, *Trends Biotechnol.* **2021**, *39*, 838.
[77] R. Novak, M. Ingram, S. Marquez, D. Das, A. Delahanty, A. Herland, B. M. Maoz, S. S. F. Jeanty, M. R. Somayaji, M. Burt, E. Calamari, A. Chalkiadaki, A. Cho, Y. Choe, D. B. Chou, M. Cronce, S. Dauth, T. Divic, J. Fernandez-Alcon, T. Ferrante, J. Ferrier, E. A. FitzGerald, R. Fleming, S. Jalili-Firoozinezhad, T. Grevesse, J. A. Goss, T. Hamkins-Indik, O. Henry, C. Hinojosa, T. Huffstater, K.-J. Jang, V. Kujala, L. Leng, R. Mannix, Y. Milton, J. Nawroth, B. A. Nestor, C. F. Ng, B. O'Connor, T.-E. Park, H. Sanchez, J. Sliz, A. Sontheimer-Phelps, B. Swenor, G. Thompson, G. J. Touloumes, Z. Tranchemontagne, N. Wen, M. Yadid, A. Bahinski, G. A. Hamilton, D. Levner, O. Levy, A. Przekwas, R. Prantil-Baun, K. K. Parker, D. E. Ingber, *Nat. Biomed. Eng.* **2020**, *4*, 407.
[78] K. Schimek, M. Busek, S. Brincker, B. Groth, S. Hoffmann, R. Lauster, G. Lindner, A. Lorenz, U. Menzel, F. Sonntag, H. Walles, U. Marx, R. Horland, *Lab Chip* **2013**, *13*, 3588.
[79] W. Zhang, Y. S. Zhang, S. M. Bakht, J. Aleman, S. R. Shin, K. Yue, M. Sica, J. Ribas, M. Duchamp, J. Ju, R. B. Sadeghian, D. Kim, M. R. Dokmeci, A. Atala, A. Khademhosseini, *Lab Chip* **2016**, *16*, 1579.
[80] J. T. Borenstein, M. M. Tupper, P. J. MacK, E. J. Weinberg, A. S. Khalil, J. Hsiao, G. García-Cardeña, *Biomed. Microdevices* **2010**, *12*, 71.
[81] M. B. Esch, D. J. Post, M. L. Shuler, T. Stokol, *Tissue Eng., Part A* **2011**, *17*, 2965.
[82] M. E. Wilson, N. Kota, Y. Kim, Y. Wang, D. B. Stolz, P. R. Leduc, O. B. Ozdoganlar, *Lab Chip* **2011**, *11*, 1550.
[83] J. S. Choi, Y. Piao, T. S. Seo, *Bioprocess Biosyst. Eng.* **2013**, *36*, 1871.
[84] L. L. Bischel, E. W. K. Young, B. R. Mader, D. J. Beebe, *Biomaterials* **2013**, *34*, 1471.
[85] A. Herland, A. D. Van Der Meer, E. A. FitzGerald, T. E. Park, J. J. F. Sleeboom, D. E. Ingber, *PLoS One* **2016**, *11*, e0150360.
[86] Y. Zheng, J. Chen, M. Craven, N. W. Choi, S. Totorica, A. Diaz-Santana, P. Kermani, B. Hempstead, C. Fischbach-Teschl, J. A. López, A. D. Stroock, *Proc. Natl. Acad. Sci. USA* **2012**, *109*, 9342.
[87] G. Ligresti, R. J. Nagao, J. Xue, Y. J. Choi, J. Xu, S. Ren, T. Aburatani, S. K. Anderson, J. W. MacDonald, T. K. Bammler, S. M. Schwartz, K. A. Muczynski, J. S. Duffield, J. Himmelfarb, Y. Zheng, *J. Am. Soc. Nephrol.* **2016**, *27*, 2370.
[88] S. Lee, M. Chung, S. R. Lee, N. L. Jeon, *Biotechnol. Bioeng.* **2020**, *117*, 748.
[89] R. Xie, W. Zheng, L. Guan, Y. Ai, Q. Liang, *Small* **2019**, *16*, 1902838.
[90] J. Liu, H. Zheng, P. Poh, H.-G. Machens, A. Schilling, *Int. J. Mol. Sci.* **2015**, *16*, 15997.
[91] A. P. Golden, J. Tien, *Lab Chip* **2007**, *7*, 720.
[92] L. E. Bertassoni, M. Cecconi, V. Manoharan, M. Nikkhah, J. Hjortnaes, A. L. Cristino, G. Barabaschi, D. Demarchi, M. R. Dokmeci, Y. Yang, A. Khademhosseini, *Lab Chip* **2014**, *14*, 2202.
[93] I. Vollert, M. Seiffert, J. Bachmair, M. Sander, A. Eder, L. Conradi, A. Vogelsang, T. Schulze, J. Uebeler, W. Holnthoner, H. Redl, H. Reichenspurner, A. Hansen, T. Eschenhagen, *Tissue Eng., Part A* **2014**, *20*, 854.
[94] H. E. Abaci, Z. Guo, A. Coffman, B. Gillette, W. H. Lee, S. K. Sia, A. M. Christiano, *Adv. Healthcare Mater.* **2016**, *5*, 1800.
[95] D. B. Kolesky, K. A. Homan, M. A. Skylar-Scott, J. A. Lewis, *Proc. Natl. Acad. Sci. USA* **2016**, *113*, 3179.
[96] W. H. Goh, M. Hashimoto, *Macromol. Mater. Eng.* **2018**, *303*, 1700484.
[97] A. Hansen, A. Eder, M. Bönstrup, M. Flato, M. Mewe, S. Schaaf, B. Aksehirlioglu, A. Schwörer, J. Uebeler, T. Eschenhagen, *Circ. Res.* **2010**, *107*, 35.
[98] J. S. Miller, K. R. Stevens, M. T. Yang, B. M. Baker, D. H. T. Nguyen, D. M. Cohen, E. Toro, A. A. Chen, P. A. Galie, X. Yu, R. Chaturvedi, S. N. Bhatia, C. S. Chen, *Nat. Mater.* **2012**, *11*, 768.
[99] D. Lei, Y. Yang, Z. Liu, B. Yang, W. Gong, S. Chen, S. Wang, L. Sun, B. Song, H. Xuan, X. Mo, B. Sun, S. Li, Q. Yang, S. Huang, S. Chen, Y. Ma, W. Liu, C. He, B. Zhu, E. M. Jeffries, F. L. Qing, X. Ye, Q. Zhao, Z. You, *Mater. Horiz.* **2019**, *6*, 1197.
[100] B. Zhang, M. Montgomery, M. D. Chamberlain, S. Ogawa, A. Korolj, A. Pahnke, L. A. Wells, S. Masse, J. Kim, L. Reis, A. Momen, S. S. Nunes, A. R. Wheeler, K. Nanthakumar, G. Keller, M. V. Sefton, M. Radisic, *Nat. Mater.* **2016**, *15*, 669.
[101] K. A. Heintz, M. E. Bregenzer, J. L. Mantle, K. H. Lee, J. L. West, J. H. Slater, *Adv. Healthcare Mater.* **2016**, *5*, 2153.
[102] S. Yasotharan, S. Pinto, J. G. Sled, S. S. Bolz, A. Günther, *Lab Chip* **2015**, *15*, 2660.
[103] S. Massa, M. A. Sakr, J. Seo, P. Bandaru, A. Arneri, S. Bersini, E. Zare-Eelanjegh, E. Jalilian, B. H. Cha, S. Antona, A. Enrico, Y. Gao, S. Hassan, J. P. Acevedo, M. R. Dokmeci, Y. S. Zhang, A. Khademhosseini, S. R. Shin, *Biomicrofluidics* **2017**, *11*, 044109.
[104] Q. Pi, S. Maharjan, X. Yan, X. Liu, B. Singh, A. M. van Genderen, F. Robledo-Padilla, R. Parra-Saldivar, N. Hu, W. Jia, C. Xu, J. Kang, S. Hassan, H. Cheng, X. Hou, A. Khademhosseini, Y. S. Zhang, *Adv. Mater.* **2018**, *30*, 1706913.
[105] M. Abudupataer, N. Chen, S. Yan, F. Alam, Y. Shi, L. Wang, H. Lai, J. Li, K. Zhu, C. Wang, *Biomed. Microdevices* **2020**, *22*, 10.
[106] M. Humayun, C. W. Chow, E. W. K. Young, *Lab Chip* **2018**, *18*, 1298.
[107] J. Cui, H. Wang, Z. Zheng, Q. Shi, T. Sun, Q. Huang, T. Fukuda, *Biofabrication* **2019**, *11*, 015016.
[108] Y. S. Zhang, A. Arneri, S. Bersini, S. R. Shin, K. Zhu, Z. Goli-Malekabadi, J. Aleman, C. Colosi, F. Busignani, V. Dell'Erba, C. Bishop, T. Shupe, D. Demarchi, M. Moretti, M. Rasponi, M. R. Dokmeci, A. Atala, A. Khademhosseini, *Biomaterials* **2016**, *110*, 45.
[109] D. Richards, J. Jia, M. Yost, R. Markwald, Y. Mei, *Ann. Biomed. Eng.* **2017**, *45*, 132.
[110] A. K. Miri, E. Mostafavi, D. Khorsandi, S. K. Hu, M. Malpica, A. Khademhosseini, *Biofabrication* **2019**, *11*, 042002.
[111] Y. Fang, R. M. Eglen, *SLAS Discovery* **2017**, *22*, 456.
[112] M. A. Lancaster, J. A. Knoblich, *Nat. Protoc.* **2014**, *9*, 2329.
[113] F. Schutgens, H. Clevers, *Annu. Rev. Pathol.: Mech. Dis.* **2020**, *15*, 211.
[114] M. W. Laschke, M. D. Menger, *Trends Biotechnol.* **2017**, *35*, 133.
[115] T. Takahashi, *Annu. Rev. Pharmacol. Toxicol.* **2019**, *59*, 447.
[116] B. Cakir, Y. Xiang, Y. Tanaka, M. H. Kural, M. Parent, Y. Kang, K. Chapeton, B. Patterson, Y. Yuan, C. He, M. S. B. Raredon, J. Dengelegi, K. Kim, P. Sun, M. Zhong, S. Lee, P. Patra, F. Hyder, L. E. Niklason, S. Lee, Y. Yoon, I. Park, *Nat. Methods* **2019**, *16*, 1169.
[117] T. Takebe, K. Sekine, M. Enomura, H. Koike, M. Kimura, T. Ogaeri, R. R. Zhang, Y. Ueno, Y. W. Zheng, N. Koike, S. Aoyama, Y. Adachi, H. Taniguchi, *Nature* **2013**, *499*, 481.
[118] C. W. van den Berg, L. Ritsma, M. C. Avramut, L. E. Wiersma, B. M. van den Berg, D. G. Leuning, E. Lievers, M. Koning, J. M. Vanslambrouck, A. J. Koster, S. E. Howden, M. Takasato, M. H. Little, T. J. Rabelink, *Stem Cell Rep.* **2018**, *10*, 751.
[119] C. L. Watson, M. M. Mahe, J. Múnera, J. C. Howell, N. Sundaram, H. M. Poling, J. I. Schweitzer, J. E. Vallance, C. N. Mayhew, Y. Sun, G. Grabowski, S. R. Finkbeiner, J. R. Spence, N. F. Shroyer, J. M. Wells, M. A. Helmrath, *Nat. Med.* **2014**, *20*, 1310.
[120] R. Vassena, C. Eguizabal, B. Heindryckx, K. Sermon, C. Simon, A. M. M. van Pelt, A. Veiga, F. Zambelli, *Hum. Reprod.* **2015**, *30*, 2014.
[121] E. Fennema, N. Rivron, J. Rouwkema, C. van Blitterswijk, J. De Boer, *Trends Biotechnol.* **2013**, *31*, 108.
[122] C. Shao, J. Chi, H. Zhang, Q. Fan, Y. Zhao, F. Ye, *Adv. Mater. Technol.* **2020**, *5*, 2000183.
[123] A. Ashok, D. Choudhury, Y. Fang, W. Hunziker, *Biotechnol. Adv.* **2020**, *39*, 107460.
[124] V. Velasco, S. A. Shariati, R. Esfandyarpour, *Microsyst. Nanoeng.* **2020**, *6*, 76.

[125] T. Takebe, K. Sekine, M. Kimura, E. Yoshizawa, S. Ayano, M. Koido, S. Funayama, N. Nakanishi, T. Hisai, T. Kobayashi, T. Kasai, R. Kitada, A. Mori, H. Ayabe, Y. Ejiri, N. Amimoto, Y. Yamazaki, S. Ogawa, M. Ishikawa, Y. Kiyota, Y. Sato, K. Nozawa, S. Okamoto, Y. Ueno, H. Taniguchi, *Cell Rep.* **2017**, *21*, 2661.
[126] Y. Takahashi, K. Sekine, T. Kin, T. Takebe, H. Taniguchi, *Cell Rep.* **2018**, *23*, 1620.
[127] C. Shao, Y. Liu, J. Chi, Z. Chen, J. Wang, Y. Zhao, *Langmuir* **2019**, *35*, 3832.
[128] E. Urich, C. Patsch, S. Aigner, M. Graf, R. Iacone, P. O. Freskgård, *Sci. Rep.* **2013**, *3*, 1500.
[129] W. L. Dissanayaka, L. Zhu, K. M. Hargreaves, L. Jin, C. Zhang, *J. Dent. Res.* **2014**, *93*, 1296.
[130] R. A. Vertrees, M. McCarthy, T. Solley, V. L. Popov, J. Roaten, M. Pauley, X. Wen, T. J. Goodwin, *Cancer Biol. Ther.* **2009**, *8*, 356.
[131] A. Przepiorski, V. Sander, T. Tran, J. A. Hollywood, B. Sorrenson, J. H. Shih, E. J. Wolvetang, A. P. McMahon, T. M. Holm, A. J. Davidson, *Stem Cell Rep.* **2018**, *11*, 470.
[132] C. Adine, K. K. Ng, S. Rungarunlert, G. R. Souza, J. N. Ferreira, *Biomaterials* **2018**, *180*, 52.
[133] I. T. Ozbolat, W. Peng, V. Ozbolat, *Drug Discovery Today* **2016**, *21*, 1257.
[134] L. Benmeridja, L. De Moor, E. De Maere, F. Vanlauwe, M. Ryx, L. Tytgat, C. Vercruysse, P. Dubruel, S. Van Vlierberghe, P. Blondeel, H. Declercq, *J. Tissue Eng. Regener. Med.* **2020**, *14*, 840.
[135] A. Soltanian, S. Mardpour, Z. Ghezelayagh, H. Baharvand, *J. Cell. Physiol.* **2019**, *234*, 9564.
[136] J. Fukuda, K. Nakazawa, *Biomicrofluidics* **2011**, *5*, 022205.
[137] K. A. Homan, N. Gupta, K. T. Kroll, D. B. Kolesky, M. Skylar-Scott, T. Miyoshi, D. Mau, M. T. Valerius, T. Ferrante, J. V. Bonventre, J. A. Lewis, R. Morizane, *Nat. Methods* **2019**, *16*, 255.
[138] K. Kusamori, M. Nishikawa, N. Mizuno, T. Nishikawa, A. Masuzawa, Y. Tanaka, Y. Mizukami, K. Shimizu, S. Konishi, Y. Takahashi, Y. Takakura, *Pharm. Res.* **2016**, *33*, 247.
[139] R. Walser, W. Metzger, A. Görg, T. Pohlemann, M. D. Menger, M. W. Laschke, *Eur. Cell Mater.* **2013**, *26*, 222.
[140] T. Okudaira, N. Amimoto, H. Mizumoto, T. Kajiwara, *J. Biosci. Bioeng.* **2016**, *122*, 213.
[141] C. Wittig, M. W. Laschke, C. Scheuer, M. D. Menger, *PLoS One* **2013**, *8*, e69975.
[142] L. A. Kunz-Schughart, J. A. Schroeder, M. Wondrak, F. Van Rey, K. Lehle, F. Hofstaedter, D. N. Wheatley, M. W. Laschke, M. D. Menger, T. Korff, H. G. Augustin, *J. Cell Biol.* **1998**, *290*, 782.
[143] J. Rezaie, M. Heidarzadeh, M. Hassanpour, H. Amini, E. Shokrollahi, M. Ahmadi, R. Rahbarghazi, in *Update on Mesenchymal and Induced Pluripotent Stem Cells* (Eds: K. A. Al-Anazi), IntechOpen, London **2020**, Ch. 6.
[144] H. Tao, Z. Han, Z. C. Han, Z. Li, *Stem Cells Int.* **2016**, *2016*, 1314709.
[145] L. Bussche, G. R. Van de Walle, *Stem Cells Transl. Med.* **2015**, *3*, 1514.
[146] S. Ho, K. Murphy, B. Binder, C. Vissers, J. K. Leach, *Stem Cells Transl. Med.* **2016**, *5*, 773.
[147] K. Zhang, L. Song, J. Wang, S. Yan, G. Li, L. Cui, J. Yin, *Acta Biomater.* **2017**, *51*, 246.
[148] R. Noguchi, K. Nakayama, M. Itoh, K. Kamohara, K. Furukawa, J. I. Oyama, K. Node, S. Morita, *J. Heart Lung Transplant.* **2016**, *35*, 137.
[149] S. H. Bhang, S. Lee, J. Y. Shin, T. J. Lee, B. S. Kim, *Tissue Eng., Part A* **2012**, *18*, 2138.
[150] J.-Y. Shin, J.-H. Jeong, J. Han, S. H. Bhang, G.-J. Jeong, M. R. Haque, T. A. Al-Hilal, M. Noh, Y. Byun, B.-S. Kim, *Tissue Eng., Part A* **2015**, *21*, 1024.
[151] L. A. Kunz-Schughart, J. A. Schroeder, M. Wondrak, F. Van Rey, K. Lehle, F. Hofstaedter, D. N. Wheatley, *Am. J. Physiol.: Cell Physiol.* **2006**, *290*, C1385.
[152] S. Hsu, P. Hsieh, *Wound Repair Regener.* **2015**, *23*, 57.
[153] M. W. Laschke, T. E. Schank, C. Scheuer, S. Kleer, S. Schuler, W. Metzger, D. Eglin, *Acta Biomater.* **2013**, *9*, 6876.
[154] R. Mishra, B. M. Roux, M. Posukonis, E. Bodamer, E. M. Brey, J. P. Fisher, D. Dean, *Biomaterials* **2016**, *77*, 255.
[155] M. T. Pham, K. M. Pollock, M. D. Rose, W. A. Cary, H. R. Stewart, P. Zhou, J. A. Nolta, B. Waldau, *NeuroReport* **2018**, *29*, 588.
[156] O. Ham, Y. B. Jin, J. Kim, M. O. Lee, *Biochem. Biophys. Res. Commun.* **2020**, *521*, 84.
[157] T. Takebe, R. R. Zhang, H. Koike, M. Kimura, E. Yoshizawa, M. Enomura, N. Koike, K. Sekine, H. Taniguchi, *Nat. Protoc.* **2014**, *9*, 396.
[158] T. Takebe, N. Koike, K. Sekine, R. Fujiwara, T. Amiya, Y. W. Zheng, H. Taniguchi, *Organogenesis* **2014**, *10*, 260.
[159] S. Grebenyuk, A. Ranga, *Front. Bioeng. Biotechnol.* **2019**, *7*, 39.
[160] F. Verseijden, S. J. Posthumus-van Sluijs, E. Farrell, J. W. Van Neck, S. E. R. Hovius, S. O. P. Hofer, G. J. V. M. Van Osch, *Cell Transplant.* **2010**, *19*, 1007.
[161] A. Lavazza, M. Massimini, *J. Med. Ethics* **2018**, *44*, 606.
[162] A. Soltanian, Z. Ghezelayagh, Z. Mazidi, M. Halvaei, S. Mardpour, M. K. Ashtiani, E. Hajizadeh-Saffar, Y. Tahamtani, H. Baharvand, *J. Cell. Physiol.* **2019**, *234*, 9564.
[163] R. D. Pedde, B. Mirani, A. Navaei, T. Styan, S. Wong, M. Mehrali, A. Thakur, N. K. Mohtaram, A. Bayati, A. Dolatshahi-Pirouz, M. Nikkhah, S. M. Willerth, M. Akbari, *Adv. Mater.* **2017**, *29*, 1606061.
[164] V. Mironov, T. Trusk, V. Kasyanov, S. Little, R. Swaja, R. Markwald, *Biofabrication* **2009**, *1*, 022001.
[165] Y. Liu, E. Kim, R. Ghodssi, G. W. Rubloff, J. N. Culver, W. E. Bentley, G. F. Payne, *Biofabrication* **2010**, *2*, 022002.
[166] L. Moroni, J. A. Burdick, C. Highley, S. J. Lee, Y. Morimoto, S. Takeuchi, J. J. Yoo, *Nat. Rev. Mater.* **2018**, *3*, 21.
[167] J. G. Nemeno-Guanzon, S. Lee, J. R. Berg, Y. H. Jo, J. E. Yeo, B. M. Nam, Y.-G. Koh, J. I. Lee, *J. Biomed. Biotechnol.* **2012**, *2012*, 956345.
[168] P. Bajaj, R. M. Schweller, A. Khademhosseini, J. L. West, R. Bashir, *Annu. Rev. Biomed. Eng.* **2014**, *16*, 247.
[169] T. Woodfield, K. Lim, P. Morouço, R. Levato, J. Malda, F. Melchels, *Compr. Biomater. II* **2017**, *5*, 236.
[170] J. Groll, T. Boland, T. Blunk, J. A. Burdick, D.-W. Cho, P. D. Dalton, B. Derby, G. Forgacs, Q. Li, V. A. Mironov, *Biofabrication* **2016**, *8*, 013001.
[171] I. T. Ozbolat, K. K. Moncal, H. Gudapati, *Addit. Manuf.* **2017**, *13*, 179.
[172] S. Derakhshanfar, R. Mbeleck, K. Xu, X. Zhang, W. Zhong, M. Xing, *Bioact. Mater.* **2018**, *3*, 144.
[173] I. Matai, G. Kaur, A. Seyedsalehi, A. McClinton, C. T. Laurencin, *Biomaterials* **2020**, *226*, 119536.
[174] W. L. Ng, J. M. Lee, M. Zhou, Y. W. Chen, K. X. A. Lee, W. Y. Yeong, Y. F. Shen, *Biofabrication* **2020**, *12*, 022001.
[175] N. A. Chartrain, C. B. Williams, A. R. Whittington, *Acta Biomater.* **2018**, *74*, 90.
[176] B. Grigoryan, S. J. Paulsen, D. C. Corbett, D. W. Sazer, C. L. Fortin, A. J. Zaita, P. T. Greenfield, N. J. Calafat, J. P. Gounley, A. H. Ta, F. Johansson, A. Randles, J. E. Rosenkrantz, J. D. Louis-Rosenberg, P. A. Galie, K. R. Stevens, J. S. Miller, *Science* **2019**, *364*, 458.
[177] H. Xu, J. Casillas, S. Krishnamoorthy, C. Xu, *Biomed. Mater.* **2020**, *15*, 055021.
[178] M. Pagac, J. Hajnys, Q.-P. Ma, L. Jancar, J. Jansa, P. Stefek, J. Mesicek, *Polymers* **2021**, *13*, 598.
[179] J. Groll, J. A. Burdick, D. W. Cho, B. Derby, M. Gelinsky, S. C. Heilshorn, T. Jüngst, J. Malda, V. A. Mironov, K. Nakayama, A. Ovsianikov, W. Sun, S. Takeuchi, J. J. Yoo, T. B. F. Woodfield, *Biofabrication* **2019**, *11*, 013001.
[180] D. Kang, G. Hong, S. An, I. Jang, W. S. Yun, J. H. Shim, S. Jin, *Small* **2020**, *16*, 1905505.
[181] L. Shao, Q. Gao, C. Xie, J. Fu, M. Xiang, Y. He, *Biofabrication* **2020**, *12*, 035014.

[182] Y. P. Jin, C. Shi, Y. Y. Wu, J. L. Sun, J. P. Gao, Y. Yang, *Chin. Med. J.* **2020**, *133*, 424.
[183] F. Maiullari, M. Costantini, M. Milan, V. Pace, M. Chirivì, S. Maiullari, A. Rainer, D. Baci, H. E. S. Marei, D. Seliktar, C. Gargioli, C. Bearzi, R. Rizzi, *Sci. Rep.* **2018**, *8*, 13532.
[184] A. Schwab, R. Levato, M. D'Este, S. Piluso, D. Eglin, J. Malda, *Chem. Rev.* **2020**, *120*, 11028.
[185] P. Datta, B. Ayan, I. T. Ozbolat, *Acta Biomater.* **2017**, *51*, 1.
[186] D. Therriault, S. R. White, J. A. Lewis, *Nat. Mater.* **2003**, *2*, 265.
[187] W. Wu, C. J. Hansen, A. M. Aragón, P. H. Geubelle, S. R. White, J. A. Lewis, *Soft Matter* **2010**, *6*, 739.
[188] L. M. Bellan, S. P. Singh, P. W. Henderson, T. J. Porri, H. G. Craighead, J. A. Spector, *Soft Matter* **2009**, *5*, 1354.
[189] R. Sooppan, S. J. Paulsen, J. Han, A. H. Ta, P. Dinh, A. C. Gaffey, C. Venkataraman, A. Trubelja, G. Hung, J. S. Miller, P. Atluri, *Tissue Eng., Part C* **2016**, *22*, 1.
[190] Q. Zou, B. E. Grottkau, Z. He, L. Shu, L. Yang, M. Ma, C. Ye, *Mater. Sci. Eng., C* **2020**, *108*, 110205.
[191] K. A. Homan, D. B. Kolesky, M. A. Skylar-Scott, J. Herrmann, H. Obuobi, A. Moisan, J. A. Lewis, *Sci. Rep.* **2016**, *6*, 34845.
[192] B. Byambaa, N. Annabi, K. Yue, G. Trujillo-de Santiago, M. M. Alvarez, W. Jia, M. Kazemzadeh-Narbat, S. R. Shin, A. Tamayol, A. Khademhosseini, *Adv. Healthcare Mater.* **2017**, *6*, 1700015.
[193] Q. Gao, Y. He, J. zhong Fu, A. Liu, L. Ma, *Biomaterials* **2015**, *61*, 203.
[194] N. Noor, A. Shapira, R. Edri, I. Gal, L. Wertheim, T. Dvir, *Adv. Sci.* **2019**, *6*, 1900344.
[195] W. Jia, P. S. Gungor-Ozkerim, Y. S. Zhang, K. Yue, K. Zhu, W. Liu, Q. Pi, B. Byambaa, M. R. Dokmeci, S. R. Shin, A. Khademhosseini, *Biomaterials* **2016**, *106*, 58.
[196] J. W. Lee, Y. J. Choi, W. J. Yong, F. Pati, J. H. Shim, K. S. Kang, I. H. Kang, J. Park, D. W. Cho, *Biofabrication* **2016**, *8*, 015007.
[197] Y. S. Zhang, J. Aleman, S. R. Shin, T. Kilic, D. Kim, S. A. M. Shaegh, S. Massa, R. Riahi, S. Chae, N. Hu, H. Avci, W. Zhang, A. Silvestri, A. S. Nezhad, A. Manbohi, F. De Ferrari, A. Polini, G. Calzone, N. Shaikh, P. Alerasool, E. Budina, J. Kang, N. Bhise, J. Ribas, A. Pourmand, A. Skardal, T. Shupe, C. E. Bishop, M. R. Dokmeci, A. Atala, A. Khademhosseini, *Proc. Natl. Acad. Sci. USA* **2017**, *114*, E2293.
[198] X. Liu, S. S. D. Carter, M. J. Renes, J. Kim, D. M. Rojas-Canales, D. Penko, C. Angus, S. Beirne, C. J. Drogemuller, Z. Yue, P. T. Coates, G. G. Wallace, *Adv. Healthcare Mater.* **2019**, *8*, 1801181.
[199] A. Leucht, A. C. Volz, J. Rogal, K. Borchers, P. J. Kluger, *Sci. Rep.* **2020**, *10*, 5330.
[200] J. Jang, H. J. Park, S. W. Kim, H. Kim, J. Y. Park, S. J. Na, H. J. Kim, M. N. Park, S. H. Choi, S. H. Park, S. W. Kim, S. M. Kwon, P. J. Kim, D. W. Cho, *Biomaterials* **2017**, *112*, 264.
[201] Y. S. Zhang, Q. Pi, A. M. van Genderen, *J. Visualized Exp.* **2017**, e55957.
[202] I. Chiesa, C. De Maria, A. Lapomarda, G. M. Fortunato, F. Montemurro, R. Di Gesù, R. S. Tuan, G. Vozzi, R. Gottardi, *Biofabrication* **2020**, *12*, 025013.
[203] W. Zhu, X. Qu, J. Zhu, X. Ma, S. Patel, J. Liu, P. Wang, C. S. E. Lai, M. Gou, Y. Xu, K. Zhang, S. Chen, *Biomaterials* **2017**, *124*, 106.
[204] A. K. Miri, D. Nieto, L. Iglesias, H. Goodarzi Hosseinabadi, S. Maharjan, G. U. Ruiz-Esparza, P. Khoshakhlagh, A. Manbachi, M. R. Dokmeci, S. Chen, S. R. Shin, Y. S. Zhang, A. Khademhosseini, *Adv. Mater.* **2018**, *30*, 1800242.
[205] H. Cui, T. Esworthy, X. Zhou, S. Y. Hann, R. I. Glazer, R. Li, L. G. Zhang, *Adv. Healthcare Mater.* **2020**, *9*, 1900924.
[206] S. Y. Hann, H. Cui, T. Esworthy, X. Zhou, S.-j. Lee, M. W. Plesniak, L. G. Zhang, *Acta Biomater.* **2021**, *123*, 263.
[207] X. Liu, S. Michael, K. Bharti, M. Ferrer, M. J. Sont, *Biofabrication* **2020**, *12*, 035002.
[208] P. D. Dalton, T. B. F. Woodfield, V. Mironov, J. Groll, *Adv. Sci.* **2020**, *7*, 1902953.
[209] Y. Tan, D. J. Richards, T. C. Trusk, R. P. Visconti, M. J. Yost, M. S. Kindy, C. J. Drake, W. S. Argraves, R. R. Markwald, Y. Mei, *Biofabrication* **2014**, *6*, 024111.
[210] C. Kucukgul, S. B. Ozler, I. Inci, E. Karakas, S. Irmak, D. Gozuacik, A. Taralp, B. Koc, *Biotechnol. Bioeng.* **2015**, *112*, 811.
[211] M. Itoh, K. Nakayama, R. Noguchi, K. Kamohara, K. Furukawa, K. Uchihashi, S. Toda, J. I. Oyama, K. Node, S. Morita, *PLoS One* **2015**, *10*, e0136681.
[212] C. Norotte, F. S. Marga, L. E. Niklason, G. Forgacs, *Biomaterials* **2009**, *30*, 5910.
[213] R. Gaebel, N. Ma, J. Liu, J. Guan, L. Koch, C. Klopsch, M. Gruene, A. Toelk, W. Wang, P. Mark, F. Wang, B. Chichkov, W. Li, G. Steinhoff, *Biomaterials* **2011**, *32*, 9218.
[214] O. Kérourédan, D. Hakobyan, M. Rémy, S. Ziane, N. Dusserre, J.-C. Fricain, S. Delmond, N. B. Thébaud, R. Devillard, *Biofabrication* **2019**, *11*, 045002.
[215] L. Lucas, A. Aravind, P. Emma, M. Christophe, C. Edwin-Joffrey, *Bioprinting* **2021**, *21*, e00119.
[216] W. Sun, B. Starly, A. C. Daly, J. A. Burdick, J. Groll, G. Skeldon, W. Shu, Y. Sakai, M. Shinohara, M. Nishikawa, J. Jang, D.-W. Cho, M. Nie, S. Takeuchi, S. Ostrovidov, A. Khademhosseini, R. D. Kamm, V. Mironov, L. Moroni, I. T. Ozbolat, *Biofabrication* **2020**, *12*, 022002.
[217] A. Bagheri, J. Jin, *ACS Appl. Polym. Mater.* **2019**, *1*, 593.
[218] J. W. Nichol, A. Khademhosseini, *Soft Matter* **2009**, *5*, 1312.
[219] Y. Du, M. Ghodousi, H. Qi, N. Haas, W. Xiao, A. Khademhosseini, *Biotechnol. Bioeng.* **2011**, *108*, 1693.
[220] R. Gauvin, A. Khademhosseini, *ACS Nano* **2011**, *5*, 4258.
[221] A. P. McGuigan, M. V. Sefton, *Proc. Natl. Acad. Sci. USA* **2006**, *103*, 11461.
[222] M. D. Sarker, S. Naghieh, N. K. Sharma, X. Chen, *J. Pharm. Anal.* **2018**, *8*, 277.
[223] T. Shimizu, H. Sekine, Y. Isoi, M. Yamato, A. Kikuchi, T. Okano, *Tissue Eng.* **2006**, *12*, 499.
[224] J. Yang, M. Yamato, T. Shimizu, H. Sekine, K. Ohashi, M. Kanzaki, T. Ohki, K. Nishida, T. Okano, *Biomaterials* **2007**, *28*, 5033.
[225] M. Y. Tondreau, F. A. Auger, in *ALTEX Proc.: Proc. of WC8* (Eds: F. Gruber) Springer, Heidelberg **2011**.
[226] N. L'Heureux, N. Dusserre, G. Konig, B. Victor, P. Keire, T. N. Wight, N. A. F. Chronos, A. E. Kyles, C. R. Gregory, G. Hoyt, R. C. Robbins, T. N. McAllister, *Nat. Med.* **2006**, *12*, 361.
[227] S. Masuda, T. Shimizu, *Adv. Drug Delivery Rev.* **2016**, *96*, 103.
[228] N. L'heureux, S. Pâquet, R. Labbé, L. Germain, F. A. Auger, *FASEB J.* **1998**, *12*, 47.
[229] K. Kim, R. Utoh, K. Ohashi, T. Kikuchi, T. Okano, *J. Tissue Eng. Regener. Med.* **2017**, *11*, 2071.
[230] L. A. Smith, P. X. Ma, *Colloids Surf., B* **2004**, *39*, 125.
[231] V. Mironov, V. Kasyanov, Z. S. Xiao, C. Eisenberg, L. Eisenberg, S. Gonda, T. Trusk, R. R. Markwald, G. D. Prestwich, *Biomaterials* **2005**, *26*, 7628.
[232] A. E. Reimer, K. M. Feher, D. Hernandez, K. Slowinska, *J. Mater. Chem.* **2012**, *22*, 7701.
[233] A. Hasan, A. Memic, N. Annabi, M. Hossain, A. Paul, M. R. Dokmeci, F. Dehghani, A. Khademhosseini, *Acta Biomater.* **2014**, *10*, 11.
[234] J. J. Stankus, L. Soletti, K. Fujimoto, Y. Hong, D. A. Vorp, W. R. Wagner, *Biomaterials* **2007**, *28*, 2738.
[235] L. Ye, J. Cao, L. Chen, X. Geng, A.-Y. Zhang, L.-R. Guo, Y.-Q. Gu, Z.-G. Feng, *J. Biomed. Mater. Res., Part A* **2015**, *103*, 3863.
[236] N. Duan, X. Geng, L. Ye, A. Zhang, Z. Feng, L. Guo, Y. Gu, *Biomed. Mater.* **2016**, *11*, 035007.
[237] P. Coimbra, P. Santos, P. Alves, S. P. Miguel, M. P. Carvalho, K. D. de Sá, I. J. Correia, P. Ferreira, *Colloids Surf., B* **2017**, *159*, 7.
[238] S. A. Sell, M. J. McClure, K. Garg, P. S. Wolfe, G. L. Bowlin, *Adv. Drug Delivery Rev.* **2009**, *61*, 1007.
[239] H. Liu, X. Li, G. Zhou, H. Fan, Y. Fan, *Biomaterials* **2011**, *32*, 3784.

[240] J. Han, P. Lazarovici, C. Pomerantz, X. Chen, Y. Wei, P. I. Lelkes, *Biomacromolecules* **2011**, *12*, 399.
[241] W. Fu, Z. Liu, B. Feng, R. Hu, X. He, H. Wang, M. Yin, H. Huang, H. Zhang, W. Wang, *Adv. Funct. Mater.* **2014**, *9*, 2335.
[242] E. Ercolani, C. Del Gaudio, A. Bianco, *J. Tissue Eng. Regener. Med.* **2015**, *9*, 861.
[243] N. Goonoo, *Biomed. Phys. Eng. Express* **2018**, *4*, 032001.
[244] T. Simón-Yarza, A. Rossi, K.-H. Heffels, F. Prósper, J. Groll, M. J. Blanco-Prieto, *Tissue Eng., Part A* **2015**, *21*, 1654.
[245] S. Salerno, F. Tasselli, E. Drioli, L. De Bartolo, *Membranes* **2020**, *10*, 112.
[246] T. P. Burton, A. Callanan, *Tissue Eng. Regener. Med.* **2018**, *15*, 301.
[247] M. Liu, X. P. Duan, Y. M. Li, D. P. Yang, Y. Z. Long, *Mater. Sci. Eng., C* **2017**, *76*, 1413.
[248] A. De Mori, M. P. Fernández, G. Blunn, G. Tozzi, M. Roldo, *Polymers* **2018**, *10*, 285.
[249] T. Wu, M. Ding, C. Shi, Y. Qiao, P. Wang, R. Qiao, X. Wang, J. Zhong, *Chin. Chem. Lett.* **2020**, *31*, 617.
[250] A. Martins, J. V. Araújo, R. L. Reis, N. M. Neves, *Nanomedicine* **2007**, *2*, 929.
[251] V. S. Joshi, N. Y. Lei, C. M. Walthers, B. Wu, J. C. Y. Dunn, *J. Surg. Res.* **2013**, *183*, 18.
[252] S. B. Orr, A. Chainani, K. J. Hippensteel, A. Kishan, C. Gilchrist, N. W. Garrigues, D. S. Ruch, F. Guilak, D. Little, *Acta Biomater.* **2015**, *24*, 117.
[253] F. Yu, W. Hunziker, D. Choudhury, *Micromachines* **2019**, *10*, 165.
[254] F. Yu, D. Choudhury, *Drug Discovery Today* **2019**, *24*, 1248.
[255] S. Knowlton, B. Yenilmez, S. Tasoglu, *Trends Biotechnol.* **2016**, *34*, 685.
[256] D. D. Monie, S. K. Bhatia, in *Bioprinting in Regenerative Medicine* (Ed: K. Turksen), Springer International Publishing, Cham **2015**, pp. 123–137.
[257] K. Fetah, P. Tebon, M. J. Goudie, J. Eichenbaum, L. Ren, N. Barros, R. Nasiri, S. Ahadian, N. Ashammakhi, M. R. Dokmeci, A. Khademhosseini, *Prog. Biomed. Eng.* **2019**, *1*, 012001.
[258] V. K. Lee, D. Y. Kim, H. Ngo, Y. Lee, L. Seo, S. S. Yoo, P. A. Vincent, G. Dai, *Biomaterials* **2014**, *35*, 8092.
[259] Y. S. Zhang, J. Aleman, A. Arneri, S. Bersini, S. R. Shin, M. R. Dokmeci, A. Khademhosseini, S. Arabia, *Biomaterials* **2016**, *110*, 45.
[260] J. Y. Park, H. Ryu, B. Lee, D. H. Ha, M. Ahn, S. Kim, J. Y. Kim, N. L. Jeon, D. W. Cho, *Biofabrication* **2019**, *11*, 015002.
[261] A. Dobos, F. Gantner, M. Markovic, J. Van Hoorick, L. Tytgat, S. Van Vlierberghe, A. Ovsianikov, *Biofabrication* **2021**, *13*, 015016.
[262] G. Gao, X. Cui, *Biotechnol. Lett.* **2016**, *38*, 203.
[263] A. K. Miri, A. Khalilpour, B. Cecen, S. Maharjan, S. Ryon, S. A. Khademhosseini, *Biomaterials* **2019**, *198*, 204.
[264] P. Sasmal, P. Datta, Y. Wu, I. T. Ozbolat, *Microphysiol. Syst.* **2018**, *2*, 9.
[265] I. S. Kinstlinger, J. S. Miller, *Lab Chip* **2016**, *16*, 2025.
[266] W. Peng, P. Datta, Y. Wu, M. Dey, B. Ayan, A. Dababneh, I. T. Ozbolat, *Cell Biology and Translational Medicine*, Vol. *3*, Advances in Experimental Medicine and Biology, Vol. *1107*, Springer, New York **2018**, pp. 53–71.
[267] J. W. Higgins, A. Chambon, K. Bishard, A. Hartung, D. Arndt, J. Brugnano, P. X. Er, K. T. Lawlor, J. M. Vanslambrouck, S. Wilson, A. N. Combes, S. E. Howden, K. S. Tan, S. V. Kumar, L. J. Hale, B. Shepherd, S. Pentoney, S. C. Presnell, A. E. Chen, M. H. Little, *bioRxiv* **2018**, 505396.
[268] A. Kjar, B. McFarland, K. Mecham, N. Harward, Y. Huang, *Bioact. Mater.* **2021**, *6*, 460.
[269] E. Maloney, C. Clark, H. Sivakumar, K. Yoo, J. Aleman, S. A. P. Rajan, S. Forsythe, A. Mazzocchi, A. W. Laxton, S. B. Tatter, R. E. Strowd, K. I. Votanopoulos, A. Skardal, *Micromachines* **2020**, *11*, 208.
[270] J. A. Brassard, M. Nikolaev, T. Hübscher, M. Hofer, M. P. Lutolf, *Nat. Mater.* **2020**, *20*, 22.
[271] M. A. Skylar-Scott, S. G. M. Uzel, L. L. Nam, J. H. Ahrens, R. L. Truby, S. Damaraju, J. A. Lewis, *Sci. Adv.* **2019**, *5*, eaaw2459.
[272] T. Takebe, B. Zhang, M. Radisic, *Cell Stem Cell* **2017**, *21*, 297.
[273] R. Vadivelu, H. Kamble, M. Shiddiky, N.-T. Nguyen, *Micromachines* **2017**, *8*, 94.
[274] A. Skardal, T. Shupe, A. Atala, *Drug Discovery Today* **2016**, *21*, 1399.
[275] B. Schuster, M. Junkin, S. S. Kashaf, I. Romero-Calvo, K. Kirby, J. Matthews, C. R. Weber, A. Rzhetsky, K. P. White, S. Tay, *Nat. Commun.* **2020**, *11*, 5271.
[276] Y. Jin, J. Kim, J. S. Lee, S. Min, S. Kim, D. Ahn, Y. Kim, S. Cho, *Adv. Funct. Mater.* **2018**, *28*, 1801954.
[277] Y. Nashimoto, T. Hayashi, I. Kunita, A. Nakamasu, Y. S. Torisawa, M. Nakayama, H. Takigawa-Imamura, H. Kotera, K. Nishiyama, T. Miura, R. Yokokawa, *Integr. Biol.* **2017**, *9*, 506.
[278] Y. Isshiki, T. Kaneko, A. Tamada, K. Muguruma, R. Yokokawa, in *2020 IEEE 33rd Int. Conf. on Micro Electro Mechanical Systems (MEMS)*, IEEE, Piscataway, NJ **2020**, pp. 1024–1027.
[279] S. Zhang, Z. Wan, R. D. Kamm, *Lab Chip* **2021**, *21*, 473.
[280] T. Grix, A. Ruppelt, A. Thomas, A.-K. Amler, B. Noichl, R. Lauster, L. Kloke, *Genes* **2018**, *9*, 176.
[281] H. Zhao, Y. Chen, L. Shao, M. Xie, J. Nie, J. Qiu, P. Zhao, H. Ramezani, J. Fu, H. Ouyang, Y. He, *Small* **2018**, *14*, 1802630.
[282] L. Serex, K. Sharma, V. Rizov, A. Bertsch, J. D. McKinney, P. Renaud, *Biofabrication* **2021**, *13*, 025006.
[283] N. S. Bhise, V. Manoharan, S. Massa, A. Tamayol, M. Ghaderi, M. Miscuglio, Q. Lang, Y. S. Zhang, S. R. Shin, G. Calzone, N. Annabi, T. D. Shupe, C. E. Bishop, A. Atala, M. R. Dokmeci, A. Khademhosseini, *Biofabrication* **2016**, *8*, 014101.
[284] A. Wnorowski, H. Yang, J. C. Wu, *Adv. Drug Delivery Rev.* **2019**, *140*, 3.
[285] A. Cochrane, H. J. Albers, R. Passier, C. L. Mummery, A. van den Berg, V. V. Orlova, A. D. van der Meer, *Adv. Drug Delivery Rev.* **2019**, *140*, 68.
[286] A. Geraili, P. Jafari, M. S. Hassani, B. H. Araghi, M. H. Mohammadi, A. M. Ghafari, S. H. Tamrin, H. P. Modarres, A. R. Kolahchi, S. Ahadian, A. Sanati-Nezhad, *Adv. Healthcare Mater.* **2018**, *7*, 1700426.
[287] J. Drost, H. Clevers, *Nat. Rev. Cancer* **2018**, *18*, 407.
[288] L. Prodanov, R. Jindal, S. S. Bale, M. Hegde, W. J. Mccarty, I. Golberg, A. Bhushan, M. L. Yarmush, O. B. Usta, *Biotechnol. Bioeng.* **2016**, *113*, 241.
[289] L. A. van Grunsven, *Adv. Drug Delivery Rev.* **2017**, *121*, 133.
[290] V. van Duinen, D. Zhu, C. Ramakers, A. J. van Zonneveld, P. Vulto, T. Hankemeier, *Angiogenesis* **2019**, *22*, 157.
[291] W. Y. Wang, D. Lin, E. H. Jarman, W. J. Polacheck, B. M. Baker, *Lab Chip* **2020**, *20*, 1153.
[292] K. H. K. Wong, J. G. Truslow, A. H. Khankhel, K. L. S. Chan, J. Tien, *J. Biomed. Mater. Res., Part A* **2013**, *101A*, 2181.
[293] M. Sato, N. Sasaki, M. Ato, S. Hirakawa, K. Sato, K. Sato, *PLoS One* **2015**, *10*, e0137301.
[294] I. Choi, S. Lee, Y. K. Hong, *Cold Spring Harbor Perspect. Med.* **2012**, *2*, a006445.
[295] A. Aspelund, M. R. Robciuc, S. Karaman, T. Makinen, K. Alitalo, *Circ. Res.* **2016**, *118*, 515.
[296] T. P. Padera, E. F. J. Meijer, L. L. Munn, *Annu. Rev. Biomed. Eng.* **2016**, *18*, 125.
[297] J. P. Wikswo, F. E. Block, D. E. Cliffel, C. R. Goodwin, C. C. Marasco, D. A. Markov, D. L. McLean, J. A. McLean, J. R. McKenzie, R. S. Reiserer, P. C. Samson, D. K. Schaffer, K. T. Seale, S. D. Sherrod, *IEEE Trans. Biomed. Eng.* **2013**, *60*, 682. Accessed Mar 2021.
[298] J. F. Wong, M. D. Mohan, E. W. K. Young, C. A. Simmons, *Biosens. Bioelectron.* **2020**, *147*, 111757. Accessed Mar 2021.
[299] S. Jalili-Firoozinezhad, F. S. Gazzaniga, E. L. Calamari, D. M. Camacho, C. W. Fadel, A. Bein, B. Swenor, B. Nestor, M. J. Cronce, A. Tovaglieri, O. Levy, K. E. Gregory, D. T. Breault, J. M. S. Cabral, D. L. Kasper, R. Novak, D. E. Ingber, *Nat. Biomed. Eng.* **2019**, *3*, 520.

[300] P. N. Joshi, in *Lab-on-a-Chip Fabrication and Application* (Eds: M. Stoytcheva, R. Zlatev), IntechOpen, London **2016**, Ch. 5.
[301] X. Wang, D. T. T. Phan, A. Sobrino, S. C. George, C. C. W. Hughes, A. P. Lee, *Lab Chip* **2016**, *16*, 282.
[302] A. Petrosyan, P. Cravedi, V. Villani, A. Angeletti, J. Manrique, A. Renieri, R. E. De Filippo, L. Perin, S. Da Sacco, *Nat. Commun.* **2019**, *10*, 4791.
[303] V. Sander, A. Przepiorski, A. E. Crunk, N. A. Hukriede, T. M. Holm, A. J. Davidson, *STAR Protoc.* **2020**, *1*, 100150.
[304] F. Jacob, R. D. Salinas, D. Y. Zhang, P. T. T. Nguyen, J. G. Schnoll, S. Z. H. Wong, R. Thokala, S. Sheikh, D. Saxena, S. Prokop, D. ao Liu, X. Qian, D. Petrov, T. Lucas, H. I. Chen, J. F. Dorsey, K. M. Christian, Z. A. Binder, M. Nasrallah, S. Brem, D. M. O'Rourke, G. li Ming, H. Song, *Cell* **2020**, *180*, 188.
[305] M. Dossena, R. Piras, A. Cherubini, M. Barilani, E. Dugnani, F. Salanitro, T. Moreth, F. Pampaloni, L. Piemonti, L. Lazzari, *Stem Cell Res. Ther.* **2020**, *11*, 94.
[306] J. Vives, L. Batlle-Morera, *Stem Cell Res. Ther.* **2020**, *11*, 72.
[307] S. N. Boers, J. J. Delden, H. Clevers, A. L. Bredenoord, *EMBO Rep.* **2016**, *17*, 938.
[308] Y. Huyan, Q. Lian, T. Zhao, D. Li, J. He, *Int. J. Bioprint.* **2020**, *6*, 53.
[309] C. Kropp, D. Massai, R. Zweigerdt, *Process Biochem.* **2017**, *59*, 244.
[310] A. J. Want, A. W. Nienow, C. J. Hewitt, K. Coopman, *Regener. Med.* **2012**, *7*, 71.
[311] C. Kropp, H. Kempf, C. Halloin, D. Robles-Diaz, A. Franke, T. Scheper, K. Kinast, T. Knorpp, T. O. Joos, A. Haverich, U. Martin, R. Zweigerdt, R. Olmer, *Stem Cells Transl. Med.* **2016**, *5*, 1289.
[312] V. Bunpetch, H. Wu, S. Zhang, H. Ouyang, *Stem Cells Dev.* **2017**, *26*, 1662.
[313] V. C. Chen, S. M. Couture, J. Ye, Z. Lin, G. Hua, H. I. P. Huang, J. Wu, D. Hsu, M. K. Carpenter, L. A. Couture, *Stem Cell Res.* **2012**, *8*, 388.
[314] C. García-Fernández, A. López-Fernández, S. Borrós, M. Lecina, J. Vives, *Biochem. Eng. J.* **2020**, *159*, 107601.
[315] J. P. K. Armstrong, T. J. Keane, A. C. Roques, P. S. Patrick, C. M. Mooney, W. L. Kuan, V. Pisupati, R. O. C. Oreffo, D. J. Stuckey, F. M. Watt, S. J. Forbes, R. A. Barker, M. M. Stevens, *Sci. Transl. Med.* **2020**, *12*, eaaz2253.
[316] Y. A. Jodat, M. G. Kang, K. Kiaee, G. J. Kim, A. F. H. Martinez, A. Rosenkranz, H. Bae, S. R. Shin, *Curr. Pharm. Des.* **2019**, *24*, 5471.
[317] B. Zhang, M. Radisic, *Lab Chip* **2017**, *17*, 2395.
[318] R. Mittal, F. W. Woo, C. S. Castro, M. A. Cohen, J. Karanxha, J. Mittal, T. Chhibber, V. M. Jhaveri, *J. Cell. Physiol.* **2019**, *234*, 8352.
[319] N. Franzen, W. H. van Harten, V. P. Retèl, P. Loskill, J. van den Eijnden-van Raaij, M. IJzerman, *Drug Discovery Today* **2019**, *24*, 1720.
[320] C. C. Miranda, J. M. S. Cabral, in *Precision Medicine for Investigators, Practitioners and Providers* (Eds: F. Gruber Elsevier, Amsterdam **2020**, Ch. 45.
[321] T. Simon-Yarza, A. Mielcarek, P. Couvreur, C. Serre, *Adv. Mater.* **2018**, *30*, 1707365.
[322] Y. Zhao, R. K. Kankala, S. Bin Wang, A. Z. Chen, *Molecules* **2019**, *24*, 675.
[323] A. Almeida, B. Sarmento, F. Rodrigues, *Int. J. Pharm.* **2017**, *519*, 178.
[324] M. Mastrangeli, S. Millet, The ORCHID partners, J. van den Eijnden-van Raaij, *ALTEX* **2019**, *36*, 650.
[325] H. Kimura, Y. Sakai, T. Fujii, *Drug Metab. Pharmacokinet.* **2018**, *33*, 43.
[326] M. Zanoni, S. Pignatta, C. Arienti, M. Bonafè, A. Tesei, *Expert Opin. Drug Discovery* **2019**, *14*, 289.
[327] M. Zanoni, M. Cortesi, A. Zamagni, C. Arienti, S. Pignatta, A. Tesei, *J. Hematol. Oncol.* **2020**, *13*, 97.
[328] S. Bartfeld, H. Clevers, *J. Mol. Med.* **2017**, *95*, 729.
[329] V. Vaira, G. Fedele, S. Pyne, E. Fasoli, G. Zadra, D. Bailey, E. Snyder, A. Faversani, G. Coggi, R. Flavin, S. Bosari, M. Loda, *Proc. Natl. Acad. Sci. USA* **2010**, *107*, 8352.
[330] Z. Gilazieva, A. Ponomarev, C. Rutland, A. Rizvanov, V. Solovyeva, *Cancers* **2020**, *12*, 2727.
[331] J. F. Dekkers, G. Berkers, E. Kruisselbrink, A. Vonk, H. R. De Jonge, H. M. Janssens, I. Bronsveld, E. A. Van De Graaf, E. E. S. Nieuwenhuis, R. H. J. Houwen, F. P. Vleggaar, J. C. Escher, Y. B. De Rijke, C. J. Majoor, H. G. M. Heijerman, K. M. De Winter-De Groot, H. Clevers, C. K. Van Der Ent, J. M. Beekman, *Sci. Transl. Med.* **2016**, *8*, 344ra84.
[332] Aspects Biosystems, Aspect Byosystems partners with Merck, GSK and McGill, **2019**.
[333] Aspects Biosystems, Aspects Biosystems annouces liver tissue collaboration with JSR, **2018**.
[334] T. Nakamura, T. Sato, *Cell. Mol. Gastroenterol. Hepatol.* **2018**, *5*, 51.
[335] G. Rossi, A. Manfrin, M. P. Lutolf, *Nat. Rev. Genet.* **2018**, *19*, 671.
[336] C. Corrò, L. Novellasdemunt, V. S. W. Li, *Am. J. Physiol.: Cell Physiol.* **2020**, *319*, C151.
[337] N. Ashammakhi, E. Elkhammas, A. Hasan, *J. Biomed. Mater. Res., Part B* **2019**, *107*, 2006.
[338] J. Yu, *Int. J. Stem Cells* **2021**, *14*, 127.
[339] M. Li, J. C. Izpisua Belmonte, *N. Engl. J. Med.* **2019**, *380*, 569.
[340] G. Kaushik, M. P. Ponnusamy, S. K. Batra, *Stem Cells* **2018**, *36*, 1329.
[341] Y. Wu, D. J. Ravnic, I. T. Ozbolat, *Trends Biotechnol.* **2020**, *38*, 594.
[342] P. Li, in *3D Bioprinting for Reconstructive Surgery: Techniques and Applications* (Eds: D. J. Thomas, Z. M. Jessop, I. S. Whitaker), Woodhead Publishing, Cambridge, UK **2018**, Ch. 11.
[343] F. Gilbert, C. D. O'Connell, T. Mladenovska, S. Dodds, *Sci. Eng. Ethics* **2018**, *24*, 73.
[344] P. Aprile, D. Letourneur, T. Simon-Yarza, *Adv. Healthcare Mater.* **2020**, *9*, 2000707.

Alessandra Dellaquila obtained her B.Sc. and M.Sc. degrees from the Department of Biomedical Engineering, Politecnico di Torino, Italy, in 2014 and 2016, respectively. After working as a research fellow for the National Research Council of Italy (CNR-ISTEC) on biomaterials for hard tissues regeneration, she has been enrolled as an early stage researcher in the Marie Skłodowska-Curie H2020 DeLIVER ITN Project (Grant No. 766181) since 2018. Her research interests are focused on microfluidics for human biology and development and characterization of biomaterials for tissue engineering applications.

Chau Le Bao is a doctoral candidate at Université Sorbonne Paris Nord. She obtained her B.Sc. in chemical engineering in the US (2016) and her M.Sc. in biomedical engineering in France (2019). Her Ph.D. project focuses on the development of vascularized hydrogel with preformed microchannels for in vitro applications. This research is funded by the French National Research Agency RHU-iLite (Recherche Hospitalo-Universitaire en santé-Innovations for Liver Tissue Engineering) project. Her main research interests are on biomaterials, specifically the use of 3D scaffolds for vascularization strategies.

Didier Letourneur obtained both his engineering degree in materials science and a master's degree in biomaterials in 1985, and his Ph.D. in chemistry in 1988 from the University of Paris Nord. He is the CNRS research director (DRCE), and the director of a large multidisciplinary research laboratory with 250 people (LVTS - INSERM U1148). He has published more than 200 publications and 18 patents. His main research interests are on biomaterials and molecular imaging from the material synthesis to the industrial and clinical transfers. He had created the company SILTISS in 2016 for the development of medical devices.

Teresa Simon-Yarza received her undergraduate degree in pharmacy and her master's degree in pharmaceutical technology from the University of Navarra, where she completed her Ph.D. in pharmacy in 2013 with a thesis focused on biomaterials for heart repair. Then, she joined the Institut Lavoisier and the Institut Galien (University Paris-Saclay) to develop metal–organic frameworks for biomedical applications. Since 2018, she has been a permanent researcher in the Laboratory for Vascular Translational Science INSERM U1148 (Paris) working on 3D hydrogels for tissue repair. With a multidisciplinary background, her main research interest focuses on biomaterials development, from the synthesis to the preclinical evaluation.

7.2. Annex 2. Publication in International Journal of Molecular Science (PDF proof)

International Journal of
Molecular Sciences

MDPI

Article

Spatial-Controlled Coating of Pro-Angiogenic Proteins on 3D Porous Hydrogels Guides Endothelial Cell Behavior

Chau Le Bao [1,*], Helen Waller [2], Alessandra Dellaquila [1], Daniel Peters [2], Jeremy Lakey [2], Frédéric Chaubet [1] and Teresa Simon-Yarza [1,*]

[1] Laboratory for Vascular Translational Science (LVTS) INSERM U1148, Université Paris Cité, Université Sorbonne Paris Nord, CEDEX 18, 75877 Paris, France
[2] Biosciences Institute, Newcastle University Biosciences Institute, Newcastle upon Tyne NE1 7RU, UK
* Correspondence: chau.le-bao@inserm.fr (C.L.B.); teresa.simon-yarza@inserm.fr (T.S.-Y.)

Abstract: In tissue engineering, the composition and the structural arrangement of molecular components within the extracellular matrix (ECM) determine the physical and biochemical features of a scaffold, which consequently modulate cell behavior and function. The microenvironment of the ECM plays a fundamental role in regulating angiogenesis. Numerous strategies in tissue engineering have attempted to control the spatial cues mimicking in vivo angiogenesis by using simplified systems. The aim of this study was to develop 3D porous crosslinked hydrogels with different spatial presentation of pro-angiogenic molecules to guide endothelial cell (EC) behavior. Hydrogels with pores and preformed microchannels were made with pharmaceutical-grade pullulan and dextran and functionalized with novel pro-angiogenic protein polymers (Caf1-YIGSR and Caf1-VEGF). Hydrogel functionalization was achieved by electrostatic interactions via incorporation of diethylaminoethyl (DEAE)–dextran. Spatial-controlled coating of hydrogels was realized through a combination of freeze-drying and physical absorption with Caf1 molecules. Cells in functionalized scaffolds survived, adhered, and proliferated over seven days. When incorporated alone, Caf1-YIGSR mainly induced cell adhesion and proliferation, whereas Caf1-VEGF promoted cell migration and sprouting. Most importantly, directed cell migration required the presence of both proteins in the microchannel and in the pores, highlighting the need for an adhesive substrate provided by Caf1-YIGSR for Caf1-VEGF to be effective. This study demonstrates the ability to guide EC behavior through spatial control of pro-angiogenic cues for the study of pro-angiogenic signals in 3D and to develop pro-angiogenic implantable materials.

Keywords: hydrogels; electrostatic interactions; spatial-controlled coating; angiogenesis; tissue engineering

Citation: Le Bao, C.; Waller, H.; Dellaquila, A.; Peters, D.; Lakey, J.; Chaubet, F.; Simon-Yarza, T. Spatial-Controlled Coating of Pro-Angiogenic Proteins on 3D Porous Hydrogels Guides Endothelial Cell Behavior. *Int. J. Mol. Sci.* **2022**, *23*, 14604. https://doi.org/10.3390/ijms232314604

Academic Editors: Axel T. Neffe and Maike Windbergs

Received: 17 October 2022
Accepted: 21 November 2022
Published: 23 November 2022

Publisher's Note: MDPI stays neutral with regard to jurisdictional claims in published maps and institutional affiliations.

1. Introduction

Tissue engineering has offered the tantalizing possibility to regenerate tissues and organs, allowing the treatment of a multitude of conditions and pathologies. Despite numerous significant progresses with in vitro and small animal studies, clinical applications have been scarce [1]. Even the most advanced solutions delivered to physicians lack sufficient vascularization within the tissue engineered constructs [2]. This is because the diffusion of oxygen and nutrient supply present major limits on the size and complexity of bioengineered scaffolds. For this reason, vascularization of biomaterials remains the highlighted focus in tissue engineering and regenerative medicines. In this context, one main current challenge in tissue engineering is the development of biomaterials that can promote angiogenesis, ultimately integrating with the host vasculature to form anastomosis.

Angiogenesis, the formation of new blood vessels from existing ones, is a complex process. During angiogenesis, quiescent endothelial cells (ECs) from pre-existing vessels are activated by the increase in concentration of pro-angiogenic factors induced by inflammation or by hypoxia [3]. Activated ECs proliferate and differentiate into tip cells,

which results in the elongation of new blood vessels in the direction of the pro-angiogenic stimulus. This sprouting process is modulated by the migration of ECs led by tip cells, characterized by lamellipodia and filopodia in their cytoskeleton, followed by stalk cells, which are found between quiescent cells and the tip cells. Stalk cells continue to proliferate and constitute the new endothelium, while ensuring a continuum with the original vessel through regulated proliferation [4,5]. Once the capillary is formed, ECs secrete attractant molecules to recruit perivascular cells, which migrate along the newly formed vessels and provide stability, support cell differentiation, and regulate vessel permeability [6].

Angiogenesis is partially modulated by the ECM, which provides essential structural support and biochemical cues for cell morphogenesis and physiological functions [7]. Numerous strategies employing hydrogels with functionalized pro-angiogenic molecules have been proposed to promote vessel formation. Most of these approaches are based on the delivery of growth factors (GFs), such as vascular endothelial growth factor (VEGF), to facilitate vascularization in vivo [8]. Recently, pre-vascularization of biomaterials has been proposed as an approach to promote in vitro vessel formation prior to implantation. The idea is to stimulate in vitro vessel formation within 3D biomaterials which present pre-formed channels. Different techniques to develop hydrogels with pre-formed channels have been investigated. These include the use of syringes or glass micropipettes [9], or sacrificial templates [10–13]. To promote cell adhesion, ECM proteins (e.g., collagen, fibrin, or fibronectin) and cell adhesive molecules (e.g., RGD, YIGSR sequences) are often incorporated into the hydrogel composition [8,14,15]. Besides interaction with the ECM, angiogenesis also depends on spatial presentation of pro-angiogenic cues that direct vessel sprouting and maturation [3]. Over the past decades, various approaches have attempted to fabricate hydrogels with spatial guidance either through direct patterning of vascular cells, or through spatial distribution of pro-angiogenic molecules (e.g., VEGF, FGF, angiopoietin, YIGSR) [16–20]. The use of ECM molecules presents promising outcomes for in vitro and in vivo vascularization. Nevertheless, clinical translation still remains a hurdle due to high cost and immunogenic potential of animal-origin ECM molecules.

Several important factors must be taken into account when designing hydrogels that favor endothelialization for tissue engineering and regenerative medicines: (1) presence of interconnected pores favoring cell–cell interactions and migration; (2) presence of a hollow channel having a wide range of diameters to mimic native vessels; (3) ability to promote EC arrangement leading to the formation of microvessel-like networks; (4) biocompatible composition (pharmaceutical-grade materials); (5) integration of basement membrane proteins (BM), such as laminin and collagen type IV, and other ECM proteins to induce endothelial proliferation and differentiation during angiogenesis; (6) easy fabrication protocol; and (7) cost efficient.

For vascularization purposes, porous 3D hydrogels are widely employed due to their ability to facilitate nutrient and oxygen diffusion, thus enabling cell migration [21,22]. Additionally, the presence of channels within porous scaffolds has been reported to promote cell growth and rapid vascularization [23,24]. The channels in 3D hydrogels play a key role in guiding EC arrangement and should also be utilized to induce angiogenic behavior in ECs.

Polysaccharides are widely employed as tissue engineered biomaterials due to their physicochemical properties that can mimic the ECM [25]. In this context, we utilized 3D porous hydrogels, composed of pullulan and dextran. Notably, our team has demonstrated in several studies the versatility of pullulan- and dextran-based hydrogels, where the scaffold geometry, mechanical properties, porosity, and swelling behavior of these hydrogels could be controlled [25–28]. The hydrogel crosslinking method was previously described in numerous publications and has been patented [29,30]. Thus, these hydrogels have been investigated in various in vitro and in vivo studies [29,31,32]. Most recently, we have demonstrated the ability to guide EC arrangement based on channel curvature on the 3D polysaccharide hydrogels [28].

In the context of promoting in vitro vessel formation, this study aimed to develop 3D porous hydrogels with different spatial presentation of pro-angiogenic signals to guide ECs towards angiogenic behavior. The challenge of this work was to functionalize the chemically crosslinked hydrogels to promote EC adhesion and to direct sprouting through spatial guidance using pro-angiogenic cues. Here, we present a simple method to produce biomimetic 3D porous hydrogels, made from pharmaceutical-grade pullulan and dextran, with preformed microchannels (Figure 1). To provide cells with pro-adhesive and pro-angiogenic signals, the hydrogels were functionalized using a recombinant, engineered bacterial protein polymer called Caf1. Caf1 subunits assemble into long, highly stable and flexible polymers, which are bioinert, allowing bioactive peptide motifs from the ECM and growth factors to be inserted and hence provide exquisite control over the biological signals supplied to the cells [33–35]. In this work, we demonstrate an innovative strategy to functionalize chemical hydrogels in a spatial-controlled manner. Capitalizing on the acidic pI of Caf1, we could functionalize hydrogels simply via electrostatic interactions induced by the coating method (Figure 1b). Then, spatial cues of the pro-angiogenic motifs were modulated through a combination of hydrogel coating and a freeze-drying process (Figure 1c).

The developed scaffolds were evaluated based on: (1) porosity; (2) presence of the hollow channels formed within the 3D scaffolds; (3) ability to promote EC cell adhesion as well as migration; (4) ability to induce pro-angiogenic behavior of ECs. Furthermore, our approach offers a facile protocol for both scaffold fabrication and functionalization. The use of Caf1 overcomes the high cost and immunogenic potential of traditional ECM molecules. The functionalized scaffolds exhibited good EC adhesion and proliferation. Scaffolds with different spatial distribution of pro-angiogenic moieties induced different EC behaviors. Based on the results obtained from this study, we report the first work, to our knowledge, in using animal-free ECM-like molecules to control the spatial cues of hydrogel-based scaffolds, which modulates EC behavior and guides them towards angiogenic sprouting.

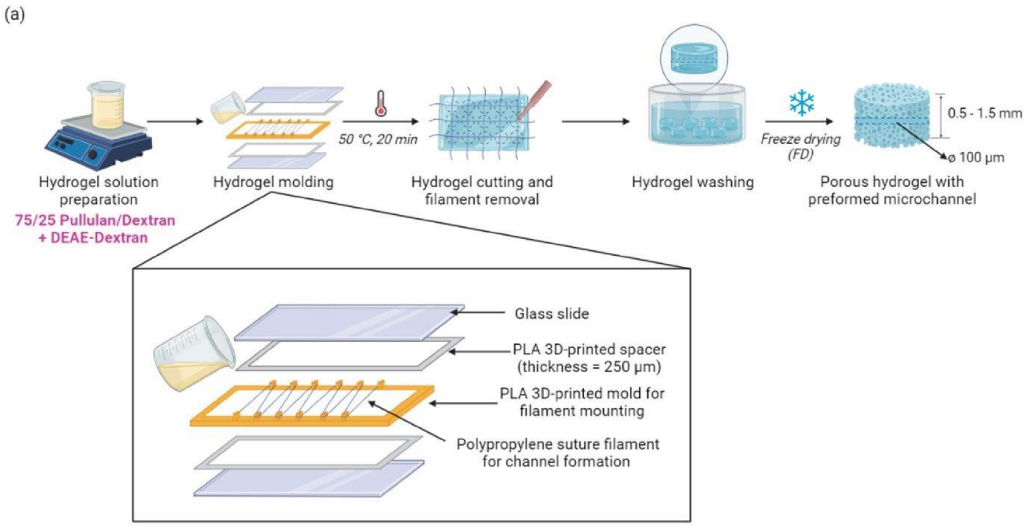

Figure 1. *Cont.*

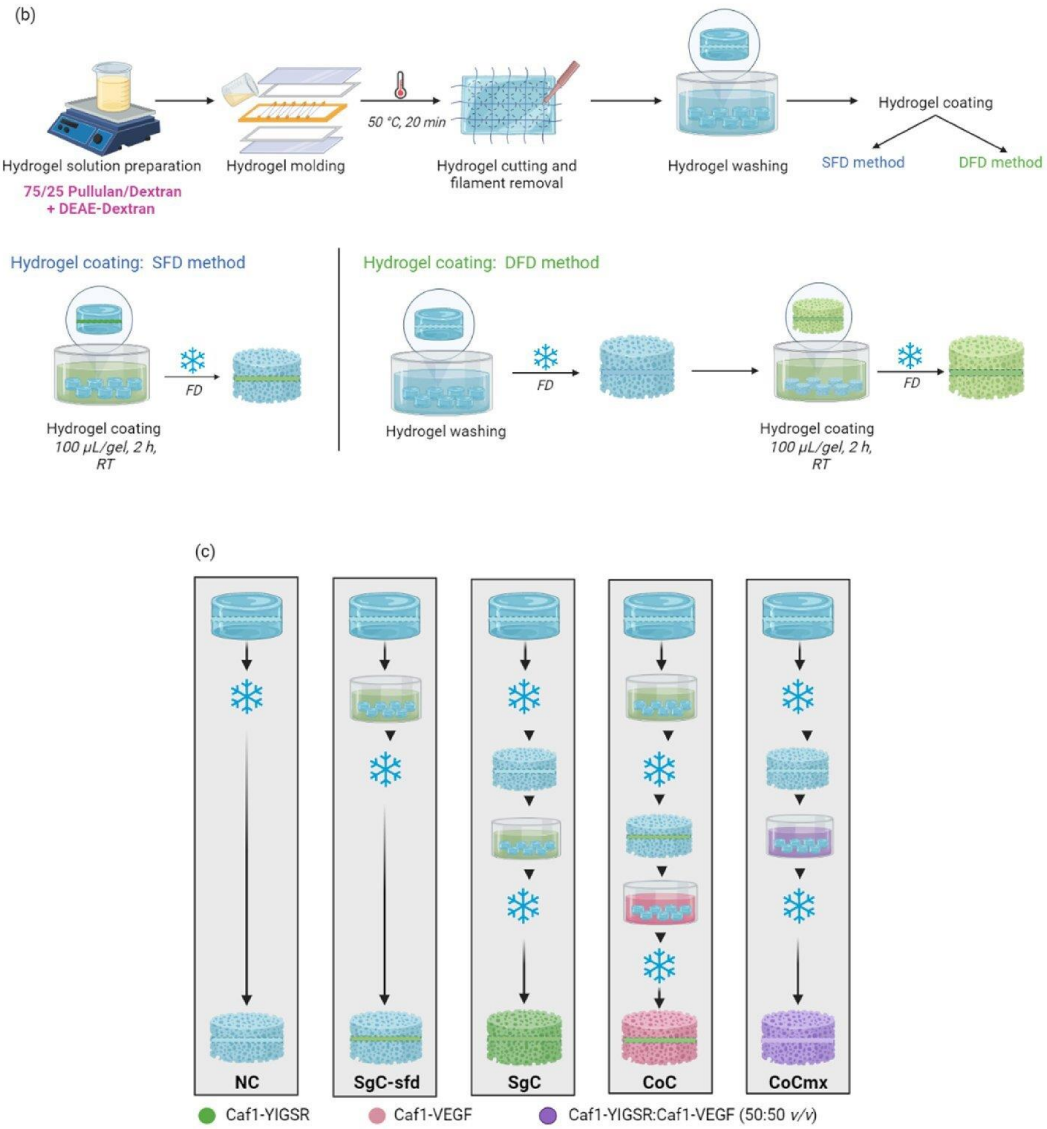

Figure 1. (**a**) Fabrication protocol of 3D porous hydrogels without coating; (**b**) Fabrication protocol of 3D porous hydrogels with coating (SFD: single freeze-drying; DFD: double freeze-drying); (**c**) Schematic plan of spatially controlled coating methods. NC: non-coated; SgC-sfd: single-coated-single-freeze-drying; SgC: single-coated; CoC: Co-coated; CoCmix: co-coated-co-mixed.

2. Results

2.1. Hydrogel Preparation and Characterization

Hydrogels molded using spacers and cut into discs had an average thickness of 550 ± 20 µm after freeze-drying. Surface pores were clearly visible with the naked eye (Figure 2a). Scanning electron microscopy (SEM) observations confirmed the porous

structure, revealing the macro- and micro-architecture of the hydrogels (Figure 2b). Larger pores (>50 µm) were present on the surface, while interconnected smaller pores (<50 µm) were seen in the cross-section of these hydrogels. Additionally, the presence of a hollow channel in the middle of the hydrogel was observed along with pores inside the channel structure (Figure 2b, bottom left).

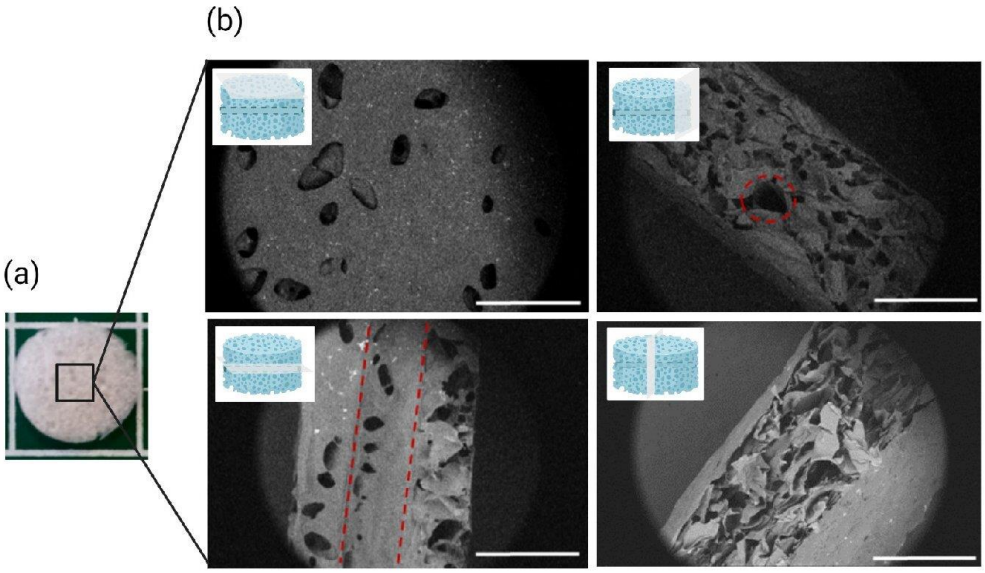

Figure 2. (**a**) Image of the hydrogel showing pores visible to the naked eyes. Scale bar = 5 mm; (**b**) SEM images of the surface, the edges and the cross-section of the hydrogel with a preformed channel. Red dash circle shows the circular cross-section of the microchannel (ø~100 µm), observed on the side of the hydrogel. Red dashed lines represent the limit between the hollow channel and the hydrogel surface. Scale bar = 1 mm.

The cationization by DEAE–Dex (DD) on pullulan–dextran-based hydrogels, previously described by our team [25–28] (referred to as PUDNA), was proven by an increase in the zeta potential of the hydrogel (from −22.3 mV to +8.28 mV) when replacing dextran with DD. Based on these results, a series of experiments were carried out to determine the optimal concentration of DD needed to facilitate electrostatic interactions between the cationized hydrogel and the negatively charged Caf1 protein polymer. Hydrogel solutions with various DD concentrations were prepared (25%, 50%, 75%, and 100% DD:Dex w/w) and hydrogels were formulated following the protocol described, as shown in Figure 1. These hydrogels were referred to as D0 for non-cationized samples, and D25, D50, D75, D100 for cationized samples with varying DD concentrations aforementioned. Upon rehydration of the hydrogels for further characterization, it was observed that the opacity increased with the increase in DD concentration added to the hydrogel (Figure 3a). Between D25 and D50, the samples were already quite opaque but the structures next to the surfaces were still visible under the microscope (Figure 3b). However, above D25, the gels were too opaque to allow observation, using confocal laser scanning microscopy (CLSM) or biphoton microscopy, of the microchannel which was embedded in the middle of the hydrogel (*z*-axis). Therefore, another opacity-coating efficiency test was conducted at the lower range of DD concentration: 5%, 10%, 15%, and 20% (DD:Dex w/w) (Figure 3). Here, all the hydrogels and their channel structures were visible via the confocal microscope

(Figure 3c). Thus, all four conditions (D5, D10, D15, D20) were used for further hydrogel characterization as well as for in vitro studies with ECs.

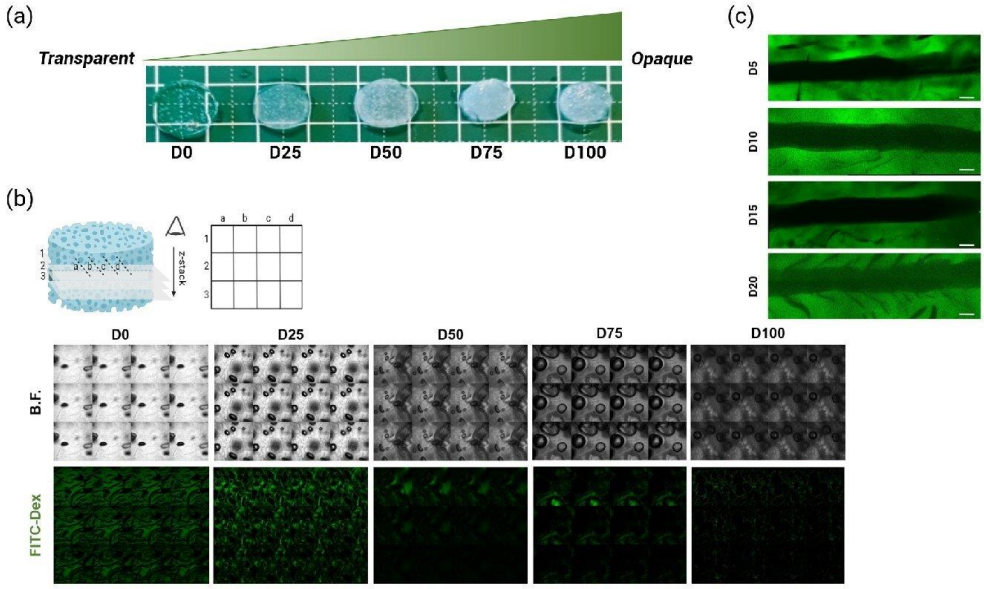

Figure 3. (**a**) Hydrogel opacity increased with an increase in DD concentration; (**b**) Hydrogel opacity as observed using CLSM: under bright-field and fluorescence (FITC). Z-stack images of hydrogels without DD (D0) and with DD 25–100% (DD:Dex w/w) were compiled as collages to demonstrate the increase in sample opacity with an increase in sample depth. (**c**) Z-projection (average intensity) of FITC-Dex hydrogels observed using CLSM.

Porosity measurements of non-cationized (PUDNA) and cationized hydrogels containing DEAE-dextran (PUDNA-D5, PUDNA-D10, PUDNA-D15, and PUDNA-D20) showed porosity values of 25–28% (Table 1). Swelling ratios for all conditions were around 12 (Table 1) meaning that water content after swelling was around 93 % (w/w). It should be noted that we did not find statistical differences between the different formulations.

Table 1. Effect of polysaccharide formulation on hydrogel properties: porosity %, swelling ratio, and water content. Results are expressed as mean values ± SD.

Scaffold Name	Porosity %	Swelling Ratio	Water Content (%)
PUDNA	26.1 ± 3.7	13.6 ± 1.8	93.1 ± 0.8
PUDNA-D5	28.0 ± 2.0	14.2 ± 3.7	94.2 ± 0.7
PUDNA-D10	25.0 ± 2.2	10.8 ±1.4	91.5 ± 0.6
PUDNA-D15	25.6 ± 4.3	12.2 ± 2.3	91.9 ± 1.3
PUDNA-D20	25.5 ± 3.1	13.2 ± 2.2	92.8 ± 0.7

The degree of crosslinking by sodium trimetaphosphate within the hydrogels was evaluated by quantifying the amount of phosphorus present after matrix degradation with HNO_3, an indicator of phosphate bridges between chains of pullulan–dextran. The phosphorus content in all hydrogel conditions ranged from 113 to 143 µmol per gram of hydrogel. These results suggest that the incorporation of DEAE–dextran did not affect the crosslinking degree of the polysaccharide-based hydrogels.

2.2. In Vitro Endothelial Cell Studies

To ensure cell adhesion on the materials, Caf1-YIGSR (a Caf1 polymer containing a pro-adhesive peptide sequence from laminin) was used to functionalize the hydrogels via electrostatic interactions. First, hydrogels were cationized by incorporating DD at various concentrations (5–20% DD:Dex w/w). Then, the cationized scaffolds were coated with the solution of Caf1-YIGSR (1 mg/mL, p.I. = 4.6) [13], at pH 7.0, room temperature (RT) via the vacuum-induced syringe method (Figure S1). This technique ensured that only the channel was coated. Subsequently, after the syringe coating step, the scaffolds were submerged in the same Caf1-YIGSR solution for 2 h, RT and immediately rinsed with PBS before the freeze-drying step (Figure 1b, SFD method). The scaffolds were exposed to UV light for at least 1 h before cell seeding experiments.

2.2.1. Selection of Cationized Hydrogel for Optimal Coating Efficiency

To establish the optimal concentration of DD required to functionalize the scaffolds via electrostatic interactions, samples with increasing DD concentration (5–20% DD:Dex w/w) were coated, then loaded with HUVECs at a seeding density of 5.0×10^6 cells/mL. Coating efficiency was determined based on cell adhesion and cell morphology. After 7 days in culture, cellularized scaffolds were fixed and stained with DAPI and phalloidin TRITC. Coated, cationized scaffolds with 5–20% DD:Dex (w/w) were referred to as PUDNA-D5C, PUDNA-D10C, PUDNA-D15C, and PUDNA-D20C, respectively.

HUVECs seeded on PUDNA-D5C formed large aggregates inside the coated channel section (Figure 4a). On PUDNA-D10C, a few polarized cells could be detected, where they exhibited filopodia and connections to neighboring cells (Figure 4a). On PUDNA-D15C scaffolds, the number of cells that adhered inside the channel appeared to increase slightly. The cell clusters seemed to reduce, while more polarized cells appeared inside the channel. Finally, on PUDNA-D20C scaffolds, cell morphology and behavior significantly improved. The entire channel edge was lined with elongated cells. These cells formed connections with their neighboring cells, showing filopodia structure and stress fibers, and less cell aggregates were detected. Regarding the porous regions outside the channel structure, numerous cell clusters were observed in the pores neighboring the channel (y-axis) as well as in the macropores outside the channel (z-axis) (Figure 4b).

Cell metabolic activity on all coated, cationized scaffolds was also investigated (Figure 4c). Overtime, there was an increase in cell metabolic activity for all coating conditions. On day 7, metabolic activity reached its peak for all conditions, with PUDNA-D20C showing the highest value and statistically greater than the metabolic activity on PUDNA-D5C and PUDNA-D10C. Although the cell metabolic activity on PUDNA-D15C vs. PUDNA-D20C did not differ, the morphological organization of HUVECs on PUDNA-D20C appeared more superior to those on PUDNA-D15C. From here on, PUDNA-D20C which showed optimal coating efficiency, was chosen as the standard cationized hydrogel for future functionalization experiments.

2.2.2. Spatial-Controlled Coating: Caf1-YIGSR Facilitated Cell Adhesion in Both SFD and DFD Coating Methods

We hypothesized that the coating of hydrogels could be modulated by integrating the coating step (via vacuum-induced syringe method) before and after the freeze-drying (FD) step (Figure 1). To confirm this hypothesis, cationized hydrogels (PUDNA-D20) were functionalized twice: the first coating was performed before FD, then the second coating was performed after FD. Samples which were coated once, were only freeze-dried once, in which only the channel was coated. These samples were named SFD and were used as controls. On the other hand, samples that were coated twice, hence freeze-dried twice, were named DFD, in which both the channel and the pores were coated.

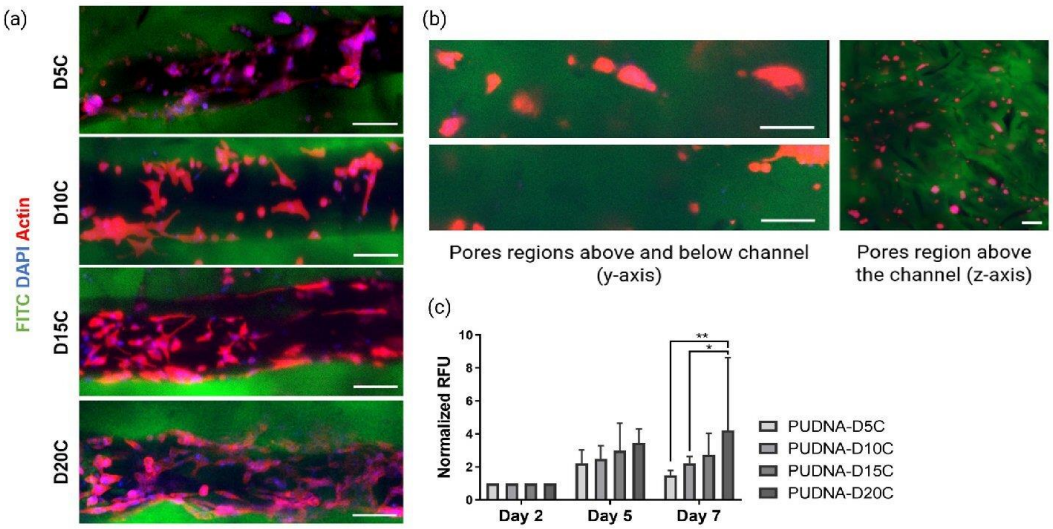

Figure 4. Cell analysis of seeded HUVECs on coated, cationized hydrogels with increasing DD concentrations: (**a**) Images represent Z-Projection, average intensity, showing cell morphology at day 7 via CLSM. Scale bar = 100 µm; (**b**) Representative image (Z-Projection) of cells in the pore region outside the channel on coated scaffold. Scale bar = 100 µm; (**c**) Cell metabolic activity determined by resazurin assay on days 2, 5, and 7. All resofurin fluorescence unit (RFU) values of each condition were normalized to their own RFU value on day 2. Statistical analysis was performed using a two-way ANOVA with multiple comparisons. * $p < 0.05$, ** $p < 0.01$.

The coated hydrogels were seeded with HUVECs at 5.0×10^6 cells/mL and cultured for 9 days. Then, cellularized scaffolds were analyzed for cell adhesion, cell morphology, and cell metabolic activity. Similar to the SFD scaffolds, cells on the DFD scaffolds adhered in a monolayer along the channel lining and more cell spreading (elongation) was detected after 7 days in culture. Additionally, more polarized cells were observed inside the channel (Figure 5a, bottom). When looking at the pores near the channel edges, migrating cells were observed: the cell filopodia reached towards the pores outside the channel and formed connections with neighboring cells residing in the pores (external of channel) (Figure 5a, bottom). Cell clusters were also detected: inside the channel, the clusters were comprised of both polarized and round cells; outside the channel, the clusters were composed of mostly round cells. On day 9 (results not shown), the cell's presence began to block visibility under the CLSM, making it inconclusive for further analysis.

Cell metabolic activity from resazurin assay (Figure 5b) was analyzed to support the cell adhesion and cell morphology observations. For both SFD and DFD scaffolds (YIGSR-SFD and YIGSR-DFD), there was an increase of metabolic activity from day 2 to day 7. After 7 days, the metabolic activity dropped. Compared to SFD, cells on DFD scaffolds had a significantly higher metabolic activity, with a peak on day 7.

2.2.3. Spatial-Controlled Coating (DFD Method): Caf1-YIGSR and Caf1-VEGF Influenced Cell Behavior Differently

Two different recombinant Caf1 proteins containing peptide sequences from laminin (YIGSR) and VEGF, were tested on DFD hydrogels. Those coated with Caf1-YIGSR and with Caf1-VEGF, were named YIGSR-DFD and VEGF-DFD, respectively. Regarding the cell morphology, cells seeded on hydrogels coated with YIGSR exhibited different shape than those seeded on VEGF-coated hydrogels (Figure 6a). On VEGF-DFD samples, very few cells adhered inside the channel and the channel edge. Those that remained adhered inside

the channel started to polarize. In contrast, on YIGSR-DFD samples, a greater number of cells adhered inside the channel and lined the channel edge while fewer cells showed signs of migration or polarization.

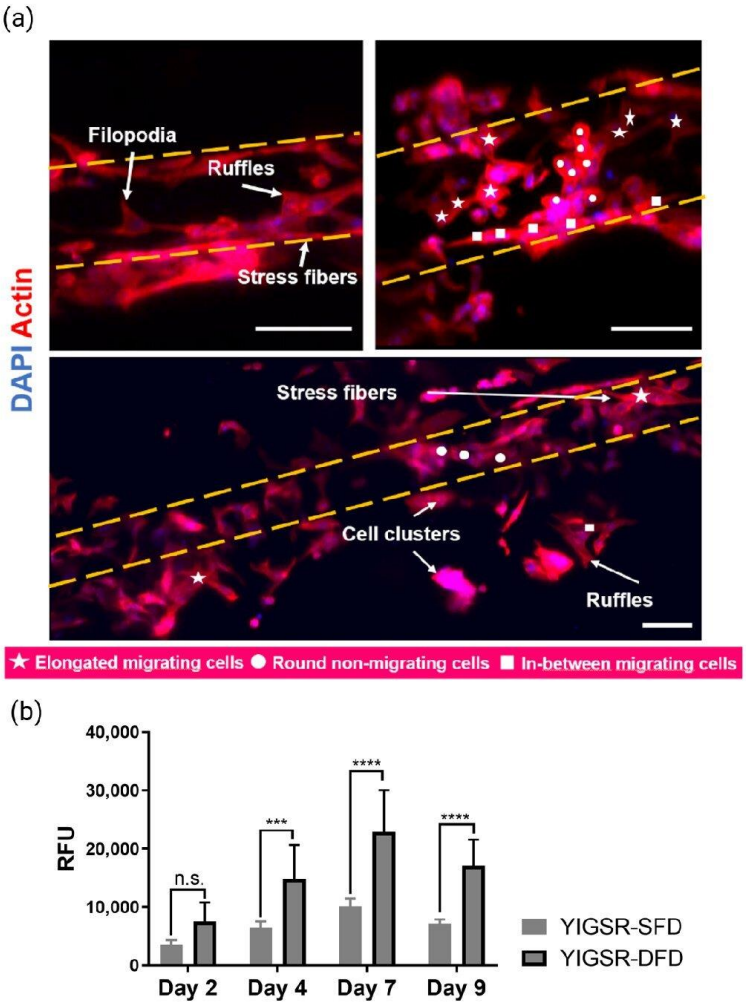

Figure 5. Cell analysis of seeded HUVECs on PUDNA-D20C scaffolds (SgC-SFD, top; SgC-DFD, bottom). (**a**) Images represent Z-Projection (average intensity) showing cell morphology at day 7 via CLSM. Scale bar = 100 μm; (**b**) Cell metabolic activity determined by resazurin assay on days 2, 5, 7, and 9. Statistical analysis was performed using a two-way ANOVA. *** $p < 0.001$, **** $p < 0.0001$.

Overtime, cell metabolic activity followed the previously observed trend, with the highest cellular activity observed on day 7 and a slight decrease on day 9. The differences in cellular activity of seeded HUVECs on YIGSR-DFD and VEGF-DFD were insignificant (Figure 6b), but the variations of cell morphology seen on the differently coated scaffolds were more obvious (Figure 6a). These results confirmed that Caf1-YIGSR had a stronger cell-adhesive effect than Caf1-VEGF.

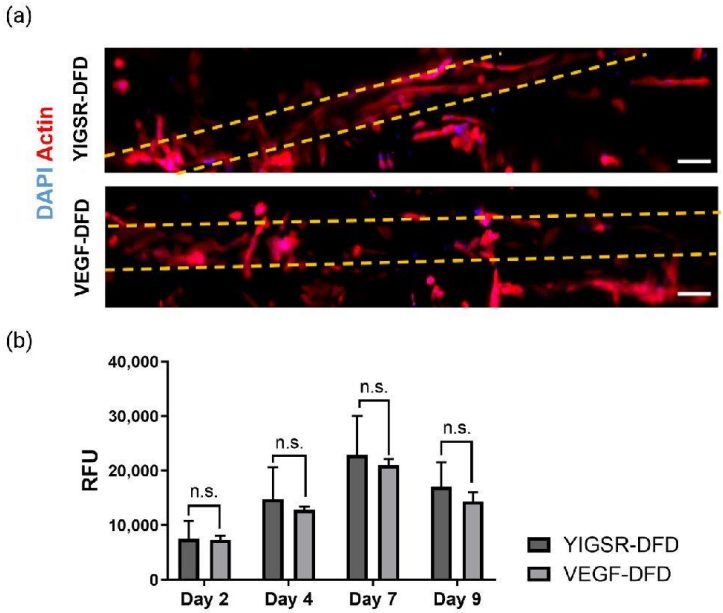

Figure 6. Cell analysis of seeded HUVECs on scaffolds functionalized with Caf1-YIGSR and Caf1-VEGF via the DFD method. (**a**) Tile-scan images represent Z-Projections (average intensity) showing cell morphology inside the scaffold channel (full length) at day 7 via CLSM. Scale bar = 100 µm. Yellow dashed lines represent the limit of the microchannel; (**b**) Cell metabolic activity of seeded HUVECs determined by resazurin assay on days 2, 4, 7, and 9. Statistical analysis was performed using a two-way ANOVA.

2.2.4. Spatial-Controlled Coating (SgC, CoC, CoCmx): Caf1-YIGSR and Caf1-VEGF Spatial Distribution on Scaffolds Can Provoke Different Angiogenic Behaviors

Using the optimal coating protocol (DFD = double freeze-drying, coating of both channel and pores), the next step was to determine whether (i) the presence of different protein types (Caf1-YIGSR and Caf1-VEGF) and (ii) their spatial presentation on the scaffolds (pores and/or microchannel) could influence cell behavior. To answer this question, several coatings were performed as described in Figure 1c. DFD scaffolds with only one type of coating (Caf1-YIGSR) were named SgC. Scaffolds with two types of coating (Caf1-YIGSR and Caf1-VEGF) were named CoC and CoCmx. In CoC, Caf1-YIGSR were coated only in the channel and Caf1-VEGF were coated in the pores. In CoCmx, both Caf1 sequences were mixed at a 50:50 ratio (v/v) so that the pores and the channel were simultaneously coated at the same time with both Caf1-YIGSR and Caf1-VEGF (Figure 4). The non-coated, cationized hydrogels (D20C) were used as control and were named NC.

As expected, the NC scaffolds did not support cell adhesion or proliferation overtime (Figure 7). On the NC scaffolds, only cell aggregates were observed inside the channel and cell metabolic activity was lower compared to those on the coated scaffolds. Initial examination of cell morphology on all the coated scaffolds (SgC, CoC, CoCmx) showed interesting outcomes. Both SgC and CoCmx resulted in elongated cells lining the channel edges, a high density of polarized cells inside the channel, large number of cells forming connections with neighboring cells. While both CoC and CoCmx scaffolds encouraged adhered cells to migrate outwards of the channel, SgC scaffolds only contained adhered cells within the channel (Figure 7a). Further observations on CoCmx scaffolds demonstrated that the co-presence of Caf1-YIGSR and Caf1-VEGF also had an effect on ECs outside the channel (Figure 8). Here, the cells in the pores did not form aggregates but rather exhibited

an elongated morphology, conforming their shape to the curvature of the pores (Figure 8a, right panel and Figure 8b).

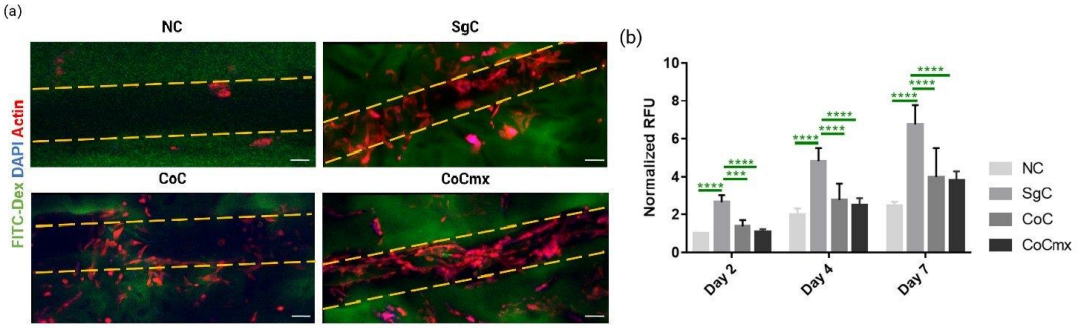

Figure 7. Cell analysis of seeded HUVECs on non-functionalized (NC) and functionalized scaffolds with a different spatial distribution of Caf1-YIGSR and Caf1-VEGF (SgC, CoC, and CoCmx) via the DFD method. (**a**) Images represent Z-Projection (average intensity) showing cell morphology at day 7 via CLSM. Scale bar = 100 µm. Yellow dashed lines represent the limit of the microchannel; (**b**) Cell metabolic activity (resazurin-based assay) at days 2, 4, and 7. Statistical analysis using two-way ANOVA of all hydrogels compared to SgC. Statistical analysis was performed using a two-way ANOVA. *** $p < 0.001$, **** $p < 0.0001$.

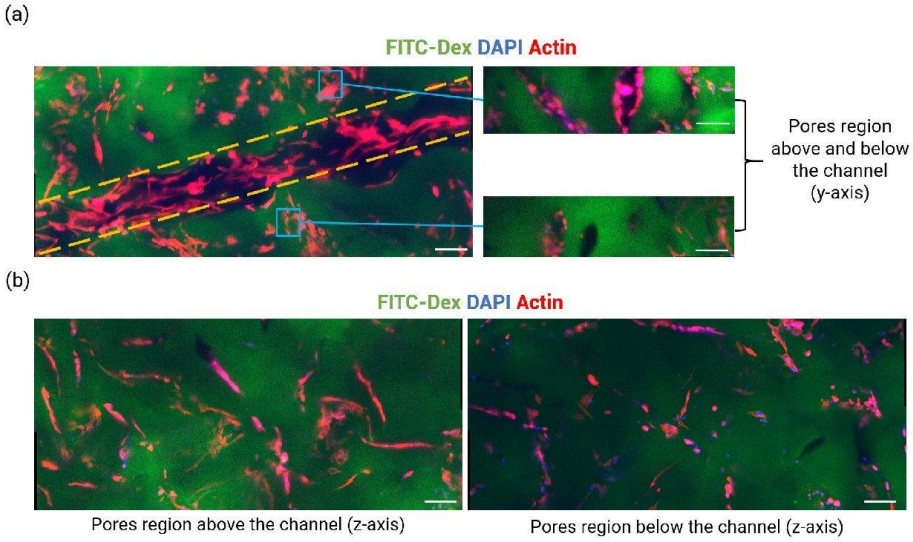

Figure 8. Cell analysis of seeded HUVECs on CoCmx scaffolds. (**a**) Images represent Z-Projection (average intensity) inside the scaffold's channel. Scale bar = 100 µm. Yellow dashed lines represent the limit of the microchannel; (**b**) Images represent Z-Projection (average intensity) of the same scaffold, in the porous regions outside the channel (z-axis). Scale bar = 100 µm.

Overall cell metabolic activity showed the expected trend with the highest activity observed on day 7 for all scaffold conditions. NC scaffolds resulted in the lowest cell metabolic activity, which is representative of the cell morphology outcome. As for coated scaffolds, the cell metabolic activity on SgC samples was significantly greater compared to those on the CoC and CoCmx scaffolds (Figure 7b).

2.2.5. Protein Bulk Concentration

Previously, we observed that the cell metabolic activity of HUVECs seeded on all functionalized hydrogels was statistically higher than on non-functionalized ones. Moreover, cell morphology drastically improved when seeded on spatially controlled coated DFD gels (SgC, CoC, CoCmx) (Figure 7a). Therefore, we hypothesized that the enhancement in cell behaviors was contributed by an increase in protein concentration on the functionalized scaffolds.

Among the SgC scaffolds where only one type of protein (Caf1-YIGSR) was employed and the coating was performed either once (SFD, channel coated only) or twice (DFD, channel and pores coated), the DFD scaffolds had a significantly greater protein concentration (µg per mg hydrogel). Similarly, when comparing all the DFD samples to the SgC-SFD samples, CoC and CoCmx showed a higher protein concentration (Figure 9). These values were expected since the DFD scaffolds were coated twice, hence the number of proteins grafted onto the hydrogels would be greater on these scaffolds.

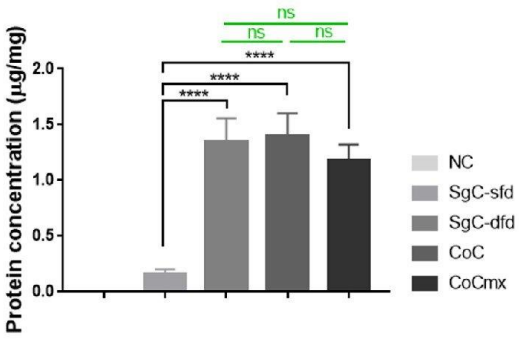

Figure 9. Protein concentration of cationized hydrogels (20% DEAE–Dextran) with spatial-control coating. Statistical analysis was performed using a one-way ANOVA. **** $p < 0.0001$.

3. Discussion

Porous hydrogels made of pullulan and dextran were synthesized by chemical crosslinking with sodium trimetaphosphate (STMP), as previously described [29]. First, the hydroxyl groups in the polysaccharides were activated at basic pH using NaOH, resulting in the opening of cyclic STMP and crosslinking between the polysaccharides, leading to hydrogel formation [36]. Previous studies have demonstrated the potential of these biocompatible hydrogels as scaffolds for 3D cell culture, tissue engineering, and cell therapy applications [25,27,37,38]. However, due to the high water content (~93%) and the chemical structures of pullulan and dextran, endothelial cells do not adhere spontaneously to these hydrogels [28,38], as shown in Figure 7a (NC sample). The neutral polysaccharides were cationized by incorporating diethylaminoethyl dextran (DEAE–Dex) to facilitate electrostatic interactions with the negatively-charged ECM-like molecules (Caf1-YIGSR and Caf1-VEGF). The shape and diameter of the channel remained 100 ± 20 µm before and after swelling. These observations are in correspondence with the swelling behavior observed in all formulations. Here, we demonstrated the ability to form straight microchannels with circular cross-section and controlled diameter.

Cell analysis of HUVECs seeded on functionalized scaffolds with various coating methods (SFD vs. DFD) and spatial distribution of the two Caf1 motifs (YIGSR and VEGF) confirmed that the Caf1 solution (p.I. = 4.6; 1 mg/mL; ζ = −23.6 mV) was adequate to facilitate electrostatic interactions with cationized hydrogels (PUDNA-D20; ζ = +29.5 mV). Through the addition of microchannels within the polysaccharide scaffolds and sufficient surface functionalization via electrostatic interactions, ECs were able to adhere, leading to good cell proliferation and cell spreading within the microchannel. In this work, spatial

control of the ECM-mimicking moieties was shown to induce different EC behaviors that could be interesting for vascularization applications. An in-depth discussion on this part is presented in Sections 3.2–3.4.

3.1. The Impact of DEAE–Dex Concentration on Hydrogel Opacity and Functionalization

As seen in Figure 3, an increase in the concentration of DEAE–Dex added to the polysaccharide solution contributed an increase in hydrogel opacity, which limited sample visibility under the microscope. Even with a multiphoton microscope or a high-resolution confocal laser scanning microscope and sufficient image treatment and analysis, it was very difficult to locate the microchannel embedded in the middle of the sample depth. Consequently, these observations suggest that a balance between hydrogel transparency and the cationic polymer concentration need to be considered to ensure sample visibility for microscopy analysis, which is essential to monitor cell behavior in the scaffolds. Moreover, this balance must also allow sufficient interactions between the charged materials in order to facilitate cell adhesion on the functionalized scaffolds.

After a series of optimization work, by synthesizing cationized hydrogels with varying DEAE–Dex concentrations (5–100% DD:Dex w/w), we were able to determine the best cationic parameters to yield optimal hydrogel opacity and favorable EC behavior outcomes. At 20% (DD:Dex w/w), the scaffold surface and microchannel were still visible under the CLSM (Figure 3a). More importantly, ECs were also observable after 7 days in culture (Figure 4a). On day 7, PUDNA-D20C scaffolds facilitated better EC adhesion, where more elongated cells were present inside the channel (Figure 4a) and cell metabolic activity was statistically higher than the metabolic activity on the rest of the other conditions (Figure 4c). These results strongly suggest that PUDNA-D20C was the optimal hydrogel condition for most favorable EC adhesion and morphology.

3.2. Caf1-YIGSR Induced Cell Adhesion on SFD Hydrogels and Enhanced Cell Proliferation on DFD Hydrogels

Cell morphology and behavior on SFD scaffolds using Caf1-YIGSR (Figure 5a) confirmed that the YIGSR sequence could be used as a cell-adhesive coating material.

Recent works on functionalized biomaterials have demonstrated the ability to modulate cell behavior by varying the concentration of cell-adhesive ligands in the scaffolds, with an increase in ligand concentration leading to an improvement in cell adhesion, spreading, and proliferation [39]. The results obtained from this study are in accordance with these findings. When both the channel and pores were coated (DFD coating method: YIGSR-DFD), the amount of Caf1 protein detected on the SgC-DFD scaffolds was higher than that on the SgC-DFD scaffolds, suggesting an increase in bulk ligand concentration (Figure 9). As a result, cell morphology on the DFD scaffolds greatly improved (Figure 5a) and greater cell metabolic activity was observed after 7 days in culture (Figure 5b). The decrease in cell metabolic activity on day 9 could be due to high cell confluency. This is supported by the fact that no signs of cell death were observed after 9 days. In conclusion, the increase in spatial distribution of the YIGSR sequence, contributed to an increase in ligand bulk concentration on the scaffold, leading to an enhancement of EC morphology and behavior.

3.3. Caf1-VEGF Induced Cell Migration and Angiogenic Sprouting Depending on Its Spatial Presentation on Porous Hydrogels

When Caf1-VEGF was used alone as the coating material in the DFD method, few cells adhered inside the channel and did not completely line the channel edge. Adhered cells showed polarization characteristics and sprouting-like behaviors. It is well known that VEGF is a pro-migratory factor that induces filopodia elongation in ECs during angiogenesis [5]. This explains why ECs in VEGF-DFD scaffolds showed filopodia structure resembling migration behaviors (Figure 5a). Additionally, cells on the top side of the channel protruded and connected to cells on the bottom side (Figure 6a). Due to lack of cell-adhesive moieties (i.e., Caf1-YIGSR), not enough cells adhered inside the channel,

resulting in lower cell proliferation, as demonstrated by the lower cell metabolic activity (Figure 6b). This drop in metabolic activity could also be linked to cell confluency on day 9.

Taking these results into consideration, CoC scaffolds were prepared, where two different Caf1 proteins were presented on the hydrogels in different spatial distribution. First, the channel was coated with Caf1-YIGSR, then the pore-filled region was coated with Caf1-VEGF (Figure 1c). On co-coating scaffolds, the cell morphology and behaviors significantly altered. Adhered cells inside the channel started to migrate outwards to the pore-filled region. Some cells even exhibited filopodia structure. These results strongly suggest that different spatial presentations of Caf1-VEGF on porous hydrogels drive distinct cell behaviors.

During the last decades, cell–ECM interaction research has shown that when cell-adhesive molecules were spatially presented to the cells in different manners, they induced different patterns of cellular behavior [40,41]. In the case of CoC hydrogels, cell adhesion was achieved thanks to the contribution of the Caf1-YIGSR coating in the channel during the first coating step (Figure 4). The presence of Caf1-YIGSR facilitated proper cell adhesion, where cells could form a strong anchor to the substrate at focal complexes [4]. The presence of Caf1-VEGF promoted protrusion formation of ECs and transformed protrusion into forward movement. This explains the observation of filopodia structure, stress fibers, and polarization of HUVECs seeded on the CoC hydrogels (Figure 7a). The adhered cells sensed migratory signals from the VEGF sequence, which stimulated cell migration processes. In other words, our results suggest that the presence of Caf1-VEGF moieties in the pores created cell directionality, leading to cells moving from the channel outwards to the porous region (exterior of the channel).

3.4. Synergistic Effects of Caf1-YIGSR and Caf1-VEGF on EC Morphologies and Behaviors

Taken the outcomes discovered from CoC hydrogels, a question regarding Caf1-YIGSR and Caf1-VEGF spatial distribution on hydrogel was considered. What will be the effect of these two Caf1 proteins on cell morphology and cell behavior, if they were both presented on the hydrogel in similar spatial organization? This question led to the creation of CoCmx hydrogels, where Caf1-YIGSR and Caf1-VEGF solutions were mixed in equal parts (50:50 v/v) and used to coat the scaffolds via the DFD method. Here, both the channel and the pores were functionalized with Caf1-YIGSR and Caf1-VEGF at the same time. Initial inspection of cell morphology on CoCmx scaffolds showed good cell adhesion (where cells fully lined the channel) and elongated filopodia (which indicated cell sprouting and migration) (Figure 7a, top panel). Moreover, migrating cells connected with non-migrating cells both inside the channel and outside the channel (Figure 7a, bottom panel). These observations suggested the synergistic effect of Caf1-YIGSR and Caf1-VEGF. Both VEGF and YIGSR are known to play a role in angiogenesis, with YIGSR contributing to cell adhesion, cell–cell interactions, and tubule formation, while VEGF stimulates cell migration [4,42,43]. The presence of both Caf1-YIGSR and Caf1-VEGF inside the channel induced a stabilizing adhesive effect on ECs. These ECs then migrated towards the VEGF stimulus that was also available in the pores of the scaffolds. Consequently, the dual presence of YIGSR and VEGF sequences, both exhibiting angiogenic effects, promoted greater EC proliferation. These ECs possibly produced their own ECM, which further stabilized the vessel-like network and induced EC differentiation towards angiogenic phenotypes. This explains why elongated migrating cells were observed in both the channel section and the porous regions outside the channel only on CoCmx scaffolds (Figure 8).

In other words, the dual presence of Caf1-YIGSR and Caf1-VEGF functionalized on our 3D porous hydrogels created a synergistic effect on seeded HUVECs. Previously, a Caf1 mosaic co-polymer containing two pro-osteogenic motifs was seen to promote the early stages of bone formation in primary human mesenchymal stromal cells in a 2D system [35]. The synergistic effect described here further demonstrates the benefits of the Caf1 system, where bioactive peptides can be easily introduced and placed in close proximity in a single material, allowing these synergistic effects to take place. Thus, these effects mimicked the

in vitro angiogenesis, where ECs adhered and became activated, then proliferated and differentiated into tip cells, resulting in elongation in the direction of the VEGF stimulus.

3.5. Comparison of the Developed Method with Current Vascularization Strategies

Over the past decades, numerous attempts have been made to develop vascularized constructs using three main strategies: microfluidic-based approaches, 3D bioprinting, and organoids/spheroids-based techniques. The readers are invited to read more on this topic in the published review [2].

The use of ECM-based membranes integrated in microfluidic platforms has allowed researchers to develop more physiologically relevant models thanks to the ability to perfuse the systems. However, most models require soft lithography for materials fabrication, which is expensive and is difficult to be used by a wide end-user's range.

The use of 3D additive manufacturing, such as fuse deposition modeling (FDM), facilitates printing of sacrificial components that better mimic in vivo vasculature. However, these techniques often require several manufacturing steps and still present major issue in terms of resolution. Most vessel geometries remain relatively simple and the vessel diameters are in the range of hundreds of microns. Channels obtained using co-axial bioprinting or with sacrificial bioinks remain in the same range. More recently, the use of laser-assisted bioprinting (LAB) offers high resolution (5–10 μm) of printed channels, automation, reproducibility, and high throughput. Similarly, the use of Vat photopolymerization-based bioprinting opens new possibility to create complex vascular patterns with high precision and high resolution. However, these approaches are still far from translation due to the high cost of equipment, and the need to work with photosensitive materials and photoinitiators further limit their application for therapy.

Spheroids and organoids are another alternative approach to promote the vascularization of hydrogel constructs. They offer the ability to recapitulate the microenvironment, thus present great potential as vascularized models. However, to reach a substantial quantity of tissue, a large number of cells are needed. The use of ECM proteins with heterogeneous composition and high immunogenic potential (e.g., collagen and Matrigel), further prevents translation of these models in the industry and clinical settings.

In this work, we employed a simple method to form microchannels at the microcapillaries range (≥100 μm). Although the filament templating/removal technique is limiting in terms of producing complex designs, it enables high reproducibility and facile fabrication. Our system, porous hydrogels with channels, functionalized in a spatial-controlled manner, present several advantages compared to other aforementioned vascularization strategies.

Compared to other hydrogel-based vascularization strategies, our polysaccharide-based hydrogels support long-term cell culture of up to 9 days, as demonstrated in this study, and could be kept up to 14 days in other studies without being degraded [27]. With a small amount of protein (~0.25–1.8 μg/mg hydrogel), we were able to induce initial cell adhesion, followed by cell proliferation and migration on functionalized scaffolds. Thus, the spatial cues (e.g., YIGSR and VEGF) further direct cell migration mimicking the first step of sprouting angiogenesis. Even though the electrostatic bonds are weaker than covalent bonds, our functionalization method was stable enough to enable observation of grafted Caf1 on the hydrogels (as shown in Figure S5). Moreover, the concomitant presence of channels and pores offers the possibility to promote vascularization of tissue constructs, while enabling co-culture with other cell types for the development of different bioengineered models. Caf1 molecules are manufactured in vitro using bacterial expression systems in high quantities and with a lower cost [33]. Thus, the animal-free origin of Caf1 would reduce immunogenic potential, making them ideal materials for implantable constructs. Our coating method based on ionic interactions is performed in a one-step process and uses green chemistry. In this study we focused on YIGSR and VEGF, but in the future, it will be possible to use the same strategy to incorporate other Caf1 peptides to confer new properties to the material. Finally, from an industrial point of view, our fabrication technique and the choice of materials are highly beneficial: The production

method is simple and can be easily scaled-up and the freeze-dried hydrogels allow for long-term storage, all contributing to low-cost production and maintenance.

4. Materials and Methods

4.1. Materials

Pullulan (Mw 200 kDa) and dextran (Mw 500 kDa) were obtained from Hayashibara Inc. (Okayama, Japan) and Pharmacosmos (Holbaeck, Denmark), respectively. FITC-dextran (dextran labeled with fluorescein isocyanate, TdB consultancy® (Prince George, BC, Canada)) was used to label the hydrogels. All other chemicals were obtained from Sigma-Aldrich® (Saint-Quentin-Fallavier, France). Caf1-YIGSR and Caf1-VEGF as freeze-dried powder were provided to us by Newcastle University (Newcastle, UK).

4.2. Hydrogel Synthesis: 3D Porous Polysaccharide-Based Hydrogel with Microchannel

Briefly, a solution of pullulan and dextran (75:25 *w*/*w*) and NaCl was prepared in ultrapure water. This solution is referred to as PUDNA. Then, NaOH 10M was added to the PUDNA solution to activate the hydroxyl groups before reacting with the crosslinker STMP (sodium trimetaphosphate) (3% *w*/*v*) at room temperature under magnetic stirring. The crosslinked solution was poured in between two glass slides, separated by polypropylene suture filaments ø 70 µm (6.0, Ethicon®) (Raritan, NJ, USA) and two spacers of 250 µm thickness, before crosslinking in an oven at 50 °C for 20 min. This incubation step was carried out to facilitate the crosslinking reaction and to form microchannels within the hydrogel. Afterwards, the hydrogels were cut into discs of 5 mm in diameter using a biopsy disc-cutter from Harris Uni-Score (Sigma-Aldrich®) (Figure 1a).

Hydrogels were neutralized in PBS 10X and washed in distilled water until equilibrium (ca. 15 µS/cm). The conductivity was measured with an Orion 145 A+ conductivity meter purchased from Thermo Fisher Scientific (Asnières-sur-Seine, France). A second wash was performed in NaCl 0.025% (Sigma-Aldrich®) until equilibrium (ca. 500 µS/cm). Finally, the hydrogels were freeze-dried to promote pore formation.

The freeze-drying protocol consisted of three stages: freezing under atmospheric pressure from 15 °C to −20 °C at a constant rate of −0.1 °C/min, followed by a phase at constant temperature of −20 °C for 90 min. Primary drying was performed at low pressure (0.001 mbar) and −5 °C for 8 h and secondary drying at 30 °C for 1 h [26].

4.3. Hydrogel Characterization

4.3.1. SEM

The topography of freeze-dried hydrogels was observed using the JEOL JSM-IT100 system (software InTouch Scope v.1.060) under low-vacuum conditions. The SEM system was located at the Institute Jacques Monod (Paris, France).

4.3.2. Porosity

The porosity of hydrogels was determined based on a published protocol which calculates the water amount absorbed in the hydrogel before and after manual squeezing tests [44]. Experiments were performed by soaking 5 samples in PBS 1X in a 24-well cell culture plate (Corning®) (Corning, NY, USA) for 2 h under mechanical shaking. Samples were then weighed after removing the excess liquid by placing them on the plastic lid. This was considered the weight of the swollen gel ($M_{swollen}$, mg). Following this step, samples were weighed again after squeezing out the remaining liquid using tissue paper and gentle pressing using a spatula. This was considered the "squeezed" weight ($M_{squeezed}$, mg). The porosity calculated by this method corresponds to the large pores that entrap water molecules free or weakly bound to the polysaccharide matrix that are release by gentle mechanical compression. The pore volume percentage was calculated using Equation (1).

At least three scaffolds were analyzed per condition. Results were expressed as mean values ± SD.

$$\text{Volume of macropores } (\%) = \frac{(M_{swollen} - M_{squeezed})}{M_{swollen}} \times 100 \quad (1)$$

4.3.3. Swelling Ratio

Scaffolds were weighed before (M_{dry}) and after ($M_{swollen}$) rehydration in PBS 1X for 48 h. The swelling ratio was determined using Equation (2). At least three scaffolds were analyzed per condition. Results were expressed as mean values ± SD.

$$\text{Swelling ratio} = \frac{(M_{swollen} - M_{dry})}{M_{dry}} \quad (2)$$

4.3.4. Water Content (WC)

The water content was calculated by using the sample weight after 48 h post-rehydration ($M_{swollen}$) and the sample weights before rehydration (M_{dry}). The water content was calculated using Equation (3). At least three scaffolds were analyzed per condition. Results were expressed as mean values ± SD.

$$WC = \frac{(M_{swollen} - M_{dry})}{M_{swollen}} \times 100 \quad (3)$$

4.4. Hydrogel Functionalization via Electrostatic Interactions

4.4.1. Caf1 Solution Preparation

To assure cell adhesion onto the polysaccharide-based hydrogels, recombinant, engineered Caf1 proteins displaying pro-adhesive and pro-angiogenic peptide motifs were used to functionalize the hydrogels. Briefly, the sequence encoding the peptide was inserted into the *caf1* gene, present on a standard expression plasmid, and the protein was expressed and purified from an *E. coli* culture using tangential flow filtration and size exclusion chromatography [33,35].

The Caf1 proteins with cell-adhesive motifs are called Caf1-YIGSR and Caf1-VEGF. Solutions of 1.0 mg/mL (ζ = −23.6 mV for Caf1-YIGSR and ζ = −21.7 mV for Caf1-VEGF) were prepared by diluting the freeze-dried powder in miliQ water at room temperature and stored at −20 °C. These solutions were then thawed on the day of hydrogel coating and allowed to cool to room temperature, before being used.

4.4.2. Cationization of Polysaccharide Hydrogel

Briefly, a predetermined amount of diethylaminoethyl (DEAE)–dextran (Mw 500 kDa) from Pharmacosmos (Holbaeck, Denmark) was added into the standard hydrogel solution to obtain a solution at various concentrations: 5–20% (DD:Dex *w*/*w*; ζ = +29.5 mV) and mixed well at room temperature (RT) until fully dissolved. The hydrogel precursor solution was degassed overnight at RT and used for hydrogel synthesis the next day.

4.4.3. Spatial-Controlled Hydrogel Coating

To facilitate electrostatic interactions, positive charges were added to the hydrogel network (by incorporation of DEAE–Dextran) to react with the negatively charged protein solution (pI = 4.46). Once the hydrogels were synthesized and rinsed thoroughly (Section 4.1), they were immediately coated via the syringe vacuum-induced method (Figure S1) (100 µL/ gel) and incubated for 2 h at RT. This coating step was performed either only before, or both before and after the freeze-drying step to coat the gel channel only (SFD coating method) or both the channel and pores (DFD coating method) (Figure 1).

4.5. Cell Culture and Cell Seeding

Human umbilical vein endothelial cells (HUVECs) (ATCC-CRL-1730) purchased from ATCC® (Manassas, VA, USA) were maintained and subcultured in T75 surface-treated flasks (Corning®) in complete endothelial growth medium (EGM-2) (Lonza) following the manufacturer's recommendations. To prevent bacterial contamination, 1% antibiotic-antimyotic (AA 100X) (Gibco™) purchased from Thermo Fisher Scientific, was also added to the complete growth medium. Cells splitting was performed according to manufacturer and kept in an incubator prior to use (37 °C, 5% CO_2).

Prior to cell seeding, hydrogels were sterilized under UV light for at least 1 h. Cells were first detached with 1 mL of Trypsin solution (1X, Gibco) at 37 °C for 5 min. Trypsin was inactivated by performing cell dispersion in EGM-2, followed by centrifugation and cell counting. Cell dilution in cell culture medium was conducted to reach the desired concentration. Cell loading was performed via the syringe vacuum-induced method to ensure cell seeding only inside the preformed microchannel. Briefly, hydrogels and cell suspension were introduced in a 10 mL syringe barrel. A 3-way stopcock was used to close the system and the plunger was pulled to make cell suspension circulate inside the channels. Then, cell-loaded hydrogels were placed in a 24 well-plate (Corning®), complete cell medium was added, and the plates were placed in an incubator.

The optimal seeding density was determined to be 5.0×10^6 cells/mL. Culture medium (EGM-2) was refreshed every 2–3 days. To facilitate cell lining of the channels, the hydrogels were turned 180° twice following the protocol described in Figure S2.

4.6. Cell Metabolic Activity

Cell metabolic activity was determined using the In Vitro Toxicology Assay Kit (Resazurin-based, TOX8-1KT, Sigma-Aldrich, France). Briefly, cells were cultured as previously described (Section 4.3). On day 2, 4, 7, and 10, cell medium was removed and 0.5 mL of fresh culture medium containing 10% resazurin solution was added. After 3 h of incubation (37 °C, 5% CO_2), 100 µL (in triplicates per sample) of the supernatant was transferred to a 96-well plate. Fluorescence was measured using an Infinite M200 Pro microplate reader (TECAN®) at 560Ex/590Em. All samples were analyzed in triplicate, in three different experiments. Results were expressed as mean values ± SD.

4.7. Cell Staining for Confocal Microscopy

Cellularized hydrogels were fixed with paraformaldehyde 4% (Sigma-Aldrich®) in PBS for 1 h at 4 °C. After rinsing with PBS, membranes were permeabilized with Triton X-100 (Sigma-Aldrich®) 0.1% in PBS for 1 h at RT. Actin filaments were labeled by incubation with TRITC-conjugated phalloidin (Sigma-Aldrich®) (1/200, 1 h incubation time at RT) and nuclei were stained with DAPI (1/2000). Samples with FITC (λ_{ex} 488 nm) and cellularized samples stained with phalloidin actin marker (λ_{ex} 561 nm) and DAPI nuclear marker (λ_{ex} 405 nm) were observed using a Leica SP8 confocal microscope. Images were acquired using the LSA-X software (LAS X Core 3.7.6) and image analysis was performed with ImageJ/Fiji software (Window, version 153, Java8).

4.8. Immunofluoresence Staining of the Caf1 Protein Polymers

In order to confirm the presence of Caf1 protein polymer functionalized on the hydrogel channel (SFD coating method), we conjugated Caf1 with fluorescent markers. Briefly, the primary antibody YPF19 (Yersinia pestis F1 antigen antibody, mouse monoclonal, GTX28275) from GeneTex (Irvine, CA, USA) was prepared in PBS (1/200) to conjugate the Caf1 presented on hydrogels. The functionalized, freeze-dried hydrogels were incubated overnight at 4 °C. After thorough washing in PBS, the samples were incubated with a secondary antibody (Alexa Fluo 647, goat anti-mouse, 1/1000) for 45 min at 37 °C. Finally, the samples were washed in PBS several times for at least 30 min. Then, the samples were observed using CLSM.

5. Conclusions

In this study, 3D porous polysaccharide-based hydrogels made of pullulan and dextran that do not promote cell adhesion, were functionalized with animal-free ECM-like molecules via electrostatic interactions promoted by the incorporation of cationized dextran (DEAE–dextran). Although the cationization resulted in slightly opaque samples, we were still able to visualize cell morphology and evaluate in vitro cellular behaviors using 3D microscopy. Our work has demonstrated that electrostatic bonding between the charged hydrogels and Caf1 molecules was stable enough to induce adequate cell adhesion and proliferation. The spatial cues on these scaffolds were controlled through a combination of hydrogel coating and a freeze-drying step. On one hand, ECs adhered and showed sprouting according to how they exposed the cell-adhesive Caf1-YIGSR. On the other hand, the VEGF-like molecule (Caf1-VEGF) functioned as a migratory factor in the presence of the adhesive moiety (Caf1-YIGSR). When ECs were exposed to both Caf1-YIGSR and Caf1-VEGF, they exhibited angiogenic behavior. These results strongly suggest that our functionalized polysaccharide-based hydrogels can provoke different EC behaviors thanks to spatially controlled presentation of these ECM-like, animal-free, pro-angiogenic molecules. Moreover, we also demonstrated that scaffold functionalization via electrostatic interactions was sufficient to promote cell adhesion and cell proliferation for a week, which allowed ECs to further differentiate into their angiogenic phenotypes when exposed properly to the different Caf1 moieties.

The novel approach described here represents an advance in the study of the effect different peptide sequences of the ECM have on ECs behavior. This work represents a proof of concept and opens the door to future studies to determine the effect of other spatial combinations using different Caf1 motifs in different cell types. The pro-angiogenic materials prepared here could be implanted in vivo for regenerative medicine applications. Furthermore, previously in the team, we have demonstrated the formation of soft tissue constructs (e.g., liver spheroids) using the non-functionalized polysaccharide hydrogels [27,45] (Le Guilcher et al., 2022 under revision). These 3D hepatic constructs showed long-term liver functions, including biliary functions, holding promise to be used as 3D models of the liver for theragnostic purposes. The developed polysaccharide hydrogels could be further optimized and integrated with the aforementioned hepatic constructs to build better organ-specific in vitro models. In the near future, we hope to contribute to the translation of vascularized constructs towards clinical applications and drug development.

Supplementary Materials: The following supporting information can be downloaded at: https://www.mdpi.com/article/10.3390/ijms232314604/s1, Figure S1: Scheme of syringe coating method which allows to selectively coat only the channel within the hydrogels before pore formation; Figure S2: Cell culture protocol of 5 mm long hydrogel channels. At day 0, endothelial cells (5.0×10^3 cells/µL) were seeded in the channels. Complete endothelial cell culture medium was changed 3 times at day 2, 4 and 6. Hydrogels were turned 180° at day 2 and 4; Figure S3: Shear storage modulus of non-coated hydrogels (NC) and coated hydrogels with different spatial-controlled coating (SgC and CoC); Figure S4: Young's modulus of hydrogels using nanoindentation mapping; Figure S5: Presence of Caf1-YIGSR on SFD coated hydrogel without cells. Scale bar = 100 µm.

Author Contributions: Conceptualization, C.L.B. and T.S.-Y.; methodology, C.L.B., A.D., F.C. and T.S.-Y.; validation, T.S.-Y., F.C., H.W., D.P. and J.L.; formal analysis, C.L.B.; investigation, C.L.B.; resources, H.W., D.P. and J.L.; data curation, C.L.B.; writing—original draft preparation, C.L.B.; writing—review and editing, C.L.B., T.S.-Y., J.L. and D.P.; visualization, C.L.B.; supervision, T.S.-Y. and F.C.; project administration, T.S.-Y. and F.C.; funding acquisition, T.S.-Y. All authors have read and agreed to the published version of the manuscript.

Funding: This research was funded by "Recherche Hospitalo-universitaire" Innovations for Liver Tissue Engineering (RHU iLite, grant number ANR-16-RHUS-0005), DILI-on-chip (grant number ANR-21-CE19-0025), EXCALYBUR (grant number ANR-20-CE18-0001), and Université Paris Cité (IDEX UP AAP EMERGENCE SIMON).

Acknowledgments: This work was supported by INSERM, Université Paris Cité, and Université Sorbonne Paris Nord. The authors would like to thank Helen Waller, Daniel Peters, and Jeremy Lakey from Newcastle University for their scientific expertise and for providing us with the recombinant peptides used in this study. The authors also greatly acknowledge Samira Benadda of the CRI U1149 Imaging Facility. Figures and illustrations were created with BioRender.

Conflicts of Interest: The co-authors declare conflict of interest. Jeremy Lakey and Daniel Peters are directors at MarraBio Limited, an active company incorporated on 10 August 2022 with the registered office located in Newcastle upon Tyne, Northumberland. The funders had no role in the design of the study; in the collection, analyses, or interpretation of data; in the writing of the manuscript; or in the decision to publish the results.

References

1. Williams, D.F. Challenges with the Development of Biomaterials for Sustainable Tissue Engineering. *Front. Bioeng. Biotechnol.* **2019**, *7*, 127. [CrossRef] [PubMed]
2. Dellaquila, A.; Le Bao, C.; Letourneur, D.; Simon-Yarza, T. In Vitro Strategies to Vascularize 3D Physiologically Relevant Models. *Adv. Sci.* **2021**, *8*, 2100798. [CrossRef] [PubMed]
3. Mastrullo, V.; Cathery, W.; Velliou, E.; Madeddu, P.; Campagnolo, P. Angiogenesis in Tissue Engineering: As Nature Intended? *Front. Bioeng. Biotechnol.* **2020**, *8*, 188. [CrossRef] [PubMed]
4. Gerhardt, H.; Golding, M.; Fruttiger, M.; Ruhrberg, C.; Lundkvist, A.; Abramsson, A.; Jeltsch, M.; Mitchell, C.; Alitalo, K.; Shima, D.; et al. VEGF guides angiogenic sprouting utilizing endothelial tip cell filopodia. *J. Cell Biol.* **2003**, *161*, 1163–1177. [CrossRef]
5. Michaelis, U.R. Mechanisms of endothelial cell migration. *Cell. Mol. Life Sci.* **2014**, *71*, 4131–4148. [CrossRef]
6. Cathery, W.; Faulkner, A.; Maselli, D.; Madeddu, P. Concise Review: The Regenerative Journey of Pericytes Toward Clinical Translation. *Stem Cells* **2018**, *36*, 1295–1310. [CrossRef]
7. Yue, B. Biology of the Extracellular Matrix: An Overview Beatri. *J. Glaucoma* **2014**, *23*, S20–S23. [CrossRef]
8. Yin, N.; Han, Y.; Xu, H.; Gao, Y.; Yi, T.; Yao, J.; Dong, L.; Cheng, D.; Chen, Z. VEGF-conjugated alginate hydrogel prompt angiogenesis and improve pancreatic islet engraftment and function in type 1 diabetes. *Mater. Sci. Eng. C* **2016**, *59*, 958–964. [CrossRef]
9. Linville, R.M.; Boland, N.F.; Covarrubias, G.; Price, G.M.; Tien, J. Physical and Chemical Signals That Promote Vascularization of Capillary-Scale Channels. *Cell Mol. Bioeng.* **2016**, *9*, 73–84. [CrossRef]
10. Tseng, T.C.; Hsieh, F.Y.; Theato, P.; Wei, Y.; Hsu, S.H. Glucose-sensitive self-healing hydrogel as sacrificial materials to fabricate vascularized constructs. *Biomaterials* **2017**, *133*, 20–28. [CrossRef]
11. Pan, B.; Shao, L.; Jiang, J.; Zou, S.; Kong, H.; Hou, R.; Yao, Y.; Du, J.; Jin, Y. 3D printing sacrificial templates for manufacturing hydrogel constructs with channel networks. *Mater. Des.* **2022**, *222*, 111012. [CrossRef]
12. Mohanty, S.; Larsen, L.B.; Trifol, J.; Szabo, P.; Burri, H.V.R.; Canali, C.; Dufva, M.; Emnéus, J.; Wolff, A. Fabrication of scalable and structured tissue engineering scaffolds using water dissolvable sacrificial 3D printed moulds. *Mater. Sci. Eng. C* **2015**, *55*, 569–578. [CrossRef] [PubMed]
13. Pimentel, C.R.; Ko, S.K.; Caviglia, C.; Wolff, A.; Emnéus, J.; Keller, S.S.; Dufva, M. Three-dimensional fabrication of thick and densely populated soft constructs with complex and actively perfused channel network. *Acta Biomater.* **2018**, *65*, 174–184. [CrossRef]
14. Rocha, L.A.; Sousa, R.A.; Learmonth, D.A.; Salgado, A.J. The role of biomaterials as angiogenic modulators of spinal cord injury: Mimetics of the spinal cord, cell and angiogenic factor delivery agents. *Front. Pharmacol.* **2018**, *9*, 164. [CrossRef]
15. Belair, D.G.; Miller, M.J.; Wang, S.; Darjatmoko, S.R.; Binder, B.Y.; Sheibani, N.; Murphy, W.L. Differential regulation of angiogenesis using degradable VEGF binding microspheres. *Biomaterials* **2016**, *93*, 27–37. [CrossRef]
16. Chiu, L.L.Y.; Radisic, M. Scaffolds with covalently immobilized VEGF and Angiopoietin-1 for vascularization of engineered tissues. *Biomaterials* **2010**, *31*, 226–241. [CrossRef] [PubMed]
17. Kuttappan, S.; Mathew, D.; Jo, J.; Tanaka, R.; Menon, D.; Ishimoto, T.; Nakano, T.; Nair, S.V.; Nair, M.B.; Tabata, Y. Dual release of growth factor from nanocomposite fibrous scaffold promotes vascularisation and bone regeneration in rat critical sized calvarial defect. *Acta Biomater.* **2018**, *78*, 36–47. [CrossRef]
18. Fittkau, M.H.; Zilla, P.; Bezuidenhout, D.; Lutolf, M.P.; Human, P.; Hubbell, J.A.; Davies, N. The selective modulation of endothelial cell mobility on RGD peptide containing surfaces by YIGSR peptides. *Biomaterials* **2005**, *26*, 167–174. [CrossRef]
19. Alsop, A.T.; Pence, J.C.; Weisgerber, D.W.; Harley, B.A.C.; Bailey, R.C. Photopatterning of vascular endothelial growth factor within collagen-glycosaminoglycan scaffolds can induce a spatially confined response in human umbilical vein endothelial cells. *Acta Biomater.* **2014**, *10*, 4715–4722. [CrossRef]
20. Rich, M.H.; Lee, M.K.; Baek, K.; Jeong, J.H.; Kim, D.H.; Millet, L.J.; Bashir, R.; Kong, H. Material-mediated proangiogenic factor release pattern modulates quality of regenerated blood vessels. *J. Control. Release* **2014**, *196*, 363–369. [CrossRef]
21. Chiu, Y.C.; Cheng, M.H.; Engel, H.; Kao, S.W.; Larson, J.C.; Gupta, S.; Brey, E.M. The role of pore size on vascularization and tissue remodeling in PEG hydrogels. *Biomaterials* **2011**, *32*, 6045–6051. [CrossRef] [PubMed]

22. Wang, Y.; Kankala, R.K.; Ou, C.; Chen, A.; Yang, Z. Advances in hydrogel-based vascularized tissues for tissue repair and drug screening. *Bioact. Mater.* **2022**, *9*, 198–220. [CrossRef]
23. Kang, Y.; Chang, J. Channels in a porous scaffold: A new player for vascularization. *Regen. Med.* **2018**, *13*, 705–715. [CrossRef] [PubMed]
24. Wang, X.; Nie, Z.; Chang, J.; Lu, M.L.; Kang, Y. Multiple channels with interconnected pores in a bioceramic scaffold promote bone tissue formation. *Sci. Rep.* **2021**, *11*, 20447. [CrossRef]
25. Lanouar, S.; Aid-Launais, R.; Oliveira, A.; Bidault, L.; Closs, B.; Labour, M.N.; Letourneur, D. Effect of cross-linking on the physicochemical and in vitro properties of pullulan/dextran microbeads. *J. Mater. Sci. Mater. Med.* **2018**, *29*, 77. [CrossRef]
26. Grenier, J.; Duval, H.; Barou, F.; Lv, P.; David, B.; Letourneur, D. Acta Biomaterialia Mechanisms of pore formation in hydrogel scaffolds textured by freeze-drying. *Acta Biomater.* **2019**, *94*, 195–203. [CrossRef] [PubMed]
27. Labour, M.N.; Le Guilcher, C.; Aid-Launais, R.; Samad, N.E.; Lanouar, S.; Simon-Yarza, T.; Letourneur, D. Development of 3D hepatic constructs within polysaccharide-based scaffolds with tunable properties. *Int. J. Mol. Sci.* **2020**, *21*, 3644. [CrossRef]
28. Simon-Yarza, T.; Labour, M.N.; Aid, R.; Letourneur, D. Channeled polysaccharide-based hydrogel reveals influence of curvature to guide endothelial cell arrangement in vessel-like structures. *Mater. Sci. Eng. C* **2021**, *118*, 111369. [CrossRef] [PubMed]
29. Autissier, A.; Le Visage, C.; Pouzet, C.; Chaubet, F.; Letourneur, D. Fabrication of porous polysaccharide-based scaffolds using a combined freeze-drying/cross-linking process. *Acta Biomater.* **2010**, *6*, 3640–3648. [CrossRef]
30. Le Visage, C.; Letourneur, D.; Chaubet, F.; Autissier, A. Method for Preparing Porous Scaffold for Tissue Engineering. U.S. Patent US9028857B2, 12 May 2015.
31. Autissier, A.; Letourneur, D.; Le Visage, C. Pullulan-based hydrogel for smooth muscle cell culture. *J. Biomed. Mater. Res. Part A* **2007**, *82*, 336–342. [CrossRef]
32. Lanouar, S. *Conception and Validation of New Tridimensional Porous Matrices for Cutaneous Wound Healing and Regeneration*; Université Sorbonne Paris Nord: Paris, France, 2020.
33. Roque, A.I.; Soliakov, A.; Birch, M.A.; Philips, S.R.; Shah, D.S.H.; Lakey, J.H. Reversible non-stick behaviour of a bacterial protein polymer provides a tuneable molecular mimic for cell and tissue engineering. *Adv. Mater.* **2014**, *26*, 2704–2709. [CrossRef] [PubMed]
34. Dura, G.; Crespo-Cuadrado, M.; Waller, H.; Peters, D.T.; Ferreira, A.M.; Lakey, J.H.; Fulton, D.A. Hydrogels of engineered bacterial fimbriae can finely tune 2D human cell culture. *Biomater. Sci.* **2021**, *9*, 2542–2552. [CrossRef] [PubMed]
35. Peters, D.T.; Waller, H.; Birch, M.A.; Lakey, J.H. Engineered mosaic protein polymers; A simple route to multifunctional biomaterials. *J. Biol. Eng.* **2019**, *13*, 54. [CrossRef] [PubMed]
36. Lack, S.; Dulong, V.; Picton, L.; Cerf, D.L.; Condamine, E. High-resolution nuclear magnetic resonance spectroscopy studies of polysaccharides crosslinked by sodium trimetaphosphate: A proposal for the reaction mechanism. *Carbohydr. Res.* **2007**, *342*, 943–953. [CrossRef]
37. Pietrzyk-Nivau, A.; Poirault-Chassac, S.; Gandrille, S.; Derkaoui, S.M.; Kauskot, A.; Letourneur, D.; Le Visage, C.; Baruch, D.; Eaves, C.J. Three-dimensional environment sustains hematopoietic stem cell differentiation into platelet-producing megakaryocytes. *PLoS ONE* **2015**, *10*, 1–19. [CrossRef]
38. Purnama, A.; Aid-Launais, R.; Haddad, O.; Maire, M.; Mantovani, D.; Letourneur, D.; Hlawaty, H.; Le Visage, C. Fucoidan in a 3D scaffold interacts with vascular endothelial growth factor and promotes neovascularization in mice. *Drug Deliv. Transl. Res.* **2015**, *5*, 187–197. [CrossRef]
39. Jeon, O.; Alsberg, E. Photofunctionalization of alginate hydrogels to promote adhesion and proliferation of human mesenchymal stem cells. *Tissue Eng. Part A* **2013**, *19*, 1424–1432. [CrossRef]
40. Akhmanova, M.; Osidak, E.; Domogatsky, S.; Rodin, S.; Domogatskaya, A. Physical, Spatial, and Molecular Aspects of Extracellular Matrix of in Vivo Niches and Artificial Scaffolds Relevant to Stem Cells Research. *Stem Cells Int.* **2015**, *2015*, 167025. [CrossRef]
41. González-pérez, F.; Alonso, M.; Torre, I.G.D.; Santos, M.; Rodríguez-cabello, J.C. Laminin-Derived Peptide Sequences within Elastin-Like Recombinamer Scaffolds Provide Spatiotemporally Synchronized Guidance of Angiogenesis and Neurogenesis. *Adv. Healthc. Mater.* **2022**, *11*, 2201646. [CrossRef]
42. Ali, S.; Saik, J.E.; Gould, D.J.; Dickinson, M.E.; West, J.L. Immobilization of Cell-Adhesive Laminin Peptides in Degradable PEGDA Hydrogels Influences Endothelial Cell Tubulogenesis. *BioRes. Open Access* **2013**, *2*, 241–249. [CrossRef]
43. Grant, D.S.; Tashiro, K.I.; Segui-Real, B.; Yamada, Y.; Martin, G.R.; Kleinman, H.K. Two different laminin domains mediate the differentiation of human endothelial cells into capillary-like structures in vitro. *Cell* **1989**, *58*, 933–943. [CrossRef] [PubMed]
44. Campodoni, E.; Montanari, M.; Dozio, S.M.; Heggset, E.B.; Panseri, S.; Montesi, M.; Tampieri, A.; Syverud, K.; Sandri, M. Blending Gelatin and Cellulose Nanofibrils: Biocomposites with Tunable Degradability and Mechanical Behavior. *Nanomaterials* **2020**, *10*, 1219. [CrossRef] [PubMed]
45. Le Guilcher, C.; Franck, G.; Dellaquila, A.; Labour, M.-N.; Aid, R.; Tordjmann, T.; Letourneur, D.; Simon-Yarza, T. Engineered Human Liver Based on Pullulan-Dextran Hydrogel Promotes Mice Survival after Liver Failure. 2022.